



**US Army Corps
of Engineers®**
Engineer Research and
Development Center

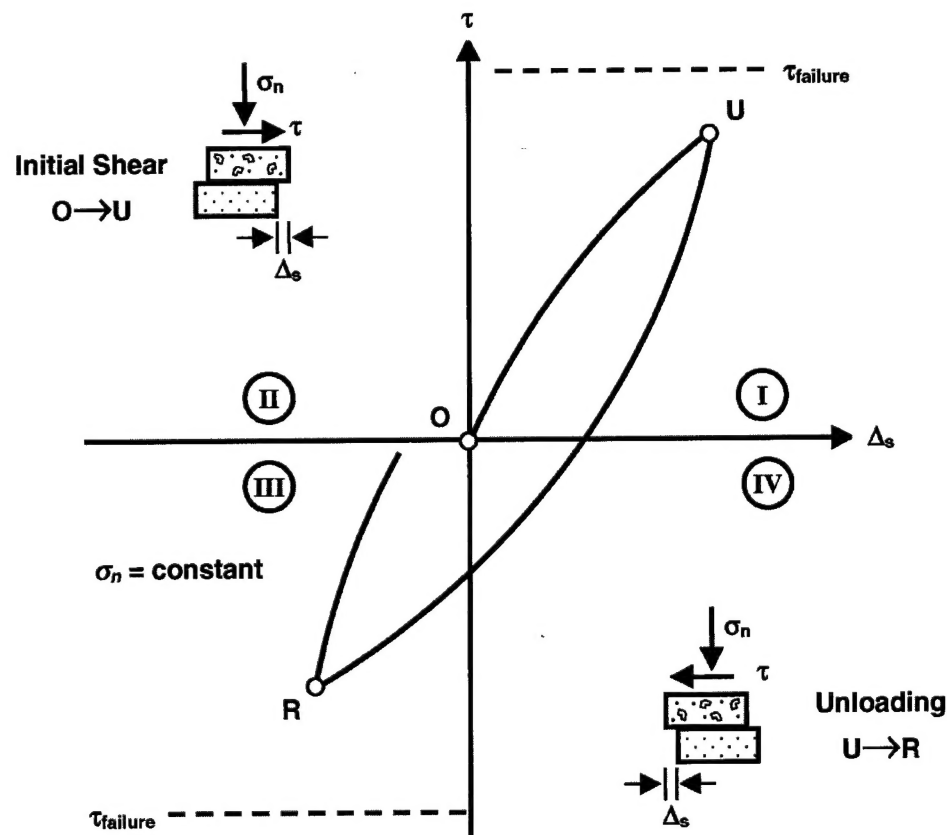
Computer-Aided Structural Engineering Project

Development of an Improved Numerical Model for Concrete-to-Soil Interfaces in Soil-Structure Interaction Analyses

**Report 2
Final Study**

Jesús E. Gómez, George M. Filz, and Robert M. Ebeling

August 2000



The contents of this report are not to be used for advertising, publication, or promotional purposes. Citation of trade names does not constitute an official endorsement or approval of the use of such commercial products.

The findings of this report are not to be construed as an official Department of the Army position, unless so designated by other authorized documents.



PRINTED ON RECYCLED PAPER

Development of an Improved Numerical Model for Concrete-to-Soil Interfaces in Soil-Structure Interaction Analyses

Report 2 Final Study

by **Jesús E. Gómez, George M. Filz**
Virginia Polytechnic Institute and State University
Blacksburg, VA 24061-0105

Robert M. Ebeling
Information Technology Laboratory
U.S. Army Engineer Research and Development Center
3909 Halls Ferry Road
Vicksburg, MS 39180-6199

Report 2 of a series

Approved for public release; distribution is unlimited

Prepared for **U.S. Army Corps of Engineers**
Washington, DC 20314-1000

Under **Work Unit 31589**

20001218 108

Engineer Research and Development Center Cataloging-in-Publication Data

Gomez, Jesus E.

Development of an improved numerical model for concrete-to-soil interfaces in soil-structure interaction analyses. Report 2, Final study / by Jesus E. Gomez, George M. Filz, Robert M. Ebeling ; prepared for U.S. Army Corps of Engineers.

401 p. : ill. ; 28 cm. -- (Technical report ITL ; TR-99-1 rept.2)

Includes bibliographic references.

1. Soil-structure interaction -- Mathematical models. 2. Soil dynamics -- Mathematical models. 3. Locks (Hydraulic engineering) -- Mathematical models. I. Filz, George Michael, 1953- II. Ebeling, Robert M., 1954- III. United States. Army. Corps of Engineers. IV. Engineer Research and Development Center (U.S.) V. Information Technology Laboratory (U.S.) VI. Computer-aided Structural Engineering Project. VII. Series: Technical report ITL ; 99-1 rept.2.
TA7 W34 no.ITL-99-1 rept.2

Contents

Preface	xx
1—Introduction.....	1
1.1 Background	1
1.2 Interface Behavior in SSI Analyses	2
1.2.1 The North Lock Wall at McAlpine Locks	3
1.2.2 Limitations of existing interface models	7
1.3 Project Scope.....	11
1.3.1 Interface testing.....	11
1.3.2 Extended hyperbolic model for interfaces	11
1.3.3 Implementation of the model in SOILSTRUCT-ALPHA.....	14
1.3.4 Lock wall simulation.....	14
1.4 Report Organization	14
2—Literature Review.....	16
2.1 Interface Testing.....	16
2.1.1 Direct Shear Box (DSB) devices	16
2.1.2 Direct Simple Shear (DSS) devices	17
2.1.3 Other devices	19
2.1.4 Summary of previous findings on interface testing and interface behavior	21
2.1.5 The Large Direct Shear Box (LDSB)	22
2.2 Interface Modeling	22
2.2.1 Interface elements	23
2.2.2 Interface constitutive models	25
2.2.3 The hyperbolic model	26
2.3 SSI Analyses of Retaining Walls.....	30
2.3.1 Review of previous work	30
2.3.2 Simplified procedure for calculating the downdrag force	32
2.4 Summary	39
3—Laboratory Testing	43
3.1 Soil Properties	43
3.1.1 Triaxial testing.....	44
3.1.2 Consolidation testing	47

3.1.3	Hyperbolic parameters	47
3.2	Concrete Specimen	48
3.2.1	Materials	48
3.2.2	Preparation of the specimen	51
3.2.3	Surface texture	51
3.3	Interface Testing Procedures	57
3.3.1	The soil box	57
3.3.2	Preparation of the interface	57
3.3.3	The Large Direct Shear Box (LDSB)	59
3.3.4	Test setup	60
3.3.5	Data reduction	61
3.4	Interface Testing Program	61
3.4.1	Testing parameters	61
3.4.2	Types of interface tests	62
3.5	Results of Interface Tests	65
3.5.1	Interface response to initial loading	65
3.5.2	Interface response to staged shear	66
3.5.3	Interface response to unloading-reloading	67
3.5.4	Interface response to multidirectional stress paths	68
3.6	Summary	69
4—	Extended Hyperbolic Model	71
4.1	Experimental Observations of Interface Response	72
4.1.1	Normalization of interface test data	72
4.1.2	Development of yield surfaces during interface shear	74
4.1.3	Loading regions	83
4.1.4	Interface response at yield	87
4.1.5	Interface response during unloading-reloading	91
4.1.6	Interface response during transition loading	91
4.2	Formulation of the Extended Hyperbolic Model for Yield-Inducing Shear	94
4.2.1	Hypothesis of interface response at yield	95
4.2.2	Mathematical formulation	98
4.2.3	Formulation of the extended hyperbolic model for interfaces at yield	102
4.2.4	Behavior of the model	103
4.3	Formulation of the Extended Hyperbolic Model for Unloading- Reloading	107
4.3.1	Version I	108
4.3.2	Version II	109
4.3.3	Version III	113
4.4	Determination of the Model Parameter Values	116
4.4.1	Determination of parameter values for interfaces at yield	116
4.4.2	Determination of interface parameter values for unloading- reloading	124
4.5	Evaluation of the Extended Hyperbolic Model	131
4.5.1	Accuracy of the model for yield-inducing shear	132
4.5.2	Accuracy of the model for unloading-reloading	137

4.5.3 Accuracy of the model for staged shear	142
4.5.4 Accuracy of the model for shearing along complex stress paths	143
4.6 Implementation of the Extended Hyperbolic Model	157
4.6.1 Incremental analyses	157
4.6.2 Identification of type of loading	158
4.6.3 Implementation of the formulation for yield-inducing shear	158
4.6.4 Implementation of Version I	161
4.6.5 Implementation of Version II	161
4.6.6 Implementation of Version III	163
4.6.7 Implementation of the extended hyperbolic model in SOILSTRUCT-ALPHA	163
4.7 Summary and Conclusions	166
5—Lock Wall Simulation	169
5.1 The IRW Facility	170
5.1.1 Components of the IRW	170
5.1.2 Preparations for the test	172
5.2 Testing Procedures	175
5.2.1 Stage 1, Backfilling	176
5.2.2 Stage 2, Surcharge	177
5.2.3 Stage 3, Inundation	177
5.3 Test Results	178
5.3.1 Results from stage 1	178
5.3.2 Results from stage 2	180
5.3.3 Results from stage 3	181
5.4 Discussion of Test Results	182
5.4.1 Response of the wall-backfill system to backfilling	182
5.4.2 Response of the wall-backfill system to surcharge	184
5.4.3 Response of the wall-backfill system to inundation	185
5.4.4 Special considerations for finite element analyses of the IRW	185
5.5 Finite Element Analysis Procedures	187
5.5.1 Summary of features of SOILSTRUCT-ALPHA	188
5.5.2 Finite element mesh	192
5.5.3 Tentative soil properties	192
5.5.4 Near-field interface properties	197
5.6 Calibration Analyses	198
5.6.1 Analysis of backfilling	198
5.6.2 Analysis of surcharge application and removal	199
5.7 Analysis of Backfill Inundation	201
5.8 Summary and Conclusions	204
6—Summary and Conclusions	206
6.1 Summary of Activities	207
6.1.1 Literature review	207
6.1.2 Laboratory testing	208

6.1.3 Extended hyperbolic model	209
6.1.4 Lock wall simulation.....	212
6.2 Recommendations for Future Work.....	214
References.....	216
Appendix A: Results of Triaxial and Consolidation Tests.....	A1
A.1 Triaxial Tests.....	A1
A.2 Consolidation Testing.....	A2
Appendix B: Determination of Hyperbolic Parameter Values of Soils.....	B1
B.1 Transformed Plots.....	B1
B.2 Hyperbolic Parameter Values.....	B2
B.2.1 Determination of K and n	B2
B.2.2 Determination of R_f	B3
B.2.3 Determination of K_b and m	B3
B.3 Comparison of Model to Test Data.....	B5
B.4 Example Calculations of Hyperbolic Parameter Values.....	B6
Appendix C: Results of Interface Tests.....	C1
Appendix D: Determination of Interface Hyperbolic Parameter Values.....	D1
D.1 Transformed Plots.....	D1
D.2 Hyperbolic Parameter Values	D2
D.2.1 Determination of K_i and n_f	D2
D.2.2 Determination of R_{ff}	D3
D.3 Comparison of Model to Test Data.....	D3
D.4 Example Calculations of Hyperbolic Parameter Values	D4
Appendix E: Example Calculations of Interface Response in the Extended Hyperbolic Model.....	E1
E.1 Interface Stiffness at Point 1	E5
E.2 Interface Stiffness at Point 2	E7
E.2.1 Version I.....	E7
E.2.2 Version II	E7
E.2.3 Version III	E8
E.3 Interface Stiffness at Point T.....	E9
E.3.1 Version I.....	E9
E.3.2 Version II	E9
E.3.3 Version III.....	E10
E.4 Interface Stiffness at Point 3	E11
E.4.1 Version I.....	E11
E.4.2 Version II	E11
E.4.3 Version III.....	E12
E.5 Interface Stiffness at Point 4	E14

E.5.1 Version I.....	E14
E.5.2 Version II	E14
E.5.3 Version III	E14
E.6 Interface Stiffness at Point 5	E15
E.7 Interface Stiffness at Point 6	E15
Appendix F: Notation	F1

SF 298

List of Figures

Figure 1-1.	Typical section, north wall of new RCC McAlpine Lock (adapted from Ebeling and Wahl 1997).....	4
Figure 1-2.	Simplified illustration of the mechanism of downdrag and shear reversal in a typical lock wall	6
Figure 1-3	Types of loading expected on the interface between a lock wall and the backfill	8
Figure 1-4.	Two models for interface shear stress-displacement response under unloading (adapted from Ebeling and Wahl 1997)	9
Figure 1-5.	Laboratory stress paths to study the response of a wall- backfill interface	12
Figure 2-1.	Distortion of the sand mass during interface tests in the DSB and DSS devices	19
Figure 2-2.	Goodman, Taylor, and Brekke (1968) zero thickness interface element and corresponding element stiffness matrix	24
Figure 2-3.	Application of the Clough and Duncan (1971) interface hyperbolic model to a typical set of test data	27
Figure 2-4.	Vertical and effective horizontal earth pressure forces on vertical plane extending from through the backfill from the heel of the monolith (adapted from ETL 1110-2-352 (HQUSACE 1994))	34
Figure 2-5.	Rock-founded retaining wall definition sketches (adapted from Filz, Duncan, and Ebeling 1997)	35

Figure 2-6.	Values of $K_{v,soil,ref}$ recommended for design (adapted from Filz, Duncan, and Ebeling 1997).....	38
Figure 2-7.	Values of $K_{v,q,ref}$ recommended for design (adapted from Filz, Duncan, and Ebeling 1997).....	39
Figure 2-8.	Values of the correction factors C_θ , C_N , and C_S (adapted from Filz, Duncan, and Ebeling 1997)	40
Figure 2-9.	Values of the correction factor C_{wt} recommended for design (adapted from EM 1110-2-2100 (HQUSACE, in preparation))	41
Figure 3-1.	Microscopic view of the sands used for interface testing.....	45
Figure 3-2.	Grain size distribution of the soils used for interface testing	46
Figure 3-3.	Hyperbolic parameter values for Density sand and Light Castle sand and comparison to values reported by Duncan et al. (1980) for similar soils.....	49
Figure 3-4.	Preparation of the concrete specimen	50
Figure 3-5.	Grain size distribution of aggregates used for the preparation of the concrete specimen.....	52
Figure 3-6.	Surface texture of representative retaining walls	54
Figure 3-7.	Preparation of sand-to-concrete interface and setup for testing	58
Figure 3-8.	View of the LDSB ready for soil-to-concrete interface testing	60
Figure 3-9.	Types of laboratory interface shear tests performed	64
Figure 4-1.	Degradation of the tangent shear stiffness during initial loading of the dense-Density-sand-to-concrete interface	73
Figure 4-2.	Diagram of normalized interface shear stiffness for the dense-Density-sand-to-concrete interface	75
Figure 4-3.	Unload-reload Test T203_15 on the dense-Density-sand-to-concrete degradation.....	76
Figure 4-4.	Staged shear Test T105_40 on the dense-Density-sand-to-concrete interface.....	79

Figure 4-5.	Diagram of normalized interface shear stiffness for unload-reload Test T203_15.....	81
Figure 4-6.	Diagram of normalized interface shear stiffness for staged shear Test T105_40	82
Figure 4-7.	Evolution of yield surfaces during interface shear.....	84
Figure 4-8.	Loading regions for Versions I and II of the extended hyperbolic model.....	85
Figure 4-9.	Comparison between the normalized stiffness diagrams for Tests T203_15 and T105_40.....	86
Figure 4-10.	Loading regions for Version III of the extended hyperbolic model.....	88
Figure 4-11.	Multidirectional stress path test T205_5 on the dense-Density-sand-to-concrete interface	89
Figure 4-12.	Multidirectional stress path Test T206_5 on the dense-Density-sand-to-concrete interface	92
Figure 4-13.	Interface response to a set of hypothetical initial loading tests.....	96
Figure 4-14.	Type of interface response assumed in the extended hyperbolic formulation	97
Figure 4-15.	Determination of the interface stiffness along an inclined stress path	99
Figure 4-16.	Interface response at yield for inclined stress paths in the extended hyperbolic model.....	104
Figure 4-17.	Interface response assumed in Version I for unloading-reloading.....	108
Figure 4-18.	Interface response assumed in Version II for unloading-reloading.....	110
Figure 4-19.	Normalized interface response during transition loading assumed in Version III.....	114
Figure 4-20.	Adjustment of the value of stiffness number n_j of the dense-Density-sand-to-concrete interface using normalized data from initial loading tests.....	119

Figure 4-21.	Normalized hyperbolic diagrams for different values of the stiffness number K_I and failure ratio R_{ff}	121
Figure 4-22.	Adjustment of the value of stiffness number K_I for the dense-Density-sand-to-concrete interface	122
Figure 4-23.	Proposed approximation for the estimation of the stiffness number for unloading-reloading K_{ur}	126
Figure 4-24.	Proposed approximation for the estimation of the scaling factor α	128
Figure 4-25.	Comparison between the extended hyperbolic model and data from initial loading tests on the dense-Density-sand-to-concrete interface	133
Figure 4-26.	Comparison between the extended hyperbolic model and data from initial loading tests on the medium-dense-Density-sand-to-concrete interface	134
Figure 4-27.	Comparison between the extended hyperbolic model and data from initial loading tests on the dense-Light-Castle-sand-to-concrete interface.....	135
Figure 4-28.	Comparison between the extended hyperbolic model and data from multidirectional stress path Test T205_5 performed on the dense-Density-sand-to-concrete interface	136
Figure 4-29.	Application of the extended hyperbolic model for unload-reload stress paths contained in Quadrant I of the τ - σ_n plane	138
Figure 4-30.	Comparison between the extended hyperbolic model and data from Test T201_5 performed on the dense-Density-sand-to-concrete interface.....	139
Figure 4-31.	Comparison between the extended hyperbolic model and data from Test T202_5 performed on the dense-Density-sand-to-concrete interface.....	140
Figure 4-32.	Comparison between the extended hyperbolic model and data from Test T203_15 performed on the dense-Density-sand-to-concrete interface.....	141
Figure 4-33.	Application of the extended hyperbolic model for staged shear stress paths	143

Figure 4-34.	Comparison between the extended hyperbolic model and data from Test T105_40 performed on the dense-Density-sand-to-concrete interface	144
Figure 4-35.	Comparison between the extended hyperbolic model and data from Test T106_15 performed on the dense-Density-sand-to-concrete interface	146
Figure 4-36.	Comparison between the extended hyperbolic model and data from multidirectional stress path Test T204_50 performed on the dense-Density-sand-to-concrete interface	148
Figure 4-37.	Comparison between the extended hyperbolic model and data from multidirectional stress path Test T206_50 performed on the dense-Density-sand-to-concrete interface	150
Figure 4-38.	Comparison between the extended hyperbolic model and data from multidirectional stress path Test T305_10 on the medium-dense-Density-sand-to-concrete interface	153
Figure 4-39.	Comparison between the extended hyperbolic model and data from multidirectional stress path Test T405_10 on the dense-Light-Castle-sand-to-concrete interface.....	155
Figure 4-40.	Procedure for the determination of the type of loading applied to an interface element during the i^{th} load step.....	159
Figure 4-41.	Flowchart for the determination of the tangent shear stiffness of an interface element at yield during the i^{th} load step	160
Figure 4-42.	Flowchart for the determination of the tangent shear stiffness of an interface element during the i^{th} load step, using Version I of the extended hyperbolic model	161
Figure 4-43.	Flowchart for the determination of the tangent shear stiffness of an interface element during the i^{th} load step, using Version II of the extended hyperbolic model.....	162
Figure 4-44.	Flowchart for the determination of the tangent shear stiffness of an interface element during the i^{th} load step, using Version III of the extended hyperbolic model	164
Figure 5-1.	The IRW test facility (after Sehn 1990).....	171
Figure 5-2.	Cross-section of the IRW	171
Figure 5-3.	IRW panels (after Sehn 1990)	173

Figure 5-4.	Stages of the lock wall simulation performed in the IRW test facility	175
Figure 5-5.	View of the IRW at different stages of the lock wall simulation	176
Figure 5-6.	Evolution of the lateral earth pressure coefficient K_h during backfilling in the IRW	183
Figure 5-7.	Lateral pressure distribution at the end of backfilling.....	183
Figure 5-8.	Evolution of the vertical shear force coefficient K_v during backfilling in the IRW	184
Figure 5-9.	Vertical shear force coefficient for surcharge $K_{v,q}$ in the IRW	186
Figure 5-10.	Values of the correction factor C_{wt} during inundation of the backfill in the IRW	187
Figure 5-11.	Finite element mesh used for the analyses.....	193
Figure 5-12.	Adjustment of stress-dependent backfill property for finite element analyses of the IRW	195
Figure 5-13.	Results of calibration analyses of backfilling and comparison of IRW test data	200
Figure 5-14.	Results of calibration analyses of surcharge and comparison to IRW test data.....	202
Figure 5-15.	Results of finite element analyses of inundation and comparison to IRW test data	203
Figure A1.	Results of CD triaxial tests on medium-dense Density sand.....	A4
Figure A2.	Results of CD triaxial tests on dense Density sand.....	A7
Figure A3.	Results of CD triaxial tests on medium-dense Light Castle sand	A10
Figure A4.	Results of CD triaxial tests on dense Light Castle sand.....	A13
Figure A5.	Results of consolidation tests on medium-dense Density sand	A16
Figure A6.	Results of consolidation tests on dense Density sand	A17

Figure A7.	Results of consolidation tests on medium-dense Light Castle sand.....	A18
Figure A8.	Results of consolidation tests on dense Light Castle sand	A19
Figure A9.	Relationship between hydrocompression strain and relative density for Light Castle sand	A20
Figure B1.	Transformed stress-strain plots from triaxial test data on medium-dense Density sand and determination of hyperbolic parameter values	B9
Figure B2.	Determination of hyperbolic parameters K and n for medium-dense Density sand	B10
Figure B3.	Determination of hyperbolic parameters K_b and m for medium-dense Density sand	B11
Figure B4.	Hyperbolic model for medium-dense Density sand and comparison to CD triaxial test data.....	B12
Figure B5.	Transformed stress-strain plots from triaxial test data on dense Density sand and determination of hyperbolic parameter values	B14
Figure B6.	Determination of hyperbolic parameters K and n for dense Dense sand.....	B15
Figure B7.	Determination of hyperbolic parameters K_b and m for dense Density sand	B16
Figure B8.	Hyperbolic model for dense Density sand and comparison to CD triaxial test data	B17
Figure B9.	Transformed stress-strain plots from triaxial test data on medium-dense Light Castle sand and determination of hyperbolic parameter values	B19
Figure B10.	Determination of hyperbolic parameters K and n for medium-dense Light Castle sand	B20
Figure B11.	Determination of hyperbolic parameters K_b and m for medium-dense Light Castle sand	B21
Figure B12.	Hyperbolic model for medium-dense Light Castle sand and comparison to CD triaxial test data.....	B22

Figure B13.	Transformed stress-strain plots from triaxial test data on dense Light Castle sand and determination of hyperbolic parameter values	B24
Figure B14.	Determination of hyperbolic parameters K and n for dense Light Castle sand	B25
Figure B15.	Determination of hyperbolic parameters K_b and m for dense Light Castle sand	B26
Figure B16.	Hyperbolic model for dense Light Castle sand and comparison to CD triaxial test data	B27
Figure B17.	Example determination of axial and volumetric strain values at 70 and 95 percent of strength. Data from CD triaxial tests on dense Light Castle sand	B29
Figure B18.	Determination of the normalized values of E_t and B for each of the CD triaxial tests performed on dense Light Castle sand (adapted from Duncan et al. 1980)	B30
Figure B19.	Determination of hyperbolic parameters K and n from the E_t/p_a values determined in column (15) of Figure B18	B31
Figure B20.	Determination of hyperbolic parameters K_b and m from the B/p_a values determined in column (16) of Figure B18	B32
Figure C1.	Results of initial loading tests on dense-Density-sand-to-concrete interface	C2
Figure C2.	Peak and residual shear strength envelopes for initial loading on dense-Density-sand-to-concrete interface	C6
Figure C3.	Results of initial loading tests on medium-dense-Density-sand-to-concrete interface	C7
Figure C4.	Peak and residual shear strength envelopes for initial loading on medium-dense-Density-sand-to-concrete interface	C11
Figure C5.	Results of initial loading tests on dense-Light-Castle-sand-to-concrete interface	C12
Figure C6.	Peak and residual shear strength envelopes for initial loading on dense-Light-Castle-sand-to-concrete interface	C16
Figure C7.	Staged shear test on dense-Density-sand-to-concrete interface, Specimen S105. Data on shear reversals are omitted	C17

Figure C8.	Staged test on dense-Density-sand-to-concrete interface, Specimen S106. Data on shear reversals are omitted.....	C19
Figure C9.	Staged tests on dense-Density-sand-to-concrete interface, Specimen S101	C21
Figure C10.	Staged tests on dense-Density-sand-to-concrete interface, Specimen S102.....	C25
Figure C11.	Staged tests on dense-Density-sand-to-concrete interface, Specimen S103	C28
Figure C12.	Unload-reload test on dense-Density-sand-to-concrete interface, $\sigma_n = 33$ kPa, Specimen S201	C30
Figure C13.	Unload-reload test on dense-Density-sand-to-concrete interface, $\sigma_n = 33$ kPa, Specimen S202	C32
Figure C14.	Unload-reload test on dense-Density-sand-to-concrete interface, $\sigma_n = 102$ kPa, Specimen S203	C34
Figure C15.	Cycle of shear reversals on dense-Density-sand-to-concrete interface, $\sigma_n = 15$ kPa, Specimen S101	C36
Figure C16.	Cycle of shear reversals on dense-Density-sand-to-concrete interface, $\sigma_n = 33$ kPa, Specimen S102	C37
Figure C17.	Cycle of shear reversals on dense-Density-sand-to-concrete interface, $\sigma_n = 102$ kPa, Specimen S103	C38
Figure C18.	Cycle of shear reversals on dense-Density-sand-to-concrete interface, $\sigma_n = 274$ kPa, Specimen S104	C39
Figure C19.	Shear reversal on medium-dense-Density-sand-to-concrete interface, $\sigma_n = 35$ kPa, Specimen S302	C40
Figure C20.	Cycle of shear reversals on medium-dense-Density-sand- to-concrete interface, $\sigma_n = 104$ kPa, Specimen S303.....	C41
Figure C21.	Cycle of shear reversals on medium-dense-Density-sand- to-concrete interface, $\sigma_n = 276$ kPa, Specimen S304.....	C42
Figure C22.	Cycle of shear reversals on dense-Light-Castle-sand-to- concrete interface, $\sigma_n = 15$ kPa, Specimen S401	C43
Figure C23.	Cycle of shear reversals on dense-Light-Castle-sand-to- concrete interface, $\sigma_n = 35$ kPa, Specimen S402	C44

Figure C24.	Cycle of shear reversals on dense-Light-Castle-sand-to-concrete interface, $\sigma_n = 104$ kPa, Specimen S403	C45
Figure C25.	Cycle of shear reversals on dense-Light-Castle-sand-to-concrete interface, $\sigma_n = 276$ kPa, Specimen S404	C46
Figure C26.	Multidirectional stress path Test T204_5 on dense-Density-sand-to-concrete interface	C47
Figure C27.	Multidirectional stress path Test T205_5 on dense-Density-sand-to-concrete interface	C49
Figure C28.	Multidirectional stress path Test T206_5 on dense-Density-sand-to-concrete interface	C51
Figure C29.	Multidirectional stress path Test T305_10 on medium-dense-Density-sand-to-concrete interface	C53
Figure C30.	Multidirectional stress path Test T405_10 on dense-Light-Castle-sand-to-concrete interface	C55
Figure D1.	Transformed plots for initial loading tests on dense-Density-sand-to-concrete interface	D6
Figure D2.	Determination of hyperbolic parameters K_l and n_j for dense-Density-sand-to-concrete interface	D7
Figure D3.	Comparison between the hyperbolic model and data from initial loading tests on dense-Density-sand-to-concrete interface	D8
Figure D4.	Transformed plots for initial loading tests on medium-dense-Density-sand-to-concrete interface	D9
Figure D5.	Determination of hyperbolic parameters K_l and n_j for medium-dense-Density-sand-to-concrete interface	D10
Figure D6.	Comparison between the hyperbolic model and data from initial loading tests on medium-dense-Density-sand-to-concrete interface	D11
Figure D7.	Transformed plots for initial loading tests on dense-Light-Castle-sand-to-concrete interface	D12
Figure D8.	Determination of hyperbolic parameters K_l and n_j for dense-Light-Castle-sand-to-concrete interface	D13

Figure D9.	Comparison between the hyperbolic model and data from initial loading tests on dense-Light-Castle-sand-to-concrete interface	D14
Figure D10.	Example determination of interface displacements at 70 and 95 percent of strength. Data from interface tests on dense Light Castle sand	D15
Figure D11.	Determination of the normalized values of K_{si} for each of the initial loading tests performed on the dense-Light-Castle-sand-to-concrete interface	D16
Figure D12.	Determination of hyperbolic parameters K_f and n_f from the K_{si}/γ_w values determined in column (12) of Figure D11	D17
Figure E1.	Multidirectional stress path Test T405_10 on dense-Light-Castle-sand-to-concrete interface	E2

List of Tables

Table 1-1	Summary of Results of SSI Analyses for the North Lock at McAlpine Locks (adapted from Ebeling and Wahl 1997)	5
Table 1-2.	Comparison of Results of SSI Analyses at Section A-A for Two Different Models of Interface Response to Unloading (adapted from Ebeling and Wahl 1997)	10
Table 2-1.	Previous Work on Direct Shear Testing of Sand-to-Concrete and Sand-to-Steel Interfaces	18
Table 2-2.	Previous Work on Direct Simple Shear Testing of Sand-to-Concrete and Sand-to-Steel Interfaces	20
Table 3-1.	Characteristics of the Soils Used for Interface Testing	44
Table 3-2.	Summary of Results of CD Triaxial Tests	45
Table 3-3.	Hyperbolic Parameter Values of Soils Used for Interface Testing	47
Table 3-4.	Mixing Proportions of Concrete	53
Table 3-5.	Physical Properties of the Concrete Mix	53
Table 3-6.	Types of Interfaces Tested	62
Table 3-7.	Summary of Interface Tests	63

Table 3-8.	Summary of Results of Initial Loading Interface Tests.....	65
Table 4-1.	Definition of Types of Loading in Interface Shear	88
Table 4-2.	Summary of the Extended Hyperbolic Model for Interfaces at Yield	103
Table 4-3.	Definition of Yield Zones in the First Quadrant and Limiting Values of the Correction Factor for Inclination of Stress Paths.....	105
Table 4-4.	Summary of Version I of the Upload-Reload Formulation in the Extended Hyperbolic Model for Interfaces.....	109
Table 4-5.	Summary of Version II of the Unload-Reload Formulation in the Extended Hyperbolic Model for Interface	113
Table 4-6.	Summary of Version III of the Extended Hyperbolic Model for Interfaces Subjected to Unloading-Reloading and Transition Loading	117
Table 4-7.	Summary of Material Properties Required in the Extended Hyperbolic Model for Interfaces.....	117
Table 4-8.	Summary of Hyperbolic Parameter Values for the Interfaces Tested.....	123
Table 4-9.	Summary of Hyperbolic Parameter Values for Interfaces between Concrete and Different Types of Soils.....	123
Table 4-10.	Comparison of the Hyperbolic Parameter Values of the Interfaces Tested to Hyperbolic Parameter Values of the Soils.....	124
Table 4-11.	Recommended Values of the Stiffness Ratio C_k	127
Table 4-12.	Recommended Values of the Scaling Factor α	130
Table 4-13.	Summary of Parameter Values for Unloading-Reloading for Interfaces Tested	131
Table 5-1.	Features of the Data Acquisition System for the Lock Wall Simulation	174
Table 5-2.	Summary of the Force Measurements during Stage 1 of the IRW Test (Backfilling).....	178
Table 5-3.	Data From Gloetzi Pressure Cells at the End of Stage 1 (Backfilling)	179

Table 5-4.	Summary of the Results of Stage 2 of the IRW (Surcharge)	179
Table 5-5.	Summary of the Results of Stage 3 of the IRW (Inundation)	180
Table 5-6.	Summary of Soil Properties Required in SOILSTRUCT- ALPHA Analyses	192
Table 5-7.	Summary of Property Values for Structural Materials in the IRW Analyses	193
Table 5-8.	Tentative Property Values for the Light Castle Sand Backfill	194
Table 5-9.	Property Values of the Wall-Backfill Interface used for the Finite Element Analyses of the IRW	198
Table 5-10.	Backfill Property Values Determined from Calibration Analyses of Stage 1 of the IRW Test	199
Table 5-11.	Backfill Property Values Determined from Calibration Analyses of Stage 2 of the IRW Test	201
Table B1.	Determination of Bulk Modulus for Medium-Dense Density Sand	B4
Table B2.	Determination of Bulk Modulus for Dense Density Sand.	B4
Table B3.	Determination of Bulk Modulus for Medium-Dense Light Castle Sand.	B4
Table B4.	Determination of Bulk Modulus for Dense Light Castle Sand	B5
Table C1.	Organization of the Figures in Appendix C	C1
Table E1.	Summary of State Parameters at Selected Points along Multidirectional Stress Path T405_10	E4
Table E2.	Summary of Hyperbolic Parameter Values for the Dense- Light-Castle-Sand-against-Concrete Interface	E4
Table E3.	Summary of Parameter Values for Unloading-Reloading of the Dense-Light-Castle-Sand-against-Concrete Interface	E5

Preface

This report summarizes the results of a final study leading to the development of an improved numerical model for concrete-to-soil interfaces for use in soil-structure interaction analyses. These improvements extend the accuracy of current interface models to include unload-reload and staged shear interface behavior. Accurate unload-reload concrete-to-soil interface behavior is important for analyses of partial or complete submergence of a lock and its backfill, commonly referred to as a postconstruction rise in the groundwater level. This research implements the resulting interface numerical model in the incremental construction, soil-structure interaction program SOILSTRUCT.

Funding for this research was provided by the Computer-Aided Structural Engineering (CASE) Project sponsored by Headquarters, U. S. Army Corps of Engineers (HQUSACE), as part of the Civil Works Research and Development Program on Structural Engineering (CWR&D). The work was performed under Civil Works Work Unit 31589, "Computer-Aided Structural Engineering (CASE)," for which Dr. Robert L. Hall, Structures Laboratory (SL), U.S. Army Engineer Research and Development Center (ERDC), is Problem Area Leader and Mr. H. Wayne Jones, Information Technology Laboratory (ITL), ERDC, is the Principal Investigator. The HQUSACE Technical Monitor is Mr. Bruce C. Riley, CECW-ED.

The work was performed at Virginia Polytechnic Institute and State University, Blacksburg, by Mr. Jesús E. Gómez, doctoral student, and Dr. George M. Filz, Associate Professor, under the guidance and supervision of Dr. Robert M. Ebeling, Computer-Aided Engineering Division (CAED), ITL. The research consisted of performing large-scale sand-to-concrete interface tests, researching current interface models for primary shear loading, and developing three interface models of varying degrees of sophistication for staged shear, primary loading, and unloading-reloading. A survey of existing concrete retaining walls was carried out by Mr. Gómez. The concrete specimen for interface testing was prepared by Mr. Gómez and Mr. Derrick Shelton at the Structures Laboratory at Virginia Tech. Mr. Gómez performed the large-scale interface test program at the Geotechnical Laboratory at Virginia Tech. The new interface model was developed by Mr. Gómez and Dr. Filz, with contributions by Dr. Ebeling. Mr. Gómez and Dr. Ebeling implemented the new interface model in SOILSTRUCT-ALPHA. Mr. Gómez performed a pilot-scale test in Virginia Tech's Instrumented Retaining Wall facility to simulate backfilling, surcharge application, and backfill inundation, and to compare the vertical force measurements to calculations performed

using the updated version of SOILSTRUCT-ALPHA. This report was prepared by Mr. Gómez, Dr. Filz, and Dr. Ebeling under the direct supervision of Mr. H. Wayne Jones, Chief, CAED, and Mr. Timothy D. Ables, Acting Director, ITL.

At the time of publication of this report, Dr. James R. Houston was Director of ERDC, and COL James S. Weller, EN, was Commander.

The contents of this report are not to be used for advertising, publication, or promotional purposes. Citation of trade names does not constitute an official endorsement or approval of the use of such commercial products.

1 Introduction

1.1 Background

Soil-Structure Interaction (SSI) analyses have proven to be powerful tools for use in analyzing, designing, and monitoring geotechnical structures. A substantial amount of the geotechnical literature of the last 30 years has dealt with the development or improvement of techniques for SSI analyses of retaining walls, piles, anchors, etc. These analyses may be performed to address key issues concerning the behavior of structures in the design stage, and often provide a means for evaluation of instrumentation data from completed structures.

SSI analyses are particularly useful in problems with complex geometry and loading conditions such as lock walls. In these cases, simple analyses are not adequate to characterize the behavior of the soil-structure system. Factors such as the placement of the backfill, filling of the lock with water, changes in the water table elevation behind the wall, temperature fluctuations, etc., play an important role in the behavior of the structure.

The first clear evidence of the importance of these factors was provided by the analyses of the Port Allen and Old River locks performed by Clough and Duncan (1969). Extensive instrumentation data suggested deformation patterns of the locks that seemed unreasonable and were thought to be the product of instrumentation errors. Clough and Duncan (1969, 1971) showed that close modeling of the construction stages of the lock and the use of a simple but adequate constitutive model for the soil and the soil-to-structure interface yielded results in close agreement with the measured data. For their analyses they used the hyperbolic model for soils proposed by Duncan and Chang (1970) following previous work by Kondner (1963) and Kondner and Zelasko (1963). The adequacy of this simple stress-strain model for use in SSI analyses is discussed in Section 4.1 of Ebeling, Peters, and Mosher (1997). This model has been extended to interface behavior, as described by Clough and Duncan (1971).

Several important contributions followed the pioneering work of Clough and Duncan. Studies of the Red River Lock and Dam No.1 (Ebeling et al. 1993; Ebeling and Mosher 1996; and Ebeling, Peters, and Mosher 1997), the North Lock Wall at McAlpine Locks (Ebeling and Wahl 1997), and Locks 27 (Ebeling, Pace, and Morrison 1997) are good examples of state-of-the-art techniques available for SSI analyses. These studies showed that the behavior of the

soil-structure interface has a significant influence on the magnitudes of the loads acting against the lock wall. They also illustrated that the pre- and post-construction stress paths followed by interface elements are complex, often involving simultaneous changes in normal and shear stresses, as well as shear stress reversals due to post-construction rise of the ground water level.

The hyperbolic interface model developed by Clough and Duncan (1971) is a very useful tool for SSI analyses. It is easy to implement, and the parameters involved in the hyperbolic fit to laboratory data have a physical meaning. Although it models interface behavior in the primary loading stage very closely, it has not been extended to accurately model simultaneous changes in shear and normal stresses, reduction of shear stress, reversals in the direction of shear, or unload-reload cycles at the interface.

The purpose of the research described in this report is the development of an improved numerical model for soil-structure interfaces that can handle a variety of stress paths. A series of interface tests were performed in the laboratory to collect data on interface response to different types of loading. An extended hyperbolic model was developed based on the test results and implemented in the finite element program SOILSTRUCT-ALPHA, which is commonly used by the U.S. Army Corps of Engineers for analysis of lock walls.

A pilot-scale lock wall simulation was carried out in the Instrumented Retaining Wall (IRW) facility at Virginia Polytechnic Institute and State University, Blacksburg (Virginia Tech), where vertical and horizontal forces exerted by the backfill on the wall were measured. Finite element calculations of the IRW simulation were performed using the updated version of SOILSTRUCT-ALPHA, which contains the formulation of the extended hyperbolic model. Comparisons between the finite element calculations and the IRW test data suggest that the extended hyperbolic model may provide accurate predictions of the magnitudes of vertical shear forces at lock wall-backfill interfaces.

This research was performed in two phases. The preliminary study (Gómez, Filz, and Ebeling 1999) contains some initial results of the interface testing program and a preliminary version of the extended hyperbolic model developed during Phase 1 of the investigation. The present Phase 2 report contains additional results of interface tests and the final version of the extended hyperbolic model. The procedure for the implementation of the model in SOILSTRUCT-ALPHA is also described. Finally, the results of the lock wall simulation are presented together with a critical evaluation of the accuracy of the model and suggestions for future work on interface modeling.

1.2 Interface Behavior in SSI Analyses

Based on SSI analyses of four hypothetical earth retaining structures, Ebeling, Duncan, and Clough (1990) concluded that the interface shear stiffness has a significant influence on the distribution of forces on the structure. They performed two different analyses of the same structure using the expected maximum and

minimum values of shear stiffness of the backfill-to-structure interface. A difference of 12.5 percent was found between the values of friction angle mobilized at the base of the structure for the two analyses. Further evidence of the importance of interface behavior in SSI analyses has been provided in a study of the North Lock wall at McAlpine Locks.

1.2.1 The North Lock Wall at McAlpine Locks

The North Lock wall at McAlpine Locks (Ebeling and Wahl 1997) has been designed as a monolith of roller-compacted concrete (RCC) directly founded on rock as illustrated in Figure 1-1. The lock wall will be 22.25 m (73 ft) high with a dense granular backfill extending from the new RCC lock to the existing lock wall as shown in the figure. The analyses were performed using the finite element program SOILSTRUCT-ALPHA (Ebeling, Duncan, and Clough 1990), which is an updated version of SOILSTRUCT (Clough and Duncan 1969) that allows for separation between the base of the wall and the foundation.

The analyses performed for the North Lock wall were completed in three phases: (a) gravity turn-on analysis prior to construction of the new lock, (b) incremental construction of the new lock and concurrent backfill placement, and (c) post-construction submergence of the backfill and flooding of the lock chamber. The lock-to-backfill, lock-to-rock, and backfill-to-rock interfaces were modeled using Goodman, Taylor, and Brekke (1968) one-dimensional interface elements. The hyperbolic models proposed by Duncan and Chang (1970) and Clough and Duncan (1971) were used for the backfill and the interfaces, respectively.

Table 1-1 shows the results of the analyses in terms of the effective horizontal and vertical forces F'_x and F_v per unit length acting on Section A-A represented in Figure 1-1.¹ The vertical force F_v is caused by downdrag on Section A-A produced by settlement of the backfill.

The earth pressure coefficients K_h and K_v , also shown in Table 1-1, are a convenient way to quantify the effective horizontal and vertical forces acting on Section A-A. They represent the ratio of these forces to the *effective overburden* and are calculated as follows (Ebeling and Wahl 1997):

$$\text{Effective Overburden} = \int_{EI370}^{EI425} \sigma'_v dy \quad (1-1)$$

$$K_v = \frac{F'_x}{\text{Effective Overburden}} \quad (1-2)$$

¹ For convenience, symbols are listed and defined in the Notation, Appendix F.

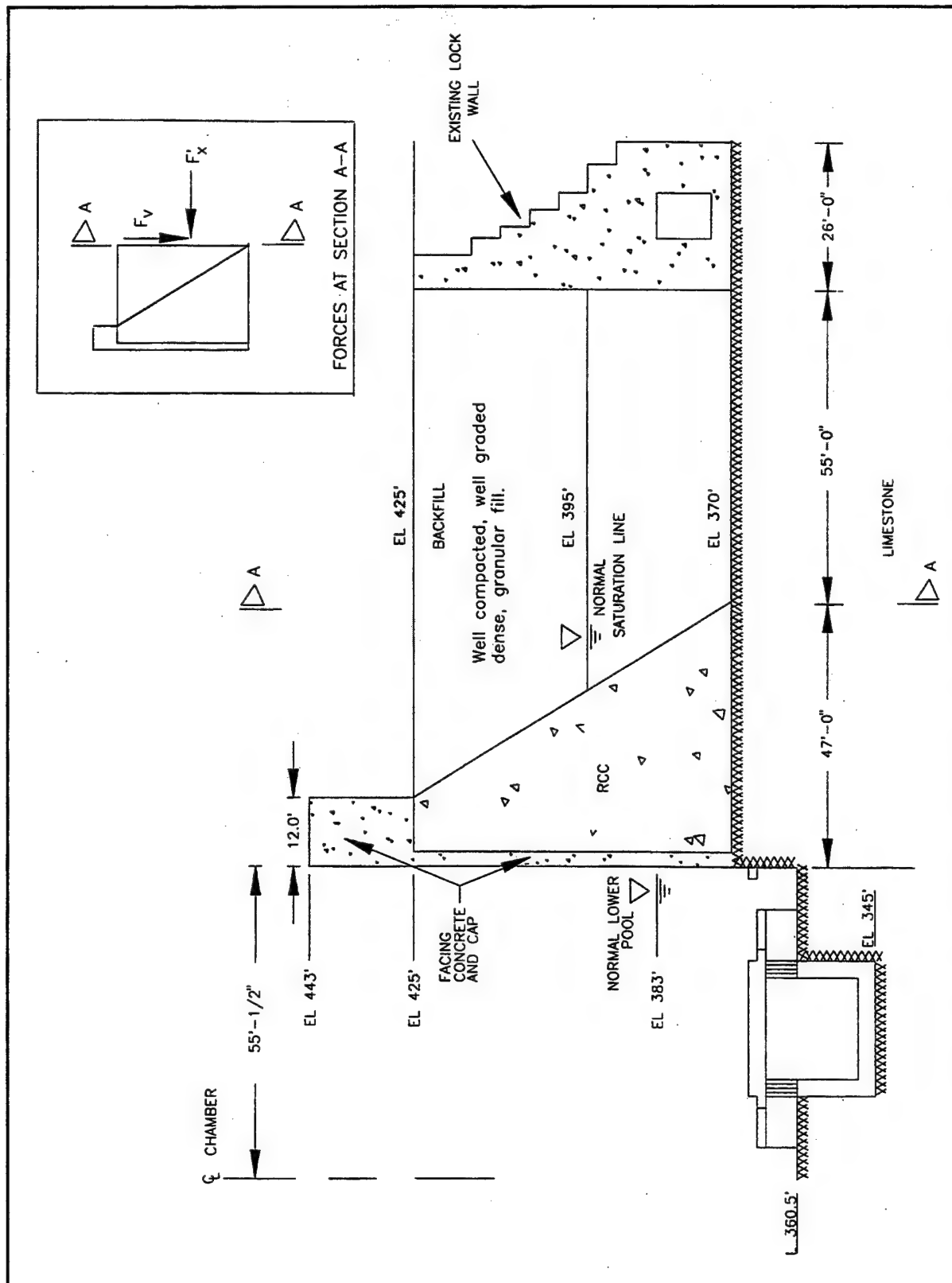


Figure 1-1. Typical section, north wall of new RCC McAlpine Lock (adapted from Ebeling and Wahl 1997) (1 ft = 0.305 m)

Table 1-1
Summary of Results of SSI Analyses for the North Lock at McAlpine Locks (adapted from Ebeling and Wahl 1997)

Condition	Effective Overburden, kN per m Run of Wall	F_x , kN per m Run of Wall	F_v , kN per m Run of Wall	K_h	K_v
After backfilling	2,782	1,217	167	0.437	0.060
After submergence	2,515	1,155	99	0.459	0.039

$$K_v = \frac{F_v}{\text{Effective Overburden}} \quad (1-3)$$

where σ_v' is the effective vertical stress acting along Section A-A.

The earth force coefficients K_h and K_v are useful for consistent comparison of results of analyses at different operational stages of the lock wall and even between retaining walls of different geometry and loading conditions. The vertical earth force coefficient K_v is also used in a simplified procedure to estimate the downdrag on retaining walls founded on rock. This simplified procedure (Appendix F in Engineer Circular (EC) 1110-2-291¹) is described in detail in Chapter 2.

The results in Table 1-1 show that after backfilling and prior to inundation, the magnitude of the downdrag on the wall is substantial and amounts to 6 percent of the effective overburden. The mechanism for generation of this downdrag during backfilling is illustrated in Figure 1-2a. The initial horizontal position of the surface of a compacted lift is shown. As the backfill placement progresses, the weight of the newly placed and compacted lifts compresses the underlying backfill. The relative movement between the compressing backfill and the wall generates shear stresses at the backfill-to-structure interface. The final configuration of the lift illustrates the nonuniform compression of the backfill due to the restraint imposed by the interface shear stresses.

Filz (1992) and Filz and Duncan (1997) showed that the distribution of the backfill-to-structure interface shear stresses is not uniform along the height of the wall. For walls founded on relatively incompressible materials, such as the rock-founded North Lock wall, there is no settlement at the bottom of the backfill due to the absence of underlying compressible material. The top of the backfill does not settle if no further loads are applied after completion of backfilling with soils that do not creep. The maximum interface shear stress occurs at some intermediate point between the top and bottom of the backfill.

¹ Starting in 1997, the Headquarters, U.S. Army Corps of Engineers (HQUSACE), began to revise and consolidate their guidance on stability criteria for concrete gravity dams and other hydraulic structures. The Corps guidance contained in this technical report is based on the summer 1999 draft of this guidance (Engineer Manual (EM) 1110-2-2100). This Corps draft guidance has undergone peer review by District engineers as EC 1110-2-291. EM 1110-2-2100 is in the final stages of preparation at the time of publication of this report.

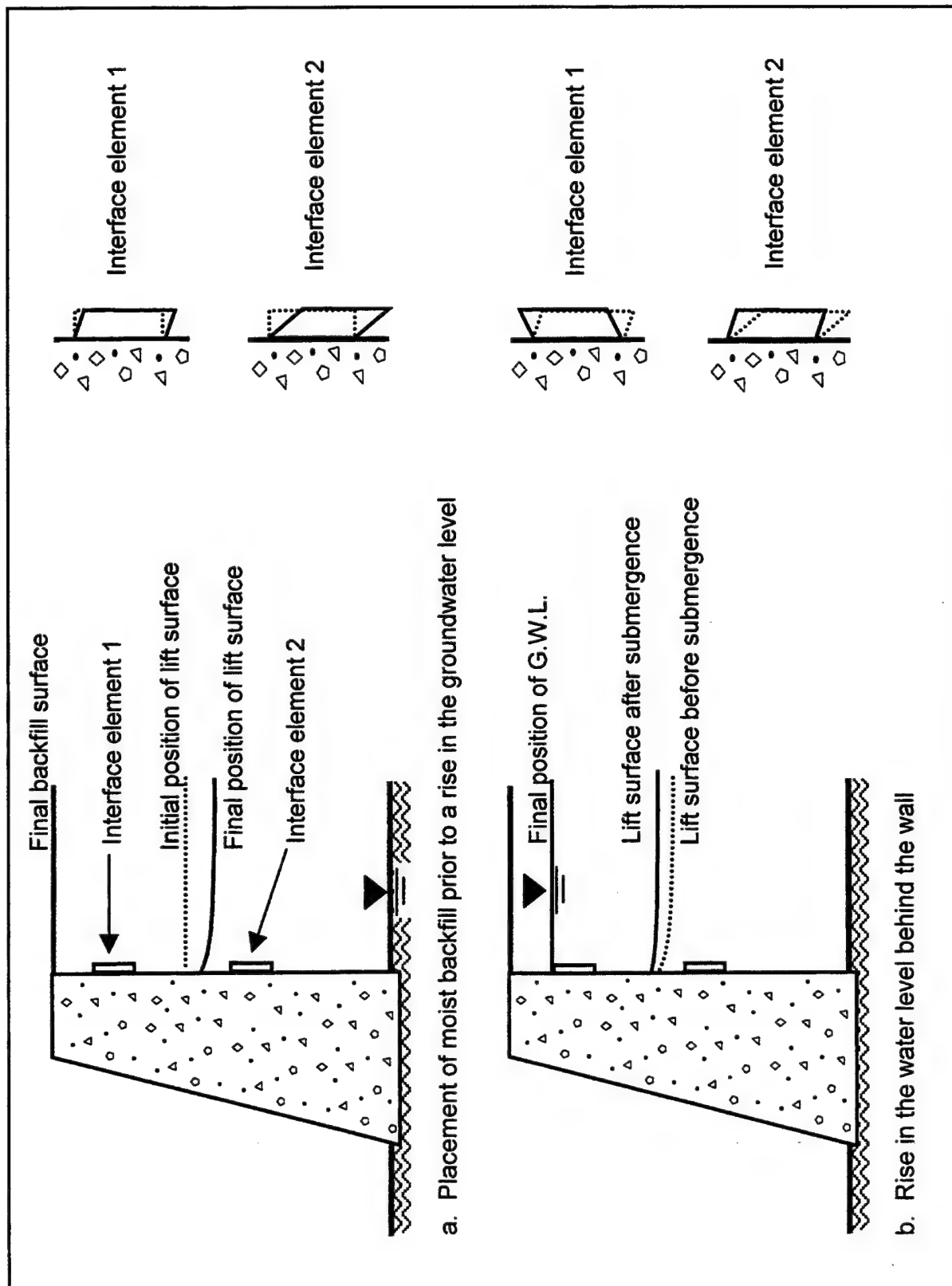


Figure 1-2. Simplified illustration of the mechanism of downdrag and shear reversal in a typical lock wall

Table 1-1 also shows the results of the analyses considering a post-construction submergence of the backfill. The vertical shear force and the vertical earth force coefficient K_v are substantially reduced compared with the analysis before submergence. The mechanism for this reduction of shear stresses is illustrated in Figure 1-2b. As the groundwater level in the backfill rises, there is a decrease in the effective stresses and, in the absence of hydrocompression, an upward movement of the backfill. As the backfill in contact with the wall rises, the shear stresses at the interface decrease.

The magnitude of the vertical shear forces acting on the back of the wall may have a significant impact on the stability of the structure. If these stabilizing forces are accounted for in the design of the structure, a more economical construction can be achieved. Reliable calculation of these forces requires an adequate constitutive model for the interface response to conditions such as those represented in Figure 1-2.

1.2.2 Limitations of existing interface models

Two interface elements are represented in the simplified lock wall scheme of Figure 1-2. The normal and shear stresses acting on these elements change simultaneously during backfill placement and subsequent submergence of the backfill. Figure 1-3a shows the typical field stress paths followed by these elements during placement of the backfill. Element 1, which is located close to the top of the backfill, follows the stress path $A-B$. Element 2, which is located at midheight of the backfill, is subjected to larger normal and shear stresses at the end of the backfill placement and may follow a stress path such as $A-C$. It also undergoes larger interface displacements than Element 1.

Figure 1-3a also illustrates the type of stress paths typically applied during laboratory testing, in which the interface is sheared to failure under constant normal stress. Although the Clough and Duncan (1971) hyperbolic model for interfaces works well for typical laboratory stress paths, the response of the interface to the actual field stress path may differ substantially from that predicted by the model.

Figure 1-3b shows the stress paths that may be followed by the two interface elements in Figure 1-2 during inundation of the backfill. Element 2 may follow the stress path $C-E$. The shear stresses acting on Element 2 decrease simultaneously with the normal stresses. The stress path for Element 1 is represented by line $B-D$. Element 1 undergoes a larger displacement along the interface because the thickness of the underlying backfill subject to rebound is larger. Due to this large displacement and the low initial shear stress acting on Element 1, inundation of the backfill may induce a reversal in the direction of shear. Further fluctuations in the water table behind the lock wall may induce unload-reload cycles on the interface.

Two different SSI analyses were performed for the North Lock wall at McAlpine Locks considering partial submergence of the backfill. Figure 1-4 shows the two different interface responses used for these analyses. In the stiff

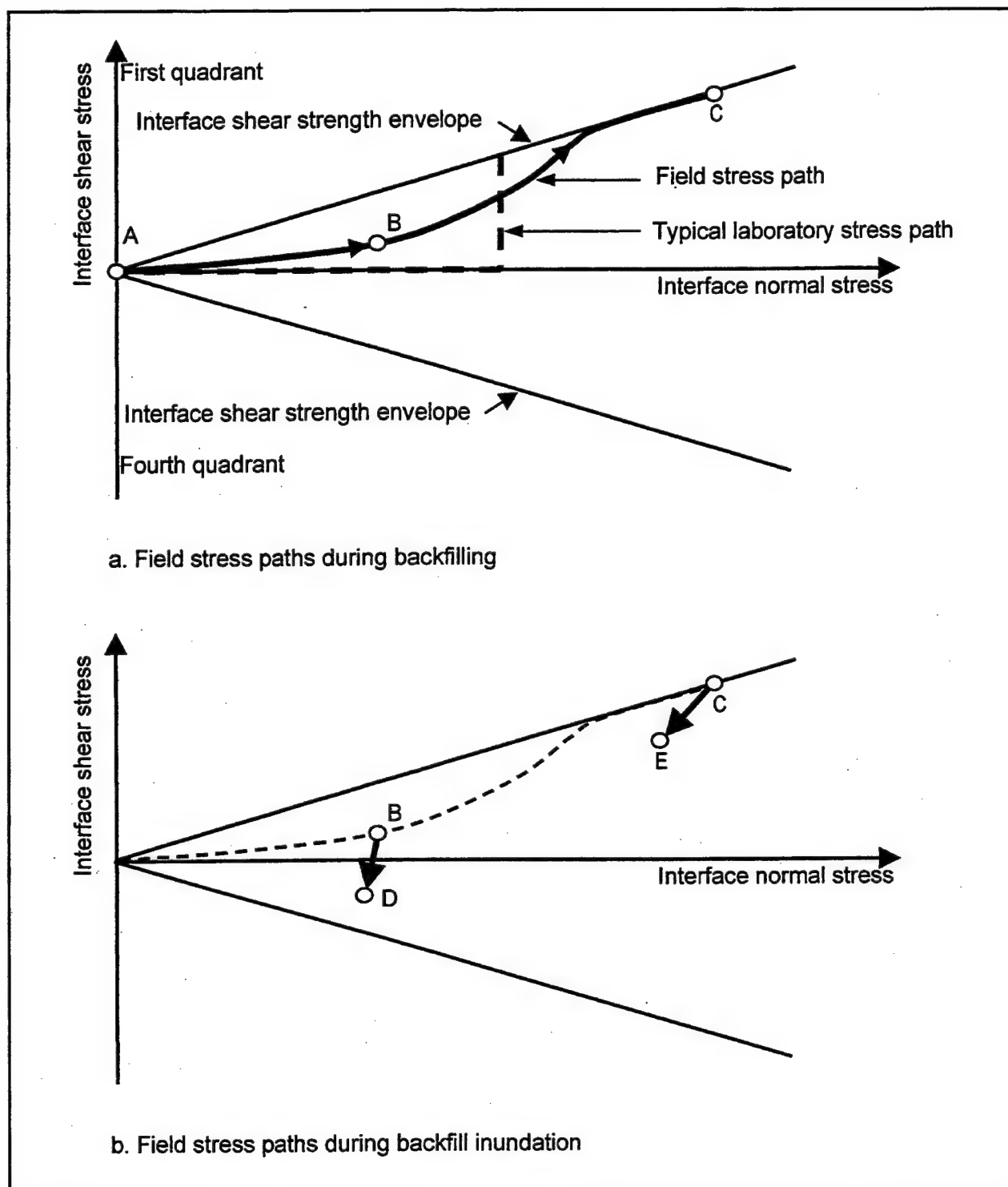


Figure 1-3. Types of loading expected on the interface between a lock wall and the backfill

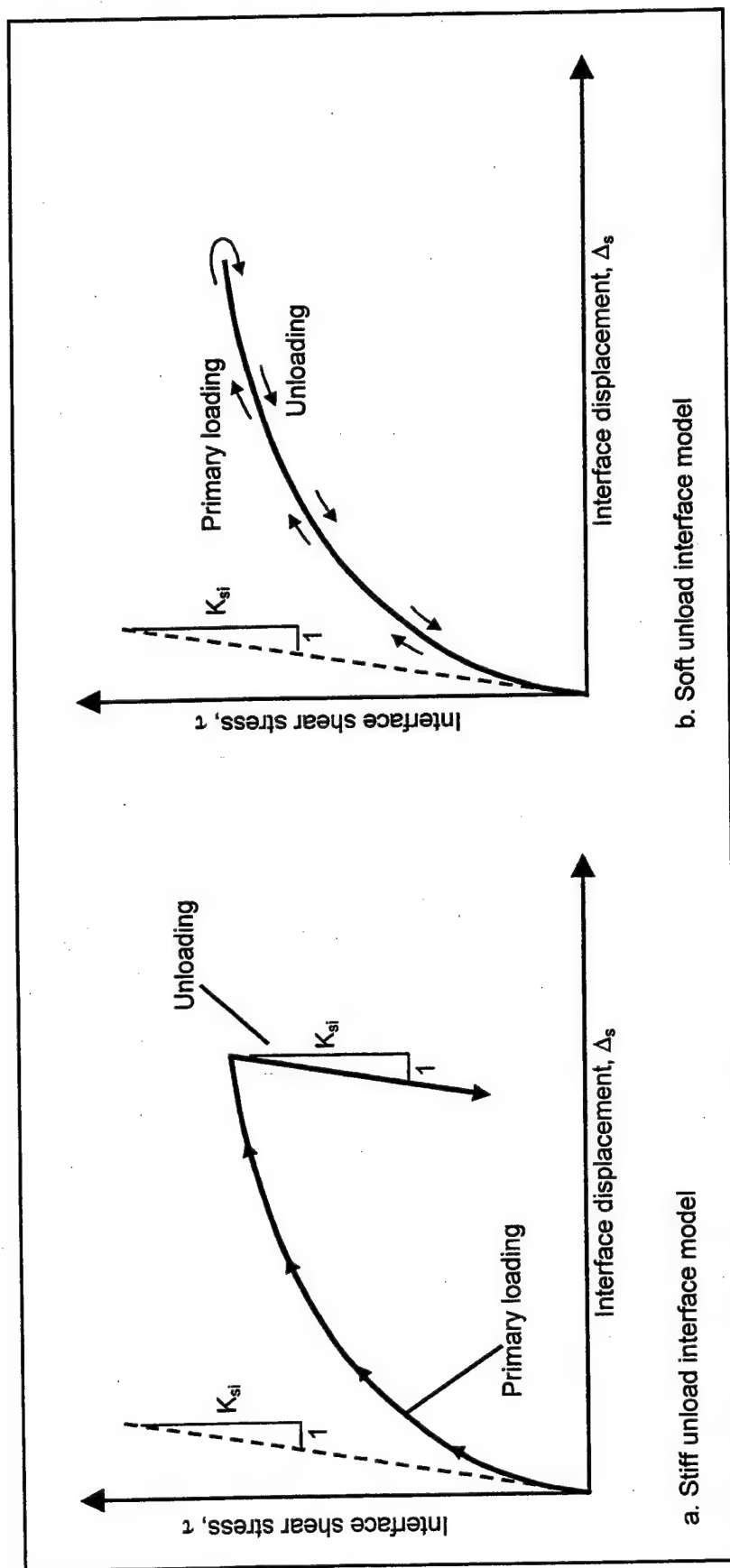


Figure 1-4. Two models for interface shear stress-displacement response under unloading (adapted from Ebeling and Wahl 1997)

unload interface model, shown in Figure 1-4a for a constant effective normal stress, the shear stiffness during reversal is assumed equal to the initial shear stiffness. Changes in effective normal stress occurred in the interface elements as the water table rose in the backfill. This resulted in a change in the interface shear stiffness used during unloading of the interface elements. In the soft unload interface model, shown in Figure 1-4b for a constant effective normal stress, the primary loading curve is also used during unloading.

The results of the two SSI analyses at Section A-A are summarized in Table 1-2. These results show that the vertical shear forces acting on the wall after partial submergence of the backfill are significantly lower for the stiff interface response model during unloading than for the soft interface response model. The computed effective base pressure below the heel of the lock wall (results not shown) is lower for the SSI analysis using the stiffer interface model during post-construction, partial submergence of the backfill. This behavior is attributed to both the lower shear force and slightly larger horizontal earth pressure acting on the back of the lock wall for the SSI analysis with the stiff interface model.

Table 1-2
Comparison of Results of SSI Analyses at Section A-A for Two
Different Models of Interface Response to Unloading (adapted from
Ebeling and Wahl 1997)

Condition	Effective Overburden, kN per m Run of Wall	F_x' , kN per m Run of Wall	F_v , kN per m Run of Wall	K_h	K_v
"Stiff" model	2,515	1,155	99	0.459	0.039
"Soft" model	2,515	1,131	130	0.450	0.052

Only very limited published information is available concerning interface response to shear stress reversals, unload and reload cycles, or simultaneous change in shear and normal stresses. One of the most significant works on the response of concrete-to-soil interfaces was performed by Peterson et al. (1976). Their results, along with those reported in Clough and Duncan (1969), have been the main source of information on interface response for SSI analyses of lock walls. Peterson et al. (1976) used a 102- by 102-mm (4- by 4-in.) shear box to test combinations of different concrete surfaces and sands. The most important variables analyzed were roughness of the concrete surface and gradation and relative density of the sand. Their work has three main limitations: (a) the frequency of the reported data points collected during interface testing is in general not adequate to model the behavior during shear reversals, (b) no tests were performed to model simultaneous changes in normal and shear stresses, and (c) end effects due to the small dimensions of the shear box may have influenced the results, especially with respect to the initial stiffness during shear load reversals.

1.3 Project Scope

This investigation included laboratory testing of soil-to-concrete interfaces and development of an improved numerical model for interfaces. The model was implemented in the finite element program SOILSTRUCT-ALPHA and was validated against the results of a lock simulation test performed using the IRW at Virginia Tech.

1.3.1 Interface testing

To introduce improvements in existing interface models, data were collected from laboratory tests performed using stress paths such as those described previously. Figure 1-5a shows a stress path in which both shear and normal stresses change simultaneously. This stress path was designed to model the type of loading expected at the wall-backfill interface during backfill placement.

Figure 1-5b illustrates stress paths applied to study the interface response to unloading-reloading and reversal in the direction of shear. These stress paths model the type of loading expected at the wall-backfill interface during inundation of the backfill.

Figure 1-5c shows a stress path designed to probe the yield surface. The interface is sheared under constant normal stress to the state of stress represented by point *S*. Subsequently, the normal stress is increased to point *S'*, while a constant shear stress is maintained. Finally, the interface is sheared to failure. This type of loading is referred to as *staged shear* in this report.

The data collected from such tests allowed the development of the extended hyperbolic model for interfaces. A series of additional interface tests were performed that combined the types of loading illustrated in Figure 1-5 into complex stress paths. The results from these tests were the basis for the evaluation of the accuracy of the extended hyperbolic model.

Virginia Tech's Large Displacement Shear Box (LDSB) was used to perform the soil-to-concrete interface shear tests. The LDSB was used previously to test clay-geomembrane interfaces (Shallenberger and Filz 1996). Several modifications to the original configuration of the LDSB were necessary to permit the kind of soil-to-concrete interface testing necessary for this project. The tests were performed on three different sand-to-concrete interfaces. The details of specimen preparation, testing procedures, and results are described in this report.

1.3.2 Extended hyperbolic model for interfaces

A new, improved numerical model was developed using the results of the interface tests performed during this investigation. The new model is based on the hyperbolic formulation developed by Clough and Duncan (1971), which has been extended to model the type of loading illustrated in Figure 1-5.

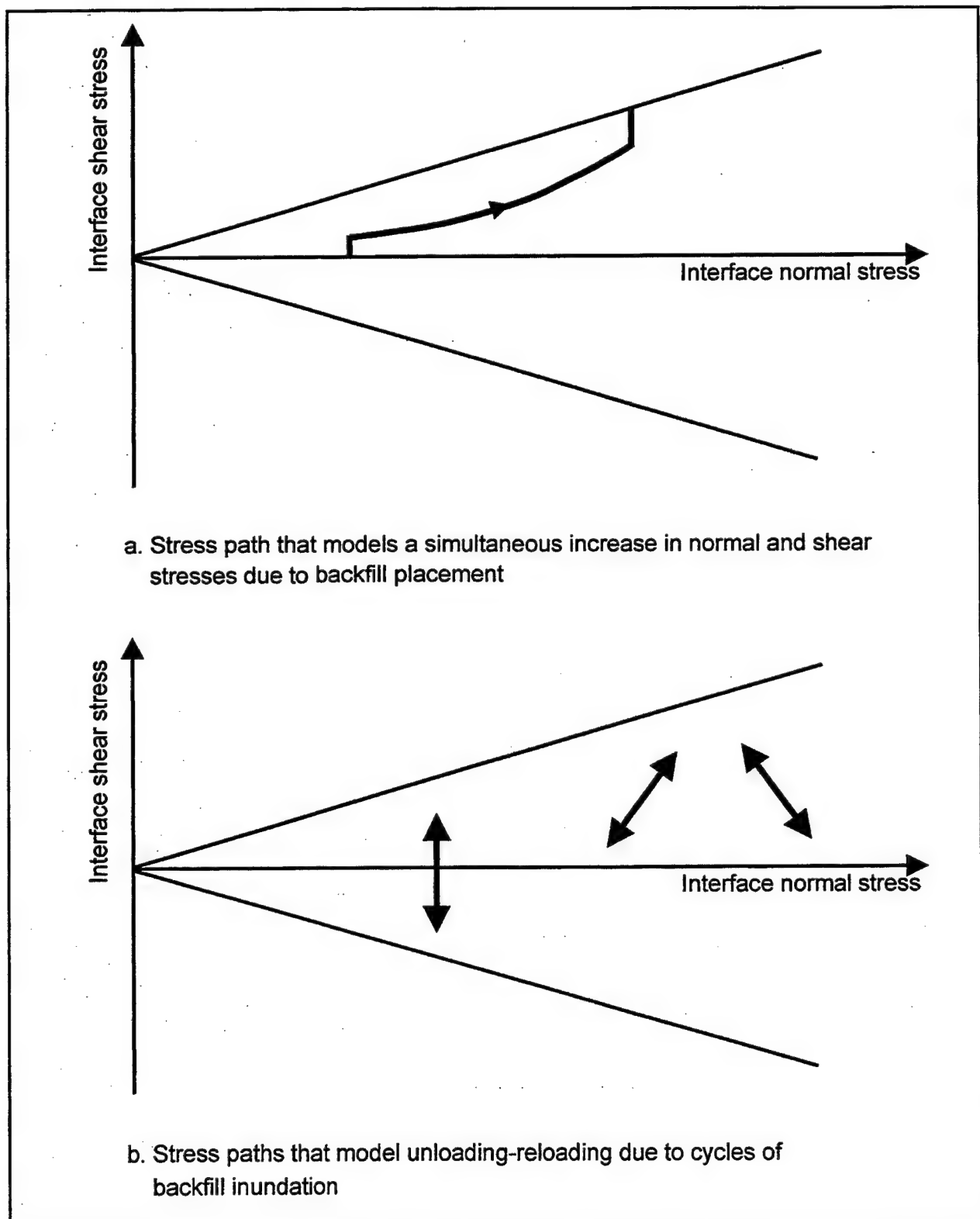


Figure 1-5. Laboratory stress paths to study the response of a wall-backfill interface (Continued)

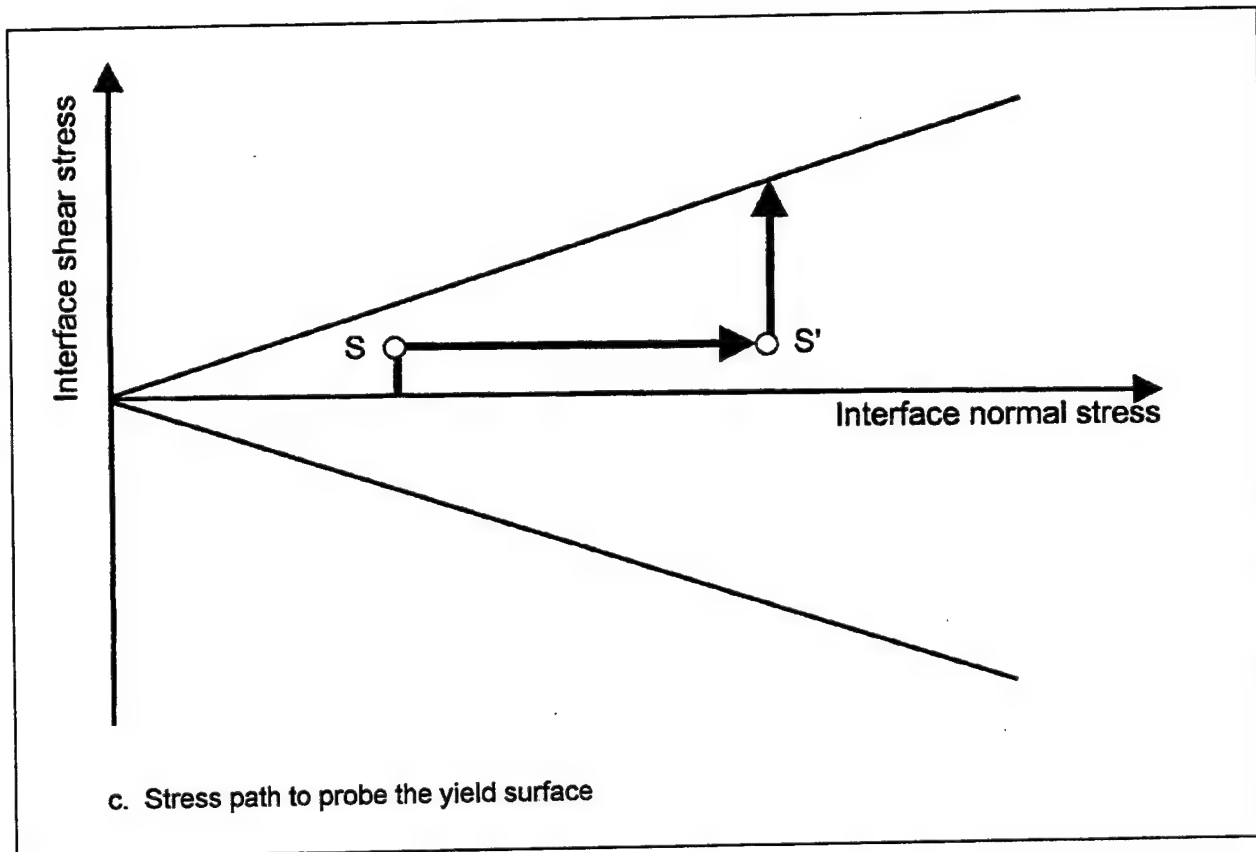


Figure 1-5. (Concluded)

The staged shear tests provided information about the evolution of the yield surface during interface shear. The model contains a formulation for interfaces undergoing yielding and a formulation for unloading-reloading and staged shear. For interfaces at yield, the extended hyperbolic model accounts for changes in the normal stress during shear, which can be applied to the type of loading illustrated in Figure 1-5a.

Three different versions of the model were developed for interfaces undergoing unloading-reloading. In Version I, a linear, normal stress-dependent interface response is assumed. Version II assumes a hyperbolic response that can model the hysteretic behavior of the interface. Version III provides a smooth transition between the reloading and yielding responses of the interface.

The model was evaluated against the results of the interface tests performed following complex stress paths. It was found that the model provides an accurate representation of interface response. Higher version numbers produce better response to complex stress paths.

1.3.3 Implementation of the model in SOILSTRUCT-ALPHA

The finite element program SOILSTRUCT-ALPHA as described in Ebeling and Wahl (1997) and Ebeling, Pace, and Morrison (1977) is frequently used for SSI analyses of Corps of Engineers structures. The program is capable of modeling the different stages of construction and operation of a lock wall. The formulation for yield-inducing shear and Version II of the unload-reload formulation were implemented in the program. The updated version of SOILSTRUCT-ALPHA was used to model the lock wall simulation performed in the IRW.

1.3.4 Lock wall simulation

A pilot-scale test was performed in Virginia Tech's IRW facility to simulate backfilling, surcharge application, and backfill inundation for a lock wall. The purpose of the test was to collect data on the behavior of the wall-backfill system during surcharge application and inundation, and to compare the vertical force measurements to calculations performed using the updated version of SOILSTRUCT-ALPHA.

It was found that the vertical force, which develops at the wall-backfill interface during backfilling, may change substantially during surcharge application and backfill inundation. Comparisons between the lock simulation data and SOILSTRUCT-ALPHA calculations suggest that the extended hyperbolic model may provide accurate predictions of interface response in SSI analyses of lock walls.

1.4 Report Organization

The report is organized in four main sections. The literature review is presented in Chapter 2, which contains a description of previous work on interface testing, interface modeling, and SSI analyses.

Chapter 3 contains a complete description of the testing equipment, testing procedures, and results of laboratory tests performed on the soils and on the soil-to-concrete interfaces used for this investigation.

The formulation of the extended hyperbolic model is presented in Chapter 4. Relevant aspects of the interface response measured during the interface tests are discussed. The hypotheses leading to the formulation of the model are introduced. The derivation of the mathematical formulation of the extended hyperbolic model is described in detail, together with the recommended procedures for the determination and adjustment of the model parameters. The model is evaluated against the results of the interface tests described in Chapter 3. Finally, an outline of the implementation of the model in the program SOILSTRUCT-ALPHA is presented.

The lock wall simulation performed in the IRW is described in Chapter 5. Details are given regarding preparation of the facility, testing procedures, and

results of the test. The finite element analyses of the IRW using SOILSTRUCT-ALPHA are presented, and the measured and the calculated magnitudes of the forces acting on the wall are compared.

Chapter 6 summarizes the results and conclusions of this investigation, and includes recommendations for future work on interface modeling and SSI analyses of lock walls.

The report also includes six appendices. Appendix A contains the results of tests performed on the soils used for interface testing. Appendix B describes the determination of the hyperbolic parameter values for the soils tested. The results of the interface tests are presented in Appendix C. The determination of the hyperbolic parameter values for the interfaces is described in Appendix D. Appendix E contains some example calculations that serve to illustrate the practical application of the extended hyperbolic model. Finally, all the symbols and abbreviations used in this report are defined in Appendix F.

2 Literature Review

This chapter is divided into the following sections:

- a. *Interface testing.* This section reviews previous work on shear testing of interfaces between soils and structural materials.
- b. *Interface modeling.* The interface models that are most commonly used in SSI analyses are reviewed. A detailed description is presented of the hyperbolic model for interfaces by Clough and Duncan (1971).
- c. *SSI analyses of retaining walls.* The development of SSI analysis techniques is outlined in this section. A simplified procedure for estimating the downdrag forces on retaining walls is described.
- d. *Summary.*

2.1 Interface Testing

Several studies have been published regarding laboratory interface testing. Most often, interface tests were performed to determine the soil-to-structure friction angle for design of geotechnical structures, such as retaining walls, buried culverts, piles, etc., and, in some cases, for the determination of parameters for constitutive modeling of interface response.

Interface tests have been performed on many types of soil-to-structure, soil-to-rock, and rock-to-rock interfaces. In this section, previous studies of soil-to-concrete and soil-to-steel interfaces are emphasized. The results of tests performed on both types of interfaces provide valuable insights into fundamental aspects of interface behavior.

2.1.1 Direct Shear Box (DSB) devices

Early systematic efforts to obtain data on the behavior of soil-to-structure interfaces were carried out by Potyondy (1961), Clough and Duncan (1971), and Peterson et al. (1976), among others. Their tests were performed using a slightly modified Direct Shear Box (DSB) in which a concrete specimen occupied one of the halves of the shear box. In most cases, the soil sample was prepared against a concrete specimen situated at the bottom. The tests were typically performed by

first increasing the normal pressure to a desired value, then shearing the interface under constant normal stress to a maximum displacement of about 12.5 mm (0.5 in.).

Peterson et al. (1976) studied the fundamental factors that influence interface behavior. They performed a large number of sand-to-concrete interface tests using a 102- by 102-mm (4- by 4-in.) DSB. In their tests, the interface was inundated and sheared, under drained conditions and constant normal load, to a maximum displacement of 12.5 mm (0.5 in.). They analyzed the influence of normal stress, interface roughness, and soil characteristics on interface behavior, and developed a database of sand-to-concrete interface friction angles.

Peterson et al. (1976) also demonstrated the usefulness of the Clough and Duncan (1971) hyperbolic formulation to model interface behavior. They developed a set of hyperbolic parameter values, which have been used as an important source of data for SSI analyses up to the present time (Ebeling et al. 1993; Ebeling and Mosher 1996; Ebeling, Pace, and Morrison 1997; Ebeling, Peters, and Mosher 1997; Ebeling and Wahl 1997).

The DSB presents two important advantages: wide availability and relatively simple test setup and sample preparation procedures. Consequently, it has been the common choice for interface testing in research and practice. Some of the most relevant studies performed using DSB-type devices are summarized in Table 2-1. Other applications of the DSB include testing interfaces such as soil to geomembrane, soil to geotextile, and geomembrane to geotextile. Commercial devices have been developed for larger interface areas of up to 305 by 305 mm (12 by 12 in.), and they can be used for soil-to-concrete testing.

Traditional DSB devices present several limitations. The maximum relative displacement that can be attained in a conventional DSB is limited; hence, the determination of the interface residual strength becomes difficult. In addition, end effects, induced by the presence of the rigid walls of the soil container, may introduce errors in the test results.

Kishida and Uesugi (1987), Fakharian and Evgin (1995), and Evgin and Fakharian (1996) have pointed out that the actual sliding displacement Δ_{actual} between the soil particles and the concrete cannot be directly measured in the DSB, as illustrated in Figure 2-1a. The displacement Δ_{meas} measured between the soil box and the concrete specimen includes the sliding displacement at the interface, as well as the deformation Δ_{dis} of the sand mass due to distortion under the applied shear stresses.

2.1.2 Direct Simple Shear (DSS) devices

Direct Simple Shear (DSS) devices have been intensively employed for interface testing during the last two decades, primarily on sand-to-steel and clay-to-steel interfaces. Sand-to-steel tests have yielded interesting results regarding the general behavior of interfaces. Many of these results are applicable to

Table 2-1
Previous Work on Direct Shear Testing of Sand-to-Concrete and Sand-to-Steel Interfaces

Source	Type of Interface and Dimensions	Type of Loading	Summary
Potyondy (1961)	Sand to concrete Sand to steel	Monotonic under constant normal stress	<ul style="list-style-type: none"> Developed a database of interface friction parameter values for interfaces between sand and concrete of varying roughness
Clough and Duncan (1971)	Sand to concrete	Monotonic shear under constant normal stress	<ul style="list-style-type: none"> Developed a hyperbolic formulation for modeling interface response
Peterson et al. (1976) and Kulhawy and Peterson (1979)	Sand to concrete 102 mm x 102 mm	Monotonic shear and shear reversal under constant normal stress	<ul style="list-style-type: none"> Analyzed the relationship between the interface response and the interface roughness, soil type, and soil density and gradation Added important contributions to the database of parameters for the Clough and Duncan (1971) hyperbolic formulation
Acar, Durgunoglu, and Turmay (1982)	Sand to concrete Sand to steel	Monotonic shear under constant normal stress	<ul style="list-style-type: none"> Studied the relationship between void ratio of the sand and interface friction angle Presented a relationship between void ratio and hyperbolic parameter values for Clough and Duncan (1971) formulation for the materials used in their tests
Desai, Drumm, and Zaman (1985)	Sand to concrete 305 mm x 305 mm	Cyclic shear under constant normal stress	<ul style="list-style-type: none"> Developed the <i>Cyclic Multi-Degree-of-Freedom</i> (CYMDOF) device for interface testing Studied the influence on interface response of the following factors: displacement and shear stress amplitude, number of loading cycles, and initial density of the sand
Bosscher and Ortiz (1987)	Sand to concrete Sand to rock	Cyclic shear under constant normal stress	<ul style="list-style-type: none"> Studied the relationship between interface roughness and interface friction angle Assessed the effect of roughness on damping ratio of the interface
Lee et al. (1989)	Sand to concrete 100 mm x 100 mm	Monotonic shear under constant normal stress	<ul style="list-style-type: none"> Developed of a set of hyperbolic parameter values for the response of the interfaces used in their tests
Hryciw and Irsyam (1993)	Sand to ribbed steel 267 mm x 76 mm	Monotonic and cyclic shear under constant normal stress	<ul style="list-style-type: none"> Studied the mechanisms of dilation and shear band formation at the interface Studied the influence of rib geometry and spacing, and soil density on the interface response

sand-to-concrete interfaces as well. Table 2-2 summarizes some of the previous work on interface behavior in which testing was performed in DSS apparatuses.

One of the main advantages of DSS devices is the ability to measure separately the total interface displacements Δ_{meas} and the soil distortion Δ_{dis} as illustrated in Figure 2-1b. According to Uesugi and Kishida (1986b), the horizontal deformation due to distortion of the sand mass is an important component of the total displacement measured in the DSS device.

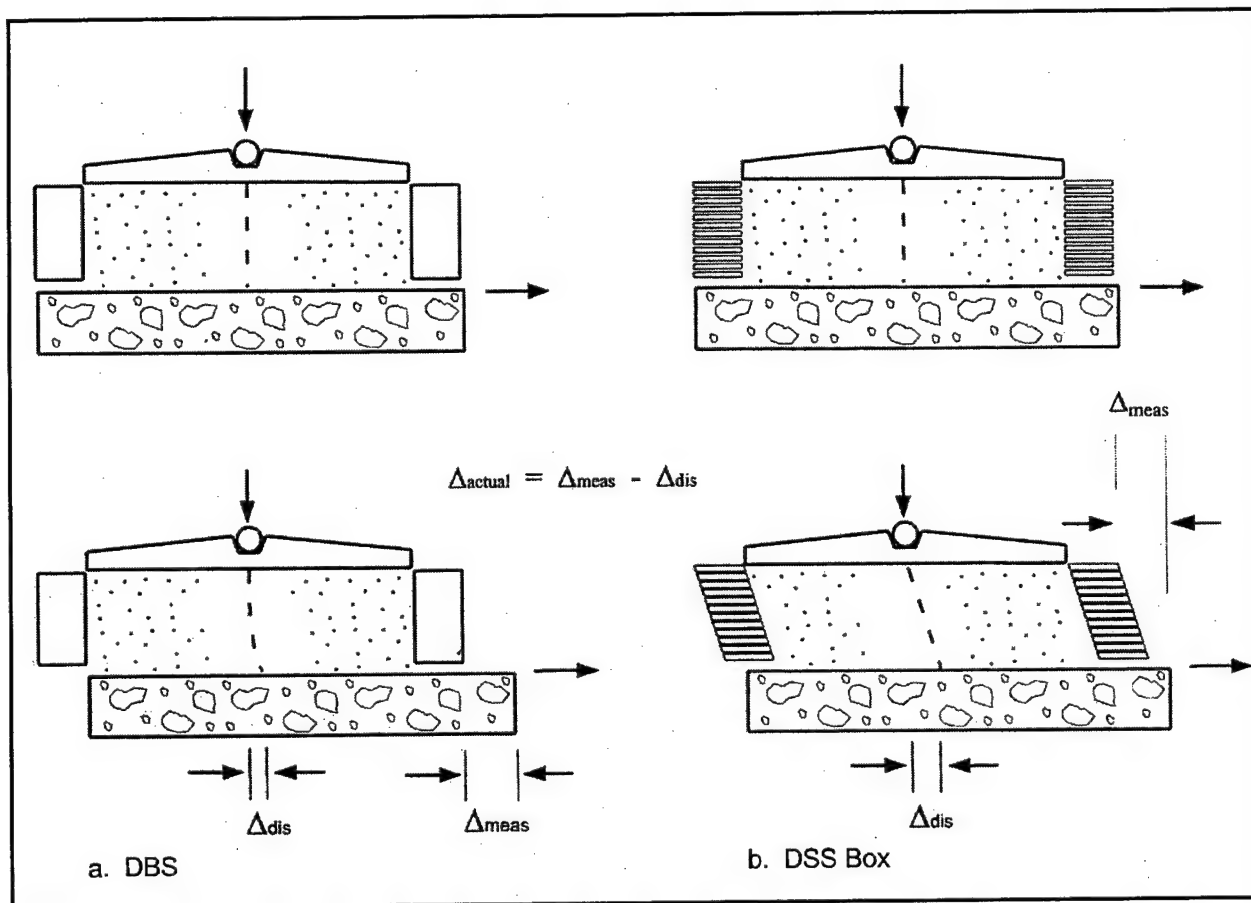


Figure 2-1. Distortion of the sand mass during interface tests in the DSB and DSS devices

DSS devices have important limitations for interface testing: (a) nonuniform distribution of stresses at the interface (Kishida and Uesugi 1987), (b) complicated sample preparation, and (c) limited maximum total displacement, which does not exceed 25.4 mm (1 in.).

2.1.3 Other devices

In order to overcome the limitations of the conventional apparatuses for interface testing, several investigators have developed special devices. Brummund and Leonards (1973) developed an annular device in which a cylindrical specimen of the structural material is embedded in sand. During testing, the specimen of structural material is pulled along its axis to failure under a confining pressure applied on the boundary of the sand sample. This device was created in an attempt to model the behavior of a pile shaft. The sample preparation for this type of test is complicated, and the normal stresses at the interface are difficult to control and depend on the relative stiffness between the structural specimen and the sand (Kishida and Uesugi 1987).

Table 2-2**Previous Work on Direct Simple Shear Testing of Sand-to-Concrete and Sand-to-Steel Interfaces**

Source	Type of Interface and Dimensions	Type of Loading	Summary
Uesugi and Kishida (1986a and 1986b)	Sand to steel 100 mm x 40 mm	Monotonic under constant normal stress	<ul style="list-style-type: none"> Concluded that distortion of the sand sample is an important component of the total displacement
Kishida and Uesugi (1987)	Sand to steel 400 mm x 100 mm	Monotonic shear under constant normal stress	<ul style="list-style-type: none"> Found direct relationship between steel roughness and interface friction coefficient
Uesugi, Kishida and Tsubakihara (1988)	Sand to steel 400 mm x 100 mm	Monotonic shear and shear reversal under constant normal stress	<ul style="list-style-type: none"> Found that slippage and rolling of sand particles occurs during shear, on rough steel surface Found that only slippage occurs on smooth steel surface Found that large volume changes of sand occur near the contact with the steel surface Reported shear band formation on rough surfaces, not on smooth surfaces
Uesugi, Kishida and Tsubakihara (1989)	Sand to steel 100 mm x 40 mm	Cyclic shear under constant normal stress	<ul style="list-style-type: none"> Confirmed observations on shear band formation by Uesugi, Kishida and Tsubakihara (1988)
Uesugi, Kishida and Uchikawa (1990)	Sand to concrete 100 mm x 40 mm	Cyclic shear under constant normal stress	<ul style="list-style-type: none"> Observed similar behavior as in sand-to-steel interfaces Found that large volume changes of the sand occur in the vicinity of the concrete surface Observed shear band formation Reported that actual sliding displacement between sand particles and concrete is small Found a direct relationship between concrete roughness and friction coefficient
Evgin and Fakharian (1996)	Sand to steel 100 mm x 100 mm	Monotonic shear under constant normal stiffness	<ul style="list-style-type: none"> Developed the <i>Cyclic 3-D Simple Shear Interface</i> (C3DSSI), from a previous DSB version by Fakharian and Evgin (1996), capable of applying shear stresses in two orthogonal directions
Fakharian and Evgin (1997)	Sand to steel 100 mm x 100 mm	Cyclic shear with constant normal stiffness	<ul style="list-style-type: none"> Studied the interface shear strength degradation during cyclic shear under constant normal stiffness
Desai and Rigby (1997)	Clay to steel and clay to rock 165-mm diameter	Cyclic shear under constant normal stress	<ul style="list-style-type: none"> Presented the CYMDOF-P device, with pore pressure measurement capabilities, which is still under development.

Ring shear devices have been used by Huck and Saxena (1981) and Yoshimi and Kishida (1981) for sand-to-concrete and sand-to-steel interface testing. According to Stark, Williamson, and Eid (1996), ring shear devices have the following advantages: (a) unlimited interface displacement, making possible the determination of residual interface shear strengths, (b) shearing along the same interface throughout the test and, and (c) no eccentric loading during shear.

The principal disadvantages of the ring shear device are as follows: (a) complicated sample preparation procedures, especially for sand-to-concrete interfaces

(Kishida and Uesugi 1987), (b) relatively narrow soil samples, which may induce scale effects in some interface tests, (c) nonuniform radial distribution of shear stresses (Stark, Williamson and Eid 1996), and (4) unknown actual sliding displacement at the interface in the case of rigid ring shear devices.

2.1.4 Summary of previous findings on interface testing and interface behavior

There seems to be no universal agreement on procedures and data interpretation for interface testing. Furthermore, little progress on the understanding of the behavior of sand-to-concrete interfaces has occurred since the work of Clough and Duncan (1971) and Peterson et al. (1976). However, several observations, which have been substantiated in more recent investigations, may be considered of special interest for this research:

- a. The Clough and Duncan (1971) hyperbolic formulation is an appropriate model for the behavior of interfaces under constant normal stress and monotonic shearing (Peterson et al. 1976; Acar, Durgunoglu, and Tumay 1982; Lee et al. 1989).
- b. The main factors affecting interface behavior under monotonic loading are interface roughness, soil density, particle angularity, and normal stress (Peterson et al. 1976; Bosscher and Ortiz 1987; Hryciw and Irsyam 1993; Uesugi and Kishida 1986a; Kishida and Uesugi 1987; Uesugi, Kishida, and Tsubakihara 1988).
- c. In all the studies reviewed, displacement softening behavior was reported in interface tests between dense sand and structural materials.
- d. The interface peak friction angle increases steadily with increasing interface roughness until a maximum is reached (Peterson et al. 1976; Bosscher and Ortiz 1987; Uesugi and Kishida 1986a; Kishida and Uesugi 1987; Uesugi, Kishida, and Uchikawa 1990). This maximum is very close to or slightly lower than the internal peak friction angle of the sand. The roughness value at which this maximum value is reached is commonly referred to as the *critical roughness*. There are several criteria to quantify the interface roughness, of which none seems to have been adopted universally. Therefore, the critical roughness values are given in units that are not consistent among different investigators.
- e. Dilation occurs during shear of a dense sand-to-concrete, or dense sand-to-steel interface (Peterson et al. 1976). The dilative deformations of sand in contact with a rough surface are usually large, and take place in a thin zone within the soil adjacent to the interface (Hryciw and Irsyam 1993; Uesugi, Kishida, and Tsubakihara 1988). Dilation is followed by the development of large displacements along the interface. In loose sand samples, compression occurs during shear and is also followed by large displacements. This zone of large volumetric changes and interface displacements is commonly known as the *shear band*. Shear band formation has not been observed on smooth interfaces.

- f. Interface behavior during cyclic shear is affected by interface roughness, soil density, particle angularity, normal stress, displacement and stress amplitude, and number of loading cycles (Desai, Drumm, and Zaman 1985; Uesugi, Kishida, and Tsubakihara 1989; Uesugi, Kishida, and Uchikawa 1990).
- g. Distortions of the sand mass above the interface are significant; consequently, the actual displacement at the interface cannot be determined in DSB devices (Uesugi and Kishida 1986a, 1986b).

2.1.5 The Large Direct Shear Box (LDSB)

Shallenberger and Filz (1996) developed a Large Displacement Shear Box (LDSB) especially designed for interface testing. The LDSB is essentially a DSB-type device with the capability to handle interfaces as large as 711 by 406 mm (28 by 16 in.). The device is capable of attaining interface displacements as large as 305 mm (12 in.) and has been used extensively for clay-to-high-density polyethylene (HDPE) geomembrane testing. The soil sample is prepared in a soil box and pressed against a moveable upper assembly containing the specimen of HDPE or structural material. An isolated test section 305 by 305 mm (12 by 12 in.) in the upper assembly, located at the center of the interface, allows the measurement of normal and shear stresses away from the edges.

Shallenberger and Filz (1996) pointed out the advantages of the LDSB over conventional devices: (a) end effects are negligible, (b) the maximum displacement of 305 mm (12 in.) allows the determination of the interface residual shear strength, and (c) no eccentric normal loads are generated during shear.

The principal disadvantage of this apparatus is that sample preparation is a time-consuming process due to the large size of the interface. Additionally, the distortion deformations of the soil sample cannot be measured; therefore, the actual interface displacements are not known.

The large displacement capabilities of the LDSB, which permit staged tests with several steps of normal pressure increments, and its reduced end effects are the main reasons for its use in this investigation. Several modifications were implemented in the device to accommodate sand-to-concrete interfaces and perform shear stress reversals. A more detailed description of the LDSB will be provided later in this report.

2.2 Interface Modeling

In SSI analyses, the soil-structure interface is represented by interface elements. Several kinds of interface elements have been developed to model the behavior of the interface under certain loading conditions. When an interface element is developed for a particular problem, an appropriate constitutive relationship must be adopted. The constitutive relationship should be capable of modeling the interface response under the expected loading conditions.

A literature review of interface elements and interface constitutive models has been performed for this investigation. The most significant contributions pertinent to this research are outlined in the following sections.

2.2.1 Interface elements

Interface elements were first introduced by Goodman, Taylor, and Brekke (1968) for finite element analysis of jointed rock masses. They were soon extended to SSI analyses of retaining walls by Clough and Duncan (1971) and Duncan and Clough (1971). The adoption of interface elements represented a significant improvement over previous methods, which assumed either of two conditions: a perfectly rough interface with no slip between soil and structure, or a perfectly smooth interface with no shear stresses developed (Clough and Duncan 1971).

The element developed by Goodman, Taylor, and Brekke (1968) is commonly referred to as *joint element* or *zero-thickness interface element*. It is a four-node element of zero thickness as illustrated in Figure 2-2. In their derivation of the joint element stiffness matrix, they used a very simple constitutive law consisting of constant values for both the shear stiffness and the normal stiffness:

$$k_n \cdot \Delta_n = \sigma_n \quad (2-1)$$

$$k_s \cdot \Delta_s = \tau \quad (2-2)$$

where

k_n = normal interface stiffness

Δ_n = displacement normal to the interface

σ_n = normal stress acting on the interface

k_s = interface shear stiffness

Δ_s = displacement along the interface

τ = interface shear stress

In this formulation, coupling effects between tangential and normal displacements along the interface are excluded, as evidenced by zero off-diagonal elements in the stiffness matrix.

Clough and Duncan (1971) observed that compressive stresses normal to the interface would induce overlapping among soil and structural elements adjacent to the interface. To minimize this effect, they proposed assigning a high value of normal stiffness to the joint element under compression. Similarly, for interface elements under tension, they proposed assigning a small value of normal stiffness to minimize the development of tensile stresses at the interface.

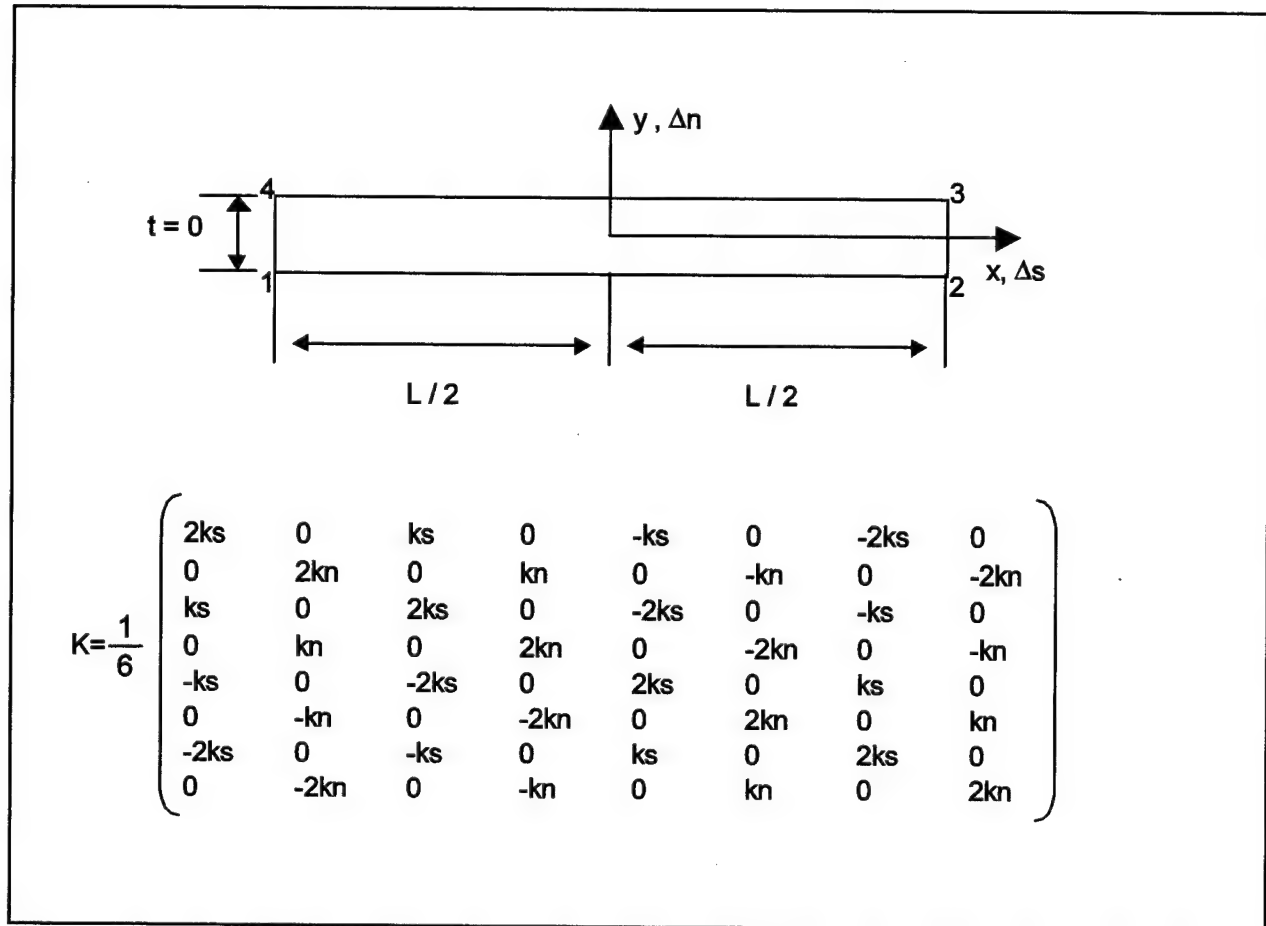


Figure 2-2. Goodman, Taylor, and Brekke (1968) zero thickness interface element and corresponding element stiffness matrix

A continuous development of improved joint elements has taken place since the original formulation by Goodman, Taylor, and Brekke (1968). Heuze and Barbour (1982) presented a review of the historical development of joint elements for analyses of jointed rock masses; most were linear and one-dimensional and did not include rotational degrees of freedom. A limited number of joint elements were developed to model displacement softening and dilation at the joints.

Morrison (1995) also presented a comprehensive review of previous investigations of interface elements. Many of the studies he reviewed described numerical integration problems arising from the use of interface elements of high normal stiffness adjacent to softer soil elements. Morrison (1995) studied an interface element formulation with relative degrees of freedom proposed by Wilson (1975) to minimize such numerical problems. Morrison (1995) showed that the Wilson (1975) formulation is not necessary if Newton-Raphson iteration is used to find the interface displacements resulting from each load increment.

Heuze and Barbour (1982) presented a zero-thickness axisymmetric joint element for finite element analyses of footings on rock, underground openings, and excavations, where dilation effects play an important role. Although no coupling terms are included in the formulation of the element, the dilation-induced normal stresses are determined explicitly based on the stiffness of the surrounding rock and the dilation angle. Yuan and Chua (1992) presented a more general formulation of the Heuze and Barbour (1982) axisymmetric element.

Matsui and San (1989) proposed an elastoplastic joint element to model interface behavior of rock joints. It accounts for the generation of normal stresses during shear, due to fully restrained dilation of the joint, in a way similar to that of Heuze and Barbour (1982).

Desai et al. (1984) and Zaman, Desai, and Drumm (1984) presented the *thin layer interface* element. It is based on the idea that interface behavior is controlled by a narrow band of soil adjacent to the interface with different properties from those of the surrounding materials. The thin layer element is treated mathematically as any other element of the finite element mesh and is assigned special constitutive relations. The Desai et al. (1984) thin layer element prevents overlapping between structural and geological materials due to its finite thickness. Desai, Muqtadir and Scheele (1986) implemented the thin layer element in interaction analyses of grouted anchors-soil systems.

Wong, Kulhawy, and Ingraffea (1989) implemented a three-dimensional version of the thin layer interface element for SSI analyses of drilled shafts under generalized loading.

2.2.2 Interface constitutive models

A number of interface constitutive models have been developed by different authors. Depending on the type of analysis performed, the interface behavior may be represented by a quasi-linear or a nonlinear model. Quasi-linear models consider a constant value of stiffness over a range of interface displacements, until yield is reached. After yield, a low constant value of stiffness is usually assigned to the interface. Quasi-linear models have been used by Goodman, Taylor, and Brekke (1968); Desai, Muqtadir, and Scheele (1986); Matsui and San (1989); and Wong, Kulhawy, and Ingraffea (1989).

In nonlinear models, the interface shear stress-displacement relationship is represented by a mathematical function of higher degree. The interface shear stiffness changes during shear, depending on the magnitude of the displacement and any other factor included in the model. Nonlinear models have been used by Clough and Duncan (1971); Zaman, Desai, and Drumm (1984); and Desai, Drumm, and Zaman (1985) among others.

Clough and Duncan (1971) developed the hyperbolic model for interfaces. This model has been used extensively in SSI analyses and design of geotechnical structures, including analyses of lock wall behavior (Ebeling et al. 1993; Ebeling and Mosher 1996; Ebeling, Peters, and Mosher 1997; Ebeling and Wahl 1997;

and Ebeling, Pace, and Morrison 1997). The hyperbolic model, described in detail in the next section, often provides an accurate approximation to the interface response under monotonic loading at constant normal stress. It has not been extended to cyclic loading or to staged shear.

Zaman, Desai, and Drumm (1984) developed a constitutive model for cyclic loading of interfaces. It is based on a polynomial formulation that includes the effects of the number of cycles, amplitude of shear displacements, and normal stress on interface response.

Desai, Drumm, and Zaman (1985) presented a *modified Ramberg-Osgood* model for interfaces under cyclic loading. The model accounts for shear stress reversals, hardening or degradation effects with number of load cycles, normal stress, relative density of the sand, and maximum displacement amplitude. Uesugi and Kishida (1985) observed that the modified Ramberg-Osgood model yields inconsistent results for shear stresses close to failure.

In all the interface models described previously, the interface yield stress is determined by the Mohr-Coulomb criterion (Goodman, Taylor, and Brekke 1968; Clough and Duncan 1971; Zaman, Desai, and Drumm 1984; Desai, Muqtadir, and Scheele 1986; and Wong, Kulhawy, and Ingraffea 1989).

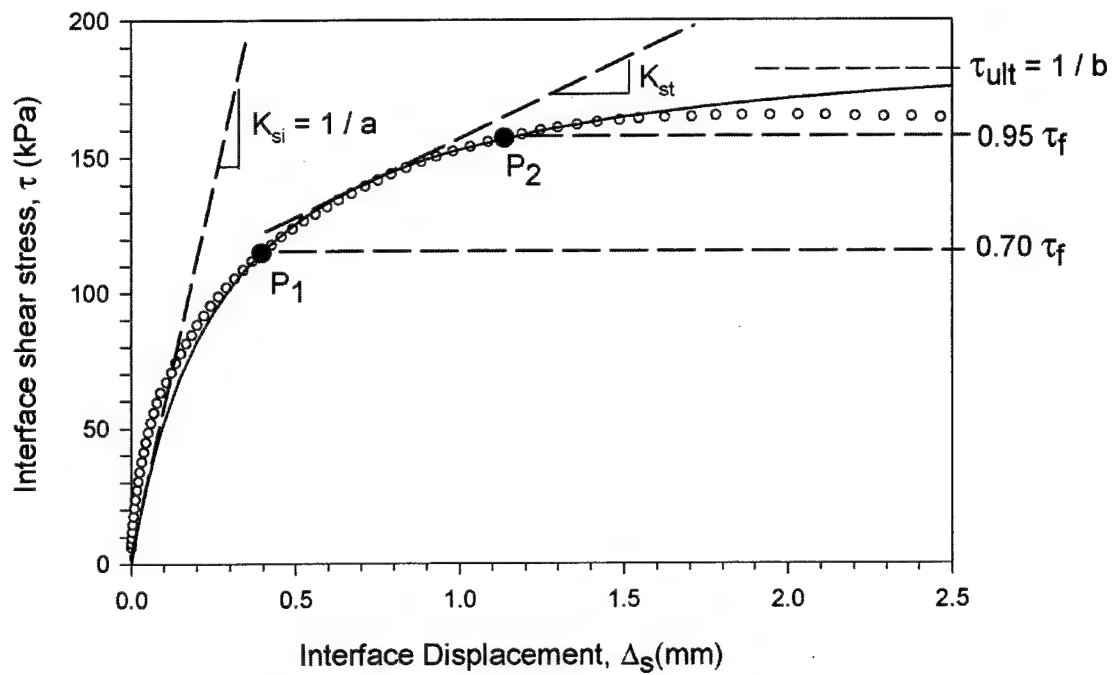
Postpeak displacement softening has been included in the formulation of some quasi-linear models that are used in conjunction with iterative finite element procedures (Wong, Kulhawy, and Ingraffea 1989). Esterhuizen (1997) presented a nonlinear constitutive formulation for clay-HDPE interfaces that accounts for work-softening behavior of the interface.

Coupling between normal and shear deformations is not included in any of the constitutive formulations found in the literature. Changes in normal stress during shear, due to restrained dilation of rock joints, are accounted for in the models proposed by Heuze and Barbour (1982) and Matsui and San (1989). This was accomplished by including an explicit formulation relating changes in normal stresses with shear displacement, dilation angle, and elastic properties of the adjacent rock mass.

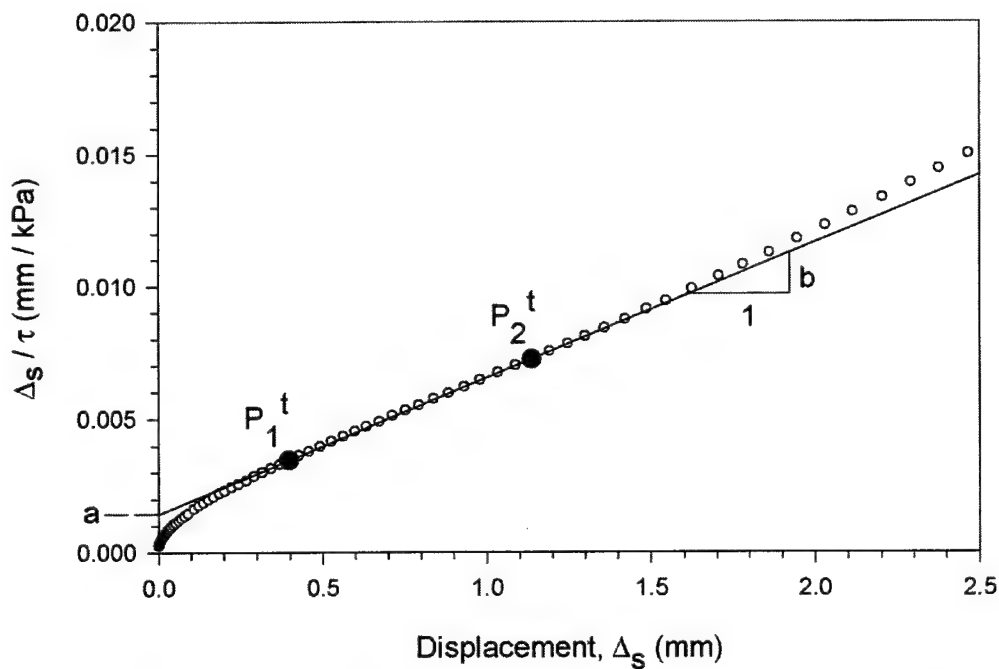
2.2.3 The hyperbolic model

Duncan and Chang (1970) presented a hyperbolic model for soil behavior following previous work by Kondner (1963) and Kondner and Zelasko (1963). The hyperbolic model was extended to interfaces by Clough and Duncan (1969, 1971) and implemented into the Goodman, Taylor, and Brekke (1968) joint element formulation.

Figure 2-3 illustrates the basic aspects of the Clough and Duncan (1971) hyperbolic model for interfaces. A hyperbola, shown in Figure 2-3a, has been used to fit a set of data from an interface shear test. The equation of the hyperbola can be written as:



a. Comparison between test data and the hyperbolic model



b. Transformed plot and determination of hyperbolic parameters a and b

Figure 2-3. Application of the Clough and Duncan (1971) interface hyperbolic model to a typical set of test data

$$\tau = \frac{\Delta_s}{a + b \cdot \Delta_s} \quad (2-3)$$

in which a and b are the parameters evaluated to fit the hyperbola to the experimental data. Equation 2-3 can be rewritten as:

$$\frac{\Delta_s}{\tau} = a + b \cdot \Delta_s \quad (2-4)$$

Figure 2-3b shows the same test data of Figure 2-3a, plotted in terms of Δ_s/τ and Δ_s . This is called the *transformed plot*. If the interface shear stress-displacement behavior follows a hyperbolic relationship, the transformed plot will be a straight line. The hyperbolic parameters a and b of Equation 2-4 will be the intercept and slope of this straight line, respectively. The actual interface test data do not exactly follow a hyperbolic relationship, and the transformed plot must then be fitted to a straight line to determine the hyperbolic parameters a and b .

Duncan and Chang (1970) observed that the transformed plot for strength test data in soils diverged from a straight line, both at low and high values of strain. They concluded that the best fit to the data was obtained when the hyperbola intersected the test data at 70 and 95 percent of the strength. Clough and Duncan (1971) adopted this same criterion for interface shear tests. Figure 2-3a shows points P_1 and P_2 corresponding to a mobilized strength of 70 and 95 percent, respectively. Points P_1' and P_2' are the corresponding representations of P_1 and P_2 in the transformed plot. A straight line is drawn between P_1' and P_2' , and the hyperbolic parameters a and b of Equation 2-4 are found as illustrated in the figure.

The hyperbolic shear stress-displacement relationship, calculated from Equation 2-3, is presented in Figure 2-3a. It can be seen that the model intersects the test data at points P_1 and P_2 .

One of the advantages of the Clough and Duncan (1971) model is that the hyperbolic parameters a and b are physically meaningful. The value of a is the reciprocal of the initial shear stiffness K_{si} of the interface. The value of b is the reciprocal of the asymptotic shear stress value τ_{ult} of the hyperbola. The value of τ_{ult} is usually larger than the actual interface shear strength τ_f . To address this discrepancy, Clough and Duncan (1971) defined the failure ratio R_f as:

$$\tau_f = R_f \cdot \tau_{ult} \quad (2-5)$$

Clough and Duncan proposed that the value of initial interface stiffness be calculated using the following expression:

$$K_{st} = K_I \cdot \gamma_w \cdot \left(\frac{\sigma_n}{p_a} \right)^{n_j} \quad (2-6)$$

where

K_I = dimensionless stiffness number

γ_w = unit weight of water

p_a = atmospheric pressure

n_j = dimensionless stiffness exponent

From a series of interface tests under different normal stresses, the hyperbolic parameter a , and consequently K_{st} , can be evaluated for each normal stress. The stiffness number K_I and stiffness exponent n_j can then be calculated by fitting K_{st} and σ_n data to Equation 2-6.

For interfaces without an adhesion intercept, the shear strength of the interface τ_f can be expressed as:

$$\tau_f = \sigma_n \cdot \tan \delta \quad (2-7)$$

where δ is the angle of interface friction, which can be also determined from a series of interface shear tests at different normal stresses σ_n . Finally, by substituting Equations 2-5, 2-6, and 2-7 into Equation 2-3, the following hyperbolic expression is obtained:

$$\tau = \frac{\Delta_s}{\frac{1}{K_I \cdot \gamma_w \cdot \left(\frac{\sigma_n}{p_a} \right)^{n_j}} + \frac{R_{ff} \cdot \Delta_s}{\sigma_n \cdot \tan \delta}} \quad (2-8)$$

For incremental analyses, it is necessary to determine the tangent stiffness value K_{st} at any point during shear. By differentiating Equation 2-8 with respect to Δ_s the following expression is obtained:

$$K_{st} = K_I \cdot \gamma_w \cdot \left(\frac{\sigma_n}{p_a} \right)^{n_j} \cdot \left(1 - \frac{R_{ff} \cdot \tau}{\sigma_n \cdot \tan \delta} \right)^2 \quad (2-9)$$

If the stress level SL is defined as:

$$SL = \frac{\tau}{\sigma_n \cdot \tan \delta} \quad (2-10)$$

the tangent stiffness K_{st} can be expressed as:

$$K_{st} = K_I \cdot \gamma_w \cdot \left(\frac{\sigma_n}{p_a} \right)^{n_j} \cdot (1 - R_{ff} \cdot SL)^2 \quad (2-11)$$

Important advantages of the Clough and Duncan (1971) hyperbolic model are as follows: (a) nonlinearity of the interface shear stress-displacement relationship is well represented by Equations 2-8 or 2-11, (b) the hyperbolic parameters have a clear physical meaning, and (c) the method is easy to implement in SSI analyses.

The Clough and Duncan (1971) hyperbolic model for interfaces has some important limitations regarding its use in SSI analyses of earth retaining structures, such as lock walls. The hyperbolic formulation does not model displacement softening of the interface and does not include any coupling effects between shear and normal displacements. It has not been extended to cases in which the shear and normal stresses both change, and it has not been fully implemented for cases of cyclic loading and shear stress reversals.

2.3 SSI Analyses of Retaining Walls

2.3.1 Review of previous work

The first systematic SSI analyses of retaining wall behavior were presented by Clough and Duncan (1969, 1971) and Duncan and Clough (1971). They used the hyperbolic constitutive relationship by Duncan and Chang (1970) to model the behavior of the backfill and extended it to model the behavior of the wall-to-soil interfaces. Relative movement at the interfaces was achieved by the use of the joint element developed by Goodman, Taylor, and Brekke (1968).

In their analyses of Port Allen and Old River U-frame locks, Clough and Duncan (1969) and Duncan and Clough (1971) demonstrated the importance of close modeling of the construction stages of the lock and backfill placement. They demonstrated that a simple linear elastic model for the soil and gravity turn-on analyses are not adequate to model the behavior of the soil-lock system. They also proved that the downdrag or vertical shear force exerted by the backfill on the wall has an important influence on the behavior of U-frame locks. Their work provided fundamental understanding of previously unknown aspects of lock wall behavior.

Clough and Duncan (1971) presented a systematic approach to SSI analyses of retaining wall behavior. They observed the importance of modeling the different stages of construction of the wall and placement of the backfill in SSI

analyses. They found that when the stages of placement of the backfill were closely modeled, the resulting horizontal and vertical loads acting on the wall were substantially larger than those obtained using classical earth pressure theories. The results of these analyses were consistent with some previous experimental work and field observations.

Ebeling, Duncan, and Clough (1990) performed a comparison between results from conventional equilibrium and finite element analyses of several hypothetical gravity walls founded on rock. Their analyses were performed with the backfill placement analysis option incorporated in SOILSTRUCT (Clough and Duncan 1969). A range of possible values of shear stiffness was assumed at the interfaces between the wall and the backfill, and between the backfill and the rock. Ebeling, Duncan, and Clough (1990) concluded that the magnitude of downdrag force is significantly affected by the concrete-to-backfill and rock-to-backfill shear stiffness values. They also concluded that conventional equilibrium analyses neglect the true process of soil-structure interaction and tend to yield very conservative results.

Ebeling et al. (1992) performed analyses of several hypothetical gravity walls founded on rock. The hypothetical walls were based on several representative examples of existing lock walls. Ebeling et al. (1992) found that conventional equilibrium analyses are very conservative because they do not account for the stabilizing effect of the downdrag forces generated by settlement of the backfill. At the time of their work, it was not known whether these vertical shear forces persisted under field conditions, and if they could be relied upon for the stability of the structure. Ebeling et al. also indicated that the behavior of retaining structures founded on soil might differ substantially from that of structures founded on rock. In soil-founded structures, the concrete-to-foundation interface is not bonded as in the case of concrete-to-rock interfaces, and greater relative interface displacements may occur, inducing more redistribution of the earth pressures.

Ebeling et al. (1993), Ebeling and Mosher (1996), and Ebeling, Peters, and Mosher (1997) presented the results of extensive SSI analyses for the soil-founded Red River Lock and Dam No. 1. A reinforced soil berm was recommended, among other alternatives, as a solution to problems induced by siltation of the lock. The SSI analysis procedures were validated against instrumentation measurements from the lock taken at the end of construction and at several operational stages. Their analyses revealed that important changes in normal stresses may occur at the soil-to-structure interface during backfill placement and operation of the lock, and underscored the importance of selecting the appropriate interface stiffness values for these loading conditions. They also noted that conventional equilibrium analyses are inadequate for the design of this type of structure.

A simplified procedure was presented in Appendix F of EM 1110-2-2100 (HQUSACE, in preparation) for evaluating the downdrag force on retaining walls founded on rock. This procedure is described in detail in the following section. It was observed that measurements in existing lock walls, as well as previous experimental data from the IRW facility at Virginia Tech (Filz 1992), showed that downdrag forces were significant and tended to increase with time.

For the case of U-frame locks and retaining structures founded on soil, the EM recommended performing complete SSI analyses. The simplified procedure has also been described in detail by Ebeling, Pace, and Morrison (1997).

Ebeling and Wahl (1997) presented the results of SSI analyses of the proposed North Lock wall at McAlpine Locks. They determined that the downdrag force was significant, and that it could be substantially affected by the response mode of the interface to unload-reload cycles. Further details were given in Chapter 1 of this report.

Filz and Duncan (1997) and Filz, Duncan, and Ebeling (1997) presented a theory for the quantification of the downdrag forces on the back of nonmoving retaining walls and described previous large-scale retaining wall tests and field measurements. They observed that post-construction settlement causes an increase in the downdrag on the back of the wall. They cited measurements at Eibach Lock in Germany, where large vertical shear forces were persistent for 10 years under repeated filling and emptying cycles and temperature fluctuations. The measured K_v remained at an approximately constant average value of 0.30. These vertical shear forces cause an important reduction in the lateral earth pressures acting on the wall.

2.3.2 Simplified procedure for calculating the downdrag force

There are some cases in which it is possible to estimate the downdrag force acting on the back of a retaining wall without performing sophisticated SSI analyses. In this section, a simplified procedure is presented for calculating the downdrag force as described by Ebeling, Pace, and Morrison (1997). It applies to retaining walls with nonyielding backfills. This is the case for rock-founded gravity retaining walls with engineered backfills that do not creep, such as soils classified as SW, SP, GW, and GP according to the Unified Soil Classification System (American Society for Testing and Materials (ASTM) 1990). It also applies to select SM backfills with nonplastic fines that do not creep. This method is based on the results of analyses performed on walls with geometrical configurations that are representative of many, but not all, Corps of Engineers rock-founded lock walls.

The simplified procedure was first reported in Engineer Technical Letter (ETL) 1110-2-352 (HQUSACE 1994). Ebeling, Pace, and Morrison (1997) presented an improved version of the original procedure, based on additional SSI analyses on rock-founded gravity walls (Filz, Duncan, and Ebeling 1997; Ebeling and Filz, in preparation). It is also described in Appendix F of EM 1110-2-2100 (HQUSACE, in preparation). This improved version is applicable to situations in which there is no water table behind the wall or when the groundwater level rises as the backfill is being placed.

The simplified procedure is based on the use of the vertical earth pressure coefficient K_v , defined in Chapter 1 of this report. Combining Equations 1-1 and 1-3, the vertical shear force F_v can be expressed as:

$$F_v = K_v \cdot \int_{heel}^{top} \sigma'_v dy \quad (2-12)$$

Figure 2-4 shows the vertical force F_v acting on a vertical plane, passing through the heel of a retaining wall with a hydrostatic water table. It also shows the diagram of vertical effective stress in the backfill. For this case, the vertical shear force can be expressed using the equation presented in ETL 1110-2-352 (HQUSACE 1994):

$$F_v = K_v \cdot \left[\frac{1}{2} \gamma_{moist} (D_1)^2 + \gamma_{moist} (D_1 D_2) + \frac{1}{2} \gamma_b (D_2)^2 \right] \quad (2-13)$$

where

γ_{moist} = moist unit weight of the backfill above the water table

D_1 = thickness of the backfill above the hydrostatic water table

D_2 = thickness of the submerged backfill above the heel of the wall

γ_b = buoyant unit weight of the submerged backfill

Equation 2-13 is valid for a horizontal backfill with no surcharge loads applied. Furthermore, Equation 2-13 applies only when the backfill is placed in a submerged condition or the groundwater level in the backfill rises concurrently with backfill placement. The case in which the groundwater level rises after construction is discussed later in this section. Filz, Duncan, and Ebeling (1997) and Ebeling and Filz (in preparation) expanded Equation 2-13 to include the effects of surcharge and sloping backfill. In the case of rock-founded gravity walls with the inclined backfill surface shown in Figure 2-5a, F_v is calculated using:

$$F_v = F_{v,soil} + F_{v,q} \quad (2-14)$$

where

$$F_{v,soil} = K_{v,soil} \cdot \left[\frac{1}{2} \gamma_{moist} (D_1)^2 + \gamma_{moist} (D_1 D_2) + \frac{1}{2} \gamma_b (D_2)^2 \right] \quad (2-15)$$

and

$$F_{v,q} = K_{v,q} \cdot q_s \cdot H \quad (2-16)$$

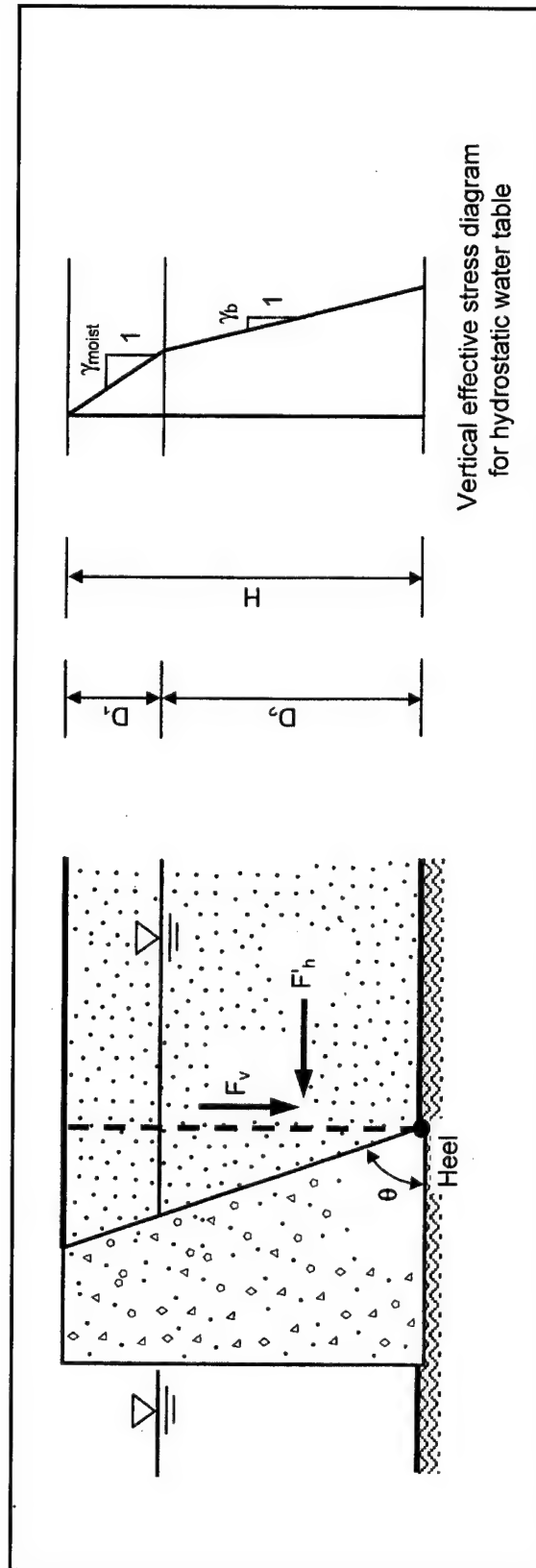
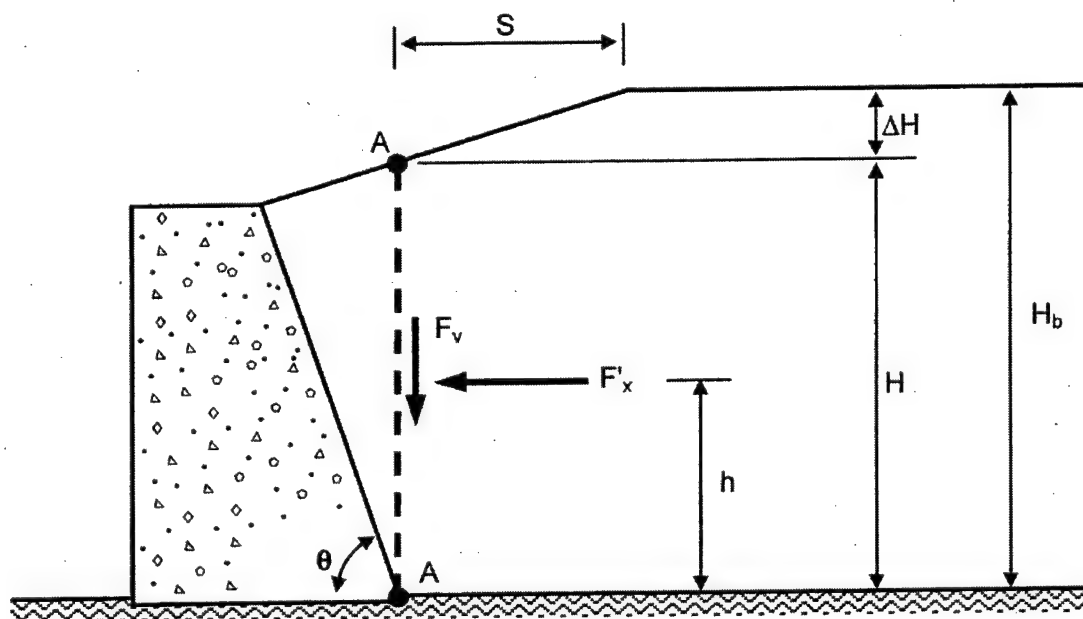
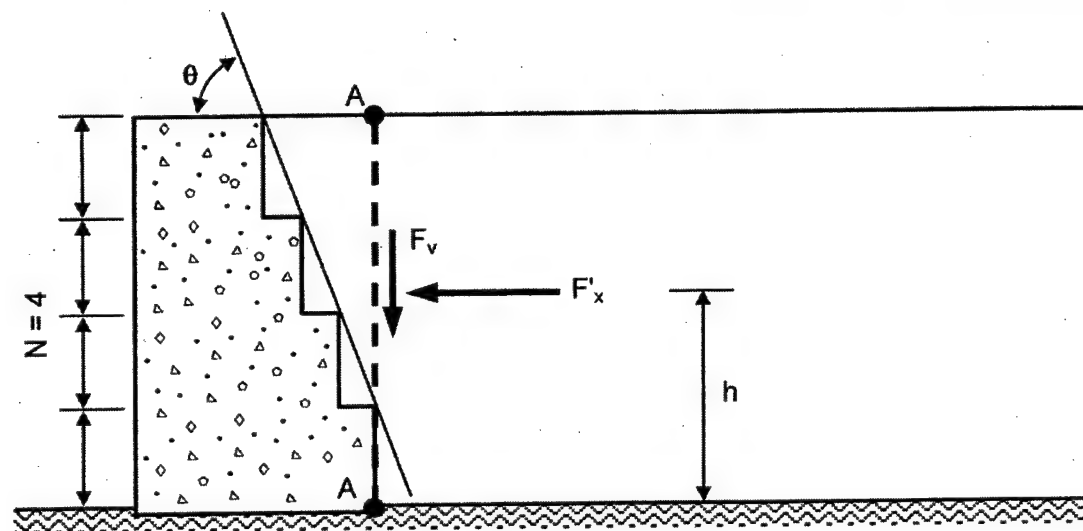


Figure 2-4. Vertical and effective horizontal earth pressure forces on vertical plane extending from the backfill from the heel of the monolith (adapted from ETL 1110-2-352 (HQUSACE 1994))



a. Mass concrete wall with a planar, sloping backside and an inclined backfill surface



b. Mass concrete wall with a stepped backside

Figure 2-5. Rock-founded retaining wall definition sketches (adapted from Filz, Duncan, and Ebeling 1997)

where

$K_{v,soil}$ = the vertical shear force coefficient for self-weight of the backfill

$K_{v,q}$ = the vertical shear force coefficient for sloping backfill and surcharge

q_s = applied surcharge pressure

H = height measured along the vertical plane A-A extending through the backfill, as indicated in Figure 2-5a.

The surcharge q_s can be determined from:

$$q_s = \Delta H \cdot \gamma_{moist} = [H_b - H] \cdot \gamma_{moist} \quad (2-17)$$

where H_b is the total backfill height measured as illustrated in the figure. The vertical shear force coefficient for self-weight of the backfill $K_{v,soil}$ is computed using:

$$K_{v,soil} = (1 - C_\theta \cdot C_N) \cdot K_{v,soil,ref} \quad (2-18)$$

where

C_θ = correction factor for inclination of the backside of a rock-founded gravity wall

C_N = correction factor for the number of steps in the backside of a rock-founded gravity wall

$K_{v,soil,ref}$ = reference value of $K_{v,soil}$ obtained for an inclination of the back of the wall θ of 90 deg

Calculation of the value for the number of steps in the back of a stepped wall N is shown in Figure 2-5b.

The vertical shear force coefficient for sloping backfill and surcharge, $K_{v,q}$, is given by:

$$K_{v,q} = C_S \cdot K_{v,q,ref} \quad (2-19)$$

where

C_S = correction factor for a rock-founded gravity retaining wall with an inclined backfill surface

$K_{v,q,ref}$ = reference value of $K_{v,q}$ obtained for a value of $S = 0$

S = horizontal distance from the vertical plane through the wall heel to the top of the backfill slope, as shown in Figure 2-5a

Given the density of the backfill and the height H as defined in Figure 2-5a, values for $K_{v,soil,ref}$ and $K_{v,q,ref}$ are obtained from Figures 2-6 and 2-7, respectively, using the curves designated as design curves. The data designated as FEM are based on the results of complete soil-structure interaction analyses using SOILSTRUCT-ALPHA (Ebeling and Filz, in preparation; or Filz, Duncan, and Ebeling 1997) and are for reference only. Correction factors C_θ , C_N , and C_S are given in Figure 2-8.

Filz, Duncan, and Ebeling (1997) presented a complete example calculation for F_v , using this simplified procedure for a 9-m- (30-ft-) high, step-tapered, rock-founded gravity wall. The wall was backfilled with dense sand and was subject to surcharge loading. No ground water table was present in the backfill. In this example, a 14 percent reduction in base width was obtained by including F_v in the analyses without compromising the design safety requirements. This illustrates the impact of including the downdrag force F_v in equilibrium calculations of a rock-founded gravity wall.

As pointed out by Ebeling, Pace, and Morrison (1997), a rebound of the backfill can occur during a post-construction rise in the groundwater level behind the wall. This may result in a reduction in the shear force F_v , as reported by Ebeling et al. (1993) and Ebeling and Mosher (1996) from their analyses of the Red River Lock No. 1. Ebeling, Pace, and Morrison (1997) indicated that, in this case, SOILSTRUCT-ALPHA (Ebeling, Duncan, and Clough 1990; Ebeling et al. 1992) can be used to perform the necessary SSI analyses to calculate F_v . These analyses must include the rise in water table and the corresponding "unloading" of the backfill (Ebeling et al. 1993; Ebeling and Mosher 1996). The work performed by Ebeling and Wahl (1997) for the new roller-compacted concrete lock at McAlpine Locks is a good example of this type of analysis.

The simplified procedure for the calculation of the downdrag force was extended to include a post-construction rise in the water table behind the wall. (Appendix F of EM 1110-2-2100 (HQUSACE, in preparation)). As illustrated in Figure 1-2b, a post-construction rise in the water table may induce rebound of the backfill, with the consequent reduction in the magnitude of the vertical shear force. The vertical shear force coefficient for backfill inundation can be calculated from:

$$K_v = K_{v,soil} \cdot C_{wt} \quad (2-20)$$

where C_{wt} is the correction factor for submergence of the backfill, which can be estimated from the following expression:

$$C_{wt} = \left(1 - \frac{D_2}{H} \right) \quad (2-21)$$

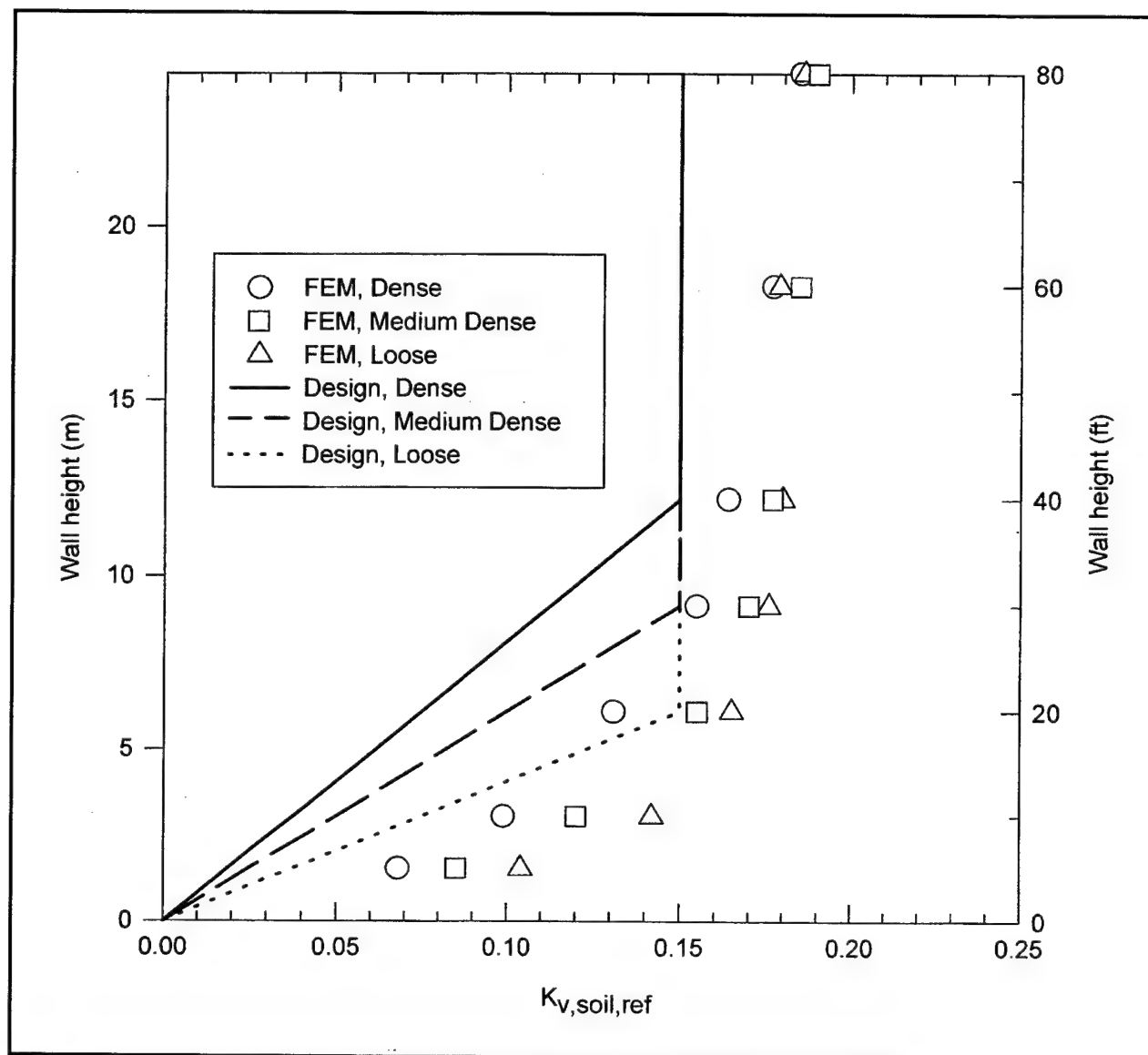


Figure 2-6. Values of $K_{v,soil,ref}$ recommended for design (adapted from Filz, Duncan, and Ebeling 1997)

For application of this method, the value of $K_{v,soil}$ for a “dry” backfill is calculated from Equation 2-18, and corrected using Equations 2-20 and 2-21. Equations 2-20 and 2-21 underestimate K_v if a post-construction rise in the water table takes place in a backfill that was placed partially submerged, or if there was a concurrent rise in the water table during backfill placement.

Figure 2-9 is a graphical representation of equation 2-21. It includes the results of a finite element analysis of the roller-compacted lock at McAlpine Locks (Ebeling and Wahl 1997). It can be seen that Equation 2-21 provides a conservative estimate of the value of the correction factor C_{wt} . This was confirmed by the results of the lock wall simulation performed for this investigation, as discussed in Chapter 5.

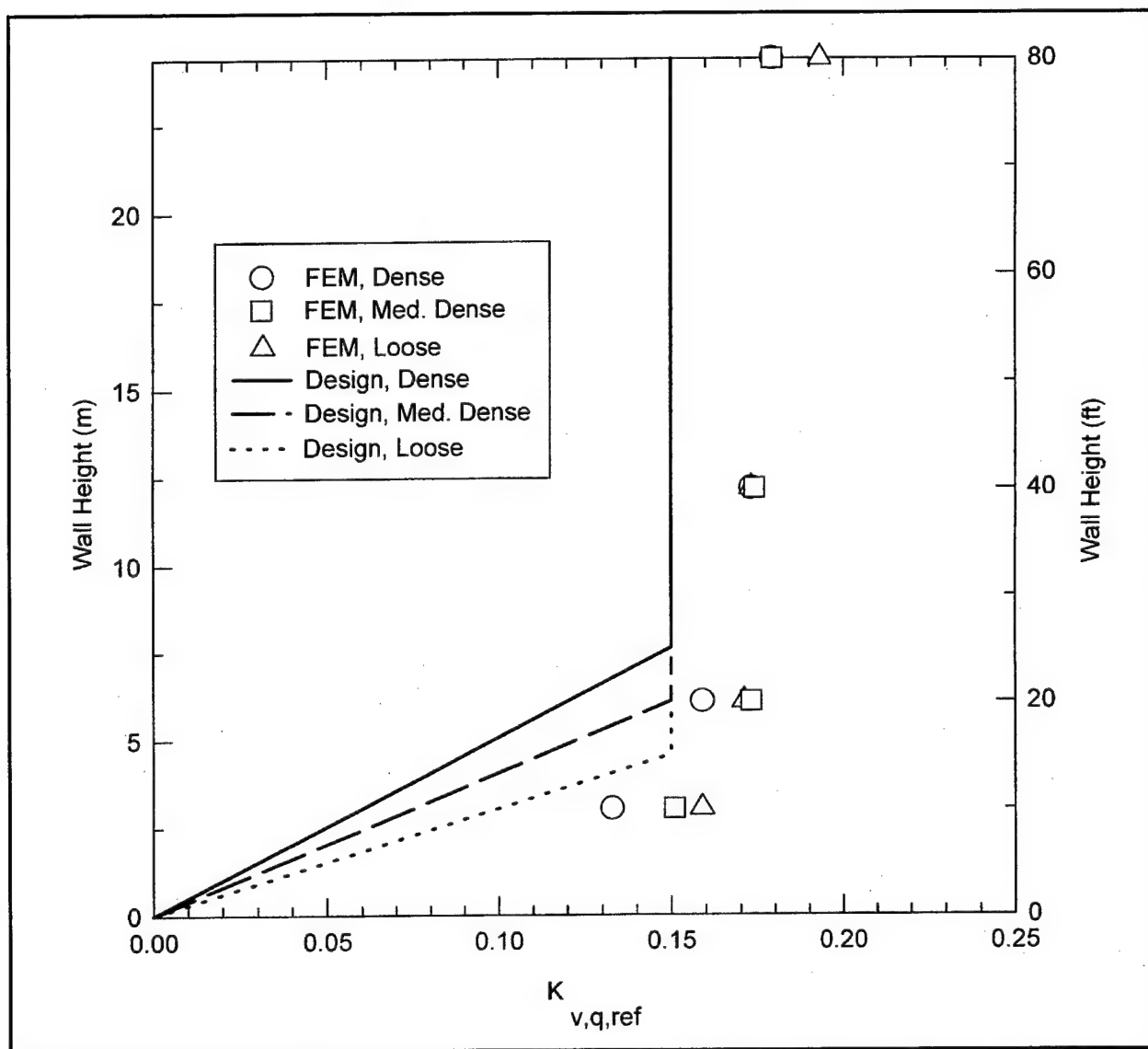


Figure 2-7. Values of $K_{v,q,ref}$ recommended for design (adapted from Filz, Duncan, and Ebeling 1997)

2.4 Summary

A literature review was carried out that included previous work on interface testing, interface modeling, and SSI analyses of retaining walls. The review focused on the most relevant issues for this investigation.

In the experimental work reviewed, the direct shear box (DSB) and the direct simple shear (DSS) are the devices most frequently used for testing of sand-to-concrete and sand-to-steel interfaces. Most of the previous work on interfaces investigated monotonic shear of the interface under constant normal stress. Some investigations have been published regarding cyclic shear of interfaces under conditions of constant normal stress or constant normal stiffness. No previous studies were found on interface response under staged shear.

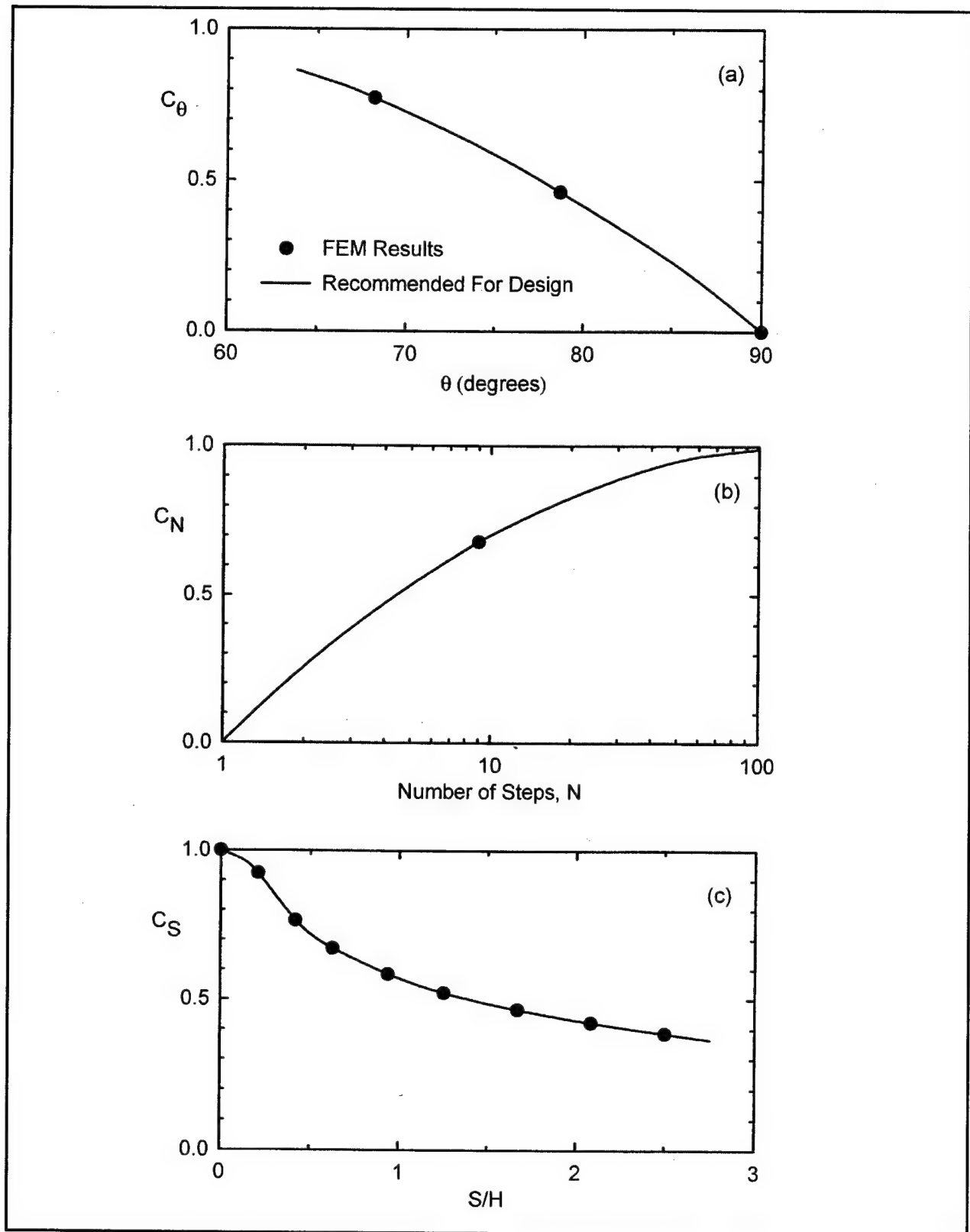


Figure 2-8. Values of the correction factors C_θ , C_N , and C_S (adapted from Filz, Duncan, and Ebeling 1997)

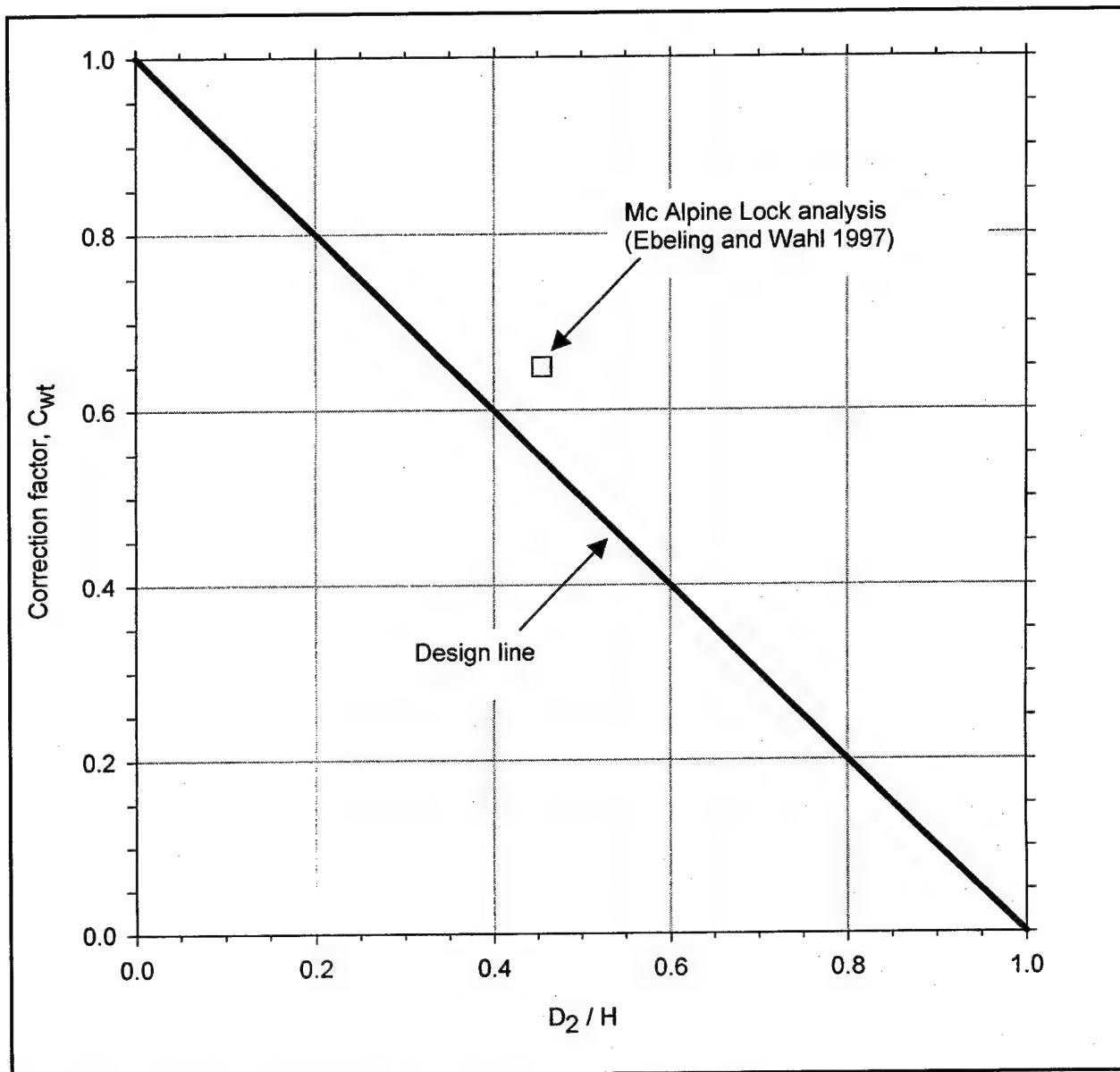


Figure 2-9. Values of the correction factor C_{wt} recommended for design (adapted from EM 1110-2-2100 (HQUSACE, in preparation))

All of the interface testing devices described in the literature present limitations. The interface sizes are limited and do not allow the determination of the residual interface strength in all cases. In addition, end effects may be present, inducing errors in the measurement of the pre-peak and peak interface response. The Large Direct Shear Box (LDSB) at Virginia Tech allows testing of interfaces as large as 711 by 406 mm under monotonic or cyclic shear. The size of the interface minimizes end effects and permits maximum interface displacements of 305 mm, allowing the determination of the residual interface strength. The large displacement capabilities of the LDSB also make possible shearing of the interface in several stages with changing normal stress.

Two types of elements are commonly implemented for modeling interfaces: the joint element and the thin layer element. The joint element, developed by Goodman, Taylor, and Brekke (1968), appears to be used most frequently due to the simplicity of its formulation.

Several models of interface response under shearing have been described in the literature. The hyperbolic formulation by Clough and Duncan (1971) was described in detail in this chapter. It has been widely used for modeling the interface response to monotonic shear under constant normal stress. It is a simple model that incorporates the most important aspects of interface behavior using parameters that have physical meaning. However, the Clough and Duncan (1971) hyperbolic formulation was not developed to model the interface response under cyclic loading or staged shear. None of the other interface models found in this literature review accounts for simultaneous changes in shear and normal stresses.

Several studies have been published regarding SSI analyses of retaining structures. From these studies, it may be concluded that the downdrag force acting on the back of a retaining wall can contribute significantly to the stability of the structure. In typical lock walls, the downdrag develops during fill placement. During this stage, the shear and normal stresses acting on the backfill-to-structure interface are changing simultaneously. During submergence and operation of the lock, the shear stresses may be reduced or even reversed. Hence, it is important to model accurately the interface response under staged shear, unloading-reloading, and shear reversals.

A detailed description of a simplified method described in Appendix F of EM 1110-2-2100 (HQUSACE, in preparation) to estimate the downdrag force was presented in this chapter. It is based on a number of SSI analyses of typical lock structures. The simplified method is useful to illustrate the importance of an adequate estimation of the downdrag force in design.

3 Laboratory Testing

A series of shear tests were performed on soil-to-concrete interfaces using the LDSB. The objective of the tests was to compile experimental data for development of the new interface model described in Chapter 4.

Before interface testing, a soil box was designed and fabricated and the LDSB was modified to accommodate soil-to-concrete interfaces. A concrete specimen was prepared with a representative surface texture, according to the results of a survey of existing concrete walls.

Two types of sands were used for the interface tests performed for this investigation: Density sand and Light Castle sand. Laboratory testing of these soils included index property tests such as gradation, minimum/maximum density, and specific gravity, as well as triaxial compression and consolidation tests to determine their mechanical properties.

This chapter is divided into five sections:

- a. *Soil properties.* Describes the gradation, mechanical properties, and hyperbolic parameter values of each of the soils used for interface testing.
- b. *Concrete specimen.* Summarizes the preparation procedures and properties of the concrete specimen used for interface testing.
- c. *Interface testing procedures.* Describes the equipment and procedures for testing the soil-to-concrete interfaces.
- d. *Interface testing program.* Lists and describes the types of interface tests.
- e. *Results of interface tests.* Summarizes the results obtained from the interface tests. These results formed the basis for development of the extended hyperbolic model.

3.1 Soil Properties

Two different sands were used for interface testing:

- a. *Density sand.* It is a fine-to-medium silica sand available commercially for in situ density determinations. Examination of the Density sand under

an optical microscope revealed that the grains are subrounded to rounded (ASTM 1993b), with a length-to-width ratio typically ranging from 1 to 2, as shown in Figure 3-1a.

- b. *Light Castle sand.* It is a fine-to-medium sand with subangular to angular grains with a length-to-width ratio ranging from 1.2 to 1.9, as shown in Figure 3-1b. This sand was used previously by Sehn and Duncan (1990) and Filz (1992) for testing at the IRW.

Table 3-1 summarizes the results of a series of laboratory tests performed to determine the gradation, maximum/minimum density, and specific gravity of the Density sand and Light Castle sand. The grain size distribution of these soils is presented in Figure 3-2. The Density sand is uniform, with grain sizes ranging from 0.2 to 0.9 mm, and has no fines. The Light Castle sand is also uniform, with grain sizes ranging from 0.1 to 2 mm, and has a negligible fraction of fines. Both soils classify as poorly graded sand SP (ASTM 1993a).

Table 3-1			
Characteristics of the Soils Used for Interface Testing			
Parameter¹	Value		Relevant Standard
	Density Sand	Light Castle Sand	
D ₁₀ , mm	0.3	0.25	D2487 (ASTM 1993a)
D ₃₀ , mm	0.42	0.32	
D ₆₀ , mm	0.55	0.45	
C _u	1.8	1.8	
C _c	1.1	0.9	
γ _{max} , kN/m ³	17.5	16.7	D4253 (ASTM 1993c)
γ _{min} , kN/m ³	15.1	13.7	D4254 (ASTM 1991)
G _s	2.65	2.66	D854 (ASTM 1992)
¹ Parameters are listed and defined in the Notation (Appendix F).			

3.1.1 Triaxial testing

Drained triaxial (CD) tests were performed to determine the internal friction angle and hyperbolic parameter values of the Density sand and the Light Castle sand for a range of relative densities D_r . Sets of medium dense and dense specimens were prepared by pluviation for each type of sand. After preparation, each sample was subjected to an internal manometric pressure of -15 to -20 kPa, which was gradually removed during application of the cell pressure. The samples were de-aired using CO₂, inundated with de-aired distilled water, and backpressure saturated. The samples in each set were consolidated under effective confining pressures ranging from 45 to 280 kPa. These values are representative of the estimated values of confining pressure within the backfill of typical lock walls. Shearing was performed at a strain rate of 0.25 %/min, which was found to be appropriate for pore pressure dissipation during previous trials.

The results of the tests are presented graphically in Figures A1 to A4 of Appendix A, and are summarized in Table 3-2. All the specimens exhibited dilation during shear and strain-softening after mobilization of the peak strength. The peak strength values measured during the tests defined curved strength

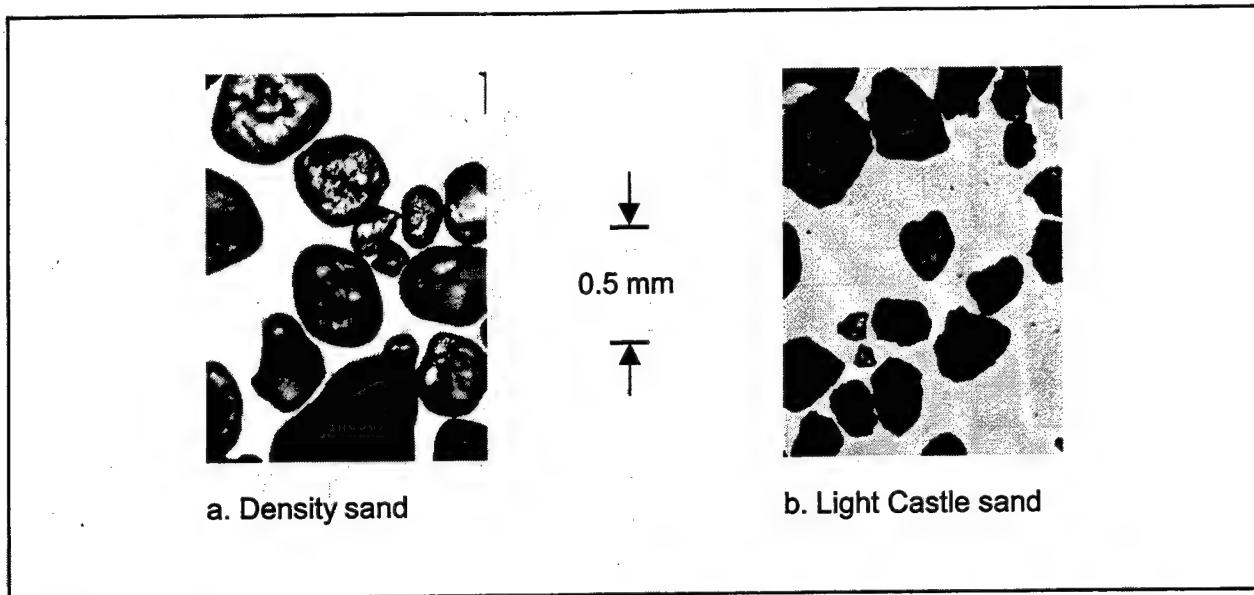


Figure 3-1. Microscopic view of the sands used for interface testing

envelopes. The peak friction angle value ϕ for a given effective confining stress σ'_3 can be calculated from the following expression (Duncan et al. 1980):

$$\phi = \phi_o - \Delta\phi \cdot \log_{10} \left(\frac{\sigma'_3}{p_a} \right) \quad (3-1)$$

where

ϕ_o = peak secant friction at a confining pressure of 101.4 kPa (1 atm)

$\Delta\phi$ = reduction in the peak friction angle value for a tenfold increase in σ'_3

The values of ϕ_o and $\Delta\phi$ for each of the soils tested are given in Table 3-2. The strength envelopes corresponding to the strength measured at a 15 percent strain are linear, and the corresponding friction angle ϕ_{cv} values are also given in Table 3-2.

Table 3-2 Summary of Results of CD Triaxial Tests				
Parameter ¹	Density Sand		Light Castle Sand	
	Medium Dense ($D_r = 41\%$)	Dense ($D_r = 92\%$)	Medium Dense ($D_r = 50\%$)	Dense ($D_r = 80\%$)
ϕ_o , deg	35	43.8	37.2	42.4
$\Delta\phi$, deg	2.5	3.2	1.4	6
ϕ_{cv} , deg	32.4	34.7	33.2	36.5
Figure	A1	A2	A3	A4
¹ Parameters are listed and defined in the Notation (Appendix F).				

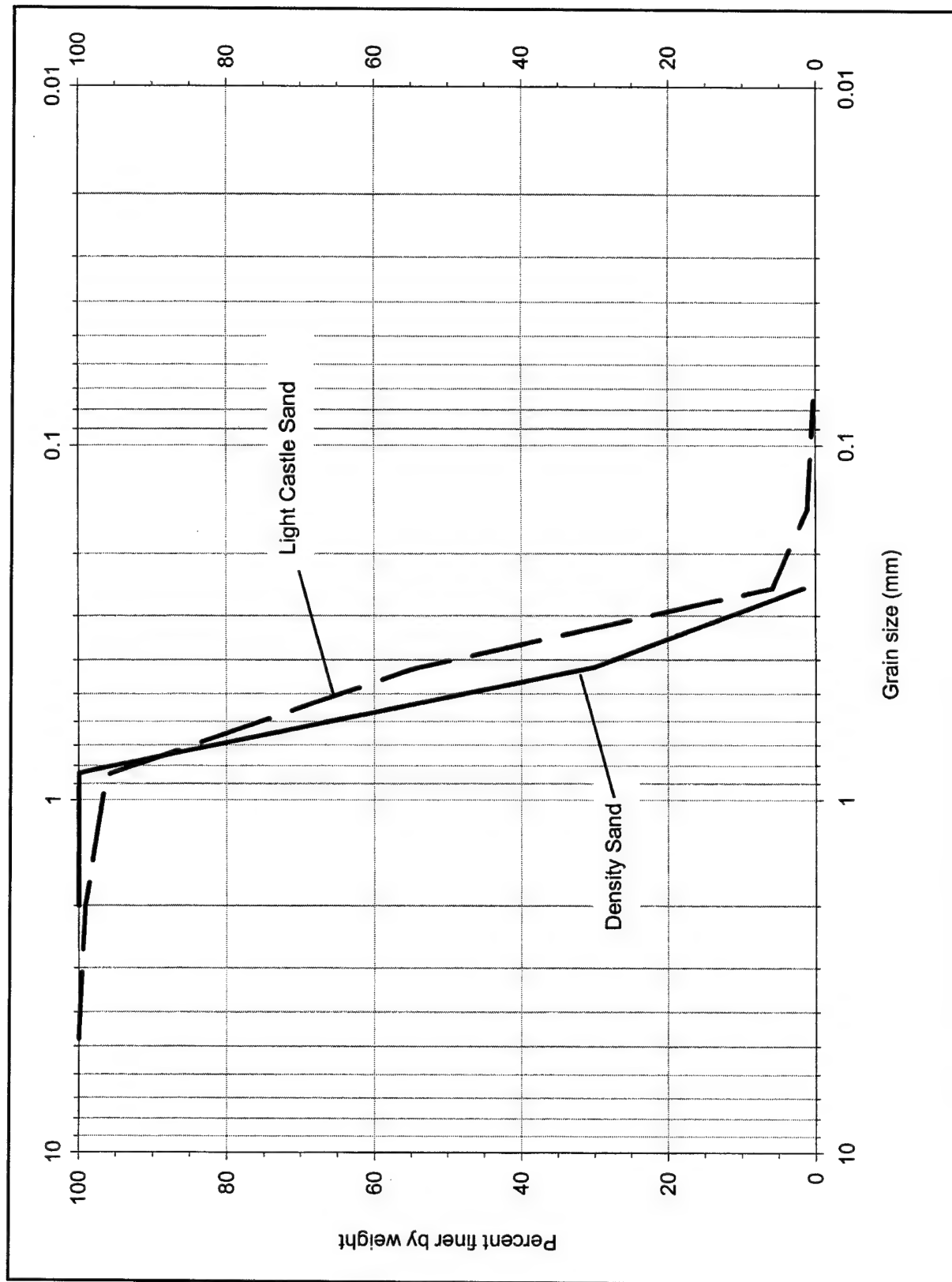


Figure 3-2. Grain size distribution of the soils used for interface testing

3.1.2 Consolidation testing

A set of consolidation tests was performed on the Density sand and Light Castle sand to provide additional data on their mechanical properties and determine their susceptibility to hydrocompression. Two specimens of each type of sand were prepared at different relative densities in a dry condition. Each specimen was consolidated under a series of vertical stress increments. Once a pre-determined stress was reached, the specimen was inundated. The ensuing hydrocompression, or vertical deformation induced by inundation, was measured. The results of these tests are presented in Figures A5 to A8 of Appendix A.

3.1.3 Hyperbolic parameters

Determination of the hyperbolic parameter values listed in Table 3-3 is described in detail in Appendix B. The triaxial and consolidation test data were used to obtain the parameter values for initial loading, according to the procedures described by Duncan et al. (1980). For the Light Castle sand, the parameter values for unloading-reloading were determined based on the unload-reload data from the consolidation tests following the method outlined by Clough and Duncan (1969).

Table 3-3 Hyperbolic Parameter Values of Soils Used for Interface Testing					
Hyperbolic Parameters ¹	Density Sand		Light Castle Sand		Reference Values for Soils of Similar Gradation (from Duncan et al. 1980)
	Medium Dense $D_r = 41\%$	Dense $D_r = 92\%$	Medium Dense $D_r = 50\%$	Dense $D_r = 80\%$	
K	780	1400	440	690	See Figure 3-3
n	0.62	0.63	0.48	0.79	0.26 - 0.79
R_f	0.852	0.850	0.880	0.813	0.77 - 0.97
K_b	530	915	290	660	See Figure 3-3
m	0.42	0.55	0.72	0.31	0.02 - 0.65
K_{ur}	—	—	880	1380	—
ϕ_o , deg	35	43.8	37.2	42.4	See Figure 3-3
$\Delta\phi$, deg	2.5	3.2	1.4	6	0 - 9
¹ Hyperbolic parameters are listed and defined in the Notation (Appendix F) and Appendix B.					

It is convenient to evaluate the accuracy of these parameter values by comparing them with values reported in the literature for soils of similar gradation. Table 3-3 shows ranges of values for the modulus exponent n , failure ratio R_f , bulk modulus exponent m , and the parameter $\Delta\phi$ reported by Duncan et al. (1980). The values of modulus number K , bulk modulus number K_b , and friction angle ϕ_o ,

presented in Table 3-3 for each of the soils, are compared in Figure 3-3 with typical values reported by Duncan et al. (1980). It can be observed that the hyperbolic parameter values of the soils tested during this investigation seem to be consistent with those reported in the literature.

Figure 3-3 allows the estimation of hyperbolic parameter values for relative densities different from those of the specimens tested. As discussed in Chapter 5, this figure was particularly useful for estimating the hyperbolic parameters of the Light Castle sand backfill for the finite element analyses of the IRW test.

A comparison between the hyperbolic stress-strain relationships calculated using the parameters in Table 3-2 for each of the sands tested and the data from the triaxial tests is presented in Figures B4, B8, B12, and B16 of Appendix B. The hyperbolic model provides a good fit of the laboratory data, especially at the higher stress levels, but it does not model the post-peak strain-softening behavior or shear-induced dilation of the soil.

3.2 Concrete Specimen

A concrete slab was prepared for the soil-to-concrete interface tests, with dimensions 635 by 305 by 25.4 mm (25 by 16 by 1 in.). The main considerations for the design of the specimen were to (a) obtain a relatively high strength to minimize surface wear during shear, (b) to create a surface texture representative of field conditions, and (c) to minimize internal deformations of the concrete specimen during interface shear. To meet these requirements, several trials were required to develop the appropriate mixing and placement procedures for the concrete.

As illustrated in Figure 3-4, the concrete specimen was poured inside an aluminum frame specially fabricated for this testing program, and topped by a 3.2-mm (0.125-in.) steel plate. This system was designed to withstand compressive and tensile forces induced by the interface shear stresses with minimal deformations. The steel plate and aluminum sides of the frame act as an external reinforcement, minimizing tensile stresses in the concrete during the interface shear tests. A set of threaded, high-strength-steel studs work as shear connectors between the concrete and the steel plate.

3.2.1 Materials

The fine aggregate for the specimen was a processed, well-graded sand, commercially available for the preparation of concrete. This sand will be referred to as Blacksburg sand throughout this report. Examination under an optical microscope revealed that the sand grains smaller than 1 mm were predominantly subangular, with length-to-width ratios ranging from 1 to 3. The larger grains tended to be more angular and flat (ASTM 1993b).

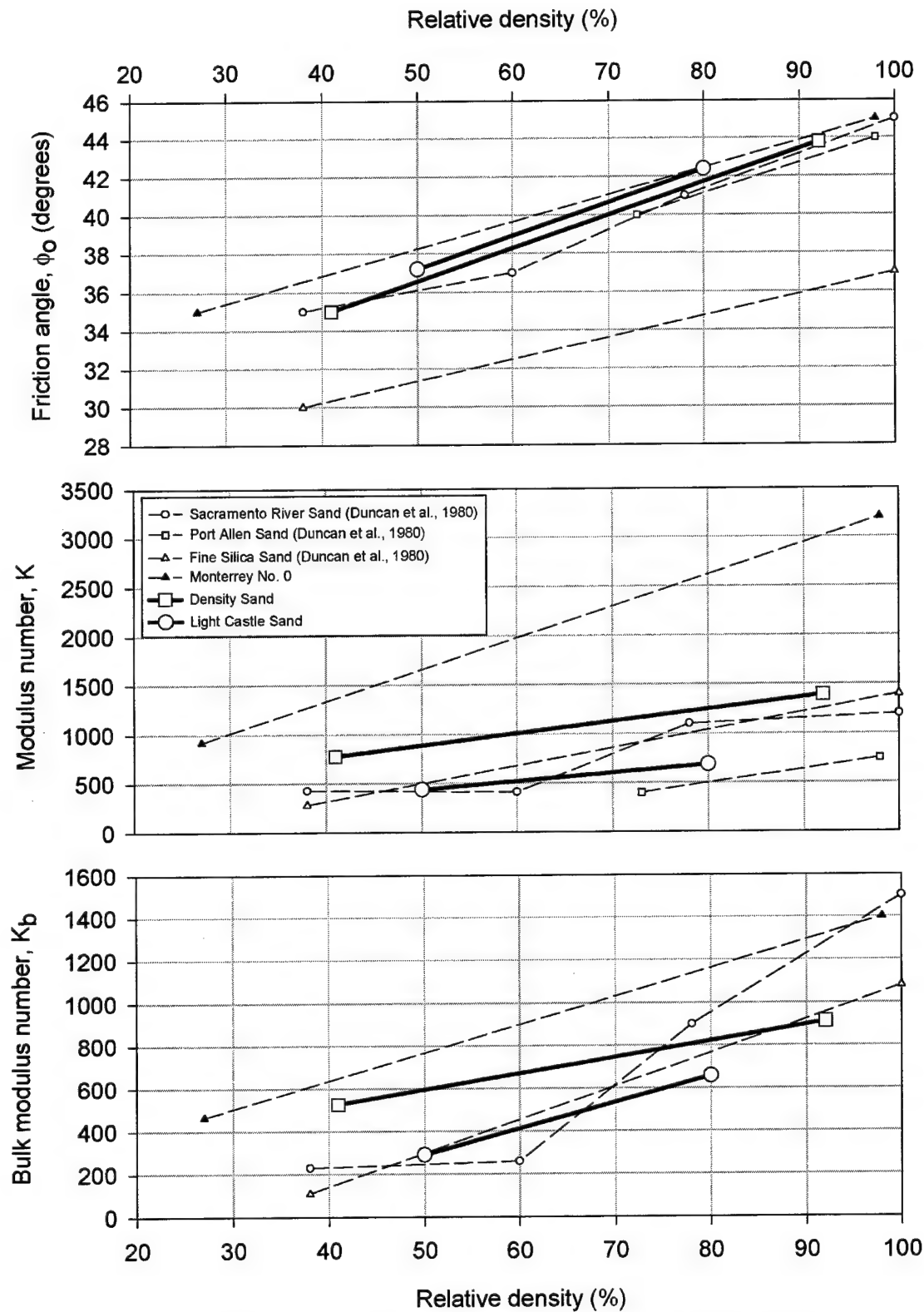


Figure 3-3. Hyperbolic parameter values for Density sand and Light Castle sand and comparison to values reported by Duncan et al. (1980) for similar soils

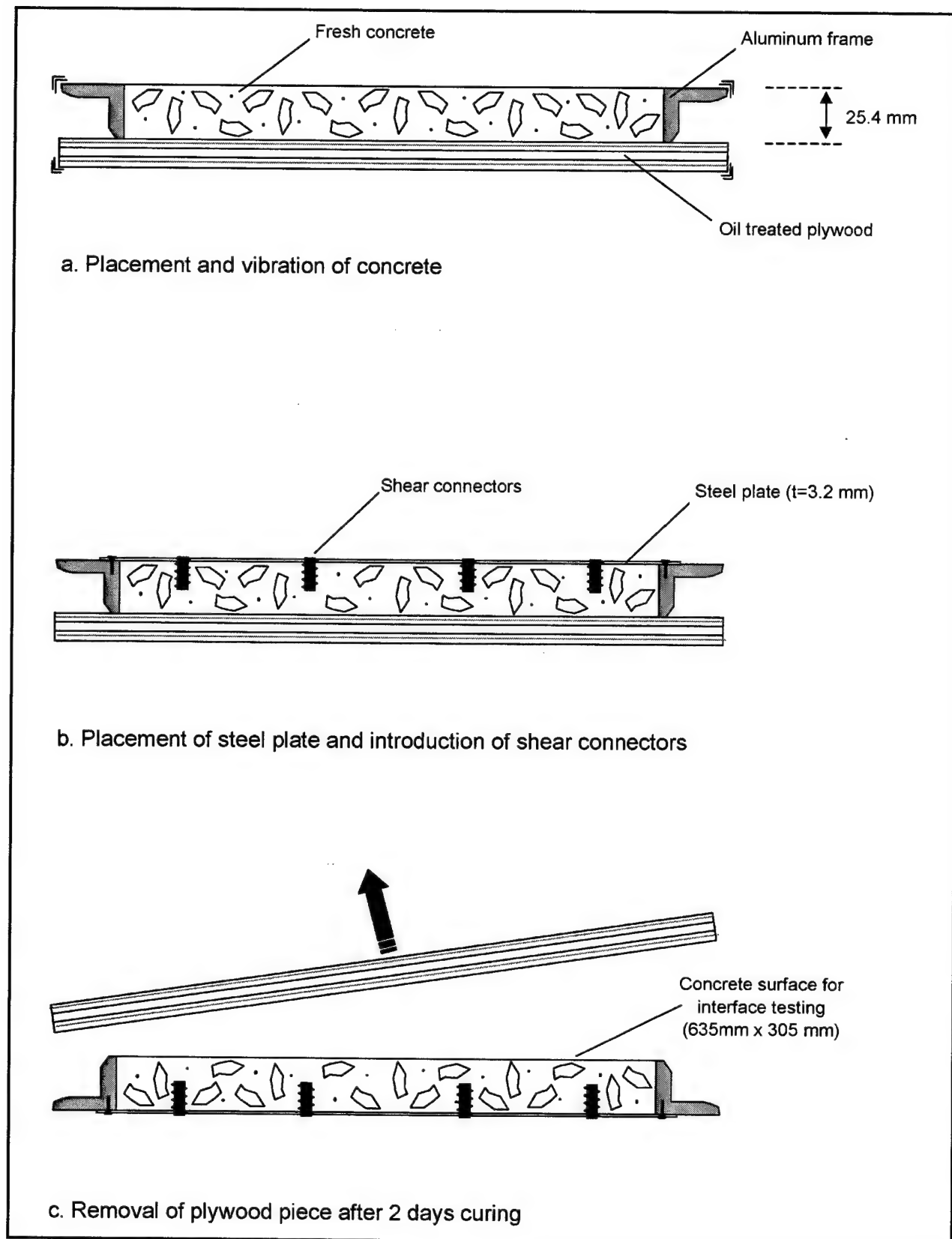


Figure 3-4. Preparation of the concrete specimen

The coarse aggregate was a crushed limestone with maximum grain size of 12.5 mm (1/2 in.), which is also commercially available for the preparation of concrete. The coarse aggregate was predominantly angular to subangular. The grain size distribution of the aggregates is presented in Figure 3-5.

To obtain an adequate workability without compromising strength, an Air-Entraining Admixture (AEA) and a High-Range Water Reducer (HRWR) were included in the concrete mix. Additionally, a corrosion inhibitor admixture was added to prevent corrosion of the steel components of the concrete frame.

3.2.2 Preparation of the specimen

The concrete was prepared following a rigorous mixing sequence. First, the aggregates were impregnated with the corrosion inhibitor. Then, the AEA, cement, water, and HRWR were added in sequence and thoroughly mixed. The mixing proportions and some physical properties of the concrete are summarized in Table 3-4.

Several trial batches were prepared until a mix with the appropriate physical properties was obtained. Tests were performed to determine the slump, air content, and compressive strength of the concrete, and the results are presented in Table 3-5.

The concrete was carefully placed onto the piece of plyform, inside the aluminum frame, as illustrated in Figure 3-4a. The concrete specimen was vibrated, trimmed, and covered with the steel plate. The plate was then attached to the aluminum frame as illustrated in Figure 3-4b. The threaded steel studs were screwed in place through the openings in the steel plate, and into the fresh concrete. The assembly was left in place for 2 days, after which the plywood piece was carefully removed, exposing the concrete surface for visual examination. At this point, an assessment was made of the surface texture of the specimen based on the results of the field survey of retaining walls, which is described in the following section. No surface treatment was applied to the specimen after its preparation. Once accepted as representative of field conditions, the specimen was placed in a wet room for 28 days, after which it was removed and used for the interface tests.

3.2.3 Surface texture

A field survey was performed to establish a range of surface textures representative of existing retaining walls. The survey, carried out throughout southwestern and northern Virginia, focused on mass and reinforced concrete retaining walls of height ranging from 3 to 7 m (10 to 23 ft), where plywood forms were used. For this investigation, four main types of surface features were identified: small-scale roughness controlled by fine aggregate of concrete, waviness controlled by the formwork material, pores, and air pockets.

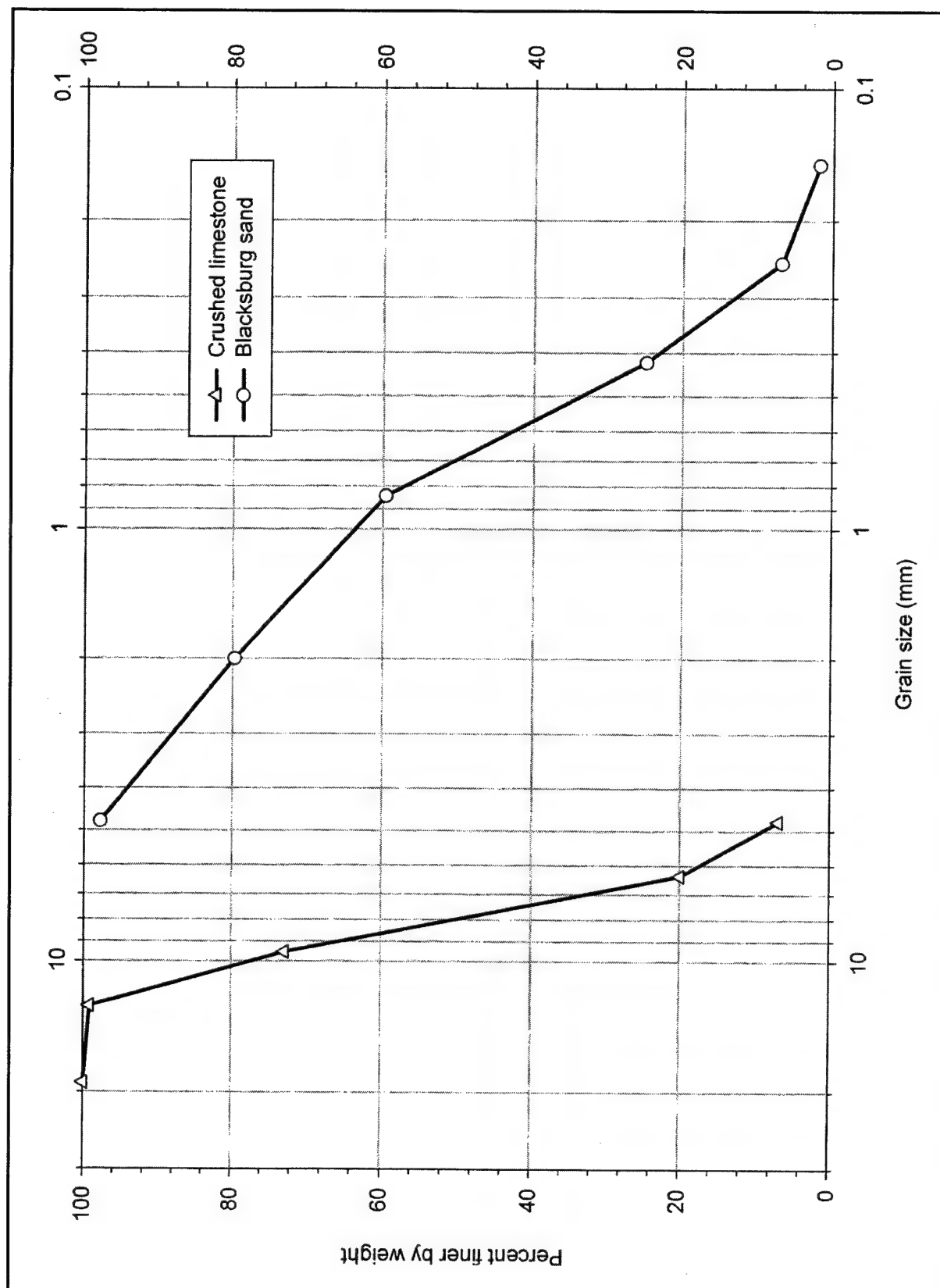


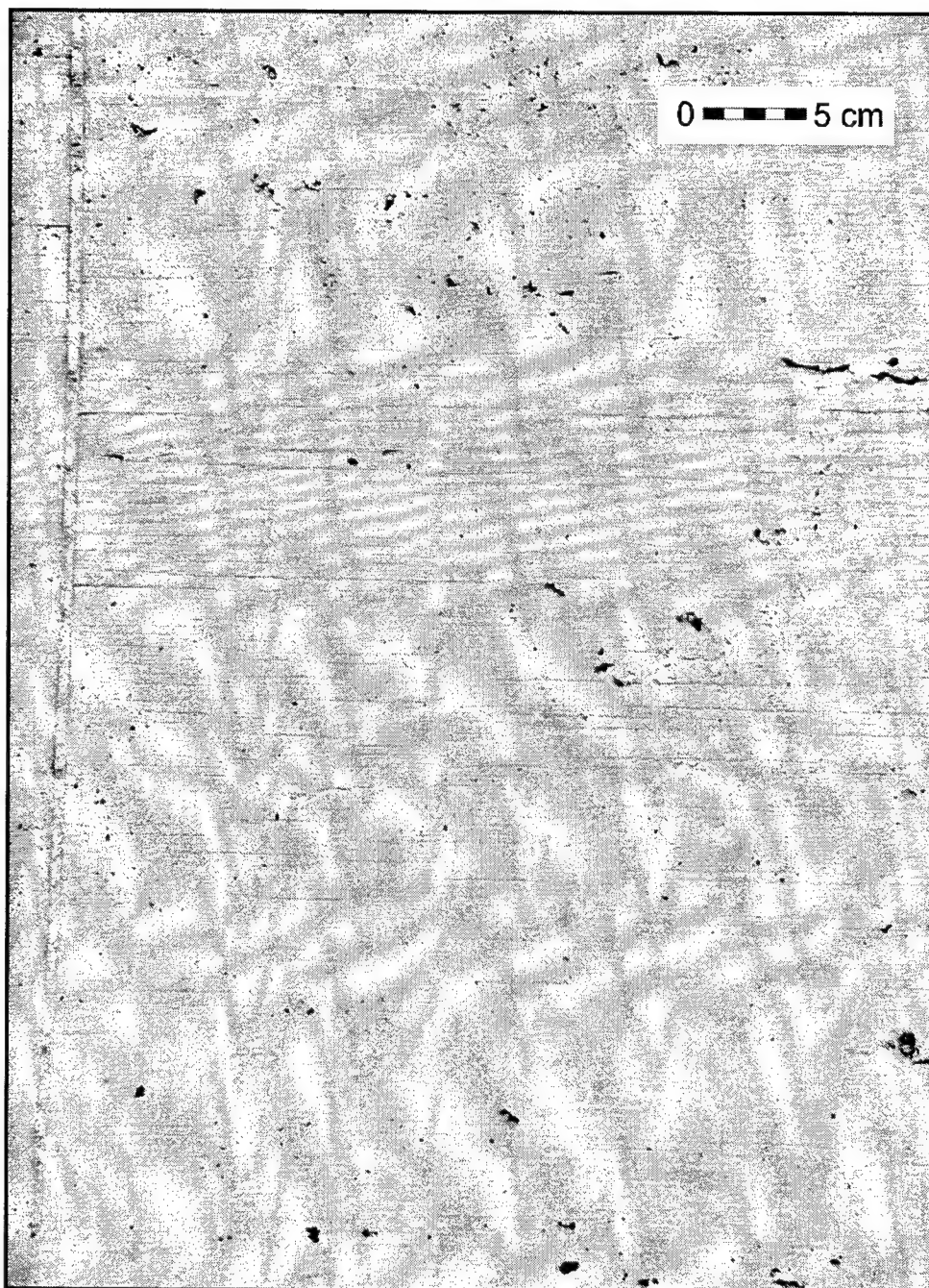
Table 3-4 Mixing Proportions of Concrete	
Coarse aggregate	600 kg/m ³
Fine aggregate (Blacksburg sand)	600 kg/m ³
Type I portland cement	264 kg/m ³
Water	105 kg/m ³
HRWR (Daracem)	850 ml/m ³
AEA (Daravair)	530 ml/m ³
Corrosion inhibitor (DCI-S)	10,420 ml/m ³

Table 3-5 Physical Properties of the Concrete Mix	
Slump	180 mm (7 in.)
Air content	7%
Compressive strength	
7 days	24,700 kPa (3,580 psi)
21 days	27,450 kPa (3,980 psi)
28 days	33,100 kPa (4,800 psi)

In total, ten retaining walls were surveyed. Two cases considered representative of all the walls surveyed are presented in Figure 3-6 at approximately the same scale. Wall A is a mass concrete retaining wall under construction, 5 m (16 ft) high and 60 m (200 ft) long, poured inside oil-treated plywood forms. The forms were reused up to six times throughout the length of the wall. The figure shows the average texture of the back of the wall, where the forms had been reused two or three times. The imprint of the plywood pattern, or waviness, is evident and is a significant component of the concrete texture. It was also observed that the waviness increased with the number of times the forms were reused. Although the concrete was vibrated after placement, air pockets are frequent.

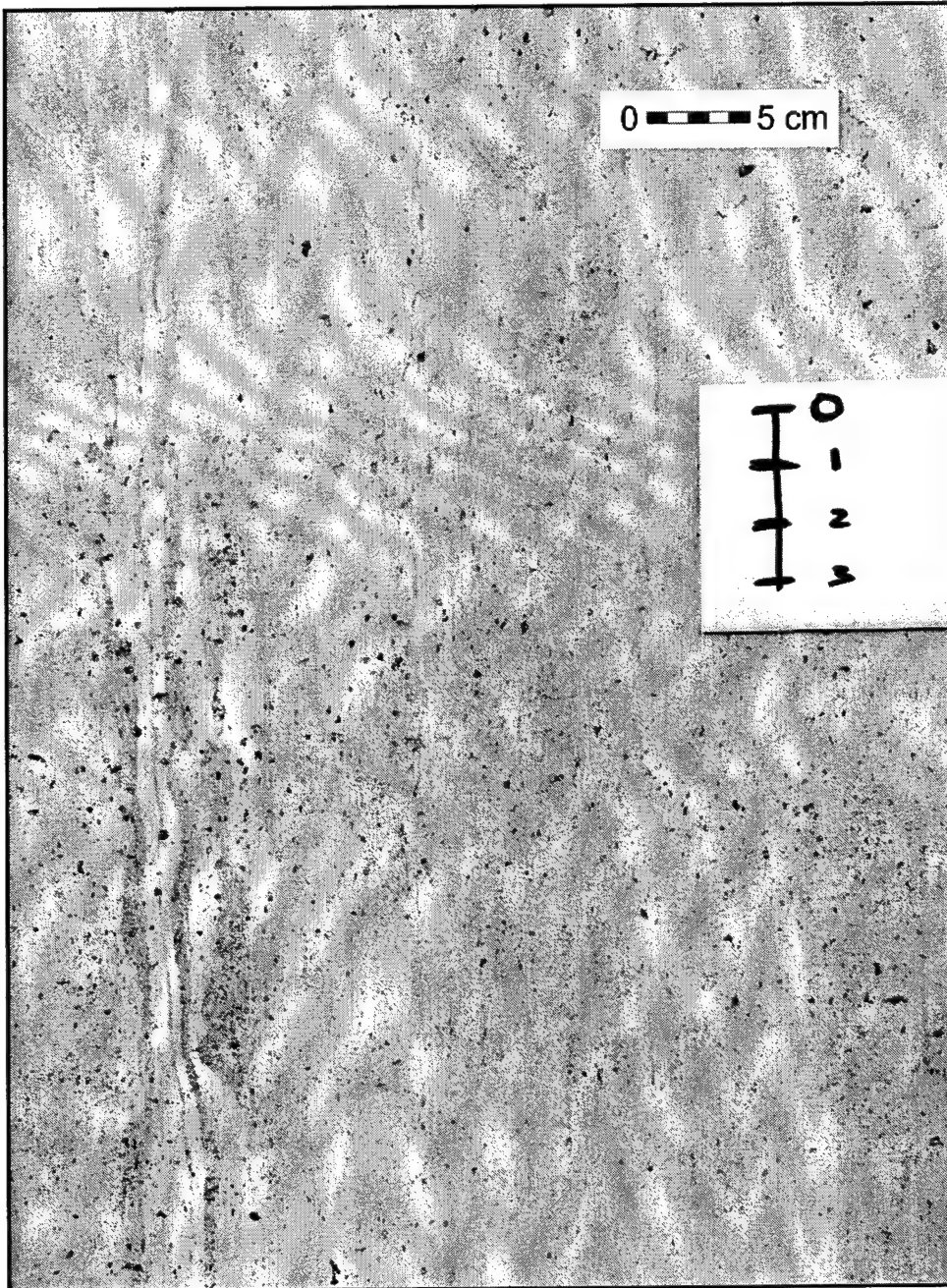
Wall B is a 7-m- (22-ft-) high reinforced concrete wall of recent construction. The figure shows the average conditions on the exposed face of the wall before any surface treatment was applied. Here the pattern of the plywood is also evident, although not as marked as in wall A. There is a much higher frequency of air pockets than in wall A.

Figure 3-6c shows the surface of the finished concrete specimen. It has surface features similar to those of the walls surveyed. The imprint of the plywood pattern is clearly visible, suggesting a degree of waviness similar to that of the field cases. The frequency of air pockets was very difficult to control during the specimen preparation. The final specimen was obtained after several trials, and it presents a frequency of air pockets similar to that of wall B.



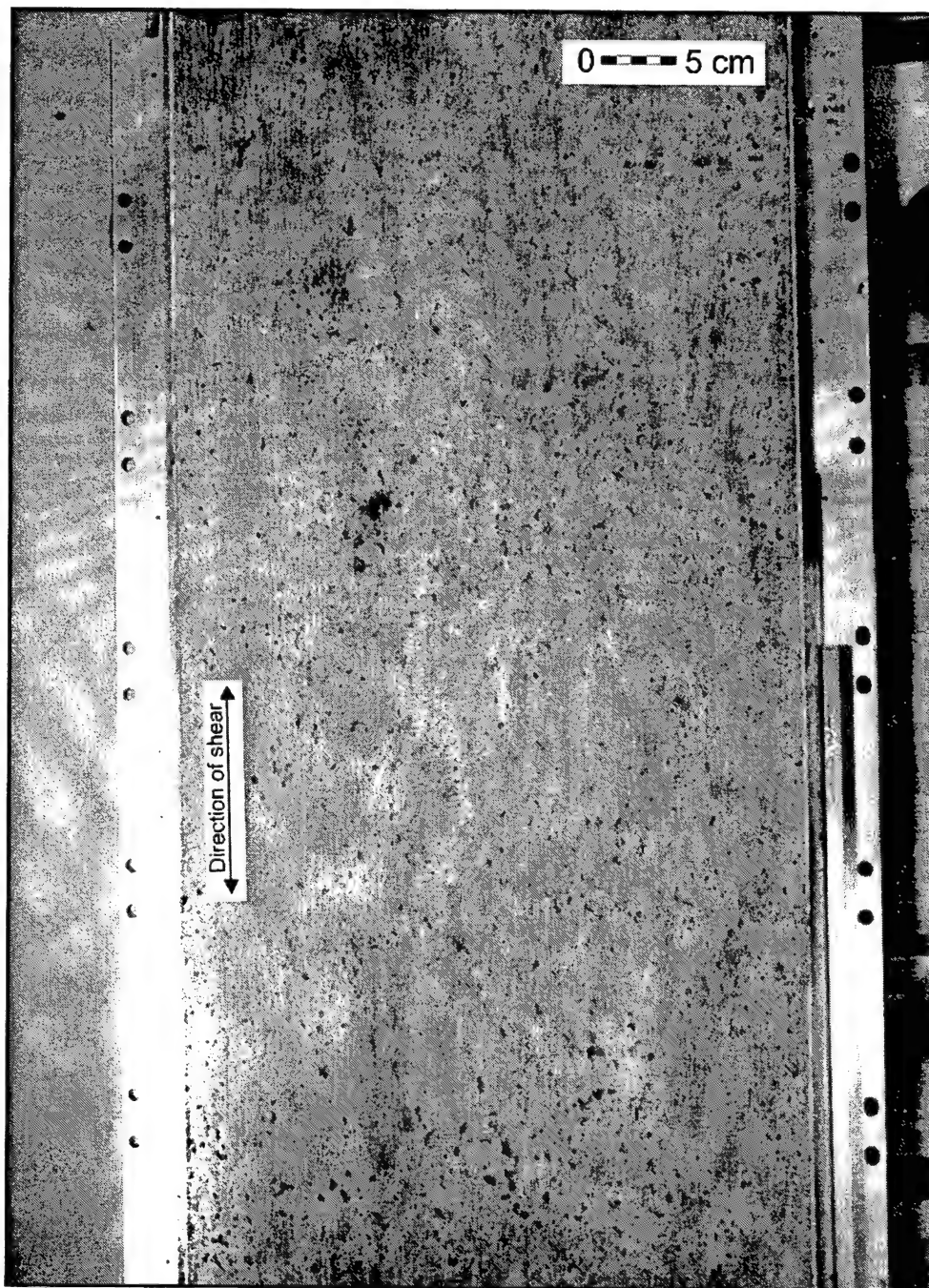
a. Wall A

Figure 3-6. Surface texture of representative retaining walls (Sheet 1 of 3)



b. Wall B

Figure 3-6. (Sheet 2 of 3)



c. Surface texture of concrete specimen

Figure 3-6. (Sheet 3 of 3)

No controls were placed on surface features such as small-scale roughness and porosity, because they are very difficult to measure in the field. However, the concrete was prepared using materials and mixing procedures that are common in the industry and considered to be representative of actual construction practices.

3.3 Interface Testing Procedures

3.3.1 The soil box

For each test, the sand specimen is compacted inside a soil box that was designed and fabricated specially for sand-to-concrete interface testing. Its inner dimensions are 635 by 406 by 25.4 mm (25 by 16 by 1 in.), and it is composed of a bottom plate and sidewalls made entirely of aluminum. The face of the bottom plate in contact with the soil is coated with several layers of polyurethane paint mixed with medium to coarse sand. This prevents slippage of the soil during interface shear testing.

The sidewalls are connected to the bottom plate by a set of structural steel bolts, which also allow the creation of the gap at the interface as described in Section 3.3.4. These bolts will be referred to as set bolts throughout this report.

A careful determination of the volume of the soil box was performed using several procedures. This was important to obtain reliable values of density of the sand sample.

3.3.2 Preparation of the interface

The sand-to-concrete interface is created by densification of the sand on top of the concrete specimen, as illustrated in Figure 3-7. The sidewalls of the soil box and an extension collar are placed on top of the slab. Four mounting brackets keep the sidewalls firmly in place throughout the entire process. To minimize the friction between the soil and the soil box, the inside of the walls is coated with vacuum grease and covered with a plastic sheeting 0.1 mm (4 mil) thick. Densification of the sand is achieved by either of two different procedures: vibration or pluviation.

In the vibration procedure, the system composed by the concrete slab, soil box, and trimming collar is attached to a 750- by 750-mm (30- by 30-in.) vibrating table. The soil is carefully placed inside the box to a height of approximately 5 mm above the trimming level, and vibrated under a 1.335-kN (300-lb) surcharge. The load and the extension collar are then removed, and the sample is trimmed as illustrated in Figure 3-7a. Theoretically, the final density of the sand can be adjusted by changing the frequency and amplitude of the vibrating table and the magnitude of the surcharge. However, it was found that the maximum relative density attainable with this setup was 70 to 80 percent. The scatter of the relative density values from one test to another was ± 5 percent. It is possible that

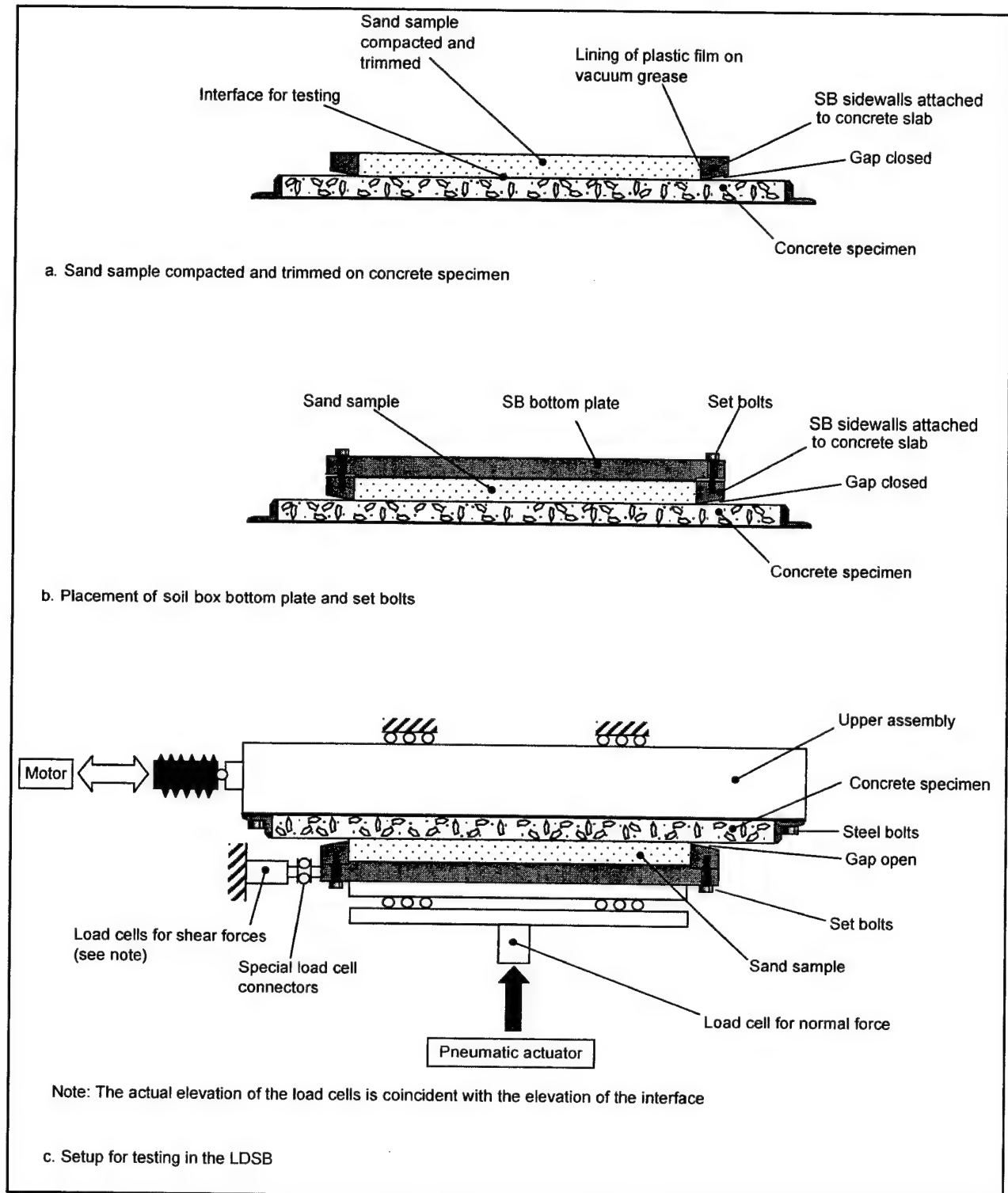


Figure 3-7. Preparation of sand-to-concrete interface and setup for testing

higher densities can be obtained with heavier surcharges; however, sample preparation may become impractical.

In the pluviation procedure, the sand is poured onto the surface of the concrete specimen. A simple *pluviation device* was constructed that allows a constant flow of sand dropping from a constant height on the concrete surface. The final density of the sand is determined by the drop height, the flow rate of sand, and the speed at which the device is translated over the concrete surface. The maximum density that can be attained by this procedure is 80 percent. The principal advantages of pluviation over vibration are a faster preparation of the specimen, and a greater repeatability with scatter in relative density values of ± 2 percent. After pluviation of the sand specimen, the extension collar is removed and the specimen is trimmed as illustrated in Figure 3-7a.

Once the soil specimen is prepared following either of these two procedures, the bottom plate is carefully placed on top of the sample, and bolted gently to the sidewalls, as illustrated in Figure 3-7b. The set bolts are tightened to generate a pressure of approximately 3.5 to 5 kPa between the bottom plate and the soil, and therefore between the soil and the concrete specimen as well. This low contact pressure maintains the rigidity of the assembly during handling, without disturbance to the interface. The assembly is then flipped and placed in position in the LDSB.

3.3.3 The Large Direct Shear Box (LDSB)

The LDSB was developed at Virginia Tech for testing of clay-to-HDPE interfaces (Shallenberger and Filz 1996). Some modifications to the LDSB were implemented to accommodate sand-to-concrete interface testing of the type described in this report. The LDSB is essentially a direct shear box type device with the capability to handle interfaces as large as 711 by 406 mm (28 by 16 in.), allowing a maximum interface displacement of 305 mm (12 in.). A view of the LDSB modified for soil-to-concrete interface testing is presented in Figure 3-8.

Shallenberger and Filz (1996) pointed out the advantages of the LDSB over conventional devices: end effects are negligible, the maximum displacement of 305 mm (12 in.) allows the determination of the interface residual shear strength, and no eccentric normal loads are generated during shear. The large displacement capabilities of the LDSB are a particularly useful feature for the type of testing performed during this investigation.

Figure 3-7c illustrates the main components of the device. The concrete specimen is rigidly attached to a moveable upper assembly by a set of structural steel bolts on each end of the slab. A screw jack transmits the action of a stepper motor to the upper assembly, which can be moved in both forward and reverse directions. The normal stress at the interface is provided by a pneumatic actuator capable of applying a force of up to 200 kN (44,000 lbf). During shear, the normal and tangential forces at the interface are measured by load cells as illustrated in the figure. The vertical and horizontal displacements at the interface are monitored by

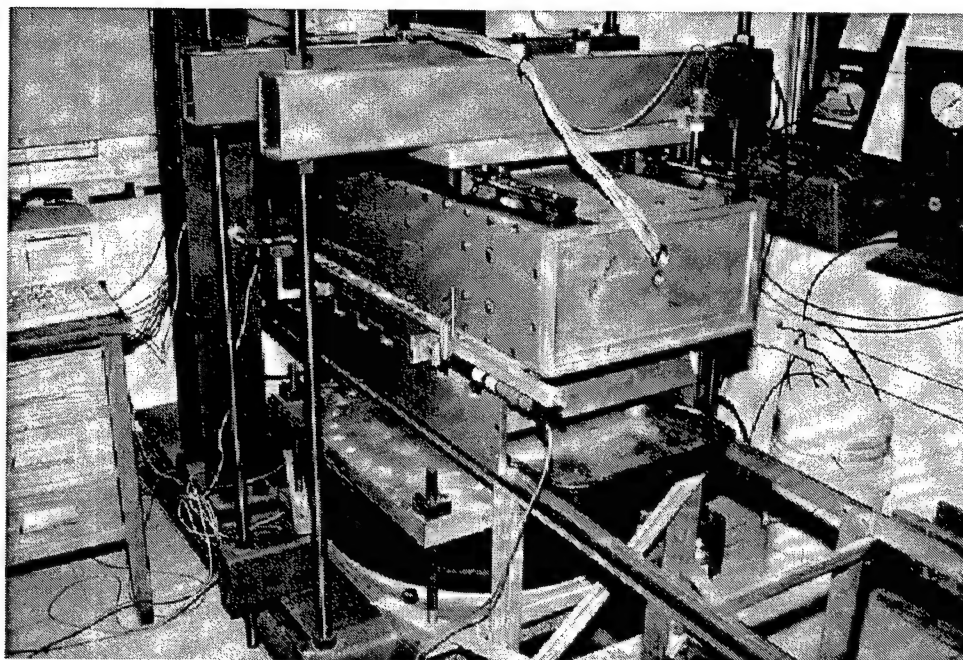


Figure 3-8. View of the LDSB ready for soil-to-concrete interface testing

a system of four linear variable displacement transducers (LVDTs), two in each direction, located on both sides of the sample. The LVDTs are capable of resolving displacements as small as 0.0025 mm (0.0001 in.).

A data acquisition system connected to a personal computer constantly monitors and records the readings from the load cells and transducers. The rate and direction of displacement along the interface are controlled by a program developed specially for this investigation. Testing features such as repeated unload-reload cycles between two predefined stress levels can be programmed or manually controlled. The program also facilitates loading of the interface along predefined stress paths. Readings are converted automatically to units of force or displacement using appropriate calibration factors.

3.3.4 Test setup

Once the sand-concrete sample is placed in the LDSB, it is lifted by the pneumatic actuator into its final position, and the concrete slab is bolted to the upper assembly. The normal pressure is increased until the initial pressure applied by the set bolts is produced. At this point, the set bolts become loose, and they can be turned by hand. The sidewalls are released from the mounting brackets and lowered by turning the set bolts to create a gap between the sidewalls and the concrete surface. The sidewalls slide gently into position due to their lubricated inner lining. The gap, illustrated in Figure 3-7c, is approximately 3.2 mm (0.125 in.) wide.

During the entire setup operation, the data acquisition system registers vertical and horizontal displacements and vertical loads. These data are checked to verify that undesired interface displacements and stresses have not occurred. After the normal pressure is increased to its final value, the soil box is connected to the horizontal load cells by special load cell connectors. These connectors restrain longitudinal displacement during shear in the forward or reverse direction. The sample is then ready for testing.

3.3.5 Data reduction

The load and displacement data recorded during the interface tests are processed using a data reduction program developed for the LDSB. The program creates a series of files containing the reduced data such as shear stress versus displacement and vertical versus horizontal displacement. These output files are copied onto a spreadsheet for processing and creation of graphic files.

3.4 Interface Testing Program

Interface tests were carried out between the concrete specimen and the soils described previously in this chapter. The purpose of the interface tests was to collect experimental data that allowed the development of a new interface model applicable to SSI analyses of lock walls. The results of these tests also add to the database on interface properties available in the literature.

3.4.1 Testing parameters

As indicated in Table 3-6, three types of interfaces were prepared: dense Density sand against concrete, medium-dense Density sand against concrete, and dense Light Castle sand against concrete. For each of the dense Density sand against concrete tests, the soil specimen was densified by vibration. For the medium-dense Density sand and dense Light Castle sand against concrete tests, the specimens were prepared by pluviation on the concrete surface. All the tests were performed at a displacement rate of 1 mm/min (0.04 in./min), under normal pressures ranging from 15 to 274 kPa (2 to 40 psi). This range of normal stresses is representative of field conditions in many lock walls.

A set of preliminary tests was performed to study the influence of inundation of the interface on the test results. The results showed that inundation does not induce any significant effect on the response of the interface. On average, the strength in inundated tests was 3.5 kPa higher than in dry tests at normal stresses ranging from 100 to 270 kPa. All subsequent tests were performed in a dry condition.

Table 3-6 Types of Interfaces Tested			
Interface Type	Average Relative Density percent	Procedure for Densification	Types of Tests Performed
Dense Density sand against concrete	75	Vibration	Initial loading Staged shear Unload-reload Multidirectional stress path
Medium-dense Density sand against concrete	49	Pluviation	Initial loading Multidirectional stress path
Dense Light Castle sand against concrete	80	Pluviation	Initial loading Multidirectional stress path

3.4.2 Types of interface tests

The types of interface tests performed for this investigation are summarized in Table 3-7, and illustrated in Figure 3-9. They can be grouped as initial loading, or virgin shear, tests; staged shear tests; unload-reload tests; and multidirectional stress path tests.

3.4.2.1 Initial loading tests. The initial loading tests were performed under constant normal stress on the newly prepared interface. In all initial loading tests, shearing continued until the residual strength was mobilized. For each type of interface, a set of initial loading tests under different normal stresses was performed to determine the peak and residual friction angle values and hyperbolic parameter values of the interface.

3.4.2.2 Staged shear tests. These tests were performed to study the interface response under a finite change in the normal pressure during shear. As illustrated in Figure 3-9b, the interface is initially sheared under a constant normal stress to a point such as *S*. Then, shearing is paused and the normal stress increased to point *S'*. Finally, shearing is resumed under this increased normal stress. The tests modeled conditions in which the normal pressure increment occurs before mobilization of the peak strength as in Figure 3-9b, or after development of the residual condition. The results of these tests were used to determine the shape of the yield surface incorporated in the extended hyperbolic model, as discussed in Chapter 4.

3.4.2.3 Unload-reload tests. These tests modeled the interface response upon a change in the direction of shear. As shown in Figure 3-9c, the interface is sheared under constant normal stress to a point such as *U*, where the shear direction is reversed. Unloading progresses to a point such as *R*, where reloading is applied to the interface. These tests provided the basis for developing a formulation for interface response under unloading-reloading, as described in Chapter 4.

Table 3-7
Summary of Interface Tests

Type of Test	Type of Interface	Specimen	Test Number	Normal Stress kPa	Figures ¹	Observations
Initial loading (virgin shear)	Dense Density sand against concrete	S101	T101_2	15	C1, C2	—
		S102	T102_5	33		
		S103	T103_15	102		
		S104	T104_40	274		
	Medium-dense Density sand against concrete	S302	T302_5	35	C3, C4	—
		S303	T303_15	104		
		S304	T304_40	276		
	Dense Light Castle sand against concrete	S401	T401_2	15	C5, C6	—
		S402	T402_5	35		
		S403	T403_15	104		
		S404	T404_40	276		
Staged shear	Dense Density sand against concrete	S105	T105_40	102 to 274	C7	Staged before peak
		S106	T106_15	33 to 102	C8	
		S101	T101_5 T101_15 T101_40	15 to 33 33 to 102 102 to 274	C9	Staged on residual condition
		S102	T102_15 T102_40	33 to 102 102 to 274	C10	
		S103	T103_40	102 to 274	C11	
Unload-reload	Dense Density sand against concrete	S201	T201_5	33	C12	Unload-reload applied before peak
		S202	T202_5	33	C13	
		S203	T203_15	102	C14	
		S101	T101_2	15	C15	Reversals applied on residual condition. Two or three cycles were performed per test.
		S102	T102_5	33	C16	
		S103	T103_15	102	C17	
		S104	T104_40	274	C18	
	Medium-dense Density sand against concrete	S302	T302_5	35	C19	
		S303	T303_15	104	C20	
		S304	T304_40	276	C21	
	Dense Light Castle sand against concrete	S401	T401_2	15	C22	
		S402	T402_5	35	C23	
		S403	T403_15	104	C24	
		S404	T404_40	276	C25	
Multidirectional stress path	Dense Density sand against concrete	S204	T204_5	35 to 280	C26	—
		S205	T205_5	35 to 240	C27	
		S206	T206_5	35 to 275	C28	
	Medium-dense Density sand against concrete	S305	T305_10	70 to 250	C29	
	Dense Light Castle sand against concrete	S405	T405_10	70 to 275	C30	

¹ Figures are included in Appendix C.

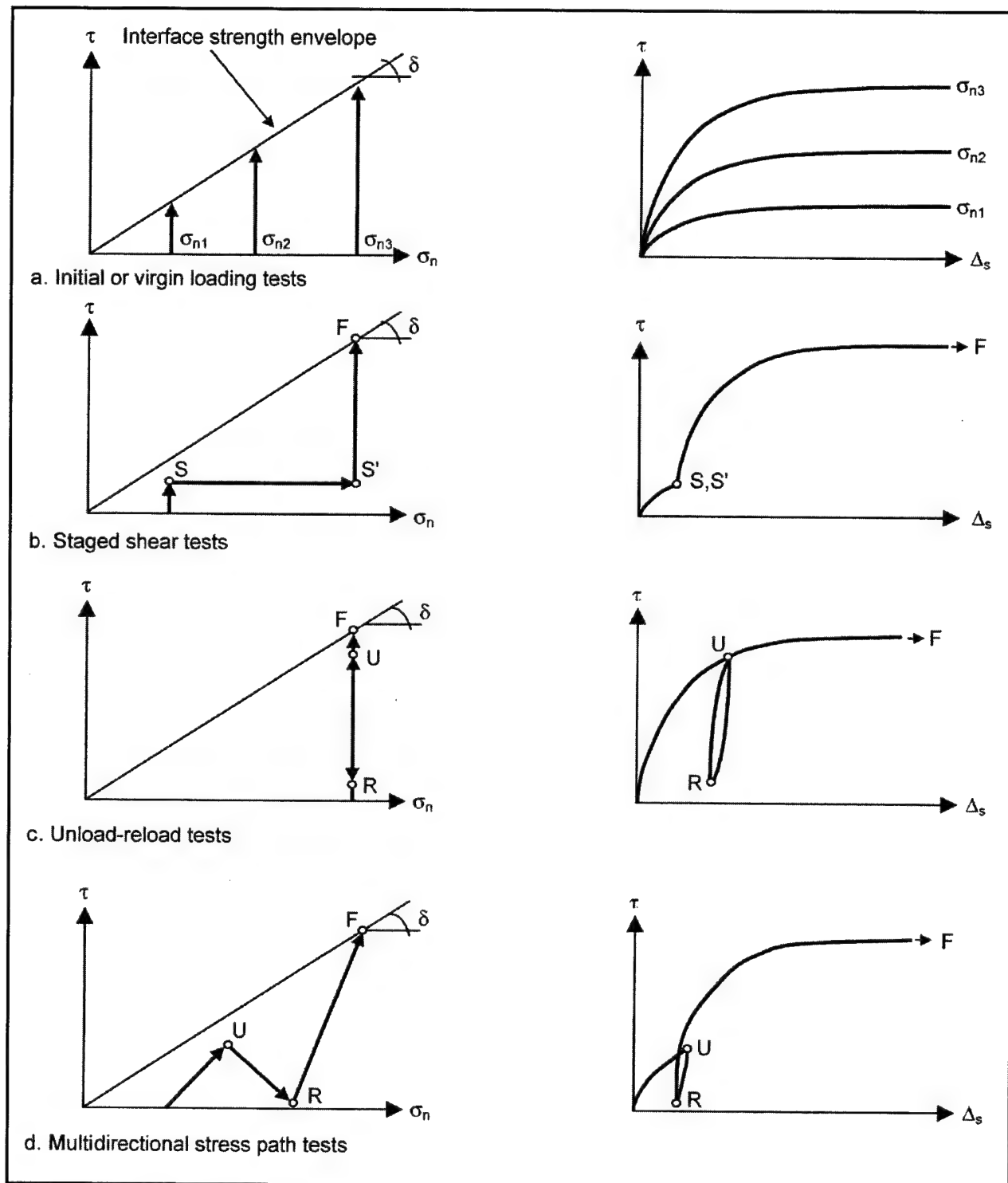


Figure 3-9. Types of laboratory interface shear tests performed

3.4.2.4 Multidirectional stress path tests. In this type of test, the interface was sheared following a stress path that involved simultaneous changes in normal and shear stresses, as illustrated in Figure 3-9d. They were intended to model loading conditions similar to those expected at the interface between a lock wall and the backfill, and to provide a basis for evaluation of the extended hyperbolic model described in Chapter 4.

Some staged shear and shear reversal tests were performed at the end of initial loading tests, after mobilization of the residual strength (Table 3-7). Although the large cyclical interface displacements required for this type of loading are not expected to take place in backfill-to-lock-wall interfaces, these results may be applicable to other Corps structures. These test results are reported in Appendix C.

3.5 Results of Interface Tests

The results of the interface tests performed for this investigation are presented in the figures of Appendix C. Table 3-7 lists the figures in Appendix C that are relevant to each interface test. In this section, the results of the interface testing are summarized. The emphasis is on the issues that are the most important for interface modeling.

3.5.1 Interface response to initial loading

The results of the initial loading tests performed on interfaces between concrete and Density sand or Light Castle sand are presented in Figures C1 to C6, and summarized in Table 3-8. In the figures, the information regarding staged shear and shear reversal cycles, which were performed at the end of initial loading tests, is omitted for the sake of clarity and will be discussed in the following sections.

Table 3-8 Summary of Results of Initial Loading Interface Tests						
Interface Type	Displacement (mm)		Interface Friction Angle, deg		Interface/Soil Friction Angle Ratio	
	To Peak Δ_{sp}	To Residual Δ_{sr}	Peak δ	Residual δ_r	δ / ϕ_o	δ_r / ϕ_{cv}
Dense Density sand against concrete	1-2	6-13	31	28	0.86	0.82
Medium-dense Density sand against concrete	2.5-3.5	12-20	29.5	28.5	0.71	0.86
Dense Light Castle sand against concrete	1-2	6-11	33.7	29.5	0.79	0.81
Note: Parameters are listed and defined in the Notation (Appendix F).						

The peak shear strength was mobilized at small displacements ranging from 1 to 3.5 mm. After mobilization of the initial peak strength, shear stresses remained practically constant before displacement softening took place. This plateau of relatively constant shear stress may exist up to displacements as large as 20 mm, as evidenced by Test T304_40 in Figure C3 of Appendix C, after which the residual condition was attained. In some cases, a secondary peak was observed in the shear stress-displacement curve. For the purposes of this investigation, the peak strength was assumed to correspond to the first peak that occurred during the test.

During shear, extension occurred in a direction normal to the interface in most of the tests. Once the residual condition was reached, no significant normal displacements took place. After removal of the concrete slab from the sand surface at the end of the tests, a layer of loose sand approximately 2 mm thick could be observed overlying the denser material immediately below. This is consistent with the observations by Uesugi, Kishida, and Tsubakihara (1988 and 1989), Uesugi, Kishida, and Uchikawa (1990), and Hryciw and Irsyam (1993). They indicate that this dilation is produced mostly by normal deformations of a thin shear band developed in the soil adjacent to the concrete surface.

The peak and residual strength envelopes are also presented in Appendix C for each type of interface. Both peak and residual strength envelopes are linear for the range of normal stresses considered, and show no apparent cohesion intercept. The peak and residual friction angle δ and δ_r values are summarized in Table 3-8, and compared to the internal friction angle ϕ_o and 15 percent strain friction angle ϕ_{cv} for each of the soils. The values of ϕ_o and ϕ_{cv} were interpolated from Figure 3-3a for the relative density values of the soil specimens prepared for interface testing. It can be seen that the values of δ and δ_r correspond to approximately 80 percent of ϕ and ϕ_{cv} , respectively.

The shear stress versus displacement plots reveal that interface displacements of less than 20 mm may not suffice for defining the value of the residual strength of sand-to-concrete interfaces. Consequently, shear box devices with displacement capabilities of less than 20 mm may not be adequate to collect data in situations where knowledge of the residual interface strength value is necessary.

The results of the initial loading tests were used to determine the hyperbolic parameter values of the three types of interface tested, as discussed in Chapter 4.

3.5.2 Interface response to staged shear

The results of the staged shear tests are presented in Figures C7 to C11 of Appendix C. These figures include the shear stress-displacement response of the interface together with the history of normal stress applied during the test and the record of displacements normal to the interface.

Two groups of staged shear tests were performed on the dense Density sand against concrete interface (Table 3-7). In the first group (Figures C7 and C8), the normal stress was increased during shear and before mobilization of the peak strength. The specimens were sheared under constant normal stress to a stress level of approximately 0.65. The relative motion of the interface was then arrested, and the normal pressure increment was applied while maintaining approximately the same magnitude of shear stress. Shearing was resumed after the normal pressure increment was completed. A significant increase of the interface shear stiffness was observed upon application of the normal stress increment. The interface peak shear strength values determined from these staged shear tests are consistent with those determined from the initial loading tests described in the previous sections.

The test results presented in Figures C7 and C8 were used to determine the shape of the yield surface included in the new extended hyperbolic model, as discussed in Chapter 4.

In the second group of staged shear tests (Figures C9 to C11), several steps of normal stress increments were applied during shear in the residual condition. These tests were carried out at the end of the initial loading tests described previously. The normal pressure steps followed the sequence: 15 to 33 kPa, 33 to 102 kPa, and 102 to 274 kPa. In most of the tests shown, some shear reversal cycles were performed, which have been omitted for the sake of clarity.

Some conclusions may be drawn from Figures C9 to C11. The residual condition established at the interface after mobilization of the peak strength and at large displacements is maintained during further shearing of the interface and under subsequent increments of the normal stress. A peak strength greater than the residual strength occurs only in the initial loading stage; for subsequent stages, the shear stress increases to the residual value and then remains constant until the application of the next normal pressure increment.

It can also be observed that the residual strength value does not depend on the stress path followed and is the same in all tests performed under the same normal stress. Therefore, it is possible to determine a complete residual strength envelope from staged shear tests, as long as the displacement capability of the equipment is enough for the development of the residual condition.

3.5.3 Interface response to unloading-reloading

A group of three unload-reload interface tests was performed on the dense Density sand against concrete interface. The results are presented in Figures C12 to C14 of Appendix C. These tests included one unload-reload cycle between two predetermined stress levels during initial loading. Tests T201 and T203 (Figures C12 and C14) were performed under constant normal stresses of 33 and 102 kPa, respectively. The unloading-reloading cycle was applied between stress levels of approximately 0.7 and 0.2. In Test T202, shown in Figure C13, the interface was unloaded from a stress level of approximately +0.75 to a stress level of -0.75, and then reloaded to failure.

A significant increase in the interface stiffness took place upon unloading and reloading of the interface. Hysteretic behavior was evident in all three tests. However, in Tests T201 and T203, in which shear stresses were always positive (shear in the first quadrant), the interface response was almost linear. In Test T202, in which unloading progressed into the fourth quadrant, the hysteretic loop was wider and the interface response was strongly nonlinear. The normal displacement plots included in the figures reveal that the interface undergoes compression during unloading and extension during reloading. These tests provided the basis for developing the unloading-reloading components of the interface model discussed in Chapter 4.

Some additional tests, performed in all three types of interfaces, consisted of one or more shear reversal cycles applied at the end of initial loading after mobilization of the residual strength. The results of such tests are presented in Figures C15 to C25 of Appendix C. It can be seen that the residual strength values are very similar or identical in both directions of shear.

3.5.4 Interface response to multidirectional stress paths

Five interface tests were performed following relatively complicated stress paths. Figures C26 to C30 in Appendix C show the stress path applied in each of these tests and the measured interface response. Test T204_5 (Figure C26) is a succession of seven staged shear tests applied on the dense Density sand against concrete interface. The normal stress was increased from 35 to 275 kPa in 35-kPa steps. Although such loading is not expected to take place at a backfill-to-wall interface, the results of the test were very useful in the validation of the new extended hyperbolic model.

Test T205_5 (Figure C27) consisted of the application of a continuously increasing normal stress during shear of the interface between dense Density sand and the concrete specimen. A similar type of loading may be expected at the interface between a wall and the backfill during placement and compaction of the backfill, as discussed in Chapter 1 (Figure 1-3a).

Tests T206_5 and T305_10 on the dense and medium-dense Density sand against concrete interfaces and T405_10 on the dense Light Castle sand against concrete interface (Figures C28 to C30) consisted of the application of more complicated stress paths. Initial loading, unloading, reloading, and simultaneous changes in shear and normal stresses were applied to the interface. The purpose of these tests was to provide a basis for a performance evaluation of the extended hyperbolic model under complicated loading paths. They also model certain aspects of the type of loading expected at the backfill-structure interface during backfill placement and operation of a lock wall.

3.6 Summary

The following laboratory and field activities were performed for this investigation:

- a.* Modifications to the LDSB.
- b.* Selection of sand specimens for interface testing.
- c.* Grain size distribution, minimum/maximum density, specific gravity, consolidation testing, and triaxial testing on the Density sand and Light Castle sand.
- d.* Field survey of existing concrete retaining walls to determine a range of representative surface textures for the concrete specimen.
- e.* Design and construction of a soil box and concrete slab.
- f.* Development of appropriate testing procedures.
- g.* Interface tests following a variety of laboratory stress paths to investigate the constitutive behavior of interfaces and to determine the interface response under field conditions for lock walls.

The LDSB was modified specifically to accommodate the soil-to-concrete interface testing for this investigation. A special aluminum soil box was designed and constructed that allows compaction of the sand sample directly onto the concrete specimen, and minimizes the disturbance of the interface during test setup operations.

A field survey of concrete walls was performed. Two representative cases were presented to convey the most common surface features of retaining walls cast against plywood. After a trial-and-error process, a concrete specimen was obtained with surface features similar to those observed in the field. The concrete specimen was contained in a frame, which was designed and constructed to act as an external reinforcement for the concrete and to minimize its deformations during interface shear.

A fine, rounded, silica sand (Density sand), and a fine, angular sand (Light Castle sand) were selected for interface testing. A series of basic laboratory tests, such as minimum/maximum density and grain size analyses, were performed on these sands. Consolidation and CD triaxial tests were also performed to determine sets of hyperbolic parameter values for these soils for a range of relative densities representative of the backfill in lock walls. These hyperbolic parameter values are consistent with values reported by Duncan et al. (1980) for soils of similar gradation.

An interface testing program was carried out that included initial loading tests, staged shear tests, unload-reload tests, and multidirectional stress path tests. Three types of interfaces were tested: dense Density sand against concrete,

medium-dense Density sand against concrete, and dense Light Castle sand against concrete. The results of these tests are presented in Appendix C.

The peak and residual interface friction angle values for the three types of interfaces tested are summarized in Table 3-8. The average ratio between the values of interface friction angle and internal friction angle of the soil was 0.8. Displacement softening was observed in all tests. The displacements required for the development of the residual condition were as large as 20 mm. Consequently, displacements of at least 20 mm are required for the determination of the residual strength of sand-to-concrete interfaces.

Staged shear tests were performed by increasing the normal pressure in steps during shear. The staged shear tests provided important information about the behavior of sand-to-concrete interfaces and were used to define the yield surfaces implemented in the extended hyperbolic model described in Chapter 4. It was found that it is possible to determine a complete residual strength envelope from staged shear tests, as long as the displacement capability of the equipment is enough for the development of the residual condition.

Several unload-reload tests were performed, in which a complete loading cycle was applied between two predetermined stress levels. These tests follow stress paths similar to field stress paths in which the shear stresses may decrease as a consequence of a rise of the water table behind a lock wall. A substantial increase in the interface shear stiffness was observed upon unloading and reloading. It was observed that compression takes place during unloading, followed by dilation during subsequent reloading of the interface. In some tests, one or several cycles of shear were performed upon mobilization of the residual strength. Similar shear stress-displacement response and residual strength values were obtained for both directions of shear in all tests.

Multidirectional stress path tests were performed on all three types of interfaces. The purpose of these tests was to provide a basis for a performance evaluation of the extended hyperbolic model under complicated loading paths. They also modelled certain aspects of the type of loading expected at the backfill-structure interface during backfill placement and operation of a lock wall. The model discussed in Chapter 4 was validated against the results of these tests.

4 Extended Hyperbolic Model

A new model for interfaces was developed for this investigation. It is based on the Clough and Duncan (1971) hyperbolic formulation, which has been extended herein to model the response of interfaces under general field loading conditions. The model captures important aspects of interface response under stress paths such as those presented in Figures 1-3a and 1-4a; yet, it retains much of the simplicity of the original Clough and Duncan (1971) formulation.

The model incorporates three new elements into the hyperbolic formulation: a yield surface, a formulation for virgin shear under continuously changing normal stress, and a formulation for unloading-reloading of the interface. The extended hyperbolic model was evaluated against the results of the interface tests, which were described in Chapter 3. It was found that the model accurately represents the response of the interface for stress paths such as those presented in Figure 3-9.

This chapter is divided into the following sections:

- a.* Experimental observations of interface response.
- b.* Formulation of the extended hyperbolic model for yield-inducing shear.
- c.* Formulation of the extended hyperbolic model for unloading-reloading.
- d.* Determination of the model parameter values.
- e.* Evaluation of the extended hyperbolic model.
- f.* Implementation of the extended hyperbolic model.
- g.* Summary and conclusions.

The most relevant observations regarding interface response during shear are presented in the first section. They correspond to the experimental data collected from the interface tests described in Chapter 3 and form the basis for the development of the new model. The subsequent sections describe the formulation of the model for yield-inducing shear and unloading-reloading, and the procedure to obtain the required interface parameter values. The performance of the extended hyperbolic model is evaluated by comparing the predicted interface response to the data collected during interface testing. An outline of the implementation of the

model in the finite element program SOILSTRUCT-ALPHA is also presented. Finally, the advantages and limitations of the model are discussed, and recommendations are given for future work on modeling backfill-to-structure interfaces.

4.1 Experimental Observations of Interface Response

This section describes important aspects of interface response measured during the laboratory testing program. The concepts of yield surfaces and loading regions in interface shear are introduced. They form the basis for formulation of the extended hyperbolic model.

4.1.1 Normalization of interface test data

Development of the extended hyperbolic model required careful interpretation of the interface test data presented in Chapter 3 and Appendix C. The interface response data collected during initial shear, staged shear, and unload-reload tests were compared. It was found that direct comparisons of the shear stress-displacement data from different types of tests did not provide an appropriate basis for study of the interface response during shear.

A procedure was devised to facilitate the comparison of the data from different types of interface tests. It is based on the normalization of tangent stiffness values determined from the test data. This procedure makes possible the study of development of yield surfaces during interface shear, and the influence of simultaneous shear and normal stress increments on interface response. It also facilitates analysis of interface response during unloading-reloading and staged shear.

The high resolution of the LDSB instrumentation and the sampling frequency of the data acquisition system made possible a continuous record of stiffness values for each of the tests. The tangent interface shear stiffness K'_{st} at any instant during the test was determined from the test data using the following expression:

$$K'_{st} = \frac{\tau^i - \tau^{i-1}}{\Delta_s^i - \Delta_s^{i-1}} \quad (4-1)$$

where

τ^{i-1} and τ^i = consecutive shear stress readings

Δ_s^{i-1} and Δ_s^i = consecutive interface displacement readings

The tangent stiffness values for the initial loading tests performed on the dense-Density-sand-against-concrete interface were determined from Equation 4-1. They are plotted against the values of stress level SL in Figure 4-1.

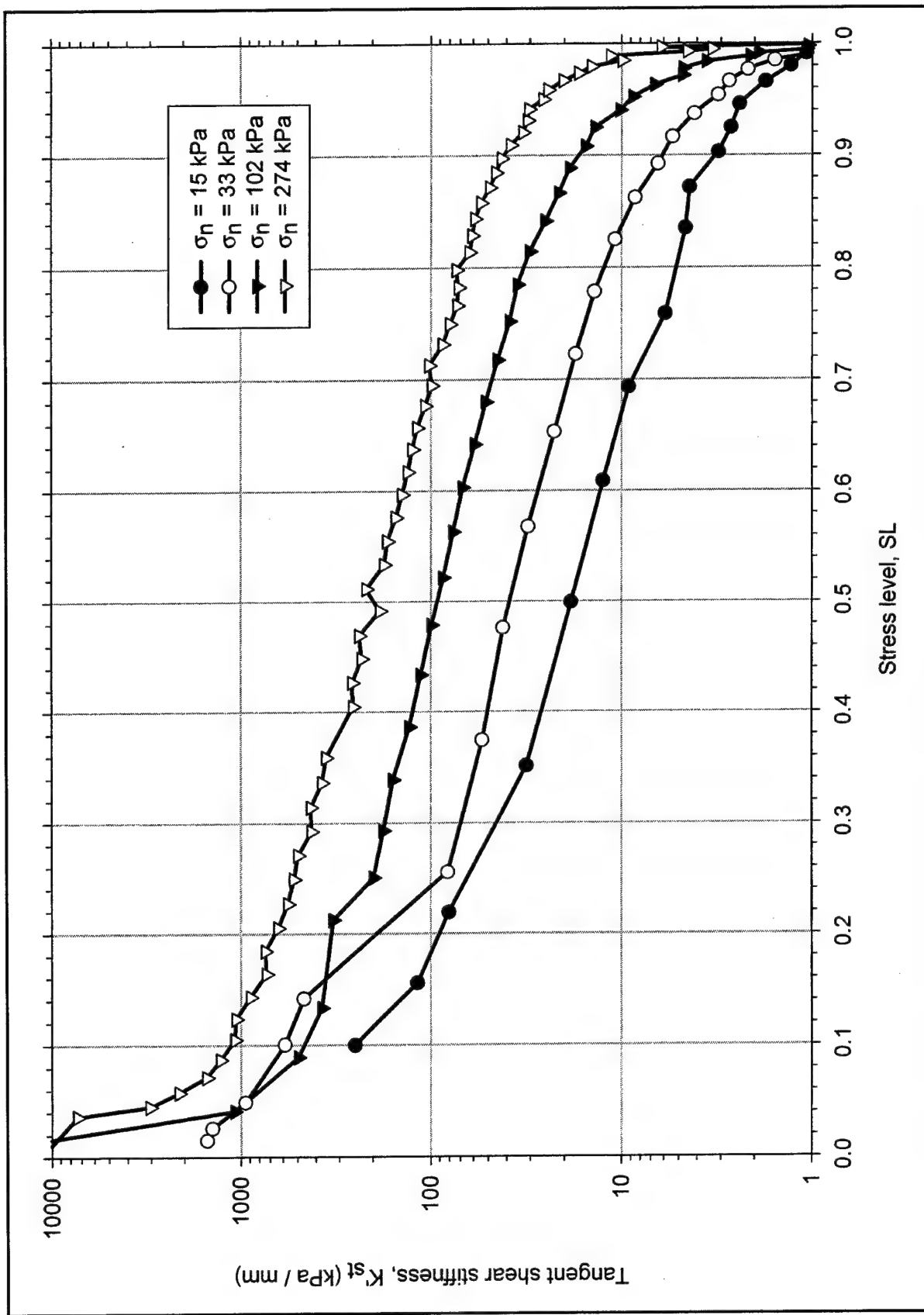


Figure 4-1. Degradation of the tangent shear stiffness during initial loading of the dense-Density-sand-to-concrete interface

In all tests, the interface stiffness decreased continuously during shear as the stress level increased. The interface stiffness values also depend on the magnitude of the normal stress, as seen in the figure.

It was found that, for all three types of interfaces tested, the interface stiffness values could be normalized using the following expression:

$$K_{sn} = \frac{K'_{st}}{\gamma_w \cdot \left(\frac{\sigma_n}{p_a} \right)^{n_j}} \quad (4-2)$$

where K_{sn} is the normalized stiffness of the interface. The parameter n_j is the stiffness exponent in the Clough and Duncan (1971) hyperbolic model discussed in Chapter 2, and it is determined as described in Appendix D.

Figure 4-2 is a *diagram of normalized stiffness*, represented in logarithmic scale, versus stress level for all initial loading tests on the dense-Density-sand-against-concrete interface. It can be seen that, for all initial loading tests, the data follow the same trend very closely. The normalized stiffness decreases rapidly from its initial value at zero stress level K_{smo} during the initial stages of shear. Between stress levels of 0.2 and 0.9, there seems to be a logarithmic relationship between the stiffness values and the stress level, as suggested by the linear shape of the diagram. Beyond a stress level of 0.9, the interface stiffness decreases rapidly until failure is attained. Significant scatter is observed at stress levels lower than 0.2 because the interface displacement increments between two consecutive data points in the initial stages of shear are comparable to the resolution of the LVDTs. The *initial loading trend line* represented by the solid line in Figure 4-2 is the basis for discussion of the development of yield surfaces during shear, which is presented in the next section.

4.1.2 Development of yield surfaces during interface shear

No information appears to be available in the literature regarding the development of yield surfaces during interface shear. During this investigation, a number of unload-reload and staged shear interface tests were performed to probe the yield surface generated during shear. These tests were described in Chapter 3.

Figure 4-3 reproduces the results of unload-reload test T203_15 performed under constant normal stress on the dense-Density-sand-to-concrete interface (more details about this test are presented in Table 3-7 of Chapter 3 and Figure C14 of Appendix C). The interface was initially sheared to point *U*, then unloaded to point *R*, and finally reloaded to failure. It can be seen in Figure 4-3b that the interface is substantially stiffer during unloading-reloading than during initial loading at the same stress levels. It can also be seen that there is a sharp transition in the shear stress-displacement plot during reloading at the previous maximum value of shear stress defined by point *U*. This point corresponds to the position of the yield surface generated during initial shear.

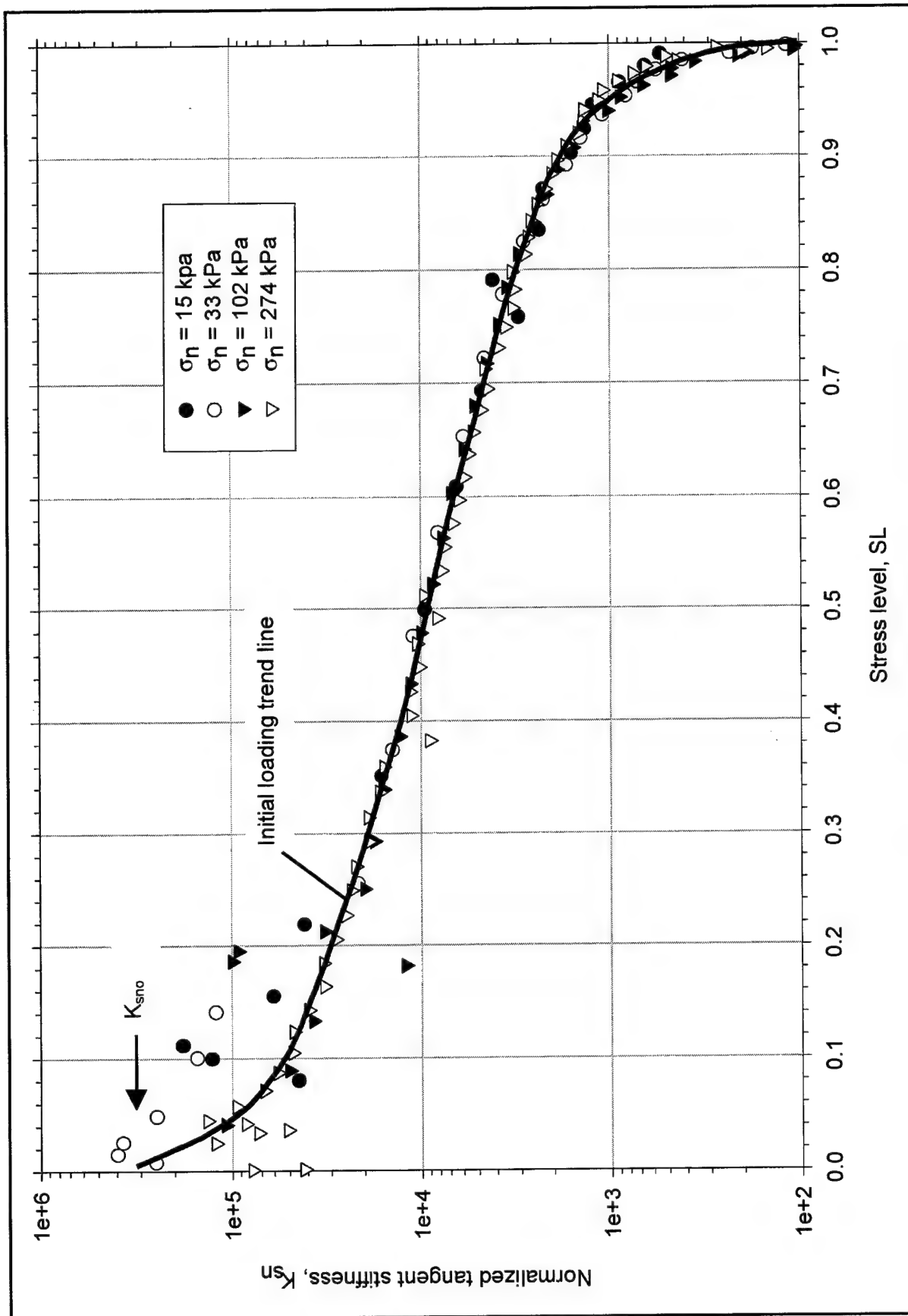


Figure 4-2. Diagram of normalized interface shear stiffness for the dense-Density-sand-to-concrete interface

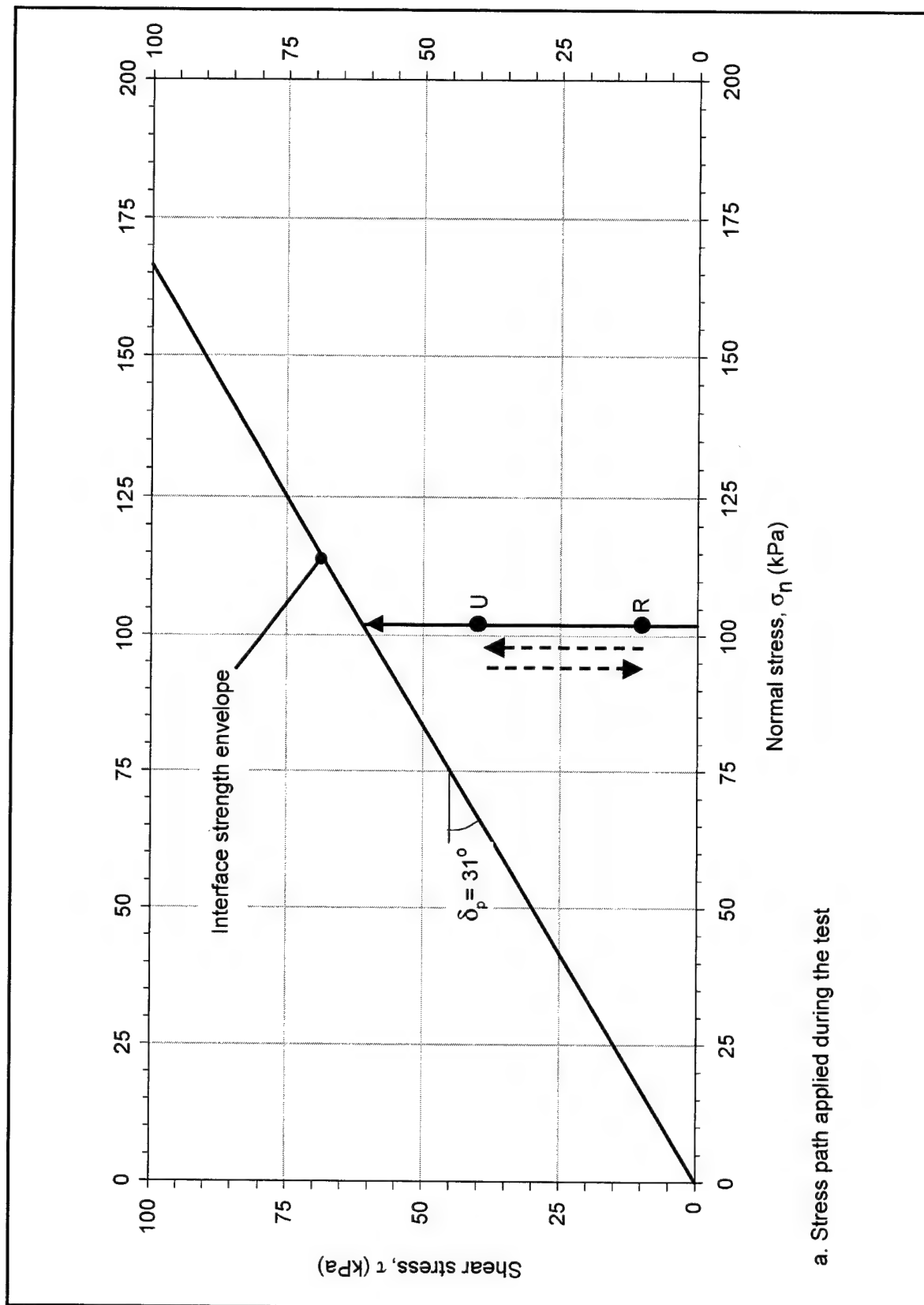


Figure 4-3. Unload-reload Test T203_15 on the dense-Density-sand-to-concrete interface (Continued)

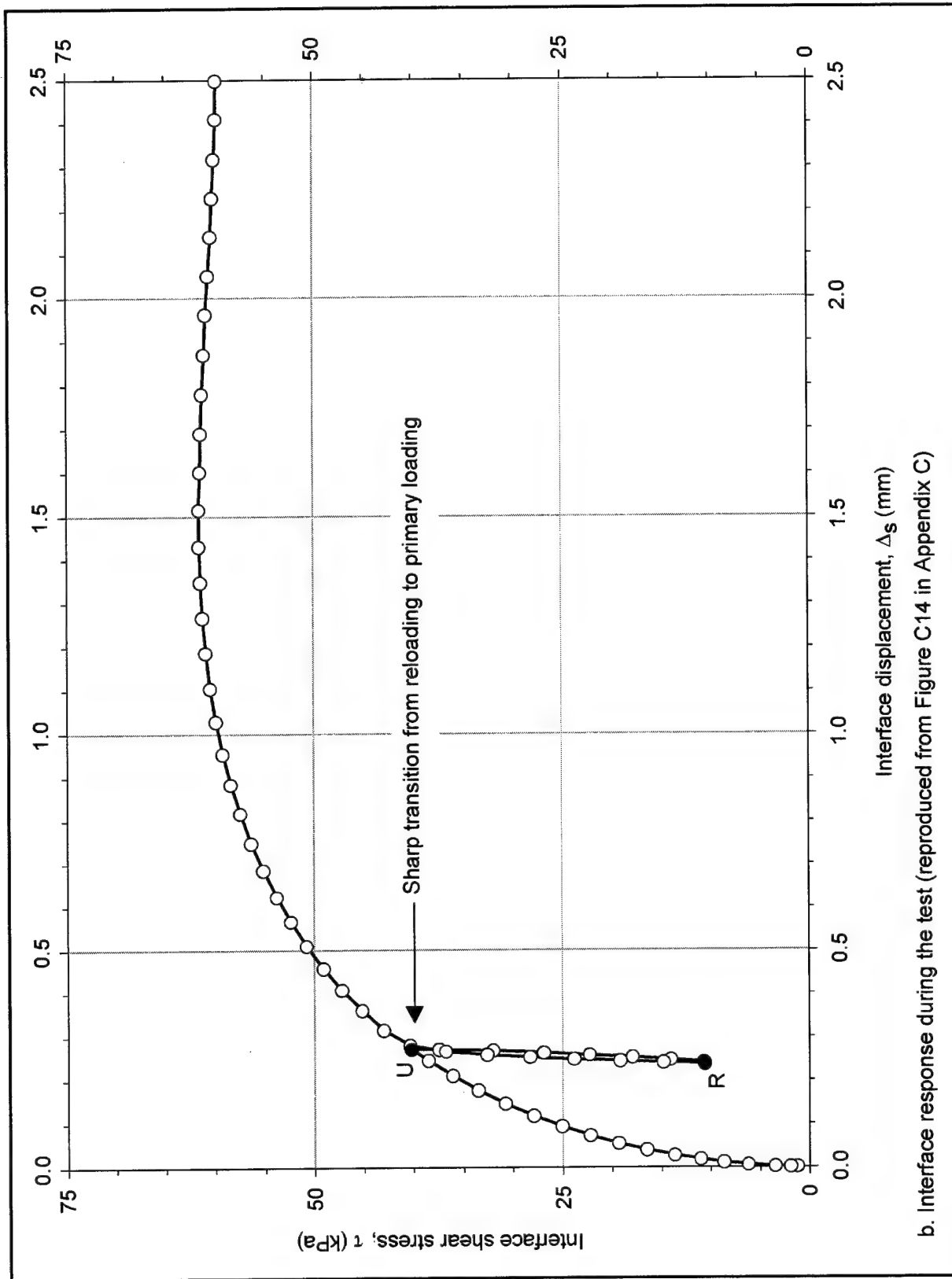


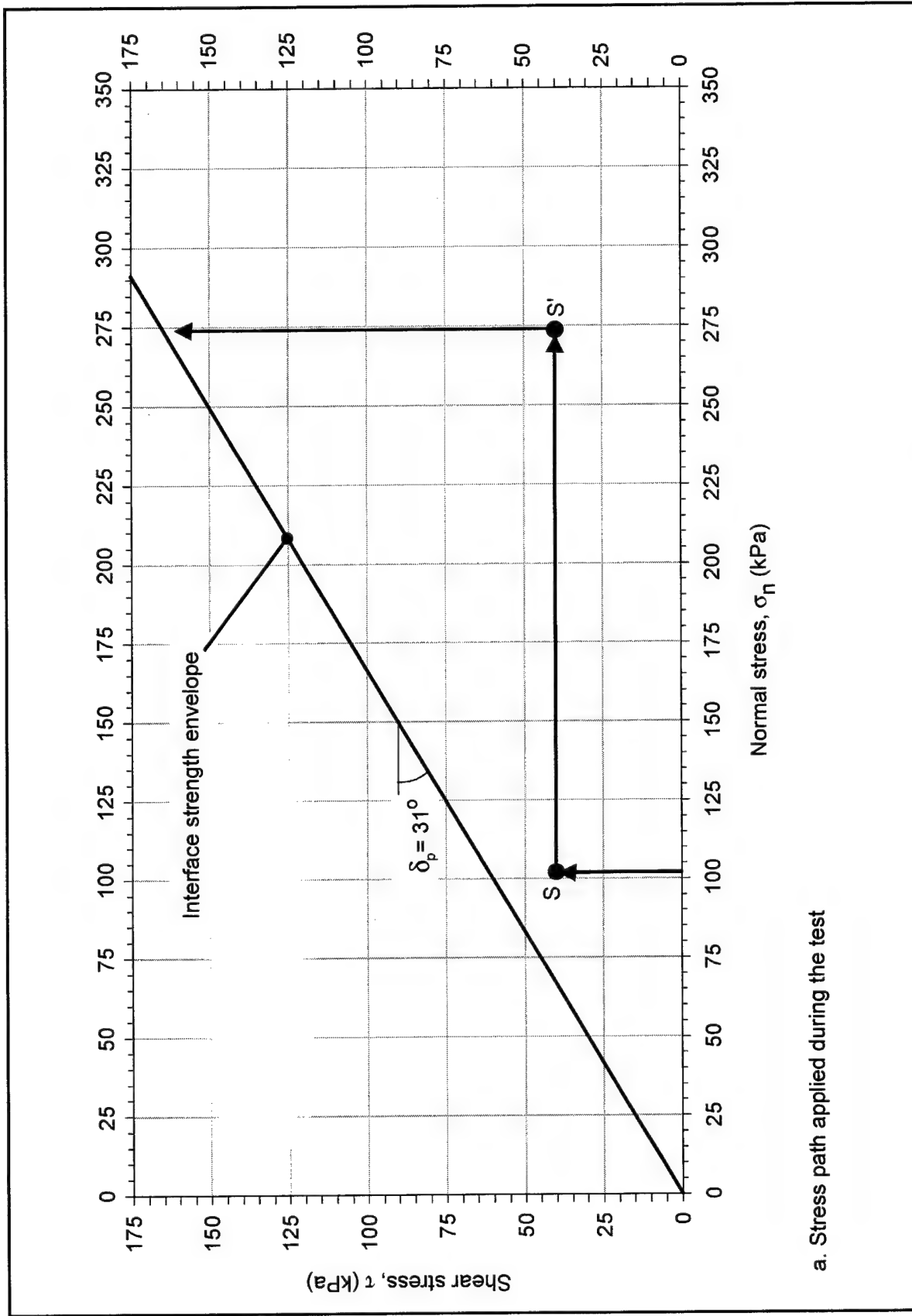
Figure 4-3. (Concluded)

The complete shape of the yield surface cannot be determined exclusively from the results of unload-reload tests. To complement the information given by tests such as T203_15, staged tests were also carried out. Figure 4-4 shows the results of staged test T105_40 performed on the dense-Density-sand-against-concrete interface (more details about this test are presented in Table 3-7 of Chapter 3 and Figure C7 of Appendix C). In this test, the interface was sheared to point *S* under a normal stress of 102 kPa. The normal stress was then increased to 274 kPa. The new state of stresses is represented by point *S'* in Figure 4-4. Shearing was resumed under this increased normal stress until failure was attained. The shear stress-displacement curve, presented in Figure 4-4b, shows a significant increase in interface stiffness after application of the normal pressure increment. This interface stiffness value decreases gradually as shearing progresses. The position of the yield surface, generated previously during virgin shear to point *S*, cannot be determined from visual inspection of Figure 4-4b because there is no sharp transition between stiff and soft response such as that observed in the unload-reload tests.

In conclusion, visual examination of the shear stress-displacement diagram of some tests may not reveal the position or shape of the yield surface generated during initial loading of the interface. As described in the following paragraphs, the procedure for normalization of the interface test data described in Section 4.1.1 facilitates detection of the position of the yield surface.

Figure 4-5 shows the diagram of normalized stiffness for unload-reload test T203_15, together with the initial loading trend line from Figure 4-2. It can be seen that, during initial loading of the interface to point *U*, the data follow the same trend given by the initial loading tests. Upon a change in the direction of shearing (points *U* and *R*), there is a significant increment in the interface stiffness values. During unloading-reloading between points *U* and *R*, the interface stiffness values decrease progressively but always remain larger than the initial loading stiffness. During reloading from point *R*, there is a significant drop in the stiffness values at approximately the past maximum stress level, given by point *U*. As loading progresses beyond point *U*, the initial loading trend line is followed.

Figure 4-6 is the diagram of normalized stiffness for staged shear test T105_40. It also shows the initial loading trend line from Figure 4-2. During initial loading to point *S*, the normalized stiffness values follow the initial loading trend line. After application of the normal stress increment from point *S* to point *S'*, the normalized stiffness value increases substantially above that given by the initial loading trend line. As shear progresses beyond point *S'*, the normalized stiffness decreases until the past maximum stress level, given by point *S*, is reached. The initial loading trend line is retaken at approximately the stress level given by point *S*. The transition from a stiffer response, after application of the normal stress increment, to a softer response during yielding, represented by the initial loading trend line, can be recognized on this normalized stiffness diagram. These observations have been confirmed for all the unload-reload, staged shear, and multidirectional stress path tests performed on all three types of interfaces tested during this investigation.



a. Stress path applied during the test

Figure 4.4. Staged shear Test T105_40 on the dense-Density-sand-to-concrete interface (Continued)

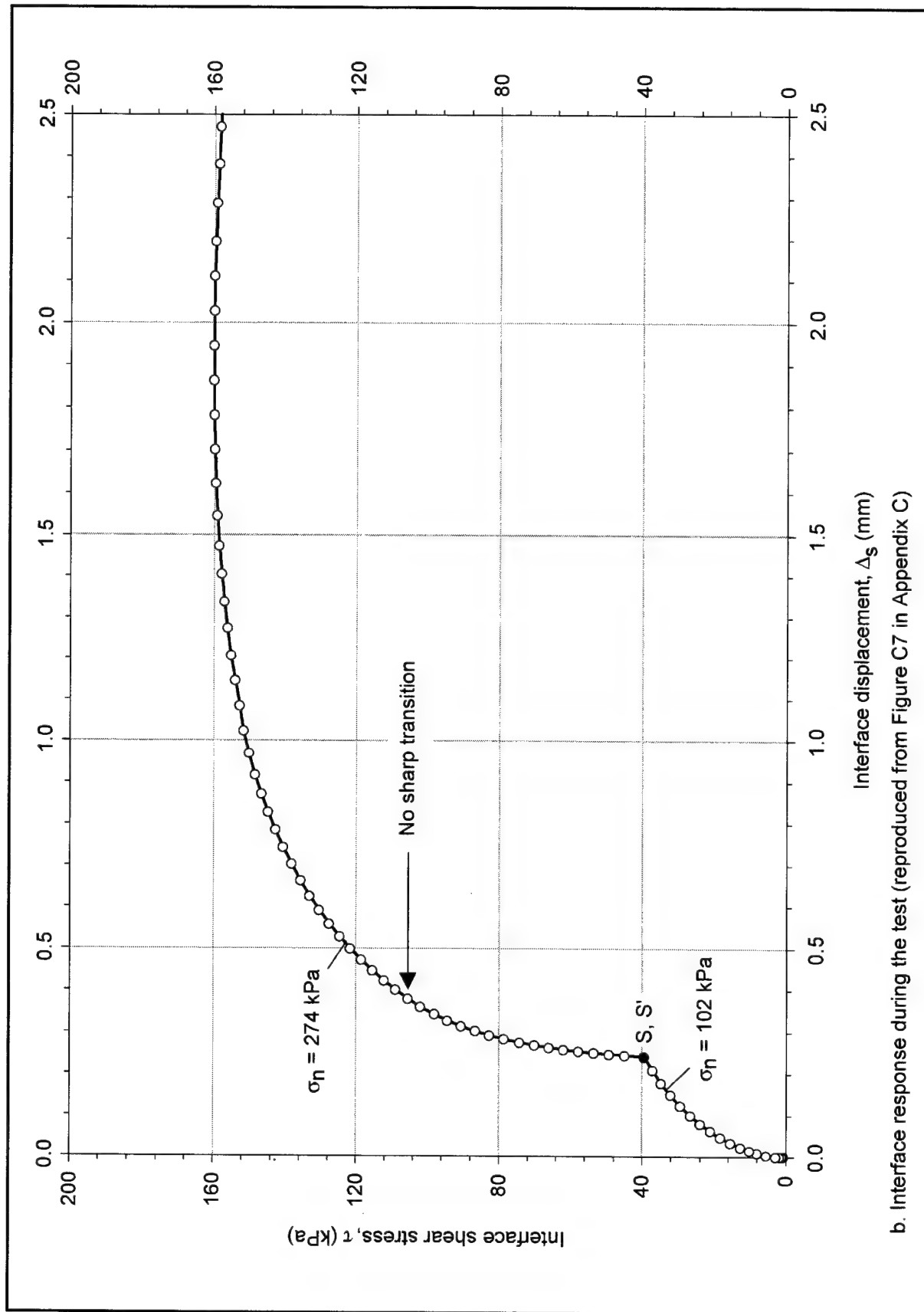


Figure 4-4. (Concluded)

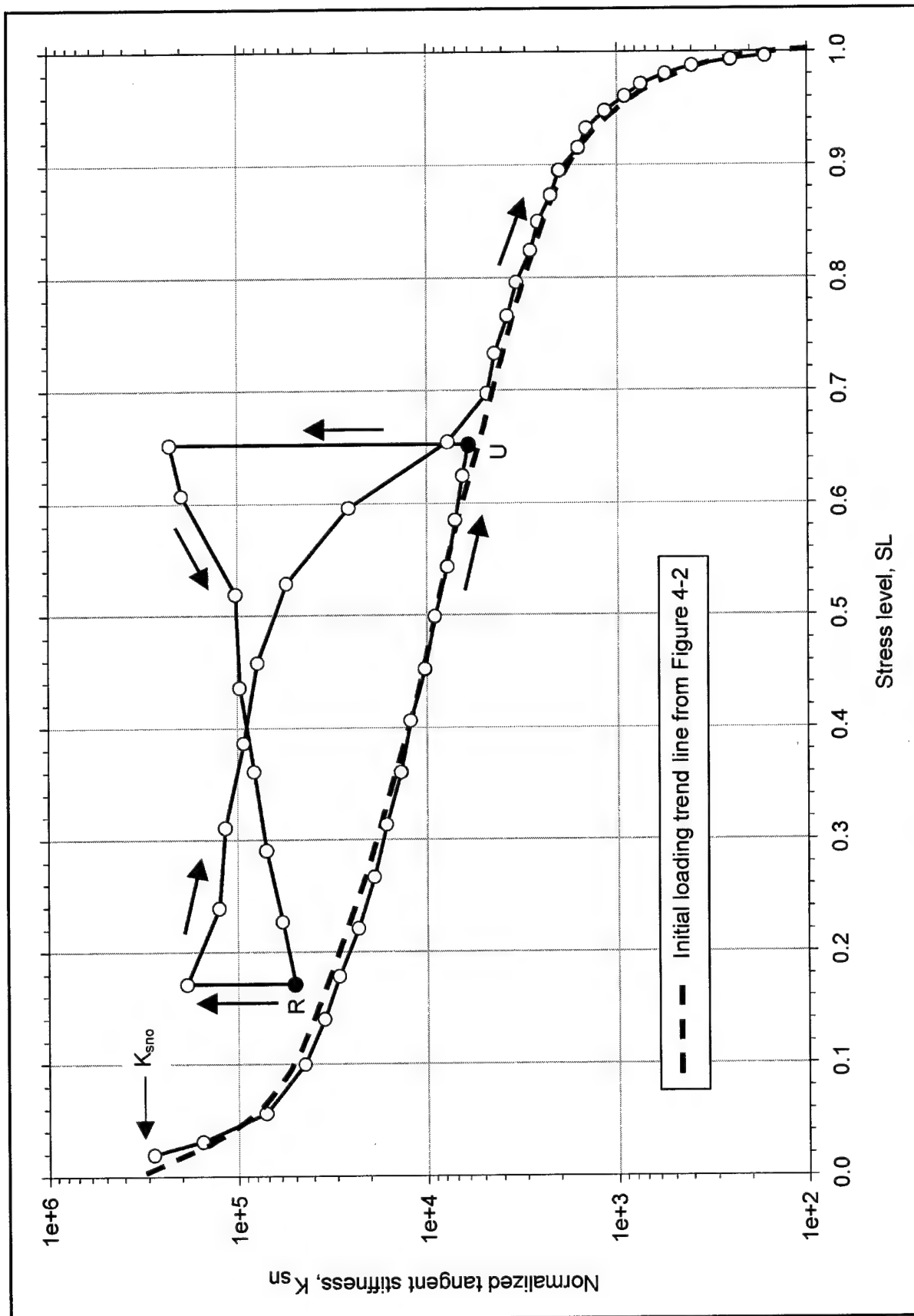


Figure 4-5. Diagram of normalized interface shear stiffness for unload-reload Test T203_15

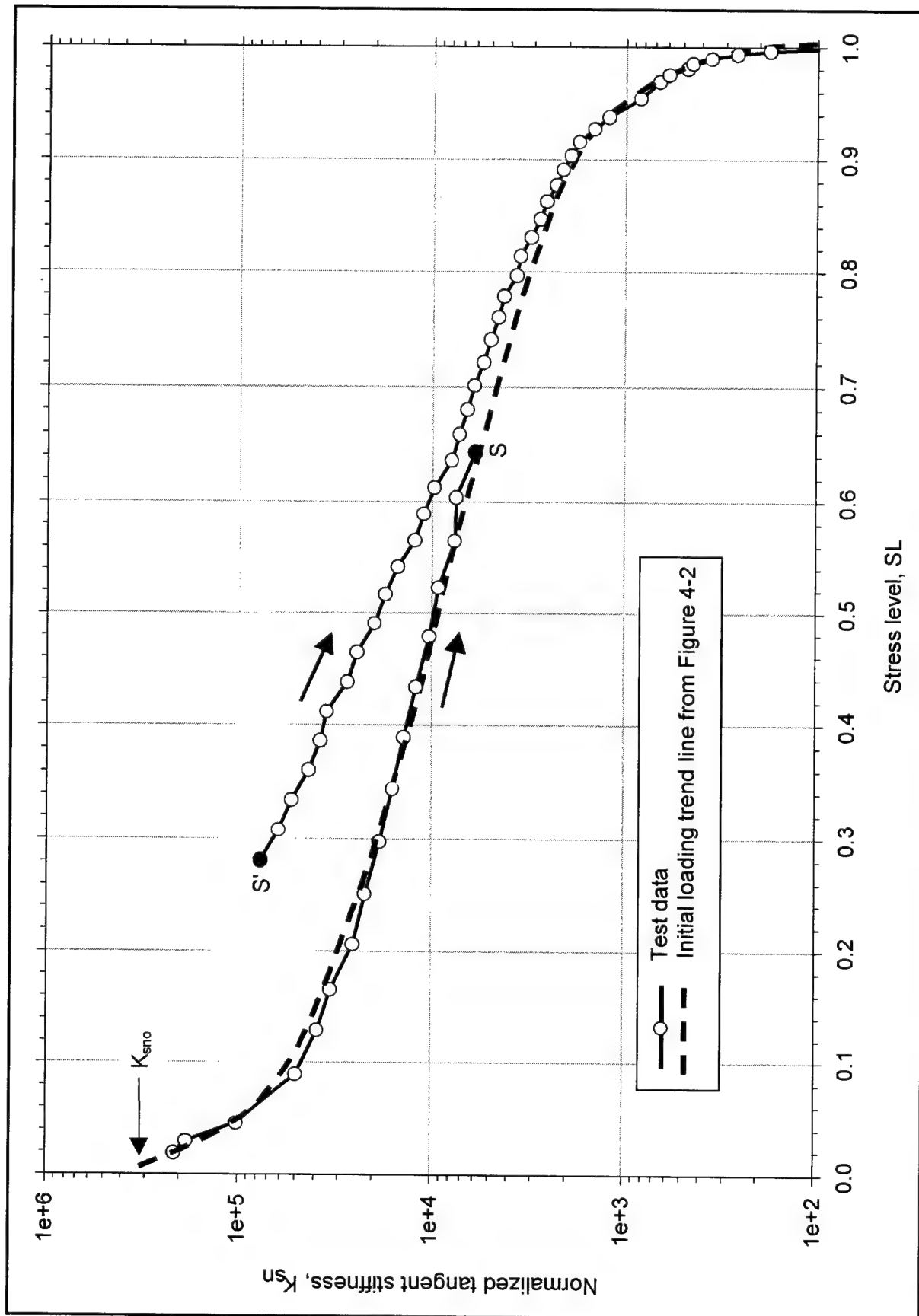


Figure 4-6. Diagram of normalized interface shear stiffness for staged shear Test T105_40

Interpretation of this phenomenon based on the test results can be illustrated by the hypothetical interface test represented in Figure 4-7. In a sand-to-concrete interface, two yield surfaces, $SL+$ and $SL-$, are generated during shear. It is assumed that they are defined by the past maximum and minimum values of stress level applied to the interface. Before shearing is applied, the two yield surfaces coincide with the normal stress axis in the σ_n - τ plane, as represented in Figure 4-7a. As the interface is sheared along a stress path such as 1-2, the upper yield surface, $SL+$, is pushed into the first quadrant to the position given by the stress level at point 2 (Figure 4-7b). During this stage, the lower yield surface, $SL-$, remains in its original position on the normal stress axis.

During subsequent shear from point 2 to point 3 (Figure 4-7c), the maximum and minimum values of stress level are not exceeded and the position of both yield surfaces remains unchanged. As shearing progresses beyond point 3, the stress level decreases below its past minimum value, and the lower yield surface, $SL-$, is pushed downward into the fourth quadrant (Figure 4-7d). The position of the lower yield surface, $SL-$, is defined by the stress level at point 4. Subsequent shearing from point 4 to point 5 does not induce any change in the positions of the yield surfaces because the minimum and maximum stress level values are not exceeded.

This concept of yield surfaces can be expressed mathematically as:

$$\begin{aligned} SL+ &= \text{past maximum stress level} \geq 0 \\ SL- &= \text{past minimum stress level} \leq 0 \end{aligned} \quad (4-3)$$

If the strength envelope is linear and the interface does not have an adhesion intercept, then the yield surfaces will be straight lines passing through the origin of the σ_n - and τ -axes.

Some authors have proposed similar definitions of yield surfaces for granular soils (Lade and Duncan 1975 and 1976; Wood 1990). In rough interfaces, as discussed in Chapter 2, the interface properties appear to be controlled by response of a thin layer of soil adjacent to the structural surface. Consequently, it appears logical that similarities exist between yield surfaces developed in sand-to-concrete interfaces and granular soils.

4.1.3 Loading regions

Plasticity-based constitutive models for soils consider two types of response to loading. An elastic response of the soil is assumed if the stress path applied to the soil is contained within the region delimited by the yield surface. If the soil undergoes yielding, a plastic response is assumed and the total strain is calculated as the sum of elastic, recoverable strains and plastic, nonrecoverable strains.

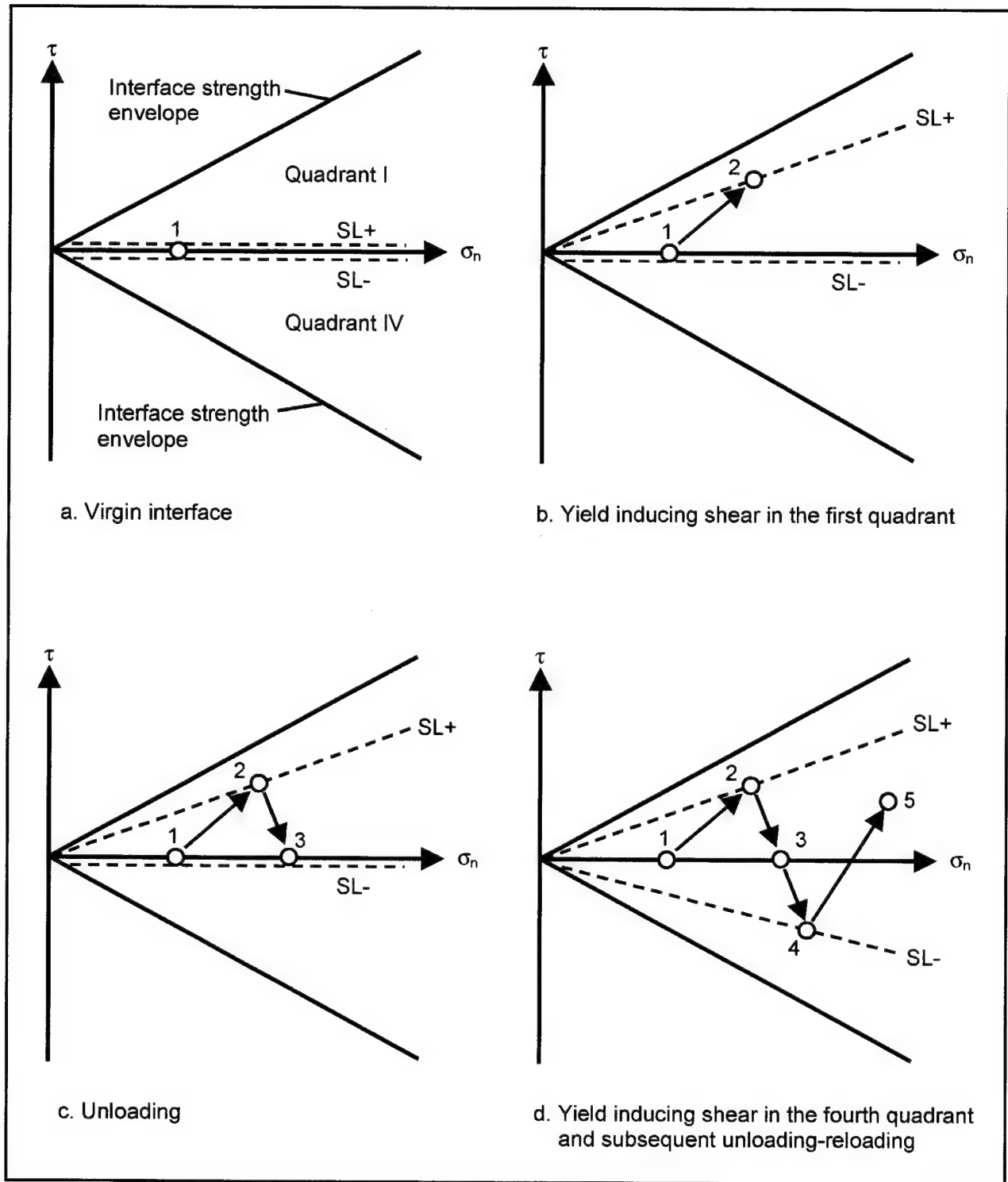


Figure 4-7. Evolution of yield surfaces during interface shear

A similar concept is proposed for use in the extended hyperbolic model. Two types of loading are defined as illustrated in Figure 4-8. *Unloading-reloading* takes place along any stress path that is contained within the region defined by the *SL+* and *SL-* surfaces. *Yielding* occurs when the stress path reaches one of the two yield surfaces. In the hypothetical test of Figure 4-7, yielding occurs along stress paths 1-2 and 3-4. Unloading-reloading takes place along stress paths 2-3 and 4-5.

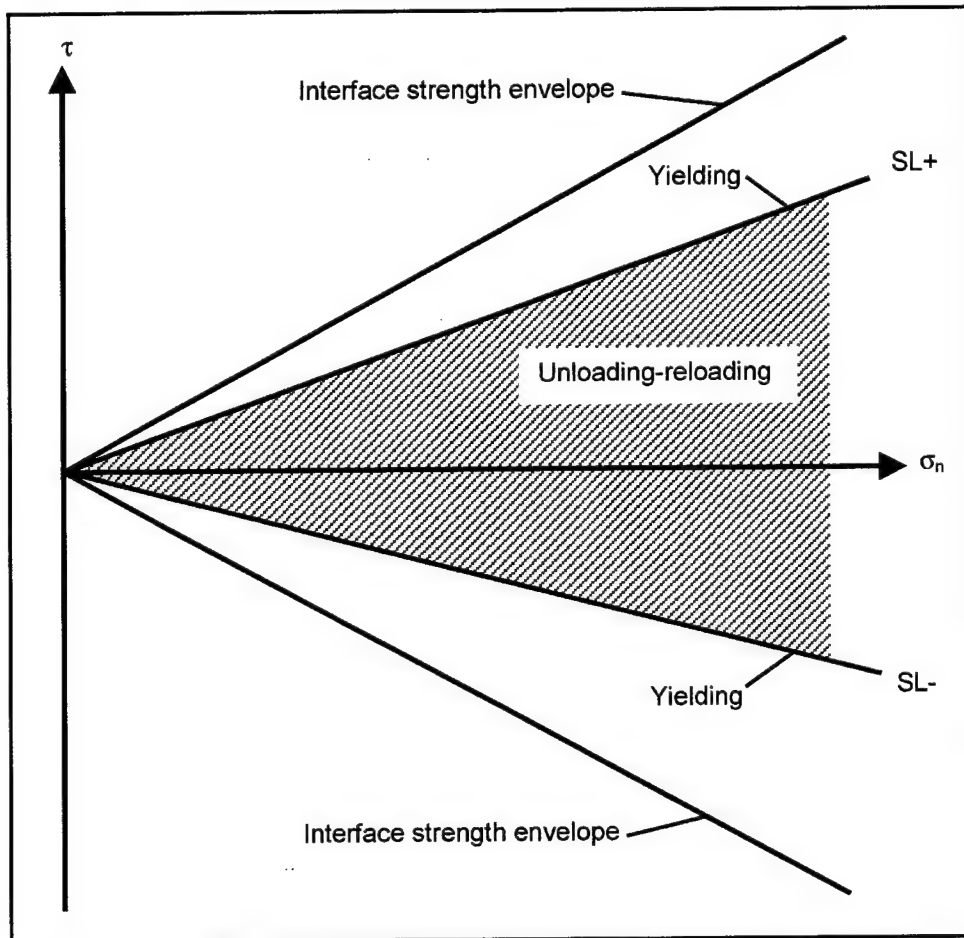


Figure 4-8. Loading regions for Versions I and II of the extended hyperbolic model

According to this concept, unload-reload tests such as T203_15 (Figure 4-3) and staged shear tests such as T105_40 (Figure 4-4) induce unloading-reloading of the interface. However, examination of the normalized stiffness diagrams for these tests (Figures 4-5 and 4-6) reveals some differences between the interface response during unload-reload tests and during staged shear.

Figure 4-9 compares the normalized stiffness diagrams for Tests T203_15 and T105_40. It can be seen that during reloading in Test T203_15, the transition of interface stiffness values from the unload-reload region to yielding is abrupt. On the other hand, there is a gradual transition in the stiffness values from

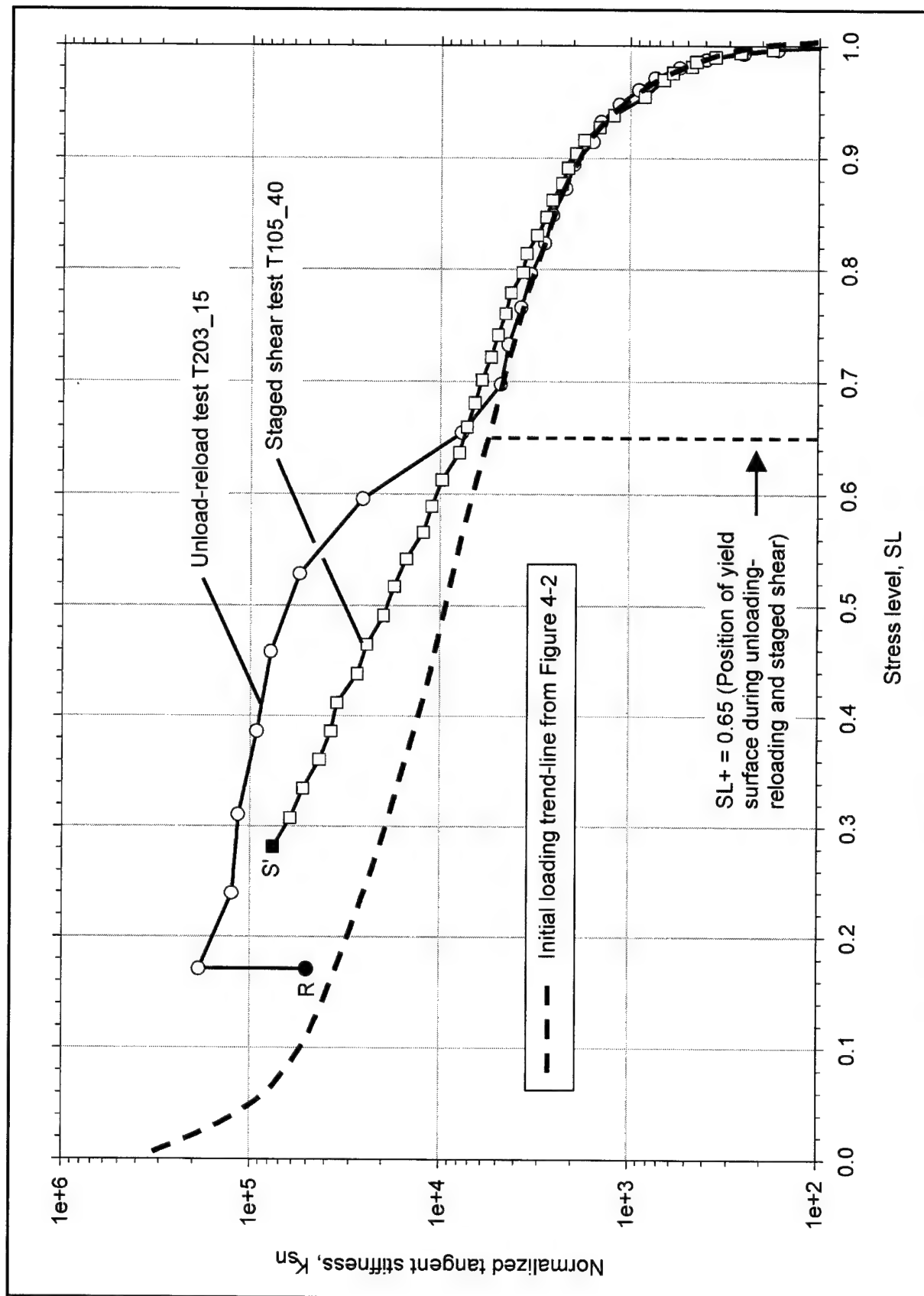


Figure 4-9. Comparison between the normalized stiffness diagrams for Tests T203_15 and T105_40

unload-reload to yielding during staged shear Test T105_40. Therefore, the stiffness values along an unloading-reloading stress path are not uniquely defined by the value of stress level, but are stress-path dependent. If this stress-path dependency is ignored, an error is introduced in the predicted interface response when lock wall-backfill interfaces are modelled. As discussed in a subsequent section, this error may be relatively small for most types of loading expected in the field.

For analyses where accurate predictions are required, it is convenient to introduce additional loading regions. Two *transition surfaces* are illustrated in Figure 4-10. They are defined as the past maximum and minimum values of shear stress. The concept of transition surfaces can be expressed mathematically as:

$$\begin{aligned}\tau+ &= \text{past maximum shear stress} \geq 0 \\ \tau- &= \text{past minimum shear stress} \leq 0\end{aligned}\tag{4-4}$$

The transition surfaces are straight lines parallel to the σ_n axis in the σ_n - τ plane. The *transition regions* are defined as the areas delimited by the $SL+$ and $\tau+$ surfaces and by the $SL-$ and $\tau-$ surfaces. A stress path corresponds to *transition loading* if it lies within any of the two transition regions. Table 4-1 summarizes the definition of loading regions.

4.1.4 Interface response at yield

As discussed previously, the data from a complete set of initial loading tests can be represented by a unique trend line of normalized stiffness. The existence and shape of this trend line reveal that the interface stiffness values are normal stress- and stress level-dependent. It appears that, regardless of past loading history, the interface response follows this initial loading trend line if yield-inducing shear takes place under constant normal stress.

When yield-inducing shear takes place along inclined stress paths, i.e. under changing normal stress, the data do not fit the initial loading trend line. Figure C27 in Appendix C shows the results of multidirectional stress path Test T205_5, which was performed on the dense-Density-sand-against-concrete interface. The interface stiffness values have been normalized and are presented in Figure 4-11, together with the initial loading trend line from Figure 4-2. According to the definition of loading regions presented in the previous section, yield-inducing shear was applied to the interface throughout this test. However, it can be seen that the interface stiffness values do not match the initial loading trend line when the direction of the stress path is not vertical.

Several important conclusions can be drawn from these observations:

- a. The interface stiffness during yield-inducing shear is significantly affected by the inclination of the stress path in the σ_n - τ plane.

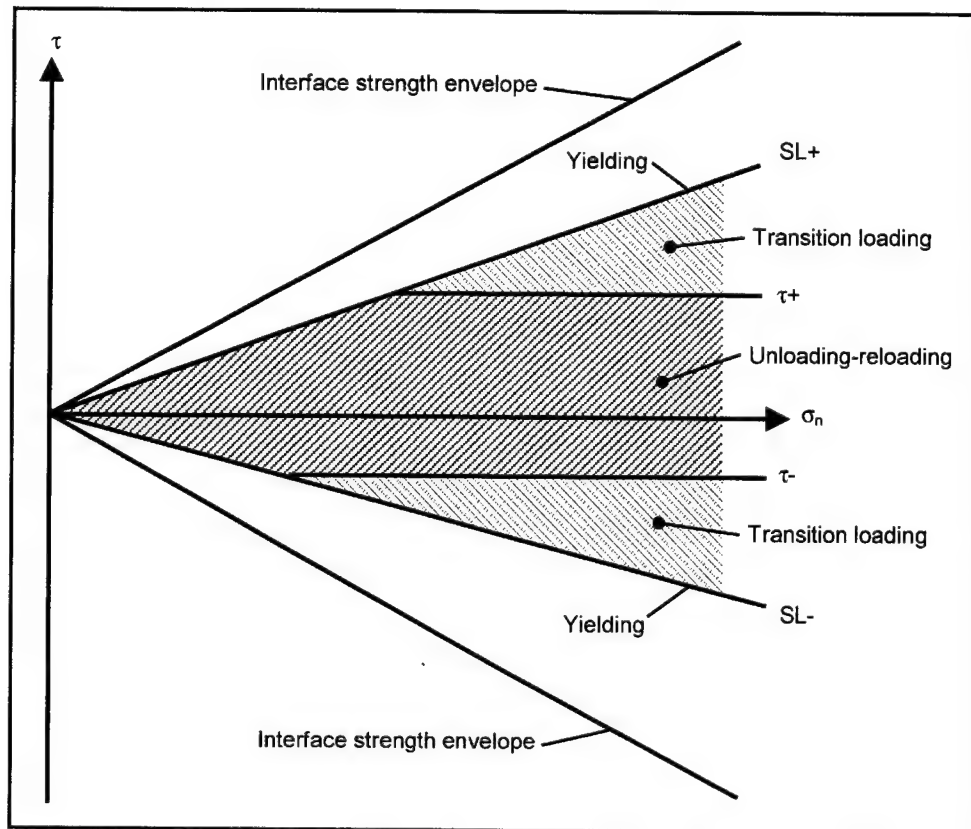


Figure 4-10. Loading regions for Version III of the extended hyperbolic model

Table 4-1 Definition of Types of Loading in Interface Shear	
Type of Loading	Condition
Yield-inducing shear	$SL = SL +$ or $SL = SL -$
Unloading-reloading	$SL < SL +$ and $\tau < \tau +$ and $SL > SL -$ and $\tau > \tau -$
Transition loading	$SL < SL +$ and $\tau \geq \tau +$ or $SL > SL -$ and $\tau \leq \tau -$

- b. During yield-inducing shear along a vertical stress path, the interface response is uniquely defined by the initial loading trend line.
- c. An accurate prediction of the interface response at yield requires a constitutive formulation that models adequately the dependence of the interface stiffness on the normal stress, stress level, and rate of change of normal stress during shearing.

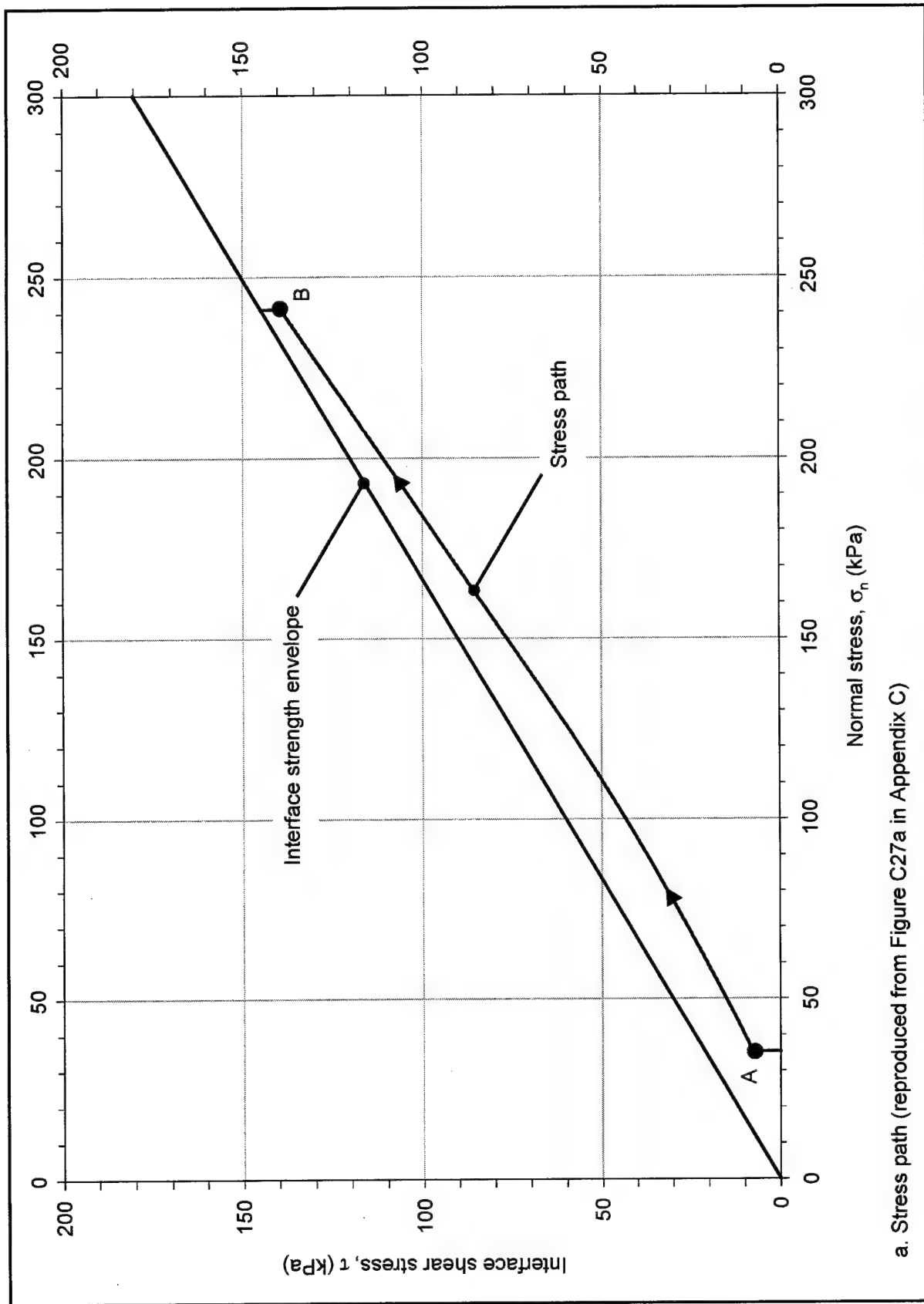


Figure 4-11. Multidirectional stress path T205_5 on the dense-Density-sand-to-concrete interface (Continued)

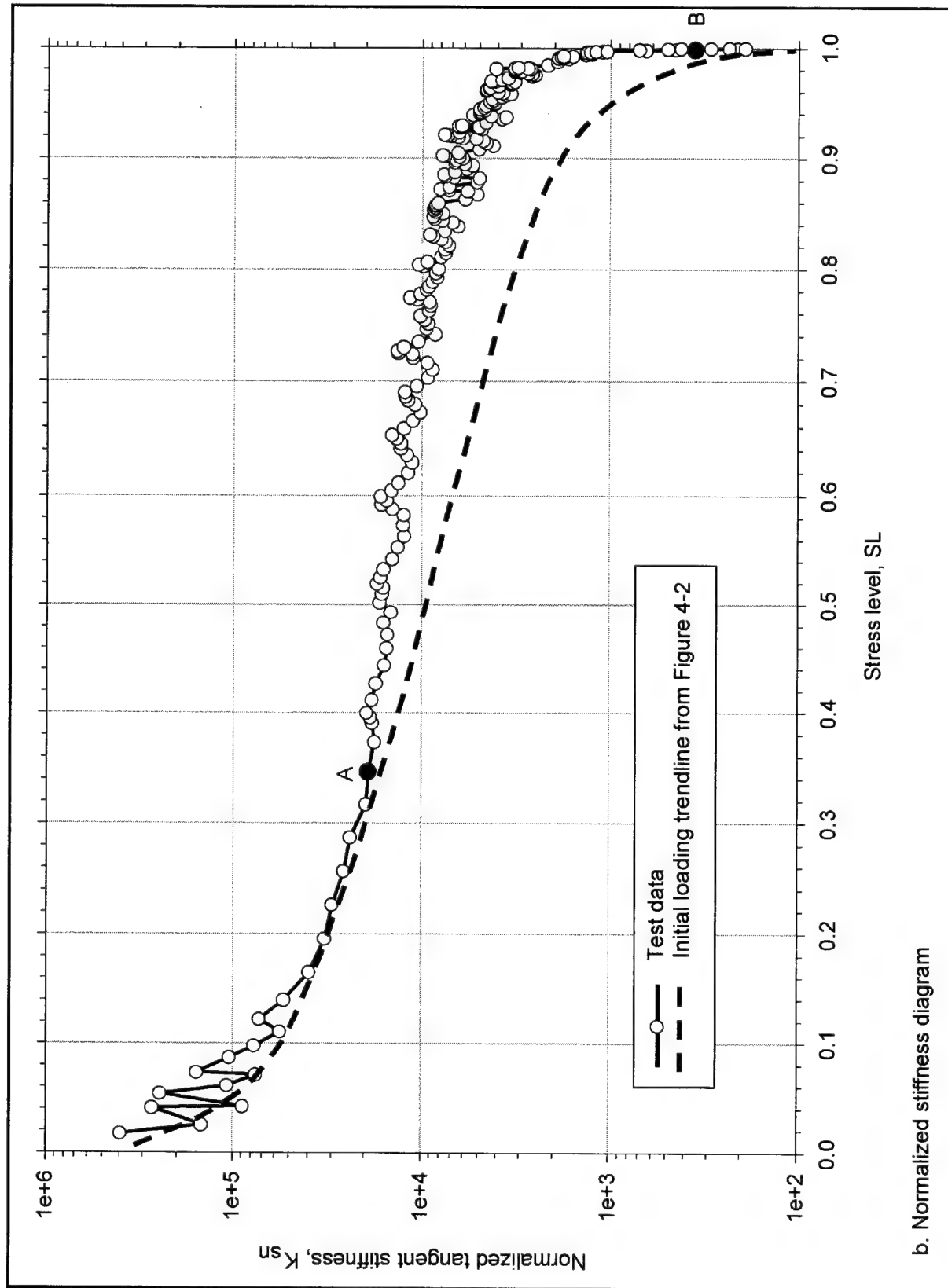


Figure 4-11. (Concluded)

4.1.5 Interface response during unloading-reloading

Examination of the normalized diagrams of unload-reload tests such as T203_15 in Figure 4-5 reveals several important aspects of the interface response. Upon unloading and reloading at points *U* and *R*, the interface stiffness value increases significantly. From the analysis of the results of all the unload-reload tests performed, it appears that the interface stiffness upon unloading or reloading always increases to a magnitude that is approximately equal to the initial interface stiffness K_{sno} .

As unloading or reloading progresses, the interface stiffness decreases gradually until yielding takes place. The rate of degradation of the interface stiffness during unloading appears to be similar to the rate of degradation during reloading, and independent of the point at which the shearing direction is reversed. Further, the normalized unload-reload data appear to follow a logarithmic relationship with the stress level, which is qualitatively similar to that found for initial loading. In most of the tests performed, the interface stiffness during unloading-reloading was greater than or equal to the interface stiffness during initial loading at the same stress level.

Finally, there is an abrupt transition between unloading-reloading and yielding in the normalized stiffness diagram. These observations can be summarized as follows:

- a. The interface stiffness value immediately after unloading or reloading appears always to be the same, and it may be possible to define this stiffness in terms of the initial interface stiffness measured at the start of an initial loading test.
- b. The type of interface response during unloading-reloading appears to be qualitatively similar to the interface response during initial loading.
- c. The transition from unloading-reloading to yielding is usually abrupt.
- d. The interface stiffness is usually greater during unloading-reloading than during initial loading for the same stress level.

4.1.6 Interface response during transition loading

It was noted previously that during transition loading, such as applied in a staged shear test, the interface stiffness values decrease gradually as the yield surface is approached. This behavior differs from unloading-reloading, where an abrupt transition is often observed when the yield surface is reached.

Figure C28 in Appendix C shows the results of multidirectional stress path Test T206_5 performed on the dense-Density-sand-against-concrete interface. A portion of the stress path applied during this test is reproduced in Figure 4-12, together with the corresponding normalized stiffness diagram. After shearing to point *C*, which defines the position of the upper yield surface, $SL+$, the interface was loaded along stress path *C-D-E-F*. Point *T1* of the stress path lies on the

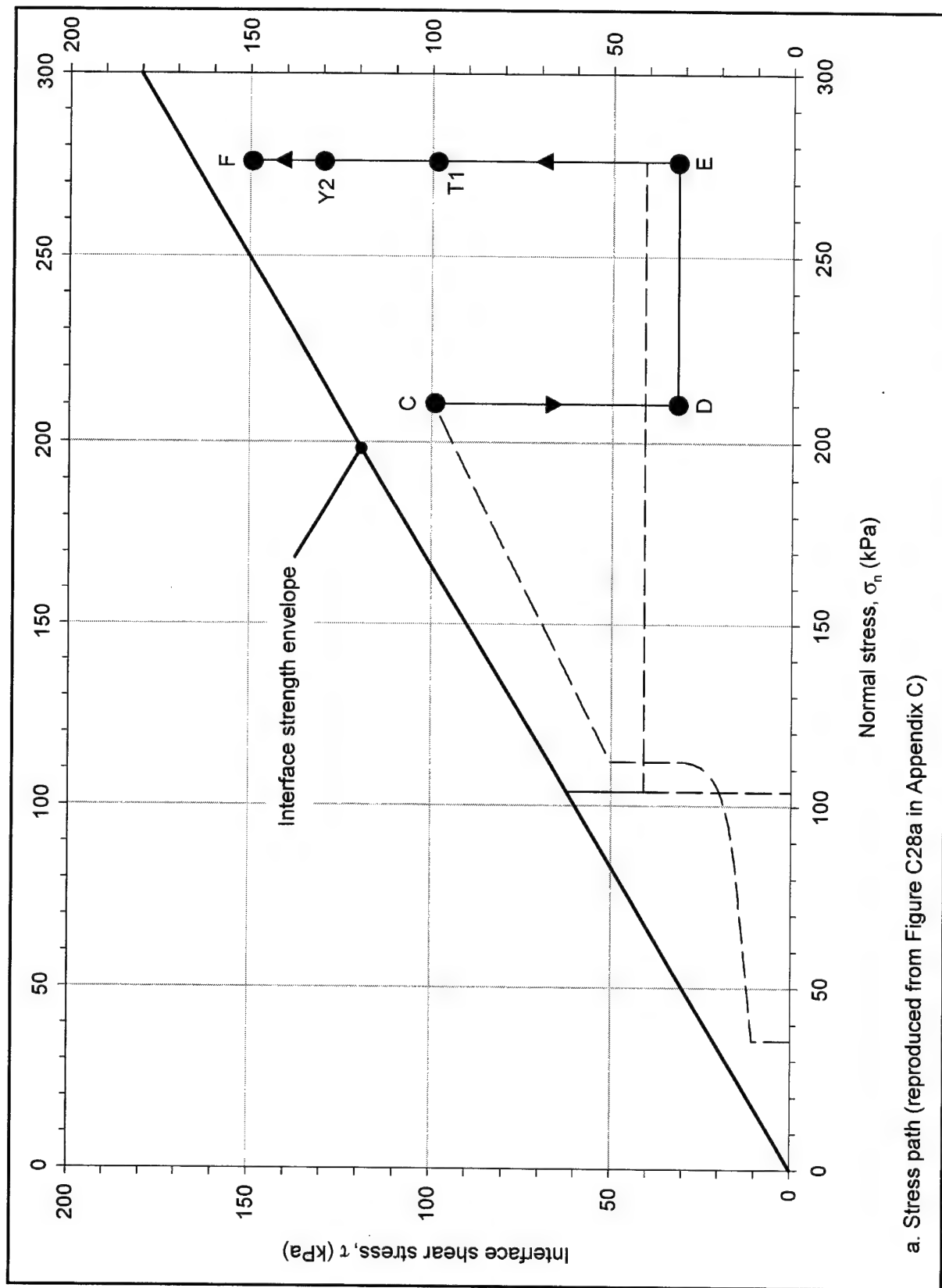


Figure 4-12. Multidirectional stress path Test T206_5 on the dense-Density-sand-to-concrete interface (Continued)

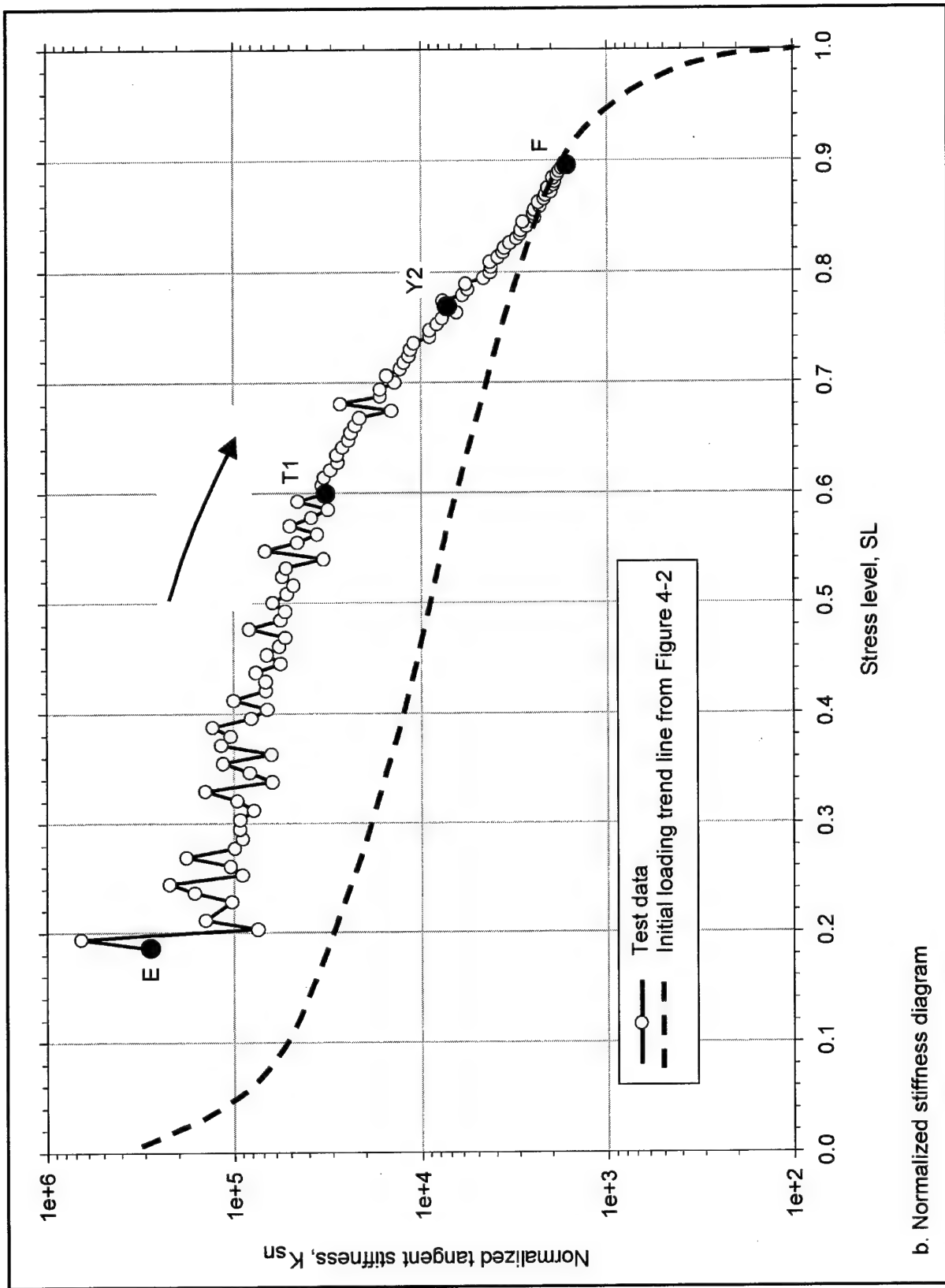


Figure 4-12. (Concluded)

transition surface, which is defined by the shear stress at point *C*. Point *Y2* lies on the yield surface, defined by the stress level at point *C*.

According to the definition of the loading regions presented in Table 4-1, segment *E-T1* of the stress path corresponds to reloading of the interface. The normalized stiffness diagram in Figure 4-12b corresponding to segment *E-F* of the stress path shows that the interface stiffness upon reloading at point *E* has a large value and, as expected, it decreases gradually during shearing to point *T1*.

Shearing from point *T1* to point *Y2* corresponds to transition loading. There is a larger rate of degradation of the interface stiffness during transition loading than during reloading, as revealed by the normalized stiffness diagram. During loading beyond point *Y2*, the initial loading trend line is retaken. Similar observations can be made regarding the results of all tests where transition loading took place.

If the normalized stiffness values at points *T1* and *Y2* are known, then the normalized stiffness at any point inside the transition region can be calculated approximately through a simple interpolation. According to the yield surface definition presented previously, a point such as *Y2* is assumed to lie on the yield surface; therefore, the normalized stiffness at *Y2* can be estimated from the initial loading trend line. The interface stiffness at a point such as *T1* depends on the previous loading history of the interface.

It can be seen in Figure 4-12 that point *Y2* does not lie exactly on the initial loading trend line. This suggests that the definition of yield surface given previously is only approximate. It must be noted, however, that the greatest divergence between theory and experimental observations regarding the position of yield surfaces corresponds to that observed in Figure 4-12b. All other experimental results showed better agreement.

In conclusion, the following observations can be made regarding the interface response during transition loading:

- a. When a stress path intersects a transition surface, the value of interface stiffness is determined by the previous loading history.
- b. The normalized interface stiffness at yield is approximately determined by the initial loading trend line and the current position of the yield surface.
- c. The normalized interface stiffness at any point inside the transition region can be determined by interpolation.

4.2 Formulation of the Extended Hyperbolic Model for Yield-Inducing Shear

The advantages of the hyperbolic model for interfaces developed by Clough and Duncan (1971) were discussed in Chapter 2. The model reproduces the non-linearity of the shear stress-displacement response of the interface and is easy to implement in SSI analyses. In incremental analyses, Equation 2-11 is used to

determine the tangent stiffness of the interface at any point during virgin shear. The interface stiffness value thus depends only on two state variables: the shear stress level and the normal stress on the interface. The interface properties are represented by the following parameters:

- a. K_I = stiffness number.
- b. n_j = stiffness exponent.
- c. R_{ff} = failure ratio.
- d. δ = interface friction angle.

Several authors have contributed to the development of a database of interface hyperbolic parameter values (Clough and Duncan 1971; Peterson et al. 1976; Acar, Durgunoglu, and Tumay 1982; Lee et al. 1989). The availability of reference interface hyperbolic parameters is an important advantage of the hyperbolic model.

The hyperbolic model was developed based on the results of virgin shear tests of interfaces under constant normal stress. It is not accurate for cases where the shear and normal stresses change simultaneously, and does not account for unloading-reloading. In the formulation of the extended hyperbolic model that was developed during this investigation the Clough and Duncan (1971) formulation is extended to model initial or virgin loading along any type of stress path, as well as unloading-reloading of the interface.

This section contains a detailed description of the formulation for yield-inducing shear in the extended hyperbolic model. This formulation is based on the experimental observations of interface response presented in the previous section. A hypothesis of interface response at yield is introduced that fits the experimental observations regarding the influence of stress path inclination on interface response. Subsequently, a general mathematical formulation is derived that can be used to extend any appropriate constitutive model available in the literature to the more general case of simultaneous changes in shear and normal stress. Finally, an extended formulation of the hyperbolic model by Clough and Duncan (1971) is derived.

4.2.1 Hypothesis of interface response at yield

Figure 4-13 illustrates the τ - Δ_n response of a hypothetical interface to loading along vertical, yield-inducing stress paths. In this type of loading, shearing occurs under constant normal stress such as in the initial loading tests described in Chapter 3. A set of τ - Δ_n curves, such as those shown in Figure 4-13b, generates a surface in the τ - Δ_n - σ_n space, as illustrated in Figure 4-14. In the extended hyperbolic model, it is assumed that the response of the interface to shear along any yield-inducing stress path is uniquely determined by this *initial loading surface*.

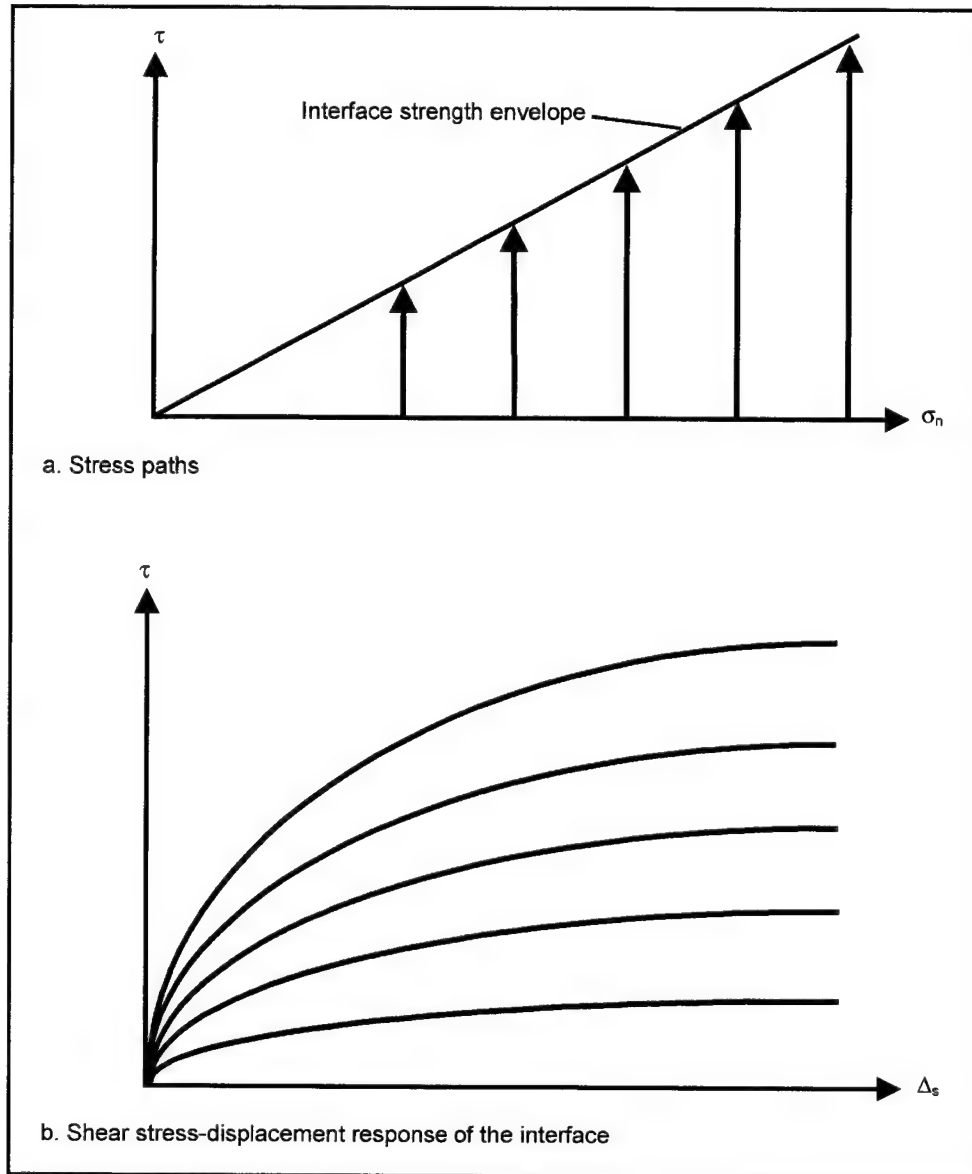


Figure 4-13. Interface response to a set of hypothetical initial loading tests

Two stress paths are illustrated in the σ_n - τ plane in Figure 4-14. Vertical stress path v corresponds to shearing under constant normal stress. The response of the interface is given by line v' on the initial loading surface in the τ - Δ_s - σ_n space. For the inclined stress path i , where both shear and normal stresses change simultaneously, the interface response is given by line i' , also on the initial loading surface. Lines v'' and i'' in the Δ_s - τ plane are the projections of lines v' and i' , respectively. They correspond to the interface response of the hypothetical interface to stress paths v and i .

Point P is located at the intersection between stress paths v and i . The interface stiffness at P during shear along stress path v is given by the slope, K_{st} , of line v'' in the Δ_s - τ plane. The stiffness at P during shear along stress path i is given by the slope, K'_{st} , of line i'' . Therefore, according to this hypothesis, the interface

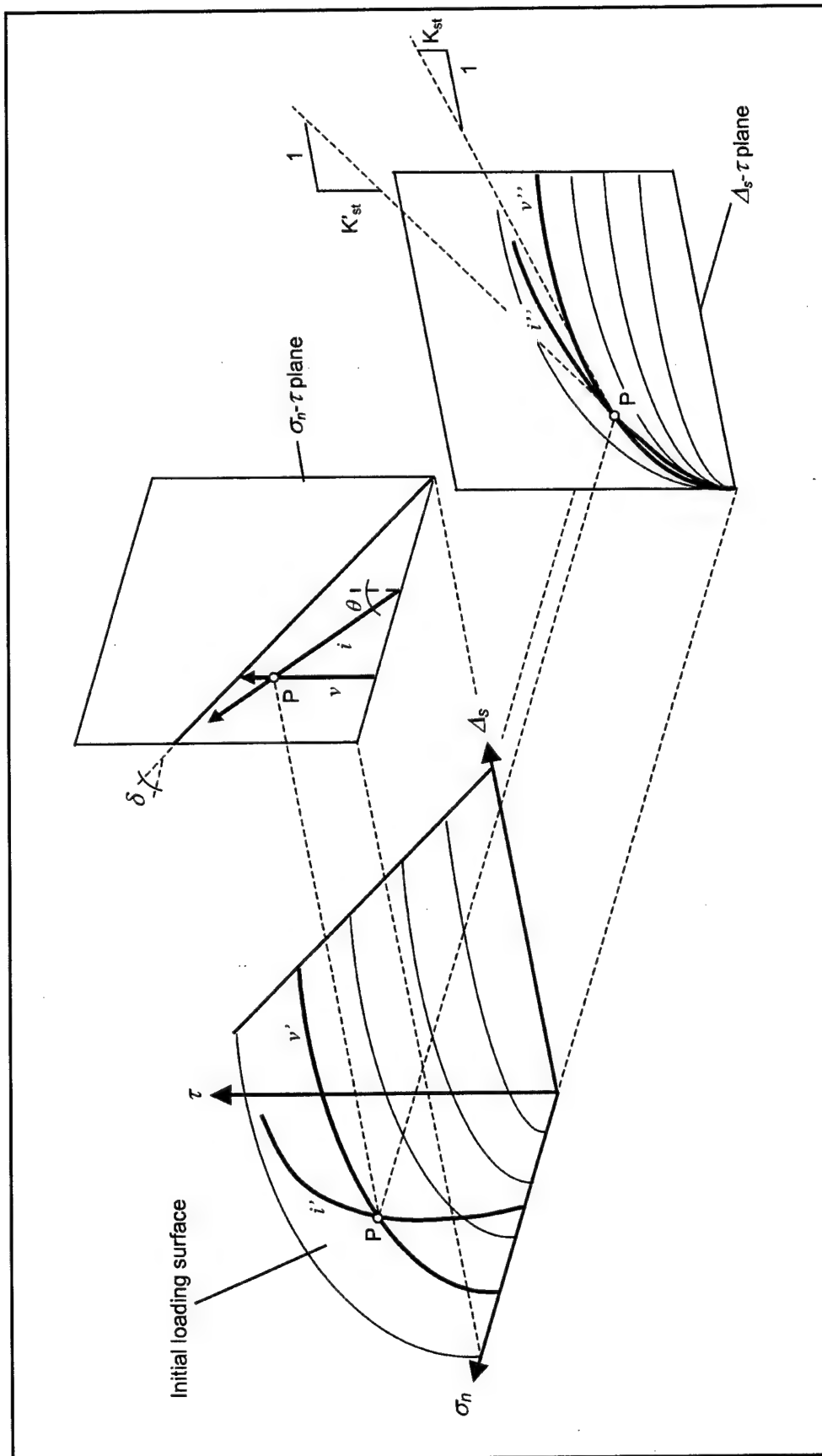


Figure 4-14. Type of interface response assumed in the extended hyperbolic formulation

shear stiffness does not depend exclusively on the magnitudes of normal stress σ_n and stress level SL as given by Equation 2-11. It also depends on the rate of change of the normal stress with respect to the shear stress, i.e., *the inclination of the stress path*.

4.2.2 Mathematical formulation

The initial loading surface illustrated in Figure 4-14 can be defined by a mathematical function such as:

$$\tau = f(\Delta_s, \sigma_n) \quad (4-5)$$

For this derivation, it is assumed that a constitutive equation such as 4-5 is available, that it is a continuous and differentiable function, and that it accurately models the interface response. Such a constitutive formulation is referred to as *base constitutive model*.

Figure 4-15 illustrates the derivation of the mathematical formulation of the model. Two points, P and Q , are located along line i' corresponding to the interface response along the inclined stress path i . Two orthogonal sections, v' and o' , of the initial loading surface are shown in the figure. Line v' , passing through P , is parallel to the Δ_s - τ plane. As discussed previously, it represents the interface response to shearing along the vertical stress path v . The orthogonal section o' , passing through Q , is parallel to the τ - σ_n plane.

The secant interface stiffness, K'_{ssec} , between points P and Q during shear along stress path i is given by:

$$K'_{ssec} = \frac{\Delta\tau^i}{\Delta\Delta_s} \quad (4-6)$$

where $\Delta\tau^i$ is the shear stress increment between points P and Q , and $\Delta\Delta_s$ is the increment of interface displacement. The shear stress increment $\Delta\tau^i$ can be expressed as:

$$\Delta\tau^i = \Delta\tau^v + \Delta\tau^o \quad (4-7)$$

where $\Delta\tau^v$ and $\Delta\tau^o$ are the components of the shear stress increment in the orthogonal directions v' and o' , respectively. Substituting Equation 4-7 into 4-6 gives the following equation:

$$K'_{ssec} = \frac{\Delta\tau^v}{\Delta\Delta_s} + \frac{\Delta\tau^o}{\Delta\Delta_s} \quad (4-8)$$

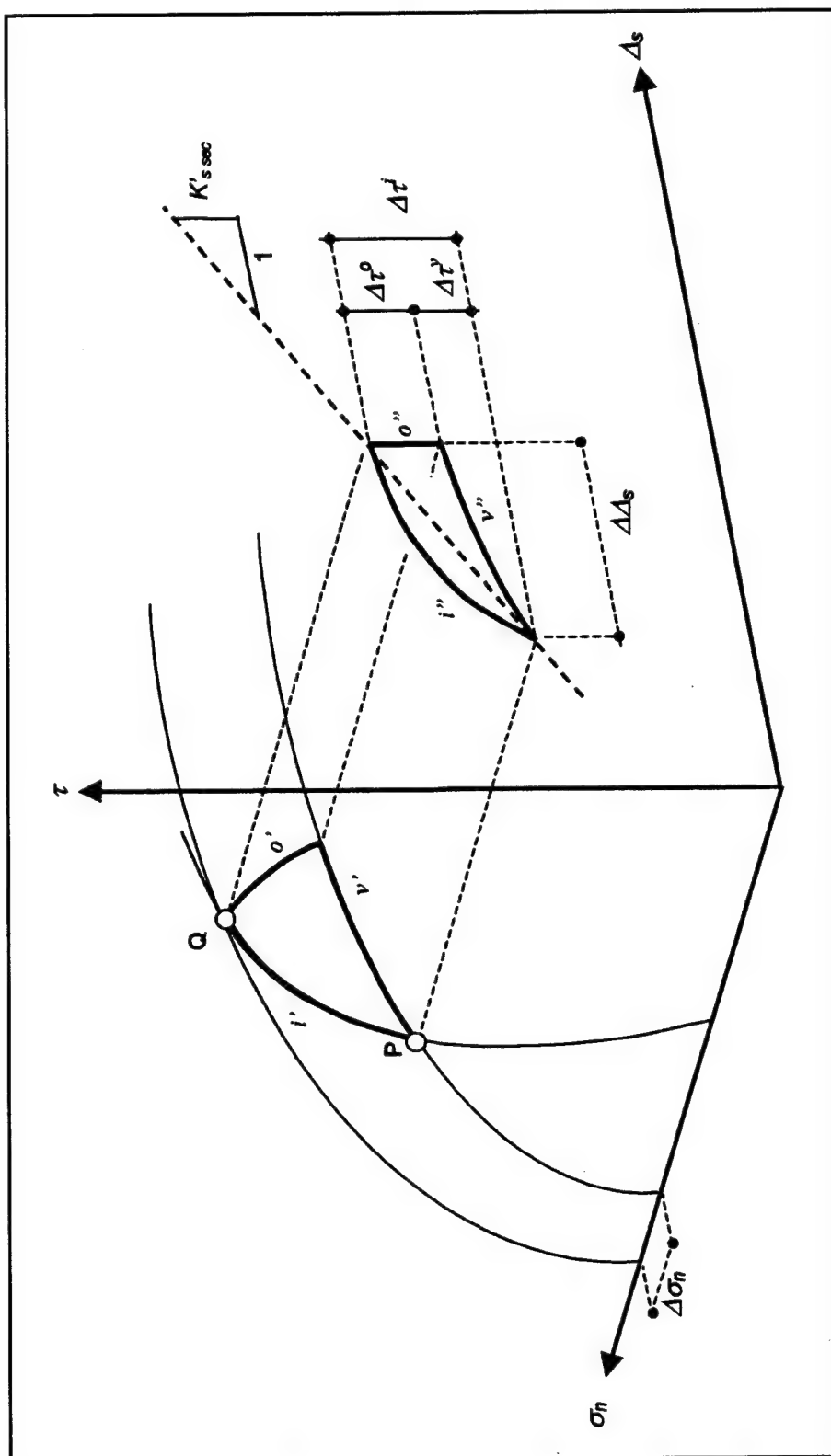


Figure 4-15. Determination of the interface stiffness along an inclined stress path

If point Q is only an infinitesimal distance away from P , Equation 4-8 becomes

$$K'_{st} = \frac{d\tau^v}{d\Delta_s} + \frac{d\tau^o}{d\Delta_s} \quad (4-9)$$

where K'_{st} is the tangent interface stiffness at point P during shear along the inclined stress path i . The first term on the right side of the equation is the interface stiffness K_{st} for loading along the vertical stress path v . Therefore, Equation 4-9 can be re-written as:

$$K'_{st} = K_{st} + \frac{d\tau^o}{d\Delta_s} \quad (4-10)$$

The differential quantity $d\tau^o$ can be expressed as

$$d\tau^o = \frac{\partial \tau}{\partial \sigma_n} \cdot d\sigma_n \quad (4-11)$$

Expression 4-11 can be rewritten as:

$$d\tau^o = \frac{\partial \tau}{\partial \sigma_n} \cdot \frac{d\sigma_n}{d\tau^i} \cdot d\tau^i \quad (4-12)$$

where $d\tau^i$ is the infinitesimal shear stress increment along inclined stress path.

Substituting Equation 4-12 into 4-10 gives the following expression:

$$K'_{st} = K_{st} + \frac{\partial \tau}{\partial \sigma_n} \cdot \frac{d\sigma_n}{d\tau^i} \cdot \frac{d\tau^i}{d\Delta_s} \quad (4-13)$$

For P and Q infinitesimally close, Equation 4-6 becomes

$$K'_{st} = \frac{d\tau^i}{d\Delta_s} \quad (4-14)$$

Equation 4-13 can then be expressed as

$$K'_{st} = K_{st} + \frac{\partial \tau}{\partial \sigma_n} \cdot \frac{d\sigma_n}{d\tau^i} \cdot K'_{st} \quad (4-15)$$

Reorganizing the terms in Equation 4-15:

$$K'_{st} = K_{st} \cdot \frac{1}{1 - \frac{\partial \tau}{\partial \sigma_n} \cdot \frac{d\sigma_n}{d\tau^i}} \quad (4-16)$$

Equation 4-16 is the mathematical formulation for yield-inducing shear along any stress path. For SSI analyses, it is convenient to rewrite Equation 4-16 as follows:

$$K'_{st} = K_{st} \cdot I \quad (4-17)$$

The term I is a correction factor for the inclination of the stress path and is determined from the following expressions:

$$I = \frac{1}{1 - \frac{\partial \tau}{\partial \sigma_n} \cdot \tan \theta} \quad (4-18)$$

$$\tan \theta = \frac{d\sigma_n}{d\tau^i} \quad (4-19)$$

where θ is the angle between the stress path direction and the τ -axis, as illustrated in Figure 4-14.

Theoretically, any base constitutive model, such as that represented by Equation 4-5, can be used with Equations 4-17, 4-18, and 4-19 to determine the interface stiffness during shear along any yield-inducing stress path. For practical purposes, it is convenient to select a base constitutive model that meets the following criteria:

- a. It is capable of accurately modeling the nonlinearity of the shear stress-displacement response of the interface under constant normal stress, i.e., along vertical stress paths.
- b. It accounts for the dependency of the interface response on the normal stress.
- c. Its mathematical formulation is simple enough to allow an easy evaluation of the term $\partial \tau / \partial \sigma_n$ in Equation 4-18.

Among the interface models available in the literature that meet these criteria, the Clough and Duncan (1971) hyperbolic formulation is especially convenient due to the simplicity of its mathematical formulation, its widespread use for SSI

analyses of lock walls, and the availability of reference hyperbolic parameter values in the literature.

4.2.3 Formulation of the extended hyperbolic model for interfaces at yield

As discussed in Chapter 2, the constitutive equation for the Clough and Duncan (1971) hyperbolic model can be written as:

$$\tau = \frac{\Delta_s}{\frac{I}{K_I \cdot \gamma_w \cdot \left(\frac{\sigma_n}{p_a}\right)^{n_j}} + \frac{R_{ff} \cdot \Delta_s}{\sigma_n \cdot \tan \delta}} \quad (2-8 \text{ bis})$$

Equation 2-8 is applicable only for initial loading into the first quadrant of the σ_n - τ plane. It can be extended to initial loading into the fourth quadrant by the introduction of a *shear direction parameter* q , as follows:

$$\tau = \frac{\Delta_s}{\frac{I}{K_I \cdot \gamma_w \cdot \left(\frac{\sigma_n}{p_a}\right)^{n_j}} + q \cdot \frac{R_{ff} \cdot \Delta_s}{\sigma_n \cdot \tan \delta}} \quad (4-20)$$

where q is equal to +1 if shearing takes place into the first quadrant ($\tau > 0$), and equal to -1 if shearing takes place into the fourth quadrant ($\tau < 0$).

Substituting Equation 4-20 into Equation 4-18 gives the following expression for the correction factor:

$$I = \frac{I}{1 + SL \cdot \left[n_j (q \cdot R_{ff} \cdot SL - 1) - q \cdot R_{ff} \cdot SL \right] \tan \delta \tan \theta} \quad (4-21)$$

In the hyperbolic model, the interface stiffness for loading under constant normal stress was defined in Chapter 2 as

$$K_{st} = K_I \cdot \gamma_w \cdot \left(\frac{\sigma_n}{p_a}\right)^{n_j} \cdot (1 - R_{ff} \cdot SL)^2 \quad (2-11 \text{ bis})$$

A similar expression is obtained by differentiating Equation 4-20 with respect to the interface displacement Δ_s :

$$K_{st} = K_I \cdot \gamma_w \cdot \left(\frac{\sigma_n}{p_a} \right)^{n_f} \cdot (1 - q \cdot R_f \cdot SL)^2 \quad (4-22)$$

The formulation for interface yielding of the extended hyperbolic model is given by Equations 4-17, 4-21, and 4-22. Table 4-2 summarizes the state variables, interface material properties, and equations necessary for the implementation of this model into SSI analyses. As observed in Table 4-2, the model does not require any interface properties in addition to those defined in the Clough and Duncan (1971) hyperbolic model.

Table 4-2 Summary of the Extended Hyperbolic Model for Interfaces at Yield	
Conditions for application	$SL = SL -$ or $SL = SL +$
State variables	SL = stress level $SL+$ = position of yield surface in first quadrant $SL-$ = position of yield surface in fourth quadrant σ_n = normal stress on the interface θ = angle between the stress path direction and the τ -axis in the σ_n - τ plane q = shear direction parameter
Interface properties	K_I = stiffness number n_f = stiffness exponent R_f = failure ratio δ = interface friction angle
Equations	$K'_s = I \cdot K_s$ $K_s = K_I \cdot \gamma_w \cdot \left(\frac{\sigma_n}{p_a} \right)^{n_f} \cdot (1 - q \cdot R_f \cdot SL)^2$ $I = \frac{1}{1 + SL \cdot [n_f(q \cdot R_f \cdot SL - 1) - q \cdot R_f \cdot SL] \tan \delta \tan \theta}$

4.2.4 Behavior of the model

Figure 4-16 illustrates the interface response predicted by the extended hyperbolic model for a series of hypothetical, yield-inducing stress paths. The hyperbolic parameter values for the dense-Density-sand-against-concrete interface were used to provide a realistic picture of the relevant features of the model. The following discussion refers to stress paths in the first quadrant, but the behavior is similar in the fourth quadrant.

Figure 4-16a shows the set of stress paths considered in this example. All the stress paths consist of initial shear of the interface, under the same normal stress to point *A*, with a stress level of 0.5. The shaded area in the figure corresponds to stress level values equal to or greater than 0.5. According to the extended hyperbolic model, once the interface is sheared to point *A*, any subsequent shear into the shaded area induces yielding of the interface, and the formulation presented previously is applicable. Conversely, any shearing into the area immediately below induces unloading of the interface, and this formulation is not valid.

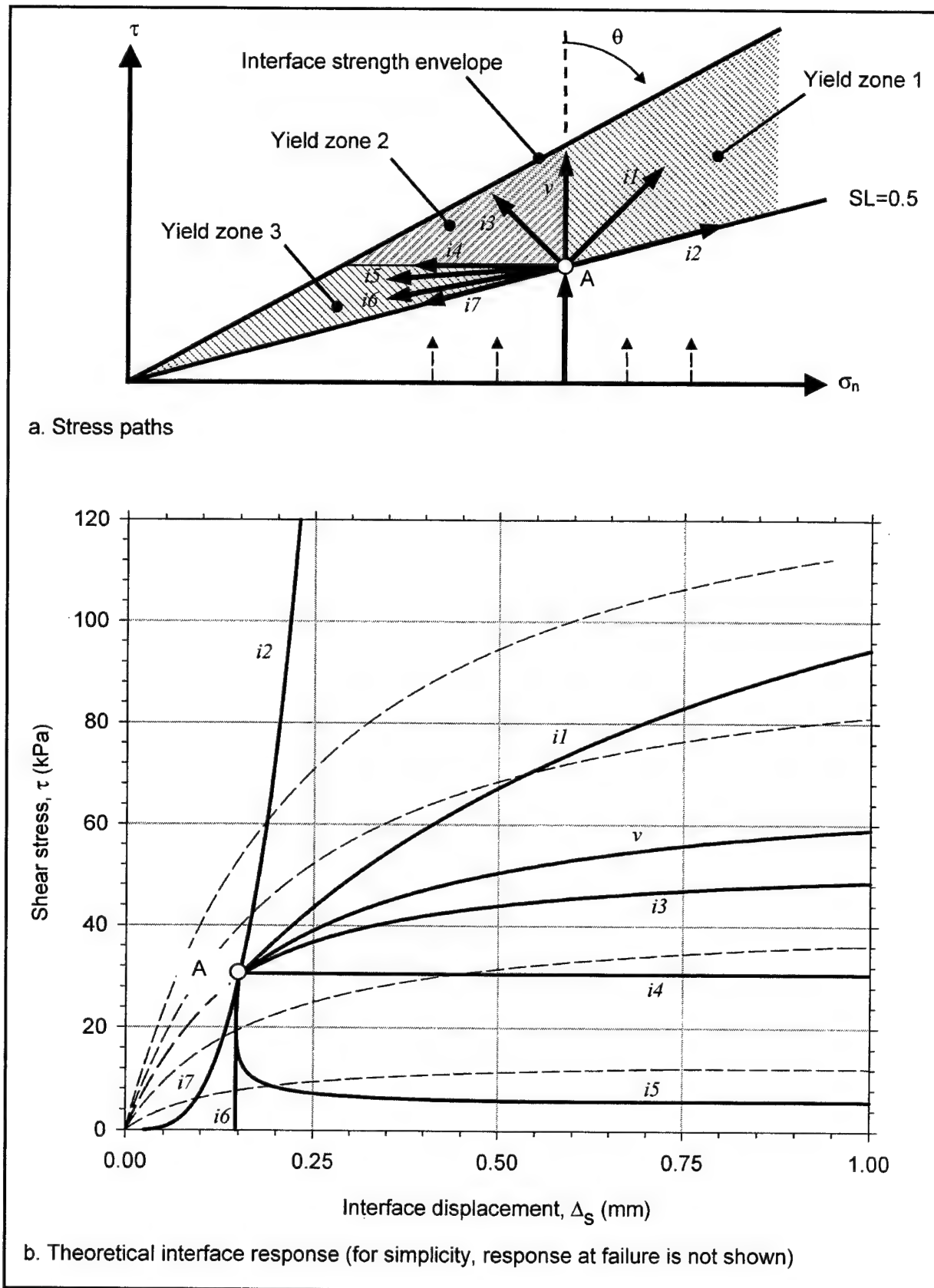


Figure 4-16. Interface response at yield for inclined stress paths in the extended hyperbolic model

At point *A*, the stress paths diverge in different directions into the shaded area. The interface response predicted by the model for each of these stress paths is presented in Figure 4-16b. For comparison, a series of dashed lines are also presented that correspond to the interface response for vertical stress paths at various normal stress magnitudes. It must be noted that, with the exception of stress path *i2*, shearing along any of the stress paths shown eventually induces failure of the interface. For simplicity, the interface response at failure, i.e., large interface displacements with no change in shear stress, is not included in the theoretical interface response diagrams presented in Figure 4-16b.

For the purpose of the following discussion, it is convenient to divide the shaded area in Figure 4-16a into several *yield zones*. Limiting values of the correction factor for each of these zones were calculated from Equation 4-21. They are summarized in Table 4-3.

Table 4-3
Definition of Yield Zones in the First Quadrant and Limiting Values of the Correction Factor for Inclination of Stress Paths

Yield Zone	Type of Loading	Tan θ	Correction Factor <i>I</i>
1	Simultaneous increase of shear and normal stresses (stress paths <i>i1</i> and <i>i2</i> in Figure 4-16)	$0 < \tan \theta \leq \frac{1}{SL \cdot \tan \delta}$	$1 < I \leq \frac{1}{1 + n_f(R_f \cdot SL - 1) - R_f \cdot SL}$
	Shear under constant normal stress (stress path <i>v</i> in Figure 4-16)	$\tan \theta = 0$	$I = 1$
2	Increasing shear stress, decreasing normal stress (stress path <i>i3</i> in Figure 4-16)	$-\infty < \tan \theta < 0$	$0 < I < 1$
	Constant shear stress, decreasing normal stress (stress path <i>i4</i> in Figure 4-16)	$\tan \theta = \pm \infty$	$I = 0$
3	Simultaneous decrease in shear and normal stresses (stress paths <i>i5</i> , <i>i6</i> and <i>i7</i> in Figure 4-16)	$\frac{1}{[R_f \cdot SL - n_f(R_f \cdot SL - 1)] \cdot SL \cdot \tan \delta} < \tan \theta < \infty$	$-\infty < I < 0$
		$\tan \theta = \frac{1}{[R_f \cdot SL - n_f(R_f \cdot SL - 1)] \cdot SL \cdot \tan \delta}$	$I = \pm \infty$
		$\frac{1}{SL \cdot \tan \theta} \leq \tan \theta \leq \frac{1}{[R_f \cdot SL - n_f(R_f \cdot SL - 1)] \cdot SL \cdot \tan \delta}$	$\frac{1}{1 + n_f(R_f \cdot SL - 1) - R_f \cdot SL} \leq I < \infty$

4.2.4.1 Yield zone 1. The hyperbolic model by Clough and Duncan (1971) predicts accurately the interface response for the case of a stress path such as *v*, where shear takes place under constant normal stress. In the extended hyperbolic model, the correction factor *I* for stress path *v* is equal to one. Therefore, the interface stiffness values from the hyperbolic model and the extended hyperbolic model are identical for this case.

For stress paths such as *i1* and *i2*, which correspond to a simultaneous increase in normal and shear stresses, the interface stiffness is calculated from the equations in Table 4-2. As indicated previously, the inclination θ of the stress path is measured clockwise with respect to the direction of the τ -axis in the σ_n - τ diagram. As the inclination increases, the correction factor I increases, and so does the value of interface stiffness K'_{st} . The maximum value of I corresponds to a stress path such as *i2* that follows the current yield surface. In this case, the interface response may show an upward concavity, indicating a continuously increasing stiffness during shear as illustrated in Figure 4-16b.

The response predicted in this loading region by the extended hyperbolic model was confirmed by the results of interface shear tests, as will be discussed in subsequent sections.

4.2.4.2 Yield zone 2. Stress path *i3* corresponds to a case where the shear stress increases as the normal stress decreases. For such a case, the correction factor I has a value lower than one, but greater than zero (Table 4-3), and the interface stiffness is lower than if shearing occurred along a vertical stress path. In such cases, the Clough and Duncan (1971) hyperbolic formulation predicts an interface response that is too stiff. The extended hyperbolic model prediction has been confirmed by the results of interface tests.

Shear stress path *i4* corresponds to a decrease in the normal stress as the shear stress remains constant. In this case, the correction factor I becomes zero suggesting zero interface shear stiffness. According to the base hypothesis of the model, the interface displacements are related to changes in both shear and normal stresses for any yield-inducing stress path (Figure 4-14). Therefore, a finite reduction in the normal stress under constant shear stress should induce a finite interface displacement. Intuitively, such assumed interface response appears correct. However, it is difficult to verify this in the LDSB, which was not designed for this type of loading. In finite element analyses, it may be necessary to assume a low value of interface stiffness for such a case to avoid numerical problems.

4.2.4.3 Yield zone 3. In this zone, loading is characterized by a simultaneous decrease in shear and normal stresses. The correction factor values in this region may be negative or positive, depending on the orientation of the stress path as indicated in Table 4-3.

For a stress path such as *i5* the correction factor values are negative. Therefore, the simultaneous decrease of normal and shear stresses induces positive interface displacements. This seems reasonable when the normal stress reduction is much larger than the shear stress reduction. There is a certain combination of the rates of change of normal and shear stresses (i.e., a certain inclination of the stress path) that induces no interface displacement at all, such as in stress path *i6* in Figure 4-16a. In this case, the correction factor takes on a value of infinity. For finite element analyses, if the interface stiffness value is negative or infinity, it may be necessary to make some assumptions regarding the response of the interface. This will be discussed in Section 4.6, "Implementation of the Extended Hyperbolic Model."

For stress paths located between $i6$ and $i7$, the correction factor is positive. For a stress path such as $i7$, lying on the yield surface, the interface stiffness at point A becomes identical to that corresponding to stress path $i2$. Only limited experimental data are available to verify the interface response assumed by the extended hyperbolic model in yield zone 3.

The foregoing discussion refers only to the effect of stress path inclination on the interface stiffness at point A . With the exception of stress path $i2$, all the stress paths in Figure 4-16a eventually induce failure of the interface. For example, when shearing takes place along stress path $i6$, the interface reaches failure at some positive value of shear stress; consequently, large displacements take place under this constant value of shear stress. For simplicity, the response of the interface at failure is not represented in the interface response diagrams of Figure 4-16b.

4.3 Formulation of the Extended Hyperbolic Model for Unloading-Reloading

As discussed in preceding sections (Figure 4-10), any stress path contained inside the region delimited by the yield surfaces $SL+$ and $SL-$ induces unloading-reloading or transition loading. During this investigation, a general formulation for unloading-reloading and transition loading was developed. It allows very accurate predictions of the response of the interface under the experimental stress paths described in Chapter 3.

To facilitate its implementation in SSI analyses, three different versions of the unload-reload formulation were developed:

- a. Version I.* The interface response is linear and normal stress-dependent. No differentiation is made between unloading-reloading and transition loading. This version may be useful for cases where unloading-reloading takes place along simple stress paths, or when a high degree of accuracy is not required for the analyses.
- b. Version II.* The interface response is nonlinear and normal stress-dependent. It follows a hyperbolic shear stress-displacement relationship. No differentiation is made between unloading-reloading and transition loading. This formulation is simple to implement in finite element programs; yet it is accurate for most loading conditions.
- c. Version III.* This is the most accurate version of the model. It is also the more complicated to implement because it introduces additional sets of state variables to differentiate between unloading-reloading and transition loading.

In all three versions of the model, the interface response is independent of the orientation of the stress path. In SSI analyses, any of the versions can be applied in conjunction with the formulation for interfaces at yield introduced previously.

Table 4-4 Summary of Version I of the Unload-Reload Formulation in the Extended Hyperbolic Model for Interfaces	
Conditions for application	$SL > SL -$ and $SL < SL +$
State variables	SL = stress level $SL+$ = yield surface in first quadrant $SL-$ = yield surface in fourth quadrant σ_n = normal stress on the interface
Interface properties	K_{urj} = stiffness number n_j = stiffness exponent δ = interface friction angle
Equations	$K'_s = K_{urj} \cdot \gamma_w \cdot \left(\frac{\sigma_n}{p_a} \right)^{n_j}$

model is very simple once a value of K_{urj} is selected. It is noted that the interface response is assumed to be independent of the inclination of the stress path.

This formulation is appropriate for analyses that do not require a high degree of accuracy. In some lock walls, the interface may be subjected to complicated unloading-reloading stress paths, and it may not be possible to select a single value of K_{urj} that provides accurate predictions of the interface response. Version II, described in the following section, accounts for nonlinearity of the interface response during unloading-reloading.

4.3.2 Version II

Figure 4-18 illustrates an unloading-reloading stress path applied to a hypothetical interface. The corresponding interface response presented in the figure is qualitatively based on the observations of unloading-reloading response of interfaces presented previously in this chapter.

In Version II, it is assumed that the shear stress-displacement response of the interface during unloading-reloading and transition loading follows a hyperbolic relationship given by:

$$\tau = \tau_o + \frac{(\Delta_s - \Delta_{so})}{\frac{1}{K_{urj} \cdot \gamma_w \cdot \left(\frac{\sigma_n}{p_a} \right)^{n_j}} + q \cdot \frac{R_{ff} \cdot (\Delta_s - \Delta_{so})}{\alpha \cdot \sigma_n \cdot \tan \delta}} \quad (4-24)$$

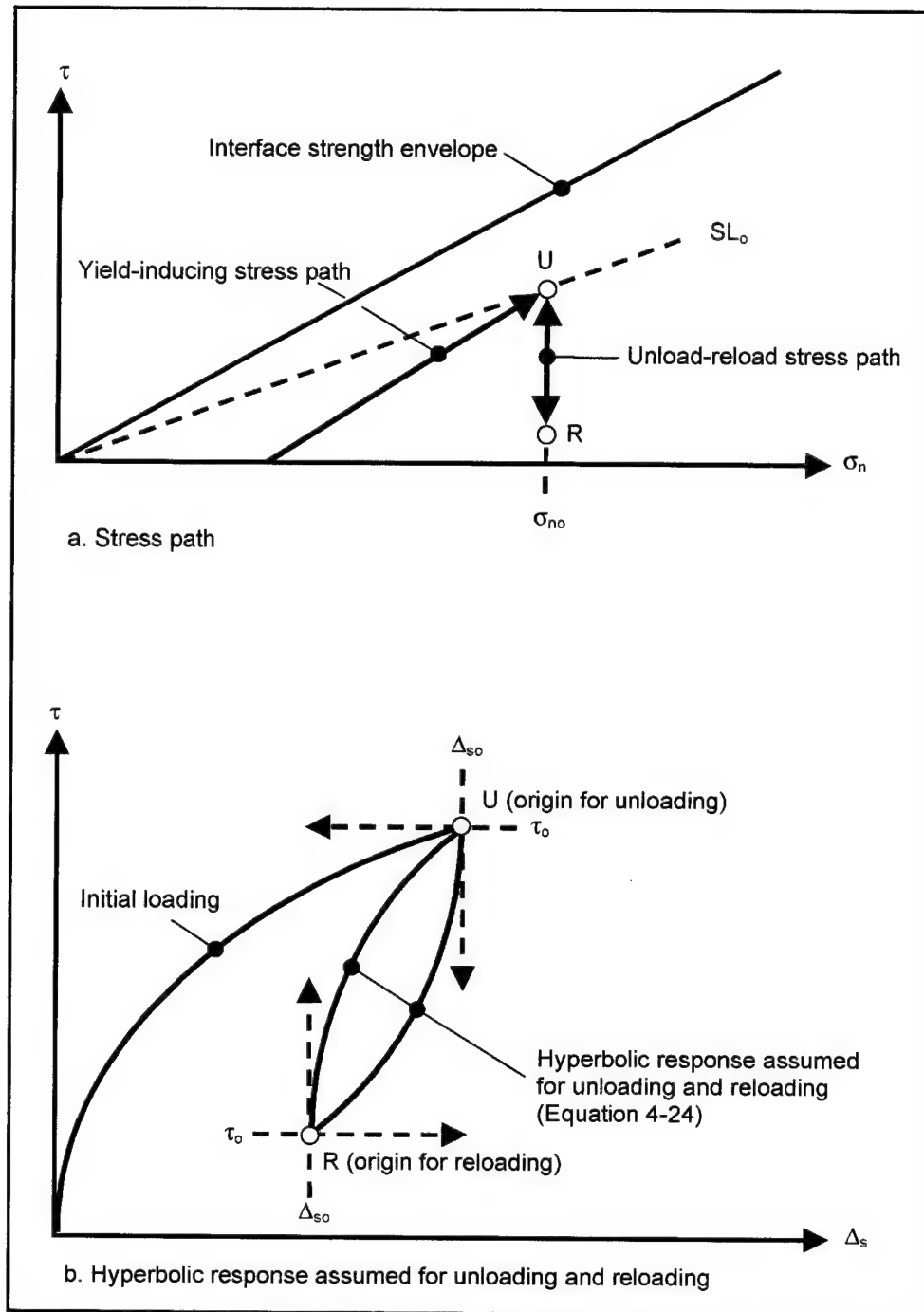


Figure 4-18. Interface response assumed in Version II for unloading-reloading

where

τ_o = shear stress at the *origin* of unloading or reloading

Δ_{so} = interface displacement at the origin of unloading or reloading

q = shear direction parameter that takes on a value of +1 or -1 if the stress level is increasing or decreasing, respectively

α = dimensionless scaling factor for unloading-reloading

The origin of unloading or reloading is defined as the point where the direction of shearing was last reversed. Accordingly, point U is the origin for unloading along $U-R$, and point R is the origin for the subsequent reloading. After a change in the shear direction, the origin remains at the same point until a new change in direction takes place.

According to this formulation, the interface response during unloading-reloading is characterized by the following features:

- a. It follows a hyperbolic shear stress-displacement relationship.
- b. This hyperbolic relationship is qualitatively identical to that assumed for yield-inducing shear (Equation 2-9).
- c. As in Equation 2-9, the first term in the denominator of Equation 4-24 controls the initial stiffness immediately after a change in the direction of shearing, i.e. upon unloading or reloading. The second term in the denominator controls the asymptotic shear stress and, therefore, the rate of degradation of the interface stiffness during unloading-reloading.
- d. In Version II, Equation 4-24 is assumed applicable to both unloading-reloading and transition loading.
- e. The interface response is assumed to be independent of the inclination of the stress path.

Expression 4-24 becomes identical to Equation 2-9 if

$$\tau_o = 0$$

$$\Delta_{so} = 0$$

$$K_{urj} = K_I$$

$$q = +1$$

$$\alpha = 1$$

If the coordinates of the origin, τ_o and Δ_{so} , are assigned values different from zero, the shear stress-displacement relationship is translated in the Δ_s - τ plane without any change in its size or shape. The possible values of the shear direction parameter q are +1 and -1. These values produce a pair of symmetrical images of the shear-stress displacement relationship, as illustrated by the unload- and reload-curves in Figure 4-18b. The value of q is equal to +1 when the stress level is increasing during unloading-reloading, and -1 if the stress level is decreasing. Different combinations of values of the origin coordinates and the shear direction

parameter create shear stress-displacement relationships that have the same shape but are shifted and rotated in the Δ_s - τ plane.

The shape and size of the shear stress-displacement relationship during unloading-reloading are controlled by the values assigned to K_{urj} and α . The value of K_{urj} controls the shape of the shear stress-displacement response. The stiffer response of the interface during unloading-reloading can be modeled by assigning a value of K_{urj} that is larger than K_I . The scaling factor α has a similar function to that of the scaling factor defined in the model for soils developed by Pyke (1979). It controls the size of the unloading-reloading curve and, therefore, the rate of degradation of the interface stiffness. As the value of α increases above one, the shear stress-displacement curve is stretched vertically in the Δ_s - τ plane.

The value of the interface stiffness number for unloading-reloading K_{urj} can be determined from unload-reload tests. Alternatively, it is also possible to relate the value of K_{urj} to the value of stiffness number for yield-inducing shear K_I as described in Section 4.4, "Determination of the Model Parameter Values."

The scaling factor α can be determined through a trial-and-error process from the results of unload-reload interface tests. It can also be related to other interface properties without the need for its experimental determination. A procedure for the determination of α from other interface properties is described in Section 4.4.

For incremental analyses, the tangent interface stiffness can be obtained by differentiating Equation 4-24 with respect to the interface displacement. The following expression is obtained:

$$K'_{st} = K_{urj} \cdot \gamma_w \cdot \left(\frac{\sigma_n}{P_a} \right)^{n_j} \cdot \left[1 - \frac{q}{\alpha} R_f \cdot (SL - SL_o) \right]^2 \quad (4-25)$$

where SL_o is the stress level at the origin of unloading-reloading, which is calculated from the following expression:

$$SL_o = \frac{\tau_o}{\sigma_{no} \cdot \tan \delta} \quad (4-26)$$

where σ_{no} is the normal stress at the origin, as shown in Figure 4-18a.

Equation 4-25 is qualitatively identical to Equation 4-22 for yield-inducing shear. As summarized in Table 4-5, this version of the model introduces two new interface properties: the stiffness number for unloading-reloading K_{urj} and the scaling factor α .

Table 4-5 Summary of Version II of the Unload-Reload Formulation in the Extended Hyperbolic Model for Interfaces	
Conditions for application	$SL > SL_-$ and $SL < SL_+$
State variables	SL = stress level SL_+ = yield surface in first quadrant SL_- = yield surface in fourth quadrant σ_n = normal stress on the interface SL_o = stress level at the origin q = shear direction parameter
Interface properties	K_{ur} = stiffness number for unloading-reloading n_f = stiffness exponent δ = interface friction angle R_f = failure ratio α = scaling factor
Equation	$K'_{st} = K_{ur} \cdot \gamma_w \cdot \left(\frac{\sigma_n}{p_a} \right)^{n_f} \cdot \left[1 - \frac{q}{\alpha} R_f \cdot (SL - SL_o) \right]^2$

4.3.3 Version III

This version is intended for use in analyses where very accurate modeling of the interface response is required. It is a more sophisticated formulation that accounts for the type of interface response observed in the transition region discussed previously in this chapter. From a practical point of view, it is not known whether Version III introduces significant gains in accuracy for modeling of lock wall-backfill interfaces with respect to Versions I and II. Implementation and use of the three versions for SSI analyses of lock walls may be required to evaluate their comparative advantages.

In this version, the interface response during unloading-reloading is identical to Version II. Therefore, for stress paths contained inside the unloading-reloading region defined in Figure 4-10, the tangent interface stiffness can be determined from Equation 4-25.

A formulation developed specifically for transition loading is introduced in this version. Based on the observations on the interface response presented previously in this chapter (Figures 4-6 and 4-12), it is assumed that the logarithm of the normalized stiffness versus stress level diagram follows a linear relationship inside the transition region. Figure 4-19 illustrates a hypothetical stress path that traverses one of the transition regions. The transition stiffness number K_{sn}^{ts} is the normalized stiffness at a point such as TS , where the stress path intersects the transition surface. The transition stress level SL^{ts} is the stress level at point TS . The stiffness degradation parameter m is the slope of the normalized stiffness diagram inside the transition region. If the values of both K_{sn}^{ts} and m are known, then the normalized stiffness K_{sn} at any point such as A , located inside the transition region, can be determined from the following equation:

$$K_{sn} = K_{sn}^{ts} \cdot 10^{m \cdot (SL - SL^{ts})} \quad (4-27)$$

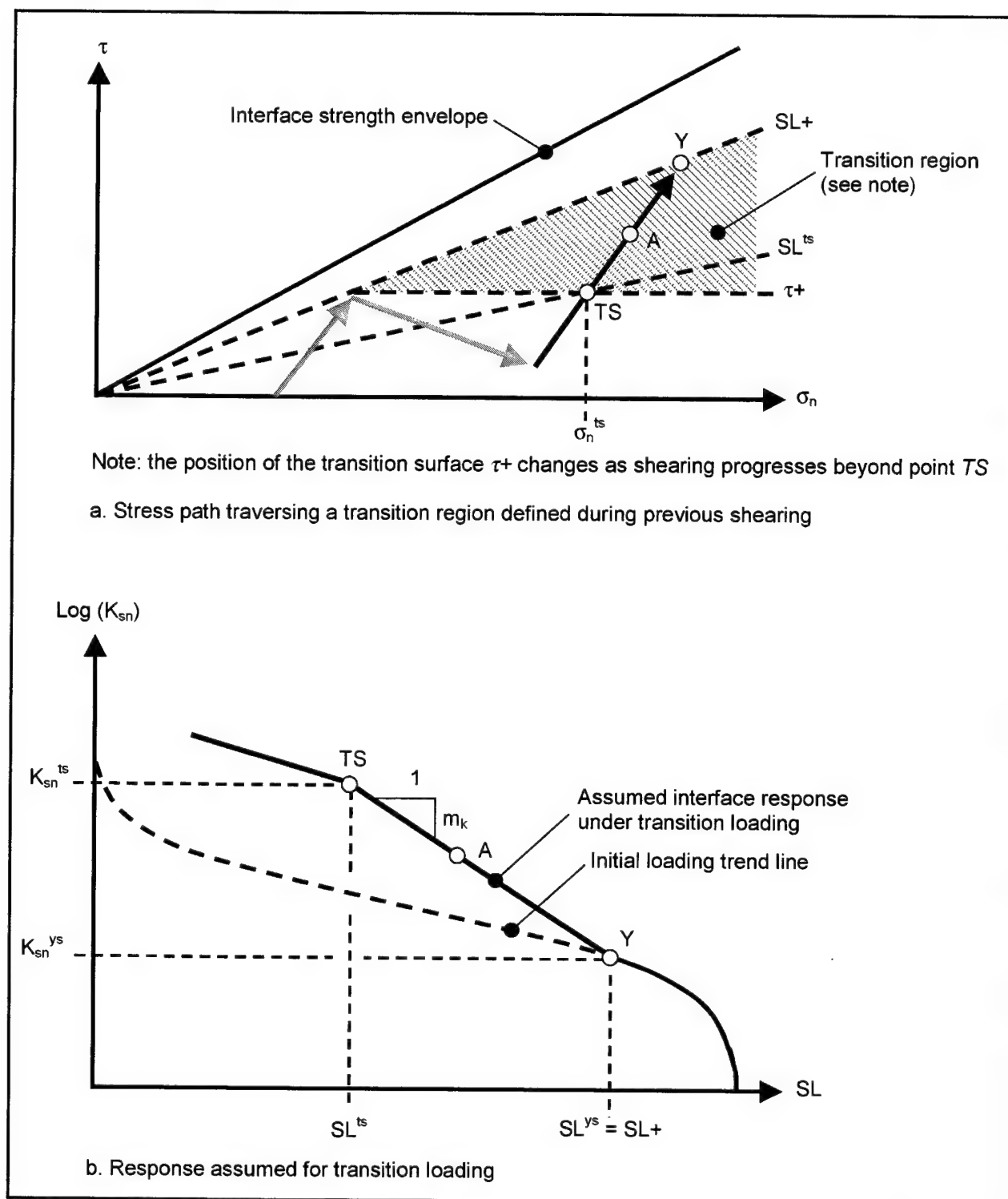


Figure 4-19. Normalized interface response during transition loading assumed in Version III

The value of interface stiffness K'_{st} can be calculated from the normalized stiffness K_{sn} . Rearranging terms in Equation 4-2 gives the following expression for the interface stiffness:

$$K'_{st} = K_{sn} \cdot \gamma_w \cdot \left(\frac{\sigma_n}{P_a} \right)^{n_j} \quad (4-28)$$

Combining Equations 4-27 and 4-28 gives the following expression for the interface stiffness at any point inside the transition region:

$$K'_{st} = K_{sn}^{ts} \cdot 10^{m(SL - SL^y)} \cdot \gamma_w \cdot \left(\frac{\sigma_n}{P_a} \right)^{n_j} \quad (4-29)$$

Equation 4-29 represents the formulation for transition loading in Version III of the extended hyperbolic model. The transition stiffness number K_{sn}^{ts} , stiffness degradation parameter m , and transition stress level SL^{ts} are three of the additional state variables required for the implementation of this formulation.

The transition stiffness number can be determined by normalizing the interface stiffness K'_{st}^{ts} at point TS , as follows:

$$K_{sn}^{ts} = \frac{K'_{st}^{ts}}{\gamma_w \cdot \left(\frac{\sigma_n^{ts}}{P_a} \right)^{n_j}} \quad (4-30)$$

where σ_n^{ts} is the normal stress corresponding to point TS .

The stiffness degradation parameter m is determined from the following expression:

$$m = \left(\frac{\log K_{sn}^{ts} - \log K_{sn}^{ys}}{SL^{ts} - SL^{ys}} \right) \quad (4-31)$$

where

K_{sn}^{ys} = yield stiffness number

SL^{ys} = stress level for the current position of the yield surface

The yield stiffness number K_{sn}^{ys} , is the value of normalized stiffness corresponding to the current position of the yield surface SL^{ys} . It can be determined from the initial loading trend line at $SL = SL^{ys}$. It is assumed that the inclination of the stress path does not influence the value of K_{sn}^{ys} ($I = 1$). From Equations 4-2, 4-17, and 4-22, the following expression for the yield stiffness number is obtained:

$$K_{sn}^{ys} = K_I \cdot (1 - q \cdot R_{ff} \cdot SL^{ys})^2 \quad (4-32)$$

The current position of the yield surface SL^{ys} can be defined mathematically as

$$\begin{aligned} SL^{ys} &= SL + \text{for shear inside the transition zone of the first quadrant} \\ SL^{ys} &= SL - \text{for shear inside the transition zone of the fourth quadrant} \end{aligned} \quad (4-33)$$

The value of the transition stress level SL^{ts} is determined from the following equation:

$$SL^{ts} = \frac{\tau^{ts}}{\sigma_n^{ts} \tan \delta} \quad (4-34)$$

where τ^{ts} is the shear stress at point TS , where the stress path intersects the transition surface.

Table 4-6 summarizes the formulation of Version III. This version of the model does not introduce any new interface properties in addition to those required in Version II. A total of five additional state variables are required for Version III.

4.4 Determination of the Model Parameter Values

Implementation of the extended hyperbolic model described in the previous sections requires determination of the values of the interface parameters listed in Table 4-7. The procedure for the determination of these values is discussed in this section. A method is described that allows the determination of K_{urj} and α using the hyperbolic parameters of the Clough and Duncan (1971) formulation.

4.4.1 Determination of parameter values for interfaces at yield

As indicated previously, implementation of the formulation for yield-inducing shear does not require any parameters in addition to those considered in the

Table 4-6
Summary of Version III of the Extended Hyperbolic Model for Interfaces Subjected to Unloading-Reloading and Transition Loading

Conditions for application	$SL > SL_-$ and $SL < SL_+$
State variables	SL = stress level SL_+ = yield surface in first quadrant SL_- = yield surface in fourth quadrant τ_+ = transition surface in first quadrant τ_- = transition surface in fourth quadrant σ_n = normal stress on the interface K_m^* = transition stiffness number m = stiffness degradation parameter SL^* = transition stress level SL_o = stress level at the origin q = shear direction parameter
Interface properties	K_i = interface stiffness number K_{ur} = stiffness number for unloading-reloading n_f = stiffness exponent δ = interface friction angle R_f = failure ratio α = scaling factor
Equations	<ul style="list-style-type: none"> Unloading-reloading When $\tau > \tau_-$ and $\tau < \tau_+$, then $K'_s = K_{ur} \cdot \gamma_w \cdot \left(\frac{\sigma_n}{p_s} \right)^{n_f} \cdot \left[1 - \frac{q}{\alpha} R_f \cdot (SL - SL_o) \right]^2$ Transition loading When $\tau \leq \tau_-$ or $\tau \geq \tau_+$, then $K'_s = K_m^* \cdot 10^{m(SL - SL^*)} \cdot \gamma_w \cdot \left(\frac{\sigma_n}{p_s} \right)^{n_f}$ <p>(Note: Additional expressions for the determination of K_m^*, m, and SL^* are presented in the text)</p>

Table 4-7
Summary of Material Properties Required in the Extended Hyperbolic Model for Interfaces

Type of Loading	Formulation	Parameters
Yield-inducing shear	Formulation for yield-inducing shear	K_i = stiffness number n_f = stiffness exponent R_f = failure ratio δ = interface friction angle
Unloading-reloading	Version I	K_{ur} = stiffness number for unloading-reloading n_f = stiffness exponent δ = interface friction angle
	Version II	K_{ur} = stiffness number for unloading-reloading n_f = stiffness exponent δ = interface friction angle R_f = failure ratio α = scaling factor
Transition loading	Version III	K_{ur} = stiffness number for unloading-reloading n_f = stiffness exponent δ = interface friction angle R_f = failure ratio α = scaling factor

Clough and Duncan (1971) hyperbolic model. A detailed description of the procedure for determination of the hyperbolic parameter values is presented in Appendix D.

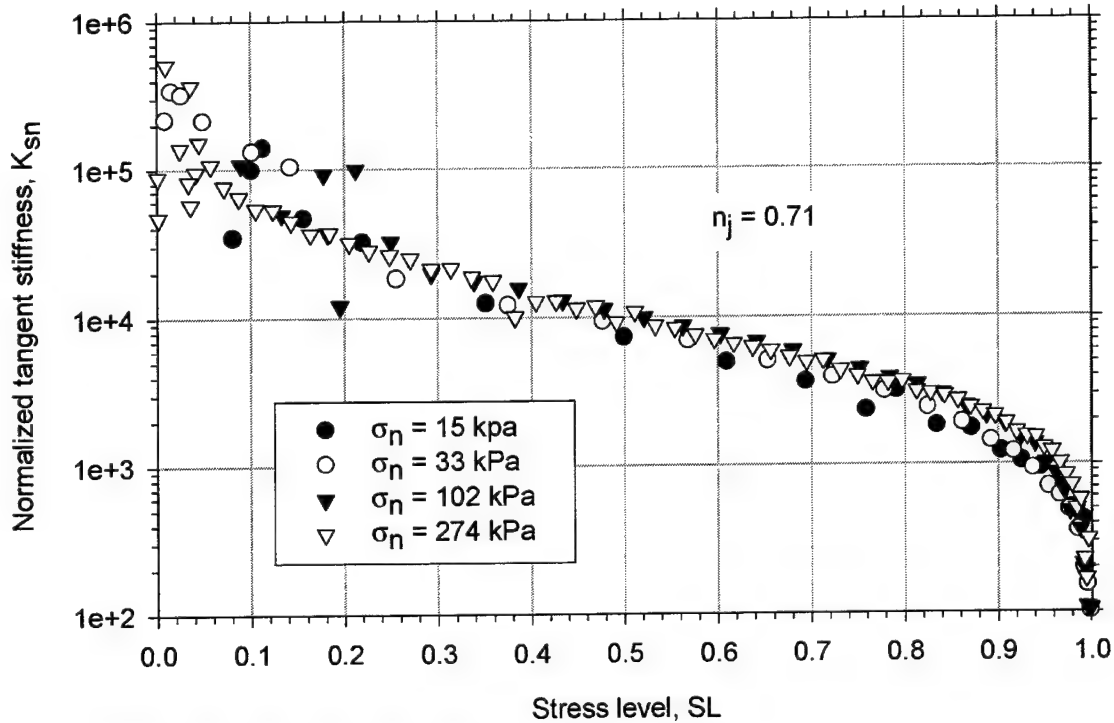
As shown in Appendix D, transformed plots of a set of initial loading test data are used to determine the values of the hyperbolic parameters. The transformed plots provide the values of initial stiffness K_{si} and asymptotic shear stress τ_{ult} for each initial loading test.

The stiffness number K_f corresponds to the initial interface stiffness value for a normal stress of 101.3 kPa (1 atm) normalized by the unit weight of water. It is determined using a best-fit straight line in a logarithmic plot of normalized initial stiffness versus normal stress. The slope of this best-fit line represents the value of the stiffness exponent n_f . The value of the failure ratio R_f is the average ratio between the shear stress at failure τ_f and the asymptotic shear stress τ_{ult} .

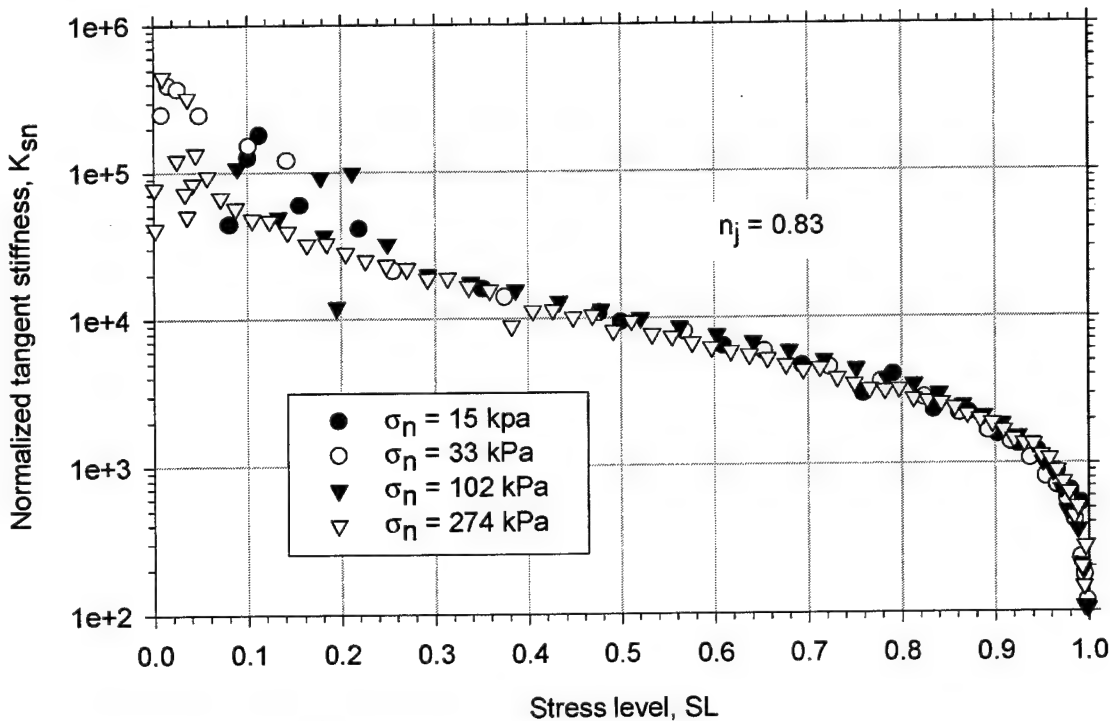
This procedure is accurate enough for implementation of the hyperbolic model (Clough and Duncan 1971) for cases of shear under constant normal stress. The formulation of the extended hyperbolic model considers the case of simultaneous changes in shear and normal stresses. As explained previously, the interface stiffness is calculated using the Clough and Duncan (1971) formulation and then multiplied by a correction factor for inclination of the stress path (Table 4-2). Large values of the correction factor can magnify errors in the interface stiffness values, which may be introduced by inaccuracies in the hyperbolic parameter values. For cases where an especially accurate determination of the interface stiffness is required, it is convenient to verify and, if necessary, adjust the hyperbolic parameter values before application of the extended hyperbolic model.

4.4.1.1 Adjustment of hyperbolic parameter values. The procedure for adjustment of the hyperbolic parameters is based on normalization of test data. It is assumed that a set of at least three initial loading tests is available for the type of interface to be analyzed. A normalized stiffness diagram is determined from the results of these tests as described previously in this chapter. For the normalization of the data, it is necessary to determine the value of the stiffness exponent n_f according to the procedure described in Appendix D. If the value of n_f is accurate, then the normalized data will show a well-defined trend line with few scattered data points. If the scatter of the data is relatively large, then the value of n_f is not accurate and can be adjusted.

Figure 4-20 shows the normalized stiffness diagram for the set of initial loading tests on the dense-Density-sand-against-concrete interface. The value of n_f , obtained according to Appendix C, produces a diagram with some scatter, as shown in Figure 4-20a. This scatter can be minimized by adjusting the value of n_f . This requires a trial-and-error process, which can be best performed in an electronic spreadsheet. Figure 4-20b shows the normalized diagram after adjusting the value of n_f . The normalized stiffness data usually present considerable scatter at low and high stress levels. The quality of the normalized stiffness plot may be best judged by examining the data in a range of stress levels between 0.2 and 0.9.



a. Normalized test data before adjustment of stiffness number n_j



b. Normalized test data after adjustment of stiffness number n_j

Figure 4-20. Adjustment of the value of stiffness number n_j of the dense-Density-sand-to-concrete interface using normalized data from initial loading tests

During this investigation, it was found that the values of n_j determined for the three interfaces tested using the procedures in Appendix D produced normalized plots with relatively small scatter. Adjustment of the n_j value was performed only for the dense-Density-sand-against-concrete interface, which presented the largest scatter.

Once a normalized stiffness diagram with minimum scatter is obtained, it is possible to verify and adjust the rest of the hyperbolic parameters. The process of verification consists of comparing the normalized test data to the normalized response of the interface calculated using the extended hyperbolic model. In the extended hyperbolic model, the interface stiffness is determined from Equations 4-17, 4-21, and 4-22. For shear under constant normal stress, the value of the correction factor, I , is equal to one, and the interface stiffness becomes:

$$K'_{st} = K_I \cdot \gamma_w \cdot \left(\frac{\sigma_n}{p_a} \right)^{n_j} \cdot (1 - R_{ff} \cdot SL)^2 \quad (4-35)$$

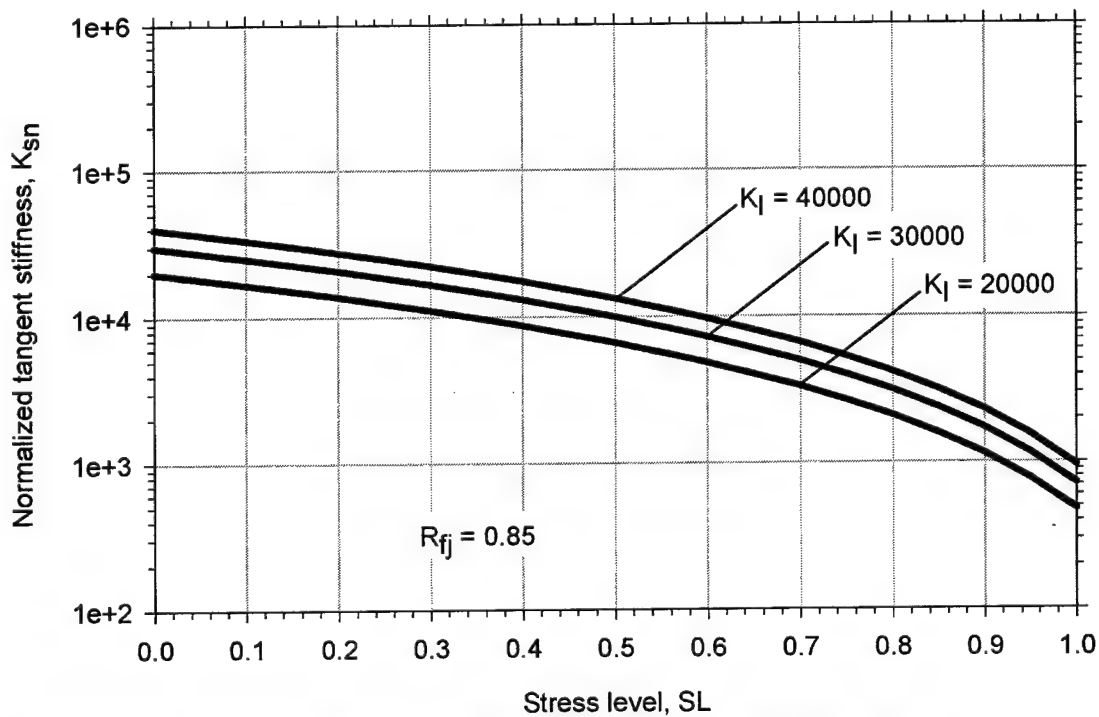
The value of K'_{st} from the extended hyperbolic model, given by Equation 4-35, can be normalized according to Equation 4-2. The resulting normalized hyperbolic stiffness is expressed as:

$$K_{sm} = K_I \cdot (1 - R_{ff} \cdot SL)^2 \quad (4-36)$$

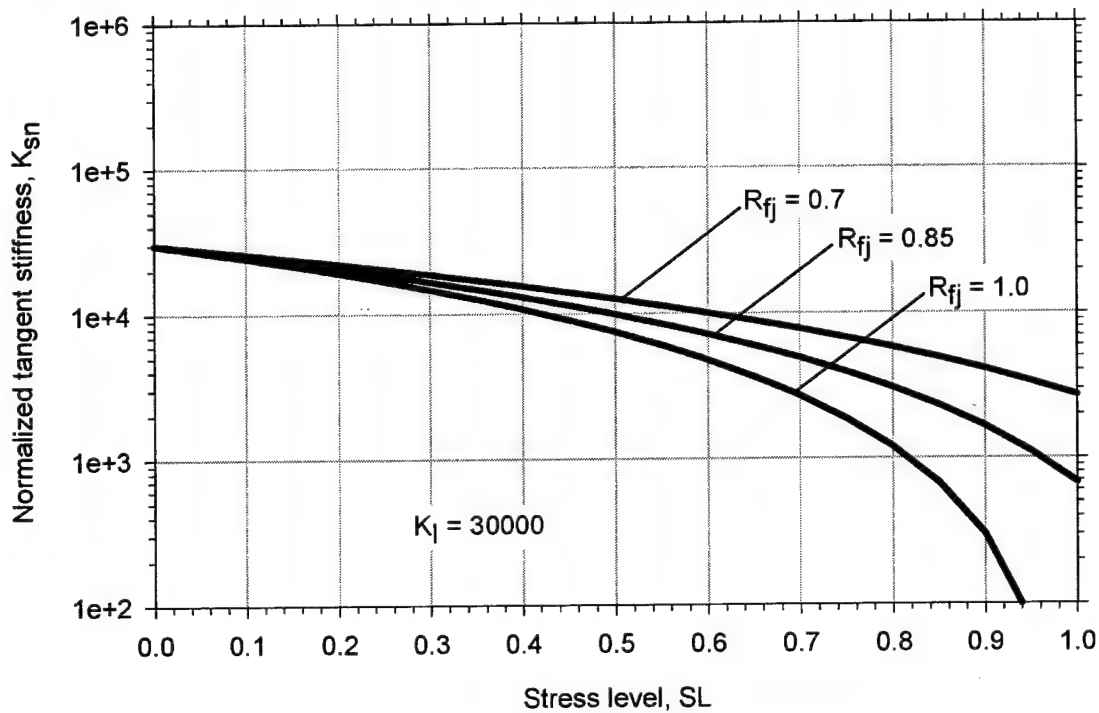
The function defined by Equation 4-36 can be plotted in a $\log K_{sm}$ versus SL diagram, as done previously for the normalized test data. Such a plot is referred to as the *normalized hyperbolic diagram*. If the model is accurate, then the normalized hyperbolic diagram fits the normalized stiffness diagram from the initial loading tests. If the model is inaccurate, the hyperbolic parameter values can be adjusted to improve the fit to the data.

Figure 4-21 illustrates the effects of adjustments in the hyperbolic parameter values on the normalized hyperbolic diagram. As can be seen in Figure 4-21a, the value of K_I controls the position of the normalized hyperbolic diagram. Different values of K_I generate a set of parallel diagrams. As shown in Figure 4-21b, the shape of the normalized hyperbolic diagram and, therefore, the rate of degradation of the interface stiffness, are controlled by the value of R_{ff} . The larger the value of R_{ff} , the larger the rate of degradation of the interface stiffness predicted by the model.

Figure 4-22 illustrates adjustment of the value of K_I for the dense-Density-sand-against-concrete interface. The dashed line is the normalized hyperbolic diagram corresponding to the hyperbolic parameter values determined from Appendix D. This diagram tends to overestimate the interface stiffness. The solid line represents the normalized hyperbolic diagram for the adjusted value of K_I which produces a better fit to the data. Adjustment of the K_I value was necessary only for the dense-Density-sand-against-concrete interface.



a. Normalized hyperbolic diagrams for different values of the stiffness number K_I



b. Normalized hyperbolic diagrams for different values of the failure ratio R_{fj}

Figure 4-21. Normalized hyperbolic diagrams for different values of the stiffness number K_I and failure ratio R_{fj}

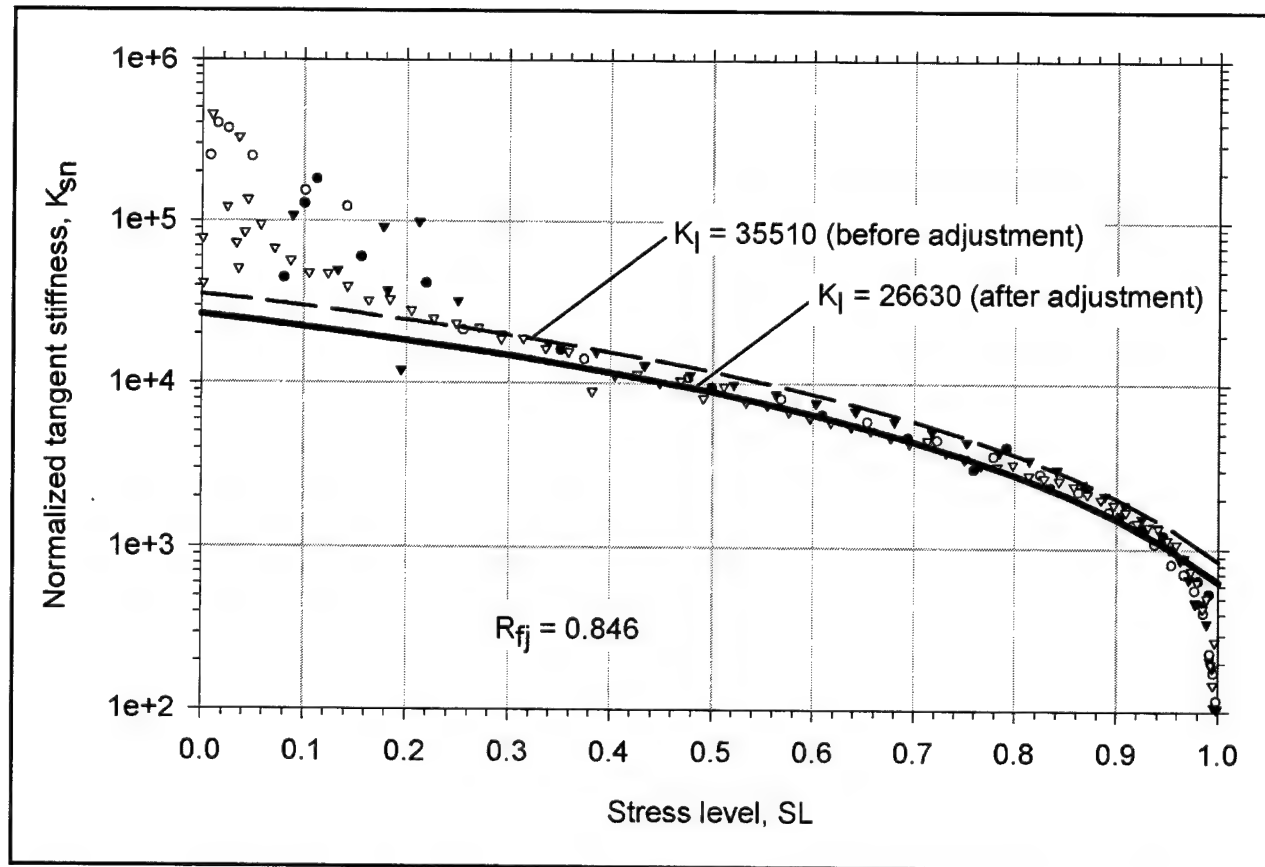


Figure 4-22. Adjustment of the value of stiffness number K_I for the dense-Density-sand-to-concrete interface

For the three types of interfaces tested, the R_{fj} values determined in Appendix D were accurate and further adjustments were not required. In cases where R_{fj} values appear inaccurate, verification of the value of the interface friction angle δ must precede any adjustments of R_{fj} . If the friction angle is accurate, then the value of R_{fj} can be adjusted using the normalized hyperbolic diagram.

4.4.1.2 Parameter values for the interfaces tested. Hyperbolic parameter values were determined for the three interfaces tested as discussed in Appendix D. They are summarized in Table 4-8. Some of these values were adjusted according to the preceding recommendations. These adjusted values are also included in Table 4-8.

Table 4-9 is a summary of adjusted hyperbolic parameters for the three interfaces tested and values reported in the literature. This table may be useful for the selection of parameter values in cases where results of initial loading tests are not available.

Table 4-8 Summary of Hyperbolic Parameter Values for the Interfaces Tested		
Parameter	Value from Appendix D	Adjusted Value for the Extended Hyperbolic Model
Dense Density Sand Against Concrete		
K_i	35510	26625
n_j	0.71	0.83
R_q	0.85	0.846
δ	31.0°	31.0°
Medium Dense Density Sand Against Concrete		
K_i	21850	No adjustments were necessary
n_j	0.81	
R_q	0.88	
δ	29.3°	
Dense Light Castle Sand Against Concrete		
K_i	20700	No adjustments were necessary
n_j	0.79	
R_q	0.79	
δ	33.7°	

Table 4-9 Summary of Hyperbolic Parameter Values for Interfaces between Concrete and Different Types of Soils						
Soil	Concrete Surface	Relative Density of Soil	K_i	n_i	R_{η}	δ , deg
Density sand	Cast against plywood	49 % (medium dense)	21850	0.81	0.88	29.3
		75 % (dense)	26625	0.83	0.85	31
Light Castle sand	Cast against plywood	80 % (dense)	20700	0.79	0.79	33.7
Uniform sand (Peterson et al. 1976)	Smooth	Loose	10200	0.87	0.71	28.2
		Medium dense	12700	0.84	0.62	31.2
		Dense	8400	1.17	0.40	32.7
	Rough	Loose	10000	0.83	0.85	28.2
		Medium dense	11900	0.71	0.78	31.2
		Dense	10400	0.70	0.41	32.7
Well-graded sand (Peterson et al. 1976)	Cast against glass plate (smooth finish)	Loose	12000	0.83	0.89	33.7
		Medium dense	9200	0.94	0.69	33.9
		Dense	10500	1.11	0.75	35.3
	Rough	Loose	7700	0.70	0.78	33.7
		Medium dense	13100	0.67	0.69	33.9
		Dense	14800	0.51	0.74	35.3
Poorly graded sand (Clough and Duncan 1969)	Smooth	Dense	75000	1	0.87	33
Ottawa sand 50-60 (Lee et al. 1989)	Smooth	Dense	19470	0.35	0.89	26.3
	Rough	Dense	19244	0.82	0.95	30.4

There are a larger number of reference values of hyperbolic parameters for soils than there are for interfaces. If neither interface test results nor reference parameters are available, it may be possible to relate the interface parameter values to the hyperbolic parameter values of the soil. Table 4-10 compares the hyperbolic parameter values for the three interfaces tested to the hyperbolic parameter values obtained from triaxial tests on isotropically consolidated soil specimens. For consistency, the hyperbolic parameter values for the soils correspond to the same relative density values attained during preparation of the interface specimens. They were determined by interpolation from Figure 3-3 in Chapter 3.

Table 4-10
Comparison of the Hyperbolic Parameter Values of the Interfaces
Tested to Hyperbolic Parameter Values of the Soils

Type of Interface	Hyperbolic Parameter Values		Interface-to-Soil Parameter Ratio
	Interface	Soil	
Medium-dense-Density-sand-to-concrete	$K_i = 26625$	$K = 870$	31
	$n_i = 0.83$	$n = 0.63$	1.32
	$R_f = 0.846$	$R_f = 0.85$	0.99
	$\delta = 31^\circ$	$\phi = 36^\circ$	0.86
Dense-Density-sand-to-concrete	$K_i = 21850$	$K = 1200$	18
	$n_i = 0.81$	$n = 0.63$	1.32
	$R_f = 0.88$	$R_f = 0.85$	1.03
	$\delta = 29.3^\circ$	$\phi = 41^\circ$	0.71
Dense-Light-Castle-sand-to-concrete	$K_i = 20700$	$K = 690$	30
	$n_i = 0.79$	$n = 0.79$	1.0
	$R_f = 0.79$	$R_f = 0.81$	0.97
	$\delta = 33.7^\circ$	$\phi = 42.4^\circ$	0.79

Ratios of interface-to-soil hyperbolic parameters are also presented in the table. These ratios are based on a limited database. They should not be used as a reference for interfaces that differ substantially from the interfaces tested during this investigation.

4.4.2 Determination of interface parameter values for unloading-reloading

In this section, recommendations for determination of the unloading-reloading parameter values are presented. It is assumed that a set of hyperbolic parameter values for the interface at yield was determined from a set of at least three initial loading tests, or from reference values as discussed in the preceding section.

4.4.2.1 Experimental determination of K_{urj} . The stiffness number for unloading-reloading K_{urj} is required for Versions I, II, and III of the extended hyperbolic model. In order to determine its value experimentally, unload-reload tests can be performed under constant normal stress, such as those described in Chapter 3 and Appendix C (Figures C12 to C14).

During this investigation, it was found convenient to relate the stiffness number for unloading-reloading K_{urj} to the stiffness number for yield-inducing shear K_I according to the following expression:

$$K_{urj} = C_k \cdot K_I \quad (4-37)$$

where C_k is the interface stiffness ratio.

The recommended process for experimental determination of K_{urj} consists of selecting an adequate starting value of C_k . The corresponding interface response calculated from the model for unloading-reloading is then compared to the interface test data. This comparison is made by plotting the model response and the test data in a shear stress-displacement diagram. The value of C_k is then adjusted until the model fits the data. The shear stress-displacement diagram should be represented at an adequate scale that conveys the degree of accuracy required.

Most often, the best performance can be obtained by selecting a different value of stiffness number for Version I than for Versions II and III. As discussed previously, Version I assumes a linear response during unloading-reloading, whereas Versions II and III assume a hyperbolic response. Consequently, the value of K_{urj} for use in Version I represents an average value of the interface stiffness, which must be lower than the value of K_{urj} for Versions II and III. It must also be equal to or larger than the value of K_I for yield-inducing shear. The assumed interface response for unloading-reloading is identical in Versions II and III; consequently, the same value of K_{urj} is used in both of these versions.

For Version I, such a trial-and-error process is simple because the interface stiffness is constant. An appropriate value of K_{urj} in Version I corresponds to the average stiffness during unloading-reloading. Due to the hysteretic behavior of interfaces, this average stiffness is controlled by the size of the unload-reload loop. Therefore, the value of the stiffness ratio C_k must be selected depending on the particular loading conditions of the interface. For Versions II and III, the determination of C_k by trial and error is more involved because both the stiffness number K_{urj} and the scaling factor α influence the assumed interface response. Therefore, the determination of K_{urj} must be carried out concurrently with the determination of α .

In addition, unload-reload testing of the interface may be difficult and time-consuming. Frequent measurements, with an adequate resolution, of the interface stresses and displacements are required for an accurate determination of the interface response. An alternative procedure is proposed for the determination of K_{urj} from other known interface properties and without the need to perform unload-reload interface tests.

4.4.2.2 Determination of K_{urj} from known interface properties. Figure 4-23 illustrates a typical hyperbolic relationship that models the response of an interface at yield. The solid portion of the line corresponds to the part of the hyperbola that models yield-inducing shear. The dashed portion corresponds to the mathematical extension of the hyperbola, given by Equation 2-9, into the third quadrant. The extension has no physical meaning for yield-inducing shear. It was found that the slope of the hyperbola at a stress level of -1 provides a good approximation to the interface stiffness upon unloading-reloading. Consequently, the value K_{urj} for Versions II and III of the model can be assumed to be equal to the normalized stiffness at a stress level of -1.

Combining Equations 4-2 and 4-22 and assigning a value of stress level of -1 gives the following expression for the stiffness number for unloading-reloading:

$$K_{urj} = K_I \cdot (1 + R_{ff})^2 \quad (4-38)$$

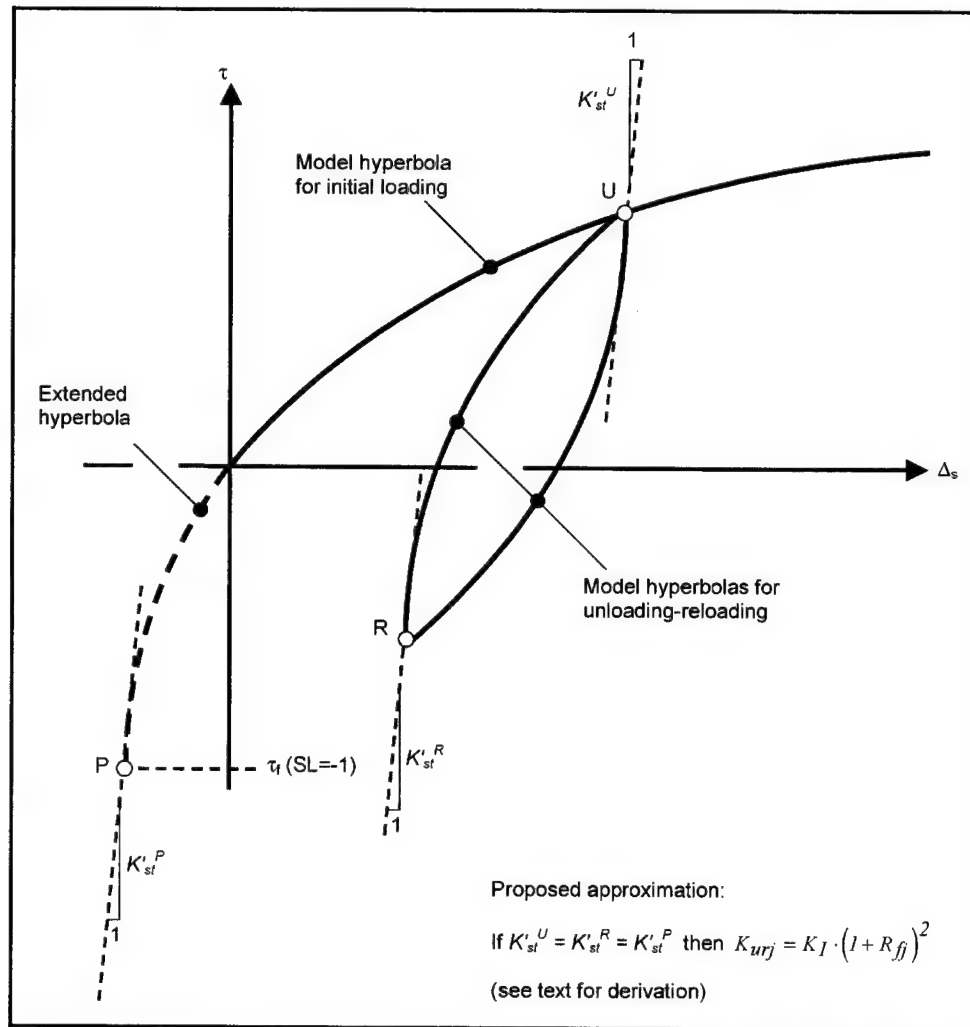


Figure 4-23. Proposed approximation for the estimation of the stiffness number for unloading-reloading K_{urj}

Recalling Equation 4-37, the following expression for the stiffness ratio can be obtained:

$$C_k = (1 + R_{ff})^2 \quad (4-39)$$

This expression is valid for Versions II and III of the model. It provides a reasonable approximation to the stiffness ratio for the three interfaces tested. For Version I, where a lower value of C_k should be used, it is recommended that half of the value given by Equation 4-39 be used, as indicated in Table 4-11. It was found that this recommended value of C_k provides reasonable estimations of the interface response for unloading-reloading cycles where the absolute change in stress level is equal to or less than one. For larger unloading-reloading cycles, it may be necessary to use a different value of C_k than that given in Table 4-11.

Table 4-11 Recommended Values of the Stiffness Ratio C_k		
Version of the Model	Correlation with R_{ff}	Expected Range
I	$C_k = 0.5 \cdot (1 + R_{ff})^2$	1 to 2
II and III	$C_k = (1 + R_{ff})^2$	2 to 4

Table 4-11 also lists ranges of values of C_k that correspond to typical values of R_{ff} (Table 4-9). It was found that, when used with the extended hyperbolic model, the expressions in Table 4-11 provide an accurate estimate of the interface stiffness for the three interfaces tested. It is anticipated that, in some cases, the parameter values given by these expressions may require further adjustment. If unload-reload testing data are available, this can be accomplished by trial and error following the procedure outlined previously.

4.4.2.3 Determination of parameter α . The scaling factor α is used in Versions II and III of the extended hyperbolic model. It can be determined experimentally from the results of unload-reload tests. As indicated previously, appropriate values of K_{urf} and α can be determined simultaneously through a trial-and-error process that consists of fitting the hyperbolic response to the data from unload-reload interface tests.

An alternative procedure is proposed to estimate the value of α from other known interface properties. It is based on the experimental observation that the normalized interface stiffness during unloading-reloading is usually equal to or greater than the interface stiffness at yield, at a given value of stress level.

Figure 4-24 illustrates the interface response during a hypothetical unload-reload test. The interface is initially sheared to point U and then unloaded to point R at a stress level of -1, which represents the onset of failure in the fourth quadrant. Finally, the interface is reloaded into the first quadrant. Large stiffness values for unloading-reloading were used in Figure 4-24 to facilitate explanation of this

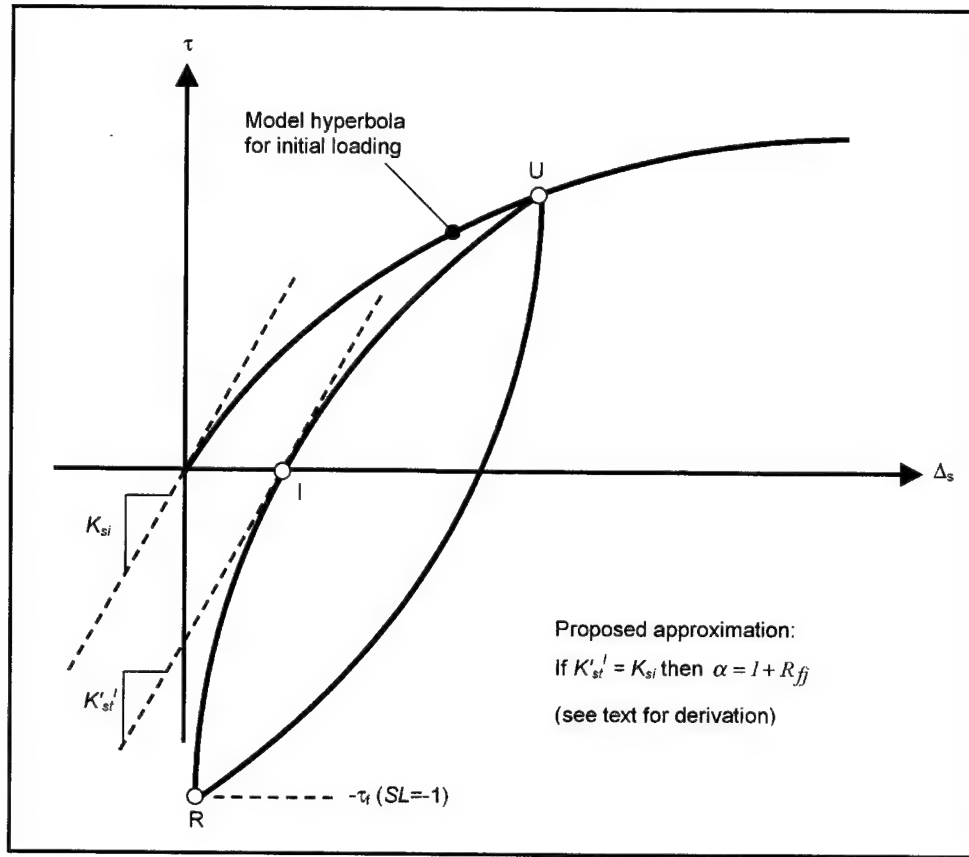


Figure 4-24. Proposed approximation for the estimation of the scaling factor α

procedure. Experimental data suggest that, during shear of a real interface, the shear stress-displacement diagram for reloading may lie closer to the virgin shear diagram (Figure C13a in Appendix C).

According to Equation 4-25, the interface stiffness during reloading from point R can be expressed as:

$$K'_{st} = K_{urj} \cdot \gamma_w \cdot \left(\frac{\sigma_n}{p_a} \right)^{n_j} \cdot \left[1 - \frac{1}{\alpha} R_{fj} \cdot (SL + 1) \right]^2 \quad (4-40)$$

The reloading diagram intersects the interface displacement axis at point I . Introducing a stress level value of zero into Equation 4-40 produces the following expression for the interface stiffness at point I :

$$K'_{st} = K_{urj} \cdot \gamma_w \cdot \left(\frac{\sigma_n}{p_a} \right)^{n_j} \cdot \left[1 - \frac{R_{fj}}{\alpha} \right]^2 \quad (4-41)$$

If it is assumed that the interface stiffness K'_{si} at point I is equal to the initial stiffness K_{si} of the interface at point O , Equation 4-41 becomes

$$K_{si} = K_{urj} \cdot \gamma_w \cdot \left(\frac{\sigma_n}{p_a} \right)^{n_j} \cdot \left[1 - \frac{R_{fj}}{\alpha} \right]^2 \quad (4-42)$$

The initial interface stiffness was defined mathematically in Chapter 2 as:

$$K_{si} = K_I \cdot \gamma_w \cdot \left(\frac{\sigma_n}{p_a} \right)^{n_j} \quad (4-43)$$

Combining Equations 4-42 and 4-43 and eliminating common terms yields the following expression:

$$K_I = K_{urj} \cdot \left[1 - \frac{R_{fj}}{\alpha} \right]^2 \quad (4-44)$$

Combining Equations 4-37 and 4-44:

$$K_I = C_k \cdot K_I \cdot \left[1 - \frac{R_{fj}}{\alpha} \right]^2 \quad (4-45)$$

Simplifying Equation 4-45 and rearranging terms:

$$\alpha = \frac{\sqrt{C_k} \cdot R_{fj}}{\sqrt{C_k} - 1} \quad (4-46)$$

An expression for the stiffness ratio C_k was given previously. Substituting Equation 4-39 into 4-46, the following expression for the scaling factor is obtained:

$$\alpha = 1 + R_{fj} \quad (4-47)$$

Equation 4-47 assumes that the hypotheses illustrated in Figures 4-23 and 4-24 are both accurate. It was found that using Equation 4-47 simplified the implementation of Versions II and III of the model substantially, and that accurate estimations of the stiffness during unloading-reloading were possible for the three interfaces tested. The expected range of values of the scaling factor is presented in Table 4-12. It was determined from Equation 4-47 and the range of reported R_{fj} values from Table 4-9.

Table 4-12
Recommended Values of the Scaling Factor α

Version of the Model	Correlation with R_f	Expected Range
I	Not applicable	-
II and III	$\alpha = 1 + R_{ff}$	1.4 to 2

This procedure for the estimation of α was selected because it ensures that the interface stiffness during unloading-reloading is always equal to or greater than the interface stiffness during virgin shear at any stress level value, as demonstrated in the subsequent paragraphs.

The following expression for the interface stiffness during unloading-reloading is obtained by substituting Equations 4-37, 4-39, and 4-47 into 4-25:

$$K'_{st} = K_I \cdot (1 + R_{ff})^2 \cdot \gamma_w \cdot \left(\frac{\sigma_n}{p_a} \right)^{n_f} \cdot \left[1 - \frac{q}{(1 + R_{ff})} R_{ff} \cdot (SL - SL_o) \right]^2 \quad (4-48)$$

For reloading from the fourth quadrant into the first quadrant ($q = +1$), Equation 4-48 becomes

$$K'_{st} = K_I \cdot \gamma_w \cdot \left(\frac{\sigma_n}{p_a} \right)^{n_f} \cdot [1 - R_{ff} \cdot SL + R_{ff} \cdot (SL_o + 1)]^2 \quad (4-49)$$

The interface stiffness for initial loading along a vertical stress path was defined as

$$K_{st} = K_I \cdot \gamma_w \cdot \left(\frac{\sigma_n}{p_a} \right)^{n_f} \cdot [1 - R_{ff} \cdot SL]^2 \quad (2-11bis)$$

The ratio between the stiffness during unloading-reloading and the stiffness at yield is obtained dividing Equation 4-49 by Equation 2-11:

$$\frac{K'_{st}}{K_{st}} = \left[1 + \frac{R_{ff}}{1 - R_{ff} \cdot SL} (SL_o + 1) \right]^2 \quad (4-50)$$

The values of stress level SL and stress level at the origin SL_o are always equal to or greater than -1, and equal to or lower than +1. The value of R_{ff} is between zero and one. Consequently, the ratio given by Equation 4-50 is always equal to or greater than one. This implies that the interface stiffness during unloading-reloading is always equal to or greater than the interface stiffness at yield for the

same stress level. This is consistent with the experimental observations on interface response discussed in previous sections.

4.4.2.4 Unload-reload parameter values for the interfaces tested. The values of the parameters K_{urj} and α for each of the interfaces tested are summarized in Table 4-13. They were determined using the criteria presented in Tables 4-11 and 4-12, and the hyperbolic parameter values listed in Table 4-8. The hyperbolic parameter values reported in Table 4-9 can be used to estimate unload-reload parameters for other types of interfaces.

Table 4-13 Summary of Parameter Values for Unloading-Reloading for Interfaces Tested		
Parameter	Value for Version I	Value for Versions II and III
Dense Density Sand Against Concrete		
K_{urj}	45365	90730
α	Not applicable	1.85
Medium Dense Density Sand Against Concrete		
K_{urj}	38450	76900
α	Not applicable	1.88
Dense Light Castle Sand Against Concrete		
K_{urj}	33160	66320
α	Not applicable	1.79

4.4.2.5 Final remarks. The recommended procedures for the estimation of parameters K_{urj} and α assume specific features in the interface response during unloading-reloading. They are based on the experimental observations on the response of the three interfaces tested.

The most accurate determination of the parameter values can be achieved from experimental data. Unload-reload testing and subsequent data interpretation may be lengthy processes. However, if an accurate determination of the interface response is required, unload-reload tests that model the type of loading expected in the field should be performed. In this case, the proposed parameter values presented in Tables 4-11 and 4-12 can be used as an initial estimate that can be adjusted by trial and error as discussed previously.

4.5 Evaluation of the Extended Hyperbolic Model

To evaluate the accuracy of the extended hyperbolic model, comparisons were made between the interface test data and the interface response calculated from the model. It was found that, for the types of testing performed, the model is accurate for yield-inducing shear. For most stress paths, Version I provides reasonable estimates of the interface response. Version II introduces a significant increase in accuracy for stress paths that induce large unloading-reloading cycles. Version III is the most accurate and can be applied for any stress path inside the unloading-reloading and transition loading regions.

In the following sections, the interface response calculated using the extended hyperbolic model is compared with the results of the interface tests. A separate discussion is presented for each of the types of interface testing performed. The comparative advantages of each of the versions of the model are also discussed.

4.5.1 Accuracy of the model for yield-inducing shear

This discussion is limited to stress paths that induce yield of the interface, and excludes cases where both yield and unloading-reloading take place.

4.5.1.1 Shear under constant normal stress. As indicated previously, the formulation of the extended hyperbolic model for vertical stress paths is identical to the formulation of the Clough and Duncan (1971) hyperbolic model. They produce the same predictions of interface response for identical interfaces sheared under the same normal stress.

Figures D3, D6, and D9 in Appendix D compare the data from initial loading tests and the interface response calculated using the Clough and Duncan (1971) formulation. The hyperbolic parameter values for the three interfaces tested determined in Appendix D were used for these comparisons. These figures are reproduced in Figures 4-25 through 4-27.

Figure 4-25 includes the interface response calculated using the extended hyperbolic model and the adjusted parameter values for the dense-Density-sand-against-concrete interface, listed in Table 4-8. For practical purposes, the difference between the estimates obtained using the two sets of parameters is negligible. However, it must be recalled that, as indicated previously, adjustment of the parameter values may be necessary when using the formulation for interfaces at yield to model interfaces subjected to simultaneous changes in shear and normal stresses. In such cases, errors in the interface stiffness values may be magnified by the correction factor for stress path inclination.

As indicated previously, it was not necessary to adjust the hyperbolic parameter values determined in Appendix D for the interfaces of medium-dense Density sand against concrete and the Light Castle sand against concrete. Consequently, only one set of interface response hyperbolas is shown for each of these interfaces in Figures 4-26 and 4-27.

4.5.1.2 Shear along inclined stress paths. The results of Test T205_5, presented in Figure C27 of Appendix C, are reproduced in Figure 4-28. A curvilinear stress path was applied to the interface, as illustrated in Figure 4-28a. Yielding of the interface was induced throughout the test. The stress path models the type of loading expected to take place on a lock-wall-to-backfill interface during placement and compaction of the backfill, as illustrated in Figure 1-3a.

The interface response for this stress path was calculated using the formulation for interfaces at yield summarized in Table 4-2. Appendix E contains an example of such calculations. The test data and the calculated interface response are compared in Figure 4-28b. The model response was determined using the

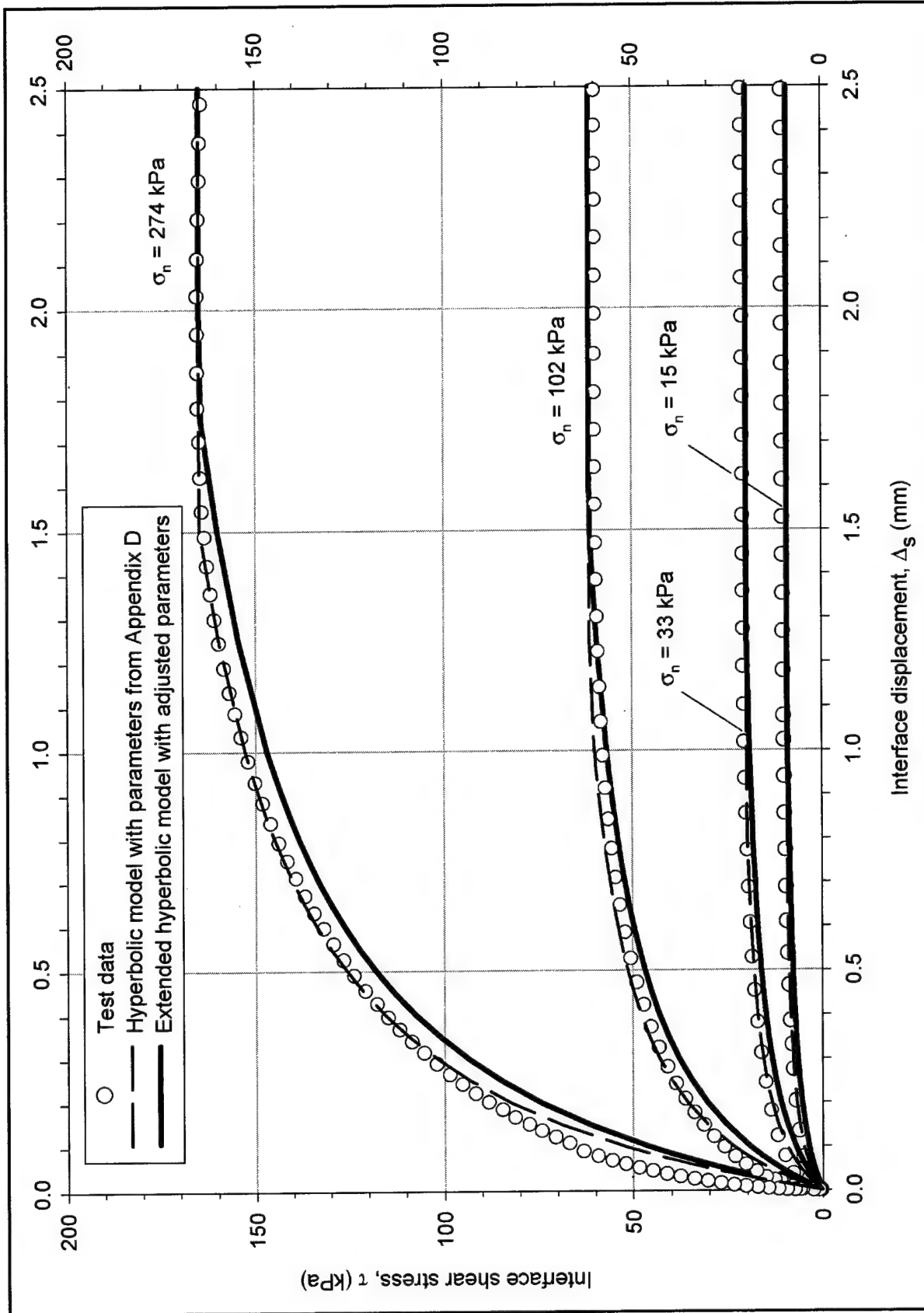


Figure 4-25. Comparison between the extended hyperbolic model and data from initial loading tests on the dense-Density-sand-to-concrete-interface

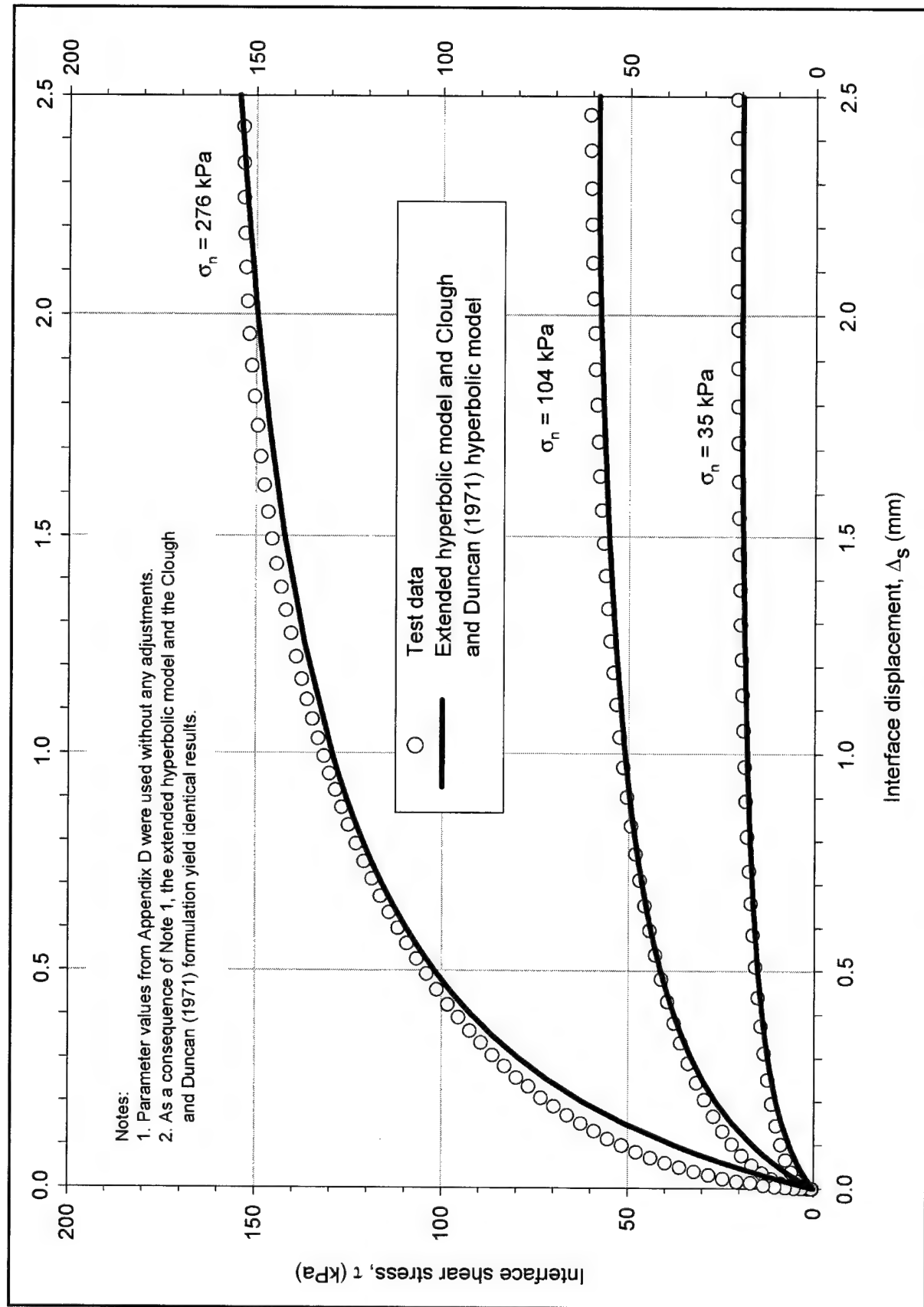


Figure 4-26. Comparison between the extended hyperbolic model and data from initial loading tests on the medium-density-sand-to-concrete interface

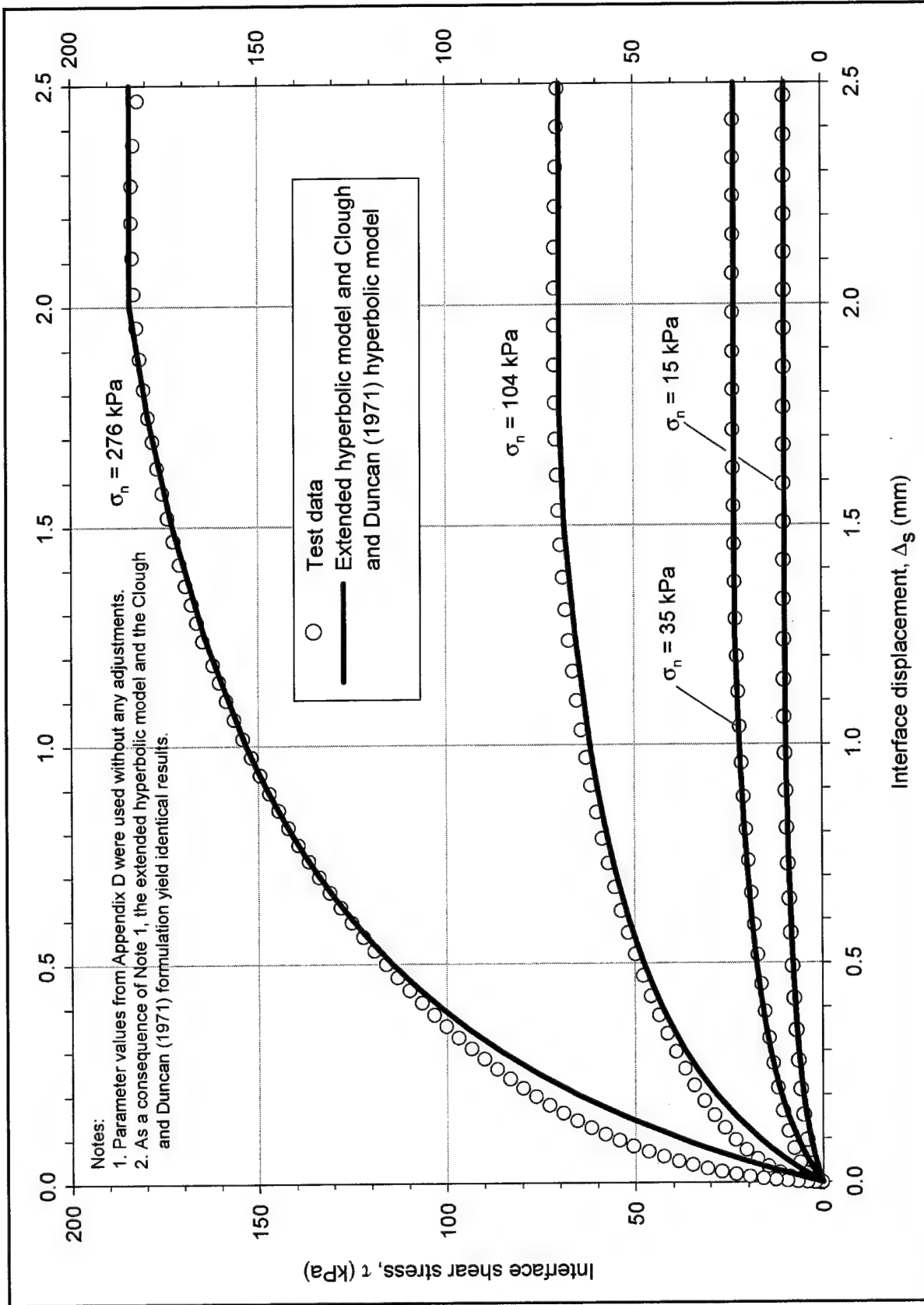


Figure 4-27. Comparison between the extended hyperbolic model and data from initial loading tests on the dense-Light-Castle-sand-to-concrete interface

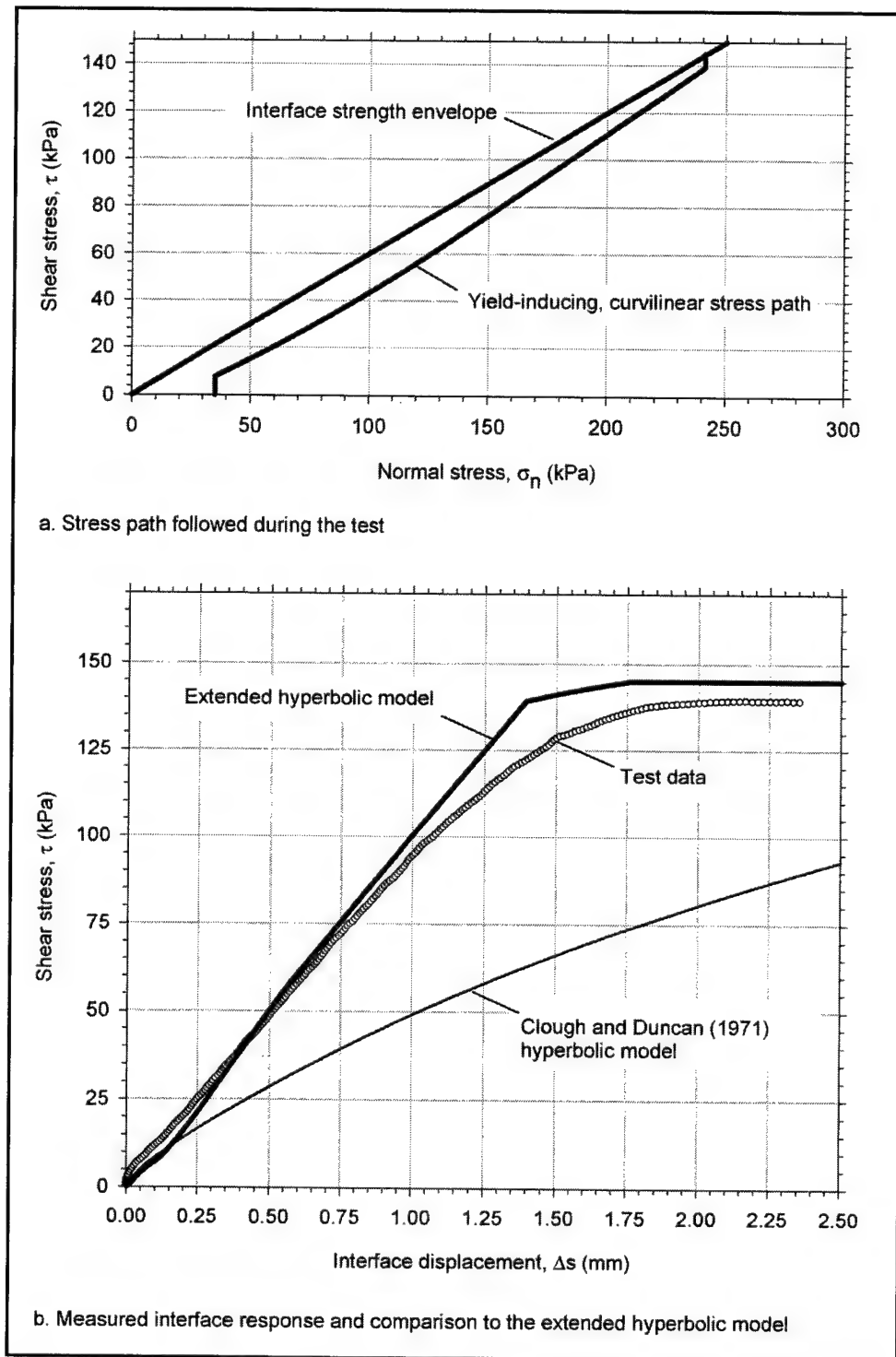


Figure 4-28. Comparison between the extended hyperbolic model and data from multidirectional stress path Test T205_5 performed on the dense-Density-sand-to-concrete interface

adjusted hyperbolic parameter values listed in Table 4-8. It can be seen that the extended hyperbolic model provides a good approximation to the measured interface response for this stress path.

The interface response calculated using the Clough and Duncan (1971) hyperbolic model is also included in the figure. The model response is much softer than the test data. This comparison reveals that, for this type of loading, substantial gains in accuracy are obtained by application of the extended hyperbolic model.

4.5.2 Accuracy of the model for unloading-reloading

This section evaluates the accuracy of the extended hyperbolic model for predicting the interface response under unloading-reloading. It excludes cases where transition loading is applied.

The results of Tests T201_5, T202_5, and T203_15 performed on the dense-Density-sand-against-concrete interface are the basis for this evaluation. Figure 4-29 illustrates the application of the extended hyperbolic model for this type of loading. As discussed previously, yielding of the interface takes place during initial loading to point *U*. Subsequently, unloading from point *U* to point *R* and reloading from point *R* are applied. Yielding occurs after the past maximum stress level, which is given by point *U*, is exceeded during reloading from point *R* and until failure of the interface.

The formulation for interfaces at yield, summarized in Table 4-2, was used to calculate the interface response for the primary loading portion of the stress path. Versions I, II, and III of the formulation for unloading-reloading, summarized in Tables 4-4, 4-5, and 4-6, respectively, were used to calculate the interface response for unloading-reloading between points *U* and *R*. The model parameter values used are those listed in Tables 4-8 and 4-13. Examples of such calculations are presented in Appendix E.

4.5.2.1 Version I. Figures 4-30a, 4-31a, and 4-32a compare the test data and the response calculated using Version I of the unload-reload formulation. For Tests T201_5 and T203_15, which have relatively small unload-reload loops contained in the first quadrant, the calculated interface response is accurate.

It can be noted that Test T202_5 has a larger unload-reload loop that extends into the fourth quadrant. The interface response calculated using Version I is linear during unloading from point *U* and until the stress path enters the fourth quadrant. Because no previous shearing occurred inside the fourth quadrant, i.e. no negative shear stresses were applied previously, the formulation for yield-inducing shear was used to model the interface response during shear to point *R* inside the fourth quadrant. Consequently, the calculated interface response for shearing from point *U* to point *R* has two components: a linear portion inside the first quadrant and a nonlinear portion inside the fourth quadrant. It can be seen that the model provides a good approximation to the measured interface response to shearing from point *U* to point *R*.

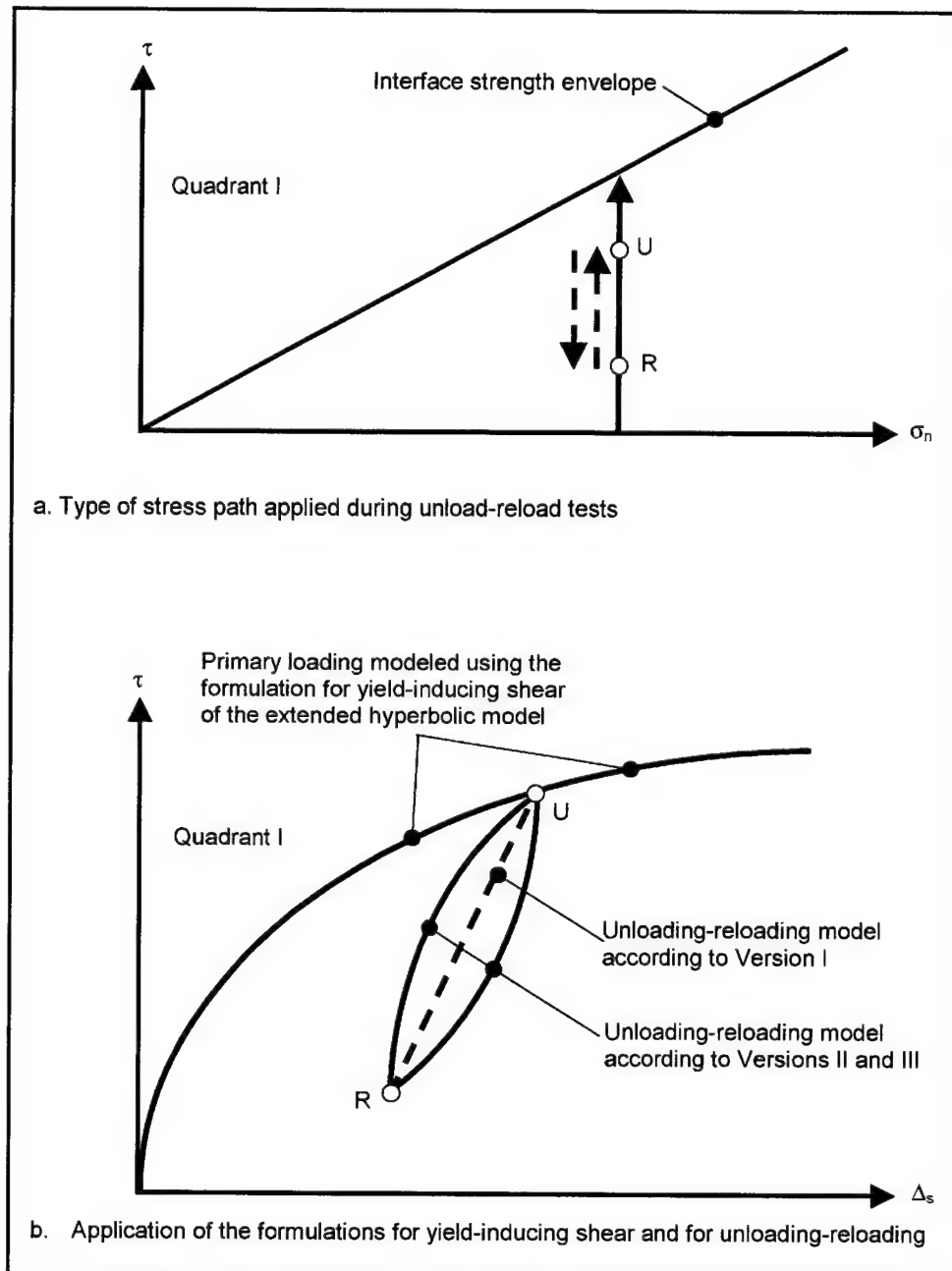


Figure 4-29. Application of the extended hyperbolic model for unload-reload stress paths contained in Quadrant I of the τ - σ_n plane

For reloading from point R , the interface response calculated using Version I is linear until the previous maximum stress level, which was reached during initial loading to point U , is attained. It is seen that the calculated interface response does not fit the test data accurately. It can be concluded that Version I does not provide good estimates of interface response for large unload-reload loops. It is important to emphasize that Version I does not model the hysteretic response of interfaces to unload-reload loops. The curvature of the shear stress-displacement response calculated using Version I for the loading applied during Test T202_5 is only a

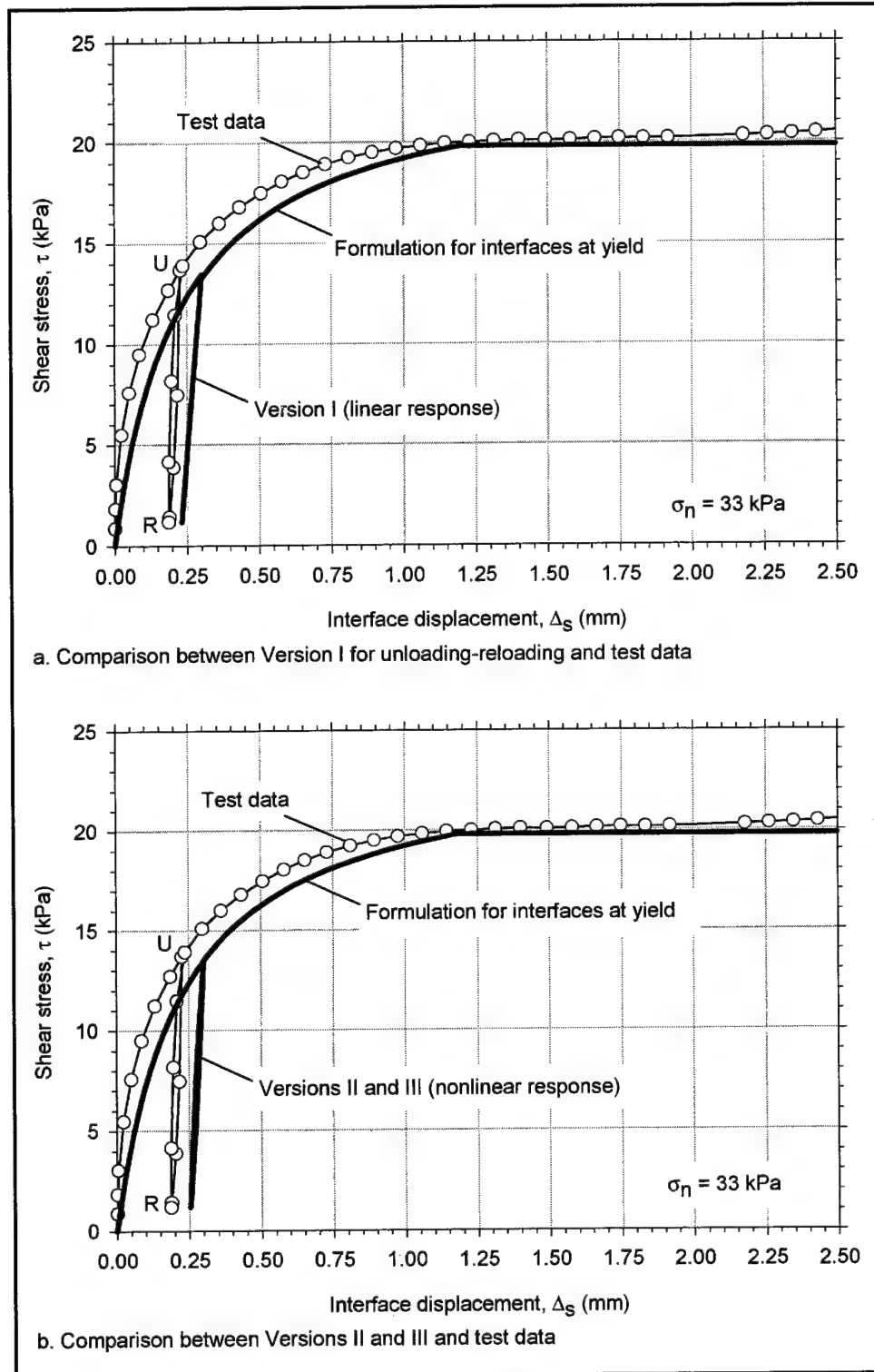


Figure 4-30. Comparison between the extended hyperbolic model and data from Test T201_5 performed on the dense-Density-sand-to-concrete interface

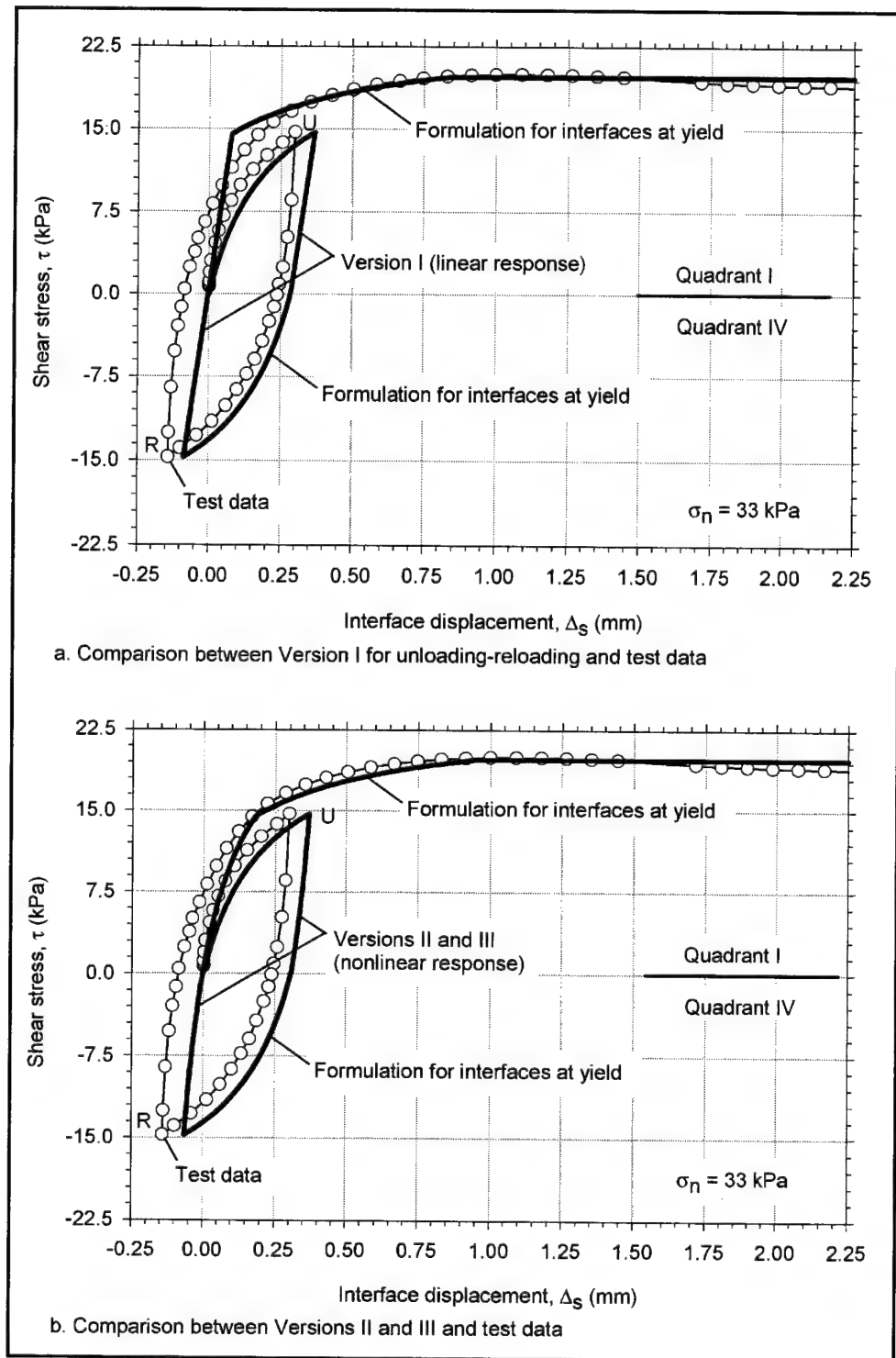


Figure 4-31. Comparison between the extended hyperbolic model and data from Test T202_5 performed on the dense-Density-sand-to-concrete interface

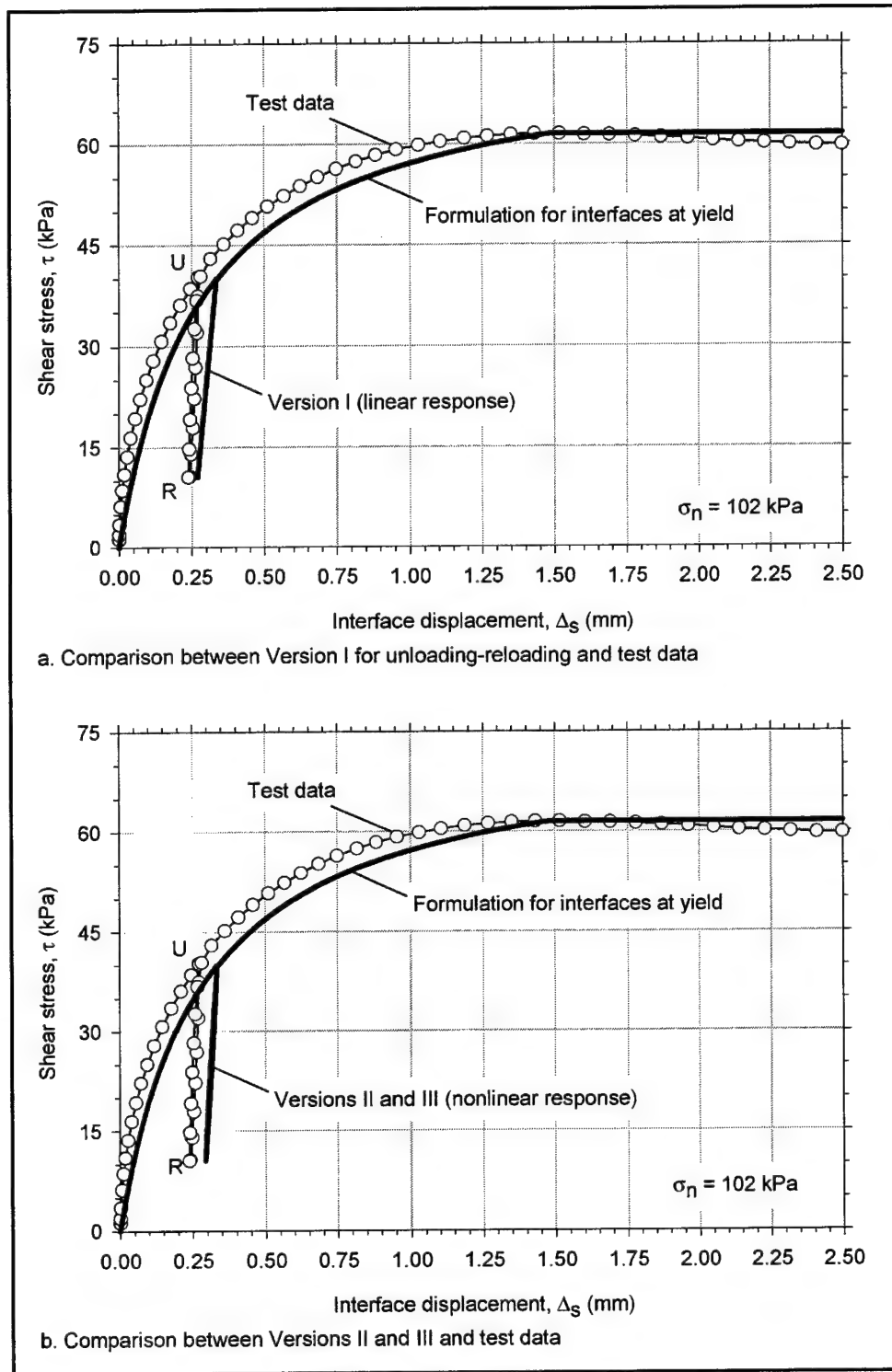


Figure 4-32. Comparison between the extended hyperbolic model and data from Test T203_15 performed on the dense-Density-sand-to-concrete interface

consequence of the nonlinear response during virgin shear into the fourth quadrant. Successive unload-reload cycles between points U and R would produce a linear, nonhysteretic response in Version I.

4.5.2.2. Versions II and III. As can be observed in Figures 4-30b, 4-31b, and 4-32b, Versions II and III provide accurate estimates of the interface response and capture the hysteretic behavior of the interface. However, for these simple stress paths, the overall gains in accuracy with respect to Version I are not very significant.

4.5.3 Accuracy of the model for staged shear

The results of Tests T105_40 and T106_15 performed on the dense-Density-sand-against-concrete interface were used to evaluate the model. The interface parameter values used for the analyses are those in Tables 4-8 and 4-12.

Figure 4-33 illustrates the application of the extended hyperbolic model for this type of loading. Initial loading to point S induces yielding of the interface. Subsequent loading along segment S - S' - Y of the stress path corresponds to transition loading of the interface. Finally, loading beyond point Y corresponds to yield-inducing shear.

The formulation for yield-inducing shear summarized in Table 4-2 was used to calculate the interface response during initial shear to point S and for loading beyond point Y . The interface response for loading along S - S' - Y was calculated using Versions I, II, and III. Appendix E contains examples of such calculations.

4.5.3.1 Versions I and II. Comparisons between the test data and the model response calculated using these two versions are shown in parts a and b of Figures 4-34 and 4-35. The interface response estimated using Versions I and II for loading along S - S' - Y , inside the transition zone, is stiffer than the measured response. The abrupt transition at point Y in the calculated shear stress-displacement curve does not match the test data. However, from a practical point of view, the approximation provided by Versions I and II is reasonable for analyses that do not require highly accurate predictions of the interface response inside the transition zone.

4.5.3.2 Version III. Comparisons between Version III of the model and the measured response during the tests are presented in Figures 4-34c and 4-35c. The model provides a very accurate approximation of the shear stress-displacement response of the interface for loading along S - S' - Y . There is a smooth transition at point Y , which fits the measured response. There are significant gains in the accuracy of stiffness values with respect to Versions I and II. It can be concluded that this version is particularly useful for cases where stress paths are applied to the interface that are mostly contained inside the transition region.

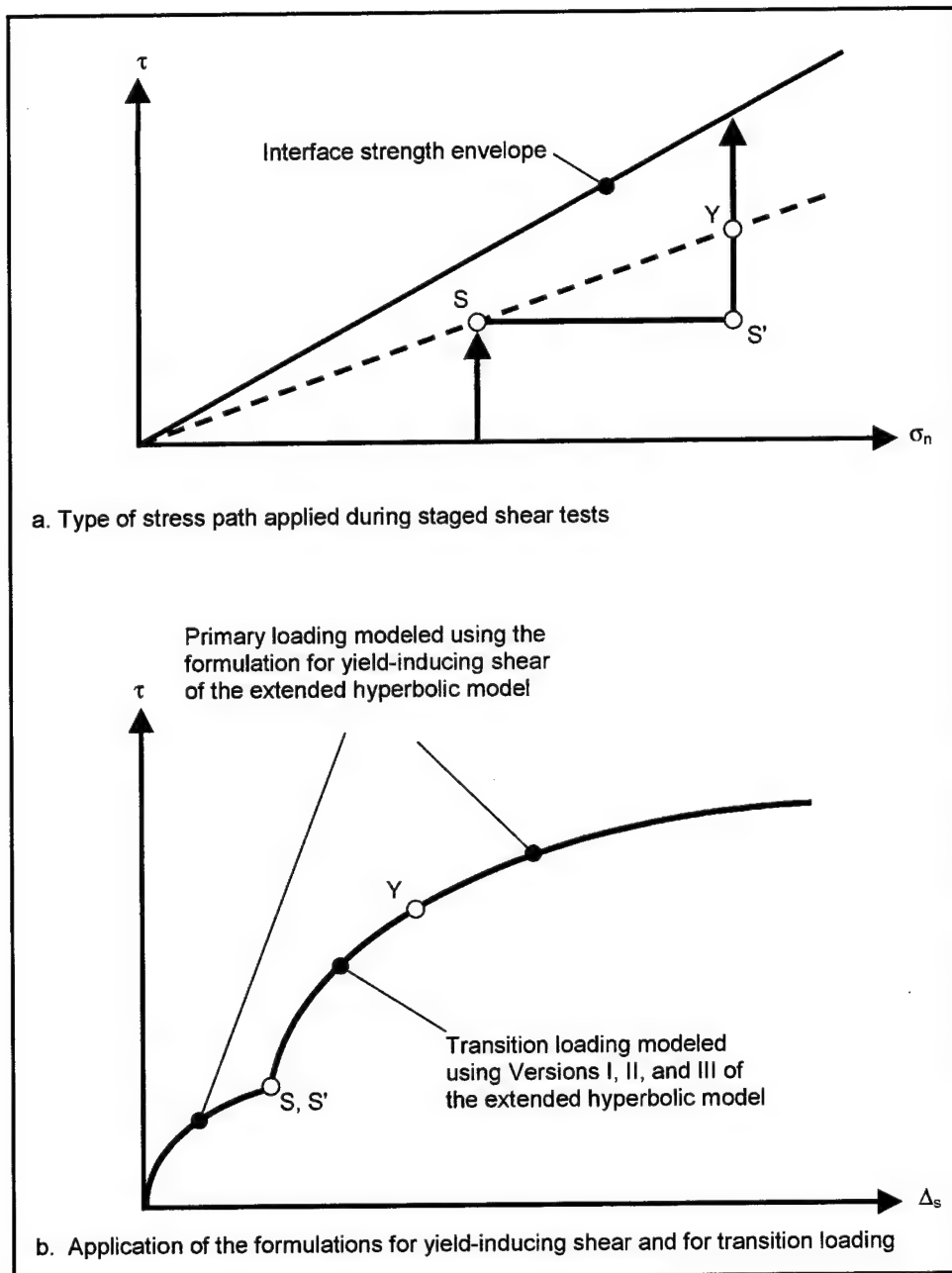


Figure 4-33. Application of the extended hyperbolic model for staged shear stress paths

4.5.4 Accuracy of the model for shearing along complex stress paths

The performance of the extended hyperbolic model for combinations of different types of loading was evaluated against data from multidirectional stress path tests. In such tests, initial loading, unloading-reloading, and transition loading were applied to the interface along stress paths with varying directions. In this

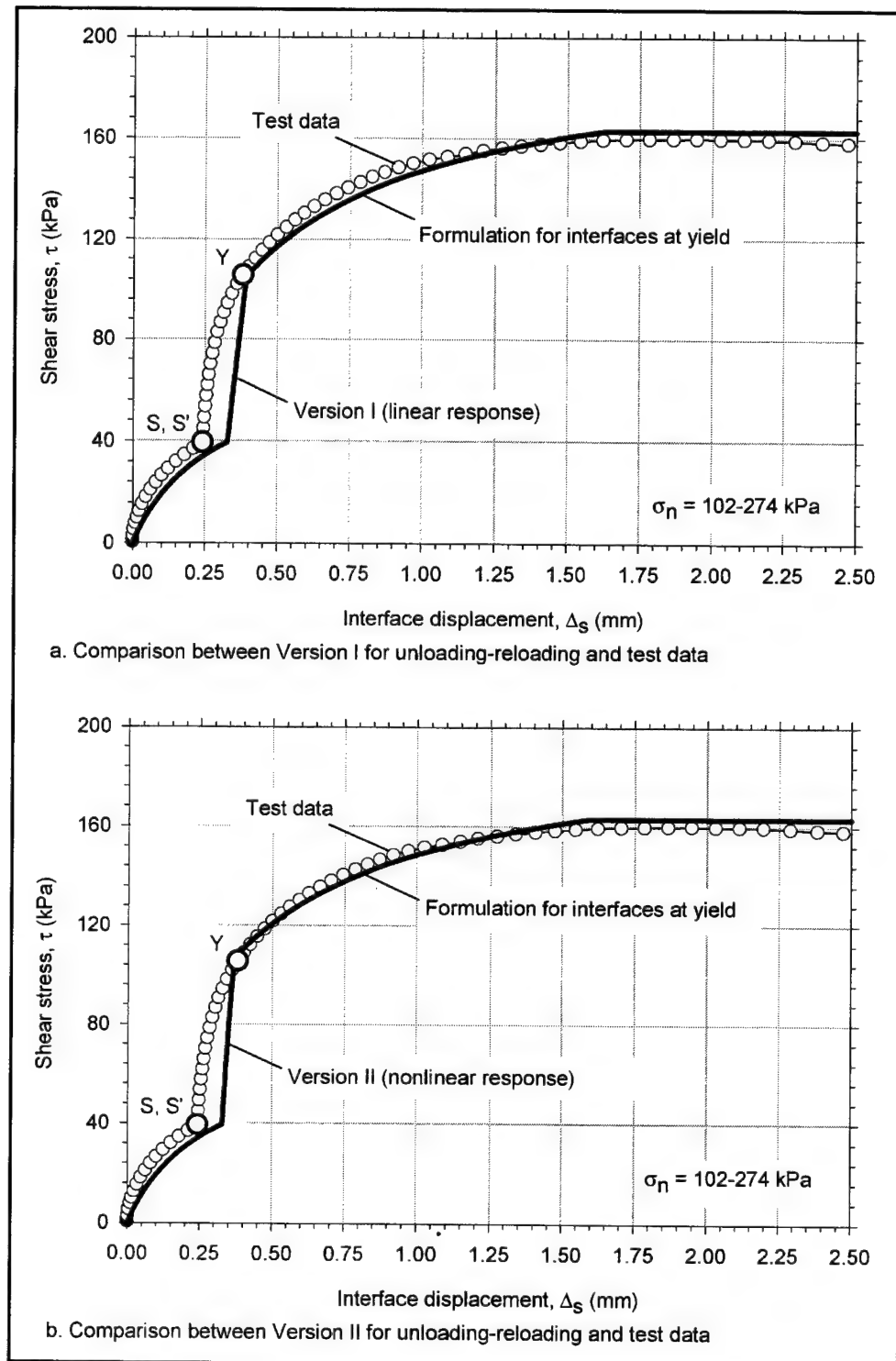


Figure 4-34. Comparison between the extended hyperbolic model and data from Test T105_40 performed on the dense-Density-sand-to-concrete interface (Continued)

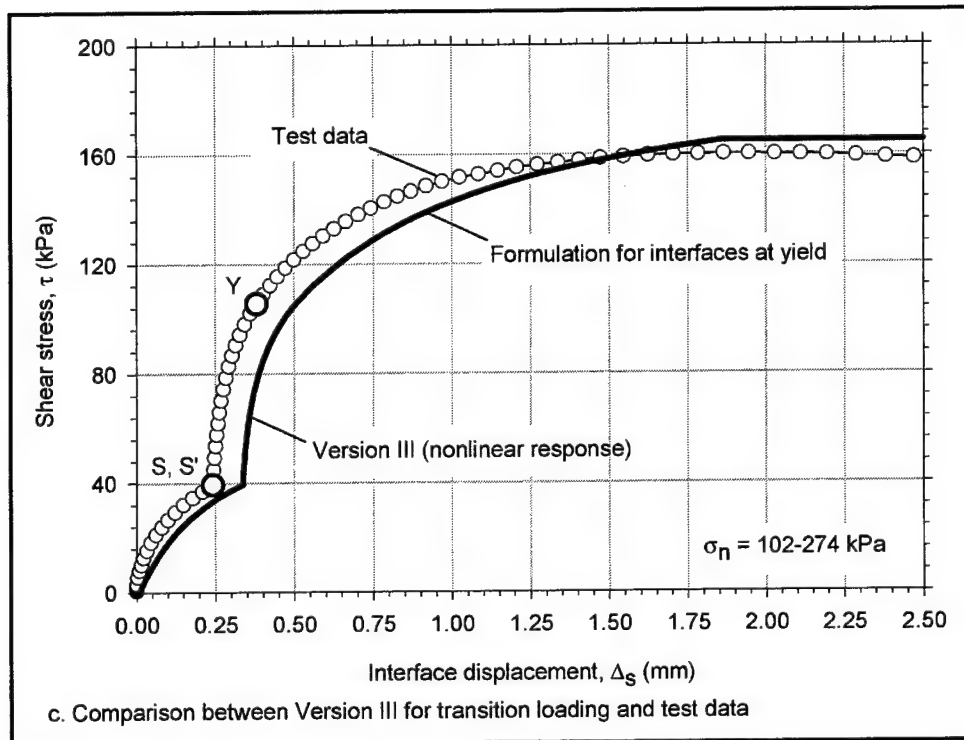


Figure 4-34. (Concluded)

section, the calculated interface response and data from the three interfaces tested are compared.

4.5.4.1 Test T204_5. This test was performed on the dense-Density-sand-against-concrete interface. It was designed to provide information on the response of the interface under transition loading along a complex stress path. Figure 4-36 reproduces the stress path applied during this test and the corresponding shear stress-displacement data. Initial shear to point *A* induced yielding of the interface. The stress level reached at point *A* was not exceeded at any point of the stress path between points *A* and *Y*; therefore, the interface was always subjected to transition loading. Loading beyond point *Y* induced yielding of the interface.

The shear stress-displacement response was estimated using all versions of the extended hyperbolic model. The interface parameter values used are those listed in Tables 4-8 and 4-13. Comparisons between the measured interface response and the predictions from Versions I, II, and III are presented in Figures 4-36b, 4-36c, and 4-36d, respectively.

Versions I and II do not provide accurate approximations to the measured interface response. The interface stiffness values calculated using both versions are larger than the measured stiffness. It is possible to improve the estimation of interface displacements in both versions by using a smaller value of the unload-reload stiffness number K_{urj} . However, such adjustment requires previous knowledge of the type of loading to take place on the interface, as well as the availability of pertinent test data.

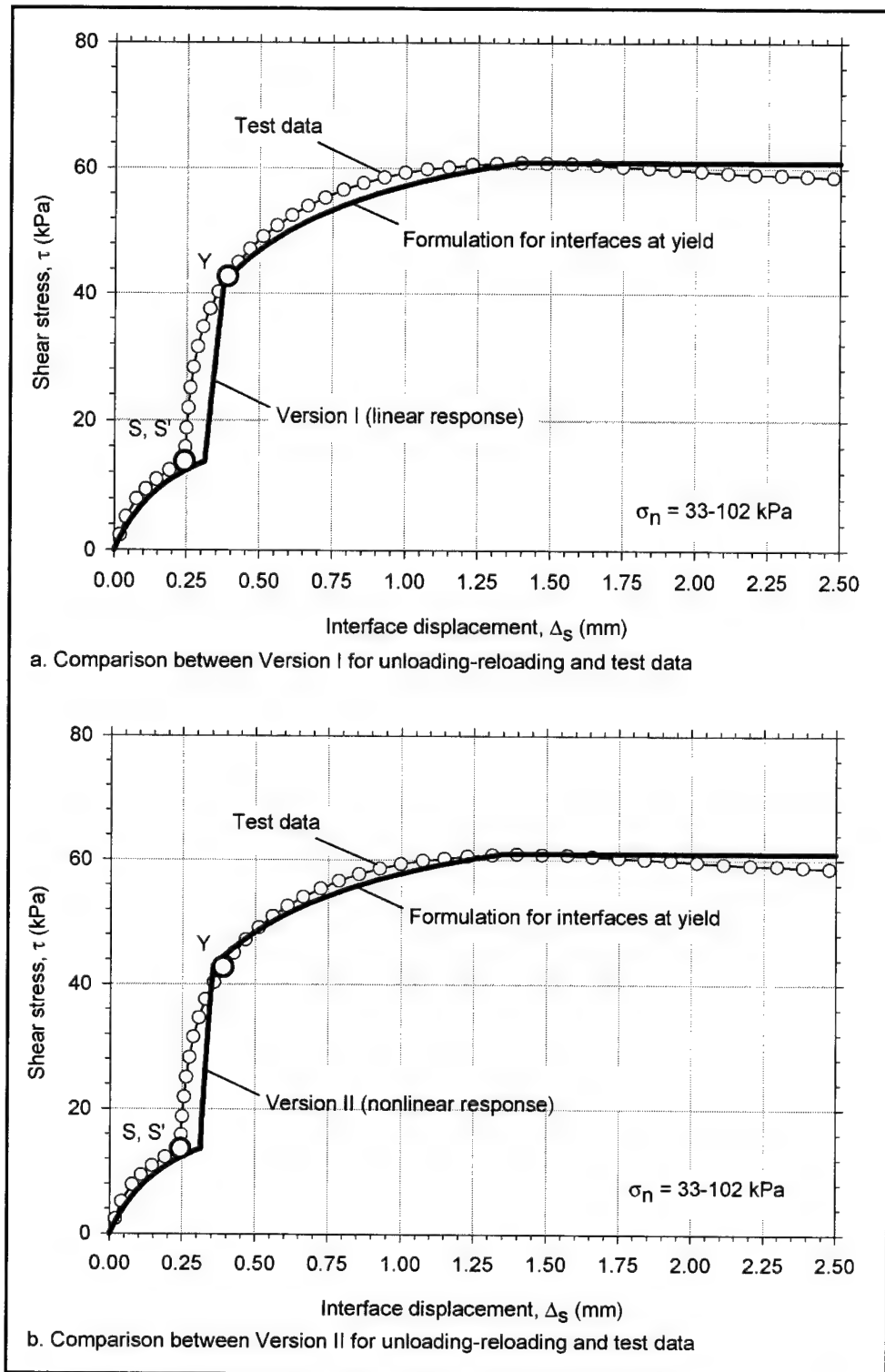


Figure 4-35. Comparison between the extended hyperbolic model and data from Test T106_15 performed on the dense-Density-sand-to-concrete interface (Continued)

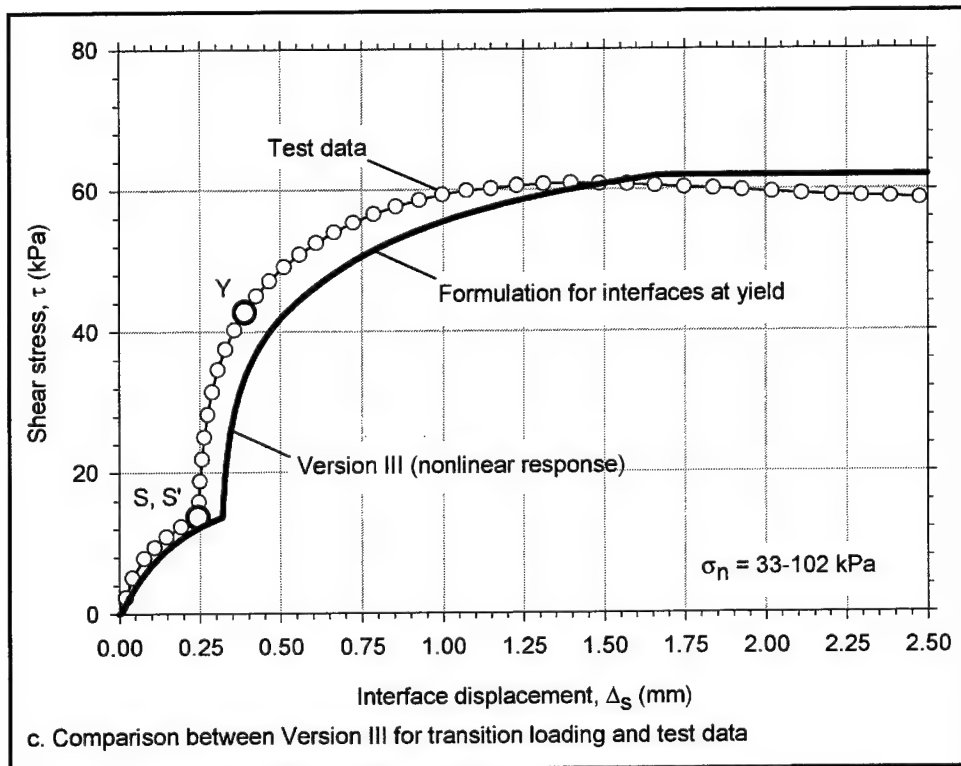


Figure 4-35. (Concluded)

Version III provides a very accurate approximation to the measured interface response. The reason for the greater accuracy of Version III is the interpolation of the interface stiffness values inside the transition region (see example calculations in Appendix E).

Figure 4-36d also shows the shear stress-displacement curve obtained from the Clough and Duncan (1971) hyperbolic model. As expected, the interface response estimated using Clough and Duncan (1971) formulation is softer than the measured response. It can be concluded that, for this type of loading, the extended hyperbolic model Version III has significant comparative advantages over the hyperbolic model.

4.5.4.2 Test 206_5. This test was performed on the dense-Density-sand-against-concrete interface. The test followed a stress path that included all three types of loading defined previously in this chapter. The purpose of the test was to provide data for a comparative evaluation of the accuracy of the three versions of the model. Figure 4-37 reproduces the stress path applied during this test and the corresponding shear stress-displacement data. According to the definitions of the loading regions presented previously, the following types of loading were applied:

- a. Initial loading to point A: yield-inducing shear.
- b. Path A-YI: transition loading.

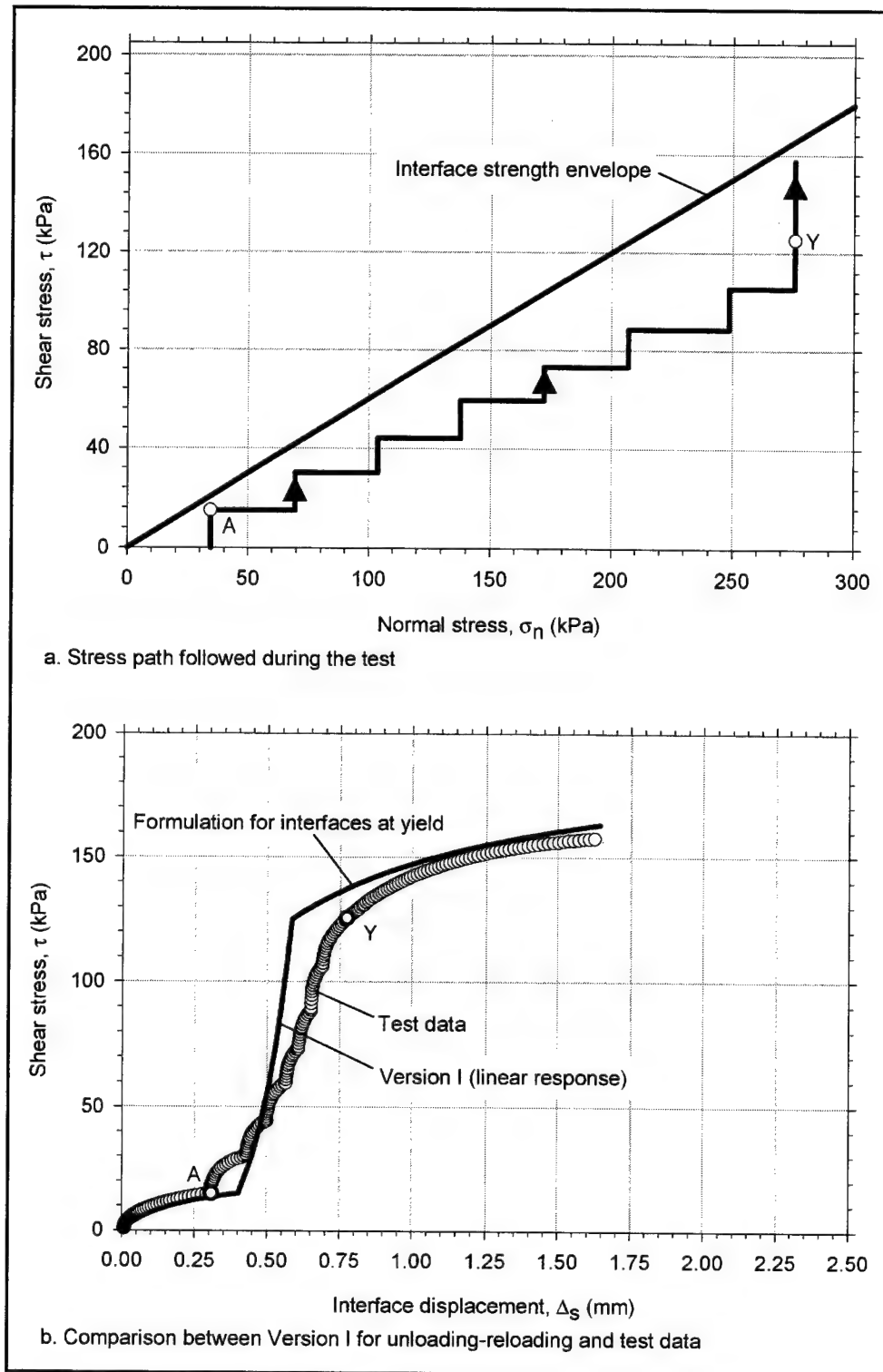


Figure 4-36. Comparison between the extended hyperbolic model and data from multidirectional stress path Test T204_50 performed on the dense-Density-sand-to-concrete interface (Continued)

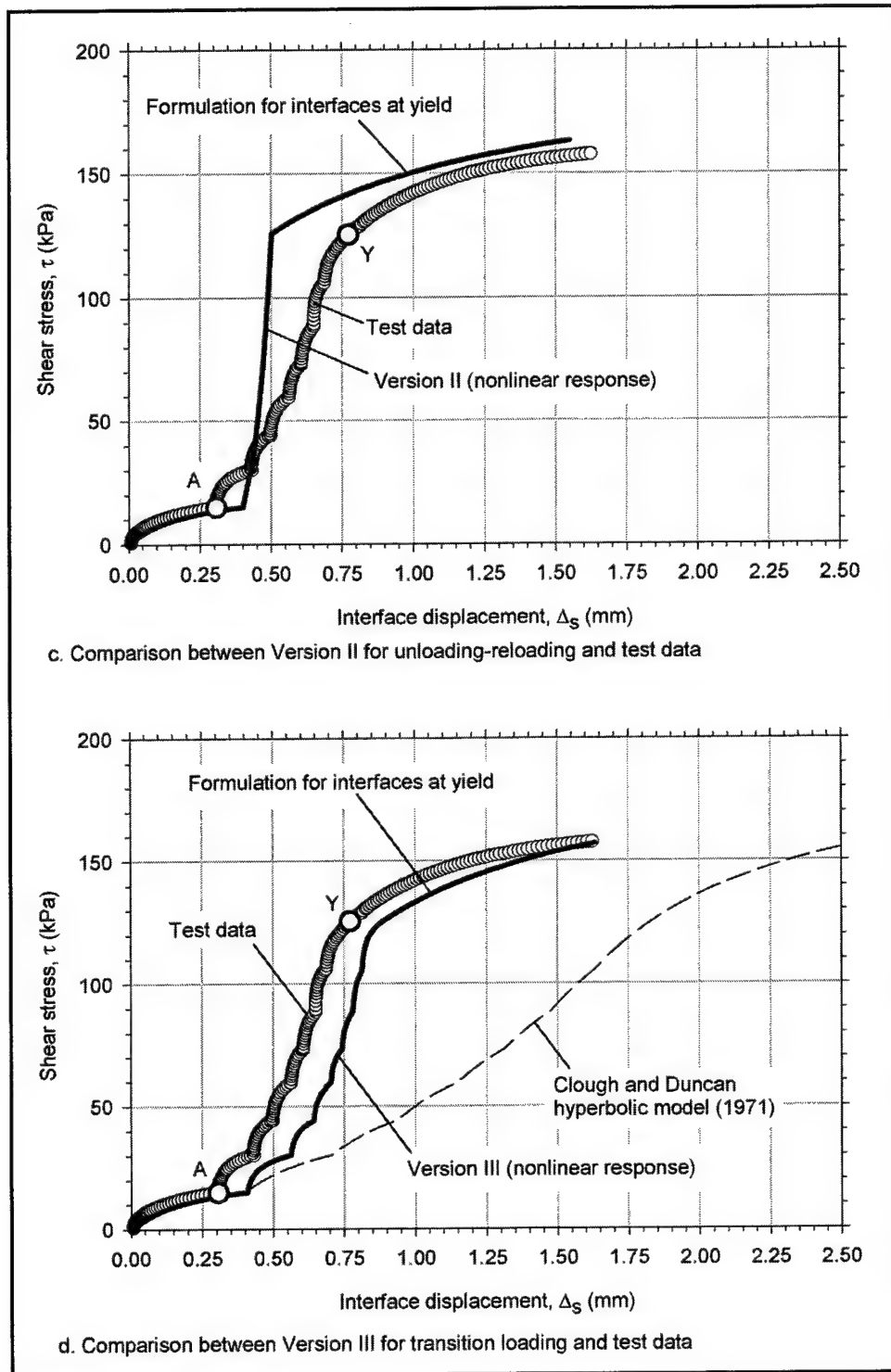


Figure 4-36. (Concluded)

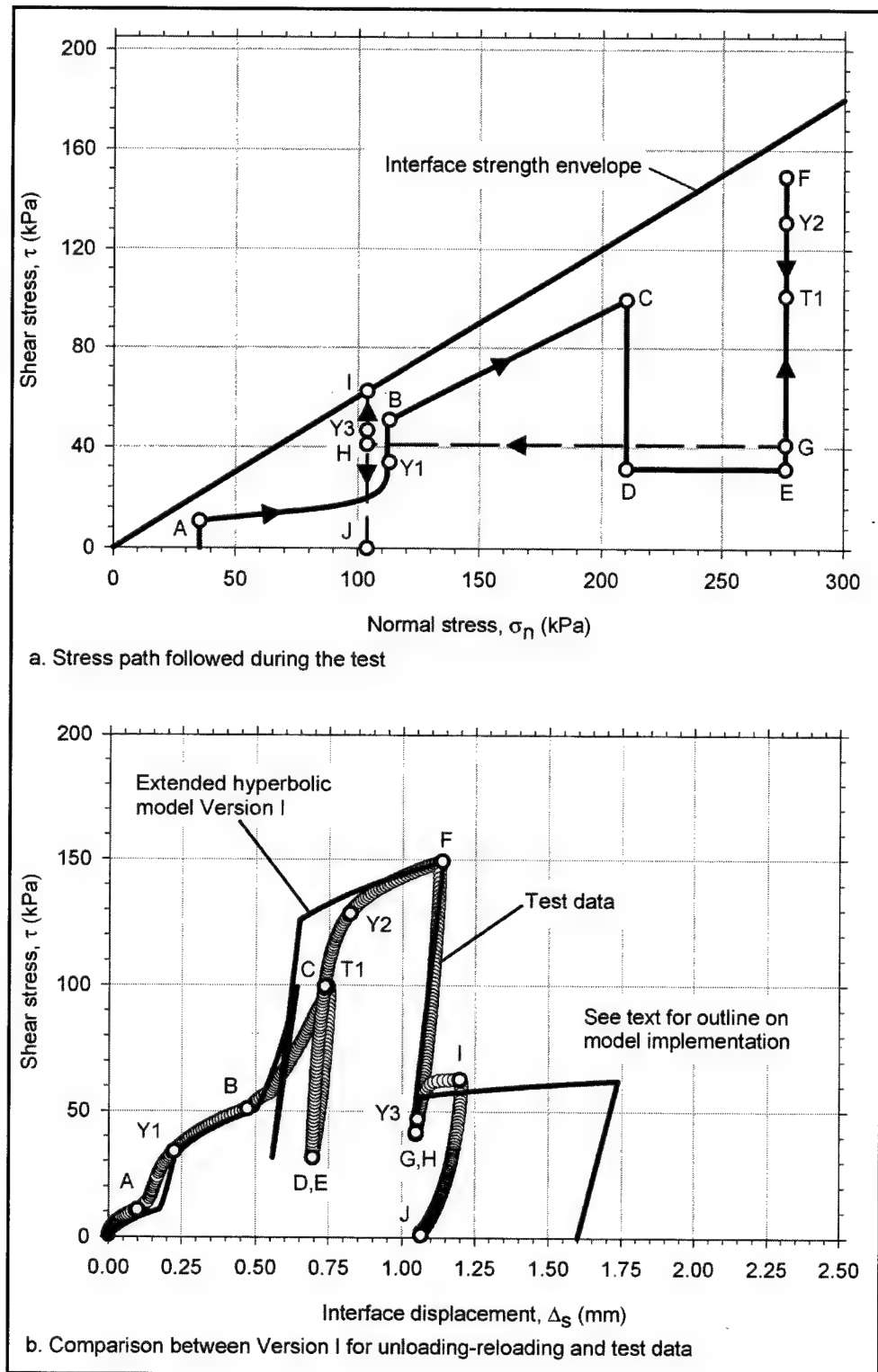
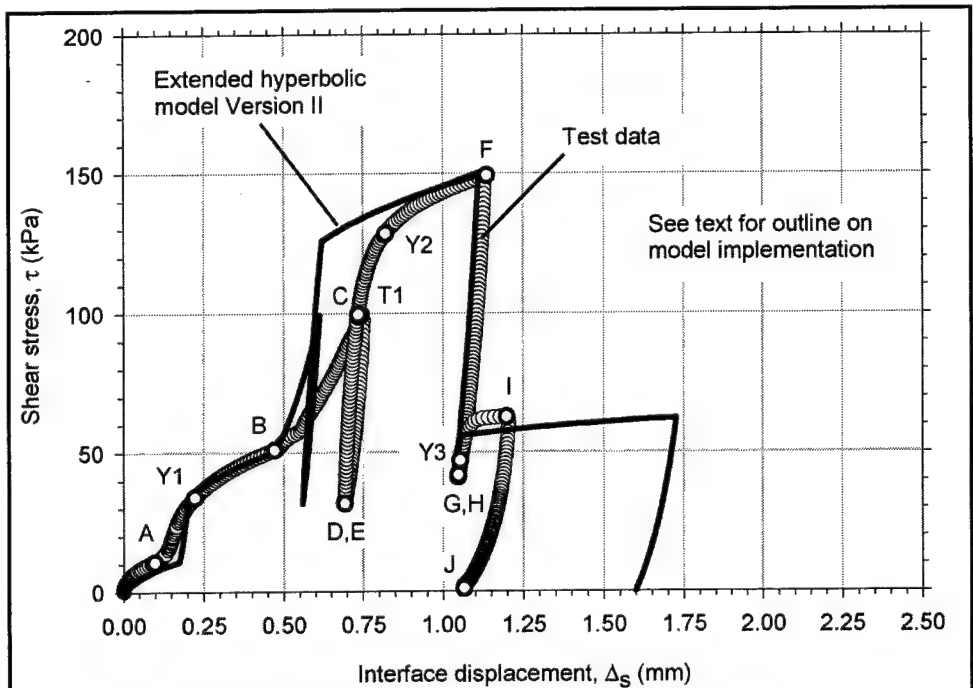
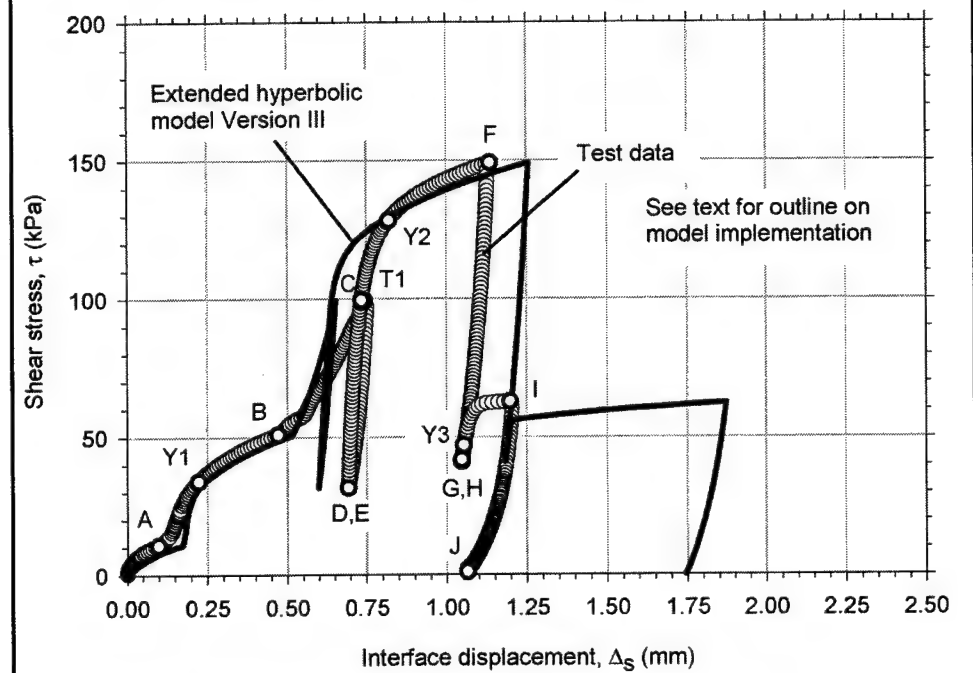


Figure 4-37. Comparison between the extended hyperbolic model and data from multidirectional stress path Test T206_5 performed on the dense-Density-sand-to-concrete interface (Continued)



c. Comparison between Version II for unloading-reloading and test data



d. Comparison between Version III for transition loading and test data

Figure 4-37. (Concluded)

- c. Path *Y1-B-C*: yield-inducing shear.
- d. Path *C-D-E-T1*: unloading-reloading.
- e. Path *T1-Y2*: transition loading.
- f. Path *Y2-F*: yield-inducing shear.
- g. Path *F-G-H-Y3*: unloading-reloading.
- h. Path *Y3-I*: yield-inducing shear.
- i. Path *I-J*: unloading.

The shear stress-displacement response was estimated using all versions of the extended hyperbolic model. The interface parameter values used are those listed in Tables 4-8 and 4-13. The measured interface response and the results obtained from Versions I, II, and III are compared in Figures 4-37b, 4-37c, and 4-37d, respectively.

The three versions of the model all provide good approximations of the interface response for this stress path. The biggest differences between the three versions correspond to the estimated interface response during transition loading from *A* to *Y1* and from *T1* to *Y2*. The interface response from *A* to *Y1*, estimated from Versions I and II, is stiffer than the measured interface response. Similar observations can be made for loading from *T1* to *Y2*. Version III, which was developed specifically for transition loading, provides more accurate values of interface stiffness for loading from *A* to *Y1* and from *T1* to *Y2*.

Finally, it is important to note that the extended hyperbolic model captured important features of the interface response. It recognized the influence of the inclination of the stress path on the interface stiffness during yield-inducing shear and the stiffer response of the interface for unloading-reloading.

4.5.4.3 Test 305_10. This test was performed on the medium-dense-Density-sand-against-concrete interface. The test was designed to provide information on the interface response at yield and during unloading-reloading along inclined stress paths. Figure 4-38 reproduces the stress path applied during this test and the corresponding shear stress-displacement data. The following types of loading can be recognized:

- a. Loading to point *B*: yield-inducing shear.
- b. Path *B-C-B-D-B*: unloading-reloading.
- c. Path *B-E*: yield-inducing shear.
- d. Path *E-F-E*: unloading-reloading.
- e. Path *E-G*: yield-inducing shear.
- f. Path *G-F*: unloading.

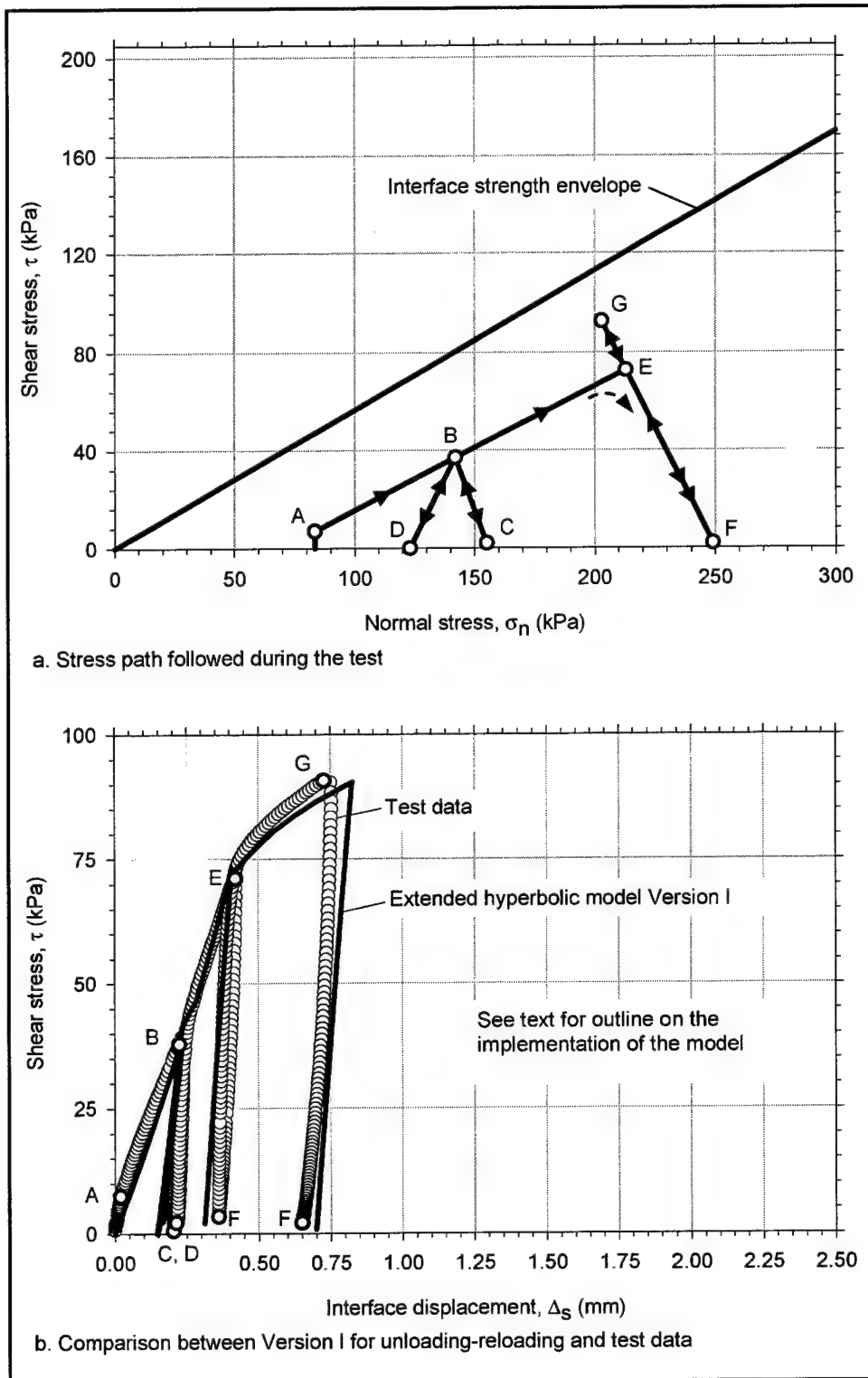


Figure 4-38. Comparison between the extended hyperbolic model and data from multidirectional stress path Test T305_10 on the medium-dense-Density-sand-to-concrete interface (Continued)

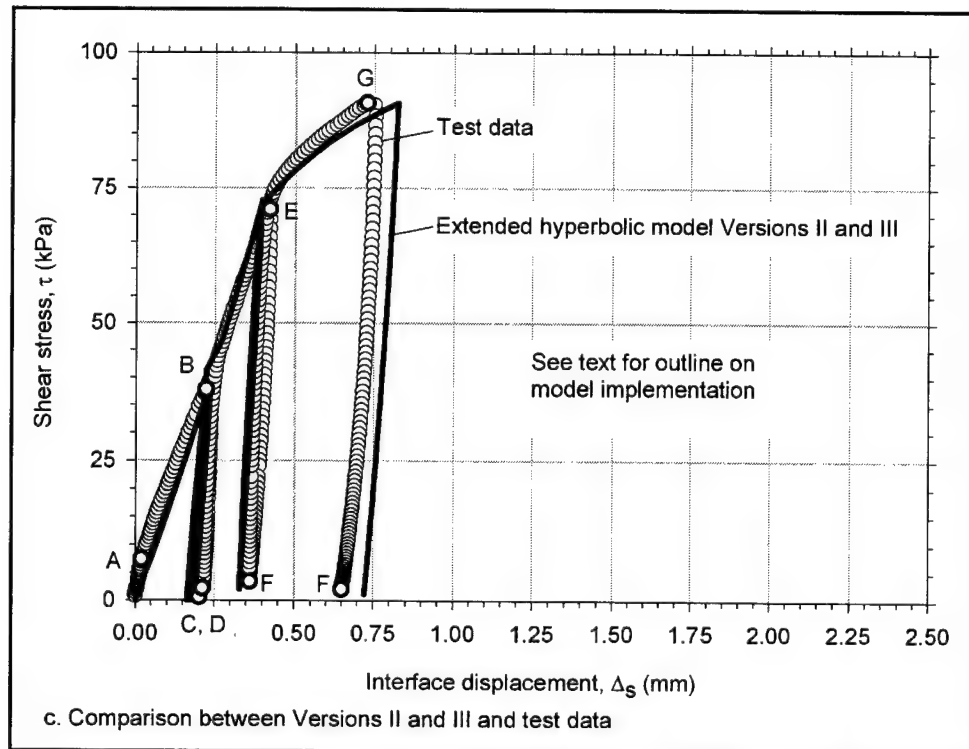


Figure 4-38. (Concluded)

The shear stress-displacement response was estimated using all versions of the extended hyperbolic model. The interface parameter values used are those listed in Tables 4-8 and 4-13. Comparisons between the measured interface response and the results obtained from Versions I, II, and III are presented in Figures 4-38b and 4-38c.

All three versions of the model provide excellent approximations of the interface response for the stress path applied in this test. The predictions given by Versions II and III are identical because transition loading was not applied to the interface.

In the extended hyperbolic model, it is assumed that the inclination of the stress path during unloading-reloading has little influence on the interface stiffness. From the analyses performed for this test, it can be concluded that the errors introduced by this assumption are small.

4.5.4.4 Test 405_10. This test was performed on the dense-Light-Castle-sand-against-concrete interface. The test was intended to provide additional information on the interface response along inclined stress paths during yield-inducing shear, unloading-reloading, and transition loading. It also served to verify the applicability of the model to an interface different from Density Sand against concrete. Figure 4-39 reproduces the stress path applied during this test and the corresponding shear stress-displacement data. The following types of loading can be recognized:

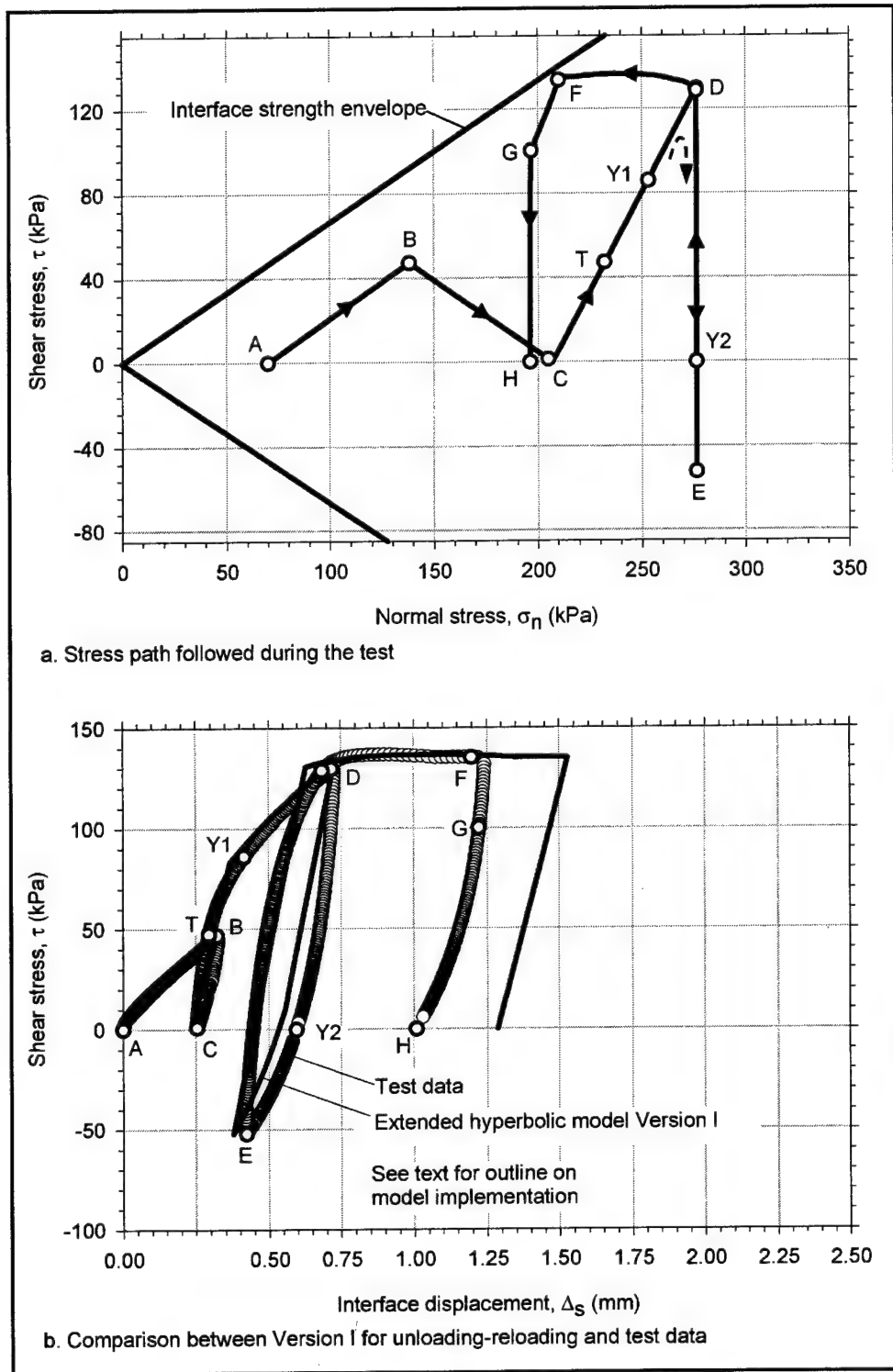


Figure 4-39. Comparison between the extended hyperbolic model and data from multidirectional stress path Test T405_10 on the dense-Light-Castle-sand-to-concrete interface (Continued)

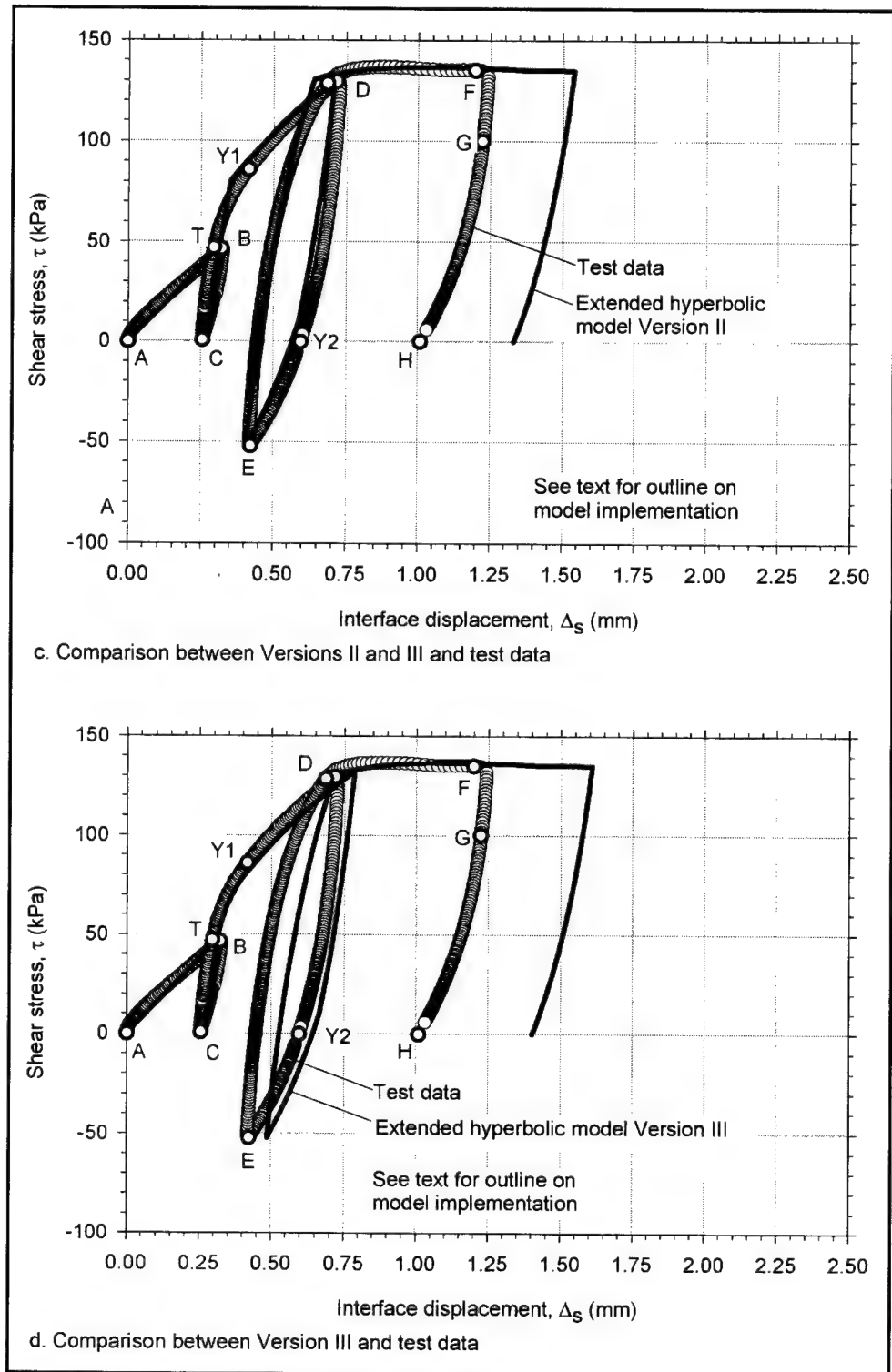


Figure 4-39. (Concluded)

- a. Path *A-B*: yield-inducing shear.
- b. Path *B-C-T*: unloading-reloading.
- c. Path *T-Y1*: transition loading.
- d. Path *Y1-D*: yield-inducing shear in first quadrant.
- e. Path *D-Y2*: unloading.
- f. Path *Y2-E*: yield-inducing shear in fourth quadrant.
- g. Path *E-Y2-D*: unloading-reloading.
- h. Path *D-F*: yield-inducing shear.
- i. Path *F-G-H*: unloading.

The shear stress-displacement response for this stress path was estimated using the three versions of the extended hyperbolic model. The interface parameter values used are those listed in Tables 4-8 and 4-13. The measured interface response and the predictions from Versions I, II, and III compared in Figures 4-39b, 4-39c, and 4-39d, respectively.

Versions I and II provide reasonable estimates of the interface displacement. They predict a stiffer than measured interface response along path *T-Y1*. The overall performance of Version II is very good, and provides an excellent approximation to the measured interface response.

The accuracy of the calculated interface displacements is similar in all three versions. However, Version III provides the most accurate approximation to the measured interface response in terms of stiffness values for transition loading between points *T* and *Y1*.

4.6 Implementation of the Extended Hyperbolic Model

This section outlines a procedure for implementation of the model in finite element analyses. Flowcharts illustrate the sequence of steps for calculation of the shear stiffness of an interface element for each incremental load step.

4.6.1 Incremental analyses

SSI analyses of lock walls often require modeling of the backfill-structure system during the construction and operation stages of the lock. In incremental analyses (Clough and Duncan 1969), boundary stress increments corresponding to each of the construction stages are transformed into sets of nodal forces. The problem consists of solving the system of equations represented by the following equation:

$$\{\Delta P\} = [K] \cdot \{\Delta u\} \quad (4-51)$$

where

$\{\Delta P\}$ = vector of nodal forces

$[K]$ = global stiffness matrix of the system

$\{\Delta u\}$ = vector of unknown incremental displacements

For each construction or operational stage, i.e., load step, the nodal displacements are determined by solving Equation 4-51. The global stiffness matrix is the assemblage of the individual element stiffness matrices, which must be updated for each load step of the analyses.

Figure 2-2 shows the expression for the stiffness matrix of the joint element developed by Goodman, Taylor, and Brekke (1968). This formulation is widely used to model backfill against lock wall interfaces. During an incremental analysis, the value of shear stiffness (K_s in the figure) of the interface element needs to be updated for each load step.

4.6.2 Identification of type of loading

In the extended hyperbolic model, calculation of the shear stiffness value requires the determination of the type of loading applied to the interface. Figure 4-40 shows a flow diagram that summarizes the steps required for this determination.

As illustrated in the figure, if the value of stress level SL^i for the current load step is equal to +1 or -1, then the interface is at failure. In this case, a low shear stiffness value is selected for the analyses. If the interface is not at failure, then the current value of stress level SL^i is compared to the state variables $SL+$ and $SL-$, which define the position of the yield surfaces in the previous load step. If the current state of stresses corresponds to yield-inducing shear, the formulation presented in Table 4-2 is applied. If the current state of stresses is inside the region delimited by the previous yield surfaces, the stiffness can be calculated using one of the three versions of the model.

If Version III is used, then it is necessary to compare the current shear stress value τ to $\tau+$ and $\tau-$, which define the position of the transition surface in the previous load increment to determine whether the current load increment induces transition loading or unloading-reloading.

4.6.3 Implementation of the formulation for yield-inducing shear

Figure 4-41 summarizes the determination of the interface stiffness at yield in an incremental finite element analysis. The interface stiffness value $K'_{st}{}^i$ for the

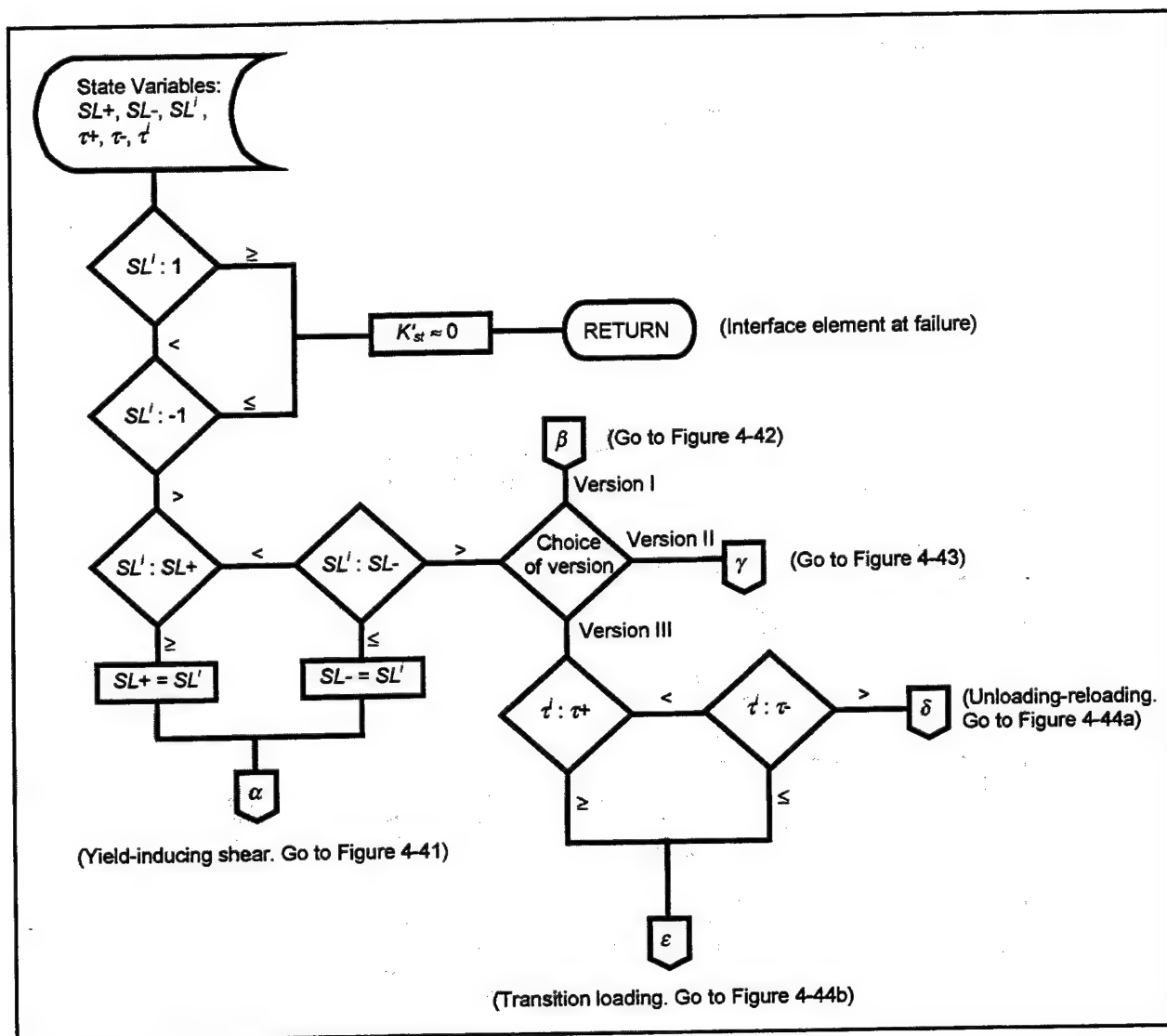


Figure 4-40. Procedure for the determination of the type of loading applied to an interface element during the i^{th} load step (Note: superscript i refers to the i^{th} load step)

current load step is determined by multiplying the value of interface stiffness for vertical stress paths K_{st}^i by the correction factor I^i for inclined stress paths.

It was indicated previously that the value of the correction factor may be equal to or lower than zero for certain inclinations of the stress path (Table 4-3). The flow diagram for the determination of the correction factor presented in Figure 4-41 identifies these cases. When the value of the correction factor is zero, such as for stress path $i4$ in Figure 4-16, a low value of shear stiffness is assigned to the interface to avoid potential numerical problems during the analyses. When the correction factor is negative or infinity, such as for stress paths $i5$ and $i6$ in Figure 4-16, a large value of interface stiffness is assumed to prevent numerical problems and minimize errors in the calculated interface displacements.

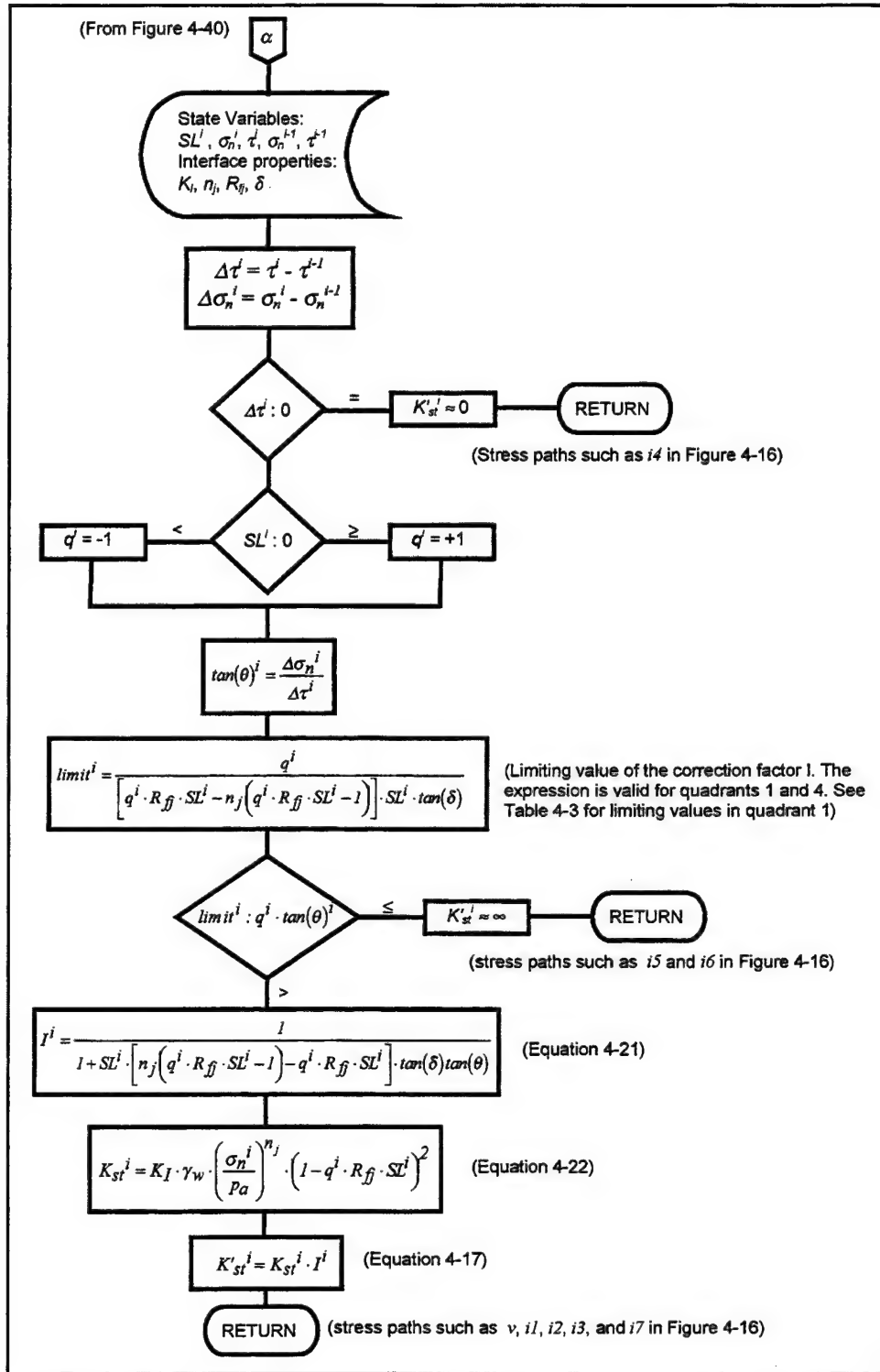


Figure 4-41. Flowchart for the determination of the tangent shear stiffness of an interface element at yield during the i^{th} load step (see Figures 4-8 and 4-10 for the definitions of loading regions)

4.6.4 Implementation of Version I

Figure 4-42 shows the flowchart for the determination of the interface stiffness in finite element analyses using Version I of the extended hyperbolic model. In the flowchart, the stiffness ratio C_k is calculated according to the recommendations presented in Table 4-11. Because C_k depends only on the value of R_{ff} , it can be calculated in any other part of the finite element code. The unload-reload stiffness number K_{urj} is obtained by multiplying the stiffness number K_I by the stiffness ratio. Alternatively, if K_{urj} is determined experimentally, it can be input as an interface property. Finally, the interface shear stiffness is calculated according to the procedure summarized in Table 4-4.

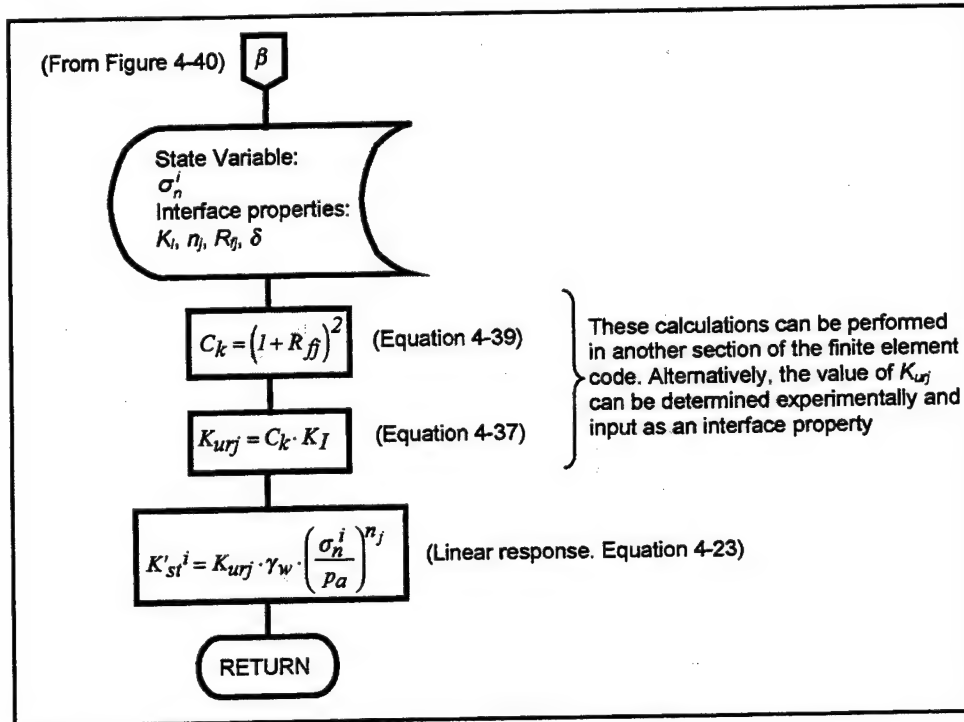


Figure 4-42. Flowchart for the determination of the tangent shear stiffness of an interface element during the i^{th} load step, using Version I of the extended hyperbolic model (see Figure 4-8 for the definition of the unloading-reloading region)

4.6.5 Implementation of Version II

As illustrated in Figure 4-43, the following state variables are necessary for implementation of this version of the model in a finite element code:

- SL^i = current value of stress level.
- SL^{i-1} and SL^{i-2} = stress level values from the two previous load steps.
- SL_0 = position of the origin.
- σ_n^i = current normal stress value.

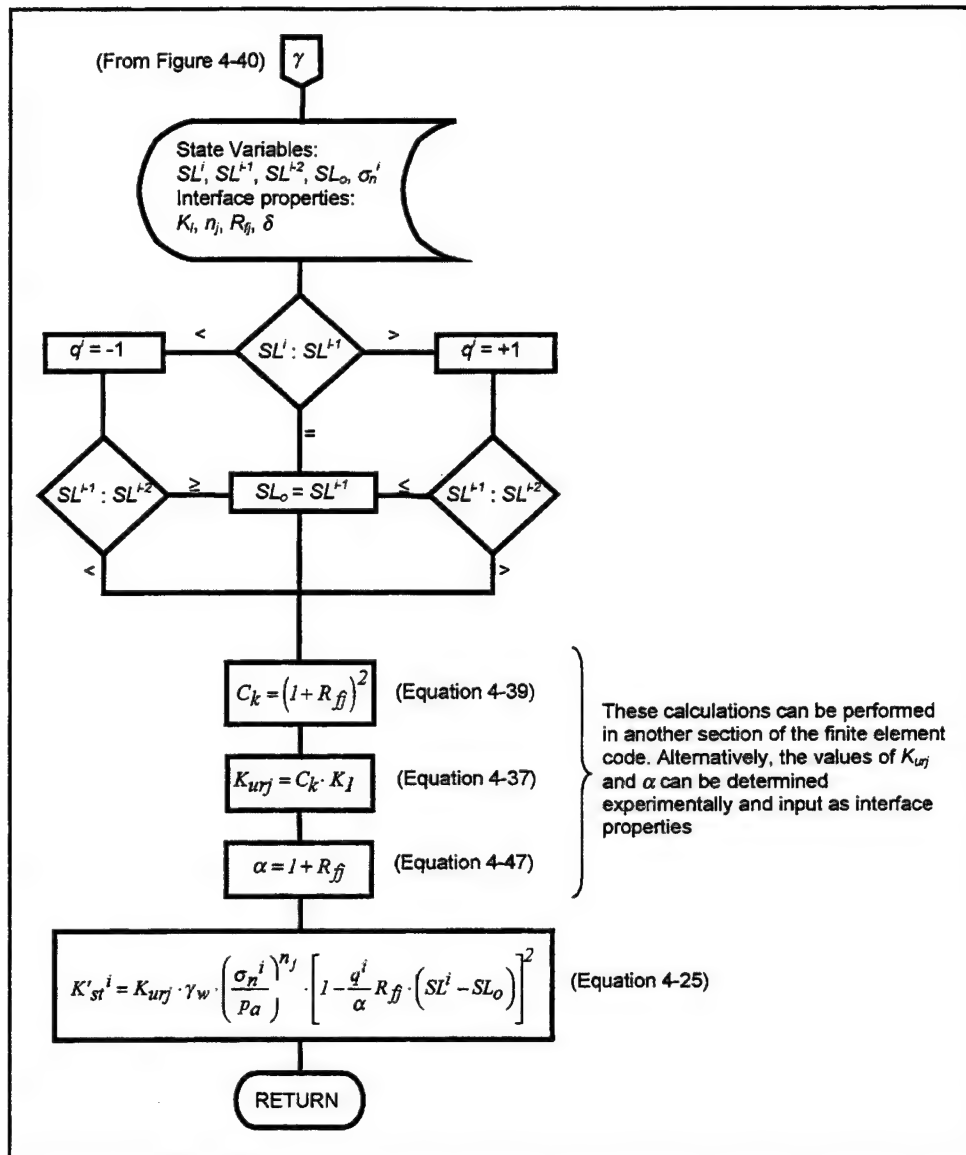


Figure 4-43. Flowchart for the determination of the tangent shear stiffness of an interface element during the i^{th} load step, using Version II of the extended hyperbolic model (see Figure 4-8 for the definition of the unloading-reloading region)

Initially, several comparisons between the values of SL^i , SL^{i-1} , and SL^{i-2} are carried out to define the value of the shear direction parameter q and the origin SL_o according to the criteria described previously in this chapter. The position SL_o of the origin is updated if there is a change in the direction of shear. Otherwise, the previous value of SL_o is maintained.

The values of the stiffness ratio C_k and the scaling factor α are determined according to the criteria presented in Tables 4-11 and 4-12. Because C_k and α depend only on the value of R_{fi} , they can be calculated in any other part of the finite element code. Alternatively, if K_{urj} and α are determined experimentally,

they can be input as interface properties. The interface shear stiffness is determined according to the formulation presented in Table 4-5.

4.6.6 Implementation of Version III

Version III differentiates between unloading-reloading and transition loading. Figure 4-44a illustrates the procedure for calculation of the interface stiffness inside the unload-reload region. The flowchart is identical to that presented in Figure 4-43 for Version II.

Figure 4-44b shows the flowchart for the case of transition loading, in which the following state variables are required:

SL^i = current value of stress level

SL^{i-1} = stress level value in the previous load step

σ_n^i = current normal stress value

σ_n^{i-1} = normal stress value in the previous load step

τ^i = current shear stress

τ^{i-1} = shear stress value in the previous load step

$\tau+$ and $\tau-$ = positions of the transition surfaces in the first and fourth quadrants, respectively

K_{st}^{i-1} = interface shear stiffness in the previous load step

First the absolute values of SL^i and SL^{i-1} are compared. If the absolute value of SL^{i-1} is greater than or equal to the absolute value of SL^i the stiffness number is assumed equal to K_{urj} .

If the absolute value of SL^{i-1} is lower than the absolute value of SL^i , a series of comparisons are performed to determine if the interface element was subjected to unloading-reloading or transition loading in the previous load increment. If the previous load increment induced unloading-reloading, then the stress path is crossing the transition surface. In this case, the values of SL^{ts} , K_{sn}^{ts} , and m , defined previously in this chapter, are determined and stored. If the previous load step induced transition loading, then the interface stiffness is calculated using the previous values of SL^{ts} , K_{sn}^{ts} , and m .

4.6.7 Implementation of the extended hyperbolic model in SOILSTRUCT-ALPHA

The finite element program SOILSTRUCT-ALPHA as described in Ebeling and Wahl (1997) and Ebeling, Pace, and Morrison (1997) is frequently used for SSI analyses of U.S. Army Corps of Engineers structures. The program is capable

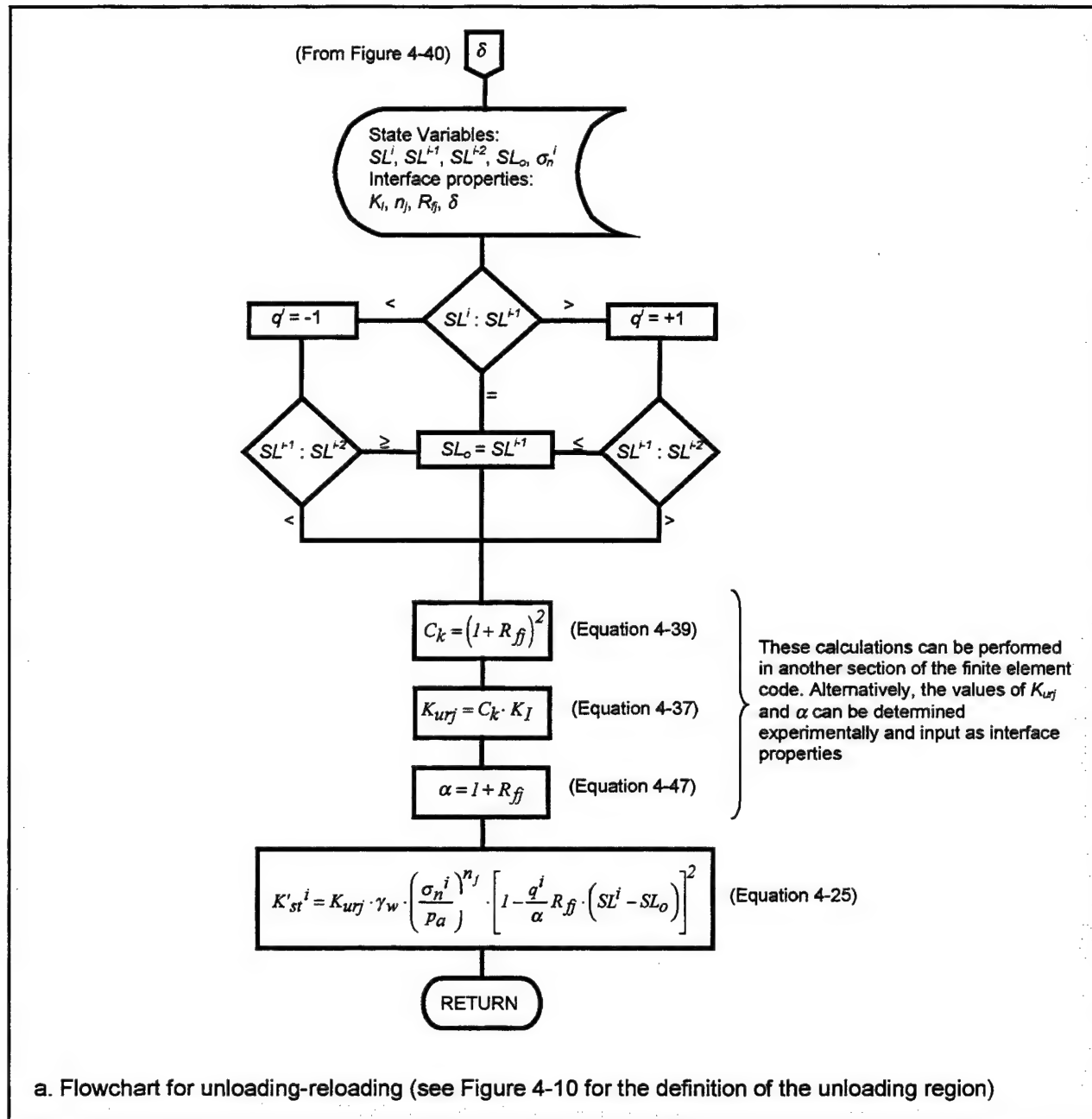


Figure 4-44. Flowchart for the determination of the tangent shear stiffness of an interface element during the i^{th} load step, using Version III of the extended hyperbolic model (see Figure 4-10 for the definition of the unloading-reloading region)

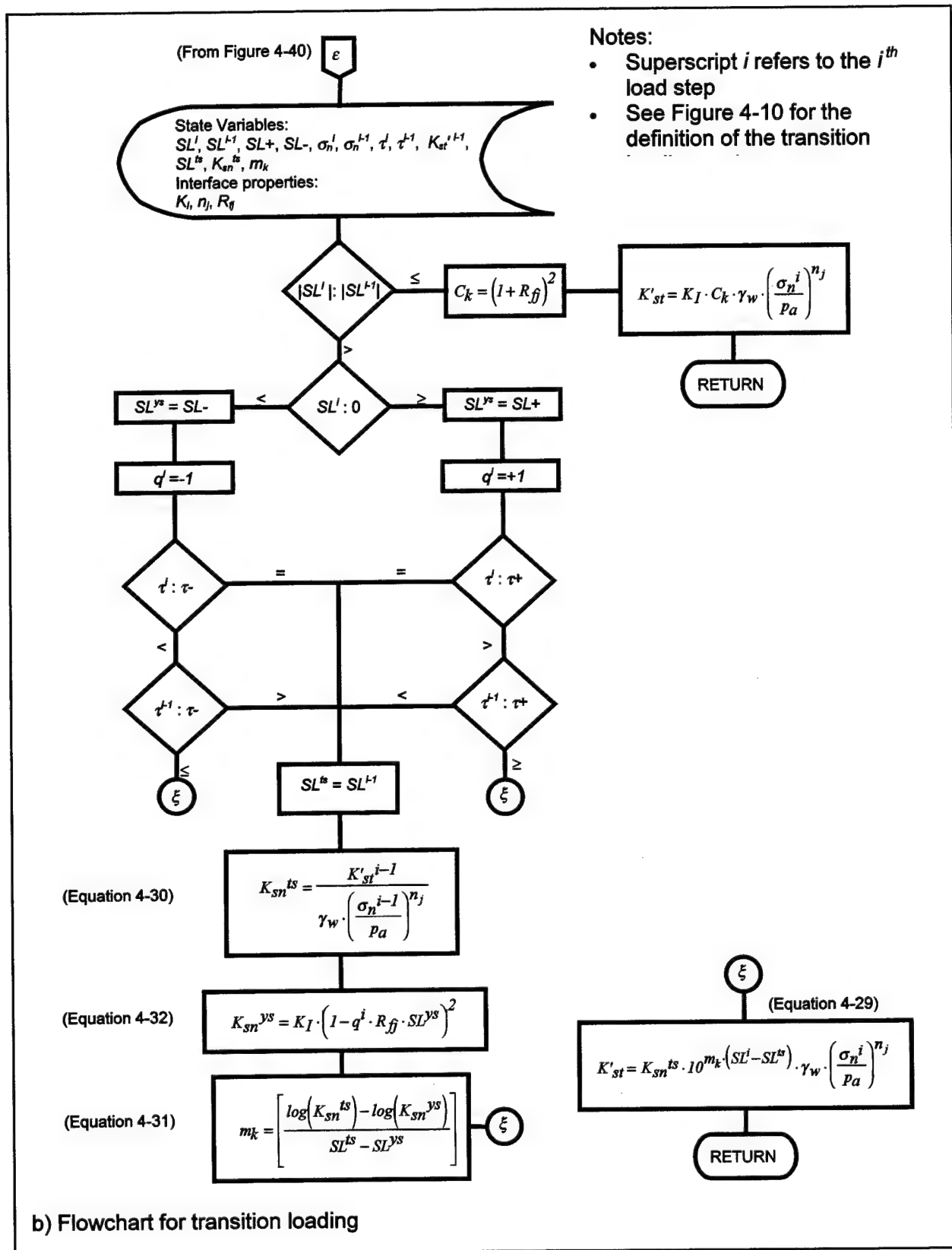


Figure 4-44. (Concluded)

of modeling the different stages of construction and operation of a lock wall. The backfill-to-structure and structure-to-foundation interfaces are modeled using the joint element developed by Goodman, Taylor, and Brekke (1968). Base separation is also modeled in SOILSTRUCT-ALPHA.

The formulation for yield-inducing shear and Version II of the unload-reload formulation were implemented in the program. The updated version of SOILSTRUCT-ALPHA contains the following subroutines:

- a. Subroutine JSTRESS. This subroutine is invoked for all the interface elements in the mesh. It identifies the elements at failure and the elements where base separation occurs. Previously, it contained the operations necessary for determination of the interface shear stiffness according to Clough and Duncan (1971) formulation. The procedure for the identification of the types of loading, illustrated in Figure 4-40, was implemented in this subroutine.
- b. Subroutine JVIRGIN. This subroutine was developed and included in SOILSTRUCT-ALPHA during this investigation. It contains the procedure for the determination of the interface stiffness at yield presented in Figure 4-41.
- c. Subroutine JUNREL. This subroutine was also developed during this investigation. It handles the cases where the interface element is subjected to unloading-reloading. The interface shear stiffness is calculated using Version II of the model, according to the procedure presented in Figure 4-43.

To verify correct implementation of the model in SOILSTRUCT-ALPHA, a single interface element was analyzed. The element was subjected to some of the stress paths applied during the interface tests. The interface response predicted by the program was identical to the results obtained by hand calculations.

4.7 Summary and Conclusions

The extended hyperbolic model for interfaces was developed during this investigation. The model captures important aspects of interface response under the type of loading expected to occur in a wall-backfill interface. The material parameters required for implementation of the model are the same as those introduced by Clough and Duncan (1971).

A procedure for normalization of interface test data was developed that facilitated the study of the interface response under a variety of experimental stress paths. Based on this study, the concepts of yield surfaces and loading regions were introduced. Two yield surfaces are defined by the past maximum and past minimum stress levels during shear. Two transition surfaces are defined by the past maximum and past minimum shear stresses on the interface. Three types of loading are considered in the extended hyperbolic model: yield-inducing shear, unloading-reloading, and transition loading.

A formulation for yield-inducing shear was developed in which the interface stiffness is determined by the normal stress, the stress level, and the rate of change of the normal stresses during shear, i.e., the inclination of the stress path. The formulation was found to predict the interface response accurately under a variety of experimental, yield-inducing stress paths.

For unloading-reloading or transition loading, one of three versions of the model can be applied, depending on the accuracy required for the analysis. In Version I, a linear, normal stress-dependent response of the interface is assumed both for unloading-reloading and for transition loading. This version does not model the hysteretic response of the interface under unloading-reloading. Comparisons of the calculated interface response with test data showed that this version may provide reasonable predictions of the interface response, provided that unloading is not too large. It is inaccurate for modeling the response of interfaces subjected to large unload-reload loops or stress paths predominantly contained inside the transition loading region. Version I is the simplest to implement and use in SSI analyses.

In Version II, a nonlinear, hyperbolic response is assumed for unloading-reloading and transition loading that accurately models the hysteretic behavior of interfaces subjected to large unload-reload loops. It provides accurate or reasonable estimates of interface response for most of the experimental stress paths considered in this investigation. However, it does not provide accurate estimates for cases in which the interface is subjected to predominantly transition loading. Although the formulation of Version II introduces some additional state variables, it is simple to implement in SSI analyses of retaining walls.

In Version III, the interface stiffness for unloading-reloading is determined in the same way as in Version II. For transition loading, on the other hand, the interface stiffness is determined by interpolation from the normalized stiffness diagram. Two normalized stiffness values are used for the interpolation: the normalized stiffness of the interface at the onset of transition loading and the normalized stiffness at yield. This version provides the most accurate estimates of interface response for all the experimental stress paths considered. It is particularly useful for cases where the interface is subjected to predominantly staged shear. Version III is the most difficult to implement in SSI analyses because it introduces several additional state variables with respect to the other two versions.

The principal advantages of the extended hyperbolic model are as follows:

- a.* It has a simple mathematical formulation.
- b.* Hyperbolic parameter values for different types of interfaces are available in the literature.
- c.* It captures the main features of the interface response under simultaneous changes in shear and normal stress and unloading-reloading.
- d.* It provides accurate estimates of the interface response for the experimental stress paths considered in this investigation.

- e. It is relatively easy to implement in SSI analyses.
- f. It establishes a framework for future work on plasticity-based interface models.

The formulations for yield-inducing shear and for unloading-reloading Version II of the extended hyperbolic model were implemented in the finite element program SOILSTRUCT-ALPHA, which is commonly used by the Corps of Engineers for analyses of lock walls. As discussed in Chapter 5, finite element analyses of the IRW lock wall simulation suggest that these formulations are effective for prediction of vertical shear forces in retaining structures.

The model has several limitations:

- a. It does not model displacements normal to the interface, and the interface thickness is implicitly assumed as zero. Consequently, in finite element analyses, a large normal stiffness must be assigned to interface elements to prevent overlapping of adjacent two-dimensional elements. In addition, it cannot model the generation of normal stresses due to restrained dilation of the interface during shear between two stiff, rough media. This may not be important for analyses of stiff retaining structures that have relatively compressible backfills.
- b. It does not model displacement softening of the interface. According to the experimental data collected during this investigation, displacement softening may take place in interfaces subjected to relative displacements of 6 to 20 mm. Therefore, in cases where larger magnitudes of interface displacement take place, the model cannot provide accurate predictions of the interface response.
- c. The model predicts interface stiffness values that are zero or negative for certain loading combinations. For implementation of the model in finite element programs, it is then necessary to use appropriate stiffness values and numerical procedures (see Stankowsky, Runesson, and Sture 1993, for example) in order to prevent numerical problems. It is believed that the model predictions for these cases are correct. However, if finite element analyses of lock walls show that these types of loading are common, it may be necessary to perform additional experimental work to verify the model predictions.
- d. As discussed in Chapter 5, the model was used successfully for the estimation of vertical shear forces in the IRW lock wall simulation. However, it has not yet been used for routine analyses of actual lock walls.

5 Lock Wall Simulation

In Chapter 4, it was shown that the extended hyperbolic model accurately predicts the interface response for a variety of experimental stress paths applied in the laboratory. It is desirable, however, to evaluate the accuracy and applicability of this new model for SSI analyses of lock walls. There are little data on lock wall response during construction and operation of locks that can be used to perform such an evaluation. The IRW at Virginia Tech provides a unique opportunity to model key aspects of lock wall construction and operation within a controlled experimental environment.

The IRW was originally developed to study the earth pressures induced by compaction of backfill. Factors such as type of backfill, compaction procedure, and lateral movements of the wall were analyzed by Sehn (1990) and Filz (1992) using the IRW. As result of their work, methods were developed for estimation of compaction-induced earth pressures against retaining walls (Duncan et al. 1991; Filz and Duncan 1997; Filz, Duncan, and Ebeling 1997).

For this investigation, a test was performed in the IRW that modeled placement and compaction of the backfill, application and removal of surcharge, and movements of the water table behind a lock wall. Light Castle sand was used as backfill material for the test. Finite element analyses of all the stages of the test were performed using the updated version of SOILSTRUCT-ALPHA, which contains the formulation of the extended hyperbolic model for interfaces. Analyses of the backfill and surcharge stages served to calibrate the backfill properties for use in analyses of the inundation stage. The test results indicate that the extended hyperbolic model provides accurate approximations of the response of the wall-backfill interface for the type of loading induced during the test.

This chapter describes the experimental procedures, results of the IRW test, and analyses of the IRW test. The chapter is divided into the following sections:

- a.* The IRW facility.
- b.* Testing procedures.
- c.* Test results.
- d.* Discussion of test results.

- e. Finite element analysis procedures.
- f. Calibration analyses.
- g. Analysis of backfill inundation.
- h. Summary and conclusions.

The first section describes the characteristics of the IRW and the modifications that were necessary to accommodate simulation of a lock wall. In subsequent sections, the testing procedures and results are described in detail. Some observations are presented regarding the backfill response to external loading and compaction that are relevant for the finite element analyses of the IRW. Details of the analyses performed using SOILSTRUCT-ALPHA are also presented. Finally, the accuracy of the extended hyperbolic model is evaluated based on comparisons of the results of the analyses and the test data.

5.1 The IRW Facility

A complete description of the components of the IRW was presented by Sehn (1990). This section summarizes the features of the IRW that are relevant for this investigation.

5.1.1 Components of the IRW

Figure 5-1 is a general view of the IRW. It is composed of a backfill area, the instrumented wall, and a reinforced concrete U-frame structure that supports the wall and encloses the backfill area. The IRW is located inside a building, isolated from the direct action of the elements. An overhead crane facilitates movement of heavy equipment and materials. The floor of the backfill area is approximately 0.90 m below the floor level of the surrounding areas in the building. The top of the instrumented wall is approximately 1.20 m above the floor level of the building. The backfill area is 1.83 m wide by 3.05 m long. A 1.83-m-wide ramp leading into the area provides access for the equipment necessary for placement and compaction of the backfill.

A cross section of the IRW is shown in Figure 5-2. The instrumented wall is composed of four 0.73-m-wide by 2.13-m-high concrete panels. Each of the panels is supported vertically by two cantilever-type load cells (Sehn 1990), which consist of a 0.1-m-long cantilever beam bolted to a support bracket at the bottom of the panel. On the free end of the beam, a roller bearing wheel allows movement on a hardened steel pad attached to the concrete floor. Each of the panels is supported horizontally by three horizontal load cells. Each of the load cells consists of a steel bar, supported on both ends by spherical bearings to minimize bending moments. The forces on the vertical and horizontal load cells are measured by strain gauges bonded to their surface at appropriate locations.

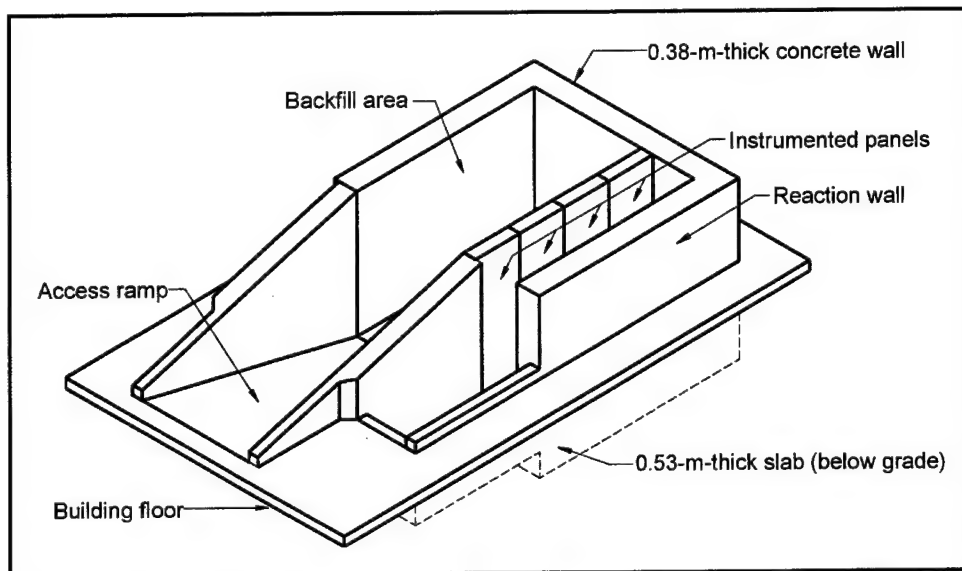


Figure 5-1. The IRW test facility (after Sehn 1990)

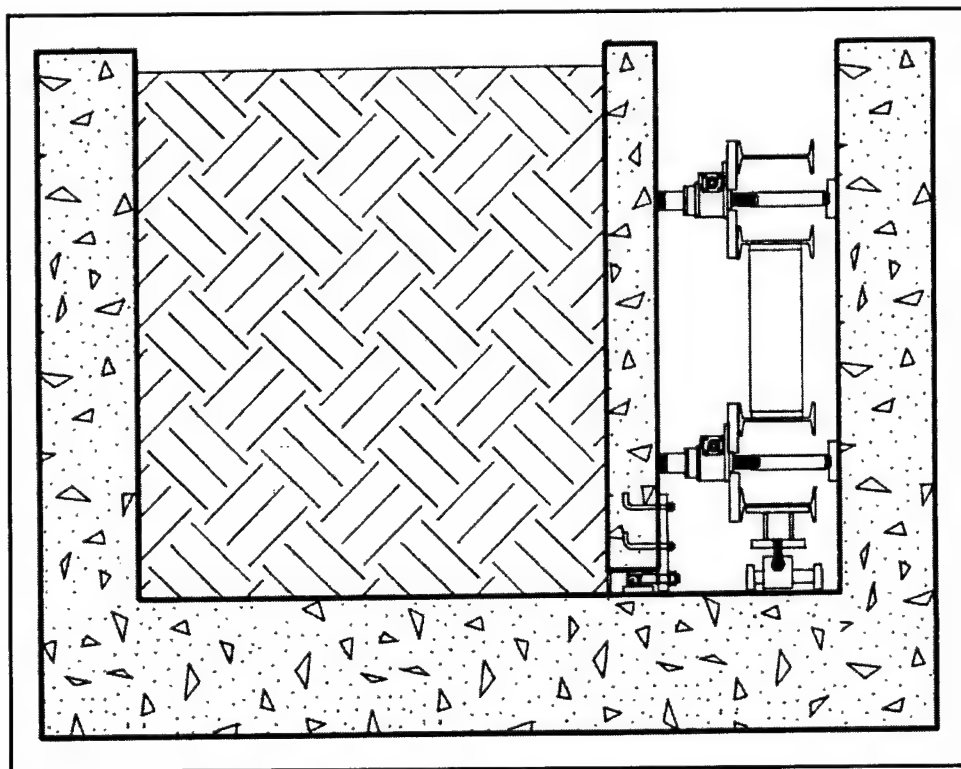


Figure 5-2. Cross-section of the IRW (after Sehn 1990)

The horizontal loads from the panels are transmitted by the load cells to a steel frame behind the panels. The frame is supported vertically by bearings that allow horizontal movements. Four screw jacks allow the application of horizontal displacements to the instrumented wall. This feature of the IRW was not used in

the lock wall simulation. The concrete panels were kept in place throughout the test.

The displacements of each of the panels during testing are monitored by two LVDTs, located at the top and bottom of the panel. The LVDTs are attached to a fixed reference beam located behind the panels.

As illustrated in Figure 5-3, the two central panels of the instrumented wall contain a variety of pressure cells for local measurements of earth pressures. Sehn (1990) presents a detailed description of the type of pressure cells embedded in the panels. For this investigation, pressures were measured using only the Gloetzl cells. The Gloetzl cells are mounted flush with the exposed wall surface. The surface of each of the cells is coated with a cement grout that resembles the surface texture of the wall. It was found that the Gloetzl cells did not provide accurate data, especially during inundation of the backfill. Filz (1992) recognized that these pressure cells may be especially sensitive to moisture migration in the surrounding mass of concrete. Nevertheless, pressure data collected during backfilling operations of the IRW provided qualitatively useful information on compaction-induced earth pressures.

A series of thermocouples are installed on both sides of the instrumented wall. The thermocouples provide data necessary for corrections of pressure and deformation readings, which may be needed when large temperature fluctuations take place during the test.

5.1.2 Preparations for the test

Simulation of a lock wall in the IRW required compaction of the backfill, application of a surcharge on the backfill surface, and inundation of the backfill. The IRW was not originally designed for surcharge application and inundation of the backfill. This section contains a description of the work performed to accommodate this type of testing in the IRW.

5.1.2.1 Construction of Bulkhead. To allow full inundation of the backfill, a bulkhead was built at the bottom of the access ramp. The bulkhead consisted of a rigid, wooden frame capable of withstanding the earth pressures generated during compaction, surcharge, and inundation. A 19-mm- (3/4-in.-) thick plywood facing was attached to the bulkhead on its backfill side. The bulkhead was pre-assembled outside the IRW and laid in place using the overhead crane. Tight tolerances were required to minimize the width of the gaps between the bulkhead and the existing concrete walls. The bulkhead was tightly attached to the walls and floor of the ramp with fifteen 12.5-mm- (1/2-in.-) steel bolts.

5.1.2.2 Water seal. To prevent significant leaks during inundation of the backfill, a sealant was applied to all the gaps existing between the instrumented panels, between the panels and the floor, and along the edges of the bulkhead. All the gaps had a maximum width of approximately 12.5 mm (0.5 in.). Caulking strips were introduced in all gaps to serve as support for the sealant. A

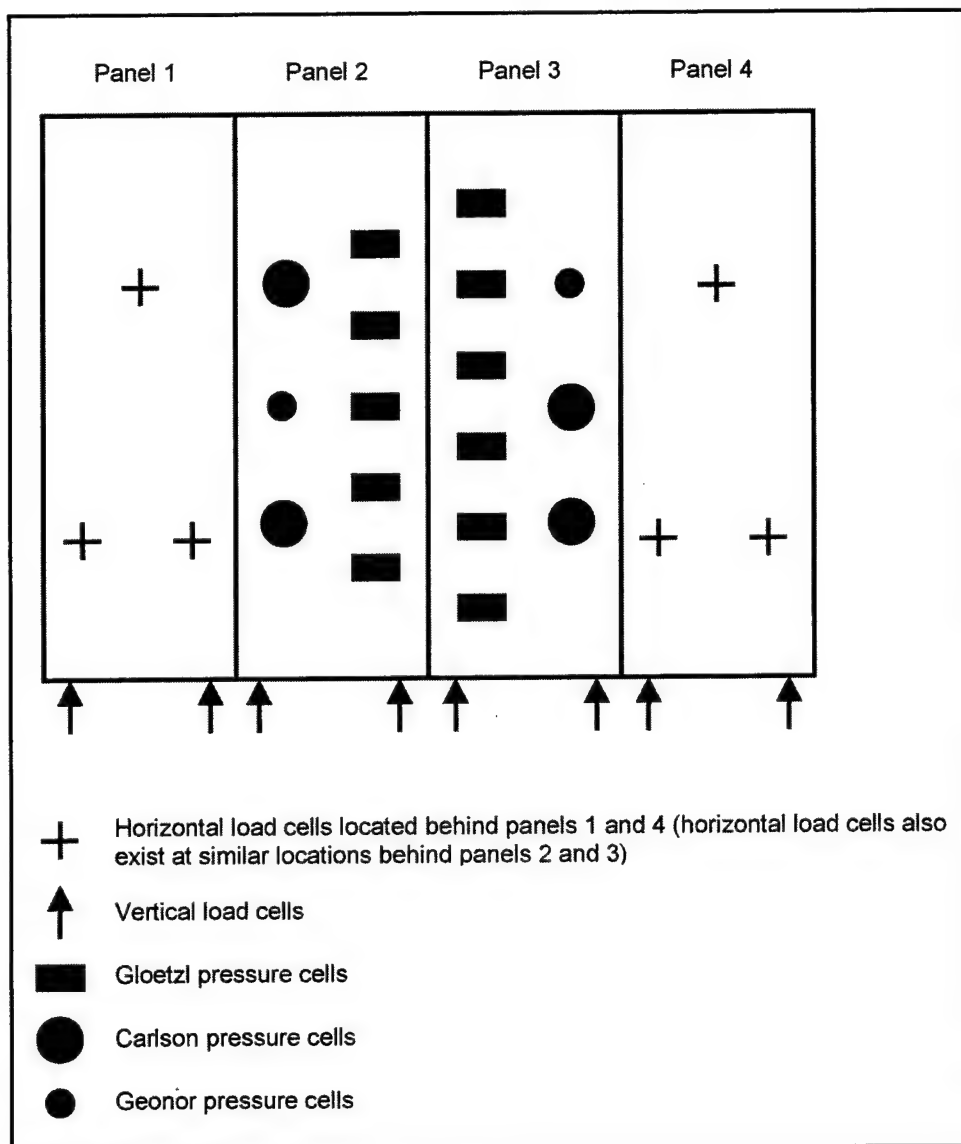


Figure 5-3. IRW panels (after Sehn 1990)

polyurethane-based, elastomeric sealant (Sikaflex-1a) was applied over the support strips with a thickness of approximately 12.5 mm (0.5 in.), and left to cure for 1 week. Once cured, the sealant has a relatively high strength and an elastic modulus ranging from 0.275 to 0.551 MPa. Application of the sealant to the bottom gap of the panels may have some influence on the force measurements of the load cells. However, this influence is minimal because the elastic modulus of the sealant is comparatively small, as confirmed by measurements performed before and after application of the sealant.

5.1.2.3 Inundation/drainage system. A simple system was devised to allow controlled inundation and drainage of the backfill. Two polyvinyl chloride (PVC) pipes were placed in the corners of the backfill area farthest from the instrumented panels. The pipes had an internal diameter of 150 mm (6 in.) and were

approximately 2.5 m (8 ft) long. The pipes were perforated and entirely covered with a geotextile fabric. In this way, inundation and drainage were possible without causing migration of fines from the soil.

One of the pipes, referred to herein as the well pipe, was selected for introduction and removal of the water during inundation and drainage. The other pipe, referred to herein as the piezometer, was used to monitor the water level inside the backfill. For drainage of the backfill, a submersible electrical pump was introduced into the well pipe.

5.1.2.4 Data acquisition. A data acquisition system was installed in the IRW, consisting of a Keithley 500A system connected to a personal computer (PC) equipped with a 486 processor. The Keithley 500A system allows use of up to ten 16-bit data acquisition cards designed for specific types of instrumentation. Table 5-1 lists some details regarding the data acquisition setup for the lock wall simulation.

Table 5-1 Features of the Data Acquisition System for the Lock Wall Simulation				
Instruments	Card type	Voltage Range	Accuracy	Sampling Frequency Hz
Horizontal load cells	AIMM3a	± 0.01 V	± 0.22 kN	5
Vertical load cells	AIMM3a	± 0.05 V	± 0.07 kN	5
Gloetzi pressure cells	AIMM3a	± 0.05 V	Not determined	5
LVDTs	AMM2	± 0.5 V	± 0.01 mm	5
Thermocouples	AMM7	± 0.25 °C	± 0.01 V	0.2

The data acquisition software provided with the Keithley 500 allows sampling of the instrumentation according to a predetermined sequence and sampling frequency. The digital output from the cards is converted into physical quantities according to calibration factors determined before the test. The software also allows graphic representation of the data.

The instruments were calibrated *in situ* before the test. The vertical and horizontal load cells were calibrated by the incremental application of forces of known magnitude at the load cell locations. Calibration of the load cells was verified after application of the sealant around the edges of the panels. It was found that the load absorbed by the sealant was negligible compared to the total loads applied to the panels. The Gloetzi pressure cells and LVDTs were calibrated following the procedures described by Sehn (1990). Several loading cycles were applied to the load cells and pressure cells to verify the repeatability of the measurements. No calibration was required for the thermocouples.

5.2 Testing Procedures

As illustrated in Figure 5-4, the test was performed in three stages:

- a. Stage 1, backfilling.
- b. Stage 2, surcharge.
- c. Stage 3, inundation.

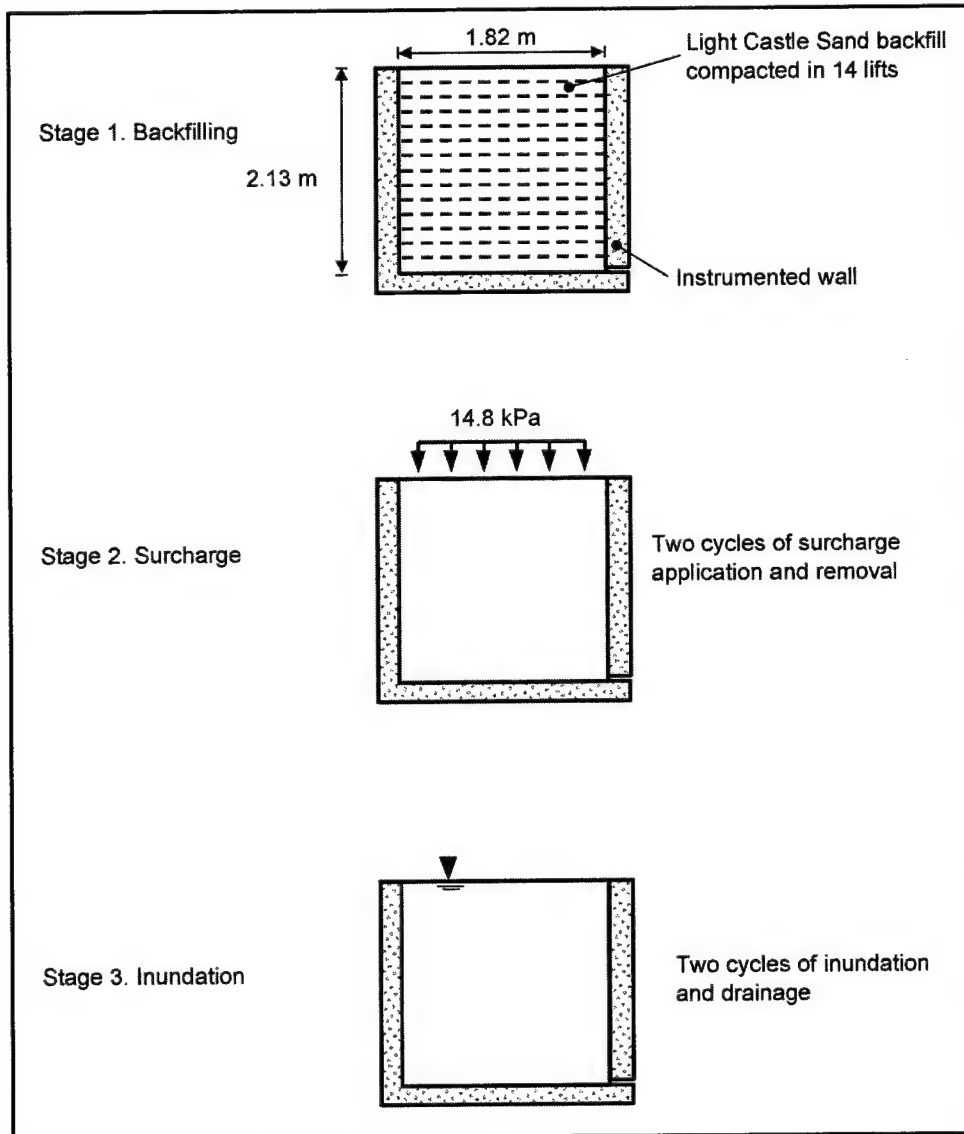


Figure 5-4. Stages of the lock wall simulation performed in the IRW test facility

The following sections describe each of the stages of the test.

5.2.1 Stage 1, Backfilling

Before the start of the backfilling operation, a nonfrictional lining was applied to the fixed walls and the bulkhead to minimize boundary effects. The lining consisted of an automotive grease coating and plastic film. Care was taken to avoid contaminating the surface of the instrumented panels or the floor of the backfill area during this process.

The backfill material was Light Castle sand. The properties of Light Castle sand are presented in Chapter 3, and Appendices A and B. The sand was air-dried to a water content below 0.2 percent, and stored inside the building until the start of the backfilling operation. The backfill was placed and compacted in 14 lifts, each with a compacted thickness of approximately 150 mm as illustrated in Figure 5-4. The sand was poured into the IRW using a hopper with bottom discharge as shown in Figure 5-5a. The weight of each batch of soil was carefully measured and recorded before pouring.

Each lift was compacted with two passes of a vibrating plate compactor as shown in Figure 5-5b. The compactor was a hand-operated Wacker model BPU2440A. After compaction of each lift, the total backfill thickness was determined by measuring the distance from the top of the backfill to a reference beam at twelve points distributed on the backfill surface. The thickness of the backfill was calculated based on the average of these readings. Measurements of horizontal and vertical forces, normal stresses, deformations, and temperatures were made after placement and after compaction of each lift.

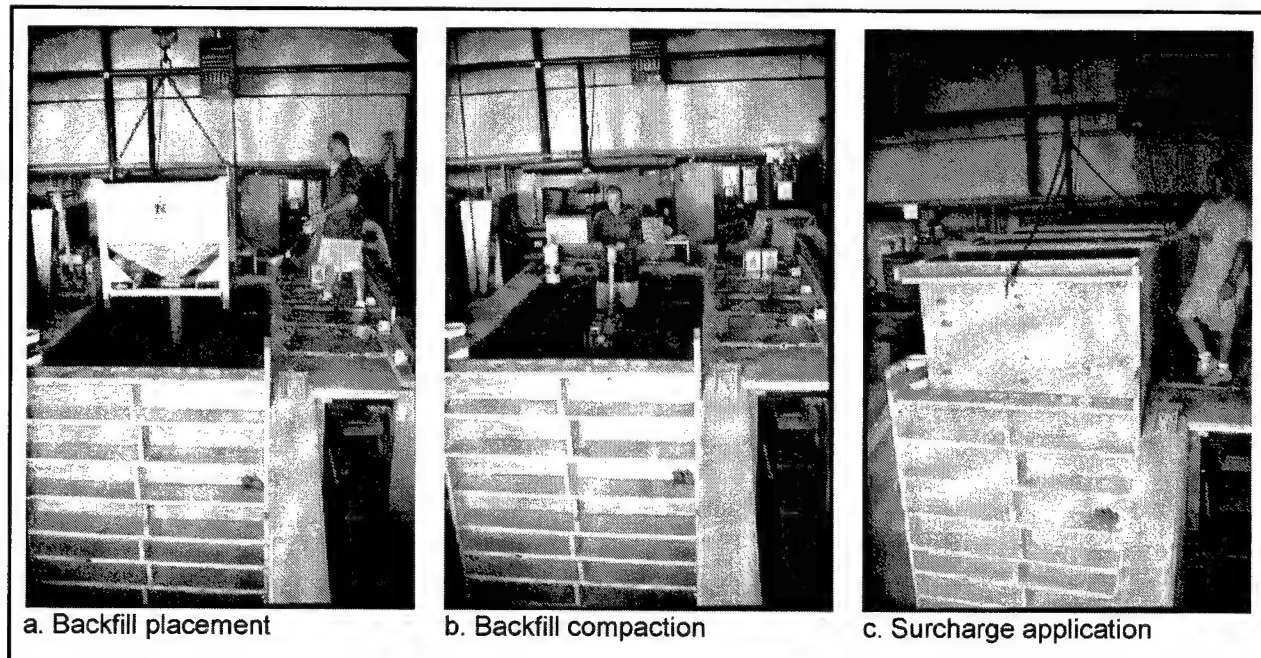


Figure 5-5. View of the IRW at different stages of the lock wall simulation

The average density of the backfill at the end of compaction was 16.8 kN/m^3 (107 lb/ft^3), which corresponds approximately to the maximum density determined in the laboratory (Table 3-1). Previous investigators reported slightly lower density values for the Light Castle sand backfill in the IRW following identical compaction procedures (Filz 1992). It is possible that the confinement provided by the wooden bulkhead helped to increase the compacted density of the backfill above the previous value. As discussed in a subsequent section, a beneficial consequence of the large backfill density was the minimization of hydrocompression effects during inundation.

5.2.2 Stage 2, Surcharge

After completion of the backfilling operation, a surcharge was placed on the surface of the backfill. The surcharge consisted of a 1.07-m (3.5-ft) wooden container filled with Light Castle sand in a loose condition. Figure 5-5c is a view of the IRW during application of the surcharge. The total weight of the sand plus the container induced a vertical pressure on the backfill surface of 14.8 kPa (310 lb/ft^2).

Two cycles of placement and removal of the surcharge were applied. After the box was carefully placed on the surface of the backfill, it was filled with sand. A uniform, horizontal surface was kept during filling to maintain a uniform surcharge on the backfill. After completion of the surcharge application, the sand was slowly removed from the box through a side opening. An identical procedure was followed for the second cycle. A precise record of the weight of sand inside the box was kept during this stage of the test. Instrumentation readings were made before, during, and after each loading cycle.

5.2.3 Stage 3, Inundation

Inundation of the backfill followed removal of the surcharge. After full inundation of the backfill, a submersible pump was introduced in the well pipe for drainage of the backfill. Two cycles of inundation and drainage were performed.

Instrumentation readings were made at several intermediate stages during inundation and drainage. Prior to each reading, the flow of water was arrested, and the water level in the pipes was monitored until equilibrium was reached. This prevented errors in the measurement of the water level inside the backfill.

Careful monitoring of flow rates during the test made possible estimation of the rate of leakage through the instrumented wall. It was found that the rate of leakage was negligible for practical purposes.

5.3 Test Results

The results of the test are summarized in Tables 5-2 to 5-5. All the data reported in the tables correspond to measurements in the two central panels (panels 2 and 3) of the instrumented wall. It is assumed that panels 2 and 3 are relatively free from any significant boundary effects induced by the presence of the endwall and the bulkhead in the IRW. Consequently, data from these panels may most closely represent a plane strain condition that can be modeled with SOILSTRUCT-ALPHA. This section discusses the results obtained from each of the three stages of the test.

Table 5-2
Summary of the Force Measurements during Stage 1 of the IRW Test (Backfilling)¹

Height of Backfill, H, m	Total Horizontal Load per Panel ² kN		Total Vertical Force per Panel ² kN		Effective Overburden kN/m	F' _x kN/m	F _v kN/m	K _h	K _v
	Panel 2	Panel 3	Panel 2	Panel 3					
0.00	0.000	0.000	0.000	0.000	0.000	0.000	0.000	-	-
0.15	0.096	0.126	0.027	-0.001	0.195	0.146	0.017	0.747	0.086
0.30	0.527	0.643	0.143	0.115	0.781	0.767	0.169	0.982	0.217
0.46	0.671	1.057	0.037	0.008	1.757	1.134	0.030	0.645	0.017
0.61	1.166	1.640	-0.083	-0.057	3.124	1.841	-0.091	0.589	-0.029
0.76	1.827	2.514	0.240	0.143	4.881	2.848	0.251	0.583	0.051
0.91	2.362	3.190	0.271	0.146	7.029	3.643	0.274	0.518	0.039
1.07	3.151	3.852	0.355	0.265	9.567	4.596	0.407	0.480	0.043
1.22	4.139	4.736	0.584	0.505	12.495	5.824	0.715	0.466	0.057
1.37	5.115	5.646	0.847	0.769	15.814	7.061	1.060	0.446	0.067
1.52	6.245	6.923	1.315	1.191	19.524	8.640	1.644	0.443	0.084
1.52	6.459	6.984	1.419	1.313	19.524	8.821	1.793	0.452	0.092
1.68	7.988	8.447	1.838	1.681	23.624	10.785	2.309	0.457	0.098
1.83	9.031	9.598	2.227	2.067	28.114	12.224	2.818	0.435	0.100
1.98	10.420	10.499	2.734	2.486	32.995	13.726	3.425	0.416	0.104
2.13	11.478	11.562	3.191	2.936	38.266	15.118	4.020	0.395	0.105
2.13	11.222	11.394	3.183	2.904	38.266	14.840	3.994	0.388	0.104

¹ See Notation (Appendix F) for definition of symbols.

² Measurements made after placement and before compaction of each lift are omitted.

5.3.1 Results from stage 1

5.3.1.1 Force measurements. Table 5-2 summarizes the vertical and horizontal force data measured in the two central panels during compaction of the backfill. The data collected after placement and before compaction of each lift have been omitted for clarity. Measurements were made before and after any interruptions of the backfill placement process. They are also included in the table. The total horizontal and total vertical loads per panel correspond to the sum of the individual load cells readings in each panel. The effective overburden

Table 5-3
Data From Gloetzl Pressure Cells at the End of Stage 1 (Backfilling)

Gloetzl Cell Number	Position of Cell ¹ m	Horizontal Pressure, σ_h KPa	
		Measured	Corrected ²
G1	1.778	12.44	10.64
G7	1.626	11.29	9.65
G2	1.473	8.83	7.55
G8	1.321	No response	-
G3	1.168	10.20	8.72
G9	1.016	9.76	8.34
G4	0.864	8.31	7.11
G10	0.711	10.15	8.68
G5	0.559	9.53	8.15
G11	0.406	8.48	7.25
G6	0.253	No response	-

¹ Measured from bottom of backfill to center of each cell.
² Obtained by dividing the measured pressure by 1.17.

Table 5-4
Summary of the Results of Stage 2 of the IRW (Surcharge)¹

Applied Surcharge, q_s , kPa	Total Horizontal Load per Panel kN		Total Vertical Force per Panel kN		F'_x kN/m	F_v kN/m	$F_{v,q}$ kN/m	$K_{v,q}$
	Panel 2	Panel 3	Panel 2	Panel 3				
0.0 ²	11.22	11.39	3.18	2.90	14.84	3.99	0.000	-
0.3	11.31	11.63	3.21	2.95	15.05	4.04	0.048	0.079
0.3	11.82	11.97	3.35	3.10	15.61	4.23	0.236	0.388
9.2	12.67	13.76	4.11	4.00	17.34	5.32	1.324	0.067
18.2	13.32	14.91	4.86	4.81	18.52	6.35	2.351	0.061
0.3	10.75	11.07	3.49	3.25	14.32	4.42	0.427	0.704
18.2	12.82	13.56	4.99	4.75	17.30	6.39	2.397	0.062
18.2	13.03	13.60	5.03	4.80	17.48	6.45	2.459	0.063
0.00	10.86	11.05	3.48	3.23	14.38	4.40	0.411	-

¹ See Notation (Appendix F) for definition of symbols.
² Corresponds to end of backfilling (last row of Table 5-2).

values are determined using Equation 1-1. The values of F'_x and F_v correspond to the horizontal and vertical forces, respectively, per unit length of wall. Definitions of the earth pressure coefficients, K_h and K_v , are presented in Chapter 1. According to Equations 1-2 and 1-3, the values of K_h and K_v are calculated by dividing the values of F'_x and F_v , respectively, by the effective overburden.

Table 5-5
Summary of the Results of Stage 3 of the IRW (Inundation)¹

Cycle		D ₂ , m	D ₂ / H	D ₁ , m	F _w kN/m	Total Horizontal Force per Panel, kN		Total Vertical Force per Panel, kN		F _x kN/m	F' _x kN/m	F _v kN/m	K _v	C _{wt}
						Panel 2	Panel 3	Panel 2	Panel 3					
1 ²	Inundation	0.00	0.00	2.13	0.00	10.86	11.05	3.48	3.23	14.38	14.38	4.40	0.115	1.000
		0.60	0.28	1.54	1.75	10.85	10.63	2.46	2.23	14.09	12.35	3.07	0.083	0.721
		0.95	0.45	1.18	4.45	12.04	11.69	1.79	1.43	15.57	11.13	2.11	0.060	0.522
		1.32	0.62	0.81	8.55	14.48	13.50	1.28	1.11	18.36	9.81	1.56	0.049	0.422
		1.52	0.71	0.61	11.38	15.67	14.90	1.12	1.08	20.06	8.68	1.44	0.048	0.416
		1.50	0.71	0.63	11.10	14.89	14.42	1.10	1.07	19.24	8.14	1.43	0.047	0.408
		1.83	0.86	0.30	16.39	17.54	16.46	0.81	0.92	22.31	5.92	1.13	0.043	0.371
		2.06	0.96	0.08	20.74	18.97	17.83	0.57	0.81	24.14	3.40	0.91	0.039	0.335
	Drainage	1.77	0.83	0.37	15.27	16.59	15.61	0.93	1.16	21.13	5.86	1.37	0.049	0.428
		1.60	0.75	0.53	12.55	15.15	14.10	0.94	1.13	19.19	6.65	1.36	0.045	0.394
		1.40	0.65	0.74	9.56	14.70	13.51	1.06	1.21	18.51	8.94	1.49	0.046	0.400
		1.19	0.56	0.94	6.98	13.83	12.51	1.34	1.49	17.29	10.31	1.86	0.054	0.470
		0.72	0.34	1.41	2.57	11.73	10.19	1.88	1.99	14.38	11.81	2.54	0.067	0.585
		0.65	0.30	1.49	2.06	11.87	10.15	1.83	1.91	14.45	12.39	2.45	0.064	0.560
		0.36	0.17	1.77	0.64	11.82	9.78	2.24	2.27	14.17	13.53	2.96	0.075	0.655
		0.33	0.15	1.80	0.53	11.57	9.25	2.55	2.55	13.66	13.13	3.35	0.085	0.741
		2	Inundation	0.88	0.41	1.26	3.76	12.33	10.14	2.07	2.14	14.74	10.98	2.76
1.70	0.80			0.43	14.19	16.86	15.17	1.18	1.40	21.02	6.83	1.70	0.059	0.514
2.13	1.00			0.01	22.31	20.09	18.53	0.75	1.05	25.35	3.04	1.18	0.053	0.458
Drainage	1.66		0.78	0.48	13.46	16.66	14.91	1.16	1.39	20.71	7.25	1.67	0.057	0.497
	1.11		0.52	1.02	6.05	13.76	12.11	1.93	2.06	16.97	10.92	2.62	0.075	0.650
	0.61		0.29	1.52	1.82	11.81	10.07	2.52	2.65	14.36	12.54	3.39	0.089	0.770
	0.32		0.15	1.81	0.51	12.01	9.83	2.93	3.03	14.33	13.82	3.91	0.099	0.864

¹ D_1 = Thickness of backfill above the water table; D_2 = height of water behind the wall; F_w = hydrostatic force on wall. See Notation (Appendix F) for definitions of other symbols.

² Corresponds to end of surcharge cycle (last row of Table 5-4).

It can be observed that the magnitudes of vertical and horizontal forces are similar for the two panels. They are also similar to the values reported by Filz (1992) for a previous IRW test using the Light Castle sand backfill.

5.3.1.2 Pressure measurements. The data from the Gloetzl pressure cells at the end of backfilling are presented in Table 5-3. Integration of these pressure values over the height of the wall yields a horizontal force magnitude of 17.35 kN per meter run of wall. This value is approximately 17 percent greater than the value of 14.84 kN/m obtained from the load cell measurements presented in Table 5-2. Table 5-3 also shows the corrected values of normal pressure, which were obtained by dividing the pressure data by 1.17.

The error in the pressure measurements suggests that Gloetzl cells do not provide data that is usable for accurate analyses of the response of the wall-backfill system. However, they provide an important insight for SSI analyses of the IRW, as discussed in the section on the interpretation of the test results.

5.3.2 Results from stage 2

Table 5-4 summarizes the data from the two cycles of application and removal of the surcharge. The vertical force increment due to surcharge application $F_{v,q}$ and the vertical shear force coefficient for sloping backfill and surcharge $K_{v,q}$ are defined in Chapter 2. The value of $F_{v,q}$ is the difference between the values of F_v

after and before the application of the surcharge. Rearranging terms in Equation 2-16 gives the following expression for the determination of $K_{v,q}$ from the IRW data:

$$K_{v,q} = \frac{F_{v,q}}{q_s \cdot H} \quad (5-1)$$

The magnitudes of the vertical shear load before and after this stage of the test are very similar. This suggests that there is little or no degradation of the vertical shear loads with cycles of application and removal of the surcharge.

5.3.3 Results from stage 3

5.3.3.1 Force measurements. The data collected during the inundation cycles of the IRW test are summarized in Table 5-5. The hydrostatic force on the wall F_w is calculated from the following expression:

$$F_w = \frac{\gamma_w \cdot D_2^2}{2} \quad (5-2)$$

The effective horizontal force F'_x is calculated by subtracting the hydrostatic force F_w from the total horizontal force F_x . The definition of the correction factor C_{wt} for a post-construction rise in the water table was presented in Chapter 2. The value of C_{wt} for the IRW test was calculated as the ratio between the K_v values during inundation and the K_v value immediately before the start of inundation (Equation 2-20).

It can be seen that the magnitude of the vertical shear force F_v decreases as the height of water in the backfill D_2 increases during inundation. Conversely, the magnitude of F_v increases as D_2 decreases during drainage. Drainage of the backfill was carried out until D_2 reached a value of approximately 0.3 m. Further lowering of the water table was not practical because the time required for full drainage of the backfill ($D_2 = 0$) was too long. However, extrapolation of the vertical force data collected during the two drainage stages reveals that the value of F_v for full drainage ($D_2 = 0$) is similar to its initial value before the start of inundation ($F_v = 4.40$ kN/m). This suggests that there is no significant degradation of the vertical shear force with cycles of inundation for the conditions of this test in the IRW.

5.3.3.2 Hydrocompression. During inundation, the elevation of the surface of the backfill was measured periodically with an accuracy of ± 1 mm. No significant changes in the backfill height were detected during inundation. This is consistent with the analysis of the hydrocompression properties of the Light Castle sand presented in Appendix A. Therefore, for the analyses of the IRW, it was assumed that hydrocompression of the backfill is negligible.

5.4 Discussion of Test Results

In this section, the backfill response observed during the test and its relevance for the finite element analyses of the IRW are discussed.

5.4.1 Response of the wall-backfill system to backfilling

5.4.1.1 Evolution of lateral earth pressures during backfilling. The values of the lateral earth pressure coefficient K_h listed in Table 5-2 are plotted against the height of the backfill in Figure 5-6. It can be seen that the value of K_h decreases as the height of the backfill increases. A value of K_h of approximately 0.4 was obtained at the end of backfilling.

For comparison, the value of the at-rest coefficient K_o determined using the approximation suggested by Jaky (1948) for an internal friction angle of the backfill of 47 deg is also illustrated in the figure. The at-rest coefficient does not account for compaction-induced lateral earth pressures behind walls with rough interfaces. Therefore, the value of K_o should be identical to the value of K_h in a nonmoving wall retaining a normally consolidated backfill and with a smooth backfill-to-wall interface. The value of K_h in the IRW is larger than the value of the at-rest coefficient throughout the backfilling stage because significant lateral stresses are locked in during compaction of the backfill.

Figure 5-7 shows the pressure distribution at the end of backfilling in the IRW test. Data from a similar test performed previously in the IRW (Filz 1992) are also shown. It can be seen that the pressure distribution on the wall is not linear and that large horizontal pressures develop throughout the height of the wall. As discussed by Duncan et al. (1991), compaction-induced earth pressures are much greater than the at-rest values near the surface of a compacted backfill. At large depths, the overburden pressure induced by the weight of the overlying backfill is significantly larger than the vertical stresses applied during compaction. Therefore, in short walls such as the IRW, the magnitude of the total horizontal force on the wall may be controlled by compaction-induced earth pressures.

In higher walls, the total horizontal force on the wall may be controlled by the at-rest pressures for normally consolidated soil backfills. As the height of the backfill increases, the value of K_h decreases. For lock walls, which are typically 12 m (40 ft) or higher and have smooth wall-to-backfill interfaces, the K_h values approach Jaky's K_o value, since the stresses induced by the overburden exceed the stresses induced by compaction.

To perform accurate analyses of short walls such as the IRW, it is necessary to account for the relatively large pressures that develop at shallow depths inside the backfill.

5.4.1.2 Evolution of vertical shear forces during backfilling. The values of the vertical force coefficient K_v measured during stage 1 of the test are plotted in Figure 5-8 against the height of the backfill. The value of K_v increases with the

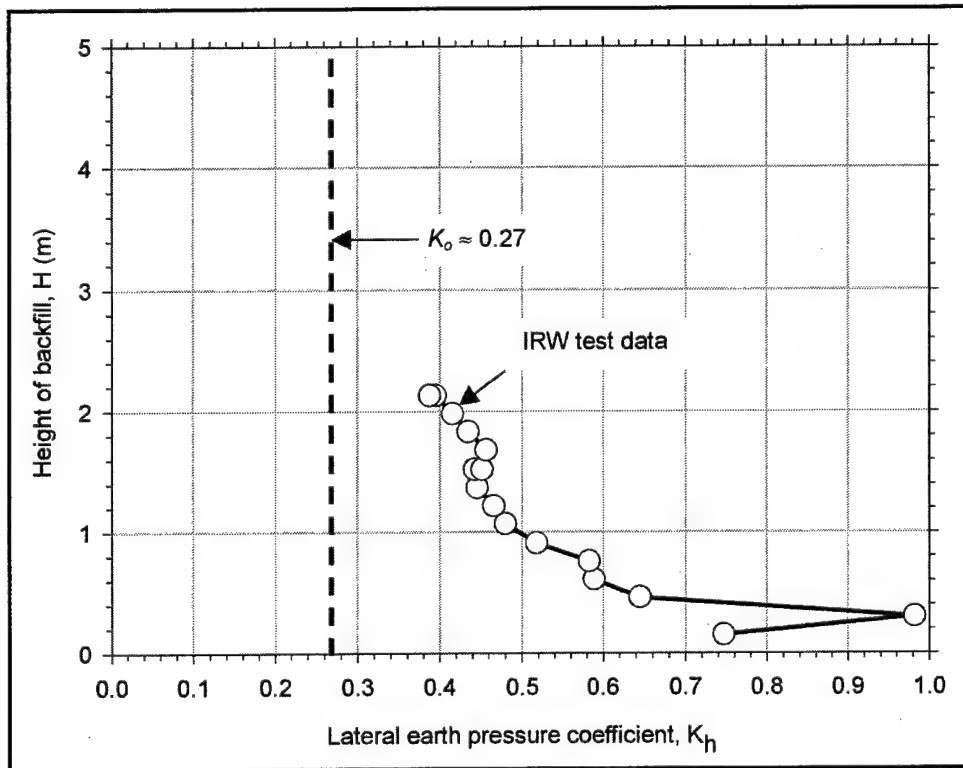


Figure 5-6. Evolution of the lateral earth pressure coefficient K_h during backfilling in the IRW

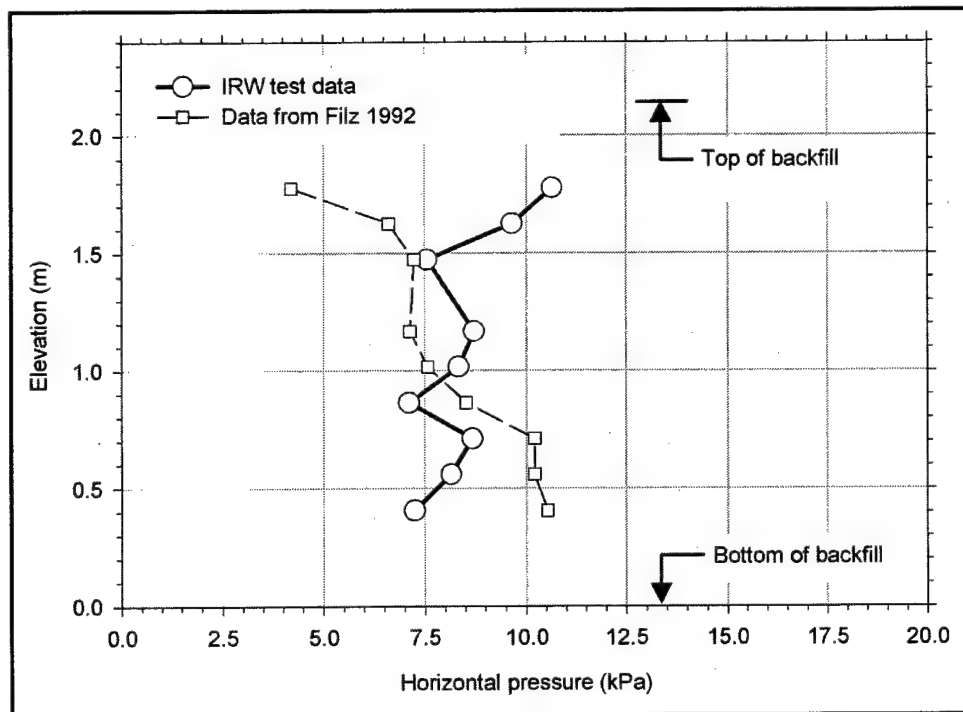


Figure 5-7. Lateral pressure distribution at the end of backfilling

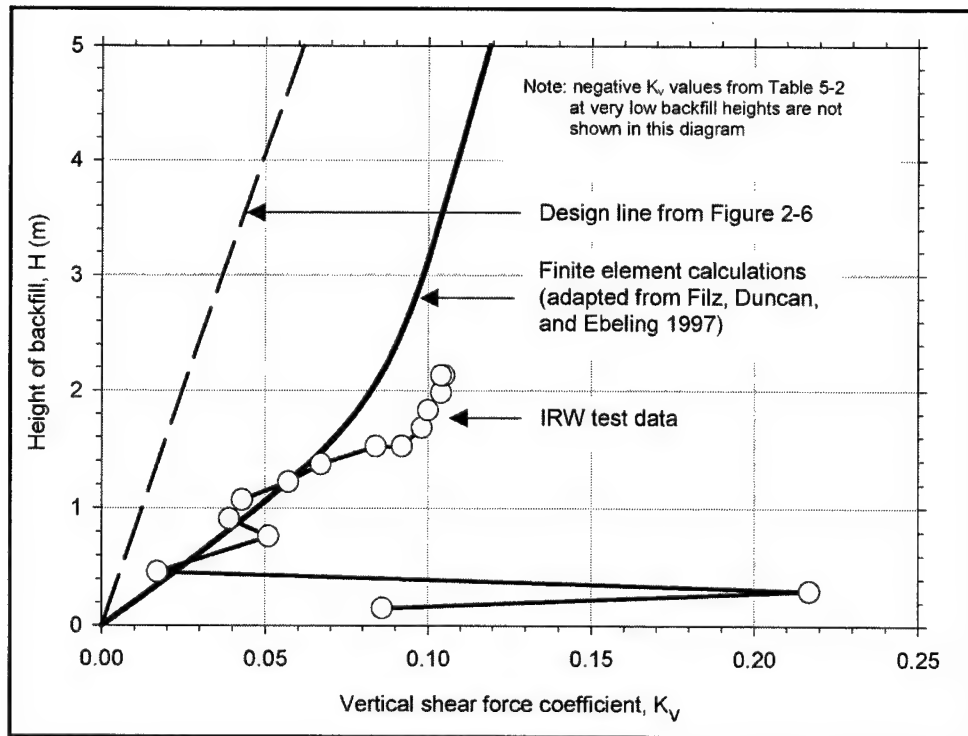


Figure 5-8. Evolution of the vertical shear force coefficient K_v during backfilling in the IRW

height of the backfill to a final value of 0.10 at the end of backfilling. This value is consistent with the results of a previous test performed in the IRW (Filz 1992).

A discussion of the development of vertical shear forces in nonmoving walls was presented by Filz and Duncan (1997) and Filz, Duncan, and Ebeling (1997). From a series of finite element analyses, they developed a set of K_v versus backfill height curves for different densities of the backfill. Figure 2-6 reproduces the results of their analyses. The calculated values of K_v for dense, granular backfills are reproduced in Figure 5-8, together with the design line recommended in Appendix F of Engineer Manual 1110-2-2100 (HQUSACE, in preparation).

It can be observed that the calculated and measured K_v values follow similar trends of variation with backfill height. However, the measured K_v values at the end of backfilling are somewhat higher than the calculated values.

The design line shown in Figure 5-8 provides conservative estimates of K_v , according to the IRW data.

5.4.2 Response of the wall-backfill system to surcharge

Values of the earth pressure coefficient for surcharge $K_{v,q}$ determined from force measurements in stage 2 are listed in Table 5-4. Neglecting the extreme values for low surcharge magnitudes, the average value of $K_{v,q}$ is 0.063. In the

IRW test, the backfill surface is horizontal and the distance from the surcharge to the wall is zero. Therefore, the concept of $K_{v,q}$ is equivalent to the concept of $K_{v,q,ref}$ discussed in Chapter 2. The average value of $K_{v,q}$ from the test is represented in a $K_{v,q,ref}$ versus backfill height diagram in Figure 5-9.

The $K_{v,q}$ values obtained by Filz, Duncan, and Ebeling (1997) from finite element analyses of nonmoving walls with dense backfills are also represented in Figure 5-9. These analyses were performed using the same backfill properties as those used in their backfilling analyses discussed in the previous section. From the theoretical plots, a value of $K_{v,q}$ of approximately 0.12 is obtained. This value is larger than the $K_{v,q}$ value determined from the IRW data. This difference between calculated and measured $K_{v,q}$ values occurs because the compressibility of the backfill assumed for the analyses is larger than the compressibility of the compacted Light Castle sand, as discussed in Sections 5.5.3 and 5.6.2.

The design line recommended in Appendix F of Engineer Manual 1110-2-2100 (HQUSACE, in preparation) is also reproduced in Figure 5-9. It provides a slightly conservative estimate of the value of $K_{v,q}$, according to the IRW data.

5.4.3 Response of the wall-backfill system to inundation

The values of the correction factor C_{wt} listed in Table 5-5 are plotted against the normalized height of water D_2/H in Figure 5-10. The test data follow a curvilinear path reaching an average final value of C_{wt} of approximately 0.4 after full inundation of the backfill ($D_2/H = 1$). The design line, recommended in Appendix F of Engineer Manual 1110-2-2100 (HQUSACE, in preparation), is also represented in the figure. It yields a good approximation to the C_{wt} values from the IRW test for D_2/H ratios lower than 0.5. For D_2/H ratios between 0.5 and 1, the design line yields conservative values of the correction factor.

5.4.4 Special considerations for finite element analyses of the IRW

A method to incorporate compaction effects into finite element analyses was developed by Seed and Duncan (1986). The compaction of each lift was modeled as the temporary application of compaction stresses on the surface of the backfill. They used a hysteretic soil model, which provided reasonable estimations of the residual earth pressures after removal of the compaction stresses.

The implementation of such a model in SOILSTRUCT-ALPHA may be a lengthy process, and it is beyond the scope of this investigation. Therefore, a simpler, alternative procedure was followed to model the response of the wall-backfill system to all types of loading applied during the test. For the analyses, different backfill property values were assigned for backfilling and for surcharge placement. The effect of compaction on the lateral pressures was modeled by assigning a larger Poisson's ratio and a lower modulus to the backfill material for stage 1 (backfilling) than for stage 2 (surcharge).

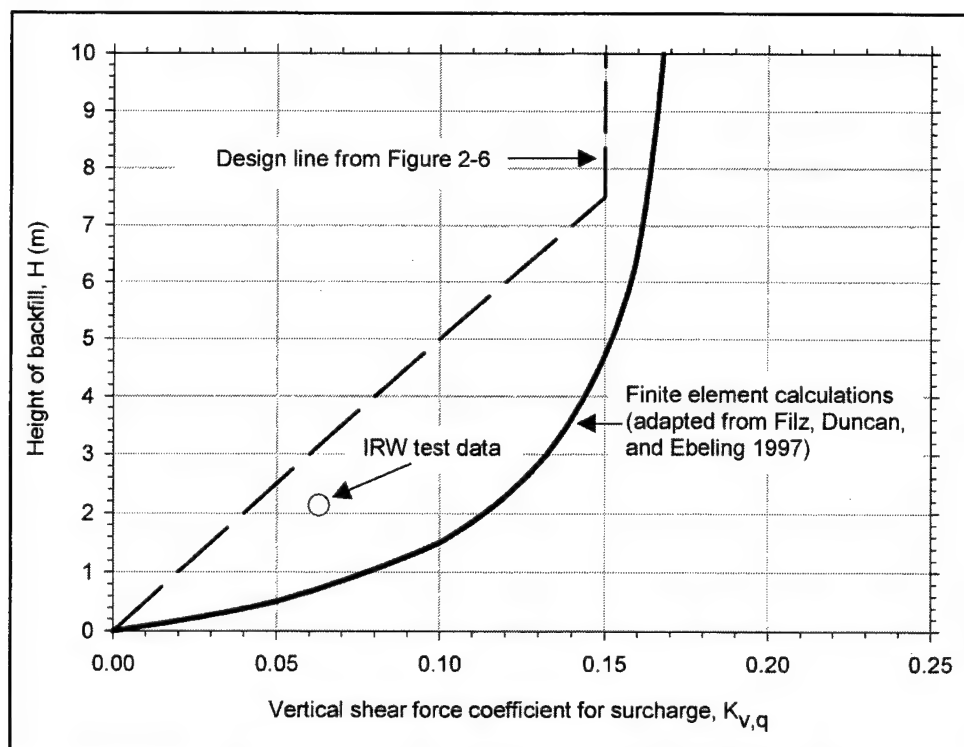


Figure 5-9. Vertical shear force coefficient for surcharge $K_{v,q}$ in the IRW

In previous sections of this report, it was observed that at the end of backfilling in the IRW, large horizontal pressures exist throughout the height of the instrumented wall, and that the pressure distribution is not linear with depth. To obtain accurate values of vertical and horizontal forces from finite element analyses of the IRW, it is necessary to account for this type of lateral pressure distribution. Finite element analyses in SOILSTRUCT-ALPHA do not provide the type of horizontal pressure distribution observed in the IRW test. In the analyses, the distribution tends to be linear, and pressures are low at shallow depths in the backfill. Consequently, the effect of the confining pressures on the backfill response to loading is not accurately modeled in the analyses. Additional adjustments of the backfill properties are required to account for the larger confining pressures that occur due to compaction.

For these reasons, limited information on the accuracy of the extended hyperbolic model can be expected from the analyses of the IRW for the backfilling and surcharge stages. The analyses of stages 1 and 2 were performed to obtain a reasonable estimate of the backfill properties and of the state of stresses existing prior to inundation. The backfill properties and state of stresses obtained from these calibration analyses were used for the analysis of inundation. The comparison between the results of the inundation analysis and the test data is the basis for the evaluation of the extended hyperbolic model.

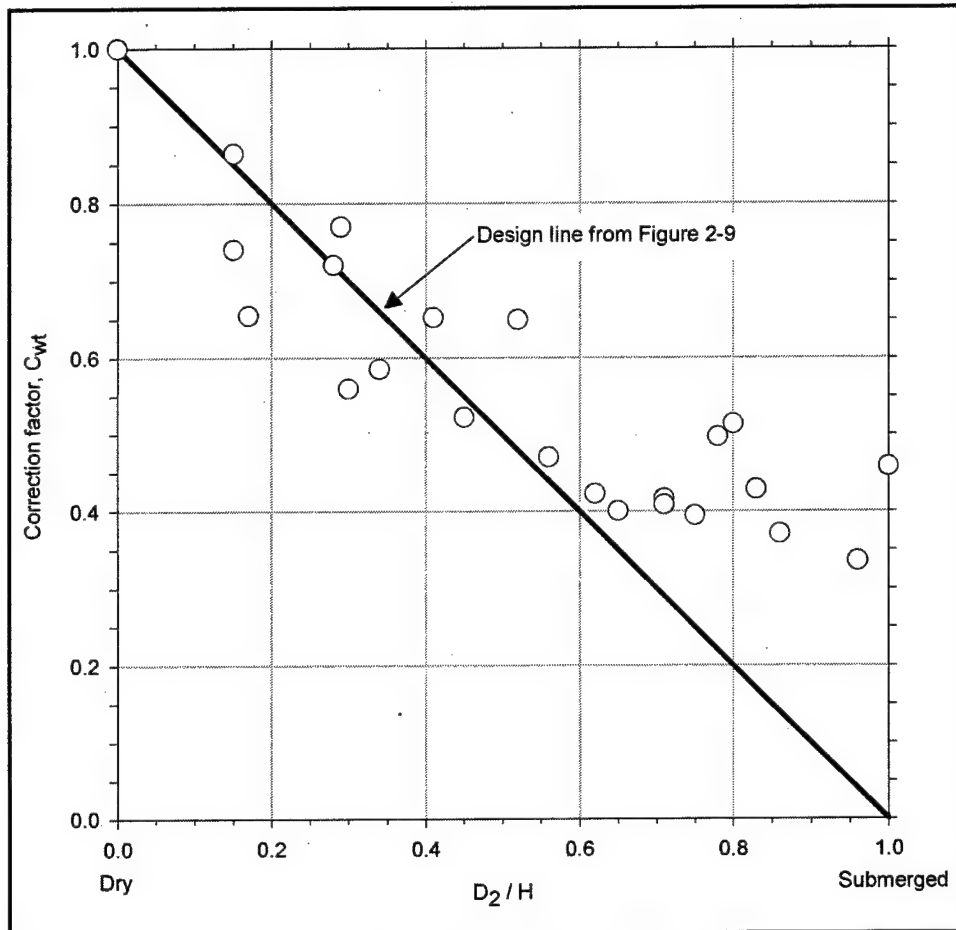


Figure 5-10. Values of the correction factor C_{wt} during inundation of the backfill in the IRW

These issues regarding the limitations of SOILSTRUCT-ALPHA analyses of the IRW may not be applicable to most lock walls. In lock walls of moderate to large height, the earth pressures are largely controlled by the self-weight of the backfill. A single set of material properties that produces reasonable estimates of earth pressures for backfilling may also produce reasonable estimates for surcharge application and for post-construction rise of the groundwater table.

5.5 Finite Element Analysis Procedures

Finite element analyses were performed to model the IRW test using the updated version of the program SOILSTRUCT-ALPHA, which contains the extended hyperbolic model presented in Chapter 4. The following steps were followed for the analyses:

- a. Selection of tentative material properties for the backfill.
- b. Calibration analyses.
- c. Inundation analysis.

Tentative values of backfill properties were determined from the results of the triaxial and consolidation tests on the Light Castle sand. These values were adjusted during the calibration analyses to match the force values measured at the end of the backfilling and surcharge stages. Finally, these adjusted properties were used for the analyses of the inundation stage.

This section summarizes features of SOILSTRUCT-ALPHA that are relevant for the analyses performed. The criteria followed for the selection of the material property values and procedures used for the calibration and backfill inundation analyses are described in detail. Finally, the analysis results are compared to the data collected during the IRW test, and the accuracy of the extended hyperbolic model for interfaces is discussed.

5.5.1 Summary of features of SOILSTRUCT-ALPHA

The program SOILSTRUCT was developed by Clough and Duncan (1969) for finite element analyses of earth retaining structures. It is a general-purpose finite element program for two-dimensional analysis of plane strain problems of soil-structure interaction. It calculates stresses and displacements due to incremental construction and/or load application, and can model nonlinear stress-strain material behavior. Two types of finite elements are used in SOILSTRUCT: two-dimensional elements for soil and structural materials, and joint elements for the interfaces between the different materials. SOILSTRUCT has undergone a continuous evolution as new developments have been introduced in soil and interface models. SOILSTRUCT-ALPHA is the latest result of this process (as described in Ebeling and Wahl 1997 and Ebeling, Pace, and Morrison 1997).

In SOILSTRUCT-ALPHA, the nonlinear response of soils to primary loading is modeled using the hyperbolic formulation by Duncan and Chang (1970). For unloading-reloading, a stress-dependent, linear response is assumed (Ebeling, Peters, and Clough 1992). The Alpha method (Ebeling, Duncan, and Clough 1990; Ebeling et al. 1992) implemented in the code allows analyses of lock walls undergoing base separation. Base separation is not a relevant issue for the IRW analyses, and it is not discussed further in this report.

As indicated in Chapter 4, the updated version of SOILSTRUCT-ALPHA, which was developed during this investigation, contains the formulation for yield-inducing shear and unloading-reloading Version II of the extended hyperbolic model for interfaces.

5.5.1.1 Incremental analysis techniques. In SOILSTRUCT-ALPHA, analyses are performed following the incremental techniques described by Clough and Duncan (1969). In the analyses, the backfill elements and structure-to-backfill

interface elements take on three different states during the analyses: air, fluid, and solid. In the initial condition before the start of backfilling, all the backfill and interface elements are assigned the properties of air and of structure-to-air interface, respectively.

Each newly placed lift is modeled as a dense fluid, with a unit weight equal to the unit weight of the compacted backfill. The pressures exerted by the new lift on the existing backfill and on the structural elements are calculated and transformed into nodal loads. The interface elements between the structure and the newly placed lift are assigned a low value of shear stiffness and, as discussed in Chapter 2, a large value of normal stiffness. Zero nodal displacements are prescribed at the surface of the newly placed lift to prevent buildup of displacements in the overlying air elements.

The value of the at-rest pressure coefficient K_0 assigned to the fluid elements is usually assumed equal to one. It determines the magnitude of the lateral pressures between the fluid elements and between the fluid elements and the retaining wall.

Upon addition of subsequent lifts to the mesh, the previously fluid elements take on a solid state. At this time, the complete set of properties of the compacted backfill and of the structure-to-backfill interface are assigned to the backfill and interface elements.

For soil and backfill, the incremental changes in stresses are related to the incremental strains through the linear relationship:

$$\begin{Bmatrix} \Delta\sigma_x \\ \Delta\sigma_y \\ \Delta\tau_{xy} \end{Bmatrix} = \frac{3 \cdot B}{9 \cdot B - E_t} \begin{bmatrix} (3 \cdot B + E_t) & (3 \cdot B - E_t) & 0 \\ (3 \cdot B - E_t) & (3 \cdot B + E_t) & 0 \\ 0 & 0 & E_t \end{bmatrix} \cdot \begin{Bmatrix} \Delta\epsilon_x \\ \Delta\epsilon_y \\ \Delta\gamma_{xy} \end{Bmatrix} \quad (5-3)$$

where

$\Delta\sigma_x$ = horizontal stress increment

$\Delta\sigma_y$ = vertical stress increment

$\Delta\tau_{xy}$ = shear stress increment

B = bulk modulus of the soil

E_t = tangent modulus of the soil

$\Delta\epsilon_x$ = horizontal strain increment

$\Delta\epsilon_y$ = vertical strain increment

$\Delta\gamma_{xy}$ = shear strain increment

For interface elements, the incremental changes in stresses and displacements are related according to the following expression:

$$\begin{Bmatrix} \Delta\tau \\ \Delta\sigma_n \end{Bmatrix} = \begin{bmatrix} K'_{st} & 0 \\ 0 & K_n \end{bmatrix} \cdot \begin{Bmatrix} \Delta_s \\ \Delta_n \end{Bmatrix} \quad (5-4)$$

where

$\Delta\tau$ = shear stress increment

$\Delta\sigma_n$ = normal stress increment

K'_{st} = tangent interface shear stiffness

K_n = interface normal stiffness

Δ_s = interface shear displacement

Δ_n = interface normal displacement

5.5.1.2 Soil properties. The tangent Young's modulus E_t of the soil for use in each load increment is computed from the following equation:

$$E_t = E_i \cdot (1 - R_f \cdot SL)^2 \quad (5-5)$$

where E_i is the initial Young's modulus of the soil.

In effective stress analyses, the initial Young's modulus E_i is determined from

$$E_i = K \cdot p_a \cdot \left(\frac{\sigma'_3}{p_a} \right)^n \quad (5-6)$$

The stress level SL in soils is determined from:

$$SL = \frac{(\sigma_1 - \sigma_3)}{(\sigma_1 - \sigma_3)_f} \quad (5-7)$$

where

σ_1 = major principal stress

σ_3 = minor principal stress

For a frictional backfill with *zero* cohesion intercept, the deviator stress at failure $(\sigma_1 - \sigma_3)_f$ is determined from:

$$(\sigma_1 - \sigma_3)_f = 2 \frac{\sigma'_3 \cdot \sin \phi'}{1 - \sin \phi'} \quad (5-8)$$

where ϕ' is the internal friction angle of the soil.

In this formulation, the parameters K , n , R_f , and ϕ' are the hyperbolic parameters defined by Duncan and Chang (1970) for modeling the response of the soil to primary loading. During unloading-reloading, a linear, stress-dependent soil response is assumed. The value of the Young's modulus for unloading-reloading E_{ur} is calculated from the following expression:

$$E_{ur} = K_{ur} \cdot p_a \cdot \left(\frac{\sigma'_3}{p_a} \right)^n \quad (5-9)$$

where K_{ur} is the unload-reload modulus number.

According to the hyperbolic formulation by Duncan and Chang (1970), the bulk modulus B of the soil is calculated from the equation:

$$B = K_b \cdot p_a \cdot \left(\frac{\sigma'_3}{p_a} \right)^m \quad (5-10)$$

where m is the bulk modulus exponent.

In SOILSTRUCT-ALPHA, the following approximate formulation is used to calculate the bulk modulus number (Ebeling, Pace, and Morrison 1997):

$$K_b = \frac{K}{3 \cdot (1 - 2 \cdot v_{nom})} \quad (5-11)$$

In Equation 5-11, it is implicitly assumed that the values of modulus exponent n and the bulk modulus exponent m are identical. The nominal Poisson's ratio v_{nom} is related to Poisson's ratio ν according to the following expression (Ebeling, Pace, and Morrison 1997):

$$\nu = \frac{1 - (1 - 2 \cdot v_{nom}) \cdot (1 - R_f \cdot SL)^2}{2} \quad (5-12)$$

The at-rest pressure coefficient K_o , used only for the analysis of the stresses induced by the newly placed lift, is usually assumed equal to one. The unit weight of the soil γ is assumed equal to the moist unit weight γ_{moist} for the portion of the backfill above the water table, and to the saturated unit weight γ_{sat} for the portion below the water table. Table 5-6 is a summary of the properties required to model soils in SOILSTRUCT-ALPHA analyses.

5.5.1.3 Interface properties. The shear stiffness K'_{st} of the interface is determined according to the formulations for yield-inducing shear and for unloading-reloading in Version II of the extended hyperbolic model introduced in Chapter 4. The normal stiffness K_n is assigned a large value to prevent overlapping of adjacent elements in the mesh.

5.5.2 Finite element mesh

Figure 5-11 shows the mesh used for the finite element analyses of the IRW. It is composed of the following elements:

- 224 two-dimensional elements for modeling the backfill.
- 32 two-dimensional elements for modeling the instrumented panels.
- 46 joint elements for modeling the interfaces between the backfill and the walls, and between the backfill and the floor of the IRW.
- 3 elastic springs to model the vertical and horizontal load cells.

The far field interface was assigned a very low stiffness to model the non-frictional lining applied to the far field wall. The instrumented wall elements were assigned common properties of reinforced concrete. The stiffness values of the springs used to model the horizontal load cells were determined from experimental load-deformation data of previous tests. The stiffness of the vertical load cell was calculated theoretically from the geometry and material properties of the load cells.

Table 5-7 lists property values that are representative of the structural materials in the IRW. These values were used for all the analyses. The following section discusses the selection of property values for the backfill and interfaces.

5.5.3 Tentative soil properties

As described in Chapter 3, hyperbolic parameter values for the Light Castle sand were determined from triaxial and consolidation tests performed on specimens compacted to relative densities of 50 and 80 percent. A relative density of approximately 100 percent was attained during compaction of the backfill in the

Table 5-6
Summary of Soil Properties
Required in SOILSTRUCT-ALPHA
Analyses

Soil Property	Definition
K	Modulus number
n	Modulus exponent
K_{ur}	Modulus number for unloading-reloading
R_f	Failure ratio
ϕ'	Internal friction angle
ν_{nom}	Nominal Poisson's ratio
K_o	At-rest earth pressure coefficient for fluid backfill
$\gamma_{moist}, \gamma_{sat}$	Moist and saturated unit weight, respectively

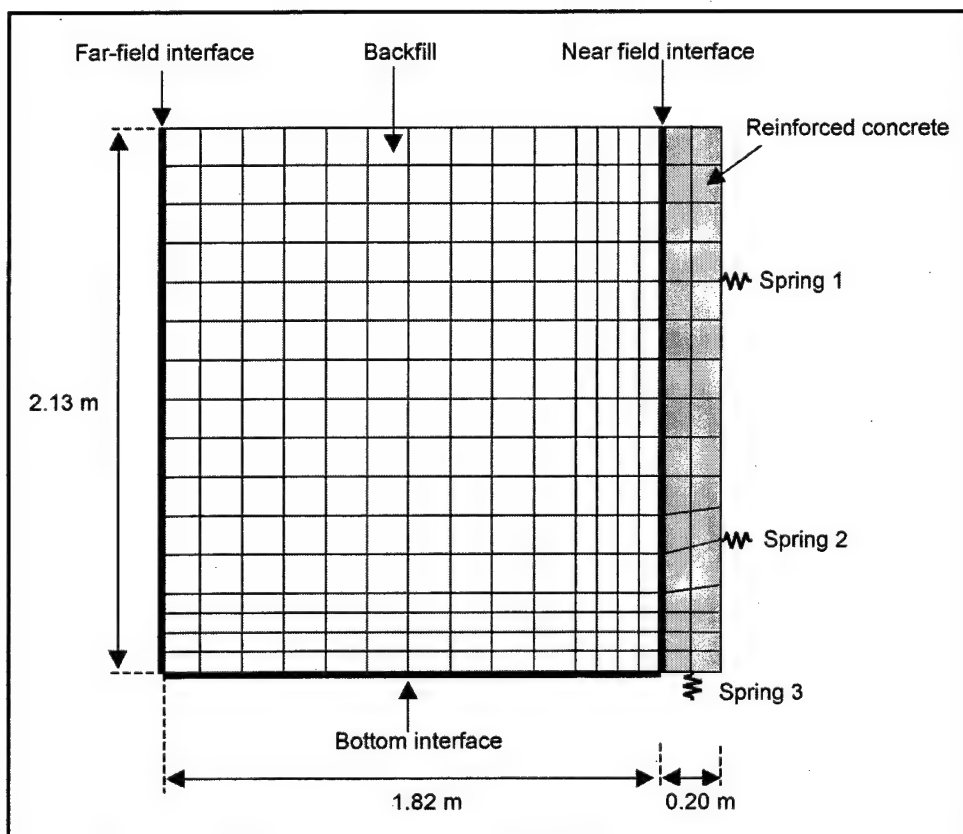


Figure 5-11. Finite element mesh used for the analyses

Table 5-7 Summary of Property Values for Structural Materials in the IRW Analyses		
Material	Property	Value
Reinforced concrete	Poisson's ratio ν	0.2
	Unit weight γ	23.6 kN/m ³
	Young's modulus E	20.7 x 10 ⁶ kPa
Spring 1	Stiffness per meter run of wall	13150 kN/m
Spring 2	Stiffness per meter run of wall	17810 kN/m
Spring 3	Stiffness per meter run of wall	24160 kN/m

IRW; consequently, no direct experimental data were available on the compacted backfill properties. Tentative property values of the compacted backfill for use in the calibration analyses were determined following the procedures described in the following paragraphs.

5.5.3.1 Estimation of stiffness number K . Duncan et al. (1980) reported hyperbolic parameter values for a number of granular soils. They noted that there is a direct relationship between the relative density of the soil and the value of

stiffness number K . The results of the tests performed on the Density sand and the Light Castle sand confirm these observations, as shown in Figure 3-3. Therefore, it is possible to estimate the value of K by extrapolation of the values determined from the triaxial tests.

A range of tentative values of K determined from extrapolation is listed in Table 5-8. Both the test results and the data reported by Duncan et al. (1980) were used for this extrapolation. These values were adjusted during the analyses of backfilling and surcharge, to account for the effects of compaction on the lateral stresses in the backfill. This is discussed in the section on calibration analyses.

5.5.3.2 Estimation of stiffness exponent n .

According to Duncan et al. (1980), the value of n does not vary significantly with relative density. Therefore, the average value of n from the triaxial tests can be used directly. However, additional considerations need to be made for the selection of n in finite element analyses of the IRW.

As discussed previously, the lateral stress distribution in the compacted backfill in the IRW is not linear. Relatively large horizontal stresses exist at shallow depths inside the backfill that are induced by the stresses applied during compaction. On the other hand, finite element analyses using SOILSTRUCT-ALPHA do not model compaction effects and produce stress distributions that tend to be linear, with lateral stresses at shallow depths being relatively small.

Figure 5-12 shows the lateral earth pressures measured at the end of backfilling in the IRW. The solid line is the pressure distribution assumed for the purposes of the following discussion. For comparison, the pressure distribution obtained from a SOILSTRUCT-ALPHA analysis is also shown. Both distributions produce approximately the same magnitude of lateral force F'_x . In the upper portion of the wall, the measured lateral stresses are larger than the stresses from the finite element analyses (Figure 5-12a). Conversely, the lateral stresses from the analyses are larger than the measured stresses in the lower portion of the wall. Although no measurements were made of the lateral stresses in the backfill away from the wall, it is reasonable to assume that a similar situation occurs throughout the soil mass.

Figure 5-12b is a hypothetical diagram of an arbitrary stress-dependent property versus confining pressure. The solid line corresponds to the relationship

Table 5-8
Tentative Property Values for the Light Castle Sand Backfill

Property ¹	Tentative Value
K	800 - 1600
n	0.20
R_f	0.85
v_{nom}	0.3 - 0.40
K_{ur}	800-1600
ϕ'	47°
γ	16.8 kN/m ³

¹ Material parameters are listed and defined in the Notation (Appendix F).

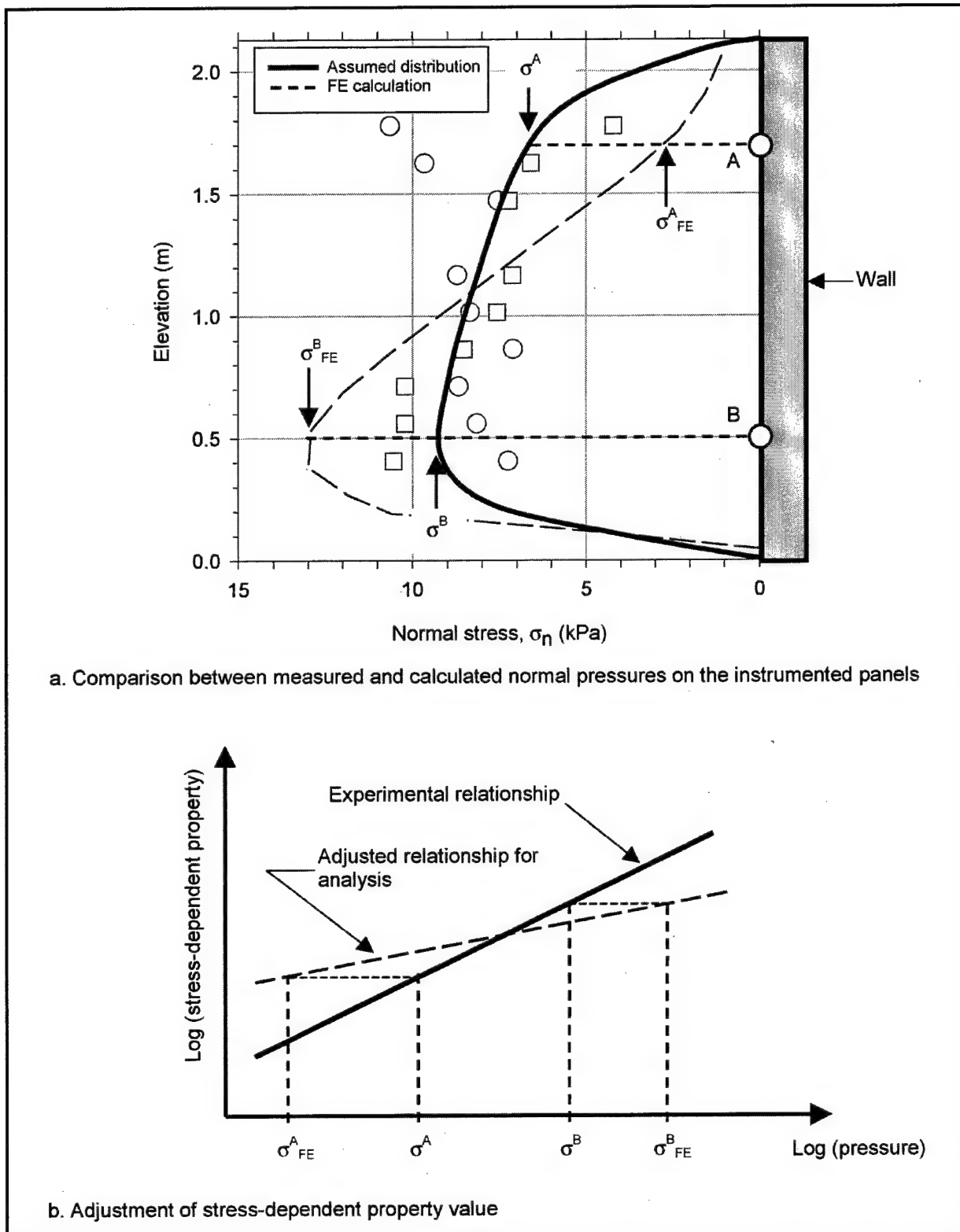


Figure 5-12. Adjustment of stress-dependent backfill property for finite element analyses of the IRW

determined from hypothetical laboratory tests. Soil properties such as the Young's modulus and the bulk modulus follow this type of relationship, as discussed in Chapter 3. The property values are inaccurate if they are determined using the solid line and the stresses from the finite element analysis. An adjusted relationship with a shallower slope, shown as a dashed line in the figure, allows estimation of approximate property values using the confining stresses from the analyses.

In order to illustrate the determination of the adjusted relationship, two points, *A* and *B*, are represented in Figure 5-12b. Point *A* is located in the upper portion of the backfill. Point *B* is located in the lower portion of the backfill. As illustrated in Figure 5-12b, the property value corresponding to the lateral stress σ^A at a point such as *A* is assigned to the lower value of stress σ_{FE}^A , calculated from the finite element analyses. Conversely, the property value corresponding to the lateral stress σ^B at a point such as *B* is assigned to the larger value of stress σ_{FE}^B , calculated from the finite element analyses. The resulting relationship has a shallower slope. If the stress-dependent property plotted in the diagram is the initial Young's modulus E_i of the soil, the slope of the relationship corresponds to the value of the modulus exponent n . Therefore, a lower value of n than that determined from the triaxial tests is required for the finite element analyses of the IRW.

Stress distributions, obtained from a series of preliminary analyses using SOILSTRUCT-ALPHA, were compared to the results of the IRW test. Based on these comparisons, an apparent value of n , listed in Table 5-8, was determined for the analyses. No further adjustments were made to the value of n during the analyses.

It must be noted that this procedure for the determination of the value of n applies only to the case of the IRW or any other walls of similar height. In lock walls, backfill heights are typically larger than 12 m (40 ft) and the lateral stresses induced by the overburden exceed the stresses induced by compaction. Consequently, adjustment of the value of n is not necessary for SOILSTRUCT-ALPHA analyses of lock walls.

5.5.3.3 Estimation of the failure ratio R_f . Duncan et al. (1980) noted that the value of R_f does not vary significantly with relative density. This was confirmed by the results of the triaxial tests performed on the Density sand and Light Castle sand, as observed in Table 3-3. The value of R_f assigned to the compacted backfill for the analyses is the average of the R_f values determined from the laboratory tests. No further adjustments were made to this value during the analyses.

5.5.3.4 Estimation of the nominal Poisson's ratio ν_{nom} . The value of ν_{nom} for analysis cannot be estimated directly from the results of laboratory tests. The one-dimensional (1-D) column analysis procedure described by Ebeling and Wahl (1997) was used for a preliminary estimation of ν_{nom} . In the 1-D column procedure, finite element analyses of a column of backfill are performed. The column is free to deform in the vertical direction under the imposed loads but fully restrained in the horizontal direction. Compaction-induced stresses are not modeled in 1-D column analyses.

The 1-D column method does not provide accurate values of v_{nom} for analyses of the IRW because significant compaction-induced lateral stresses take place in walls of low height. Additionally, vertical shear forces on the wall-backfill interface are comparatively large. A range of tentative values of v_{nom} for analysis of the IRW is presented in Table 5-8. These values correspond to lateral loads in the 1-D column that are equal to or larger than the measured loads in the IRW. Adjustment of these tentative values of v_{nom} was required to account for compaction effects in the IRW. For lock walls, 1-D column analyses may provide v_{nom} values that are adequate for analysis because, due to the larger height of the lock walls, the effects of compaction on the magnitude of lateral stresses are not as significant as in the IRW.

5.5.3.5 Estimation of the unload-reload modulus K_{ur} . As discussed previously, the assumed response of the soil to unloading-reloading is linear and stress-dependent in SOILSTRUCT-ALPHA. It was assumed that a value of K_{ur} identical to the value of K may provide a reasonable approximation to the modulus value during hysteretic unload-reload cycles. The values of K and K_{ur} were adjusted simultaneously in the calibration analyses of the IRW.

5.5.3.6 Estimation of the friction angle ϕ' . There is a direct relationship between the value of ϕ_o and the relative density of the soil (Duncan et al. 1980). The value of ϕ_o of the compacted backfill was estimated by extrapolation from Figure 3-3. The extrapolated value of ϕ_o and the average value of $\Delta\phi$ were used to determine the internal friction angle of the backfill according to Equation 3-1. The magnitude of the confining stress σ'_3 used for calculation of ϕ' was the average of the horizontal stress measurements in the IRW test.

5.5.4 Near-field interface properties

Property values were determined for the interface between dense Light Castle sand and concrete as described in Chapter 4. Soil specimens for interface tests were prepared with relative densities of 80 percent; therefore, no direct experimental data are available on the interface properties corresponding to the Light Castle sand compacted to 100 percent of relative density.

There are no established criteria to predict the interface parameters based on the density of the soil. The results reported by Peterson et al. (1976) suggest that interface properties may or may not vary with relative density. In some cases, lower stiffness values were observed in dense specimens than in medium dense specimens of the same soil. In other cases, the variation in interface properties was not substantial for large changes in the soil void ratio.

Based on this information, the interface property values for the compacted backfill were assumed identical to those determined from the interface tests on the dense Light Castle sand against concrete interface. These values, listed in Table 5-9, were used for all the analyses without further adjustments.

As discussed previously, the earth pressure distribution on the wall calculated from finite element analyses differs from the pressures measured in the IRW. For the backfill, an adjusted value of n was determined as illustrated in Figure 5-12 to account for the effect of the pressure distribution on the value of the Young's modulus. Similar analyses can be performed to determine an adjusted value of n_f that accounts for the effect of the pressure distribution on the value of interface stiffness. However, sensitivity analyses showed that n_f has negligible influence on the magnitude of the forces acting on the wall. Consequently, the value of n_f determined from the interface tests was used for the analyses.

Table 5-9

Property Values of the Wall-Backfill Interface used for the Finite Element Analyses of the IRW

Parameter ¹	Value (Determined in Chapter 4)
K_i	20700
n_f	0.79
R_f	0.79
δ	33.7°

¹ Material parameters are listed and defined in the Notation (Appendix F) and Appendix B.

5.6 Calibration Analyses

A series of preliminary analyses were performed for the backfilling and surcharge stages of the IRW test. The purposes of these analyses were

- To adjust the tentative backfill parameter values determined from the laboratory tests on Light Castle sand specimens.
- To provide a reasonable approximation of the stresses existing in the wall-backfill system before the start of the inundation stage.

The values of horizontal and vertical forces F'_x and F_v , measured in the IRW at the end of compaction and at the end of surcharge, were the target values for the calibration analyses. The backfill property values were adjusted until the results of the analyses were approximately equal to the target values. The adjusted parameter values for the surcharge stage were used for the analysis of backfill inundation.

5.6.1 Analysis of backfilling

During the backfilling analyses, the target magnitudes of F_v and F'_x at the end of backfilling were attained by adjusting the values of modulus number K and nominal Poisson's ratio ν_{nom} . An increase in the value of K produces a decrease in vertical displacements in the backfill and, consequently, a decrease in the shear force at the wall-backfill interface. An increase in ν_{nom} produces an increase in the horizontal force magnitude. A trial-and-error process is necessary because changes in K and ν_{nom} also induce changes in F'_x and F_v , respectively.

Table 5-10
Backfill Property Values
Determined from Calibration
Analyses of Stage 1 of
the IRW Test

Property ¹	Value
K	1000
n	0.20
R_f	0.85
v_{nom}	0.36
K_{ur}	-
ϕ'	47°
γ	16.8 kN/m ³
¹ Material parameters are listed and defined in the Notation (Appendix F)	

Table 5-10 lists the property values determined from this iteration process. Figure 5-13 compares the measured and calculated values of F'_x and F_v .

The analysis showed that varying K and v_{nom} within their expected range of values listed in Table 5-8 produces large variations in the results of the analyses. Therefore, it is not possible to make first-order predictions of backfilling in the IRW using the property values obtained from laboratory tests. However, once the target values of the forces at the end of backfilling are attained, the results of the analysis for intermediate backfill heights are in excellent agreement with the test

data, as shown in Figure 5-13. This suggests that the procedures followed for the analyses are adequate, and that the models of soil and interface provide reasonable approximations to their actual response.

5.6.2 Analysis of surcharge application and removal

The analysis of the surcharge stage was performed consecutively after the backfilling analysis. Therefore, the initial forces acting on the wall before surcharge application corresponded to the values measured at the end of backfilling. The surcharge analyses were performed in two steps:

- The values of K and v_{nom} were adjusted during the analyses to match the target values of F_v and F'_x for full surcharge application.
- An analysis of surcharge removal was performed using the same parameter values determined in Step 1 and assuming a value of K_{ur} identical to the value of K .

The parameter values of the backfill determined from these analyses are listed in Table 5-11. It can be observed that a larger value of K is necessary to model surcharge application than to model backfilling. Conversely, a smaller value of v_{nom} is necessary to model surcharge application than to model backfilling. As discussed previously, the differences in the values of K and v_{nom} between backfilling and surcharge application are due to the existence of compaction effects during backfilling that are not modeled in SOILSTRUCT-ALPHA. The values of K and v_{nom} in Table 5-10 were selected to account for these compaction effects, and they are not representative of the properties of the compacted backfill. The soil property values listed in Table 5-11, on the other hand, are believed to be representative of the compacted backfill, and were used for the analysis of inundation described in the following section.

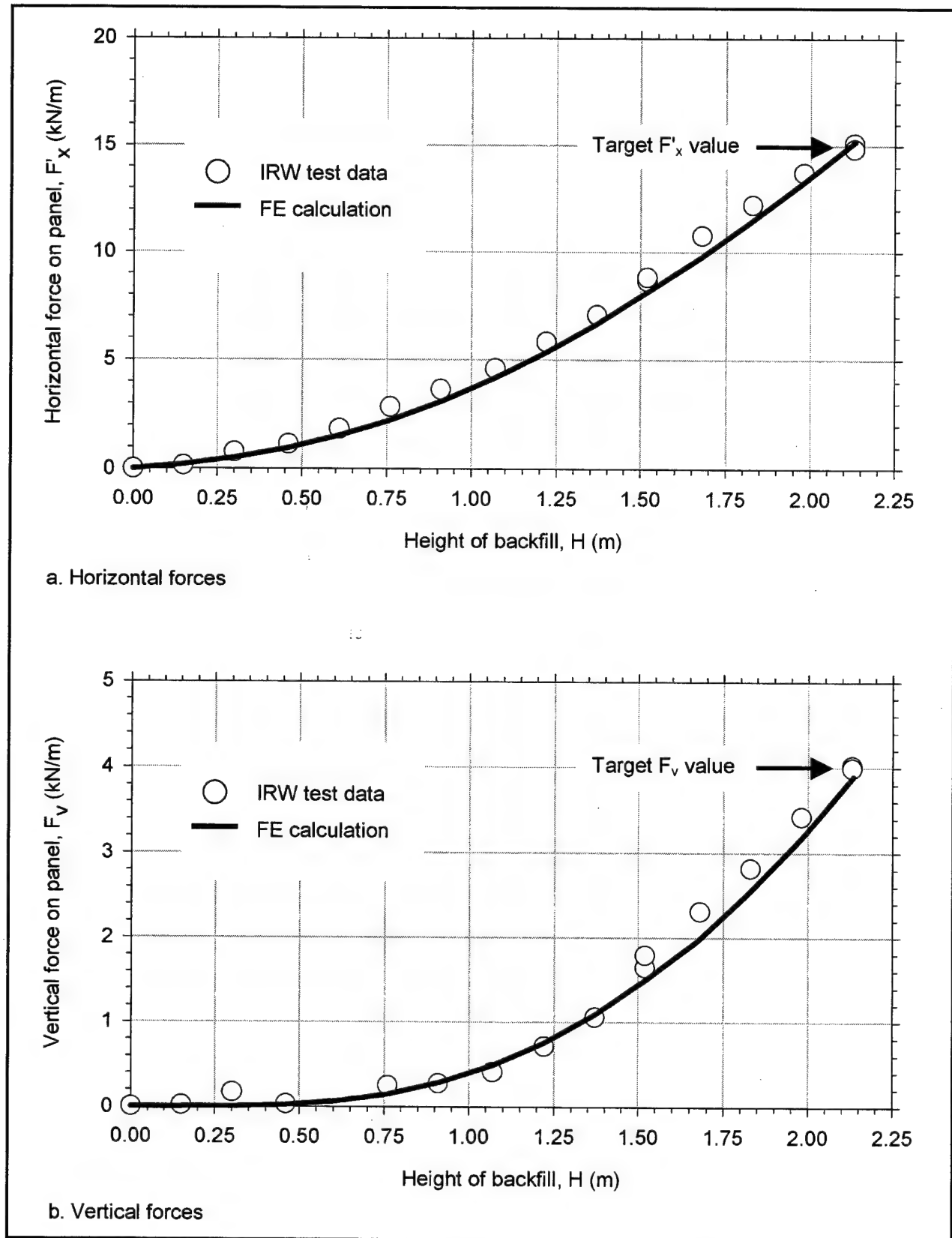


Figure 5-13. Results of calibration analyses of backfilling and comparison of IRW test data

The value of K obtained from these analyses is larger than the expected value from the laboratory tests. This may be due to the following:

- a. The laboratory specimens were prepared by pluviation, whereas the backfill was compacted by vibration. The difference in the preparation procedures may account for differences between the properties of the laboratory specimens and the compacted backfill.
- b. Compaction stresses applied to each lift induce preloading of the backfill. Because the height of the IRW is relatively small, it is possible that these preloading stresses are not exceeded throughout the soil mass during subsequent application of the surcharge. Consequently, surcharge application may correspond to reloading and induce a stiffer backfill response, especially at shallow depths.

Table 5-11
Backfill Property Values
Determined from
Calibration Analyses
of Stage 2 of the IRW Test

Property ¹	Value
K	2500
n	0.20
R_f	0.85
v_{nom}	-0.06
K_{ur}	2500
ϕ'	47°
γ	16.8 kN/m ³

¹ Material parameters are listed and defined in the Notation (Appendix F).

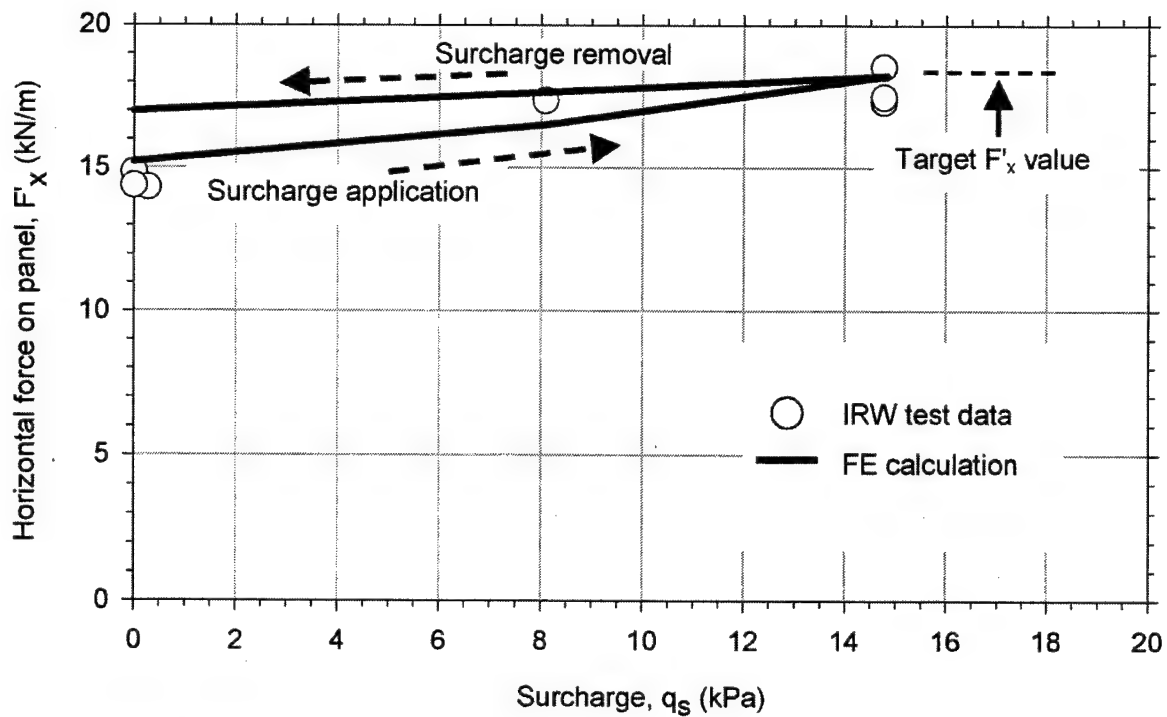
The value of v_{nom} is negative. It must be recalled that v_{nom} does not have direct physical meaning. Considering an average stress level of the backfill of 0.23, determined from the analyses, and using Equation 5-12, an average value of the Poisson's ratio ν of 0.14 is obtained.

Figure 5-14 compares the measured and calculated values of F'_x and F_v . In the finite element analyses, the initial values of F'_x and F_v are different from the residual values after removal of the surcharge because the responses of the backfill and the interface are different during primary loading from those during unloading. Due to the scatter of the test data, it is unclear if this aspect of the analyses is representative of the actual response of the wall-backfill system.

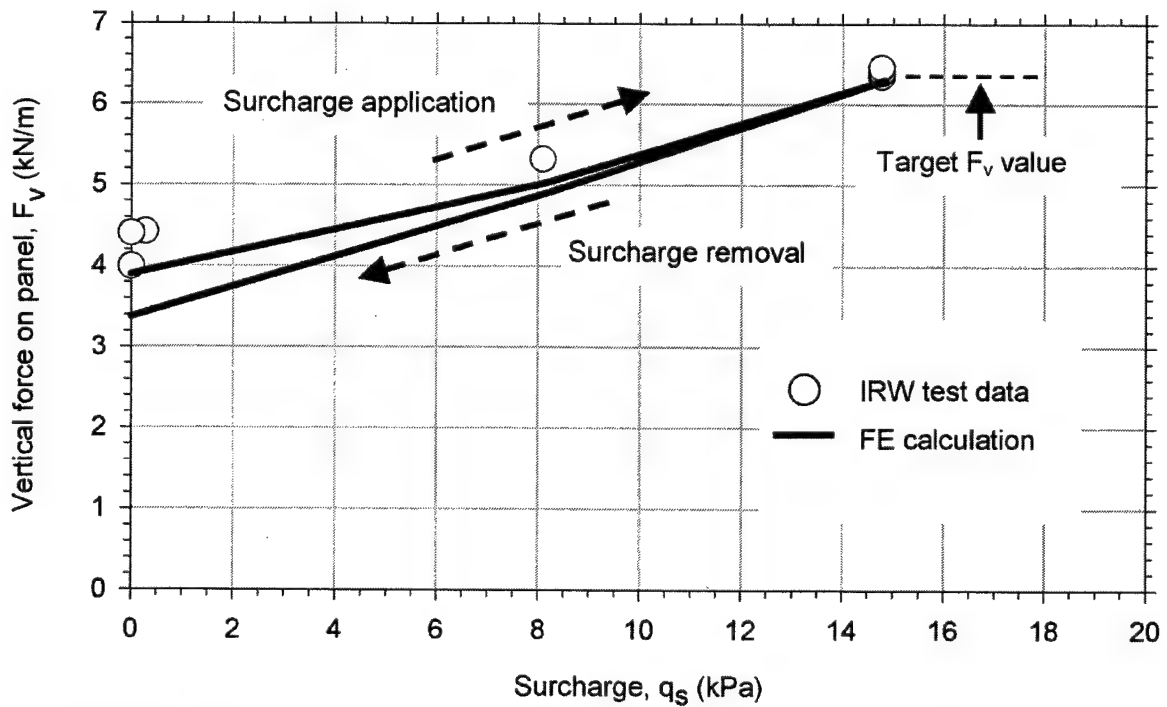
5.7 Analysis of Backfill Inundation

An analysis was performed of the inundation stage of the IRW test consecutively after the analysis of backfilling and surcharge described in the previous section. The backfill property values listed in Table 5-11 were used for the analysis. The rise of the water level from the bottom to the top elevation of the wall was modeled in 14 incremental steps.

The results of the analyses are represented graphically in Figure 5-15 and compared to the test data. The analysis provides a very good approximation to the values of F'_x and F_v measured during the test. Three important conclusions can be made from the analysis results:

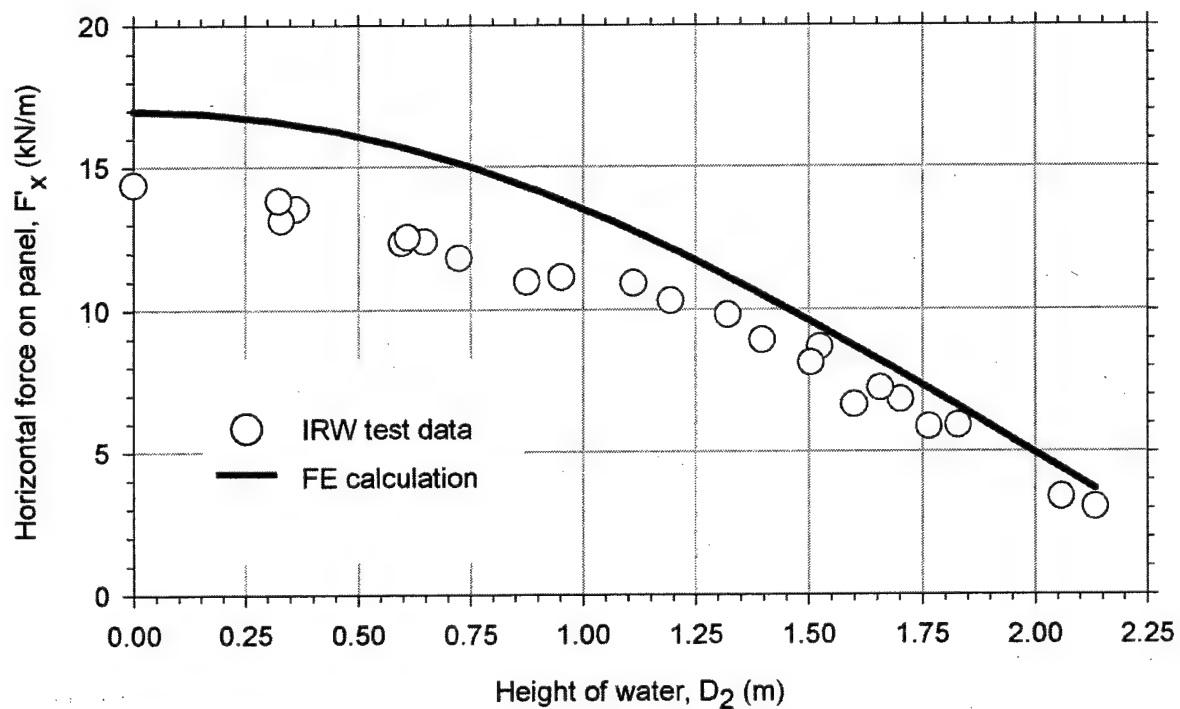


a. Horizontal forces

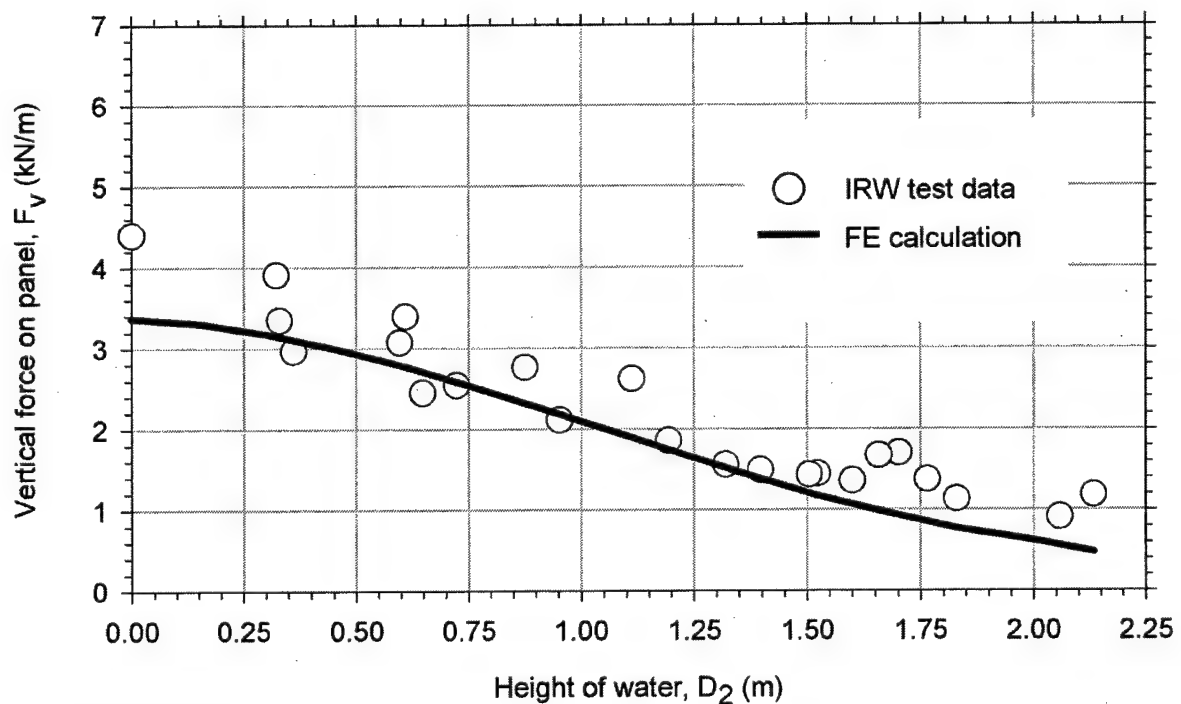


b. Vertical forces

Figure 5-14. Results of calibration analyses of surcharge and comparison to IRW test data



a. Horizontal forces



b. Vertical forces

Figure 5-15. Results of finite element analyses of inundation and comparison to IRW test data

- a. The implementation of the extended hyperbolic model in SOILSTRUCT-ALPHA was successful.
- b. The soil and interface models used in the analyses are accurate for the type of loading that takes place during inundation of the IRW backfill.
- c. It may be inferred that the interface model may be accurate for analyses of actual lock walls of greater height. Therefore, use of the interface model for lock wall analyses is recommended for further validation of its accuracy and advantages.

5.8 Summary and Conclusions

A pilot-scale test was performed in the IRW to simulate construction and operation of a lock wall. The test was carried out in three stages: backfilling, surcharge application, and backfill inundation. Light Castle sand was used as backfill material for the test. The properties of the backfill and of the wall-backfill interface were estimated from the results of the laboratory tests described in Chapter 3.

The IRW was not originally designed for surcharge application and inundation of the backfill. Consequently, preparations were necessary to accommodate the intended simulation. To allow full inundation of the backfill, a wooden bulkhead was designed and constructed at the bottom of the access ramp. A sealant was applied to all the gaps existing between the instrumented panels, between the panels and the floor, and along the edges of the bulkhead to prevent significant leaks during inundation of the backfill. Two perforated polyvinyl chloride pipes were installed for inundation and drainage of the backfill. A soil box was prepared to contain the soil used as surcharge. Before the start of the test, all the instruments were calibrated in situ and a data acquisition system was installed in the IRW.

The test results show that a significant vertical shear force develops at the wall-backfill interface during placement and compaction of the backfill. This shear force increases significantly during surcharge application, and decreases during inundation of the backfill. However, it was observed that the final magnitude of the vertical shear force at the end of the test, after drainage of the backfill, was similar to the shear force at the end of backfilling. This suggests that there is no significant degradation of the vertical shear force with cycles of surcharge application and backfill inundation.

The vertical shear force coefficient K_v was calculated from the vertical force measurements during backfilling. It was found that it increases with increasing backfill height. The measured values of K_v are greater than the values predicted using the design line recommended in Appendix F of Engineer Manual 1110-2-2100 (HQUSACE, in preparation). This is a result of the conservatism employed in establishing the design line and the relatively large effect of compaction-induced stresses in short walls such as the IRW. It is not recommended here that the K_v values given by the design line be exceeded for design of lock walls.

The vertical shear force coefficient for surcharge $K_{v,q}$ was determined from the test measurements from the surcharge application stage. It was found that the design line (Appendix F of Engineer Manual 1110-2-2100 (HQUSACE, in preparation)) provides a slightly conservative approximation to the measured $K_{v,q}$ value.

The correction factor C_{wt} for determining the vertical shear force coefficient during inundation was determined from the vertical force measurements during inundation and drainage of the backfill. It was found that the design line (Appendix F of Engineer Manual 1110-2-2100 (HQUSACE, in preparation)) provides a good approximation of the C_{wt} value for water-to-wall height ratios D_2/H that are less than 0.5. For larger ratios, the design values are conservative.

Compaction-induced stresses are significant in the IRW because of its short height. Because the influence of compaction on the stresses decreases with increasing wall heights, accurate finite element analyses of lock walls do not commonly require modeling the stresses applied during compaction. However, for the finite element analyses of the IRW, it is important to account for these compaction effects.

The finite element analyses of the IRW were performed using the updated version of SOILSTRUCT-ALPHA, which contains the extended hyperbolic model for interfaces. For finite element analyses of the IRW, different properties were assigned to the backfill during backfilling than were assigned during surcharge application. For the backfilling analysis, a lower modulus and larger Poisson's ratio than suggested by laboratory test data were assumed, which provided appropriate vertical and horizontal stresses at the wall-backfill interface. For the surcharge placement analysis, a stiffer backfill with a reduced Poisson's ratio were assumed. The properties of the backfill were adjusted by trial and error until the analysis results matched the target values of F_v and F'_x measured in the IRW at the end of compaction and surcharge application. It was found that, once a match to the target F_v and F'_x values was obtained from the analyses, the analysis results for intermediate stages also matched the test data. This suggests that the procedures followed for the analyses are adequate, and that the models of soil and interface provide reasonable approximations to their actual response.

A finite element analysis of backfill inundation was performed using the backfill properties determined from the calibration analysis of surcharge placement. The analysis provides a very good approximation to the values of F'_x and F_v measured during the test. It can be concluded that the implementation of the extended hyperbolic model in SOILSTRUCT-ALPHA was successful, and that the soil and interface models used in the analyses are accurate for inundation analyses of the IRW. It may be inferred that the model may be accurate for analyses of actual lock walls of greater height. Therefore, use of the model for lock wall analyses is recommended for further validation of its accuracy and advantages.

6 Summary and Conclusions

An earth retaining structure such as a lock wall may be subjected to a significant downdrag force generated during placement of the backfill. This downdrag force has a stabilizing effect that could produce a substantially more economical design if accounted for in the design of the wall. Accurate estimation of the downdrag force requires use of an appropriate model for the interface between the backfill and the wall. The model must provide accurate predictions of the interface response to the type of loading applied during placement of the backfill, inundation of the lock, and subsequent operational stages.

The hyperbolic formulation developed by Clough and Duncan (1971) has been used extensively in soil-structure interaction (SSI) analyses for modeling the interface response under monotonic loading. However, it is not applicable to cases where the interface undergoes unloading-reloading or simultaneous changes in shear and normal stresses such as in the backfill-to-structure interface in lock walls. An extended hyperbolic model was developed during this investigation that can predict the interface response to simultaneous changes in shear and normal stresses as well as unloading-reloading and staged shear.

The accuracy of the model was evaluated against the results of interface tests performed for this investigation. In addition, the model was implemented in the finite element program SOILSTRUCT-ALPHA. A pilot-scale test was performed at the Instrumented Retaining Wall (IRW) at Virginia Tech to simulate backfilling, application and removal of surcharge, and changes in the elevation of the water table behind a lock wall. Finite element analyses of all the stages of the test were performed using SOILSTRUCT-ALPHA. Comparisons between the test measurements and the results of the finite element analyses indicate that the extended hyperbolic model provides accurate approximations of the interface response.

This chapter summarizes the activities performed and the conclusions from this investigation. The advantages and limitations of the extended hyperbolic model are presented, as well as recommendations regarding future work on interface modeling for lock wall analyses.

6.1 Summary of Activities

This section summarizes all the activities completed for this investigation: literature review, laboratory testing, the extended hyperbolic model, and lock wall simulation.

6.1.1 Literature review

The literature review (Chapter 2) focused on interface testing, interface modeling, and SSI analyses of retaining walls.

In the experimental work reviewed, the direct shear box (DSB) and the direct simple shear (DSS) are the devices most frequently used for testing sand-to-concrete and sand-to-steel interfaces. Most of the previous work on interfaces investigated monotonic shear of the interface under constant normal stress. Some investigations have been published concerning cyclic shear of interfaces under conditions of constant normal stress or constant normal stiffness. No previous studies of interface response under staged shear were found in the literature.

All of the interface testing devices described in the literature present limitations. The interface sizes are limited and do not allow the determination of the residual interface strength in all cases. In addition, end effects may be present, inducing errors in the measurement of the pre-peak and peak interface response. The Large Direct Shear Box (LDSB) at Virginia Tech allows testing of interfaces as large as 711 mm by 406 mm under monotonic or cyclic shear. The size of the interface minimizes end effects and permits maximum interface displacements of 305 mm, allowing the determination of the residual interface strength. The large displacement capabilities of the LDSB also make possible shearing of the interface in several stages with changing normal stress.

Two types of elements are commonly implemented for modeling interfaces: the joint element and the thin layer element. The joint element, developed by Goodman, Taylor, and Brekke (1968), appears to be used most frequently due to the simplicity of its formulation.

Several models of interface response under shearing have been described in the literature. The hyperbolic formulation by Clough and Duncan (1971) was described in detail in Chapter 2. It has been widely used for modeling the interface response to monotonic shear under constant normal stress. It is a simple model that incorporates the most important aspects of interface behavior using parameters that have physical meaning. However, the Clough and Duncan (1971) hyperbolic formulation was not developed to model interface response under cyclic loading or staged shear. None of the other interface models found in this literature review accounts for simultaneous changes in shear and normal stresses.

Several studies have been published concerning SSI analyses of retaining structures. From these studies, it may be concluded that the downdrag force acting on the back of a retaining wall can contribute significantly to the stability of the

structure. In typical lock walls, the downdrag develops during fill placement. During this stage, the shear and normal stresses acting on the backfill-to-structure interface are changing simultaneously. During submergence and operation of the lock, the shear stresses may be reduced or even reversed. Hence, it is important to model accurately the interface response under staged shear, unloading-reloading, and shear reversals.

A detailed description of a simplified method (Appendix F of Engineer Manual 1110-2-2100 (HQUSACE, in preparation) to estimate the downdrag force was presented in Chapter 2. It is based on a number of SSI analyses of typical lock structures. The simplified method is useful to illustrate the importance of an adequate estimation of the downdrag force in design.

6.1.2 Laboratory testing

The following laboratory and field activities (Chapter 3) were performed for this investigation:

- a.* Modifications to the LDSB.
- b.* Selection of sand specimens for interface testing.
- c.* Grain size distribution, minimum/maximum density, specific gravity, consolidation testing, and triaxial testing on the Density sand and Light Castle sand.
- d.* Field survey of existing concrete retaining walls to determine a range of representative surface textures for the concrete specimen.
- e.* Design and construction of a soil box and concrete slab.
- f.* Development of appropriate testing procedures.
- g.* Interface tests following a variety of laboratory stress paths to investigate the constitutive behavior of interfaces and to determine the interface response under field conditions for lock walls.

The LDSB was modified specifically to accommodate soil-to-concrete interface testing for this investigation. A special aluminum soil box was designed and constructed that allows compaction of the sand sample directly onto the concrete specimen and minimizes the disturbance of the interface during test setup operations.

A field survey of concrete walls was performed. A concrete specimen was prepared with surface features similar to those observed in the field. The concrete specimen was contained in a frame, which was designed and constructed to act as an external reinforcement for the concrete and to minimize its deformations during interface shear.

A fine, rounded, silica sand (Density sand), and a fine, angular sand (Light Castle sand) were selected for interface testing. A series of basic laboratory tests,

such as minimum/maximum density and grain size analyses, were performed on these sands. Consolidation and CD triaxial tests were also performed to determine sets of hyperbolic parameter values for these soils for a range of relative densities representative of the backfill in lock walls.

An interface testing program was carried out that included initial loading tests, staged shear tests, unload-reload tests, and multidirectional stress path tests. Three types of interfaces were tested: dense Density sand against concrete, medium-dense Density sand against concrete, and dense Light Castle sand against concrete.

From the results of the interface tests, it was found that the average ratio between the values of interface friction angle and internal friction angle of the soil was 0.8. Displacement softening was observed in all tests. The displacements required for the development of the residual condition were as large as 20 mm.

Staged shear tests were performed by increasing the normal pressure in steps during shear. The staged shear tests provided important information about the behavior of sand-to-concrete interfaces and were used to define the yield surfaces implemented in the extended hyperbolic model. It was found that it is possible to determine a complete residual strength envelope from staged shear tests, as long as the displacement capability of the equipment is enough for the development of the residual condition.

Several unload-reload tests were performed during which a complete loading cycle was applied between two predetermined stress levels. These tests follow stress paths similar to field stress paths in which the shear stresses may decrease as a consequence of a rise of the water table behind a lock wall. A substantial increase in the interface shear stiffness was observed during unloading and reloading. It was observed that compression takes place during unloading, followed by dilation during subsequent reloading of the interface. In some tests, one or more cycles of shear were performed upon mobilization of the residual strength. Similar shear stress-displacement response and residual strength values were obtained for both directions of shear in all tests.

Multidirectional stress path tests were performed on all three types of interfaces. The purpose of these tests was to provide a basis for a performance evaluation of the extended hyperbolic model under complicated loading paths. They also modeled certain aspects of the type of loading expected at the backfill-structure interface during backfill placement and operation of a lock wall. The extended hyperbolic model was validated against the results of these tests.

6.1.3 Extended hyperbolic model

An extended hyperbolic model for interfaces was developed during this investigation (Chapter 4). The model captures important aspects of interface response under the type of loading expected to occur in a wall-backfill interface. The material parameters required for implementation of the model are the same as those introduced by Clough and Duncan (1971).

A procedure for normalization of interface test data was developed that facilitated the study of interface response under a variety of experimental stress paths. Based on this study, the concepts of yield surfaces and loading regions were introduced. Two yield surfaces are defined by the past maximum and past minimum stress levels during shear. Two transition surfaces are defined by the past-maximum and past-minimum shear stresses on the interface.

Three types of loading are considered in the extended hyperbolic model: yield-inducing shear, unloading-reloading, and transition loading (Table 4-1). Yield-inducing shear occurs if the stress path reaches one of the yield surfaces. Transition loading in the first quadrant of the τ - σ_n plane occurs if the stress level is lower than the past maximum stress level and the shear stress is equal to or greater than the past maximum shear stress. Conversely, transition loading in the fourth quadrant occurs if the stress level is greater than the past minimum stress level and the shear stress is equal to or lower than the past minimum shear stress. Unloading-reloading takes place if the stress level is lower than the past maximum stress level and greater than the past minimum stress level, and if the shear stress is lower than the past maximum shear stress and greater than the past minimum shear stress.

A formulation for yield-inducing shear was developed in which the interface stiffness is determined by the normal stress, the stress level, and the rate of change of the normal stresses during shear, i.e., the inclination of the stress path. The formulation was found to predict the interface response accurately under a variety of experimental, yield-inducing stress paths.

For unloading-reloading or transition loading, one of three versions of the model can be applied, depending on the accuracy required for the analysis. In Version I, a linear, normal stress-dependent response of the interface is assumed both for unloading-reloading and for transition loading. This version does not model the hysteretic response of the interface under unloading-reloading. Comparisons of the calculated interface response with test data showed that this version may provide reasonable predictions of the interface response for unloading-reloading cycles that are not too large. It is inaccurate for modeling the interface response to large unload-reload loops or interfaces subjected predominantly to transition loading. Version I is the simplest to implement and use in SSI analyses.

In Version II, a nonlinear, hyperbolic response is assumed for unloading-reloading and transition loading that accurately models the hysteretic behavior of interfaces subjected to large unload-reload loops. It provides accurate or reasonable estimates of interface response for most of the experimental stress paths considered in this investigation. However, it does not provide accurate estimates for cases in which the interface is subjected predominantly to transition loading. Although the formulation of Version II introduces some additional state variables, it is simple to implement in SSI analyses of retaining walls.

In Version III, the interface stiffness for unloading-reloading is determined in the same way as in Version II. For transition loading, on the other hand, the interface stiffness is determined by interpolation from the normalized stiffness diagram. Two normalized stiffness values are used for the interpolation: the

normalized stiffness of the interface at the onset of transition loading and the normalized stiffness at yield. This version provides the most accurate estimates of interface response for all the experimental stress paths considered. It is particularly useful for cases where the interface is subjected predominantly to staged shear. Version III is the most difficult to implement in SSI analyses because it introduces several additional state variables with respect to the other two versions.

The principal advantages of the extended hyperbolic model are as follows:

- a. It has a simple mathematical formulation.
- b. Hyperbolic parameter values for different types of interfaces are available in the literature.
- c. It captures the main features of the interface response under simultaneous changes in shear and normal stress and unloading-reloading.
- d. It provides accurate estimates of the interface response for the experimental stress paths considered in this investigation.
- e. It is relatively easy to implement in SSI analyses.
- f. It establishes a framework for future work on plasticity-based interface models.

The formulations for yield-inducing shear and for unloading-reloading Version II of the extended hyperbolic model were implemented in the finite element program SOILSTRUCT-ALPHA, which is commonly used by the U.S. Army Corps of Engineers for analyses of lock walls. Finite element analyses of the IRW lock wall simulation suggest that these formulations are effective for prediction of vertical shear forces in retaining structures.

The model has several limitations:

- a. It does not model displacements normal to the interface, and the interface thickness is implicitly assumed as zero. Consequently, in finite element analyses, a large normal stiffness must be assigned to interface elements in order to minimize overlapping of adjacent two-dimensional elements. In addition, it cannot model the generation of normal stresses due to restrained dilation of the interface during shear between two stiff, rough media. This may not be important for analyses of stiff retaining structures that have relatively compressible backfills.
- b. It does not model displacement softening of the interface. According to the experimental data collected during this investigation, displacement softening may take place in interfaces subjected to relative displacements of 6 to 20 mm. Therefore, in cases where larger magnitudes of interface displacement take place, the model cannot provide accurate predictions of the softening response.
- c. The model predicts interface stiffness values that are zero or negative for certain loading combinations. For implementation of the model in finite

element programs, it is then necessary to use appropriate stiffness values and adequate numerical procedures to prevent numerical problems. It is believed that the model predictions for these cases are correct. However, if finite element analyses of lock walls show that these types of loading are common, it may be necessary to perform additional experimental work to verify the model predictions.

As discussed in Chapter 5, the model was used successfully for the estimation of vertical shear forces in the IRW lock wall simulation. However, it has not yet been used for routine analyses of actual lock walls.

6.1.4 Lock wall simulation

A pilot-scale test was performed in the IRW to simulate construction and operation of a lock wall (Chapter 5). The test was carried out in three stages: backfilling, surcharge application, and backfill inundation. Light Castle sand was used as backfill material for the test.

The IRW was not originally designed for surcharge application and inundation of the backfill. Consequently, preparations were necessary to accommodate the intended simulation. To allow full inundation of the backfill, a wooden bulkhead was designed and constructed at the bottom of the access ramp and all the gaps between the instrumented panels were sealed. Two perforated polyvinyl chloride pipes were installed for inundation and drainage of the backfill. A soil box was prepared to contain the soil used as surcharge. Before the start of the test, all the instruments were calibrated in situ and a data acquisition system was installed in the IRW.

The test results show that a significant vertical shear force develops at the wall-backfill interface during placement and compaction of the backfill. This shear force increases significantly during surcharge application, and decreases during inundation of the backfill. However, it was observed that the final magnitude of the vertical shear force at the end of the test, after drainage of the backfill, was similar to the shear force at the end of backfilling. This suggests that there is not a significant degradation of the vertical shear force with cycles of surcharge application and backfill inundation.

The vertical shear force coefficient K_v was calculated from the vertical force measurements during backfilling. It was found to increase with increasing backfill height. The measured values of K_v are greater than the values predicted using the design line recommended in Appendix F of Engineer Manual 1110-2-2100 (HQUSACE, in preparation). This is a result of the conservatism employed in establishing the design line and the relatively large effect of compaction-induced stresses in short walls such as the IRW. It is not recommended here that the K_v values given by the design line be exceeded for design of lock walls.

The vertical shear force coefficient for surcharge $K_{v,q}$ was determined from the test measurements from the surcharge application stage. It was found that the design line (Appendix F of Engineer Manual 1110-2-2100 (HQUSACE, in

preparation)) provides a slightly conservative approximation of the measured $K_{v,q}$ value.

The correction factor C_{wt} for determination of the vertical shear force coefficient during inundation was determined from the vertical force measurements during inundation and drainage of the backfill. It was found that the design line (Appendix F of Engineer Manual 1110-2-2100 (HQUSACE, in preparation)) provides a good approximation of the C_{wt} value for water-to-wall height ratios D_2/H less than 0.5. For larger ratios, the design values are conservative.

Compaction-induced stresses are significant in the IRW because of its short height. Because the influence of compaction on the stresses decreases with increasing wall heights, accurate finite element analyses of lock walls do not commonly require modeling the stresses applied during compaction. However, for the finite element analyses of the IRW, it is important to account for these compaction effects.

The finite element analyses of the IRW were performed using the updated version of SOILSTRUCT-ALPHA, which contains the extended hyperbolic model for interfaces. For finite element analyses of the IRW, different properties were assigned to the backfill during backfilling than were assigned during surcharge application. For the backfilling analysis, a lower modulus and larger Poisson's ratio than suggested by laboratory test data were assumed, which provided appropriate vertical and horizontal stresses at the wall-backfill interface. For the surcharge placement analysis, a stiffer backfill and a reduced Poisson's ratio were assumed. The properties of the backfill were adjusted by trial and error until the analysis results matched the target values of F_v and F'_x measured in the IRW at the end of compaction and surcharge application. It was found that, once a match to the target F_v and F'_x values was obtained from the analyses, the analysis results for intermediate stages also matched the test data. This suggests that the procedures followed for the analyses are adequate, and that the models of the soil and interface provide reasonable approximations to their actual response.

A finite element analysis of backfill inundation was performed using the backfill properties determined from the calibration analysis of surcharge placement. The analysis provided a very good approximation to the values of F'_x and F_v measured during the test. It can be concluded that the implementation of the extended hyperbolic model in SOILSTRUCT-ALPHA was successful, and that the soil and interface models used in the analyses are accurate for inundation analyses of the IRW. It may be inferred that the model may be accurate for analyses of actual lock walls of greater height. Therefore, use of the model for lock wall analyses is recommended for further validation of its accuracy and usefulness.

6.2 Recommendations for Future Work

According to the findings from this investigation, the following recommendations are presented for future work on interface modeling and SSI analyses of lock walls:

- a. It is recommended that the updated version of the program SOILSTRUCT-ALPHA be used for analyses of lock walls to further verify the applicability of the extended hyperbolic model for interfaces. Such analyses would also serve to detect numerical problems, if any, arising from the implementation of the extended hyperbolic model in SOILSTRUCT-ALPHA.
- b. The relative significance of Versions I, II, and III could be assessed by adding Versions I and III to SOILSTRUCT-ALPHA and then comparing the results of analyses of lock walls.
- c. The extended hyperbolic model does not account for displacement softening of interfaces. If peak strengths are used in cases where displacement softening takes place at the wall-backfill interface, SOILSTRUCT-ALPHA analyses may overestimate the magnitude of the downdrag force. It is therefore recommended to calculate the range of relative displacement magnitudes at the interface between backfill and interface from the results of SOILSTRUCT-ALPHA analyses of typical lock walls with varying foundation conditions. Such analyses may reveal the type of lock wall configurations where displacement softening behavior of the wall-backfill interface needs to be modelled to obtain accurate estimates of downdrag forces. According to the results of the interface tests performed during this investigation, displacement softening may occur after relative displacements of 5 to 20 mm at the interface. Alternatively, residual interface strengths could be used to produce a conservative analysis.
- d. The extended hyperbolic formulation does not model displacements normal to the interface. According to the results from the interface tests performed, dilation takes place at the interface between sand and concrete. Although the model provides accurate estimates of the interface response to simultaneous changes in normal and shear stresses, it cannot predict changes in normal stresses during shear induced by restrained dilation of the interface. Restrained dilation of interfaces is known to occur in rock joints, and rock joint models have been developed that allow the calculation of normal stress changes induced by this phenomenon. However, it is not known whether restrained dilation can occur at a wall-backfill interface. Relatively simple finite element analyses can be performed using SOILSTRUCT-ALPHA to estimate the magnitude of changes in normal stress at the wall-backfill interface due to dilation, and the results can be used to evaluate the importance of these normal stress changes for design of lock walls.
- e. If interface dilation is found to be an important issue for design of lock walls or other Corps of Engineers structures, it may be convenient to

develop a new interface element formulation for use in finite element analyses. This new formulation could incorporate features of the extended hyperbolic model and account for coupled tangential and normal displacements. The formulation of the thin layer interface element developed by Desai et al. (1984) could be a convenient starting point for the development of such a coupled interface model.

References

- Acar, Y. B., Durgunoglu, H. T., and Tumay, M. T. (1982). "Interface properties of sand," *Journal of the Soil Mechanics and Foundations Division*, ASCE, 108(GT4), 648-654.
- American Society for Testing and Materials. (1990). "Standard test method for classification of soils for engineering purposes," Practice No. D2487-90, *1990 Book of ASTM Standards*, 04.08, Philadelphia, PA.
- _____. (1991). "Standard test method for minimum index density and unit weight of soils and calculation of relative density," ASTM D4254-91, West Conshohocken, PA.
- _____. (1992). "Standard test method for specific gravity of soils," ASTM D854-92, West Conshohocken, PA.
- _____. (1993a). "Standard classification of soils for engineering purposes (Unified Soil Classification System)," ASTM D2487-93, West Conshohocken, PA.
- _____. (1993b). "Standard practice for description and identification of soils (visual-manual procedure)," ASTM D2488-93, West Conshohocken, PA.
- _____. (1993c). "Standard test method for maximum index density and unit weight of soils using a vibratory table," ASTM D4253-93, West Conshohocken, PA.
- Bosscher, P. J., and Ortiz, C. (1987). "Frictional properties between sand and various construction materials," *Journal of Geotechnical Engineering*, ASCE, 113(9), 1035-1039.
- Brandon, T. L., Duncan, J. M., and Gardner, W. S. (1990). "Hydrocompression settlement of deep fills," *Journal of Geotechnical Engineering*, ASCE, 116(10), 1536-1548.
- Brummund, N. F., and Leonards, G. A. (1973). "Experimental study of static and dynamic friction between sand and typical construction materials," *Journal of Testing and Evaluation*, ASTM, 1(2), 162-165.

- Clough, G. W., and Duncan, J. M. (1969). "Finite element analyses of Port Allen and Old River Locks," Report No. TE-69-3, U.S. Army Engineer Waterways Experiment Station, Vicksburg, MS.
- Clough, G. W., and Duncan, J. M. (1971). "Finite element analyses of retaining wall behavior," *Journal of the Soil Mechanics and Foundations Division*, ASCE, 97(SM12), 1657-1673.
- Desai, C. S., and Rigby, D. B. (1997). "Cyclic interface and joint shear device including pore pressure effects," *Journal of Geotechnical and Geoenvironmental Engineering* 123(6), 568-579.
- Desai, C. S., Drumm, E. C., and Zaman, M. M. (1985). "Cyclic testing and modeling of interfaces," *Journal of Geotechnical Engineering*, ASCE, 111(6), 793-815.
- Desai, C. S., Muqtadir, A., and Scheele, F. (1986). "Interaction analyses of anchor-soil systems," *Journal of Geotechnical Engineering*, ASCE, 112(5), 537-553.
- Desai, C. S., Zaman, M. M., Lightner, J. G., and Siriwardane, H. J. (1984). "Thin-layer elements for interfaces and joints," *International Journal for Numerical and Analytical Methods in Geomechanics* 8(1), 19-43.
- Duncan, J. M., and Chang, C. Y. (1970). "Nonlinear analysis of stress and strain in soils," *Journal of the Soil Mechanics and Foundations Division*, ASCE, 96(SM5), 1629-1653.
- Duncan, J. M., and Clough, G. W. (1971). "Finite element analyses of Port Allen Lock," *Journal of the Soil Mechanics and Foundations Division*, ASCE, 97(SM8), 1053-1067.
- Duncan, J. M., Byrne, P., Wong, K. S., and Mabry, P. (1980). "Strength, stress-strain and bulk modulus parameters for finite element analyses of stresses and movements in soil masses," Report No. UCB/GT/80-01, Department of Civil Engineering, University of California, Berkeley.
- Duncan, J. M., Williams, G. W., Sehn, A. L., Seed, R. B. (1991). "Estimation earth pressures due to compaction," *Journal of Geotechnical Engineering* 117(12), 1833-1847.
- Ebeling, R. M., and Filz, G. M. "Soil-structure interaction analyses of rock founded gravity and cantilevered walls" (in preparation), U.S. Army Engineer Research and Development Center, Vicksburg, MS.
- Ebeling, R. M., and Mosher, R. L. (1996). "Red River U-Frame Lock No. 1 backfill-structure-foundation interaction," *ASCE Journal of Geotechnical Engineering* 122(3), 216-225.

- Ebeling, R. M., and Wahl, R. E. (1997). "Soil-structure-foundation interaction analysis of new roller-compacted concrete North Lock Wall at McAlpine Locks," Technical Report ITL-97-5, U.S. Army Engineer Waterways Experiment Station, Vicksburg, MS.
- Ebeling, R. M., Duncan, J. M., and Clough, G. W. (1990). "Methods of evaluating the stability and safety of gravity earth-retaining structures founded on rock - Phase 2 study," Technical Report ITL-90-7, U.S. Army Engineer Waterways Experiment Station, Vicksburg, MS.
- Ebeling, R. M., Pace, M. E., and Morrison, E. E. (1997). "Evaluating the stability of existing massive concrete gravity structures founded on rock," Technical Report REMR-CS-54, U.S. Army Engineer Waterways Experiment Station, Vicksburg, MS.
- Ebeling, R. M., Peters, J. F., and Clough, G. W. (1992). "User's guide for the incremental construction soil-structure interaction program SOILSTRUCT," Technical Report ITL-90-6, U.S. Army Engineer Waterways Experiment Station, Vicksburg, MS.
- Ebeling, R. M., Peters, J. F., and Mosher, R. L. (1997). "The role of non-linear deformation analyses in the design of a reinforced soil berm at Red River U-Frame Lock No. 1," *International Journal for Numerical and Analytical methods in Geomechanics* 21, 753-787.
- Ebeling, R. M., Clough, G. W., Duncan, J. M., and Brandon, T. L. (1992). "Methods for evaluating the stability and safety of gravity earth retaining structures founded on rock," Technical Report REMR-CS-29, U.S. Army Engineer Waterways Experiment Station, Vicksburg, MS.
- Ebeling, R. M., Mosher, R. L., Abraham, K., and Peters, J. F. (1993). "Soil-structure interaction study of Red River Lock and Dam No. 1 subjected to sediment loading," Technical Report ITL-93-3, U.S. Army Engineer Waterways Experiment Station, Vicksburg, MS.
- Esterhuizen, J. J. (1997). "Progressive failure of slopes in lined waste impoundments," Ph.D. Diss., Geotechnical Engineering Division, Department of Civil Engineering, Virginia Polytechnic Institute and State University, Blacksburg.
- Evgin, E., and Fakharian, K. (1996). "Effect of stress paths on the behaviour of sand-steel interfaces," *Canadian Geotechnical Journal* 33(6), 853-865.
- Fakharian, K., and Evgin, E. (1995). "Simple shear versus direct shear tests on interfaces during cyclic loading." *Proceedings Third International Conference on Recent Advances in Geotechnical Earthquake Engineering and Soil Dynamics*, St. Louis, MO, April 2-7, 1995. S. Prakash, ed., University of Missouri at Rolla, III, 13-16.

- Fakharian, K., and Evgin, E. (1996). "An automated apparatus for three-dimensional monotonic and cyclic testing of interfaces," *Geotechnical Testing Journal* 19(1), 22-31.
- _____. (1997). "Cyclic simple-shear behavior of sand-steel interfaces under constant normal stiffness condition," *Journal of Geotechnical and Geoenvironmental Engineering* 123(12), 1096-1105.
- Filz, G. M. (1992). "An analytic and experimental study of earth loads on rigid retaining walls," Ph.D. Diss., Geotechnical Engineering Division, Department of Civil Engineering, Virginia Polytechnic Institute and State University, Blacksburg.
- Filz, G. M., and Duncan, J. M. (1997). "Vertical shear loads on nonmoving walls. I: Theory," *ASCE Journal of Geotechnical Engineering* 123(9), 856-862.
- Filz, G. M., Duncan, J. M., and Ebeling, R. M. (1997). "Vertical shear loads on nonmoving walls. II: Applications," *ASCE Journal of Geotechnical Engineering* 123(9), 863-873.
- Gómez, J. E., Filz, G. M., and Ebeling, R. M. (1999). "Development of an improved numerical model for concrete-to-soil interfaces in soil-structure interaction analyses; Report 1, Preliminary study," Technical Report ITL-99-1, U.S. Army Engineer Research and Development Center, Vicksburg, MS.
- Goodman, R. E., Taylor, R. L., and Brekke, T. L. (1968). "A model for the mechanics of jointed rock," *Journal of the Soil Mechanics and Foundations Division*, ASCE, 94(SM3), 637-659.
- Headquarters, U.S. Army Corps of Engineers. (1994). "Stability of gravity walls, vertical shear," Engineer Technical Letter 1110-2-352, Washington, DC.
- _____. "Stability analyses of concrete structures" (in preparation), Engineer Manual 1110-2-2100, Washington, DC.
- Heuze, F. E., and Barbour, T. G. (1982). "New models for rock joints and interfaces," *ASCE Journal of the Geotechnical Engineering Division* 108(GT5), 757-776.
- Hryciw, R. D., and Irsyam, M. (1993). "Behavior of sand particles around rigid ribbed inclusions during shear," *Soils and Foundations* 33(3), 1-13.
- Huck, P. J., and Saxena, S. K. (1981). "Response of soil-concrete interface at high pressure." *Proceedings of the Tenth International Conference on Soil Mechanics and Foundation Engineering*, Stockholm, 15-19 June 1981. A. A. Balkema, Rotterdam, The Netherlands, 2, 141-144.

- Jaky, J. (1948). "The coefficient of earth pressure at rest," *Journal of the Society of Hungarian Architects and Engineers*, 1944.
- Janbu, N. (1963). "Soil compressibility as determined by oedometer and triaxial tests." *European Conference on Soil Mechanics and Foundation Engineering*, Wiesbaden, Germany, 1, 19-25
- Kishida, H., and Uesugi, M. (1987). "Tests of the interface between sand and steel in the simple shear apparatus," *Géotechnique* 37(1), 45-52.
- Kondner, R. L. (1963). "Hyperbolic stress-strain response: Cohesive soils," *Journal of the Soil Mechanics and Foundations Division*, ASCE, proc. Paper 3429, 89(SM1), 115-143.
- Kondner, R. L., and Zelasko, J. S. (1963). "A hyperbolic stress-strain formulation for sands." *Proceedings, 2nd Pan-American Conference on Soil Mechanics and Foundations Engineering*, Sao Paulo, Brazil, July 16-24 1963. I, 289-324.
- Kramer, S. L. (1996). *Geotechnical earthquake engineering*. Prentice-Hall, Upper Saddle River, NJ.
- Kulhawy, F. H., and Peterson, M. S. (1979). "Behavior of sand-concrete interfaces." *Proceedings of the 6th Panamerican Conference on Soil Mechanics and Foundation Engineering*, Lima, Peru, December 2-7, 1979. II, 225-236.
- Lade, P. V., and Duncan, J. M. (1975). "Elastoplastic stress-strain theory for cohesionless soil," *ASCE Journal of the Geotechnical Engineering Division* 101(GT10), 1037-1053.
- _____. (1976). "Stress-path dependent behavior of cohesionless soil," *ASCE Journal of the Geotechnical Engineering Division* 102(GT1), 51-68.
- Lee, P. A., Kane, W. F., Drumm, E. C., and Bennett, R. M. (1989). "Investigation and modeling of soil-structure interface properties." *Foundation engineering: Current principles and practice*. ASCE Geotechnical Special Publication 22, 580-587.
- Matsui, T., and San, K. C. (1989). "An elastoplastic joint element with its application to reinforced slope cutting," *Soils and Foundations* 29(3), 95-104.
- Morrison, C. S. (1995). "The development of a modular finite element program for analyses of soil-structure interaction," Ph.D. Diss., Geotechnical Engineering Division, Department of Civil Engineering, Virginia Polytechnic Institute and State University, Blacksburg.
- Peterson, M. S., Kulhawy, F. H., Nucci, L. R., and Wasil, B. A. (1976). "Stress-deformation behavior of soil-concrete interfaces," Contract Report B-49 to Niagara Mohawk Power Corporation, Syracuse, NY.

- Potyondy, J. G. (1961). "Skin friction between various soils and construction materials," *Géotechnique* 11(4), 339-353.
- Pyke, R. (1979). "Nonlinear soil models for irregular cyclic loadings," *ASCE Journal of the Geotechnical Engineering Division* 105(GT6), 715-726.
- Seed, R. B., and Duncan, J. M. (1986). "FE analyses: Compaction-induced stresses and deformations," *Journal of Geotechnical Engineering* 112(1), 23-43.
- Sehn, A. L. (1990). "Experimental study of earth pressures on retaining structures," Ph.D. Diss., Geotechnical Engineering Division, Department of Civil Engineering, Virginia Polytechnic Institute and State University, Blacksburg.
- Shallenberger, W. C., and Filz, G. M. (1996). "Interface strength determination using a large displacement shear box." *Proceedings of the Second International Congress on Environmental Geotechnics*, Osaka, Japan, 5-8 November 1996. M. Kamon, ed., A. A. Balkema, Rotterdam, The Netherlands.
- Stankowski, T., Runesson, K., and Sture, S. (1993). "Fracture and slip of interfaces in cementitious composites. I: Characteristics," *Journal of Engineering Mechanics*, ASCE, 119(2), 292-314.
- Stark, T. D., Ebeling, R. M., and Vettel, J. J. (1994). "Hyperbolic stress-strain parameters for silts," *Journal of Geotechnical Engineering*, ASCE, 120(2), 420-441.
- Stark, T. D., Williamson, T. A., and Eid, H. T. (1996). "HDPE geomembrane/geotextile interface shear strength," *Journal of Geotechnical Engineering* 122(3), 197-203.
- Uesugi, M., and Kishida, H. (1985). "Discussion: Cyclic testing and modeling of interfaces," *Journal of Geotechnical Engineering*, ASCE, 113(9), 1086-1087.
- _____. (1986a). "Frictional resistance at yield between dry sand and mild steel," *Soils and Foundations* 26(4), 139-149.
- _____. (1986b). "Influential factors of friction between steel and dry sands," *Soils and Foundations* 26(2), 33-46.
- Uesugi, M., Kishida, H., and Tsubakihara, Y. (1988). "Behavior of sand particles in sand-steel friction," *Soils and Foundations* 28(1), 107-118.
- _____. (1989). "Friction between sand and steel under repeated loading," *Soils and Foundations* 29(3), 127-137.

- Uesugi, M., Kishida, H., and Uchikawa, Y. (1990). "Friction between dry sand and concrete under monotonic and repeated loading," *Soils and Foundations* 30(1), 115-128.
- Wilson, E. L. (1975). "Finite elements for foundations, joints and fluids." *Finite Elements in Geomechanics*. G. Gudehus, ed., John Wiley, London.
- Wong, P. C., Kulhawy, F. H., and Ingraffea, A. R. (1989). "Numerical modeling of interface behavior for drilled shaft foundations under generalized loading." *Foundation Engineering: Current Principles and Practice*, ASCE Geotechnical Special Publication 22, 565-579.
- Wood, D. M. (1990). *Soil behavior and critical state soil mechanics*. Cambridge University Press, New York.
- Yoshimi, Y., and Kishida, T. (1981). "A ring torsion apparatus for evaluating friction between soil and metal surfaces," *Geotechnical Testing Journal* 4(4), 145-152.
- Yuan, Z., and Chua, K. M. (1992). "Exact formulation of axisymmetric-interface-element stiffness matrix," *Journal of Geotechnical Engineering* 118(8), 1264-1271.
- Zaman, M. M., Desai, C. S., and Drumm, E. C. (1984). "Interface model for dynamic soil-structure interaction," *Journal of Geotechnical Engineering* 110(9), 1257-1273.

Appendix A

Results of Triaxial and Consolidation Tests

Triaxial and consolidation tests were performed on specimens of the soils used for interface testing. The objectives of these tests were as follows:

- a. Determination of the internal friction angle of the soils.
- b. Determination of the hyperbolic parameters of the soils.
- c. Evaluation of hydrocompression strains induced by inundation of the soils.

This appendix describes the procedures and results of the tests performed on specimens of Density sand and Light Castle sand. The procedure for the determination of the internal friction angle of the soils from the results of the triaxial tests is presented. Hydrocompression properties of the soils are evaluated based on the results of the consolidation tests. The procedure for determination of the hyperbolic parameter values of each of the soils is presented in Appendix B.

A.1 Triaxial Tests

Two different sands were used for the tests:

- a. *Density sand*. It is a fine to medium silica sand with subrounded to rounded grains, available commercially for in situ density determinations.
- b. *Light Castle sand*. It is a fine to medium sand with subangular to angular grains.

A more complete description of the properties of these soils is presented in Chapter 3 of this report.

Drained triaxial (CD) tests were performed to determine the internal friction angle and hyperbolic parameter values of the Density sand and the Light Castle sand for a range of relative densities. Sets of medium dense and dense specimens

were prepared by pluviation for each type of sand. After preparation, each sample was subjected to an internal manometric pressure of -15 to -20 kPa, which was gradually removed during application of the cell pressure. The samples were de-aired using carbon dioxide, inundated with de-aired distilled water, and back-pressure saturated. The samples in each set were consolidated under effective confining pressures ranging from 45 to 280 kPa. These values are representative of the estimated values of confining pressure within the backfill of typical lock walls. Shearing was performed at a strain rate of 0.25 %/min, which was found to be appropriate for pore pressure dissipation during previous trials.

The results of the tests are presented graphically in Figures A1 to A4.¹ All the specimens exhibited dilation during shear and strain softening after mobilization of the peak strength. Because the peak strength envelopes of both soils are curved, the value of secant friction angle ϕ for a given confining pressure σ'_3 , can be calculated from the following expression (Duncan et al. 1980):²

$$\phi = \phi_o - \Delta\phi \cdot \log_{10} \left(\frac{\sigma'_3}{p_a} \right) \quad (A1)$$

where

ϕ_o = peak secant friction at a confining pressure of 101.4 kPa (1 atm)

$\Delta\phi$ = reduction in the peak friction angle value for a tenfold increase in σ'_3

p_a = atmospheric pressure

The values of friction parameters ϕ_o and $\Delta\phi$ are determined using diagrams of secant friction angle versus normalized confining pressure σ_3/p_a such as those shown in Figures A1c, A2c, A3c, and A4c.

The procedure for the determination of the hyperbolic parameter values of the soils is presented in Appendix B.

A.2 Consolidation Testing

Consolidation tests were performed on specimens of Density sand and Light Castle sand to provide additional data on their mechanical properties and determine their susceptibility to hydrocompression (Brandon, Duncan, and Gardner 1990).

Two specimens of each type of sand were prepared at different relative densities in a dry condition. Each specimen was consolidated under a series of vertical stress increments. Once a predetermined stress was reached, the specimen

¹ For convenience, symbols are listed and defined in the Notation (Appendix F).

² References cited in this Appendix are included in the References at the end of the main text.

was inundated after primary consolidation was attained. The results of these tests are presented as strain versus stress diagrams in Figures A5 to A8.

During inundation, compressive vertical strain was observed in all specimens tested. The strain that takes place during inundation includes deformation due to secondary compression of the sand and collapse of the structure due to inundation. The value of the strain induced by hydrocompression in each test was determined from strain versus time plots following the procedure suggested by Brandon, Duncan, and Gardner (1990).

Figure A9 is a diagram of hydrocompression strain versus relative density determined from the consolidation tests on Light Castle Sand specimens. Two specimens, prepared at different relative densities, were inundated under a vertical stress of 32.3 kPa. It is seen that hydrocompression strains decrease for increasing soil densities. A straight line was drawn through the data points corresponding to these two tests and extended through the entire range of relative densities shown. Lines parallel to this extended line were drawn through the single data points corresponding to vertical stresses of 7.8 and 17 kPa.

In the Instrumented Retaining Wall (IRW) described in Chapter 5, the vertical stress in the backfill ranges from zero at the top of the backfill to 33.6 kPa at the bottom. The extended lines shown in Figure A9 allow the estimation of hydrocompression strains throughout the height of the backfill. It can be seen that hydrocompression strains may range from zero to 0.0015 for a relative density of 100 percent. Assuming an average vertical stress of 17 kPa, the average hydrocompression strain of the backfill during inundation is 0.0002. This value corresponds to a vertical settlement at the top of the backfill of less than 0.5 mm. This is consistent with the negligible settlements observed during inundation in the IRW test.

It must be noted that the procedure followed for estimation of hydrocompression strains in the IRW backfill is only approximate. There is not enough information to support the assumed linear relationship between hydrocompression strains and relative density. In addition, an accurate estimate of the backfill settlement can be obtained only by integration of the hydrocompression strains over the height of the backfill. However, given the relatively small height of the IRW backfill, it can be assumed that the error in the estimation of the hydrocompression settlement is small.

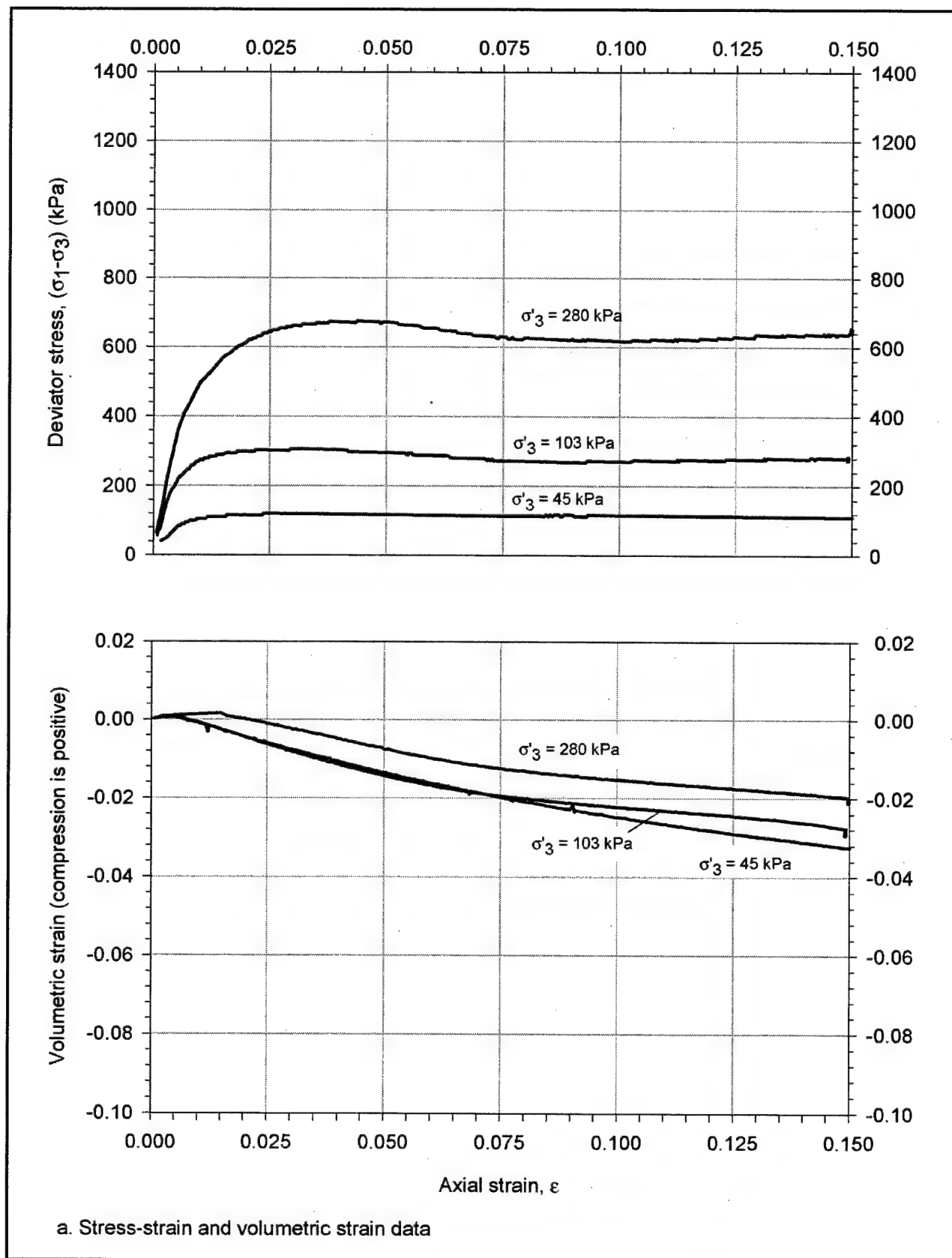


Figure A1. Results of CD triaxial tests on medium-dense Density sand (Sheet 1 of 3)

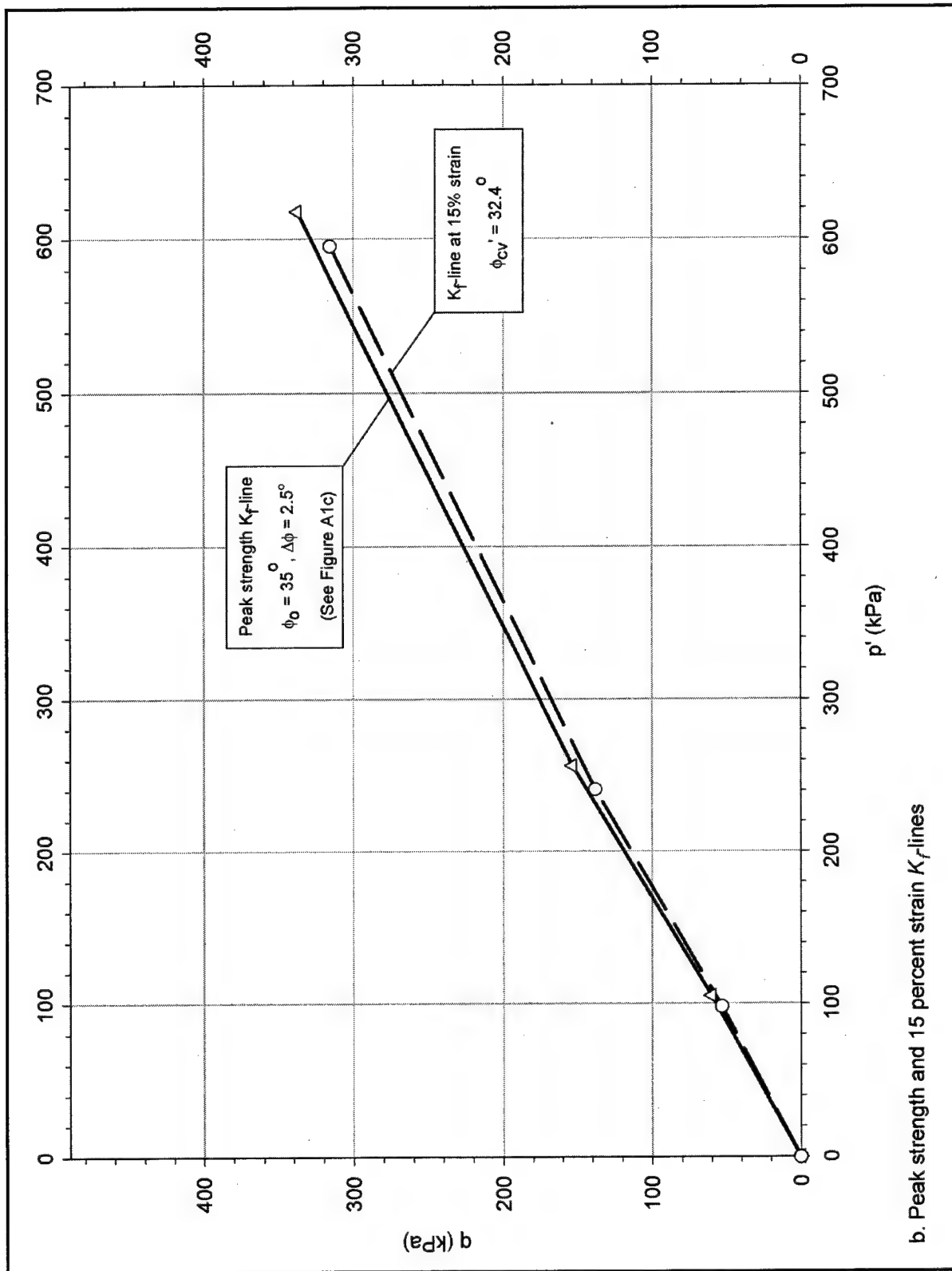


Figure A1. (Sheet 2 of 3)

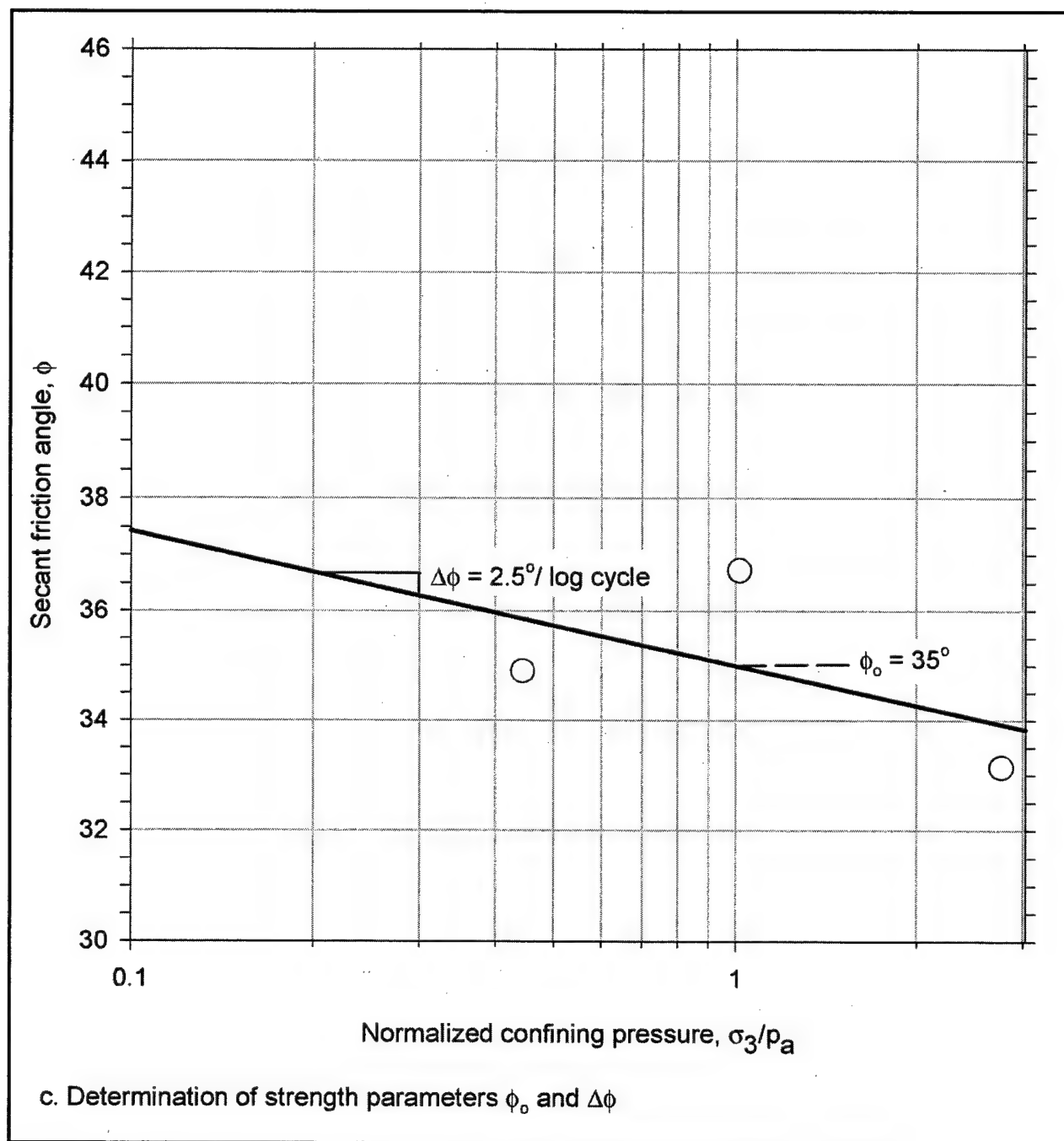


Figure A1. (Sheet 3 of 3)

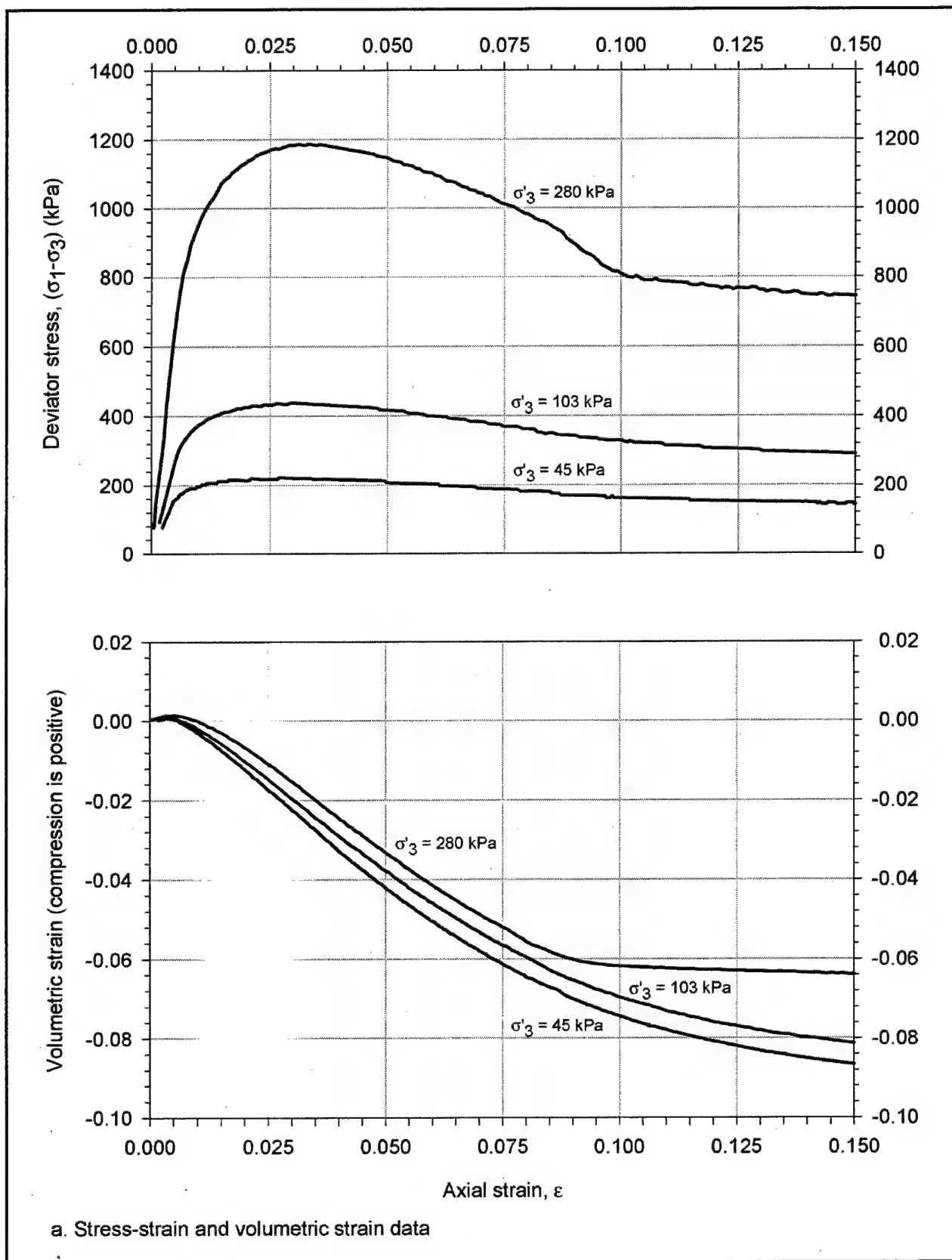


Figure A2. Results of CD triaxial tests on dense Density sand (Sheet 1 of 3)

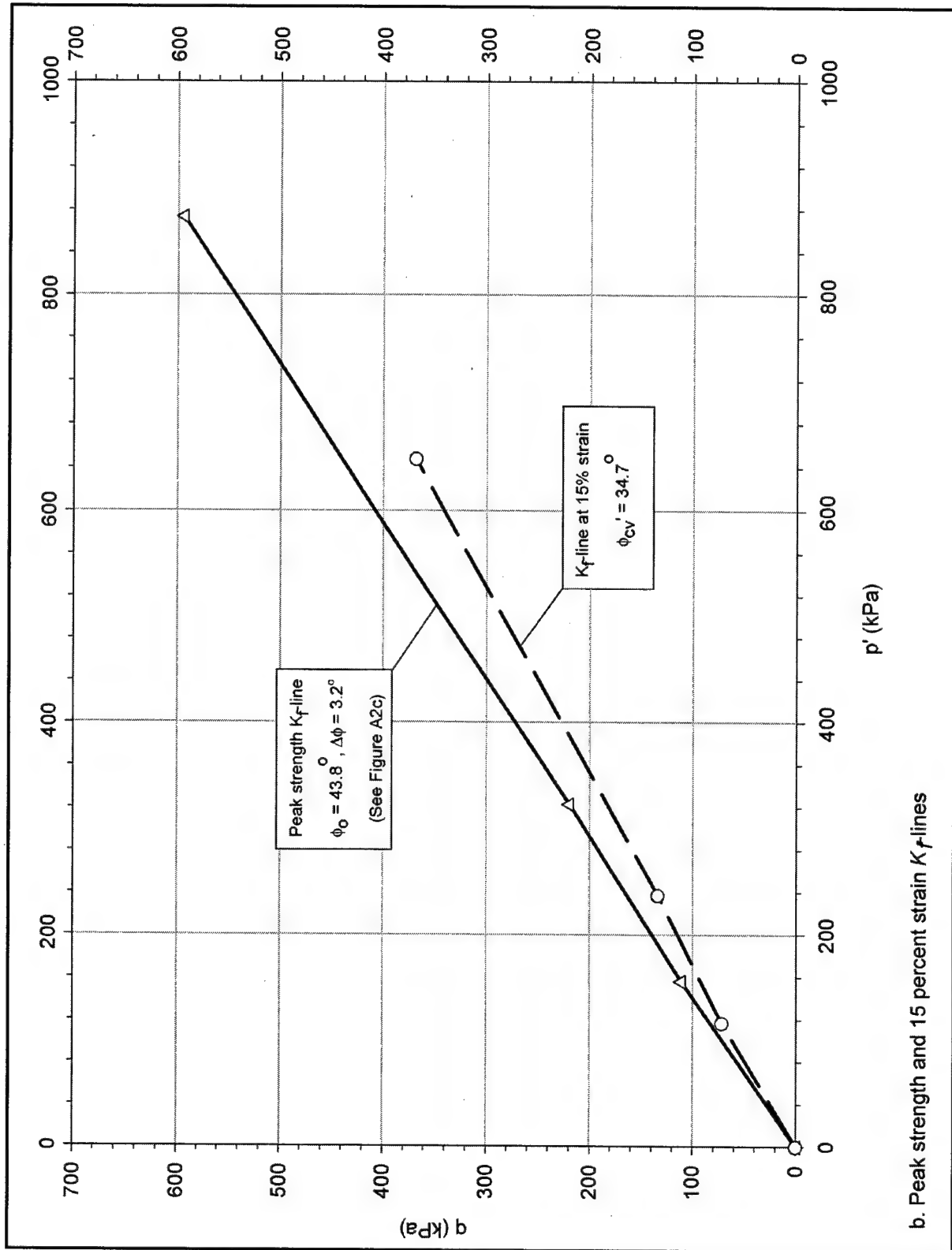


Figure A2. (Sheet 2 of 3)

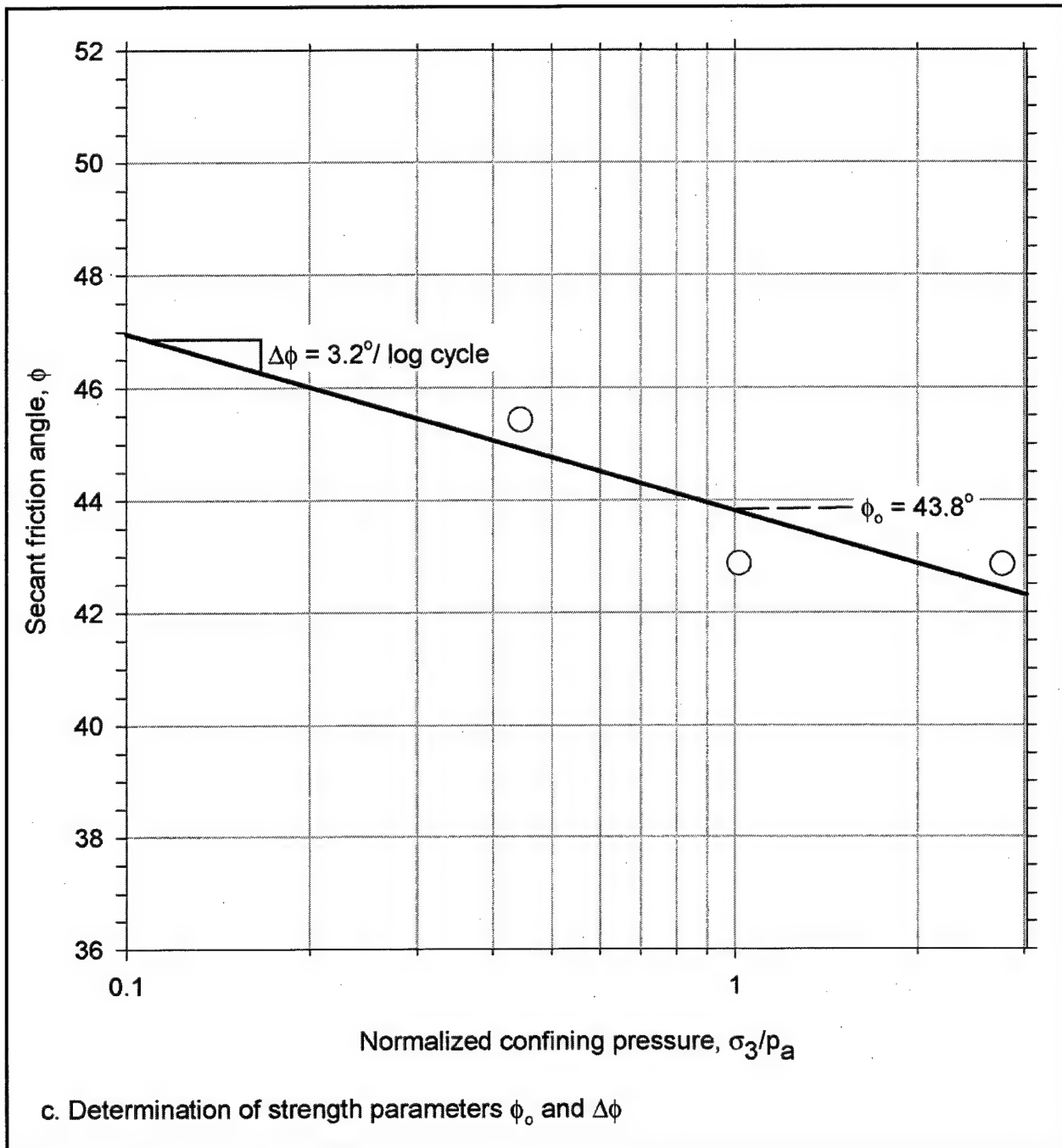


Figure A2. (Sheet 3 of 3)

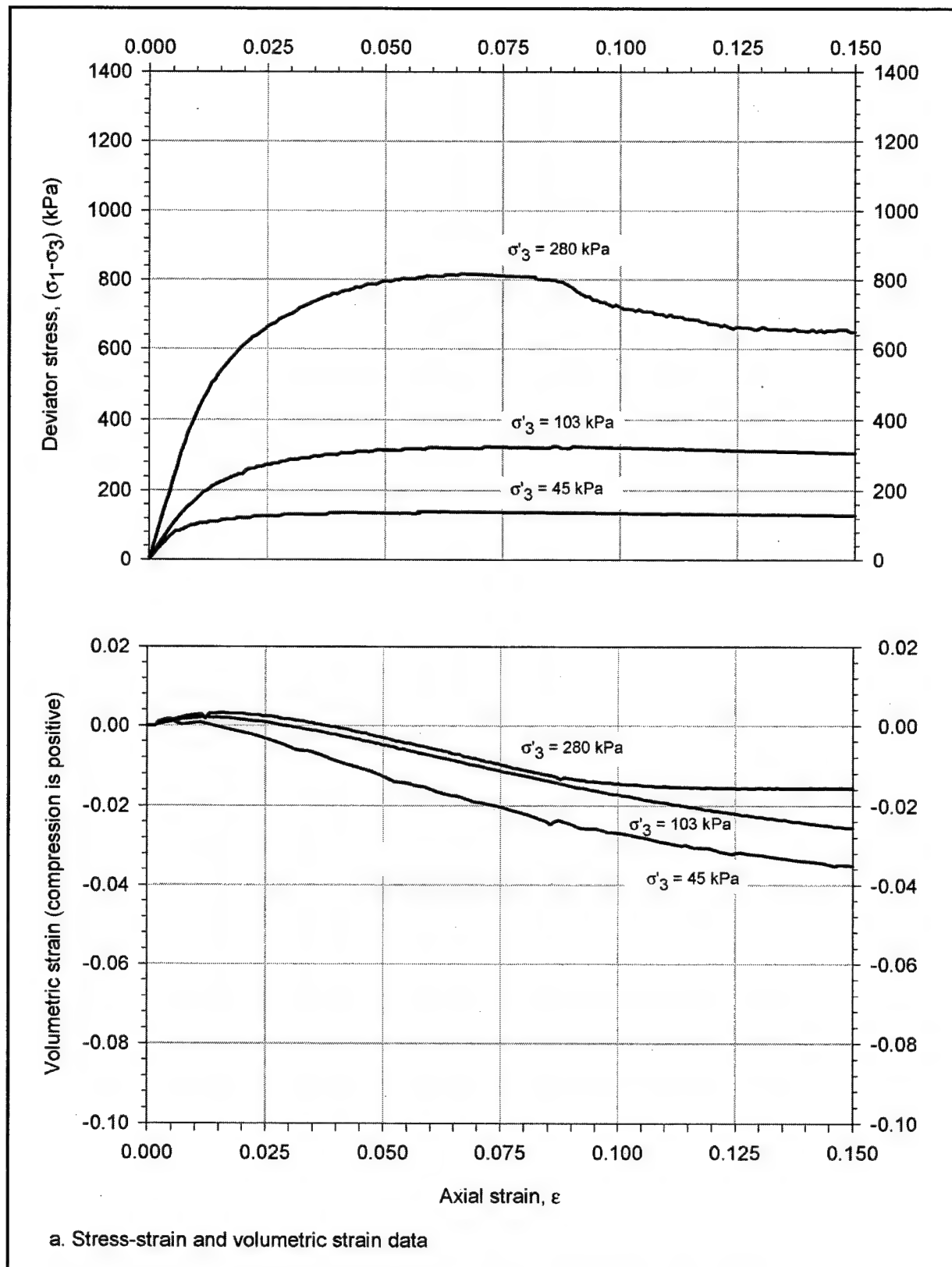


Figure A3. Results of CD triaxial tests on medium-dense Light Castle sand (Sheet 1 of 3)

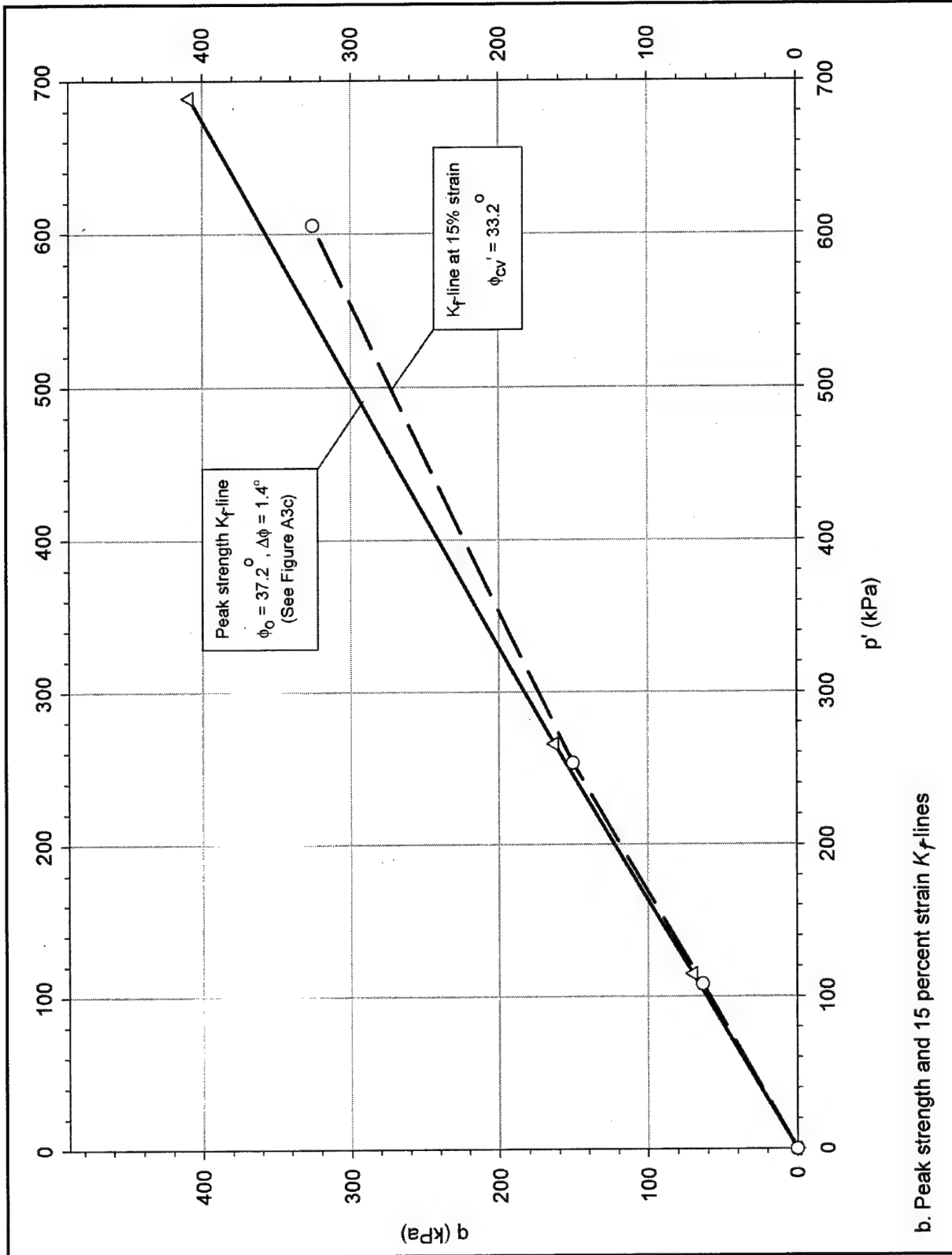


Figure A3. (Sheet 2 of 3)

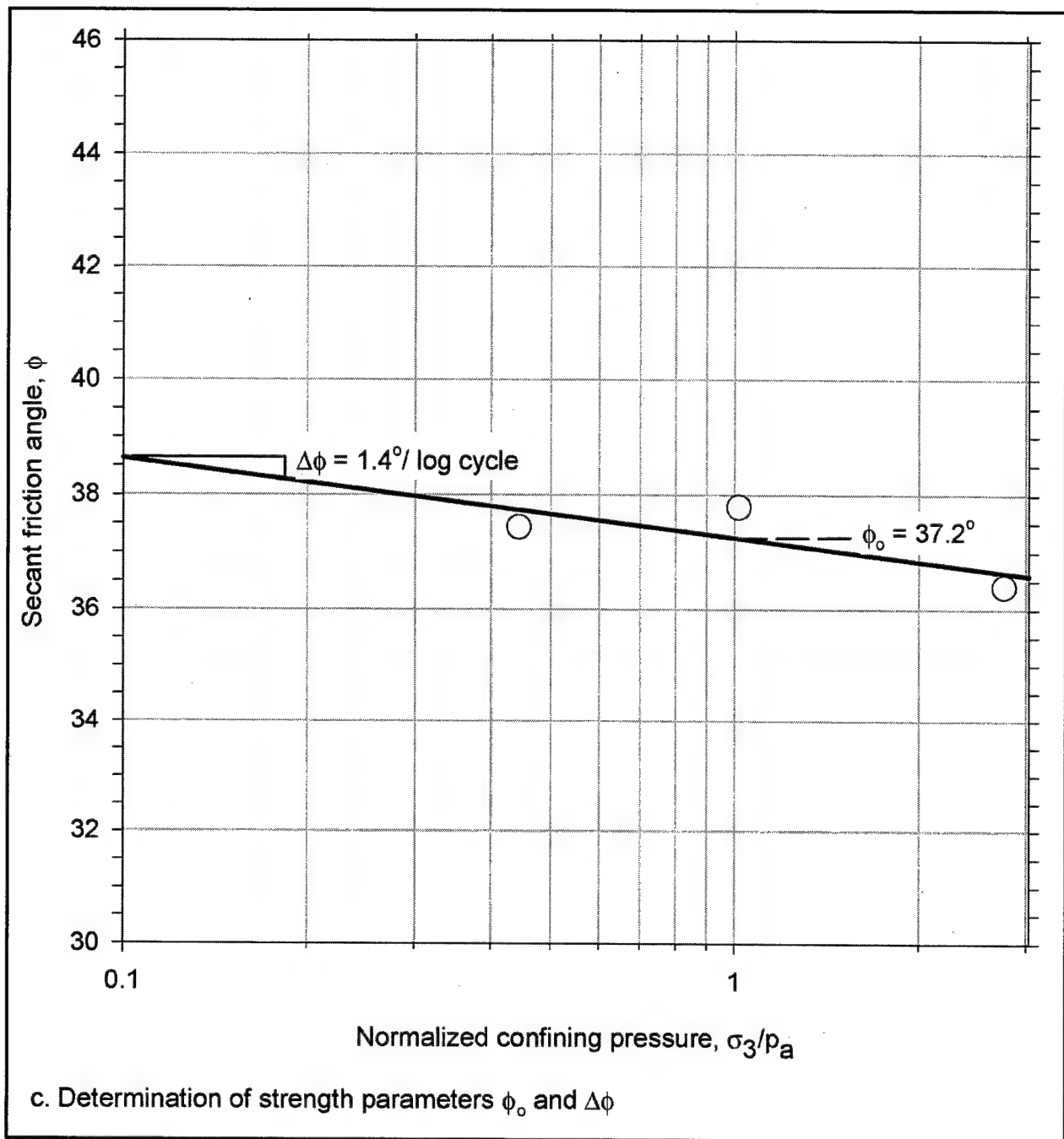


Figure A3. (Sheet 3 of 3)

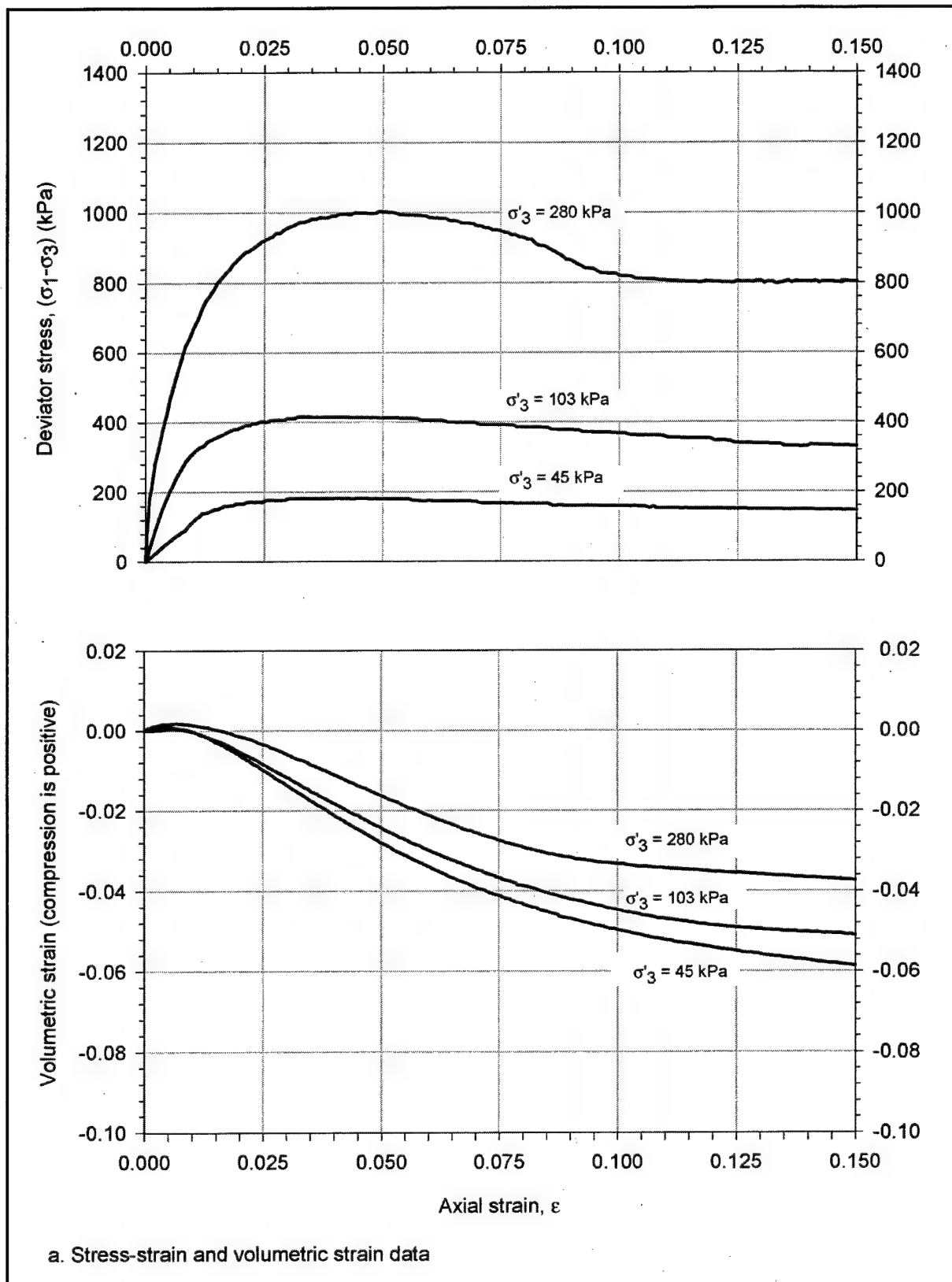


Figure A4. Results of CD triaxial tests on dense Light Castle sand (Sheet 1 of 3)

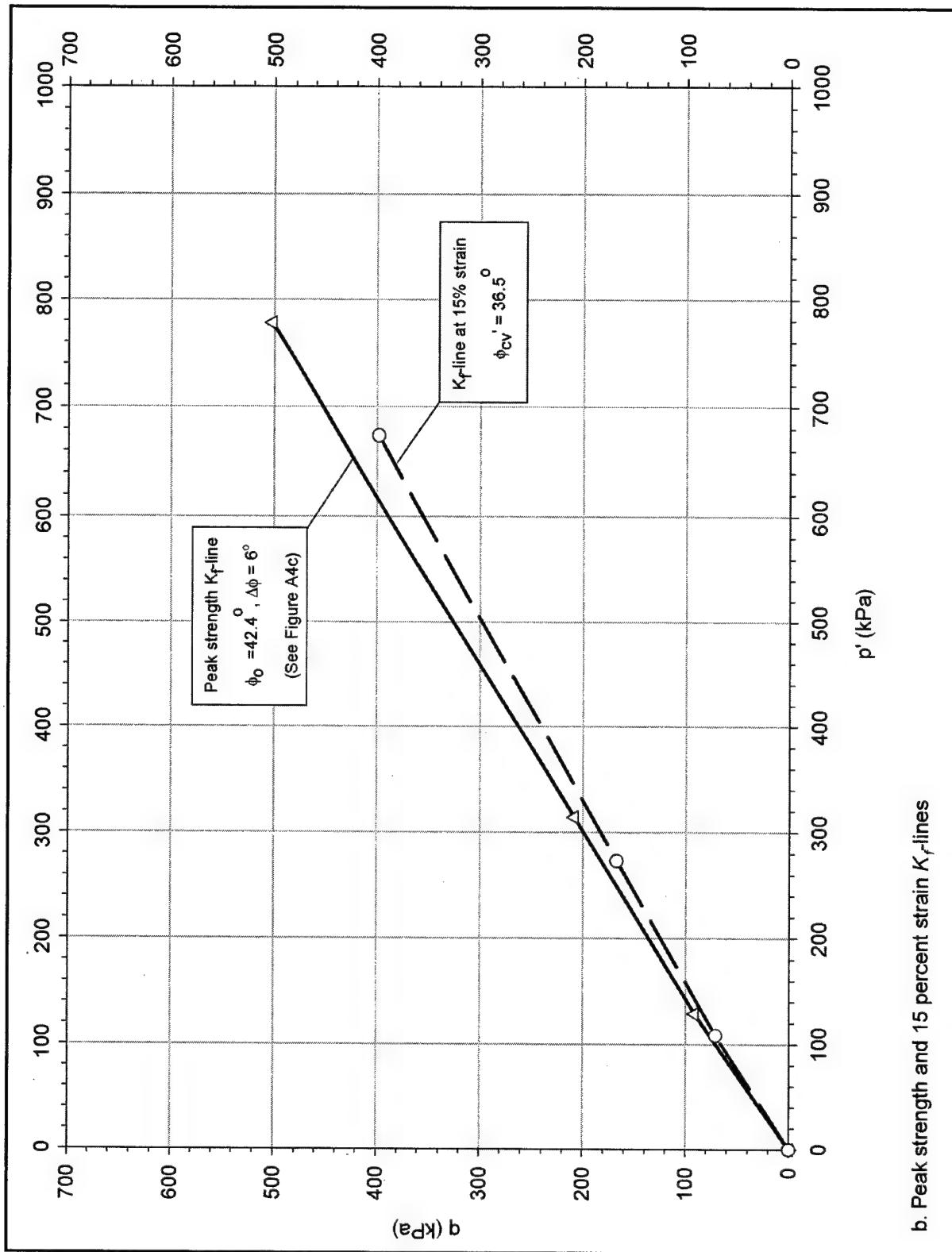


Figure A4. (Sheet 2 of 3)

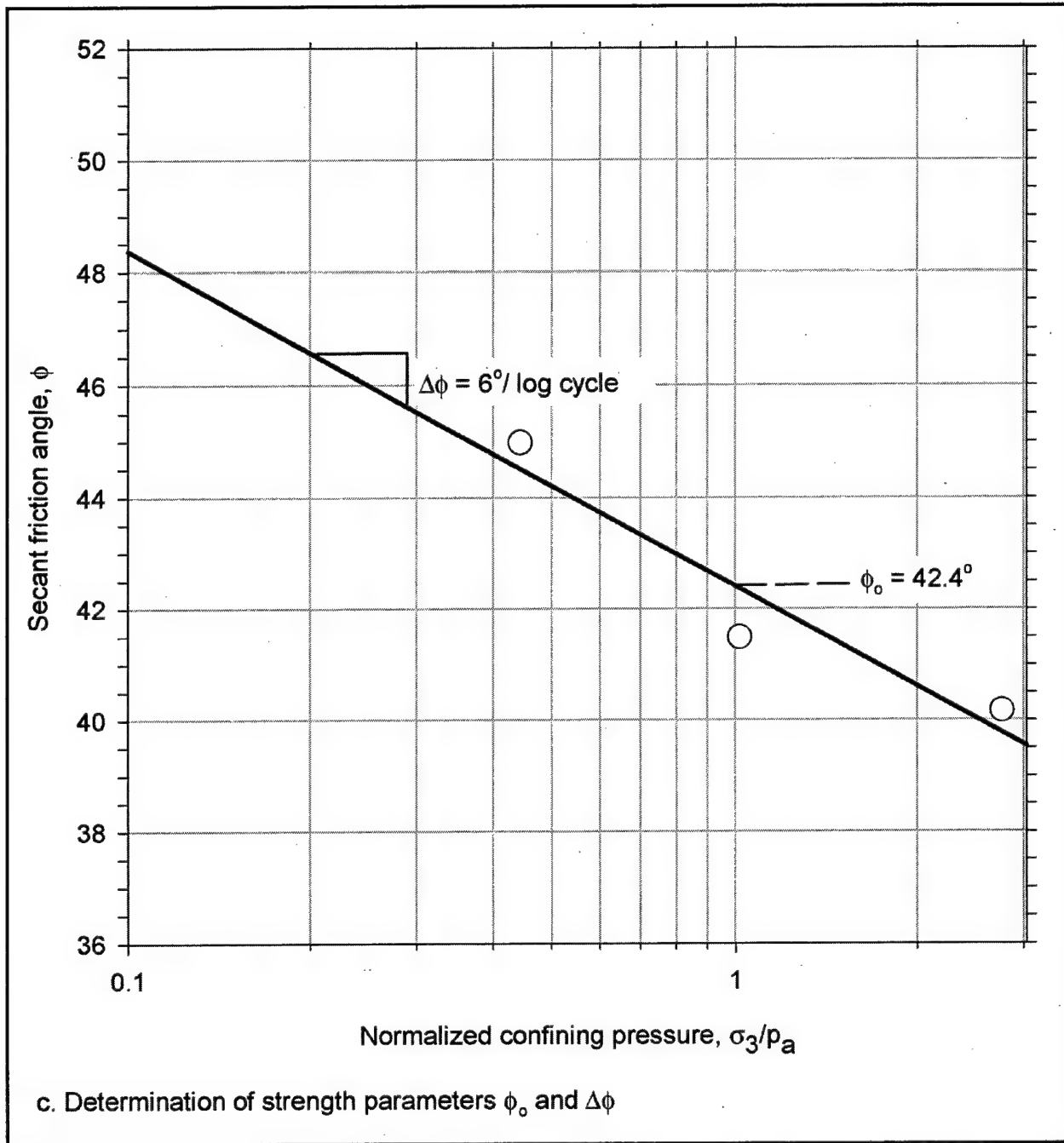


Figure A4. (Sheet 3 of 3)

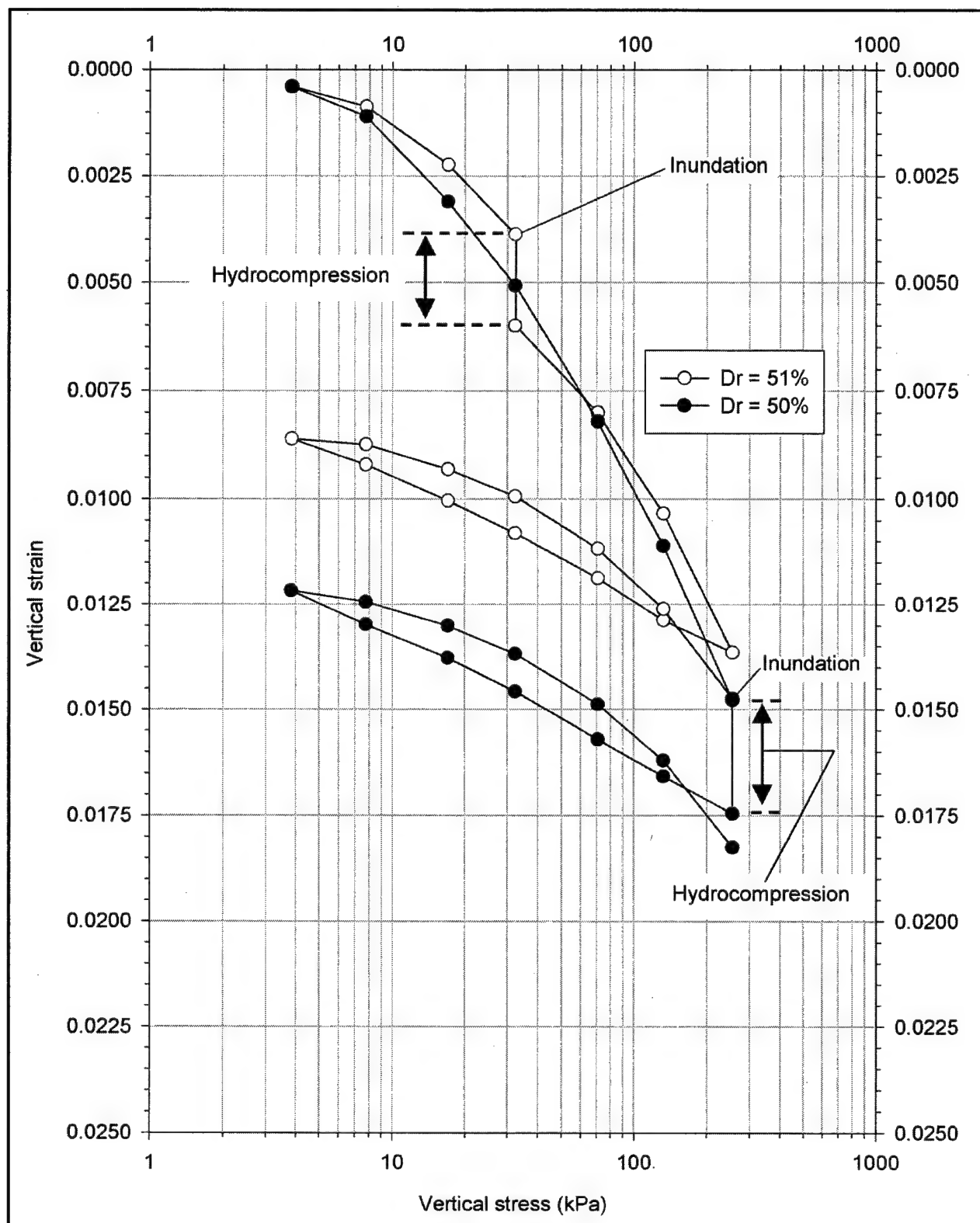


Figure A5. Results of consolidation tests on medium-dense Density sand

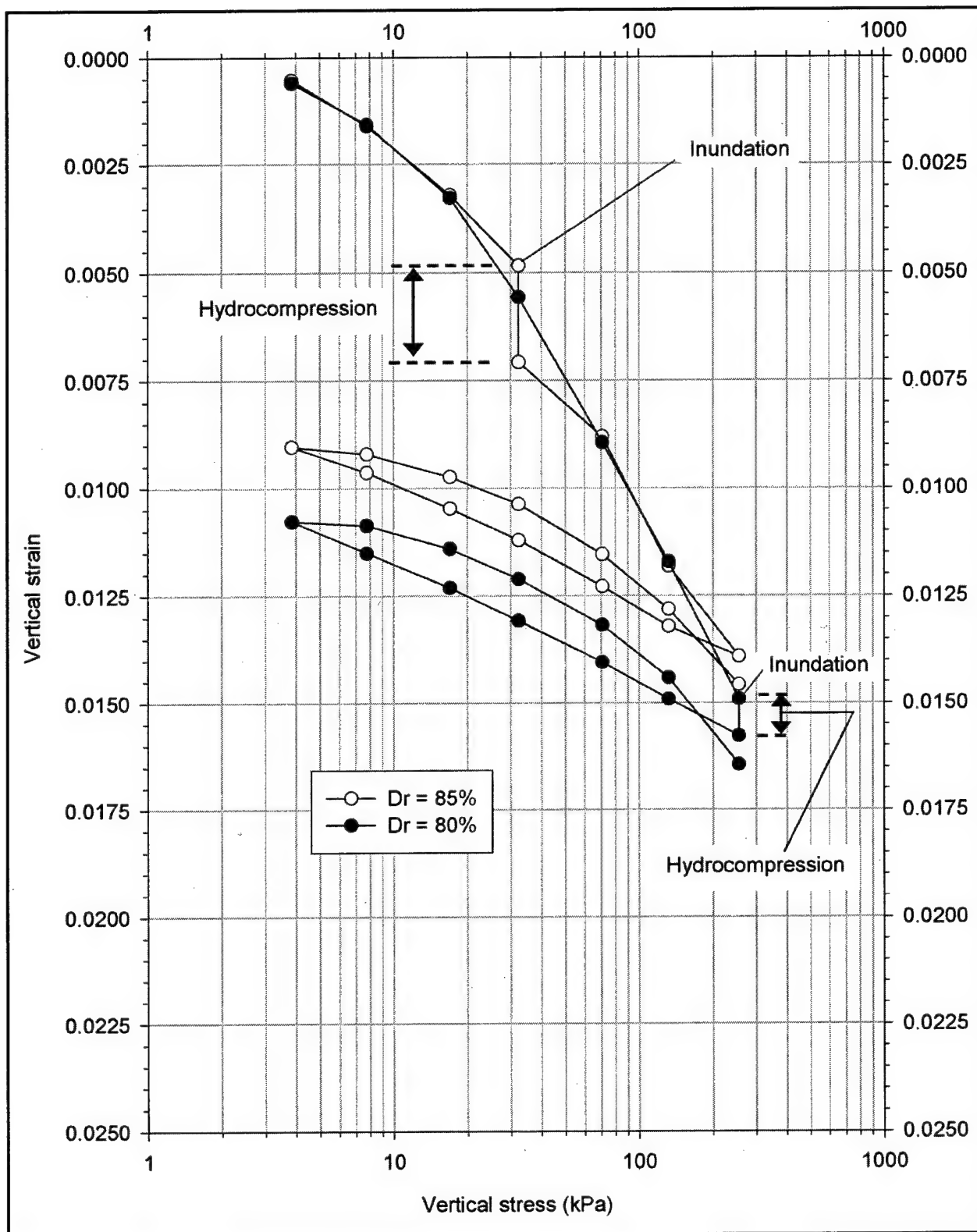


Figure A6. Results of consolidation tests on dense Density sand

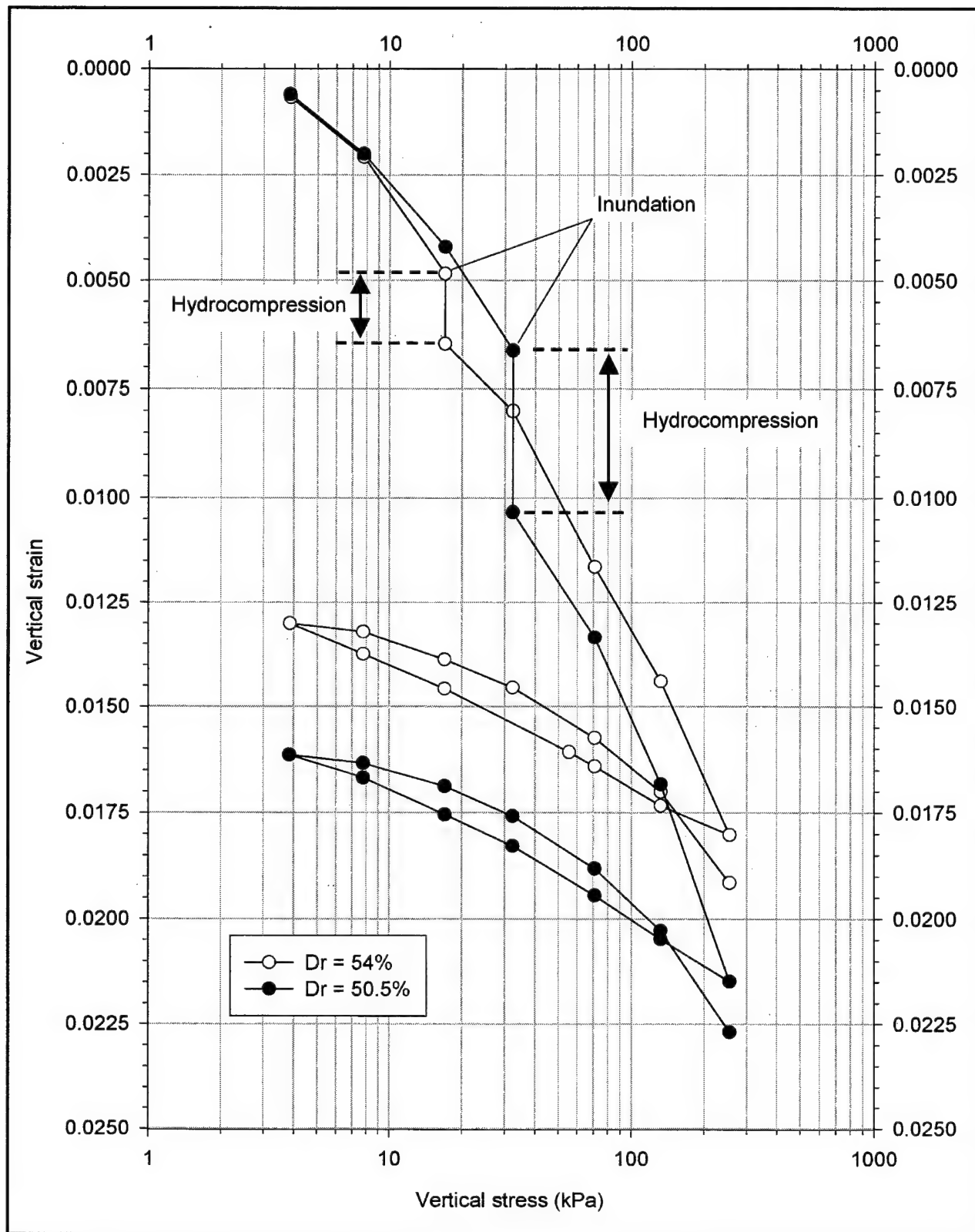


Figure A7. Results of consolidation tests on medium-dense Light Castle sand

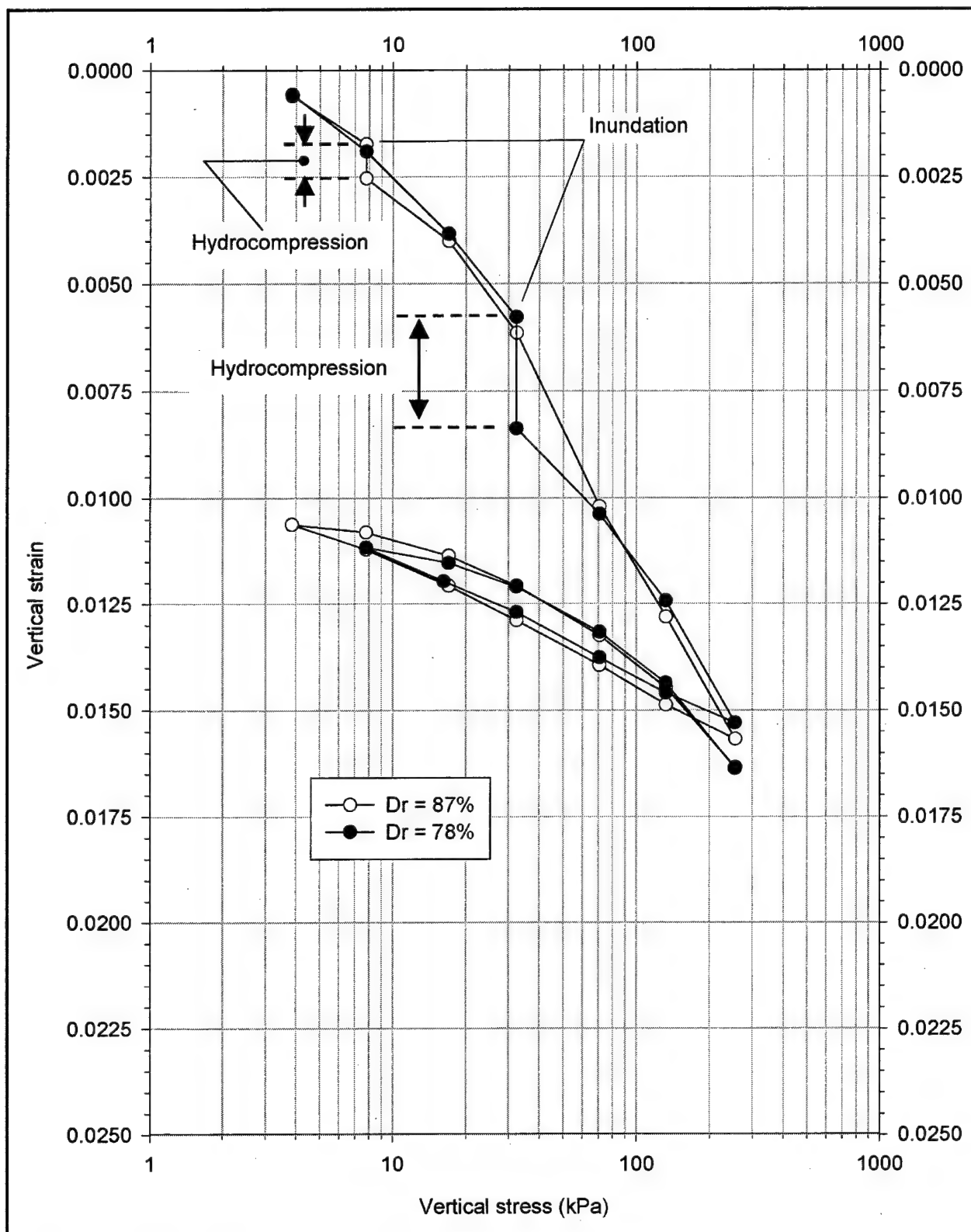


Figure A8. Results of consolidation tests on dense Light Castle sand

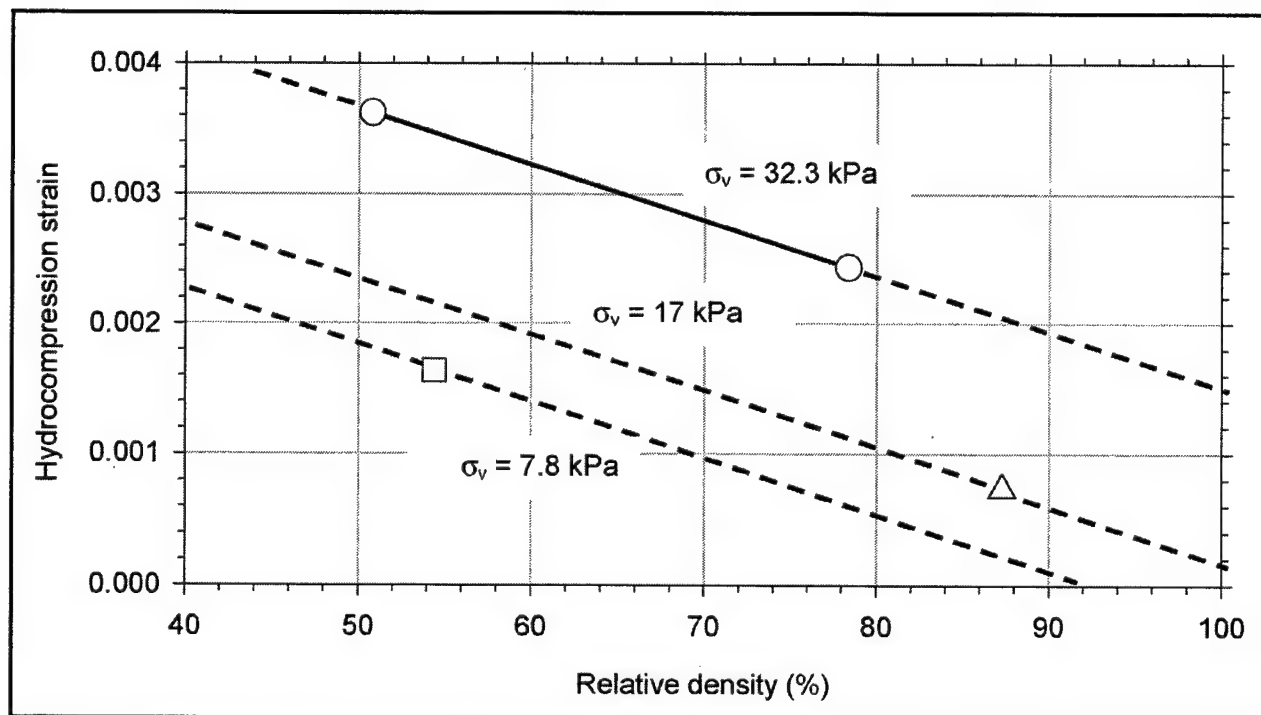


Figure A9. Relationship between hydrocompression strain and relative density for Light Castle sand

Appendix B

Determination of Hyperbolic Parameter Values of Soils

This appendix describes the procedure suggested by Duncan et al. (1980)¹ for the determination of hyperbolic parameter values for soils from results of triaxial tests. Hyperbolic parameter values of Density sand and Light Castle sand are determined based on the results of the triaxial tests presented in Appendix A. Figures B1 through B16 show the determination of the hyperbolic parameter values for all the sands tested. Figures B1 through B4, corresponding to the determination of parameter values for medium-dense Density sand, are used in the following description to illustrate the procedure followed. Example calculations of hyperbolic parameter values for dense Light Castle sand are presented in the last section of this appendix.

B.1 Transformed Plots

The procedure for the determination of hyperbolic parameter values of medium-dense Density sand is illustrated in Figures B1 through B4. The triaxial test stress-strain data shown in Figure A1 of Appendix A is represented in a transformed plot in Figure B1. In this transformed diagram, the value of axial strain² ϵ measured during the test is divided by the corresponding value of deviator stress $\sigma_1 - \sigma_3$ and plotted against the axial strain. If the stress-strain relationship measured during the triaxial test is hyperbolic, the transformed diagram is a straight line. The intercept a of this straight line on the $\epsilon/(\sigma_1 - \sigma_3)$ axis is the reciprocal of the initial Young's modulus E_i of the soil specimen. The slope b of the line is the reciprocal of the asymptotic deviator stress $(\sigma_1 - \sigma_3)_{ult}$.

The stress-strain relationship of a soil usually differs from a hyperbola. Duncan et al. (1980) indicated that the values of parameters a and b can be determined from a straight line passing through the points in the transformed plot that correspond to 70 and 95 percent of the strength.

¹ References cited in this Appendix are included in the References at the end of the main text.

² For convenience, symbols are listed and defined in the Notation (Appendix F).

The transformed plot in Figure B1 shows the 70 and 95 percent strength data points for each of the tests performed on medium-dense Density sand. Straight lines are drawn through each pair of these points. For comparison, the complete set of transformed data from the tests is also shown in the figure. It is seen that the lines drawn through the 70 and 95 percent data points match closely the transformed data sets. Such a comparison may be useful for minimizing errors in the determination of hyperbolic parameter values that can arise from inconsistencies in the data. Transformation of the entire set of test data is easily achieved in an electronic spreadsheet. The use of a spreadsheet also facilitates modification of the values of parameters a and b to obtain the best possible fit to the data.

B.2 Hyperbolic Parameter Values

B.2.1 Determination of K and n

The values of the parameters a and b determined from the transformed plots are presented in the table included in Figure B1. The values of initial Young's modulus and asymptotic deviator stress are determined using the following equations:

$$E_i = \frac{1}{a} \quad (\text{B1})$$

$$(\sigma_1 - \sigma_3)_{ult} = \frac{1}{b} \quad (\text{B2})$$

The values of E_i and $(\sigma_1 - \sigma_3)_{ult}$ for each of the tests performed on medium-dense Density sand are presented in the table in Figure B1. It can be seen that the values of initial Young's modulus E_i increase with increasing confining pressure σ'_3 . Janbu (1963) suggested the following relationship between the initial Young's modulus and confining pressure:

$$E_i = K \cdot p_a \left(\frac{\sigma'_3}{p_a} \right)^n \quad (\text{B3})$$

where

K = modulus number

p_a = atmospheric pressure

n = modulus exponent

Equation B3 can be used for both undrained and drained compression. For undrained compression, the value of σ_3 is used instead of σ'_3 . This relationship implies that there is a linear relationship between the logarithm of the initial

Young's modulus and the logarithm of the confining pressure. Figure B2 is a logarithmic diagram showing the values of normalized Young's modulus E_i/p_a , determined from the table in Figure B1, represented against the values of normalized confining stress σ'_3/p_a . A best-fit straight line is drawn through the data points. The value of the modulus number K is equal to the value of normalized Young's modulus given by this best-fit line for a confining stress of one atmosphere. The slope of the line is the modulus exponent n .

B.2.2 Determination of R_f

The table in Figure B1 shows the values of deviator stress at failure $(\sigma_1 - \sigma_3)_f$, determined from the stress-strain plots of the tests, which are presented in Figure A1 of Appendix A. It can be seen in the table that the values of $(\sigma_1 - \sigma_3)_{ult}$ are larger than the values of $(\sigma_1 - \sigma_3)_f$ in all the tests. The value of the failure ratio, R_f , for each of the tests is determined from the following expression:

$$R_f = \frac{(\sigma_1 - \sigma_3)_f}{(\sigma_1 - \sigma_3)_{ult}} \quad (B4)$$

The table contains the values of R_f determined for each of the tests. For modeling, an average value of R_f is determined from the test results as shown at the bottom of the table. Typical values of R_f range between 0.5 and 0.9 for most soils (Duncan et al. 1980).

B.2.3 Determination of K_b and m

In the hyperbolic model, it is assumed that the value of bulk modulus B is independent of stress level and dependent of confining pressure (Duncan et al. 1980). The following expression is used for the calculation of the bulk modulus:

$$B = \frac{(\sigma_1 - \sigma_3)}{3 \cdot \epsilon_v} \quad (B5)$$

where $(\sigma_1 - \sigma_3)$ is the deviator stress and ϵ_v is the volumetric strain.

In reality, application of deviator stress during a triaxial test induces volume changes in the soil specimen. Consequently, the value of bulk modulus determined from triaxial test data depends on which points on the stress-strain and volumetric strain-axial strain curves are selected for the calculation. The following criteria are used for the selection of points in the volumetric strain-axial strain data (Duncan et al. 1980):

- a. If the volumetric strain-axial strain data plot does not reach a horizontal tangent (zero volume change) before mobilization of 70 percent of the strength, the points on the stress-strain and volumetric strain-axial strain

curves corresponding to a stress level of 70 percent are used for bulk modulus determination.

- b. If the volumetric strain-axial strain curve reaches a horizontal tangent before mobilization of 70 percent of the strength, the point where the volumetric strain-axial strain curve becomes horizontal and the corresponding point on the stress-strain curve are used for bulk modulus determination.

For Density sand and Light Castle sand, it was found that dilation was significant and that the volumetric strain-axial strain curve presented a horizontal tangent before mobilization of 70 percent of the strength. Therefore, the second criterion was used for the determination of the bulk modulus B for all the specimens tested, as shown in Tables B1 through B4.

Table B1 Determination of Bulk Modulus for Medium-Dense Density Sand			
Confining Stress σ_3' kPa	Deviator Stress ($\sigma_1 - \sigma_3$) kPa	Volumetric Strain ϵ_v %	Bulk Modulus B^1 kPa
45	78.6	0.073	36146
103	133.7	0.082	54107
280	388.5	0.158	82023
$B = \frac{(\sigma_1 - \sigma_3)}{\epsilon_v}$			

Table B2 Determination of Bulk Modulus for Dense Density Sand			
Confining Stress σ_3' kPa	Deviator Stress ($\sigma_1 - \sigma_3$) kPa	Volumetric Strain ϵ_v %	Bulk Modulus B^1 kPa
45	120.8	0.071	56471
103	184.0	0.067	91446
280	684.2	0.140	163358
$B = \frac{(\sigma_1 - \sigma_3)}{\epsilon_v}$			

Table B3 Determination of Bulk Modulus for Medium-Dense Light Castle Sand			
Confining Stress σ_3' kPa	Deviator Stress ($\sigma_1 - \sigma_3$) kPa	Volumetric Strain ϵ_v %	Bulk Modulus B^1 kPa
45	72.8	0.170	14277
103	210.7	0.210	33451
280	555.9	0.320	57901
$B = \frac{(\sigma_1 - \sigma_3)}{\epsilon_v}$			

Table B4 Determination of Bulk Modulus for Dense Light Castle Sand			
Confining Stress σ_3' kPa	Deviator Stress ($\sigma_1 - \sigma_3$) kPa	Volumetric Strain ϵ_v %	Bulk Modulus B^1 kPa
45	73.8	0.047	52340
103	199.2	0.109	60917
280	548.3	0.190	96192
$^1 B = \frac{(\sigma_1 - \sigma_3)}{\epsilon_v}$			

It can be seen in Tables B1 through B4 that the values of bulk modulus increase with confining pressure. The relationship between bulk modulus and confining pressure is approximated by the following relationship:

$$B = K_b \cdot p_a \left(\frac{\sigma_3'}{p_a} \right)^m \quad (B6)$$

where K_b is the bulk modulus number and m is the bulk modulus exponent.

The values of K_b and m are determined in a logarithmic diagram of normalized bulk modulus B/p_a versus normalized confining stress σ_3'/p_a . The values presented in Table B1 for the medium-dense Density sand were used to create the B/p_a versus σ_3'/p_a diagram of Figure B3. A best-fit straight line was drawn through the data points. The value of bulk modulus number K_b is equal to the value of normalized bulk modulus given by this best-fit line for a confining stress of 1 atm. The slope of the line is the bulk modulus exponent m .

B.3 Comparison of Model to Test Data

Once the hyperbolic parameter values are determined, it is necessary to compare the model response to the test data. The stress-strain response from the model is calculated using the following expression:

$$(\sigma_1 - \sigma_3) = \frac{\epsilon}{\frac{1}{K \cdot p_a \left(\frac{\sigma_3'}{p_a} \right)^n} + R_f \cdot \frac{\epsilon}{(\sigma_1 - \sigma_3)_f}} \quad (B7)$$

The deviator stress at failure $(\sigma_1 - \sigma_3)_f$ is calculated from the following equation:

$$(\sigma_1 - \sigma_3)_f = 2 \frac{\sigma_3 \cdot \sin \phi'}{1 - \sin \phi'} \quad (\text{B8})$$

where ϕ' is the internal friction angle.

The volumetric strain-axial strain response is calculated using the following equation:

$$\varepsilon_v = \frac{(\sigma_1 - \sigma_3)}{3 \cdot K_b \cdot p_a \cdot \left(\frac{\sigma'_3}{p_a} \right)^m} \quad (\text{B9})$$

The stress-strain and volumetric strain-axial strain responses of the sands tested were calculated using Equations B7, B8, and B9, and the hyperbolic parameters determined following the procedure described previously. Figures B4, B8, B12, and B16 compare the test data and the calculated hyperbolic response. In the figures, the stress-strain hyperbolas are interrupted at the value of deviator stress at failure $(\sigma_1 - \sigma_3)_f$. A horizontal stress-strain relationship, i.e., zero Young's modulus, is used to model the response of the soil at failure.

It can be seen that the hyperbolic model provides an accurate approximation to the stress-strain response measured during the tests. The volumetric strain-axial strain response calculated using the hyperbolic model also provides a good approximation to the test data for the initial stages of shear, in which compression takes place. It does not model subsequent dilation of the soils.

B.4 Example Calculations of Hyperbolic Parameter Values

This section presents an example of the determination of hyperbolic parameter values. The data from the CD triaxial tests performed on dense specimens of Light Castle sand are used for this example. The example follows the procedure described by Duncan et al. (1980).

The first step in the determination of hyperbolic parameter values is checking for inconsistencies in the data from the CD triaxial tests. Figure B17 shows the results of the tests performed on dense Light Castle sand. The data shown in the figure are identical to those shown in Figures A4 and B16. Close examination of Figure B17 reveals that the data present some minor inconsistencies. To minimize these inconsistencies, a smooth response of the soil to triaxial testing was assumed for the determination of the hyperbolic parameter values. This assumed response corresponds to the solid lines in Figure B17.

The next step is the determination of the deviator stress at failure $(\sigma_1 - \sigma_3)_f$ for each confining stress. The values of $(\sigma_1 - \sigma_3)_f$ can be determined from the deviator stress-axial strain plots of the tests. Column (2) in the table presented in

Figure B18 contains the values of deviator stress at failure determined from Figure B17. The values of deviator stress corresponding to 70 and 95 percent of $(\sigma_1 - \sigma_3)$ are calculated as shown in columns (3) and (6), respectively.

The values of axial strain corresponding to 70 and 95 percent of the strength are determined from the deviator stress-axial strain plots. Columns (4) and (7) in Figure B18 contain the strain values determined as shown in Figure B17.

The values in columns (2), (3), (4), (6), and (7) are the basis for the determination of the values of initial Young's modulus E_i and failure ratio R_f . The sequence of calculations leading to the determination of the values of E_i and R_f is shown in Figure B18, and corresponds to the procedure presented in the previous sections.

It must be noted that in the method presented in Figure B18 the data are not plotted in transformed coordinates. Only the two data points corresponding to 70 and 95 percent of the strength are transformed as shown in columns (5) and (8). Although not strictly necessary, it is recommended always to plot the complete data set in transformed coordinates. The transformed plots are useful to check the data for inconsistencies and for verifying the values of Young's modulus and failure ratio determined from the procedure presented in Figure B18. Transforming the data following the procedure described previously in this appendix can be accomplished easily with electronic spreadsheets.

The value of failure ratio R_f to be used for modeling is the average of the values determined in Figure B18. The values of K and n are determined by plotting the normalized values of initial Young's modulus against the normalized confining stress in logarithmic scale as shown in Figure B19.

Figures B17 and B18 also illustrate the determination of the values of bulk modulus B from the triaxial test data. If the volumetric strain-axial strain plot does not reach a horizontal tangent before mobilization of 70 percent of the strain, the volumetric strain corresponding to 70 percent of the strength is used for the determination of B . If the volumetric strain-axial strain plot reaches a horizontal tangent before mobilization of 70 percent of the strength, the maximum value of volumetric strain is used for the determination of B .

The volumetric strain-axial strain plots of dense Light Castle sand shown in Figure B17 reach a horizontal tangent before mobilization of 70 percent of the strength. The maximum values of volumetric strain are determined as shown in the figure. They are copied to column (10) of the table in Figure B18. The deviator stress corresponding to the point of maximum volumetric strain is also determined from the figure and copied to column (9) in Figure B18. These two values are used to determine the value of B for each of the confining stresses applied. The values of K_b and m are determined from a logarithmic plot of normalized bulk modulus versus normalized confining stress, as shown in Figure B20.

It must be noted that none of the values presented in Figure B18 was determined graphically. They were obtained directly or by interpolation of data in an

electronic spreadsheet. Although graphical determination of values of stress and strain from a figure such as B17 may provide less significant decimal places than their numerical determination, the overall precision of the values of the hyperbolic parameters is similar using both procedures. The use of an electronic spreadsheet is recommended, not for increased precision, but for ease in the calculations and verification of the results.

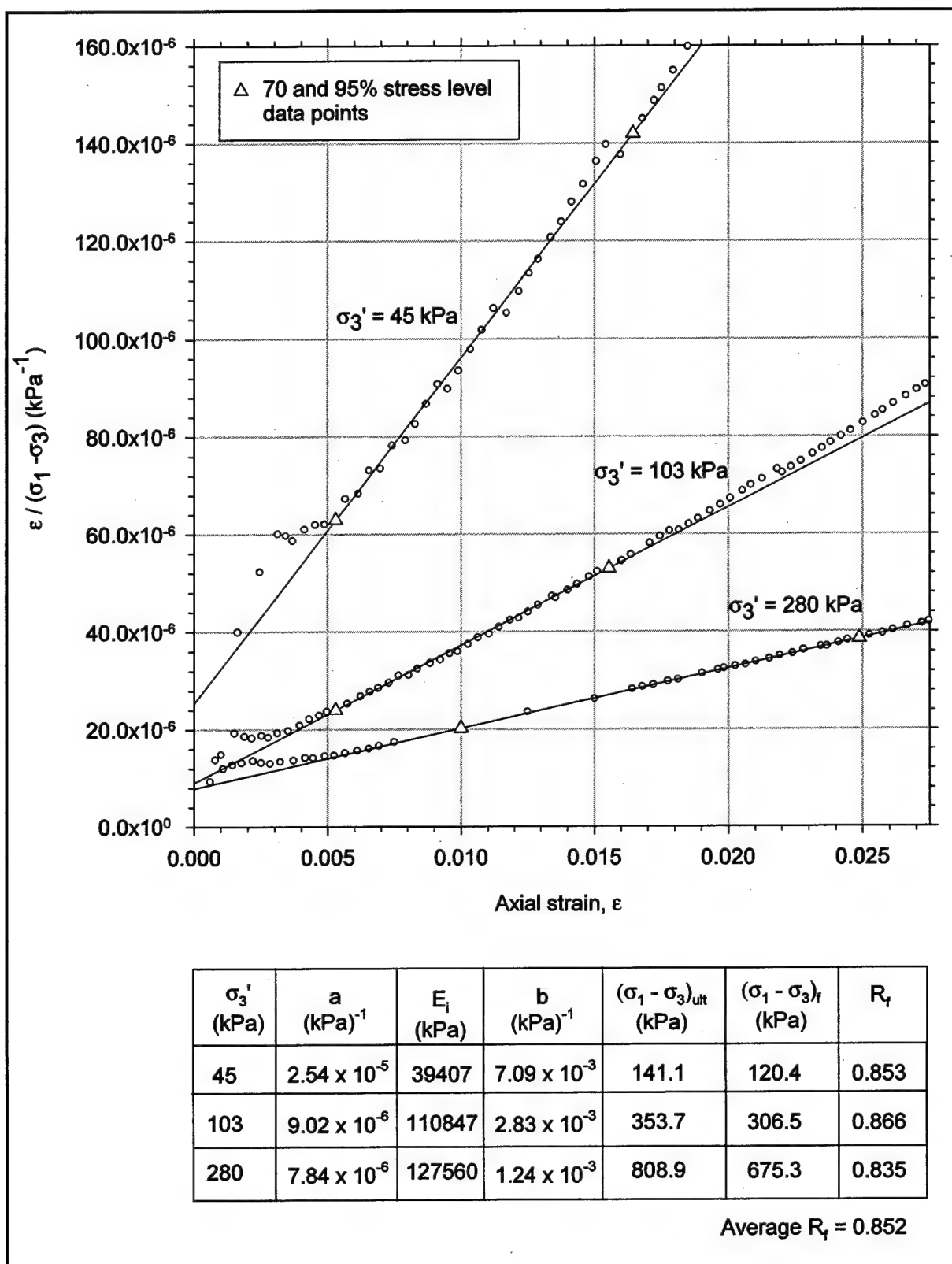


Figure B1. Transformed stress-strain plots from triaxial test data on medium-dense Density sand and determination of hyperbolic parameter values

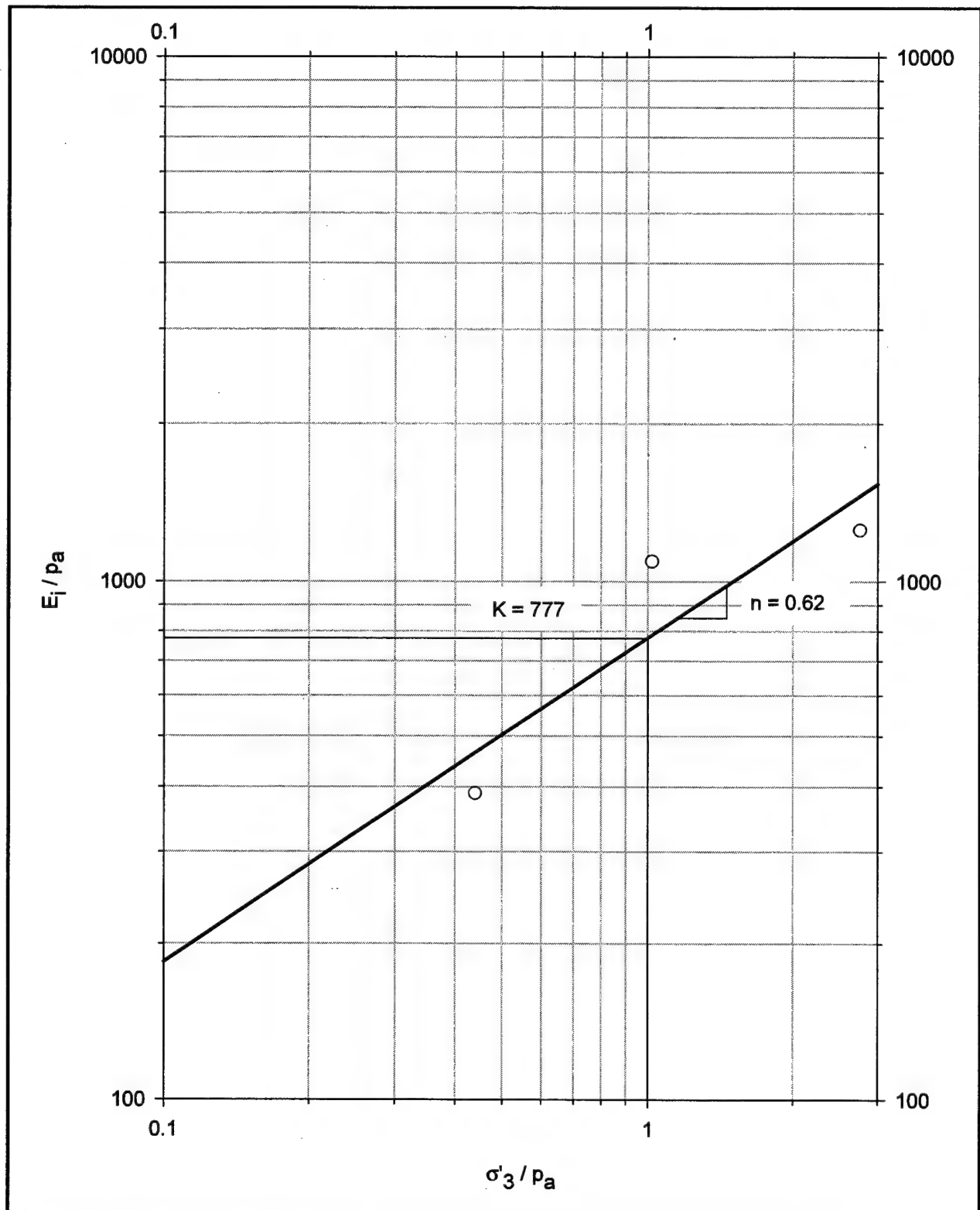


Figure B2. Determination of hyperbolic parameters K and n for medium-dense Density sand

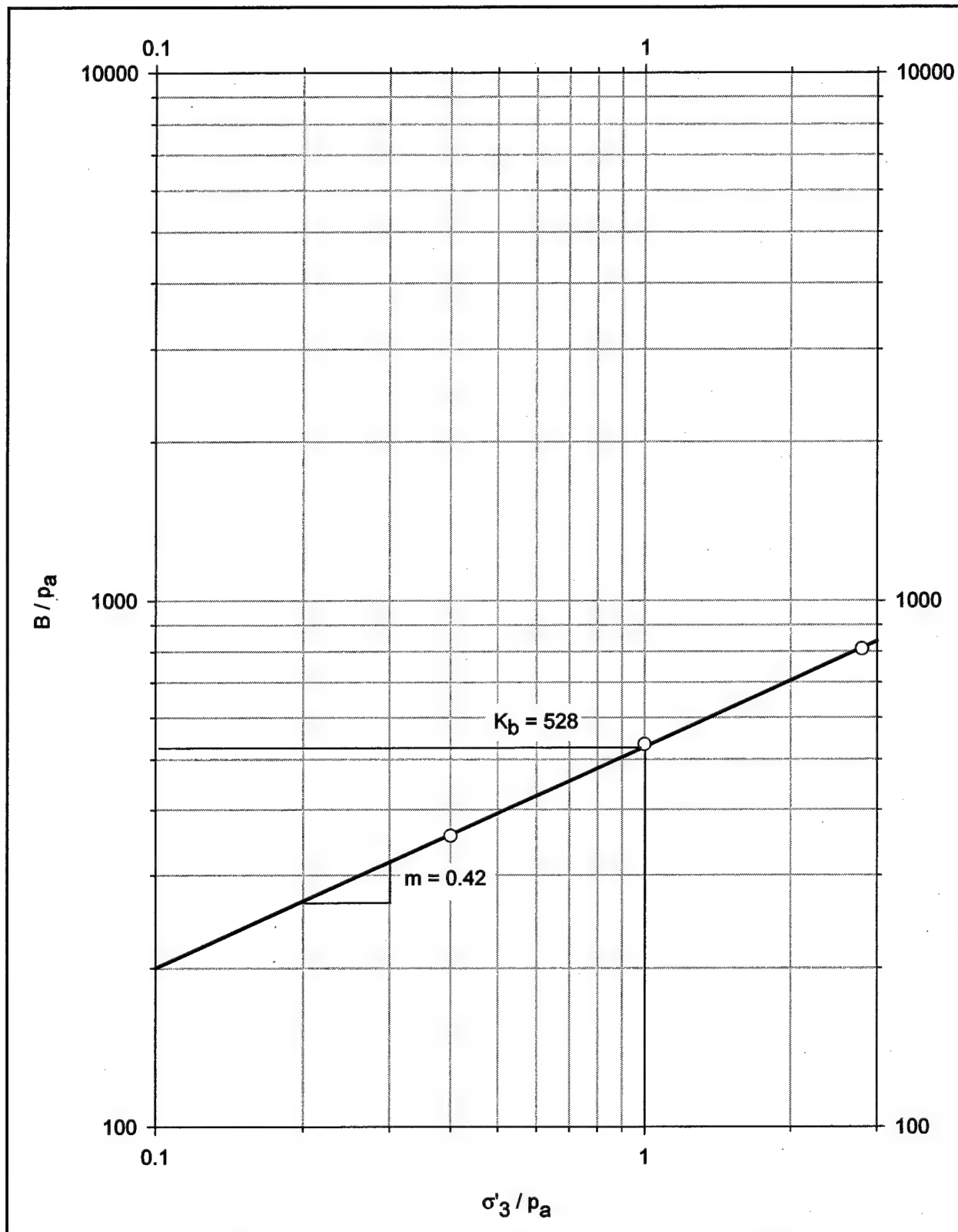


Figure B3. Determination of hyperbolic parameters K_b and m for medium-dense Density sand

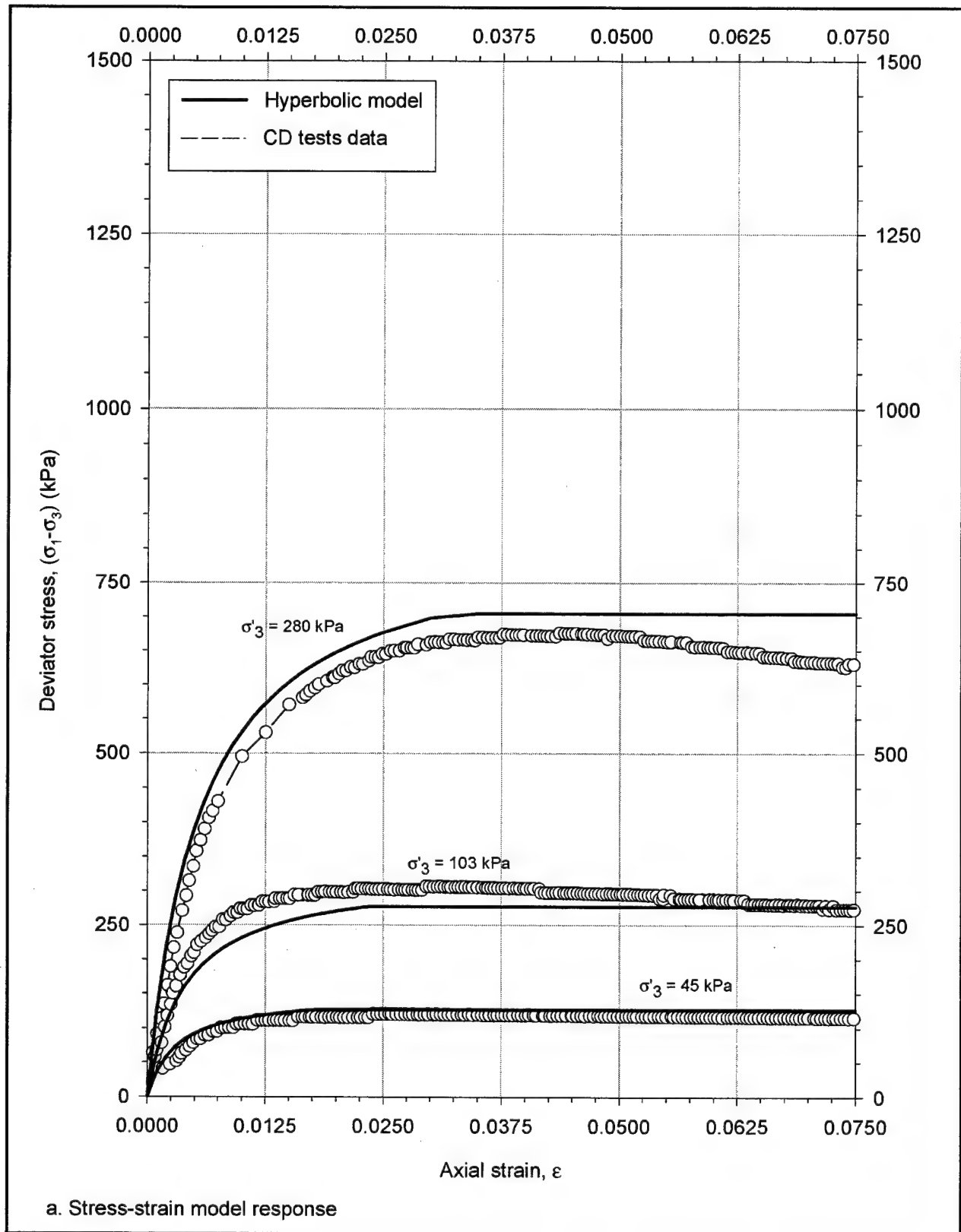


Figure B4. Hyperbolic model for medium-dense Density sand and comparison to CD triaxial test data
(Continued)

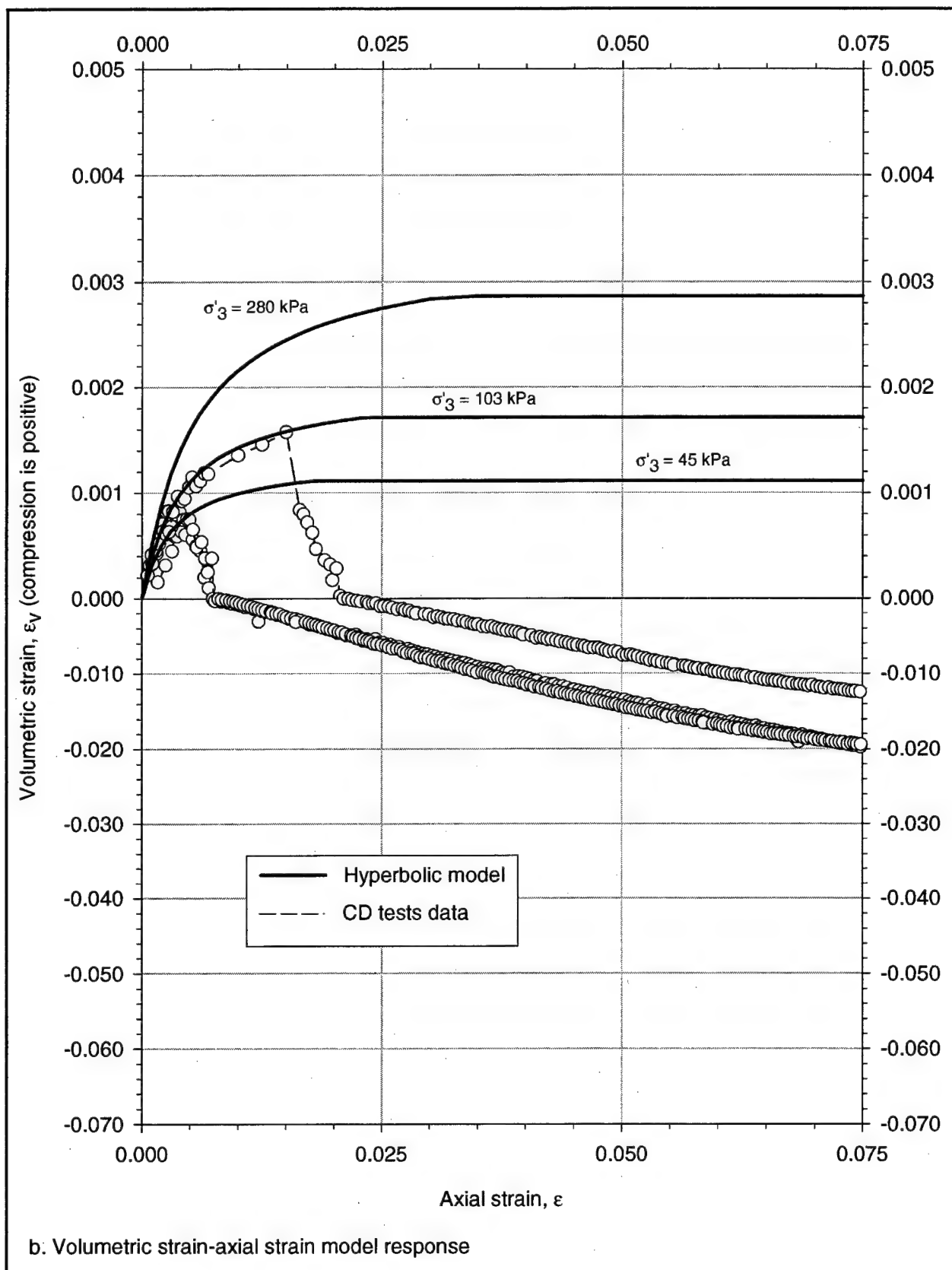


Figure B4. (Concluded)

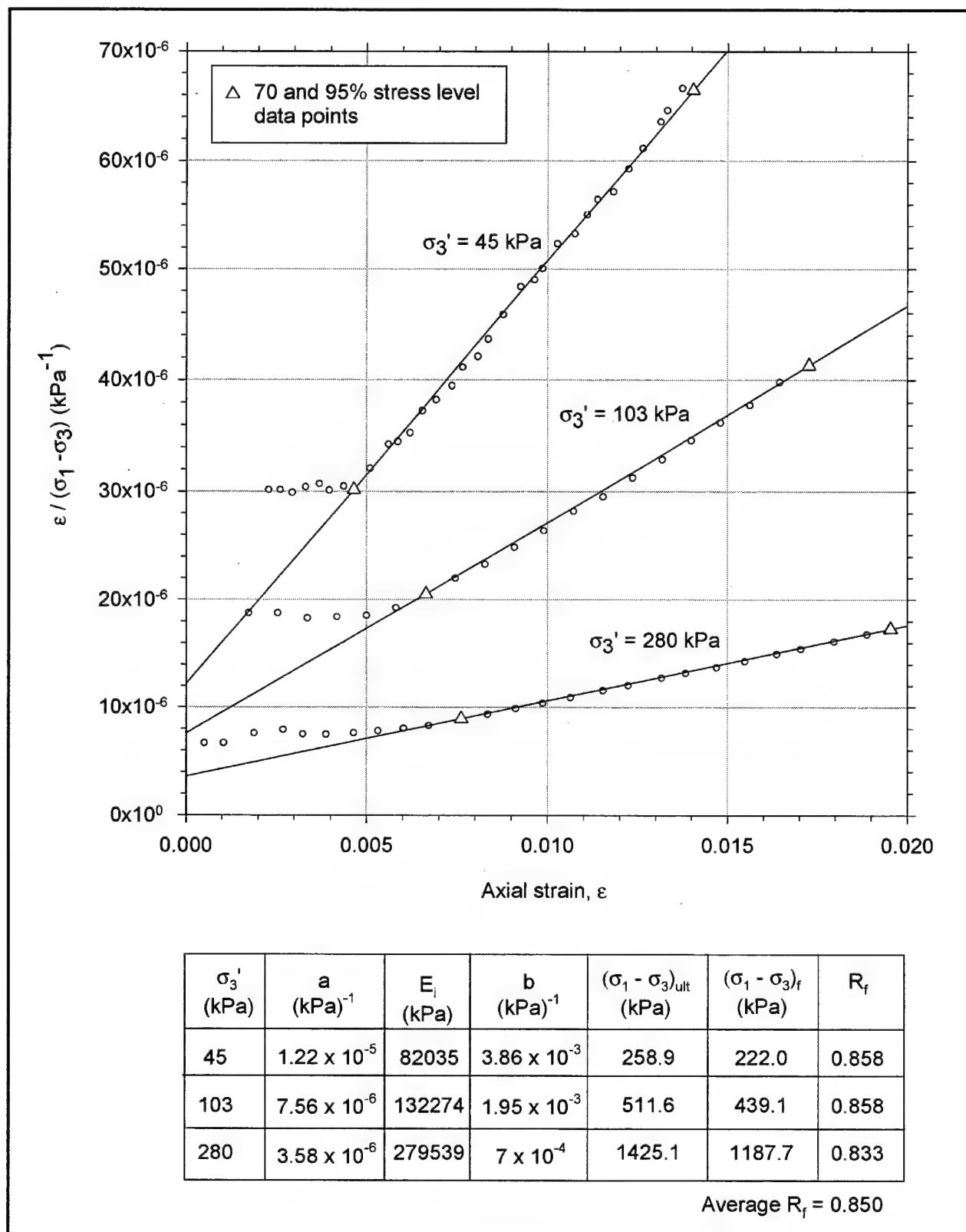


Figure B5. Transformed stress-strain plots from triaxial test data on dense sand and determination of hyperbolic parameter values

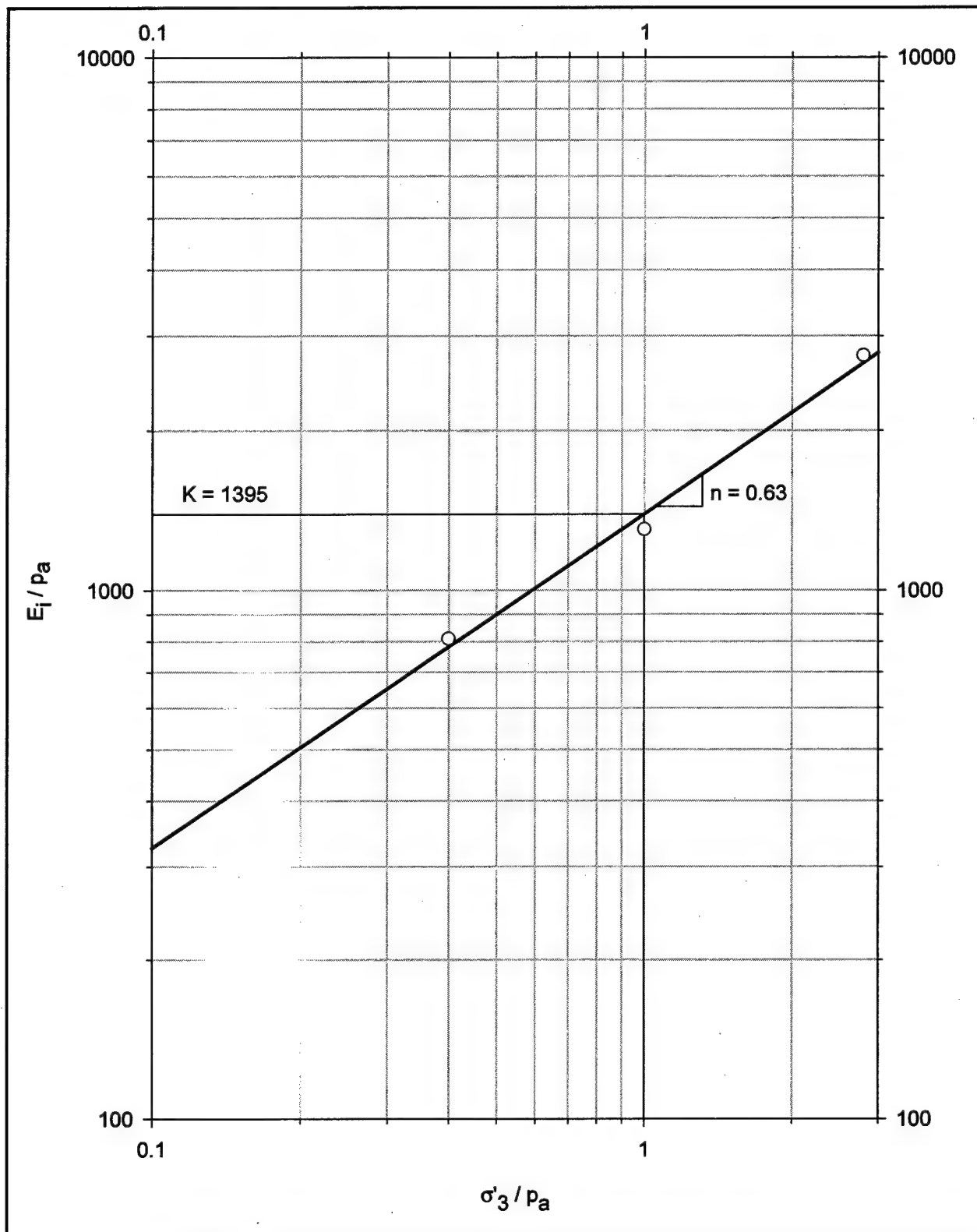


Figure B6. Determination of hyperbolic parameters K and n for dense Density sand

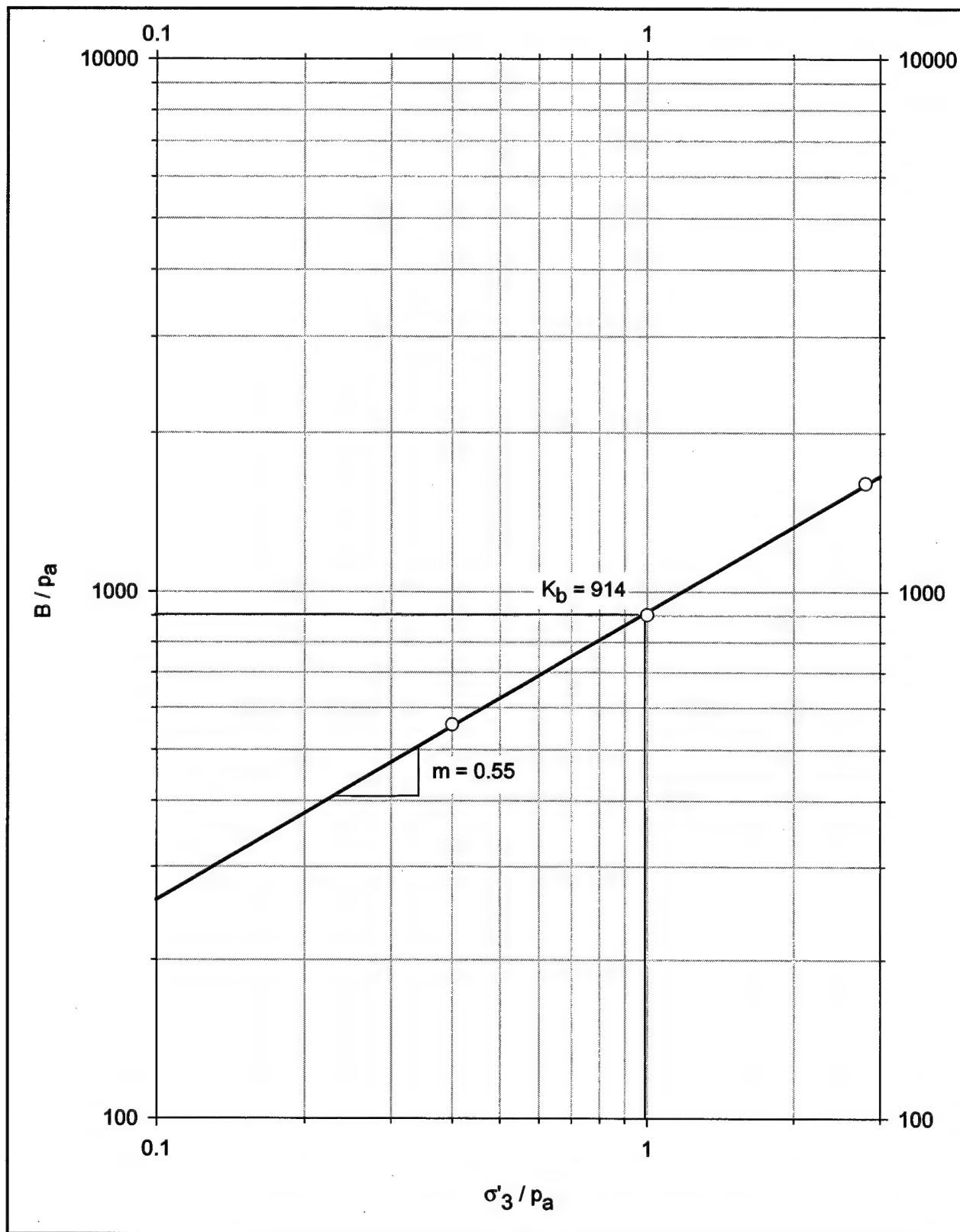


Figure B7. Determination of hyperbolic parameters K and m for dense Density sand

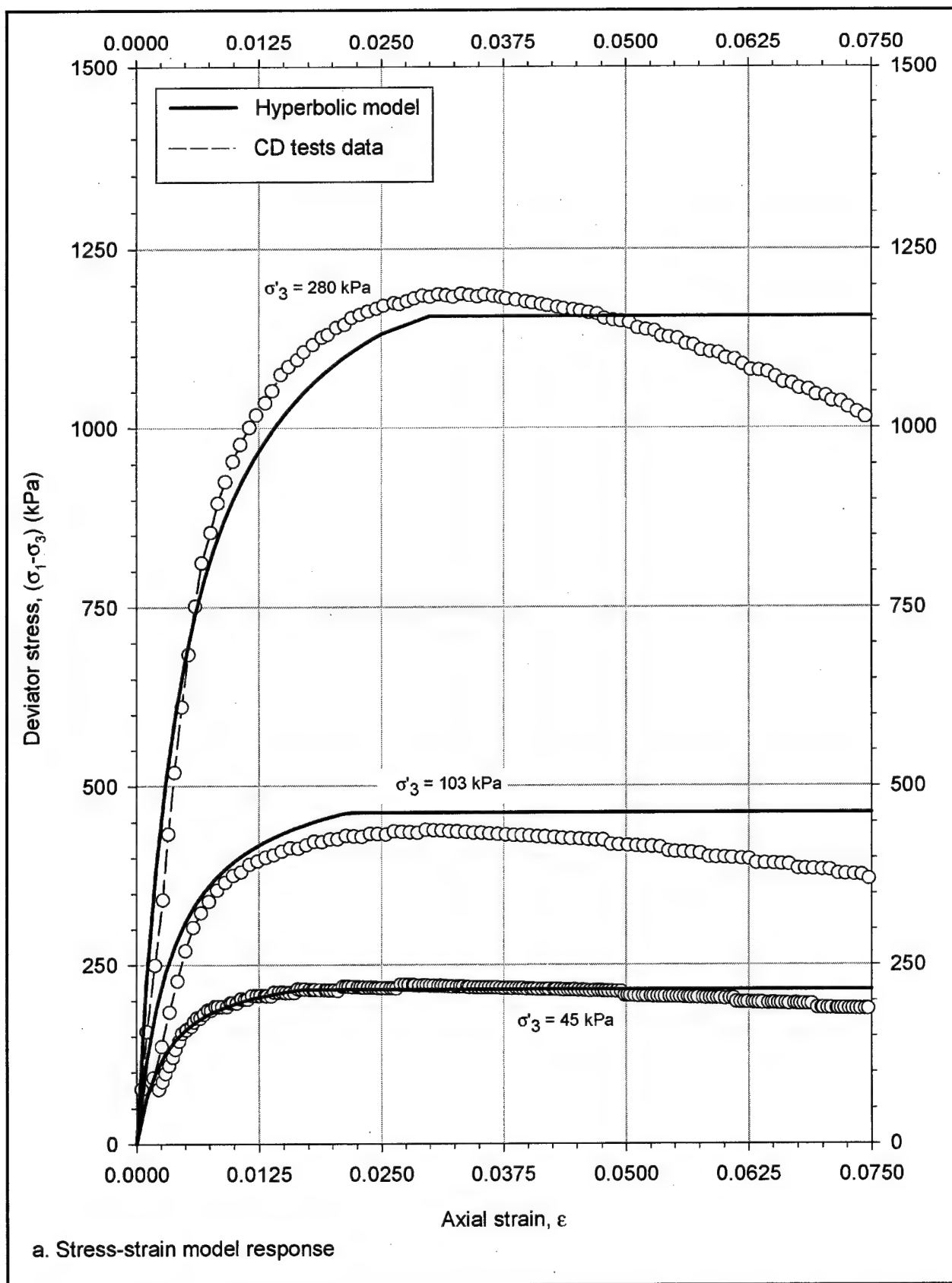


Figure B8. Hyperbolic model for dense Density sand and comparison to CD triaxial test data (Continued)

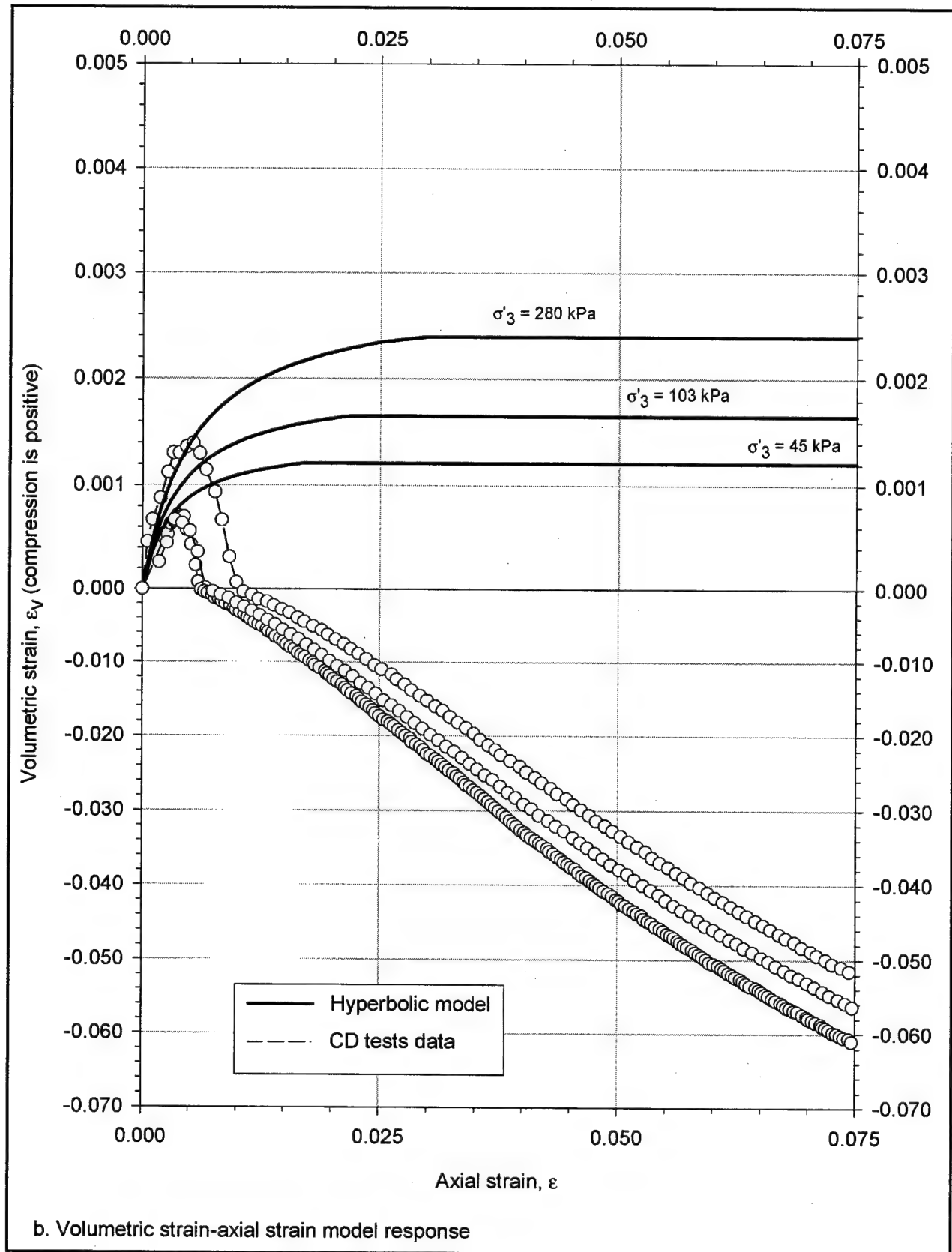
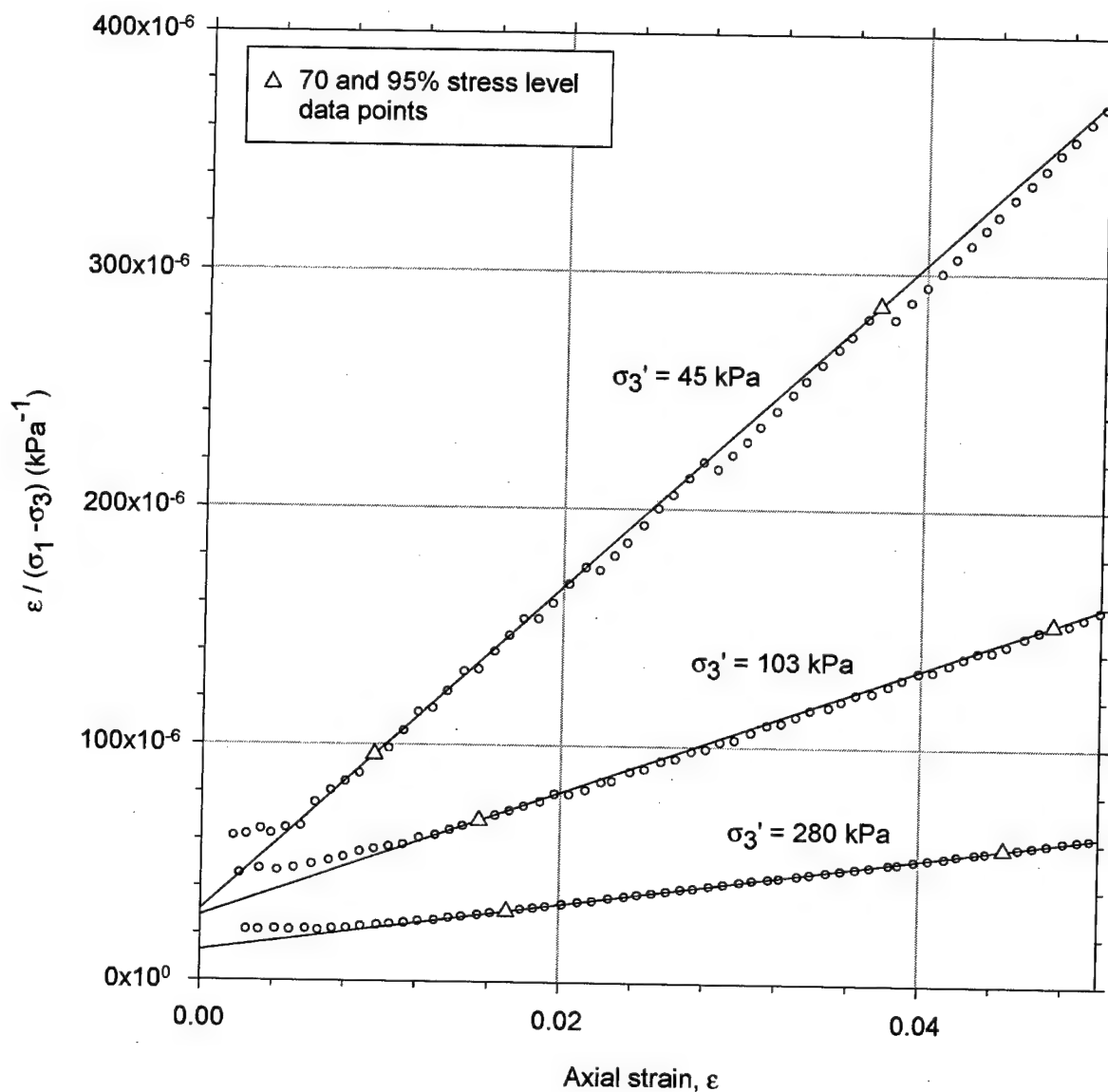


Figure B8. (Concluded)



σ_3' (kPa)	a (kPa) ⁻¹	E_i (kPa)	b (kPa) ⁻¹	$(\sigma_1 - \sigma_3)_{ult}$ (kPa)	$(\sigma_1 - \sigma_3)_f$ (kPa)	R_f
45	2.99×10^{-5}	33451	6.86×10^{-3}	145.8	139.5	0.957
103	2.73×10^{-5}	36640	2.64×10^{-3}	378.1	326.0	0.862
280	1.27×10^{-5}	78834	1×10^{-3}	996.2	817.2	0.820

Average $R_f = 0.880$

Figure B9. Transformed stress-strain plots from triaxial test data on medium-dense Light Castle sand and determination of hyperbolic parameter values

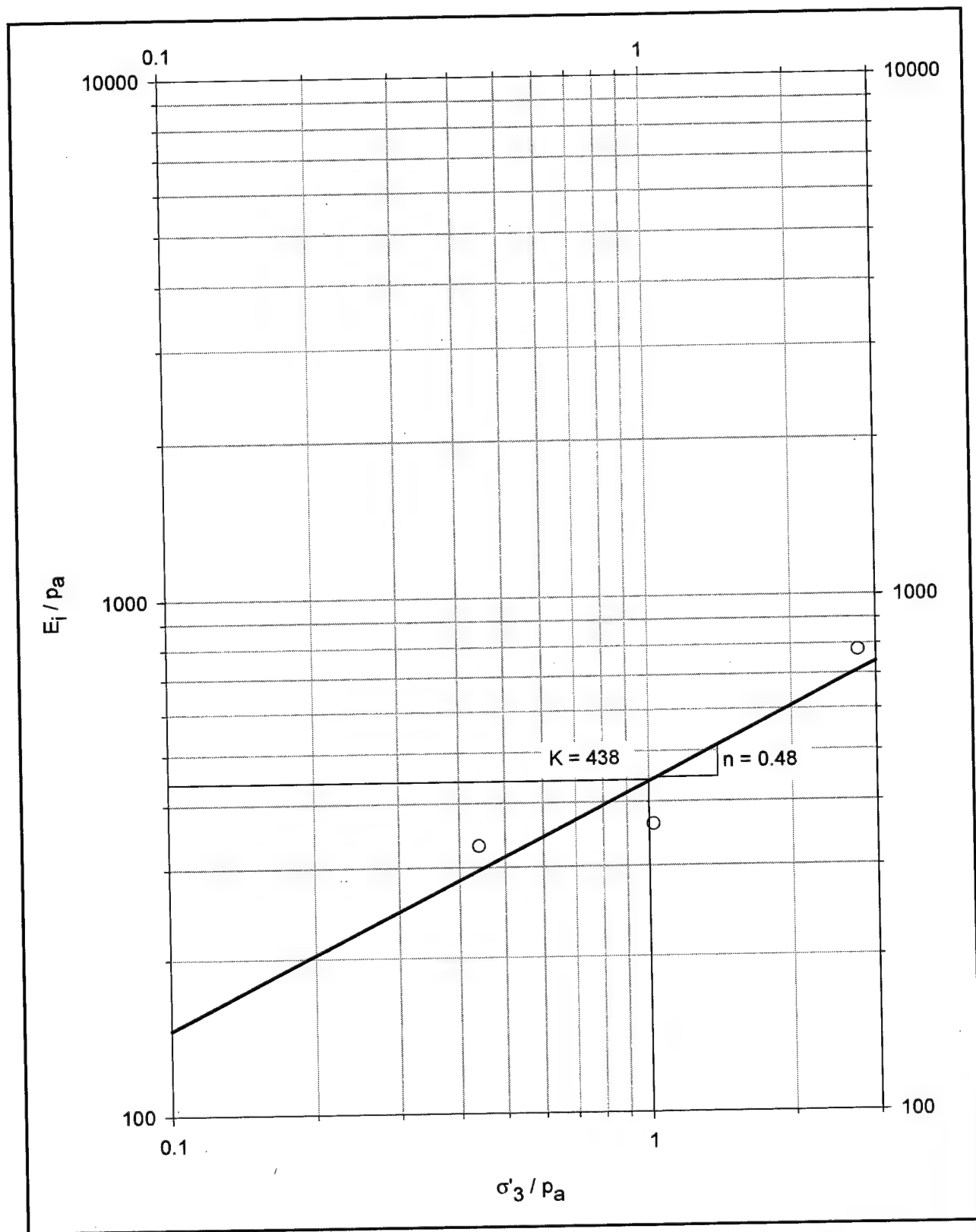


Figure B10. Determination of hyperbolic parameters K and n for medium-dense Light Castle sand

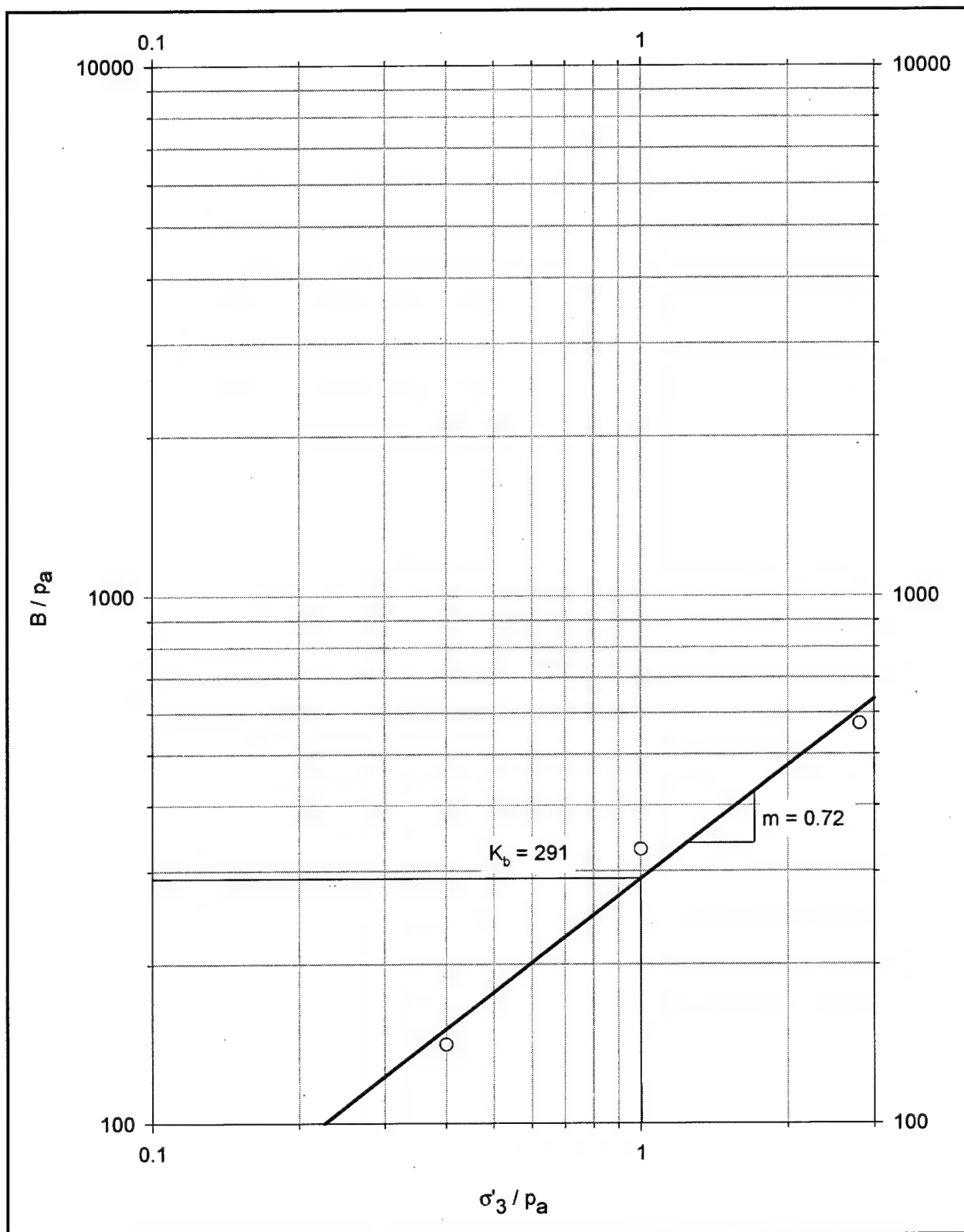


Figure B11. Determination of hyperbolic parameters K_b and m for medium-dense Light Castle sand

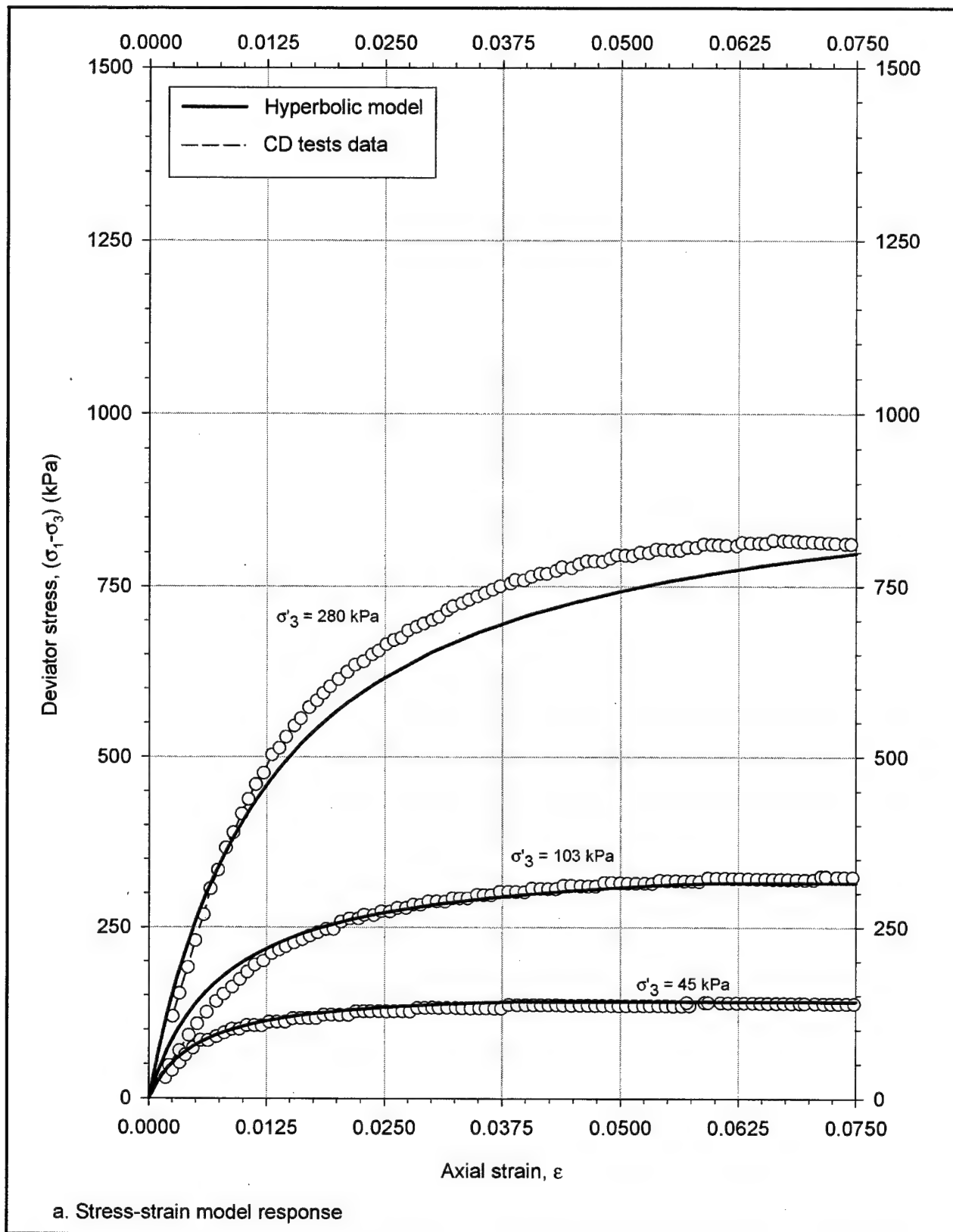


Figure B12. Hyperbolic model for medium-dense Light Castle sand and comparison to CD triaxial test data (Continued)

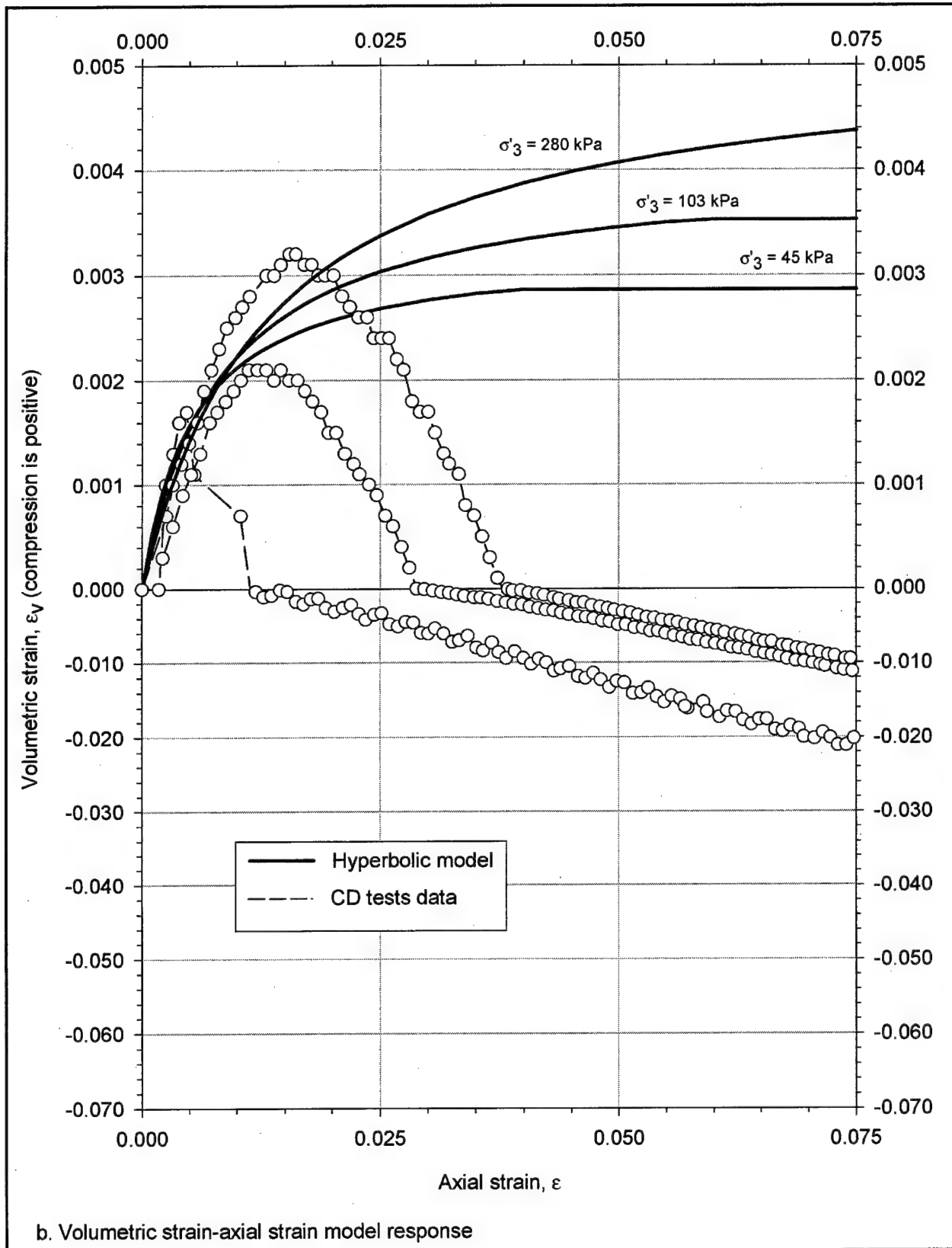


Figure B12. (Concluded)

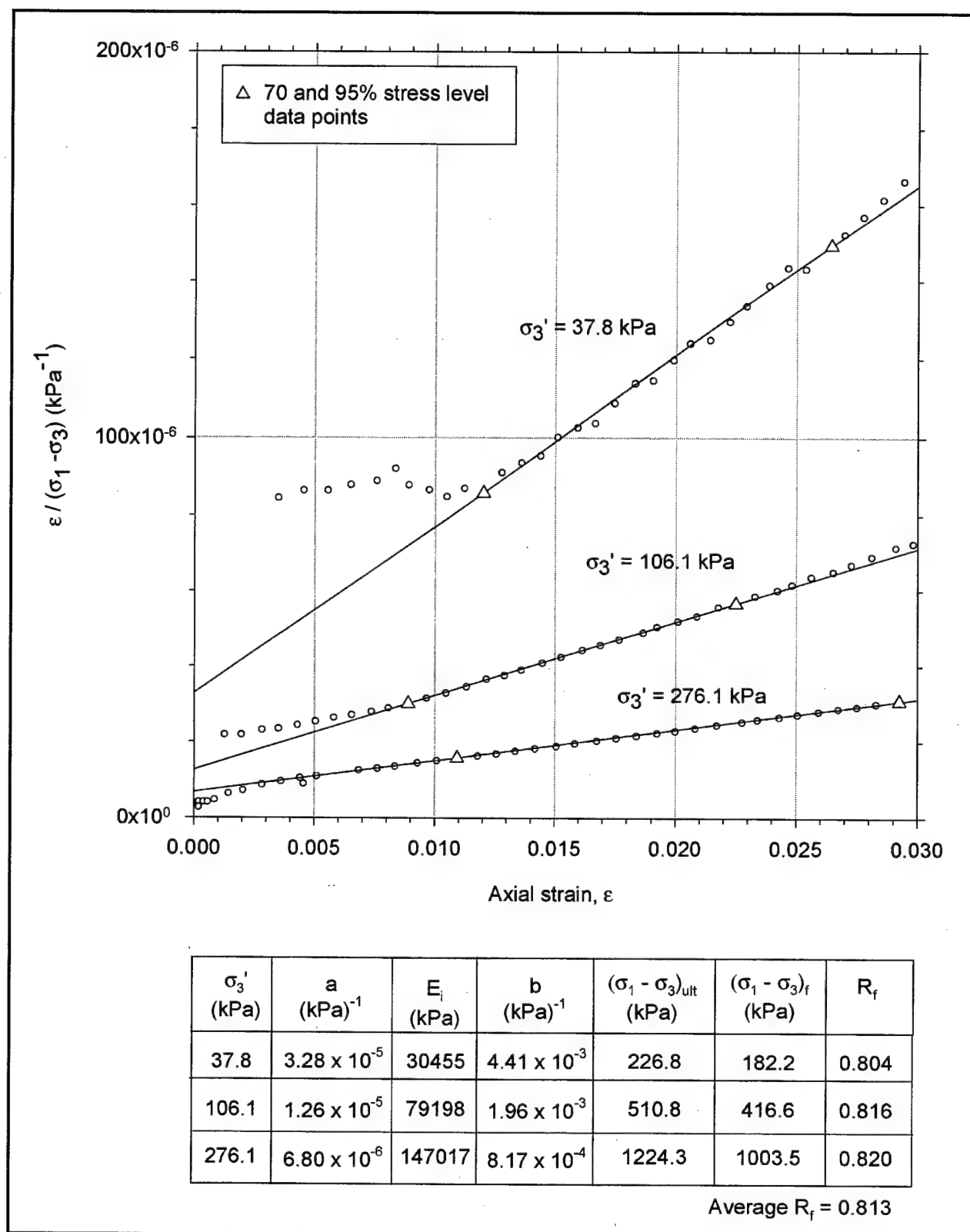


Figure B13. Transformed stress-strain plots from triaxial test data on dense Light Castle sand and determination of hyperbolic parameter values

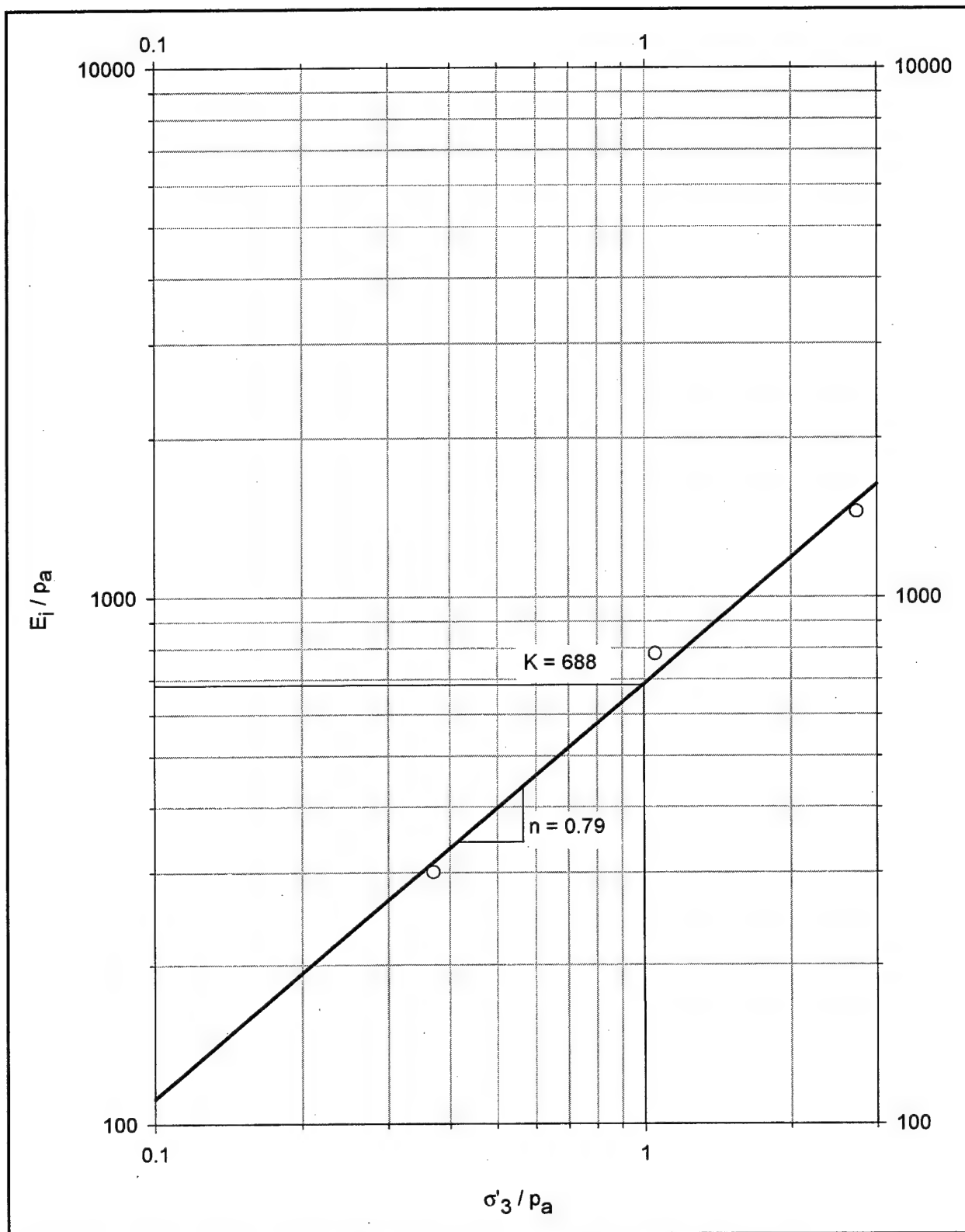


Figure B14. Determination of hyperbolic parameters K and n for dense Light Castle sand

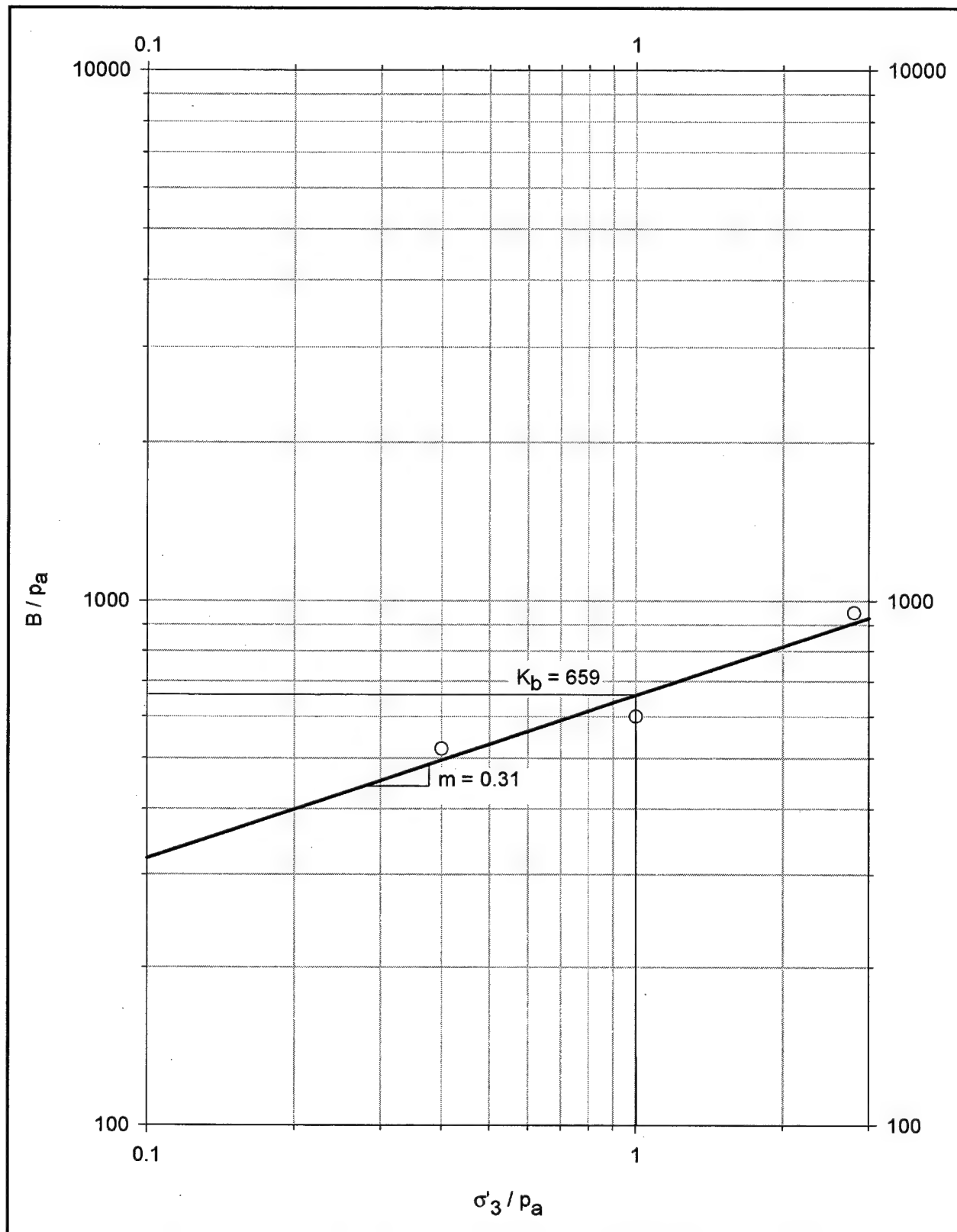


Figure B15. Determination of hyperbolic parameters K_b and m for dense Light Castle sand

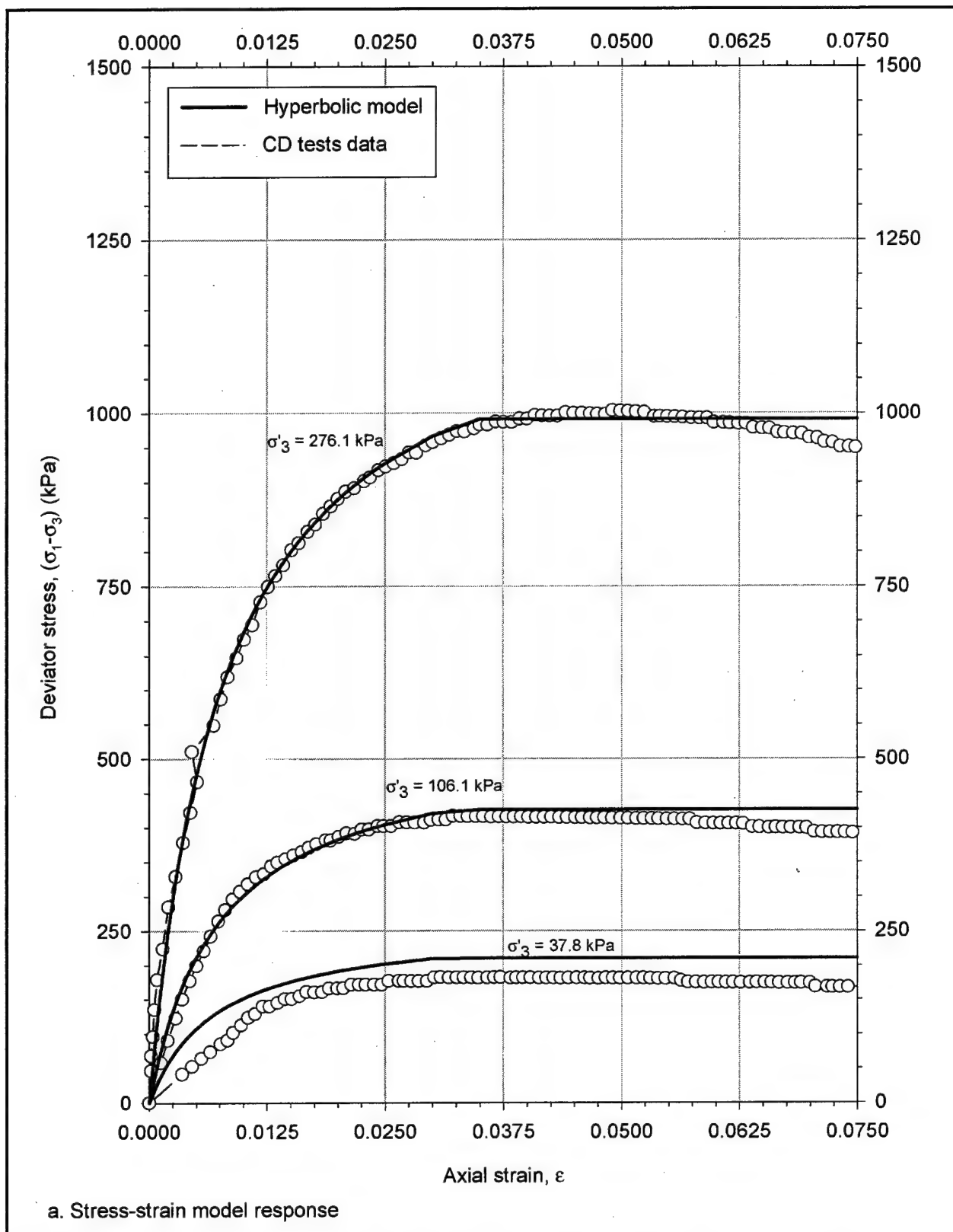


Figure B16. Hyperbolic model for dense Light Castle sand and comparison to CD triaxial test data
(Continued)

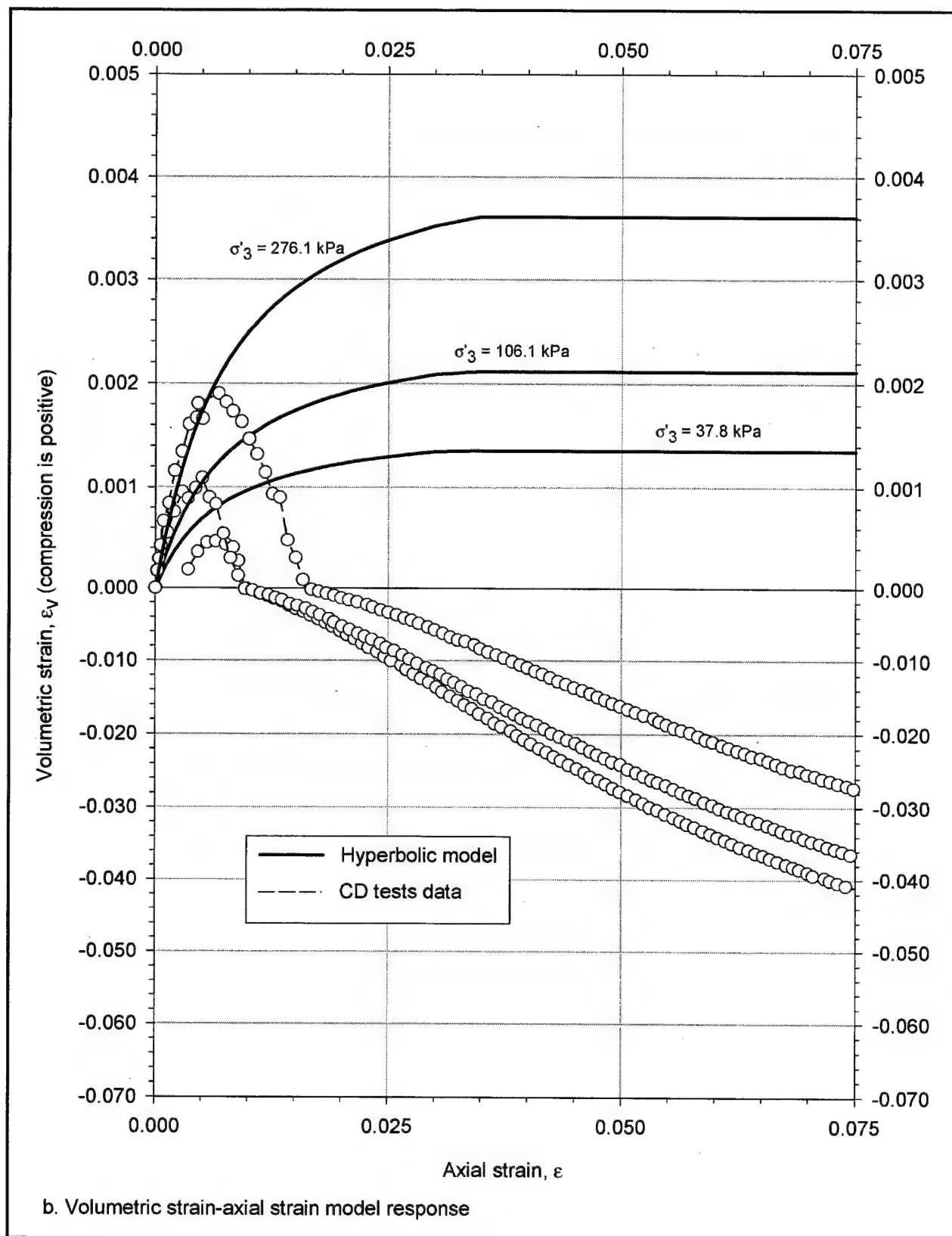


Figure B16. (Concluded)

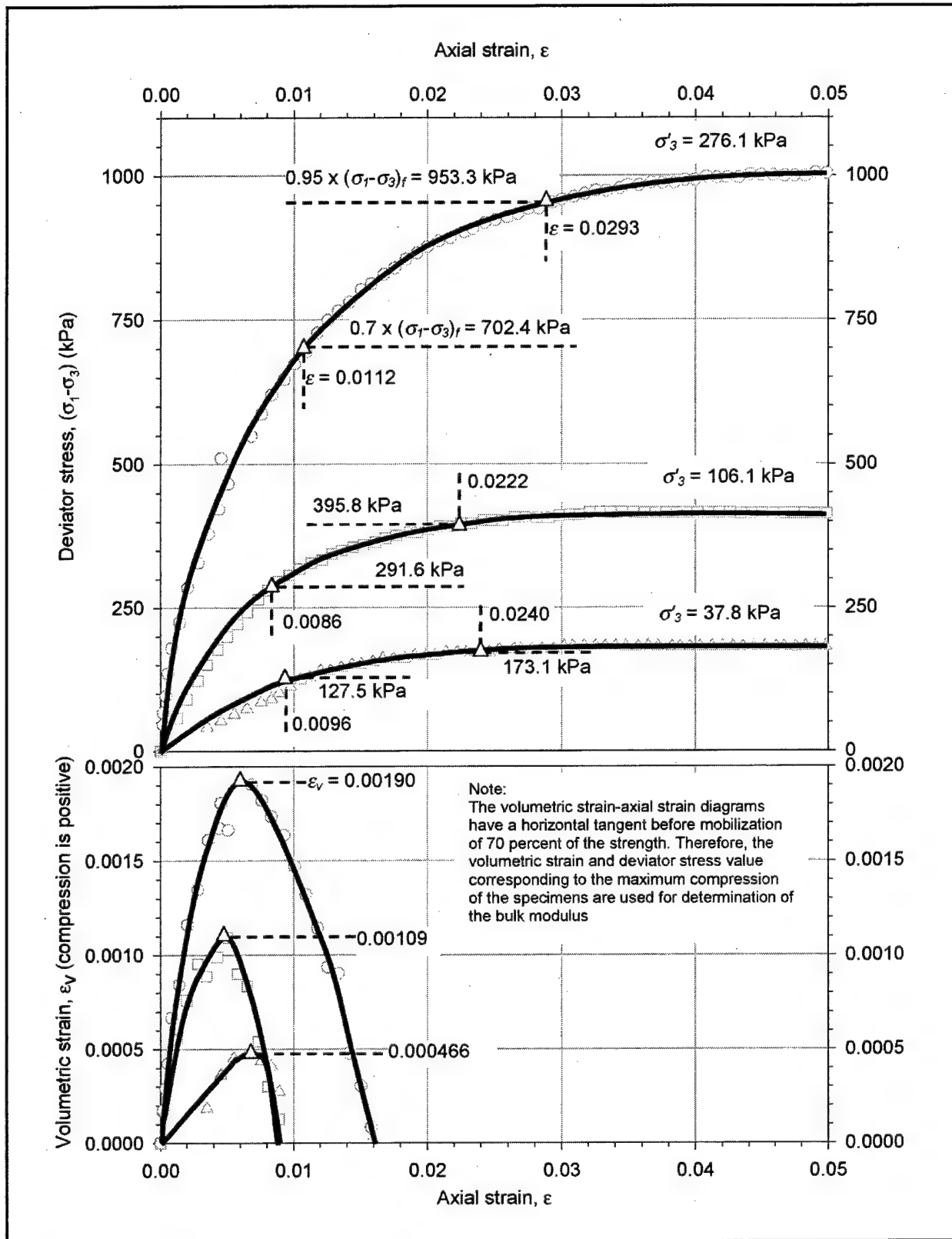


Figure B17. Example determination of axial and volumetric strain values at 70 and 95 percent of strength. Data from CD triaxial tests on dense Light Castle sand

σ'_3 (kPa)	Data for Determination of Hyperbolic Parameters K and n					Data for Determination of Hyperbolic Parameters K_b and m				
	70% Stress Level		95% Stress Level							
	$(\sigma_1 - \sigma_3)_f$ (kPa)	ε	$(\sigma_1 - \sigma_3)$ (kPa)	ε	$\frac{\varepsilon}{(\sigma_1 - \sigma_3)}$ (kPa ⁻¹)	$(\sigma_1 - \sigma_3)$ (kPa)	ε	$(\sigma_1 - \sigma_3)$ (kPa)	ε_v	$\frac{(\sigma_1 - \sigma_3)}{3 \cdot \varepsilon_v}$ (kPa)
(1)	(2)	(4)	(3)	(5)	(6)	(7)	(8)	(9)	(10)	(11)
38	182.2	0.0096	127.5	7.53×10^{-5}	173.1	0.0240	1.39×10^{-4}	73.8	0.00047	52340
106	416.6	0.0086	291.6	2.95×10^{-5}	395.8	0.0222	5.61×10^{-5}	199.2	0.00109	60917
276	1003.5	0.0112	702.4	1.59×10^{-5}	953.3	0.0293	3.07×10^{-5}	548.3	0.00190	96192

Notes:

- $p_a = 101.3$ kPa
- Figure B17 illustrates the procedure for the determination of the values of deviator stress, axial strain, and volumetric strain for this example
- See Appendix B for a complete explanation of the hyperbolic model and procedure for determination of hyperbolic parameter values
- In this example, the organization of calculations is based on Figure 21 of Duncan et al. (1980). Numerical values correspond to the dense Light Castle Sand used for this investigation

$\frac{\sigma'_3}{p_a}$	$\frac{1}{(\sigma_1 - \sigma_3)_{ult}}$ (kPa) ⁻¹	R_f	$\frac{E_i}{p_a}$	$\frac{B}{p_a}$
(12)	(13)	(14)	(15)	(16)
0.38	4.42×10^{-3}	0.805	300	517
1.05	1.96×10^{-3}	0.816	782	601
2.72	8.18×10^{-4}	0.820	1465	950

- (1) Confining stress. Use effective confining stress, σ'_3 , for effective stress analyses. Use total confining stress, σ_3 , for total stress analyses
 (2) Deviator stress at failure. Determined from the deviator stress-axial strain plots of the data of each test.

$$(3) \quad 70 \text{ percent of } (\sigma_1 - \sigma_3)_f \quad (4) \quad \text{Axial strain corresponding to (3) determined as illustrated in Figure B17} \quad (5) \quad \frac{\varepsilon}{(\sigma_1 - \sigma_3)} = \frac{(4)}{(3)}$$

$$(6) \quad 95 \text{ percent of } (\sigma_1 - \sigma_3)_f \quad (7) \quad \text{Axial strain corresponding to (6) determined as illustrated in Figure B17} \quad (8) \quad \frac{\varepsilon}{(\sigma_1 - \sigma_3)} = \frac{(7)}{(6)}$$

- (9) Deviator stress for determination of bulk modulus, B. Use (3) if the ε_v - ε curve does not reach a horizontal tangent in compression before (3) is mobilized. Otherwise, use $(\sigma_1 - \sigma_3)$ corresponding to the maximum ε_v (compression) as illustrated in Figure B17
 (10) Volumetric strain for determination of B. Use ε_v corresponding to (3) if the ε_v - ε curve does not reach a horizontal tangent in compression before (3) is mobilized. Otherwise, use the maximum ε_v (compression) as illustrated in Figure B17

$$(11) \quad \frac{(\sigma_1 - \sigma_3)}{3 \cdot \varepsilon_v} = \frac{(9)}{3 \cdot (10)} \quad (12) \quad \frac{\sigma'_3}{p_a} = \frac{(1)}{101.3 \text{ kPa}} \quad (13) \quad \frac{1}{(\sigma_1 - \sigma_3)_{ult}} = \frac{(8) - (5)}{(7) - (4)} \quad (14) \quad R_f = \frac{(2) \cdot (13)}{(5) + (8) - (13)} \cdot \frac{(4) + (7)}{(4) + (7)} \cdot \frac{1}{p_a}$$

$$(16) \quad \frac{B}{p_a} = \frac{(11)}{p_a}$$

Figure B18. Determination of the normalized values of E_i and B for each of the CD triaxial tests performed on dense Light Castle sand (adapted from Duncan et al. 1980)

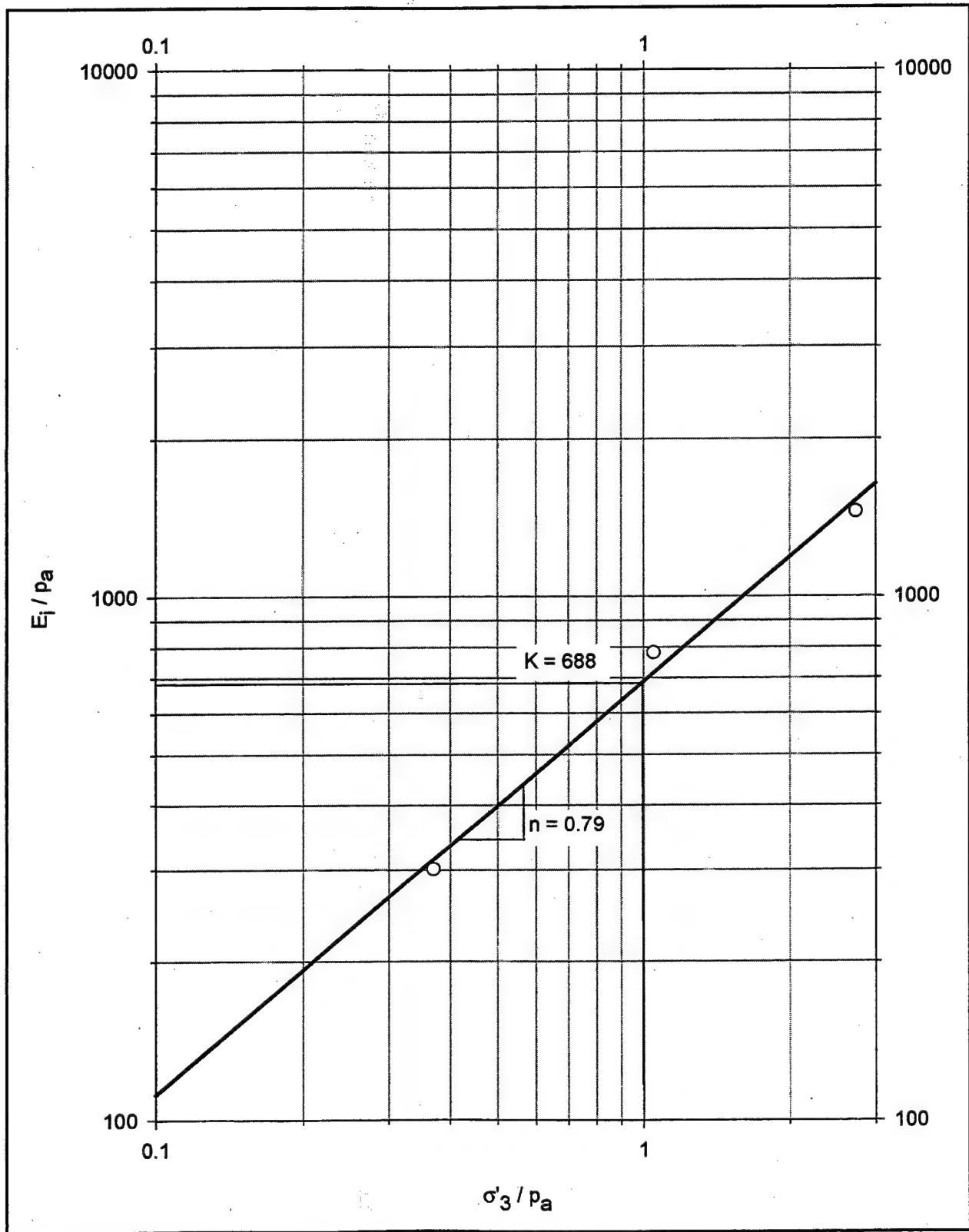


Figure B19. Determination of hyperbolic parameters K and n from the E_i / p_a values determined in column (15) of Figure B18

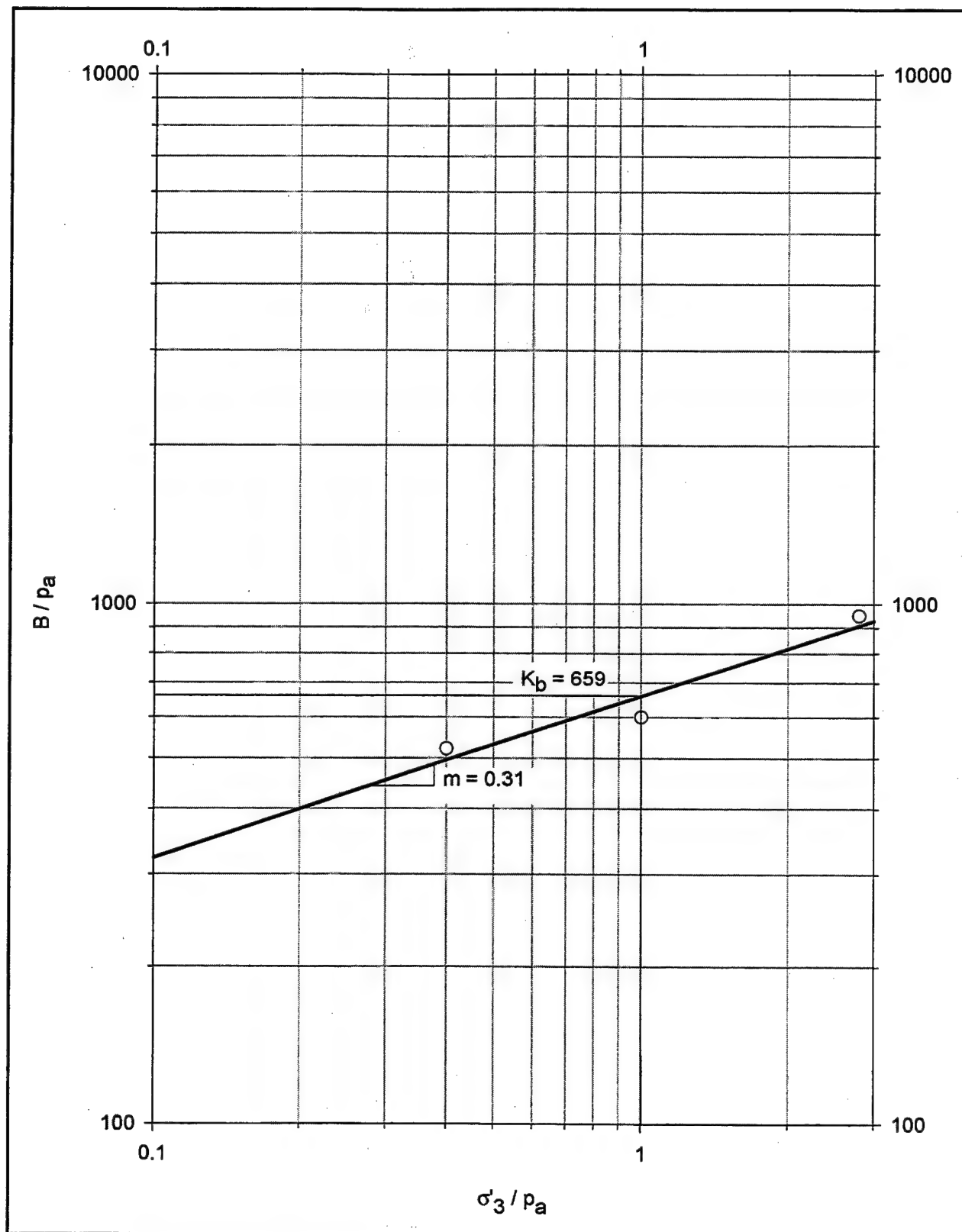


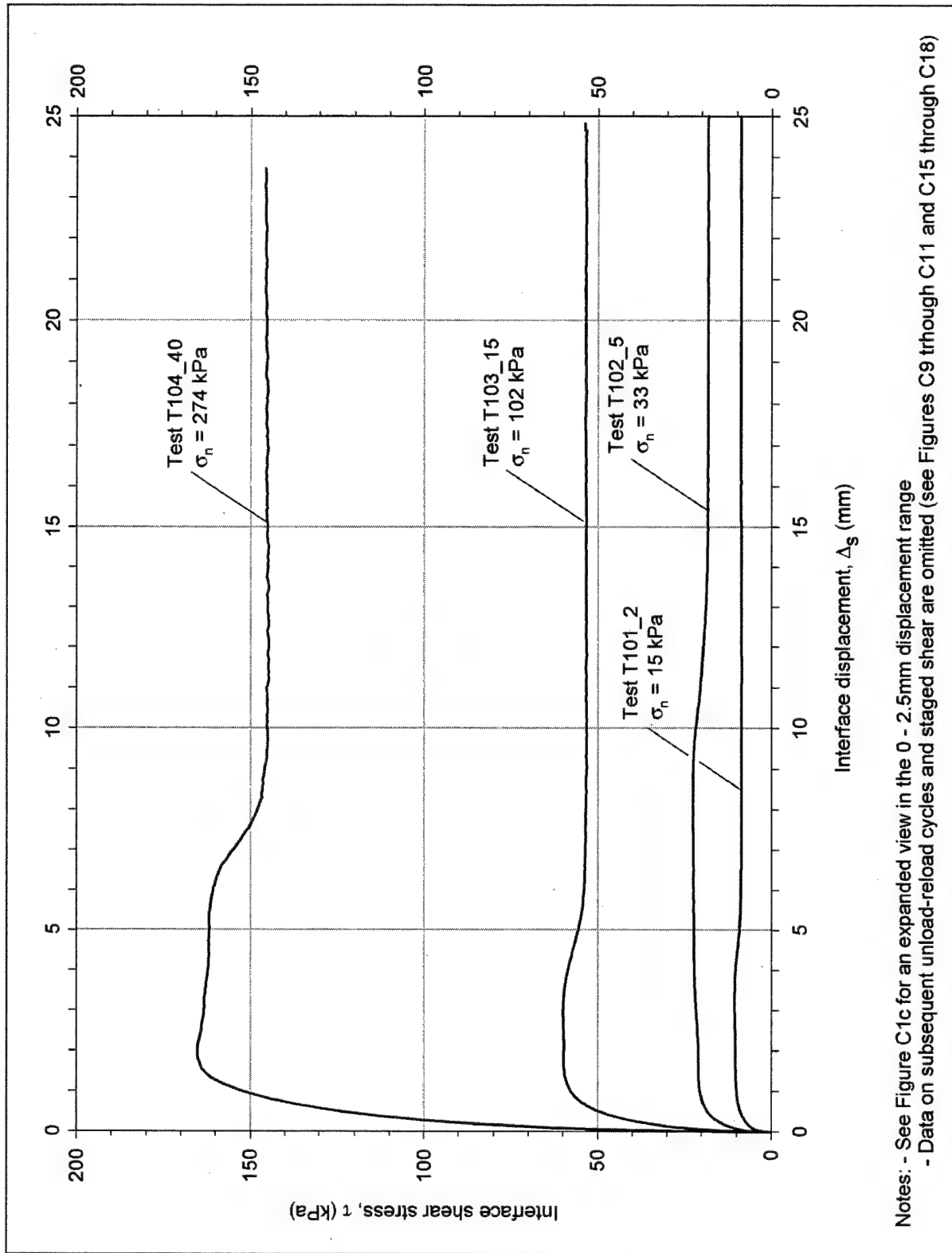
Figure B20. Determination of hyperbolic parameters K_b and m from the B/p_a values determined in column (16) of Figure B18

Appendix C

Results of Interface Tests

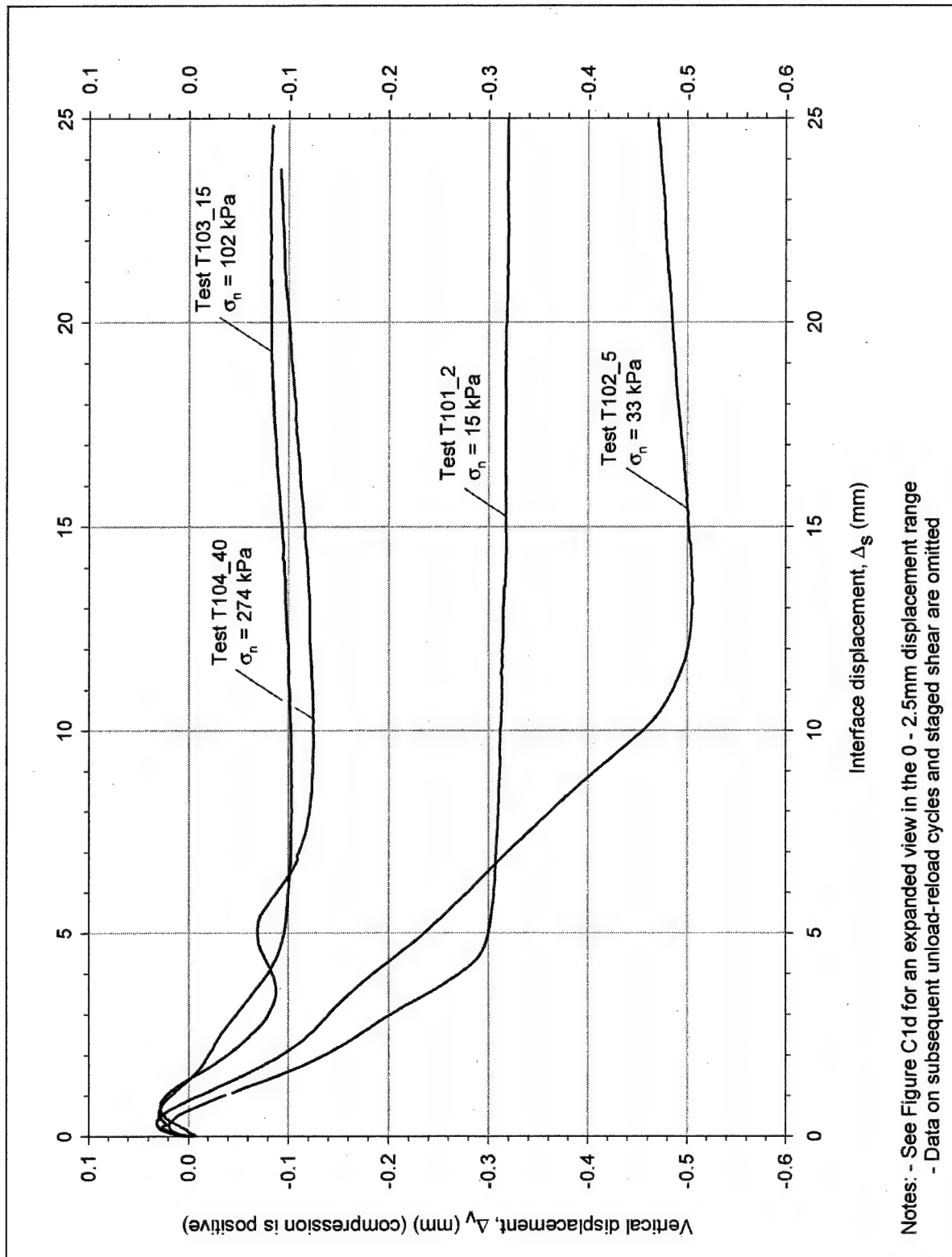
This appendix contains the results of all the interface tests performed during this investigation. Table C1 shows the organization of the figures. Symbols used in this appendix are listed and defined in the Notation (Appendix F).

Table C1 Organization of the Figures in Appendix C			
Type of Test	Dense Density Sand Against Concrete	Medium Dense Density Sand against Concrete	Dense Light Castle Sand against Concrete
Initial loading (virgin shear)	C1 and C2	C3 and C4	C5 and C6
Staged shear	C7 through C11	-	-
Unload-reload	C12 through C18	C19 through C21	C22 through C25
Multidirectional stress path	C26 through C28	C29	C30



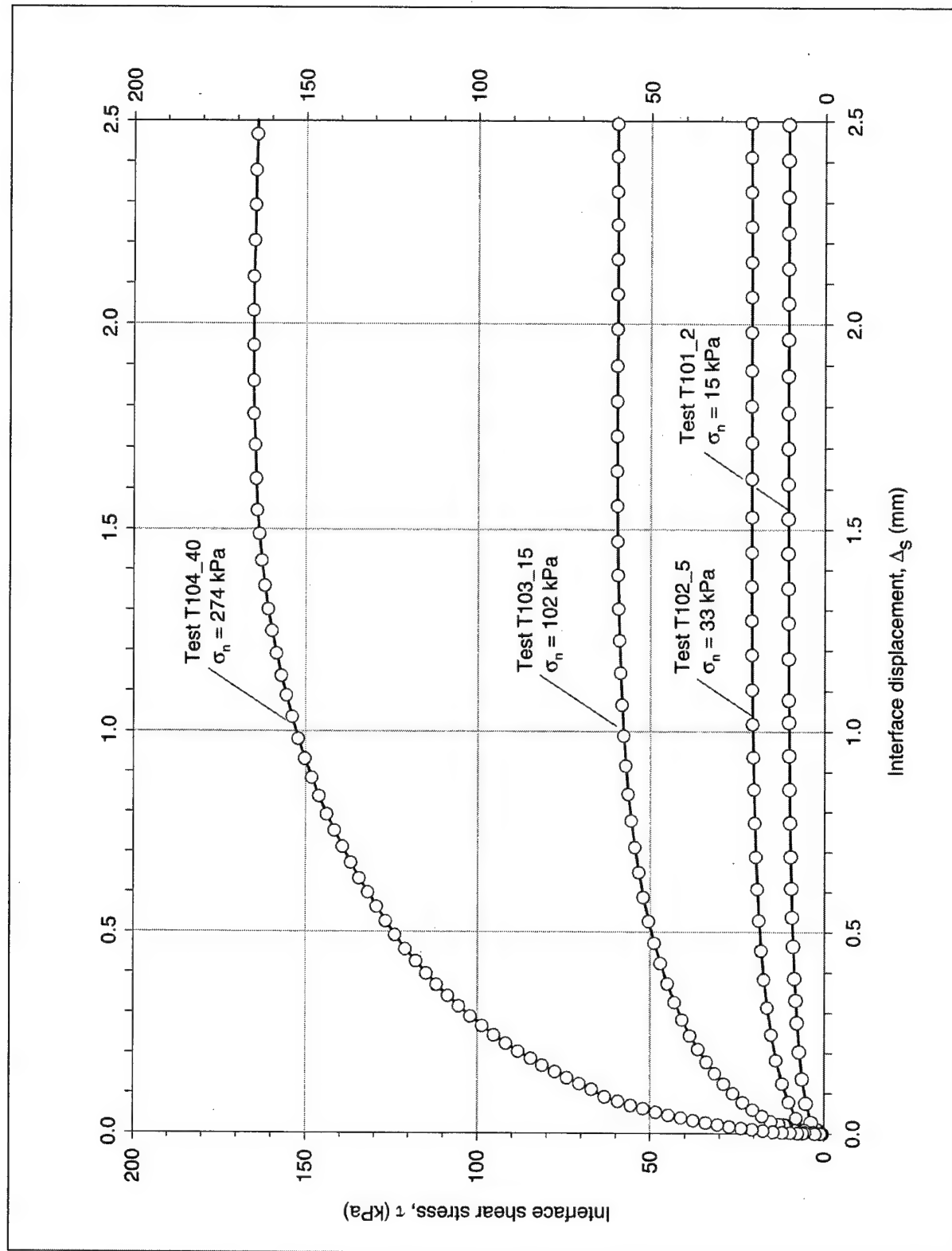
a. Shear stress versus interface displacement data

Figure C1. Results of initial loading tests on dense-Density-Sand-to-concrete interface (Sheet 1 of 4)



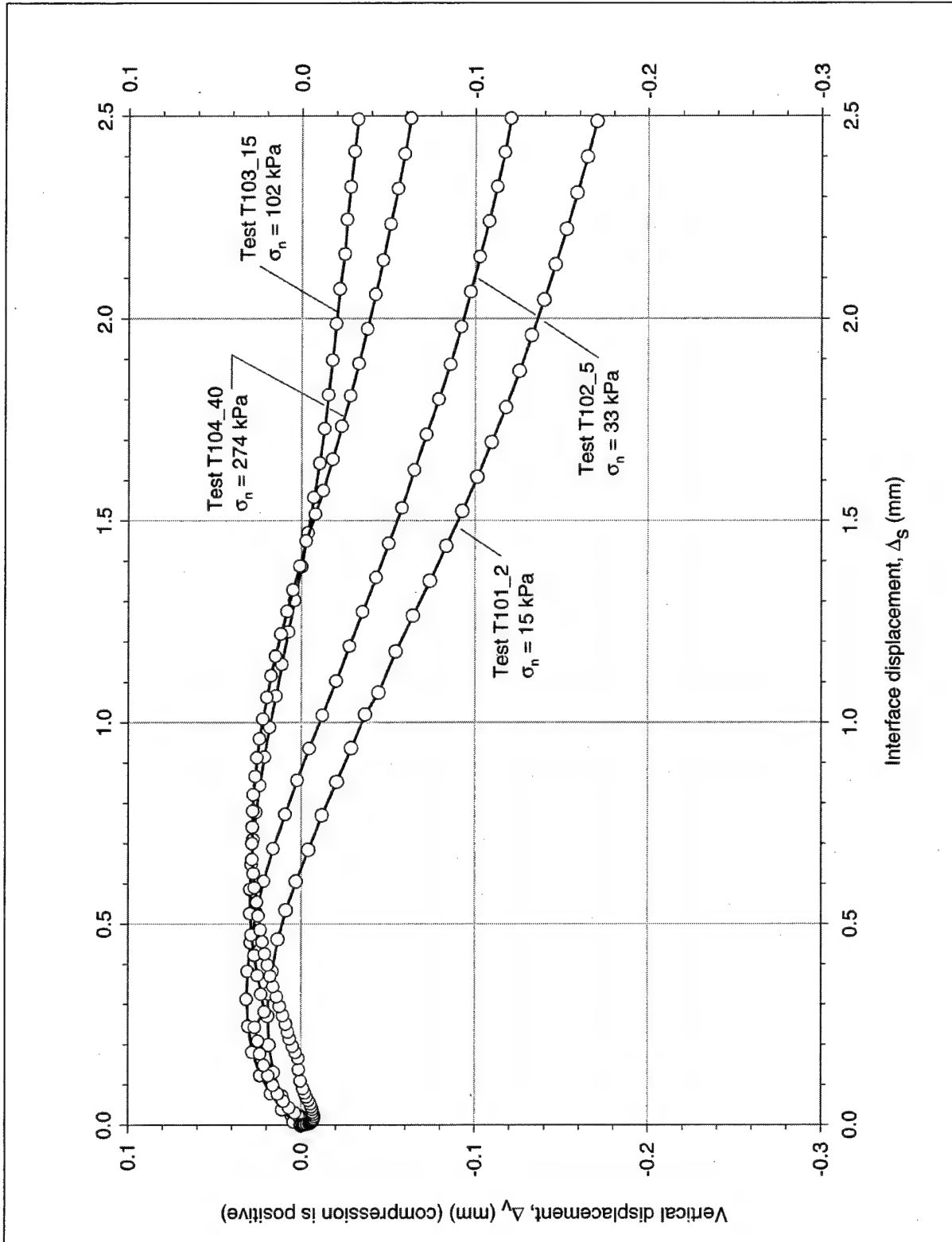
b. Vertical versus horizontal interface displacement data

Figure C1. (Sheet 2 of 4)



c. Enlargement of Figure C1a

Figure C1. (Sheet 3 of 4)



d. Enlargement of Figure C1b

Figure C1. (Sheet 4 of 4)

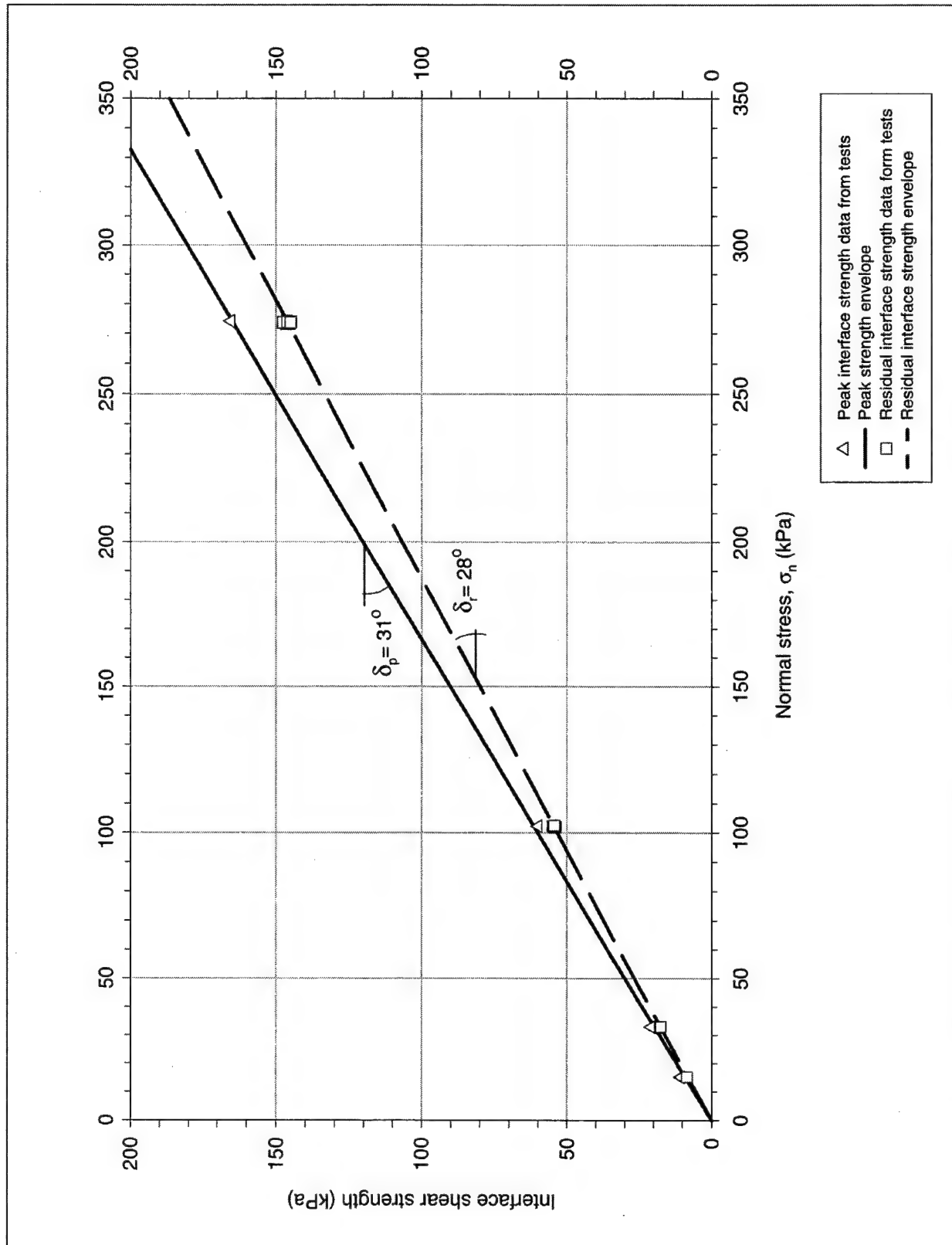
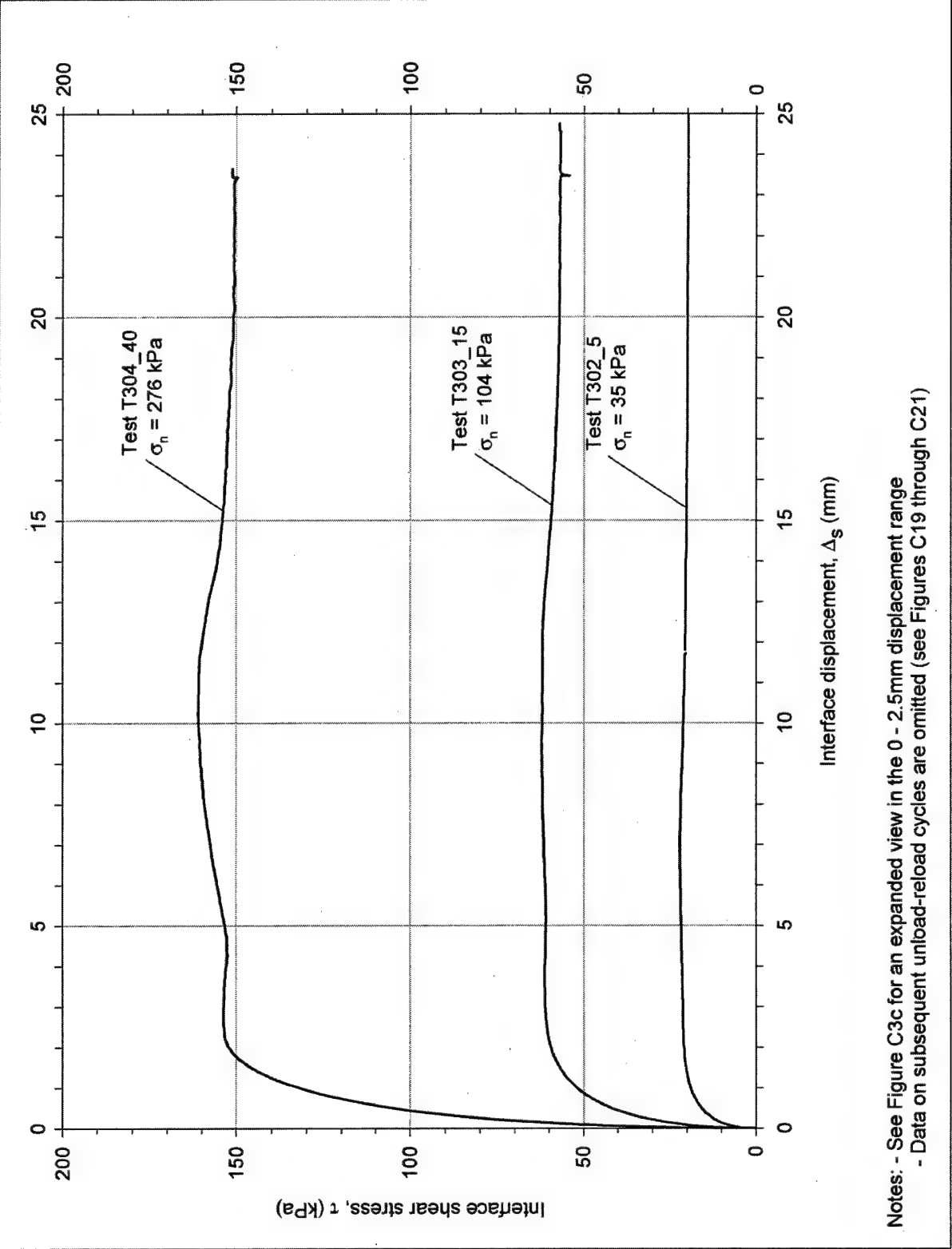
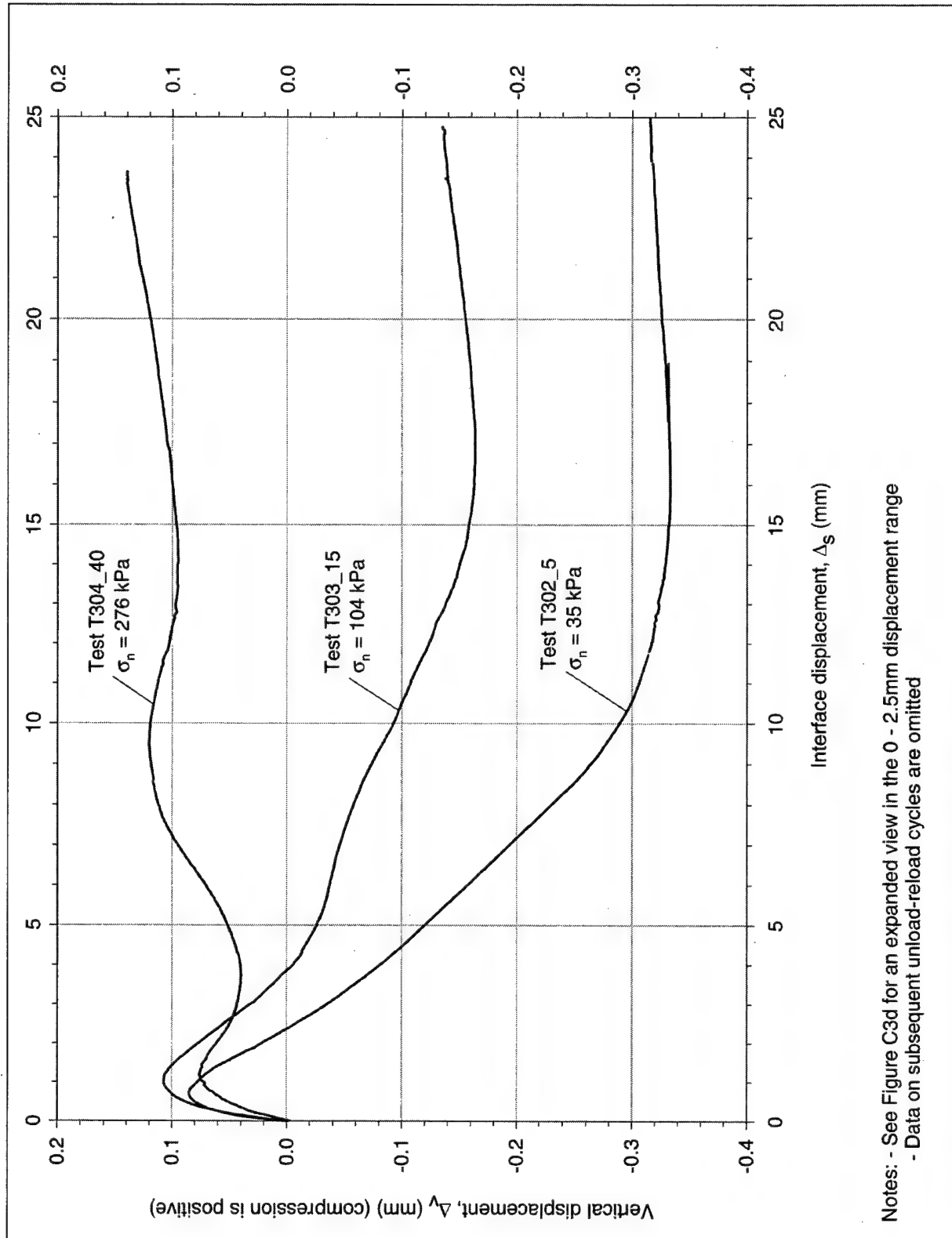


Figure C2. Peak and residual shear strength envelopes for initial loading on dense-Density-sand-to-concrete interface

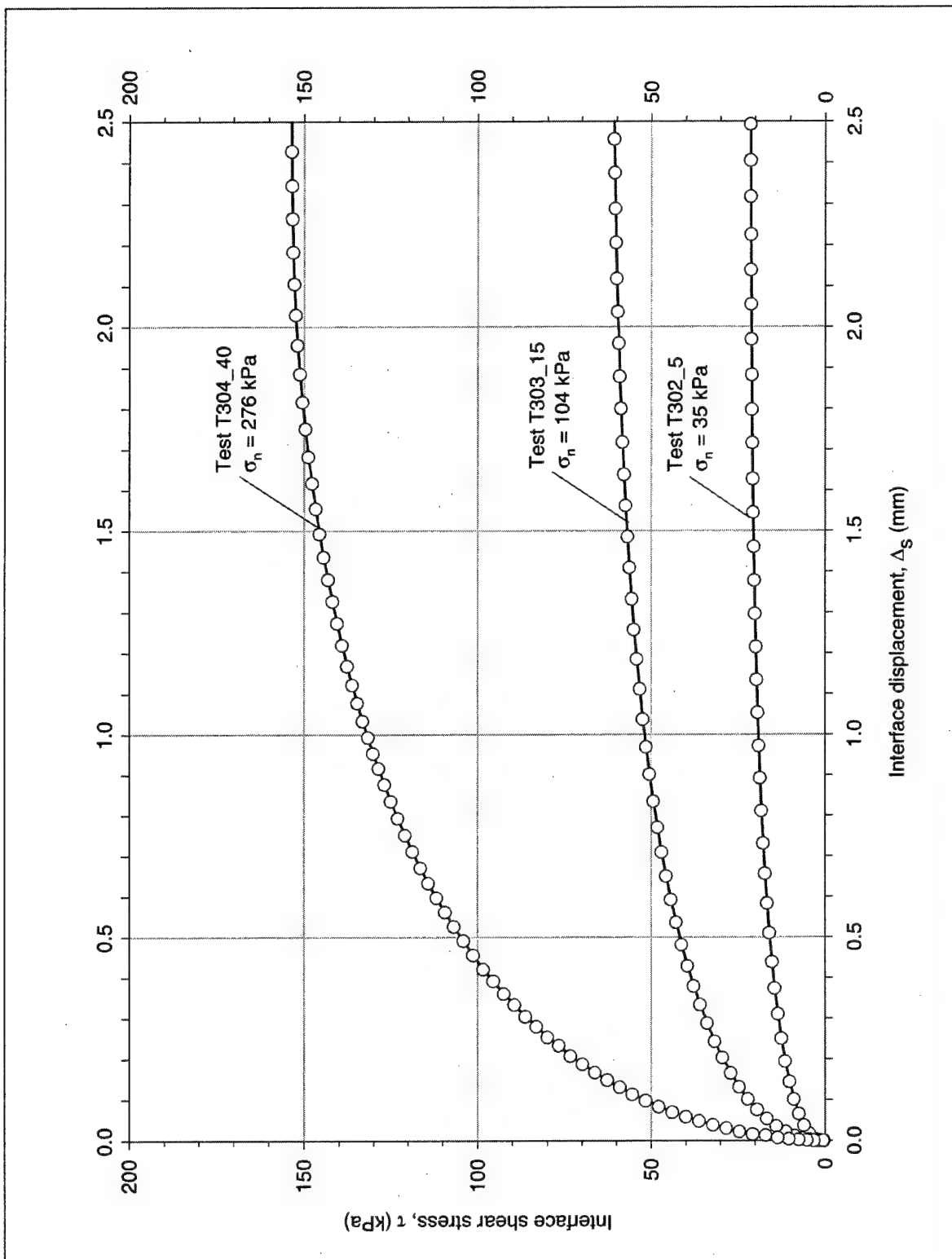


a. Shear stress versus interface displacement data

Figure C3. Results of initial loading tests on medium-dense-Density-sand-to-concrete interface (Sheet 1 of 4)

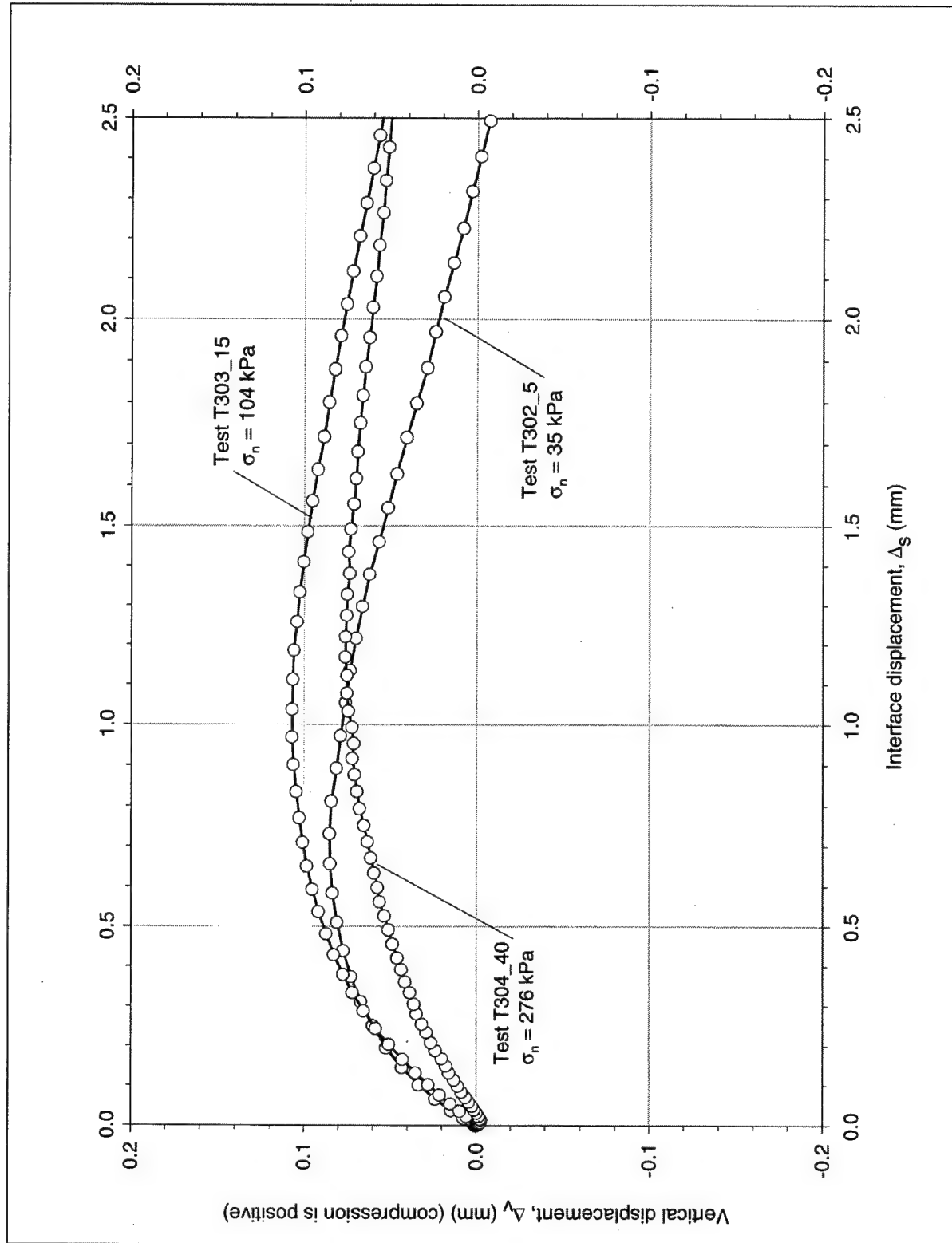


b. Vertical versus horizontal interface displacement data
Figure C3. (Sheet 2 of 4)



c. Enlargement of Figure C3a

Figure C3. (Sheet 3 of 4)



d. Enlargement of Figure C3b
Figure C3. (Sheet 4 of 4)

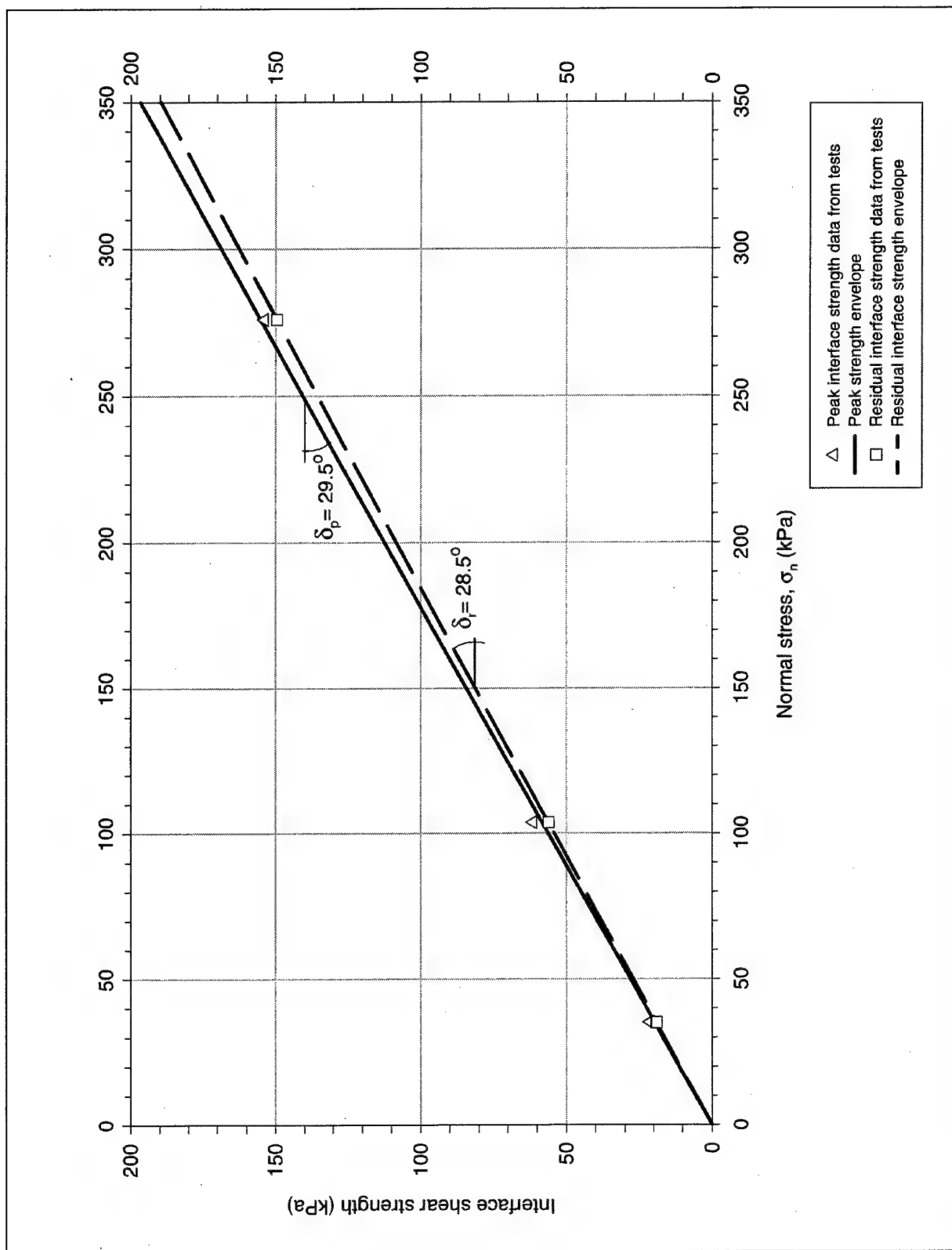
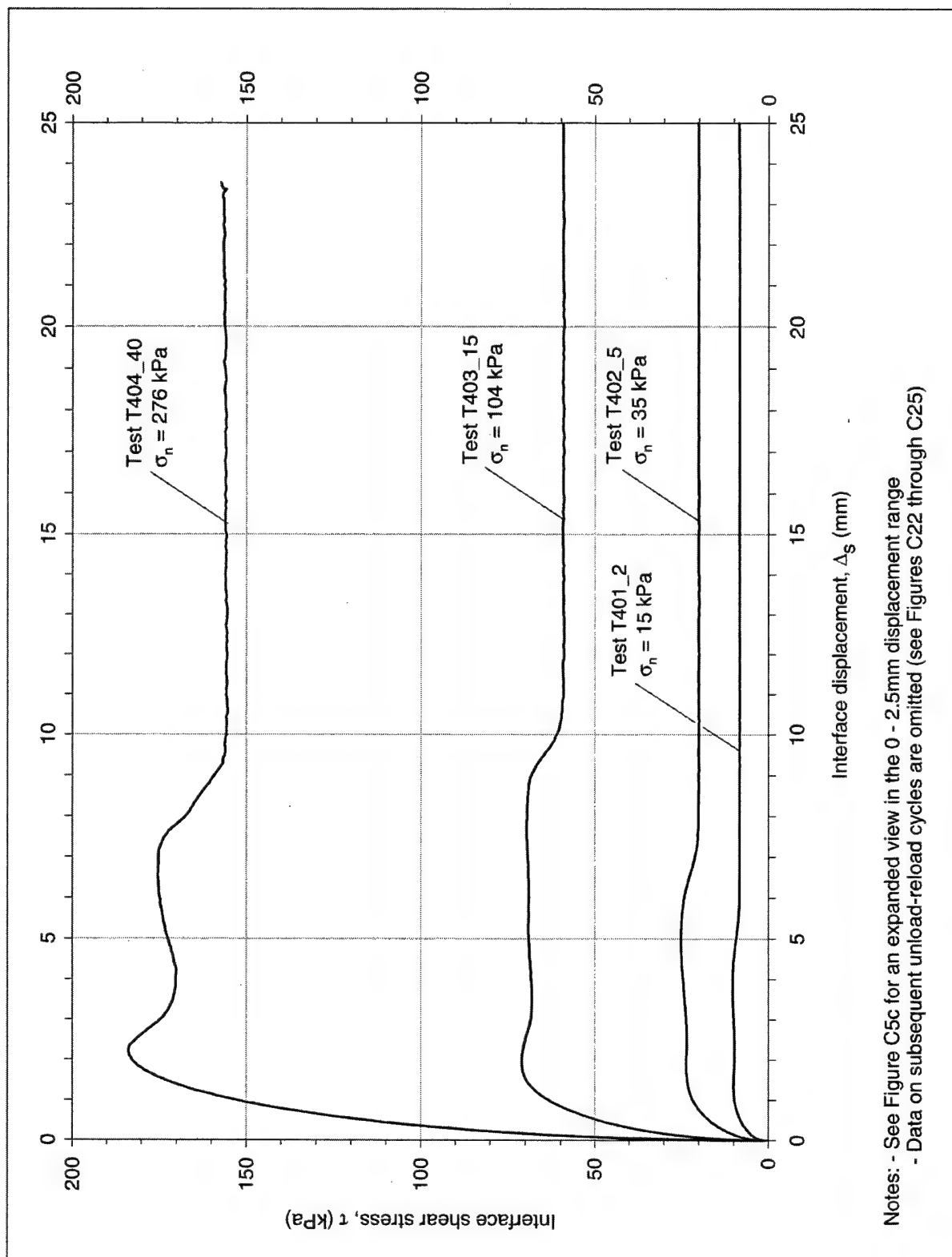
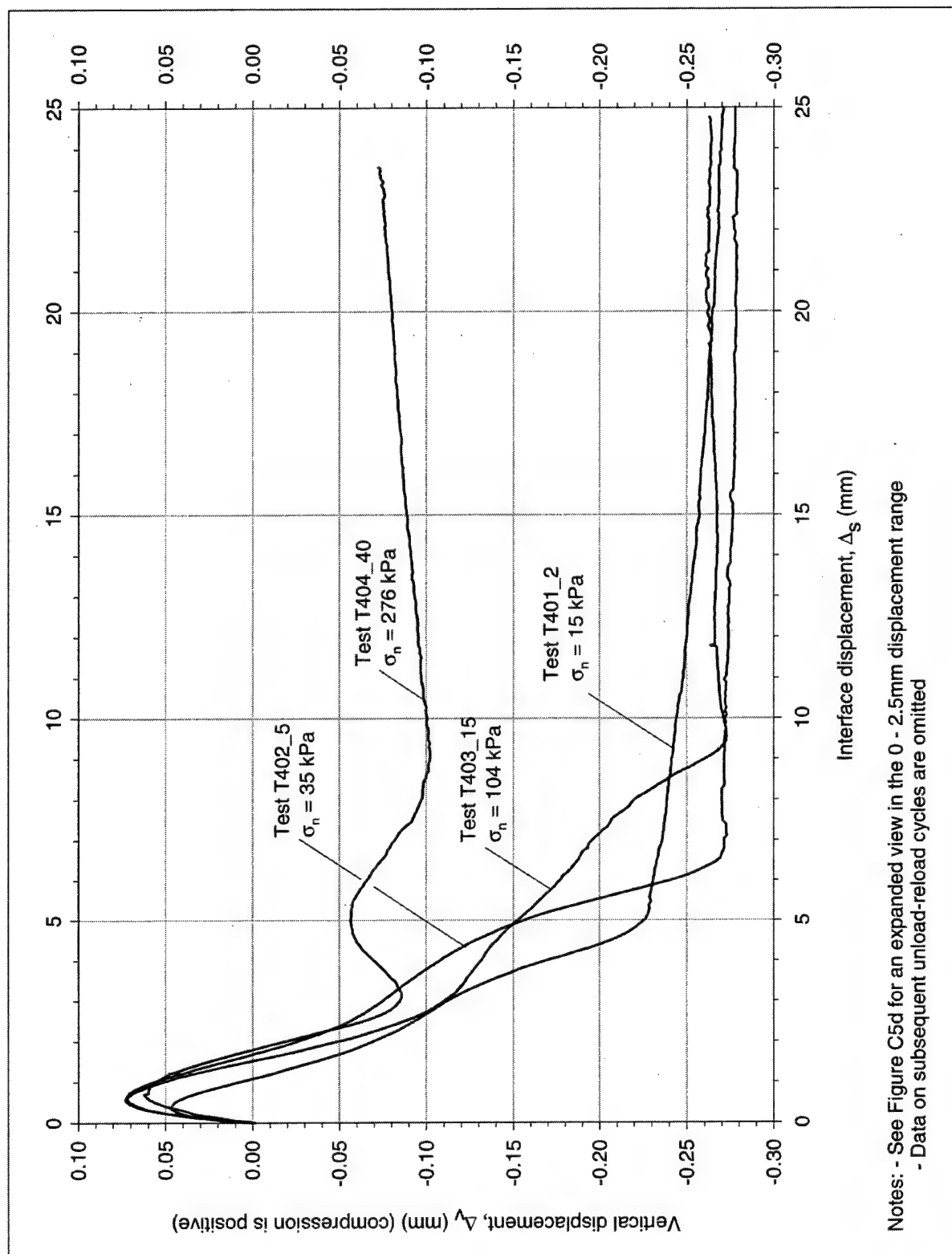


Figure C4. Peak and residual shear strength envelopes for initial loading on medium-dense-Density sand-to-concrete interface

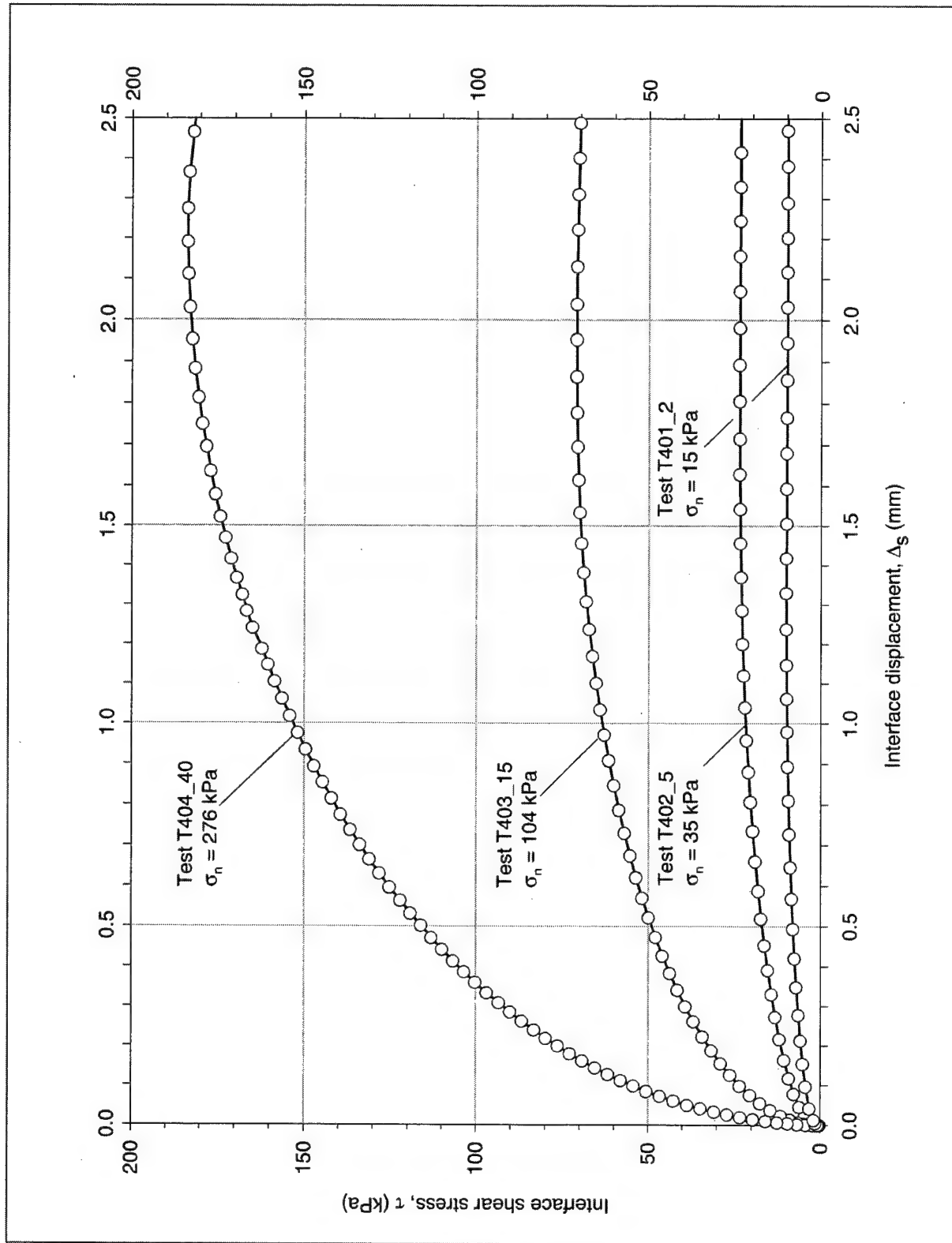


a. Shear stress versus interface displacement data

Figure C5. Results of initial loading tests on dense-Light-Castle-sand-to-concrete interface (Sheet 1 of 4)

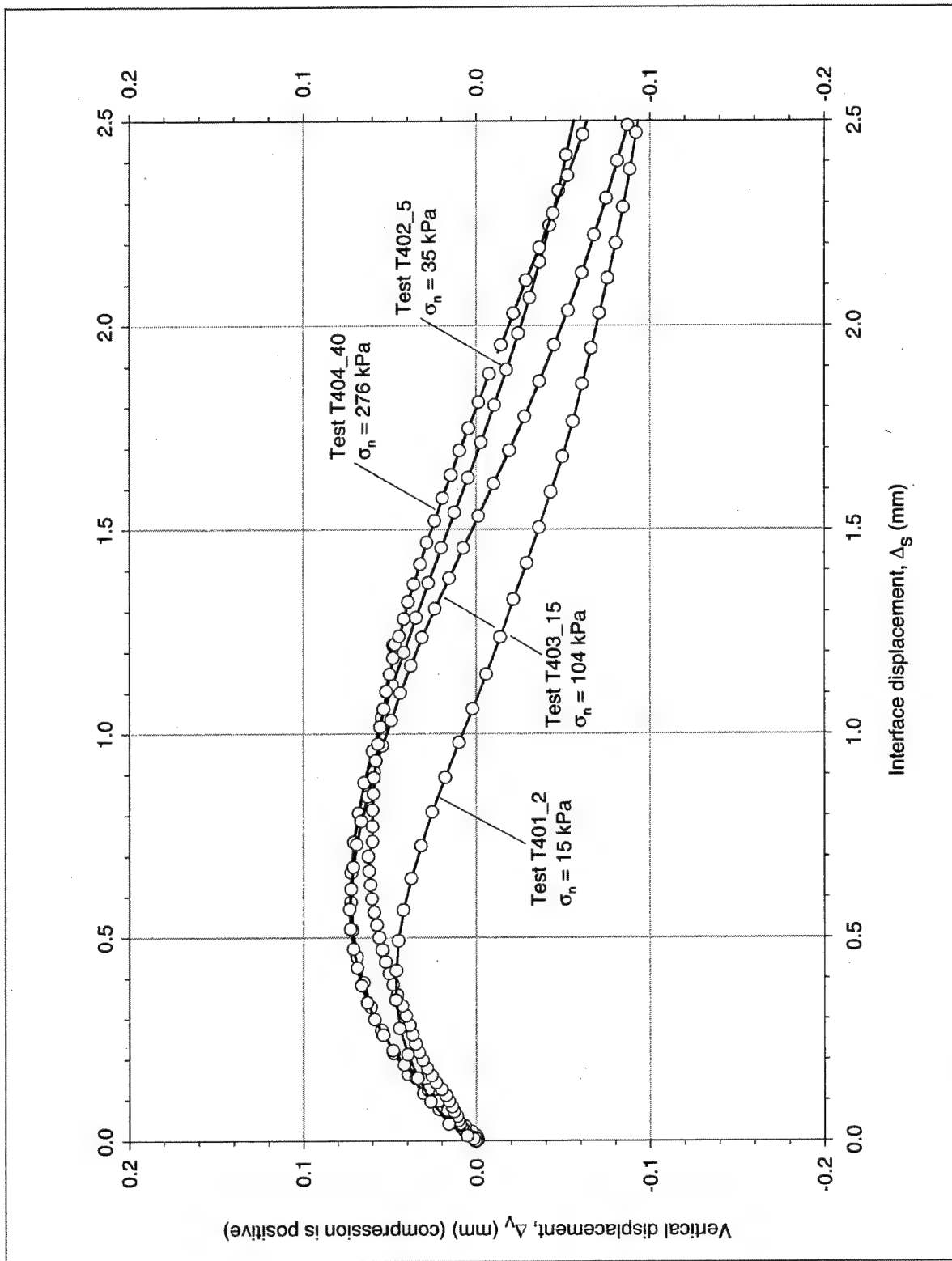


b. Vertical versus horizontal interface displacement data
 Figure C5. (Sheet 2 of 4)



c. Enlargement of Figure C5a

Figure C5. (Sheet 3 of 4)



d. Enlargement of Figure C5b

Figure C5. (Sheet 4 of 4)

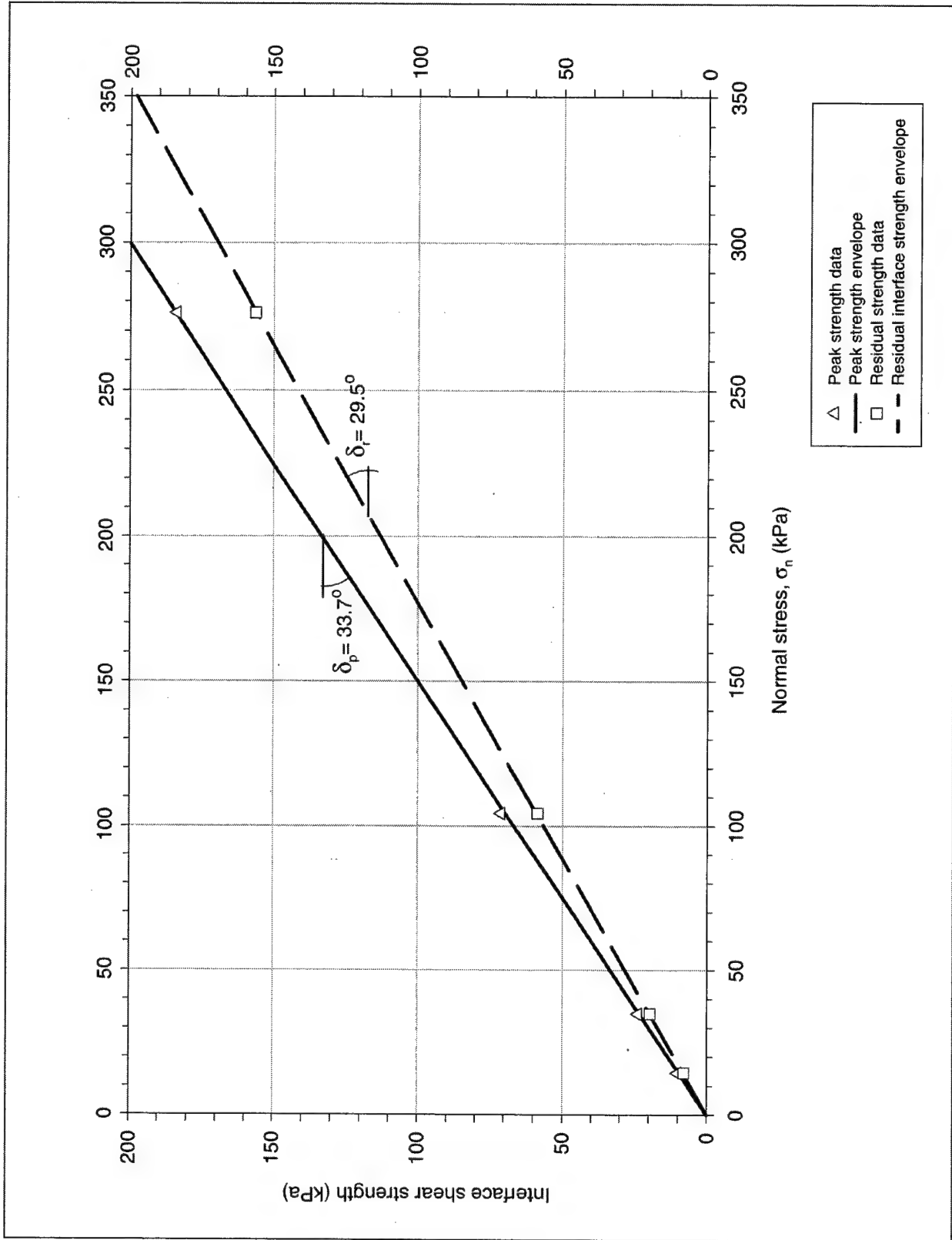
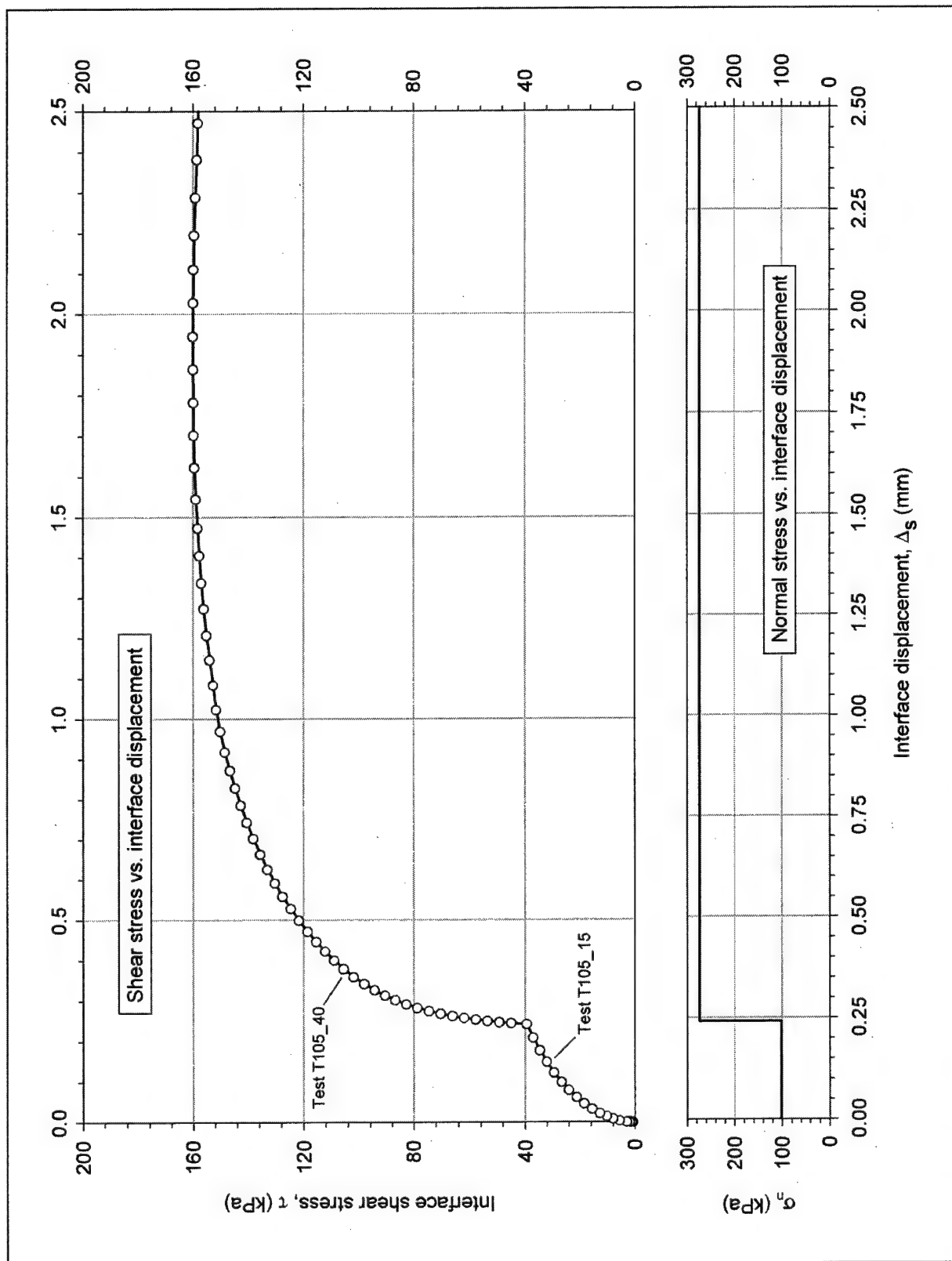
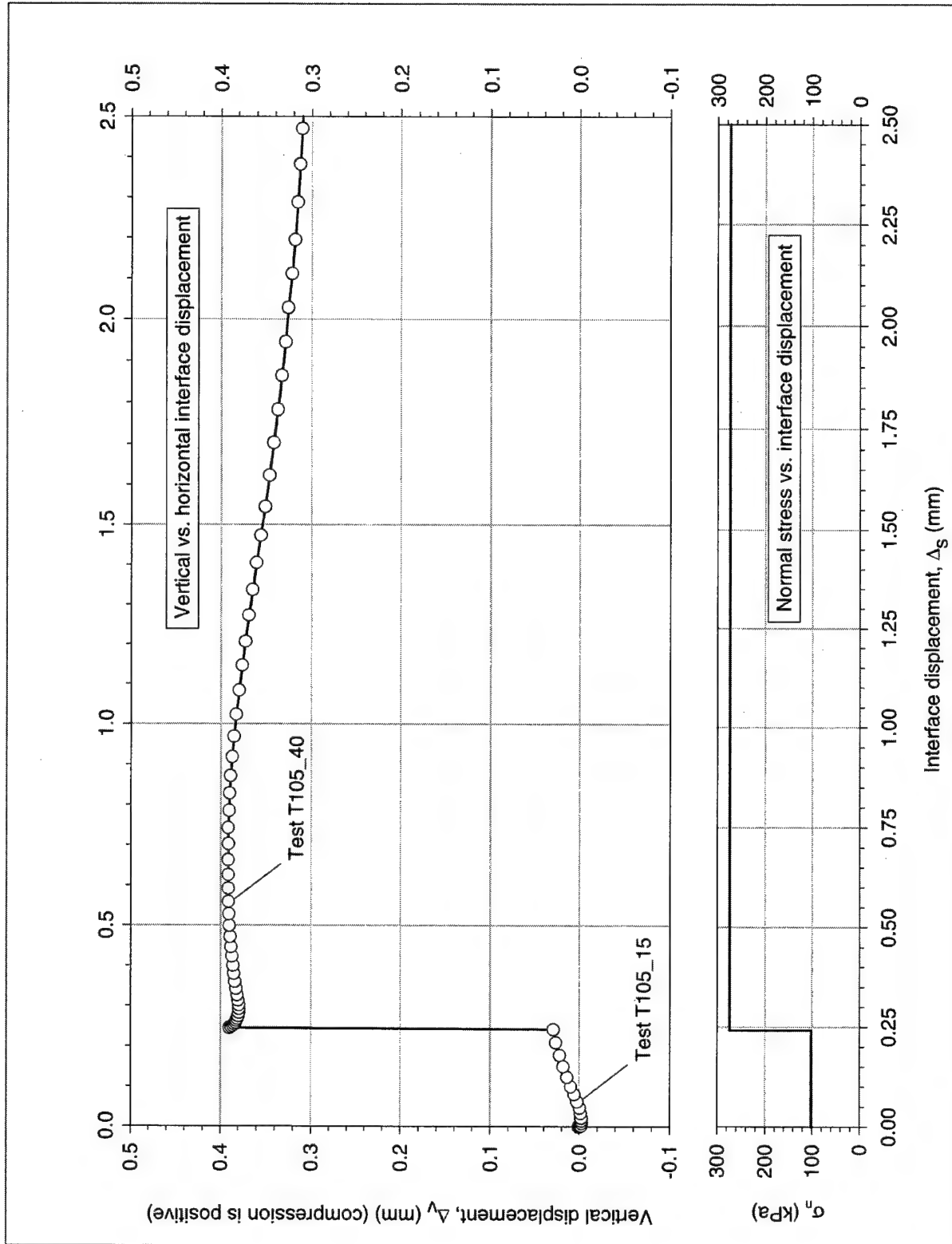


Figure C6. Peak and residual shear strength envelopes for initial loading on dense-Light-Castle-sand-to-concrete interface

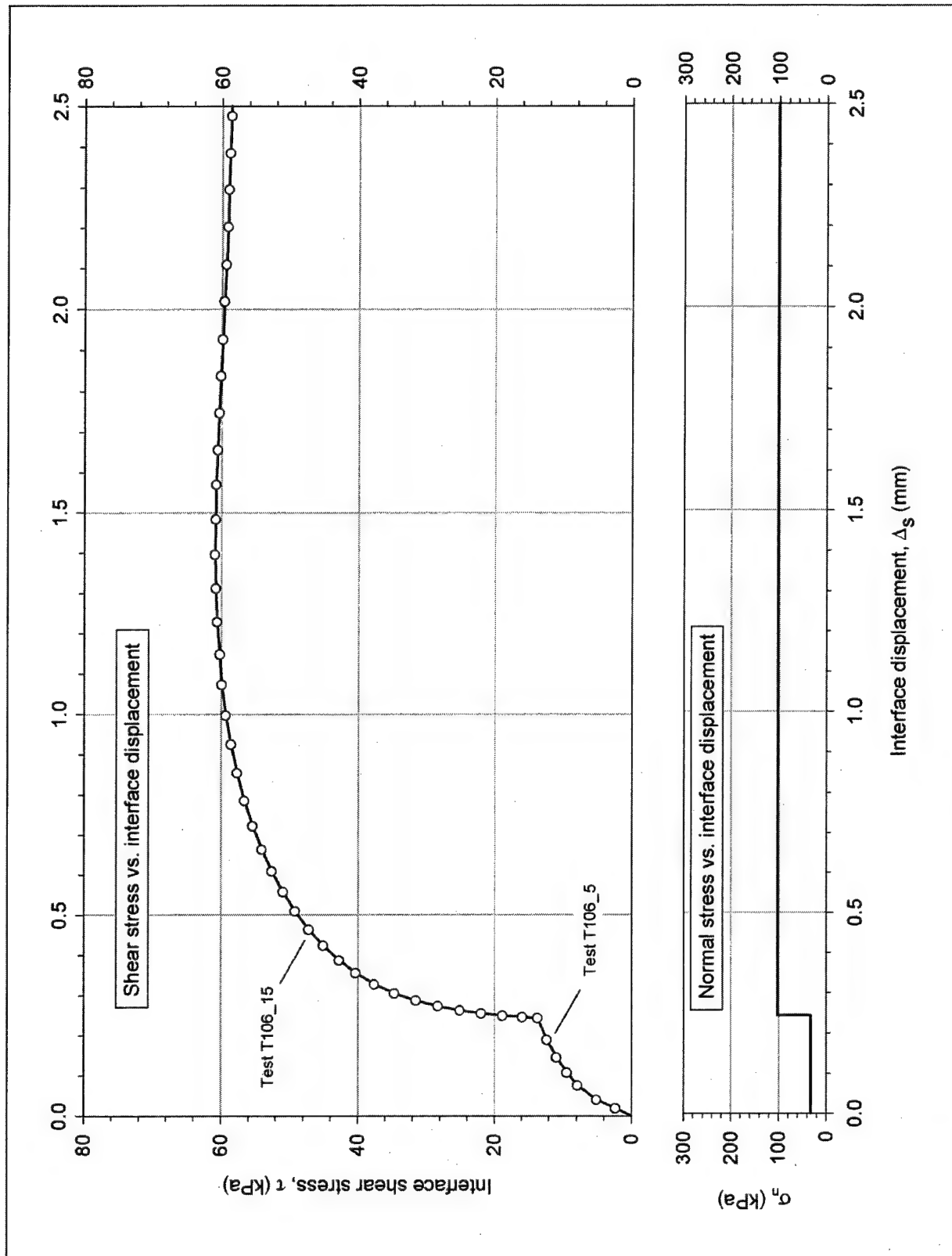


a. Shear stress versus interface displacement data
Figure C7. Staged shear test on dense-Density-sand-to-concrete interface, Specimen S105. Data on shear reversals are omitted (Continued)



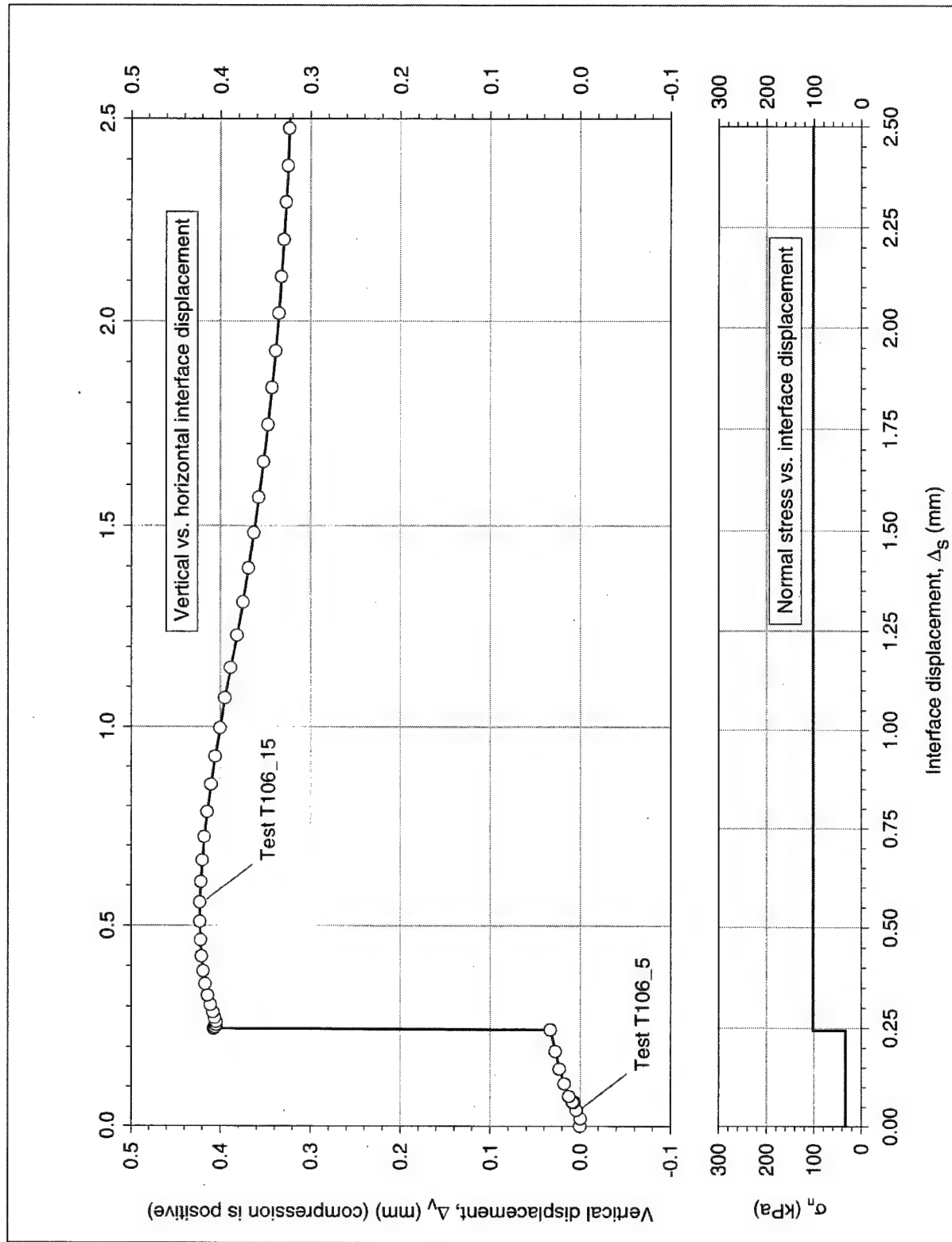
b. Vertical versus horizontal interface displacement data

Figure C7. (Concluded)



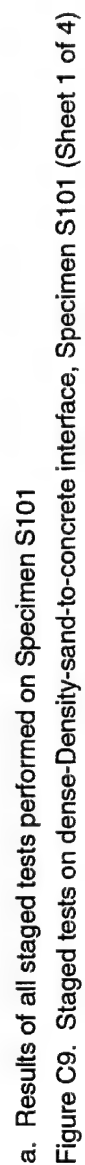
a. Shear stress versus interface displacement data

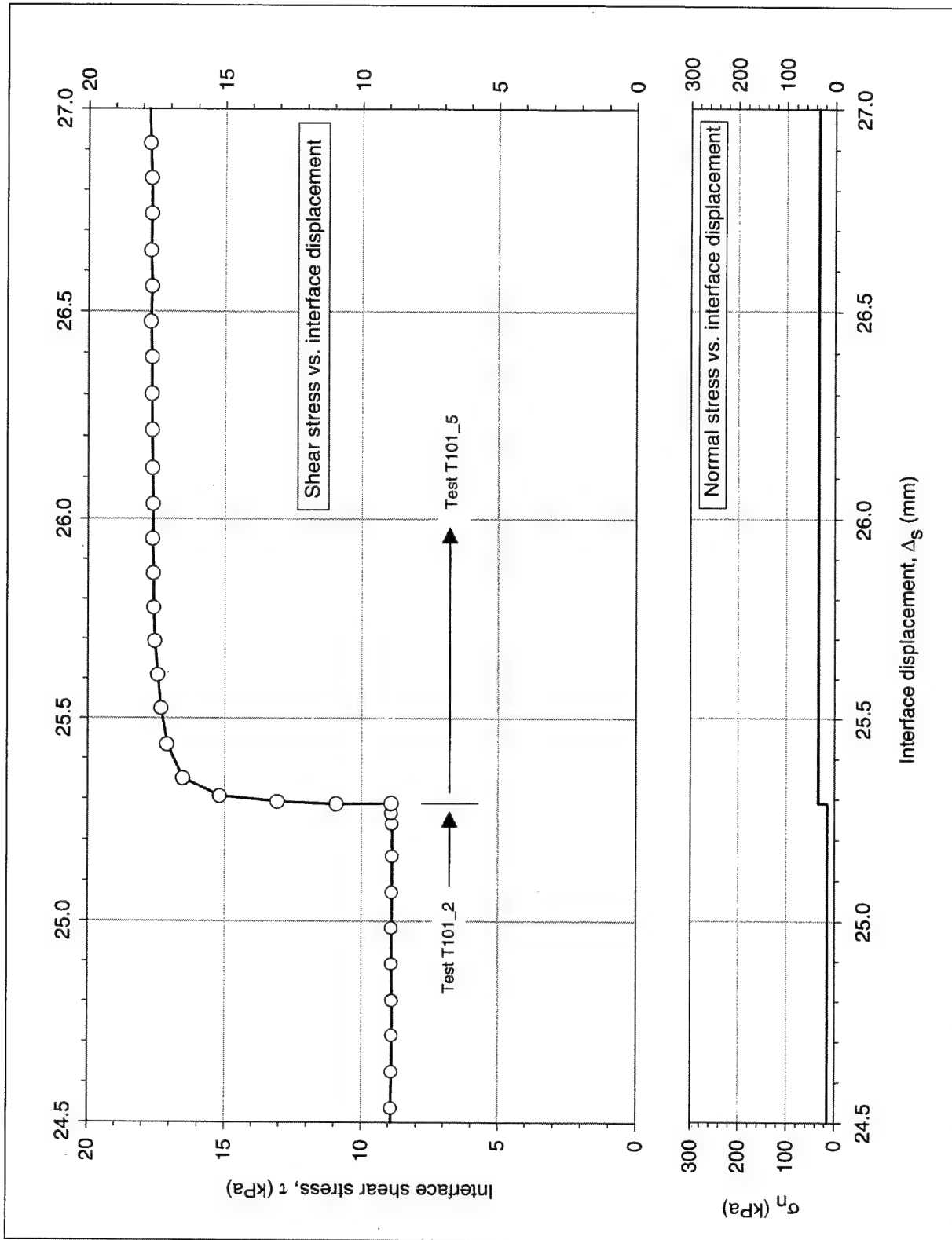
Figure C8. Staged test on dense-Density-sand-to-concrete interface, Specimen S106. Data on shear reversals are omitted (Continued)



b. Vertical versus horizontal interface displacement data

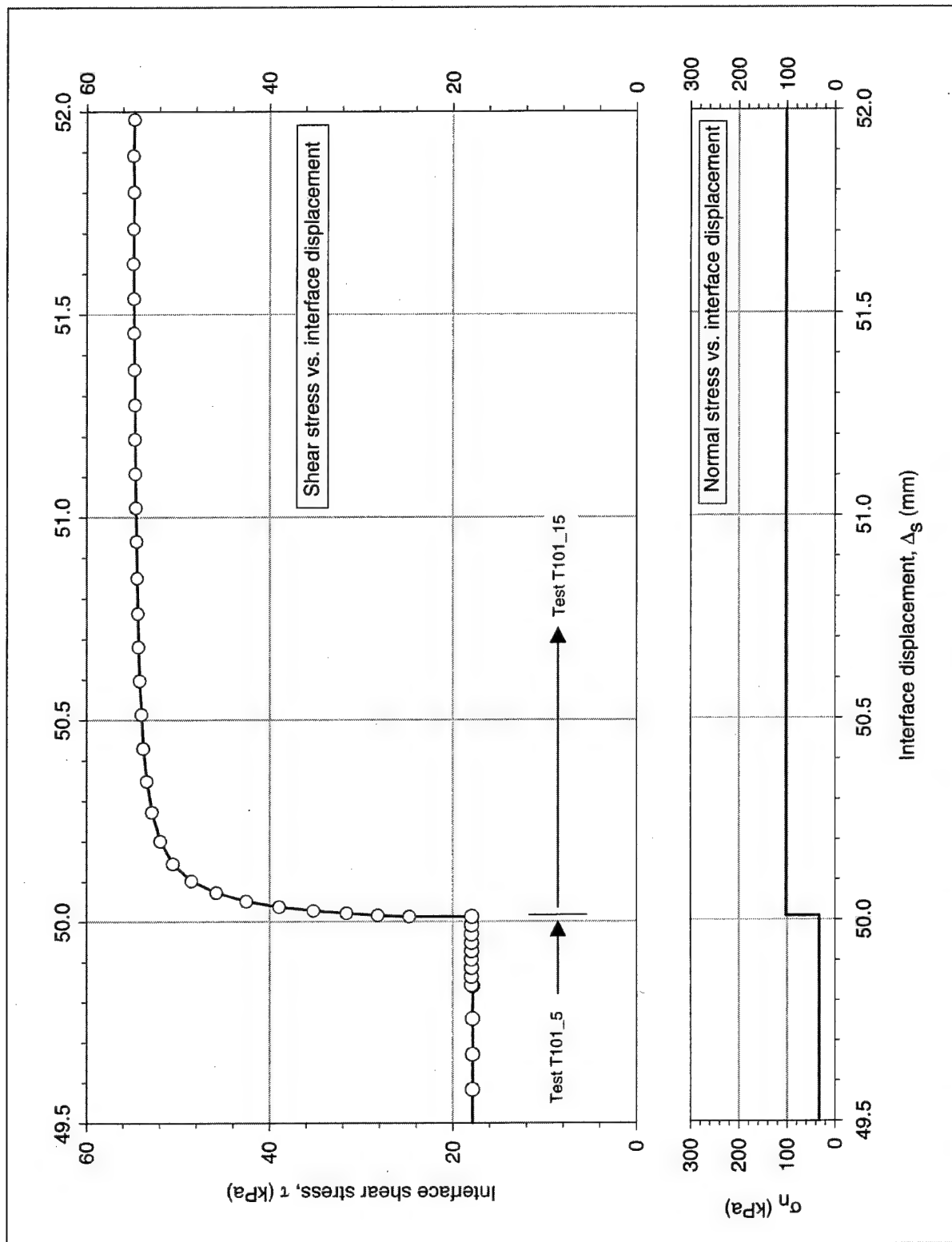
Figure C8. (Concluded)



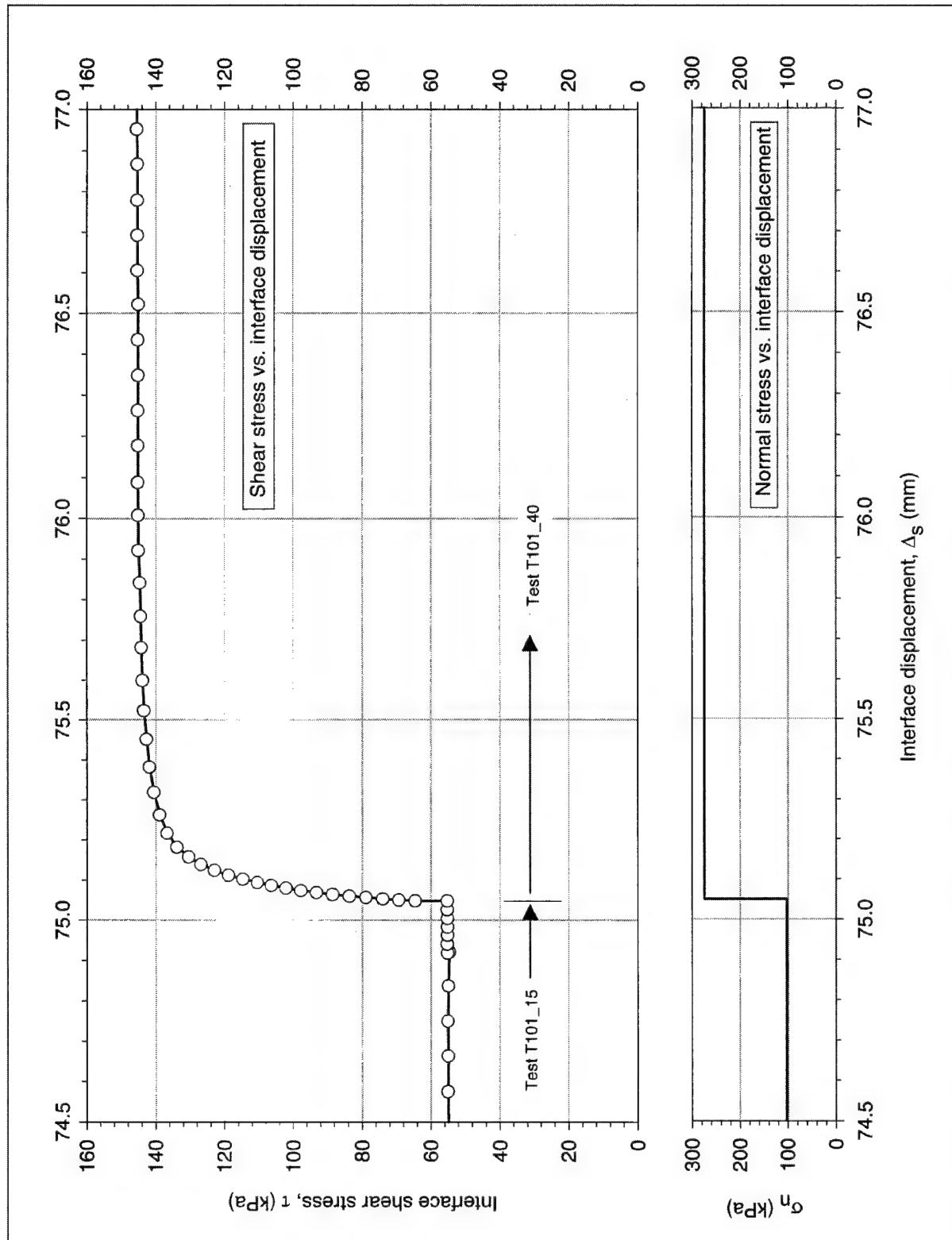


b. Detail of shear stress-displacement response for staged shear Test T101_5. Normal stress increased from 15 to 33 kPa

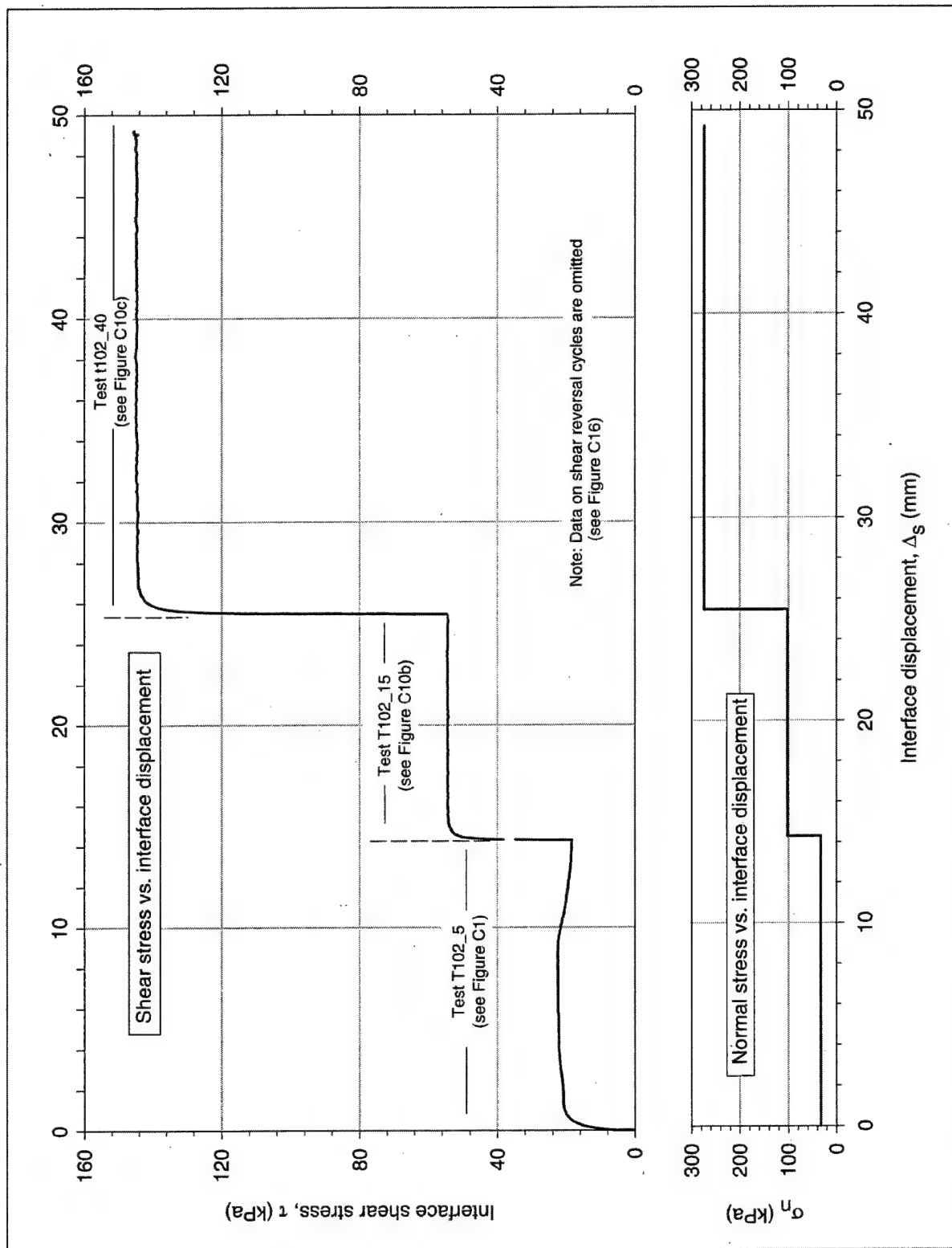
Figure C9. (Sheet 2 of 4)



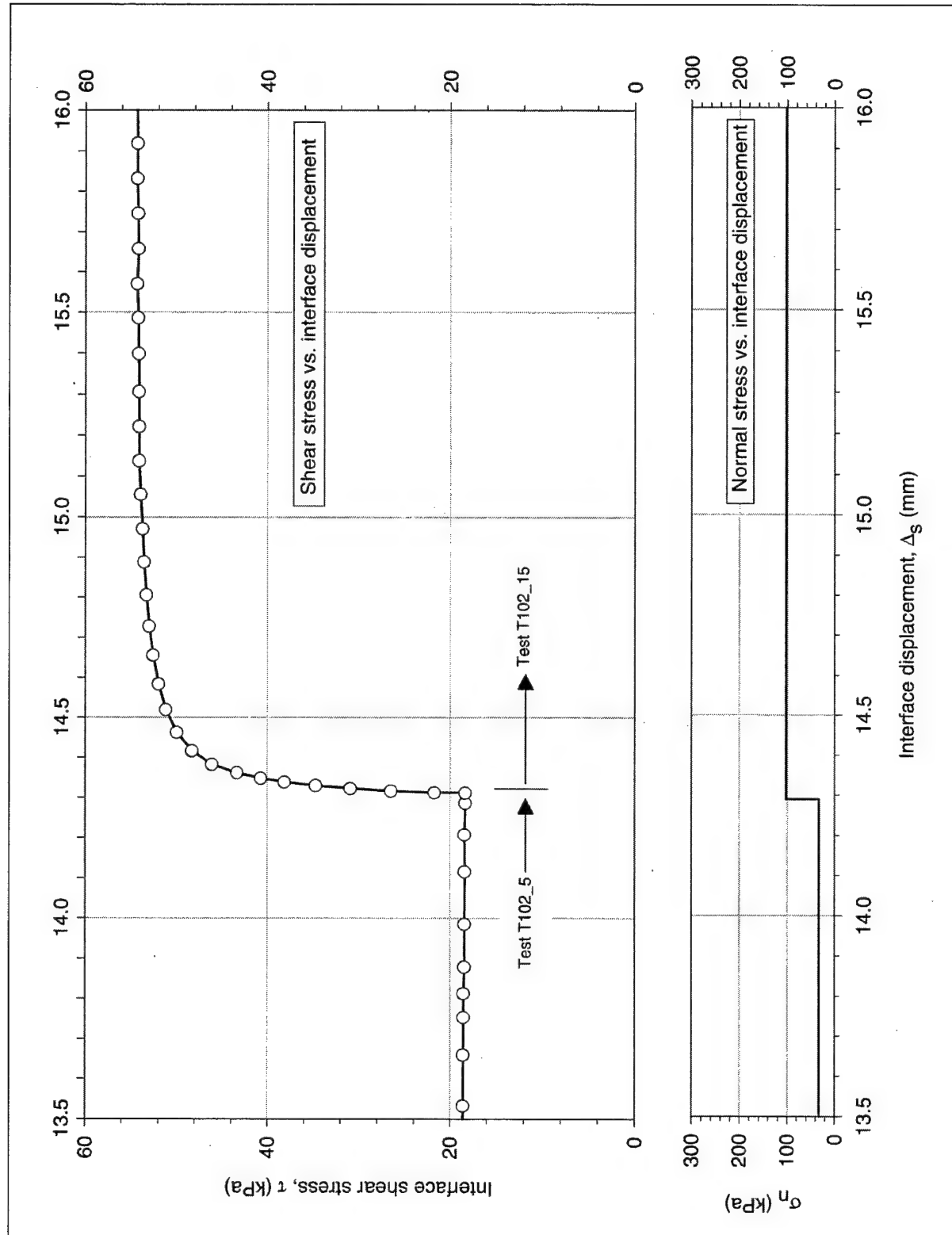
c. Detail of shear stress-displacement response for staged shear Test T101_15. Normal stress increased from 33 to 102 kPa
 Figure C9. (Sheet 3 of 4)



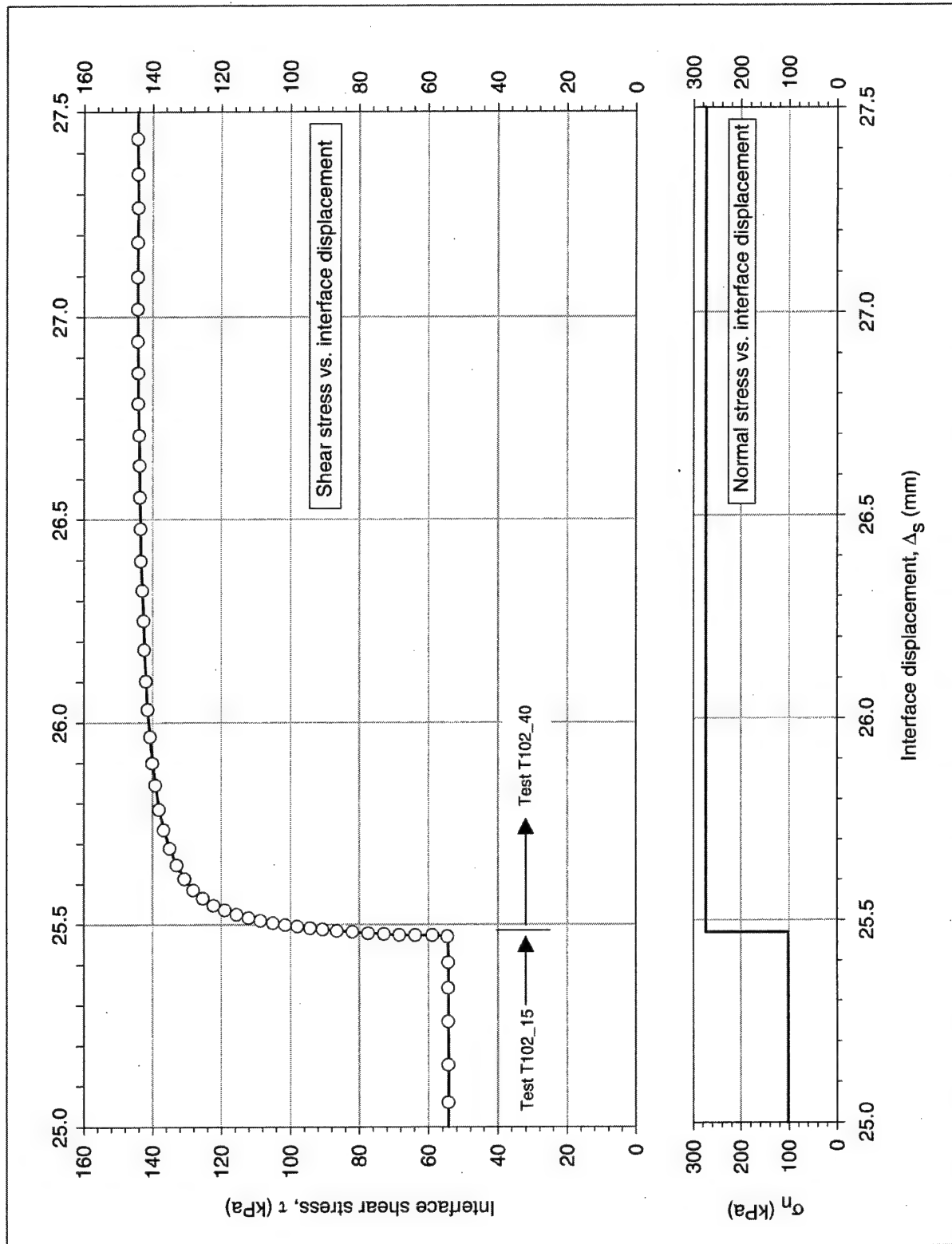
d. Detail of shear stress-displacement response for staged shear Test T101_40. Normal stress increased from 102 to 274 kPa
 Figure C9. (Sheet 4 of 4)



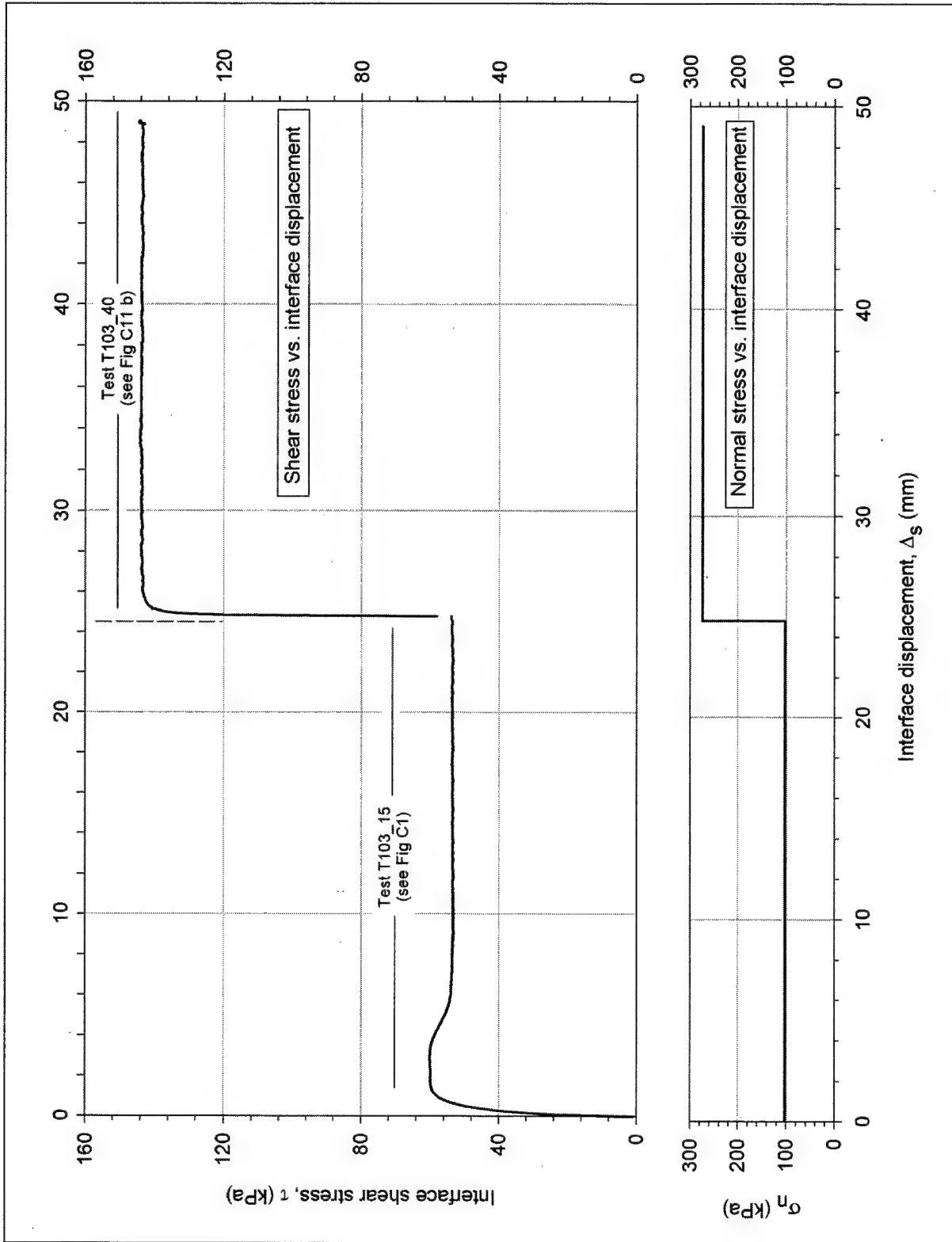
a. Results of all staged tests performed on Specimen S102
Figure C10. Staged tests on dense-Density-sand-to-concrete interface, Specimen S102 (Sheet 1 of 3)



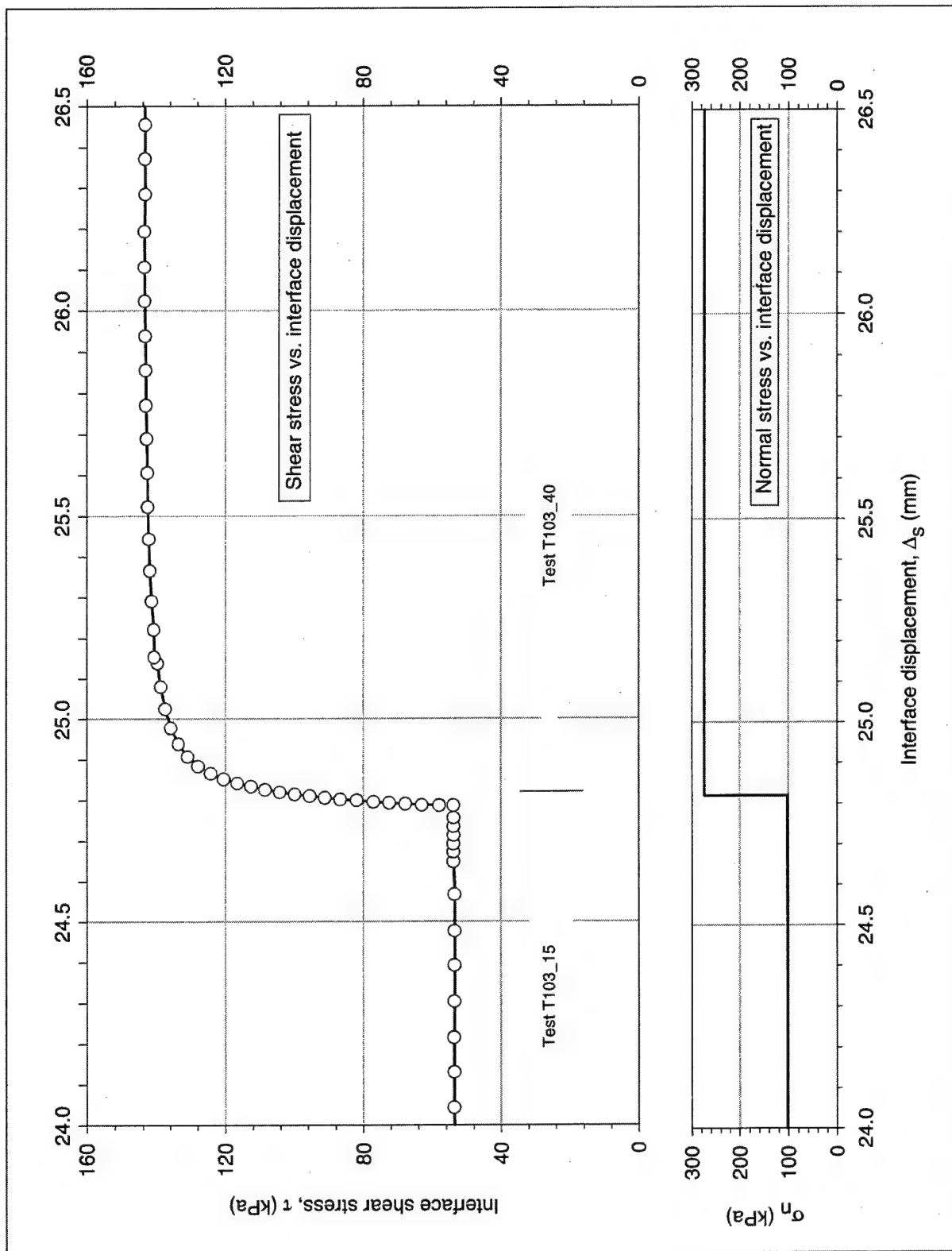
b. Detail of shear stress-displacement response for staged shear Test T102_15. Normal stress increased from 33 to 102 kPa
Figure C10. (Sheet 2 of 3)



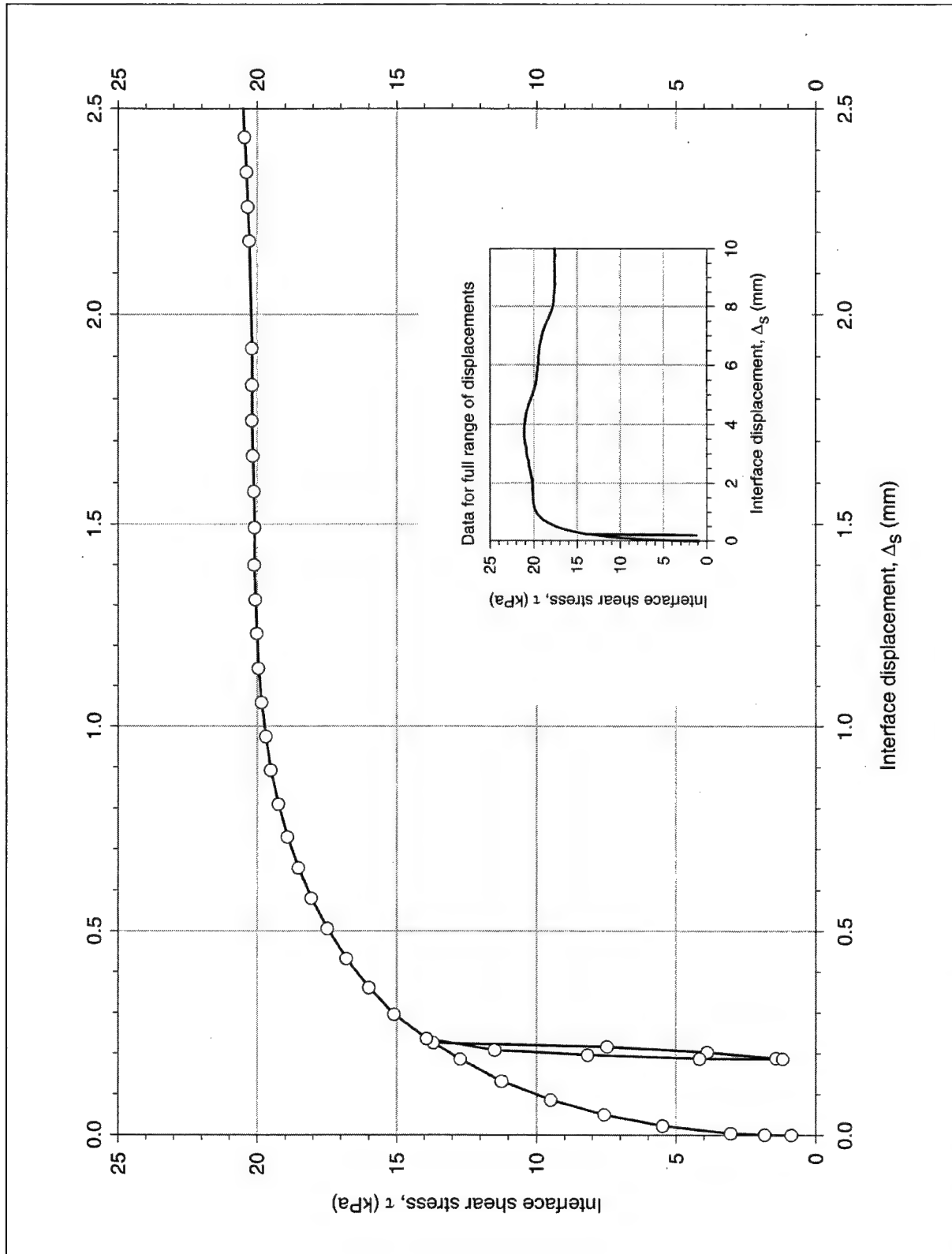
c. Detail of shear stress-displacement response for staged shear Test T102_40. Normal stress increased from 102 to 274 kPa
Figure C10. (Sheet 3 of 3)



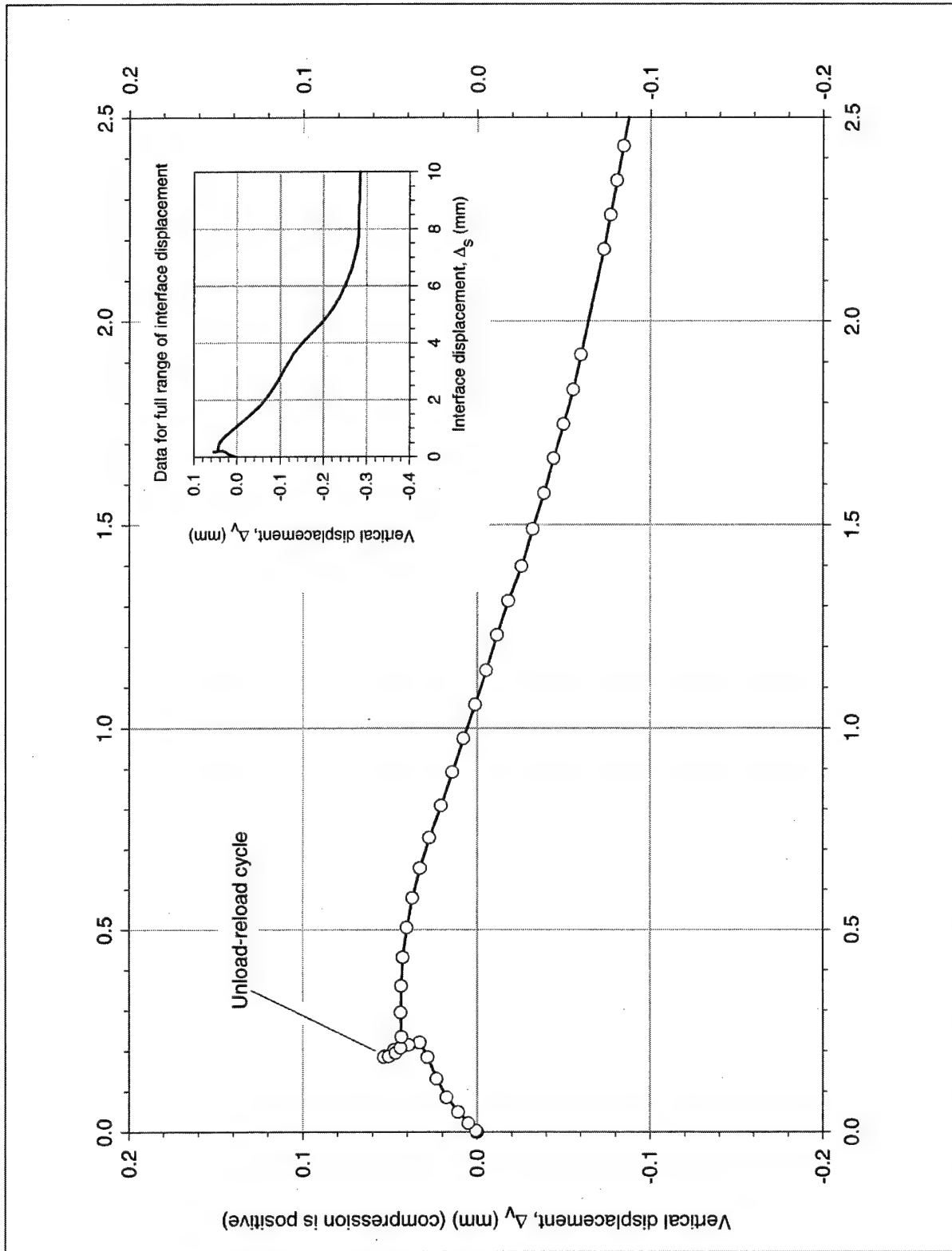
a. Results of all staged tests performed on Specimen S103
 Figure C11. Staged tests on dense-Density-sand-to-concrete interface, Specimen S103 (Continued)



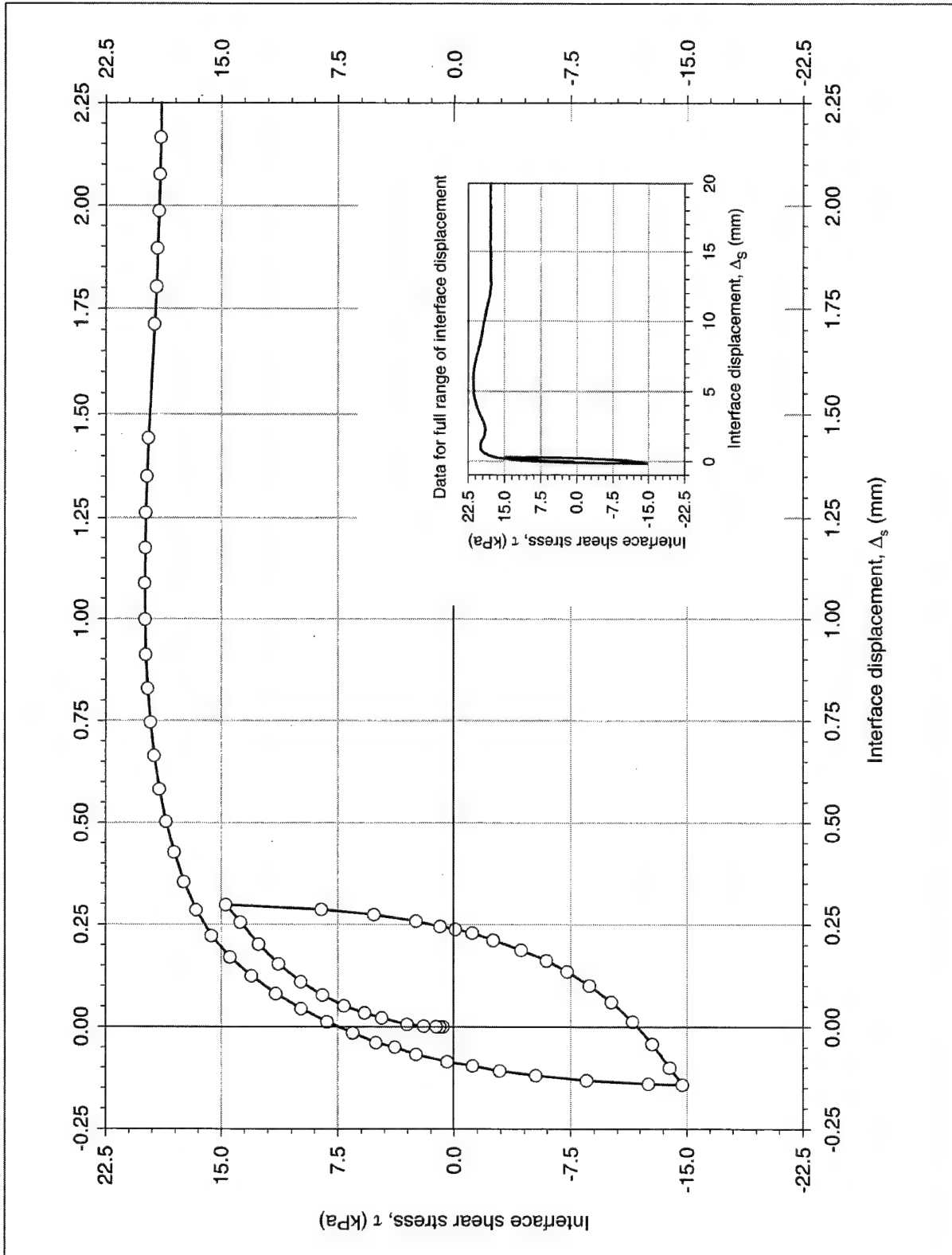
b. Detail of shear stress-displacement response for staged shear Test T103_40. Normal stress increased from 102 to 274 kPa
Figure C11. (Concluded)



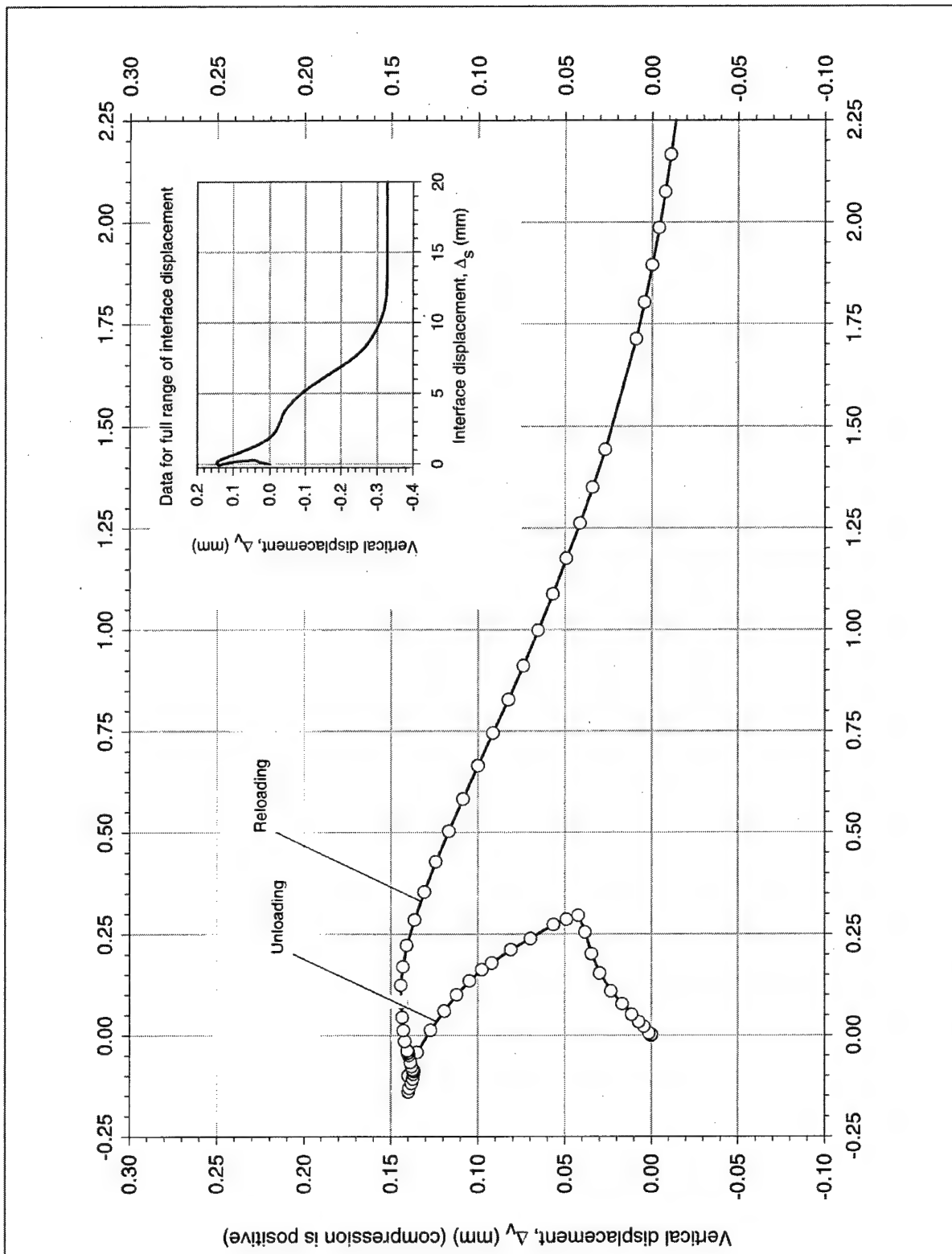
a. Detail of unload-reload cycle. Inset shows data for full range of interface displacement
 Figure C12. Unload-reload test on dense-Density-sand-to-concrete interface, $\sigma_n = 33$ kPa, Specimen S201 (Continued)



b. Vertical versus horizontal interface displacement data
Figure C12. (Concluded)

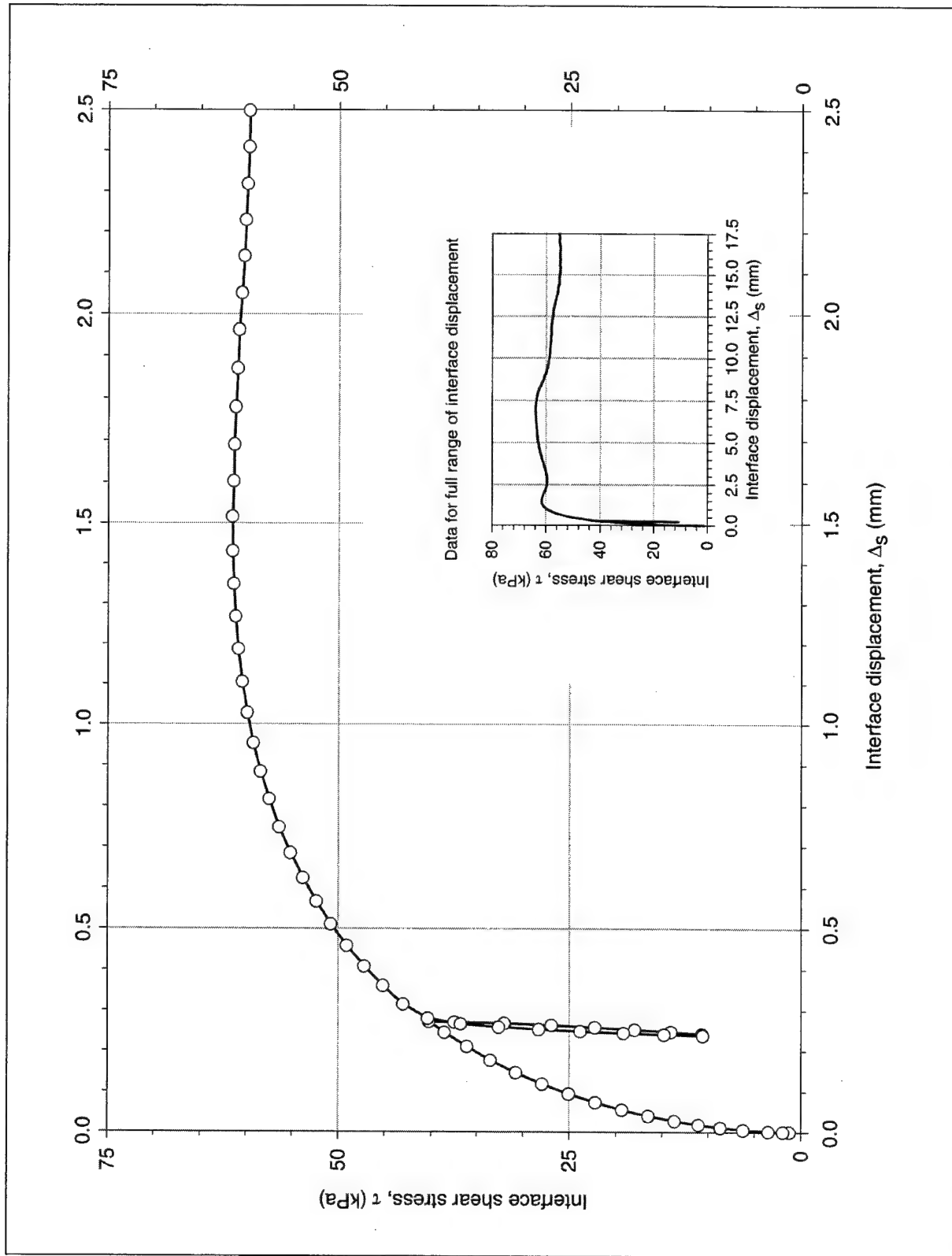


a. Detail of unload-reload cycle. Inset shows data for full range of interface displacement
 Figure C13. Unload-reload test on dense-Density sand-to-concrete interface, $\sigma_n = 33$ kPa, Specimen S202 (Continued)

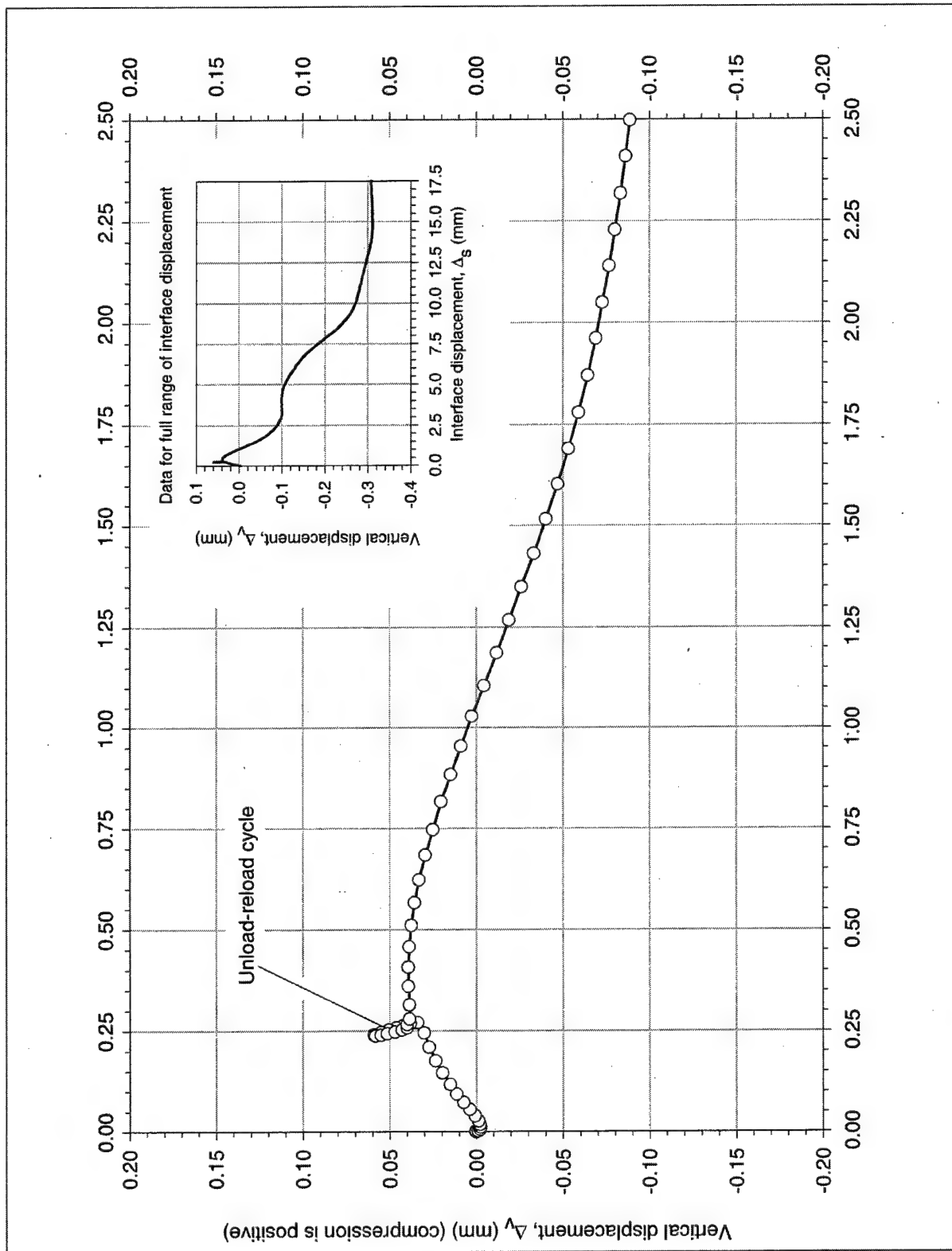


b. Vertical versus horizontal interface displacement data

Figure C13. (Concluded)



a. Detail of unload-reload cycle. Inset shows data for full range of interface displacement
 Figure C14. Unload-reload test on dense-Density-sand-to-concrete interface, $\sigma_n = 102$ kPa, Specimen S203 (continued)



b. Vertical versus horizontal interface displacement data
Figure C14. (Concluded)

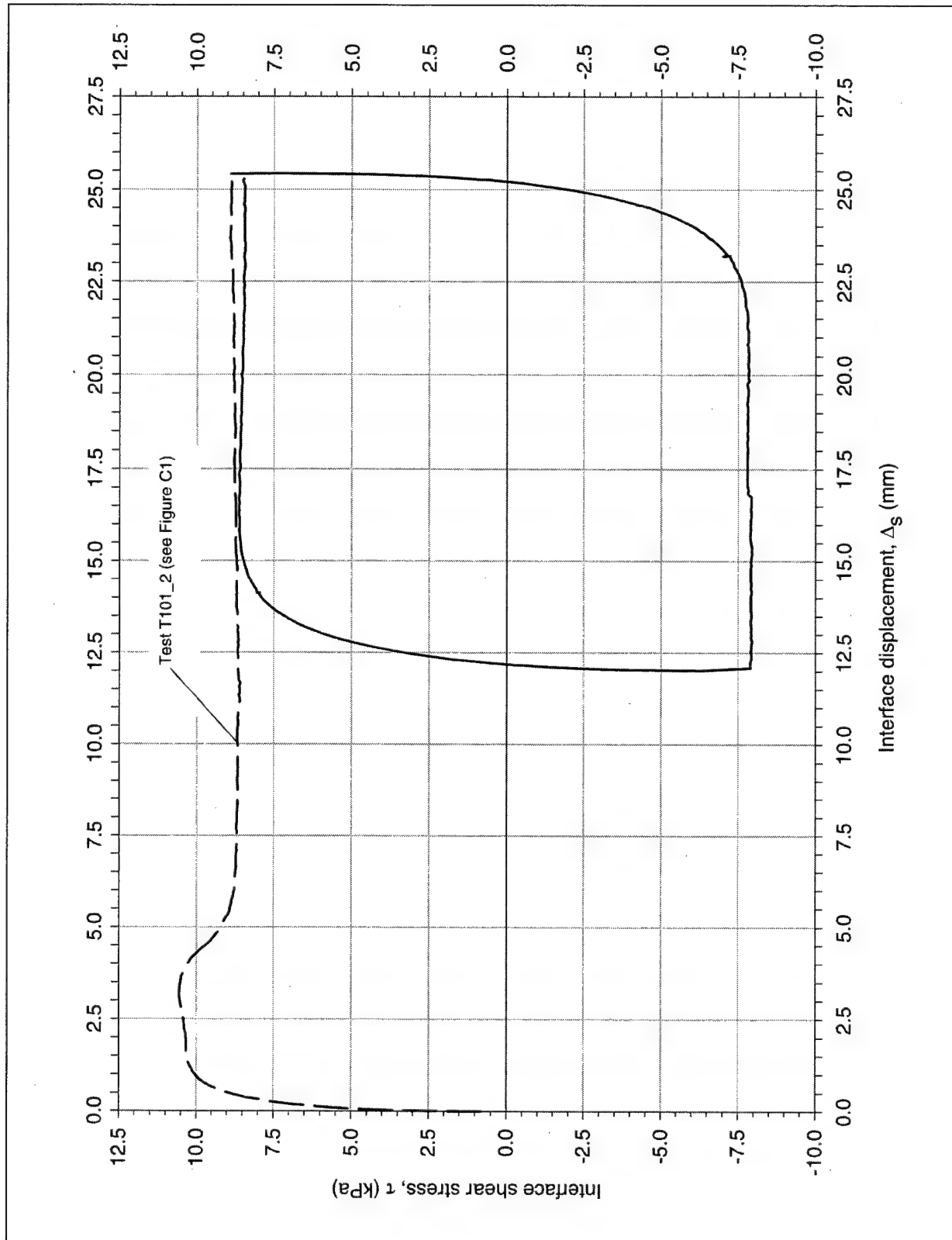
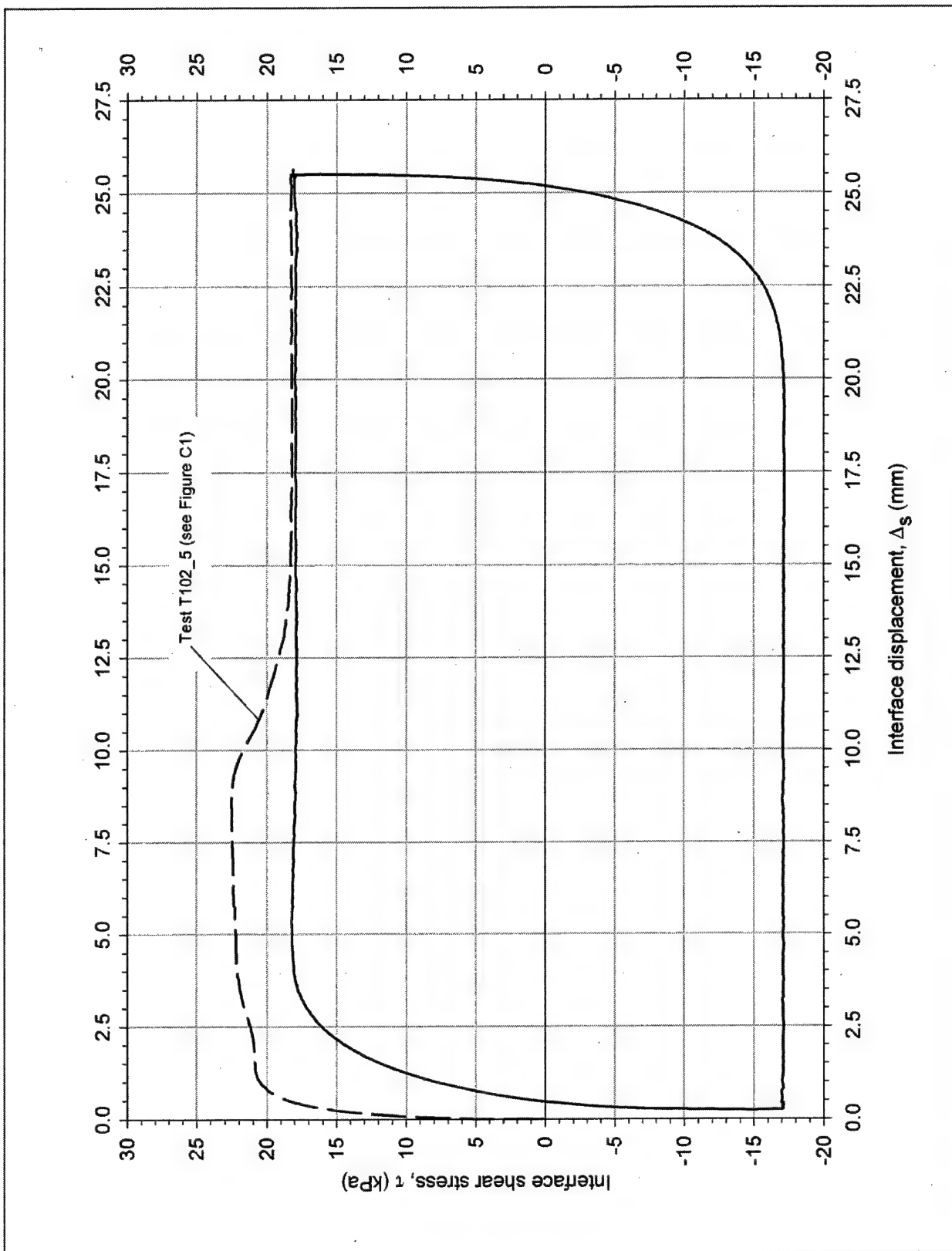


Figure C15. Cycle of shear reversals on dense-Density-sand-to-concrete interface, $\sigma_n = 15$ kPa, Specimen S101

Figure C16. Cycle of shear reversals on dense-Density-sand-to-concrete interface, $\sigma_n = 33$ kPa, Specimen S102

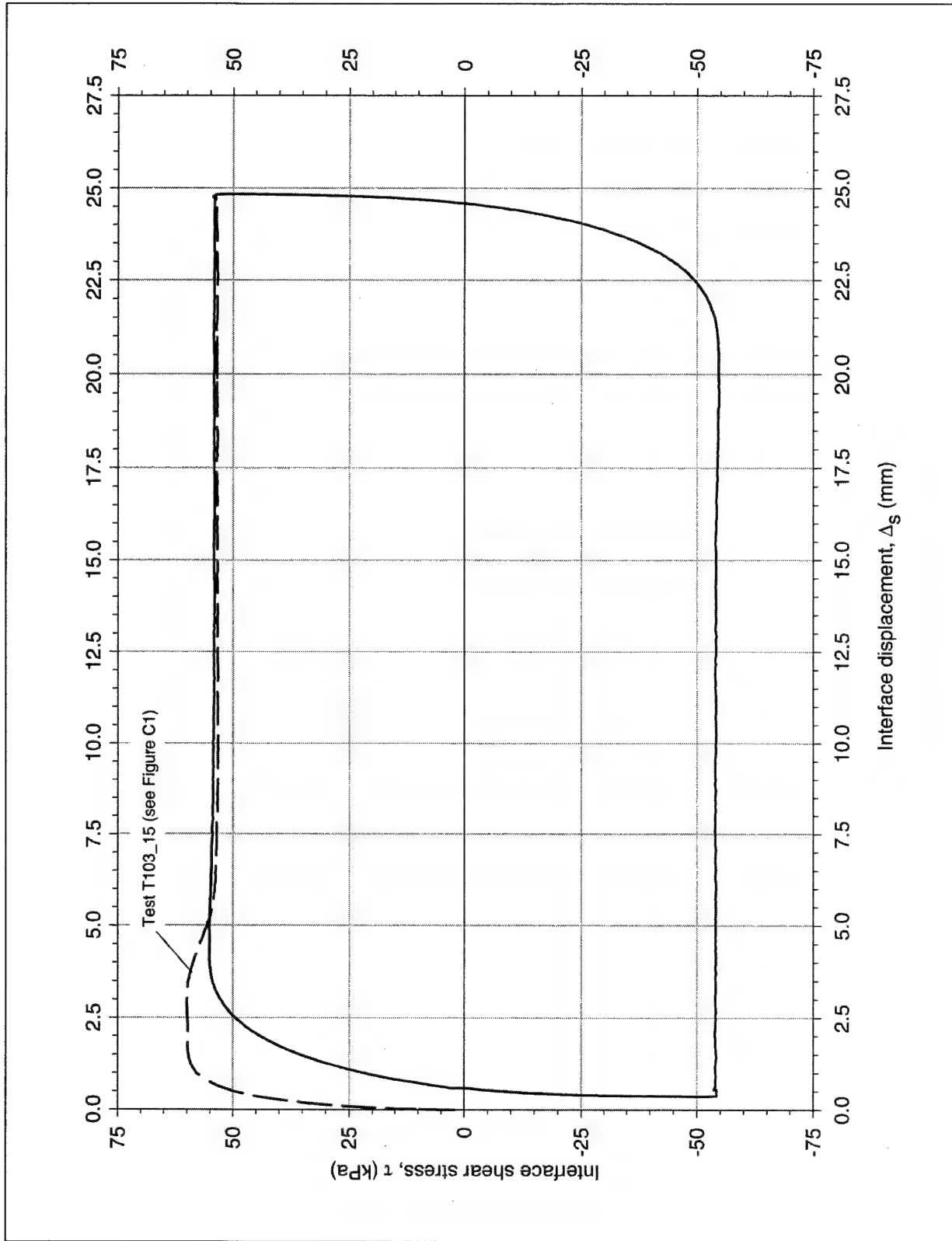


Figure C17. Cycle of shear reversals on dense-Density sand-to-concrete interface, $\sigma_n = 102$ kPa, Specimen S103

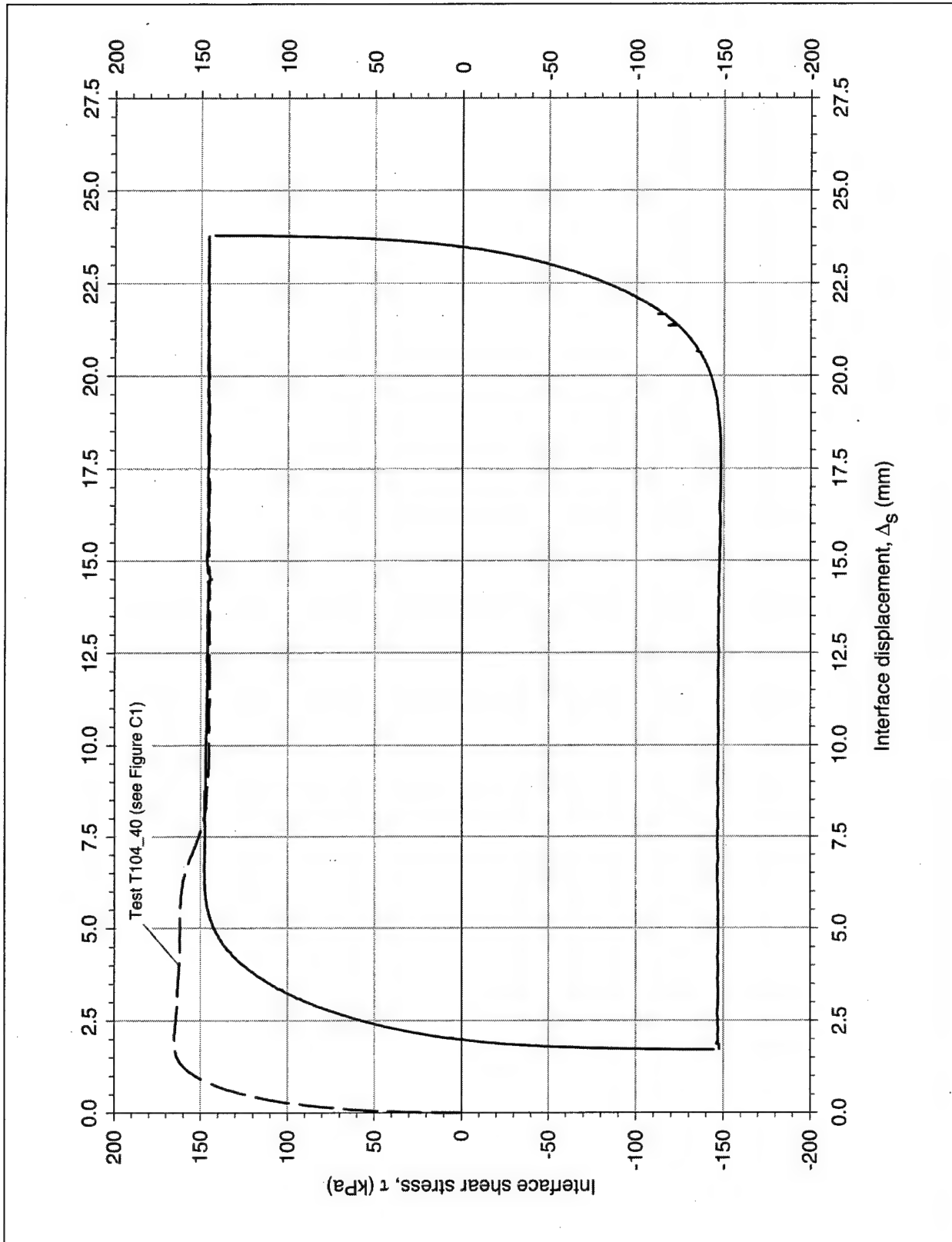


Figure C18. Cycle of shear reversals on dense-Density-sand-to-concrete interface, $\sigma_n = 274$ kPa, Specimen S104

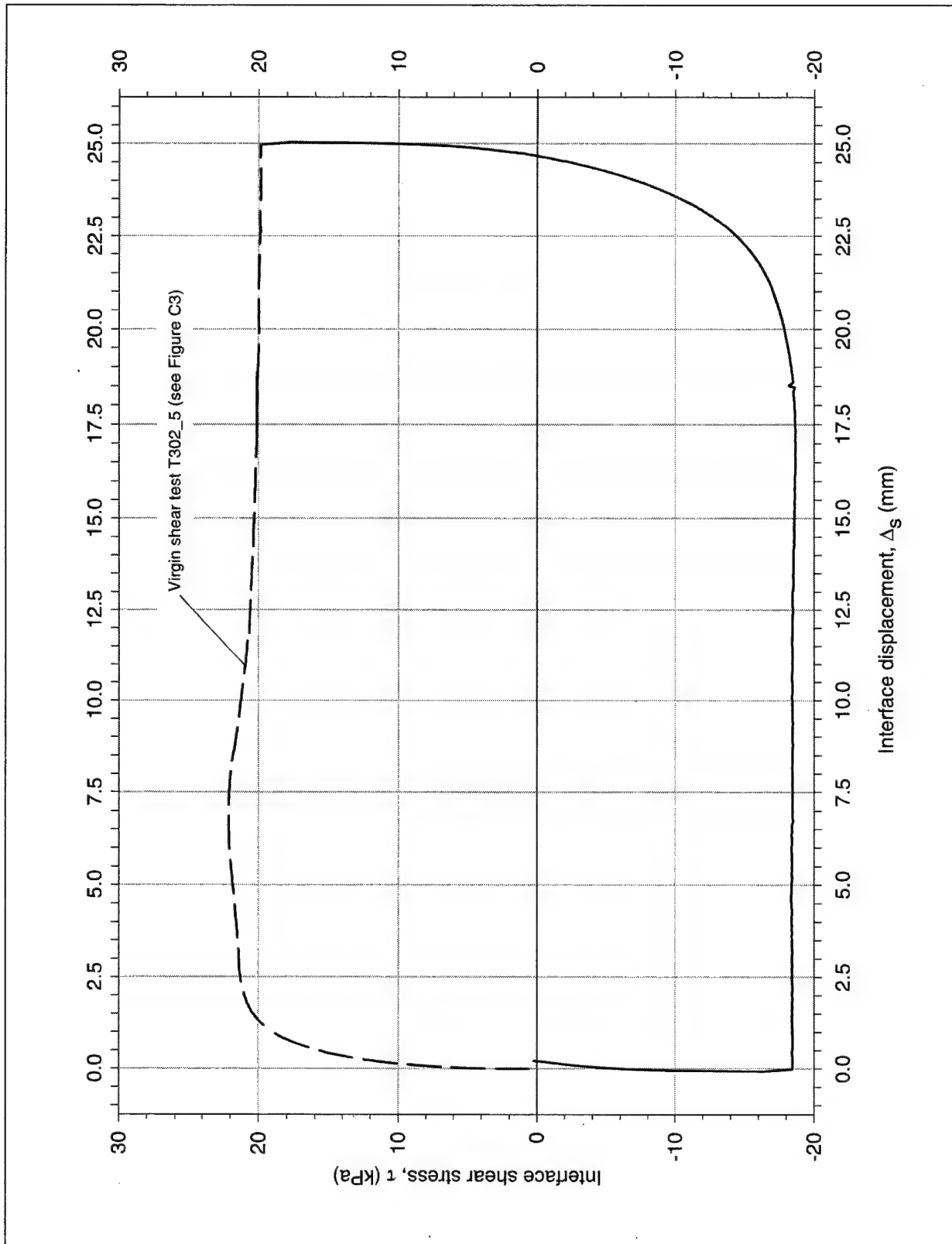


Figure C19. Shear reversal on medium-dense-Density-sand-to-concrete interface, $\sigma_n = 35$ kPa, Specimen S302

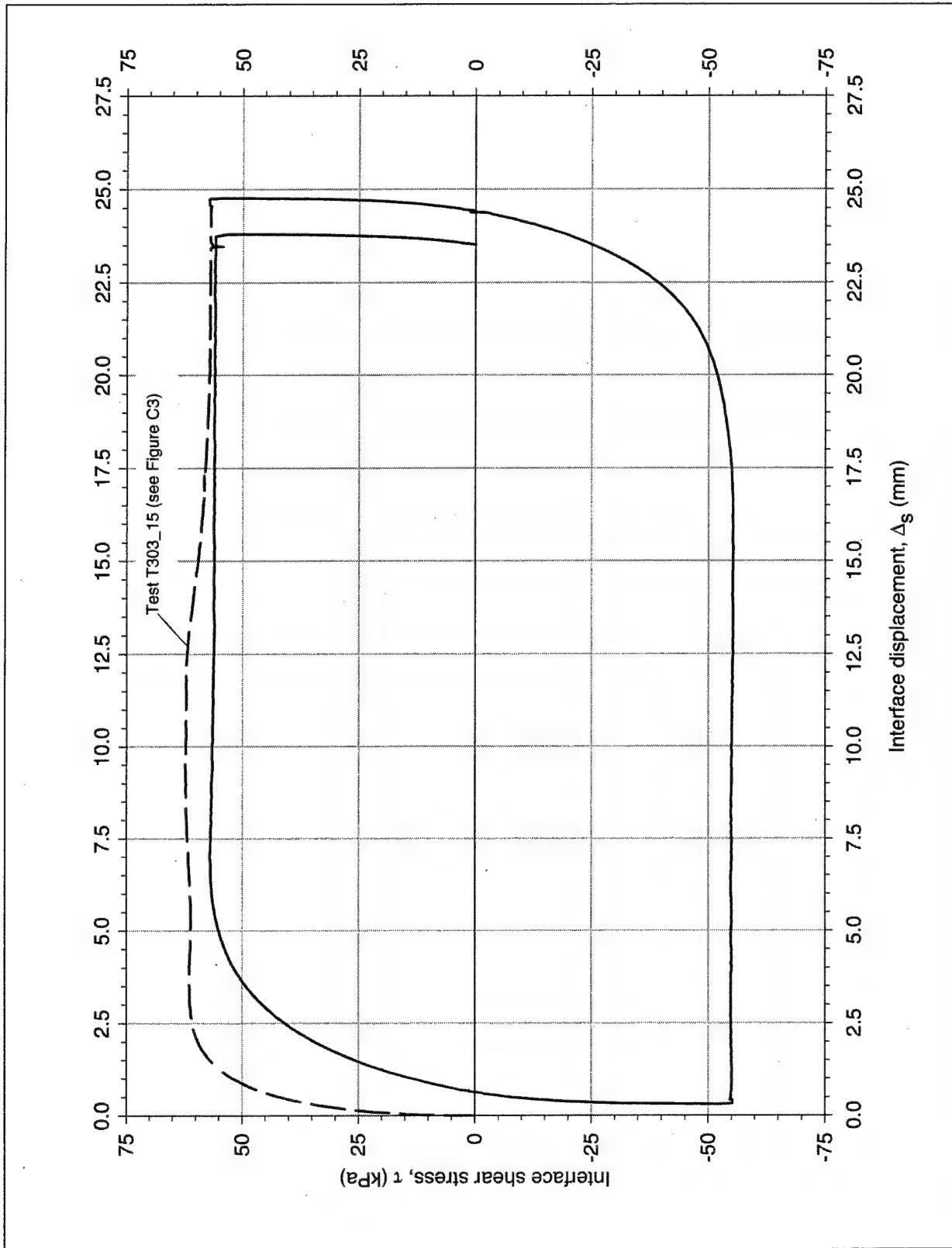


Figure C20. Cycle of shear reversals on medium-density sand-to-concrete interface, $\sigma_n = 104$ kPa, Specimen S303

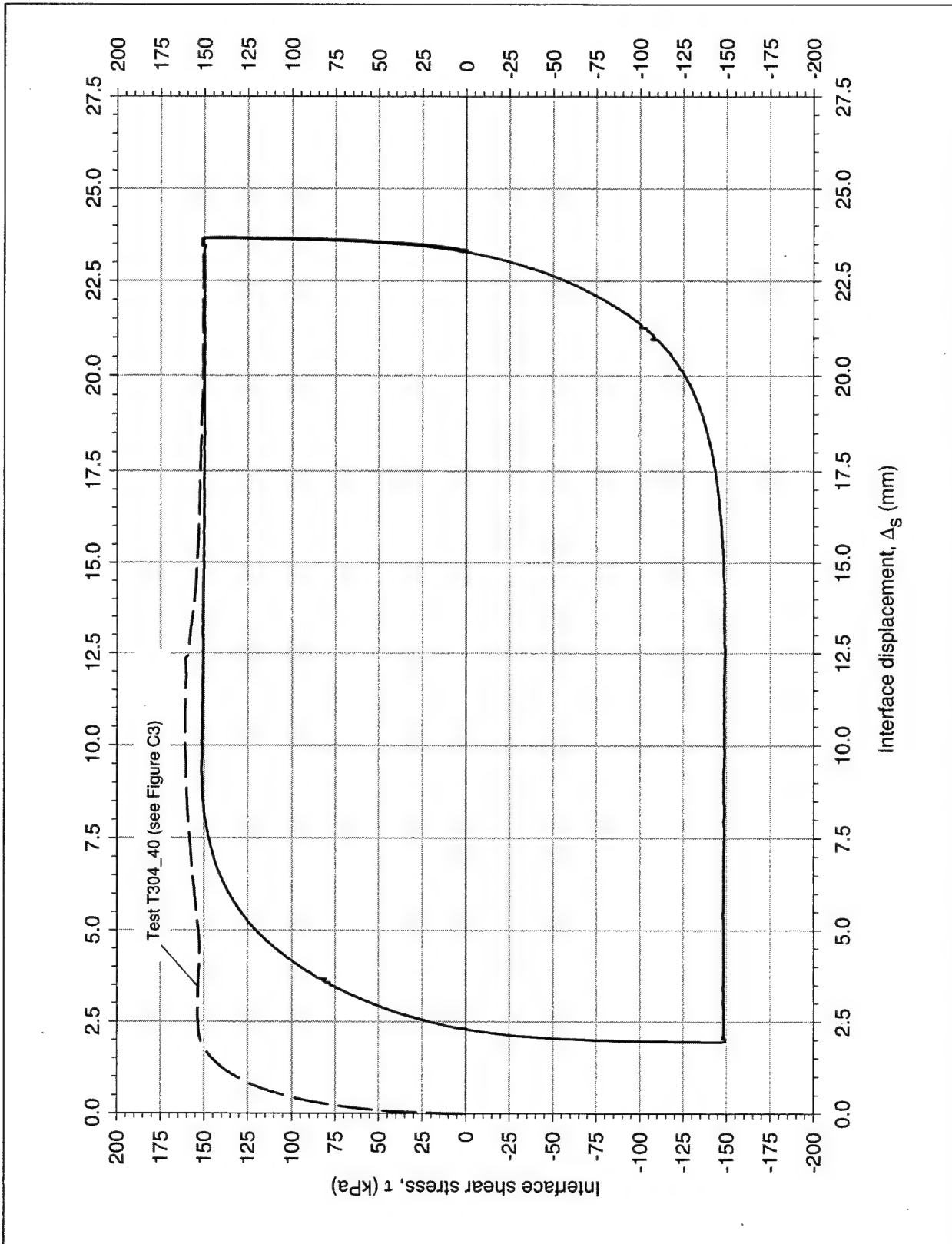


Figure C21. Cycle of shear reversals on medium-dense-Density-sand-to-concrete interface, $\sigma_n = 276$ kPa, Specimen S304

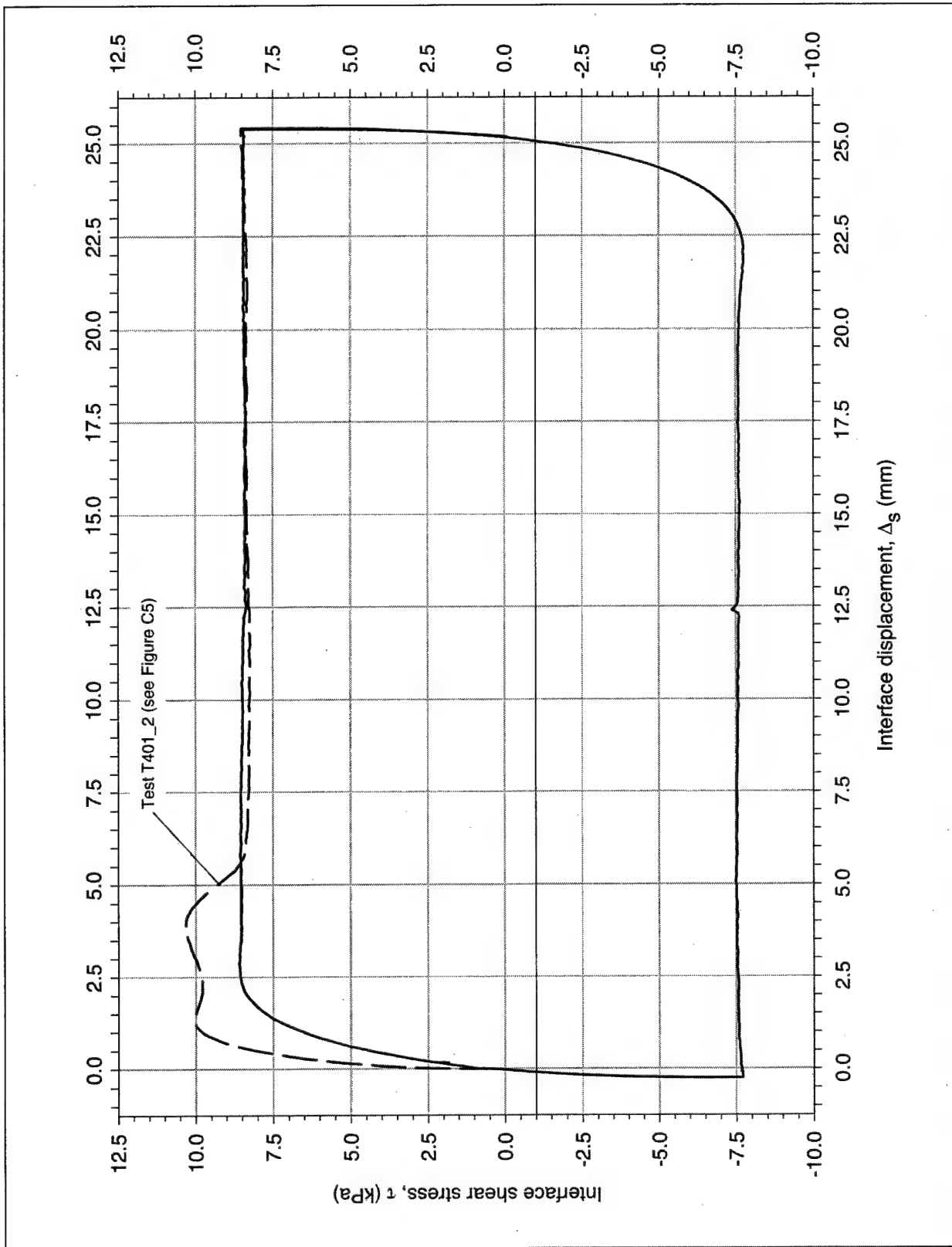


Figure C22. Cycle of shear reversals on dense-Light-Castle-sand-to-concrete interface, $\sigma_n = 15$ kPa, Specimen S401

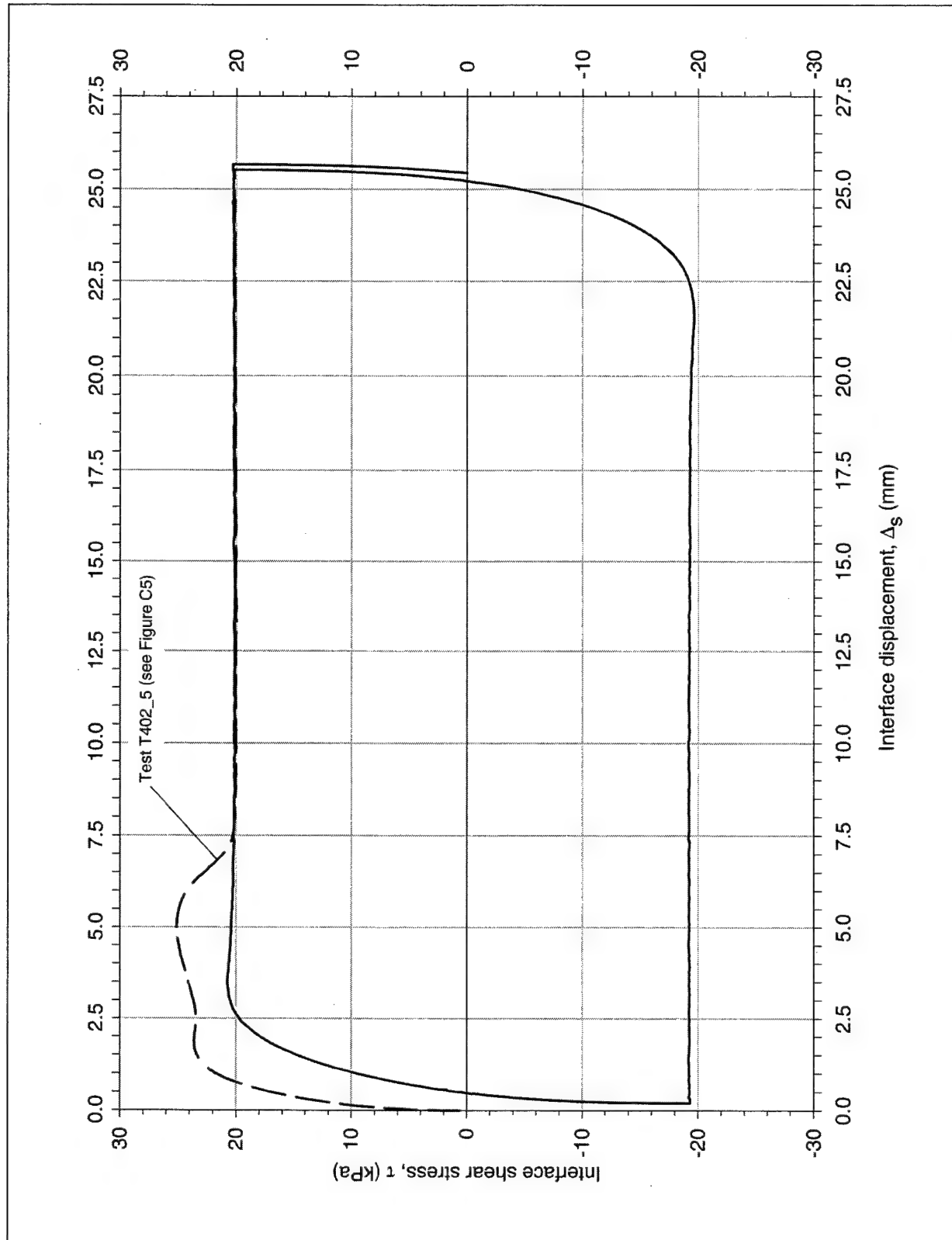


Figure C23. Cycle of shear reversals on dense-Light-Castle-sand-to-concrete interface, $\sigma_n = 35$ kPa, Specimen S402

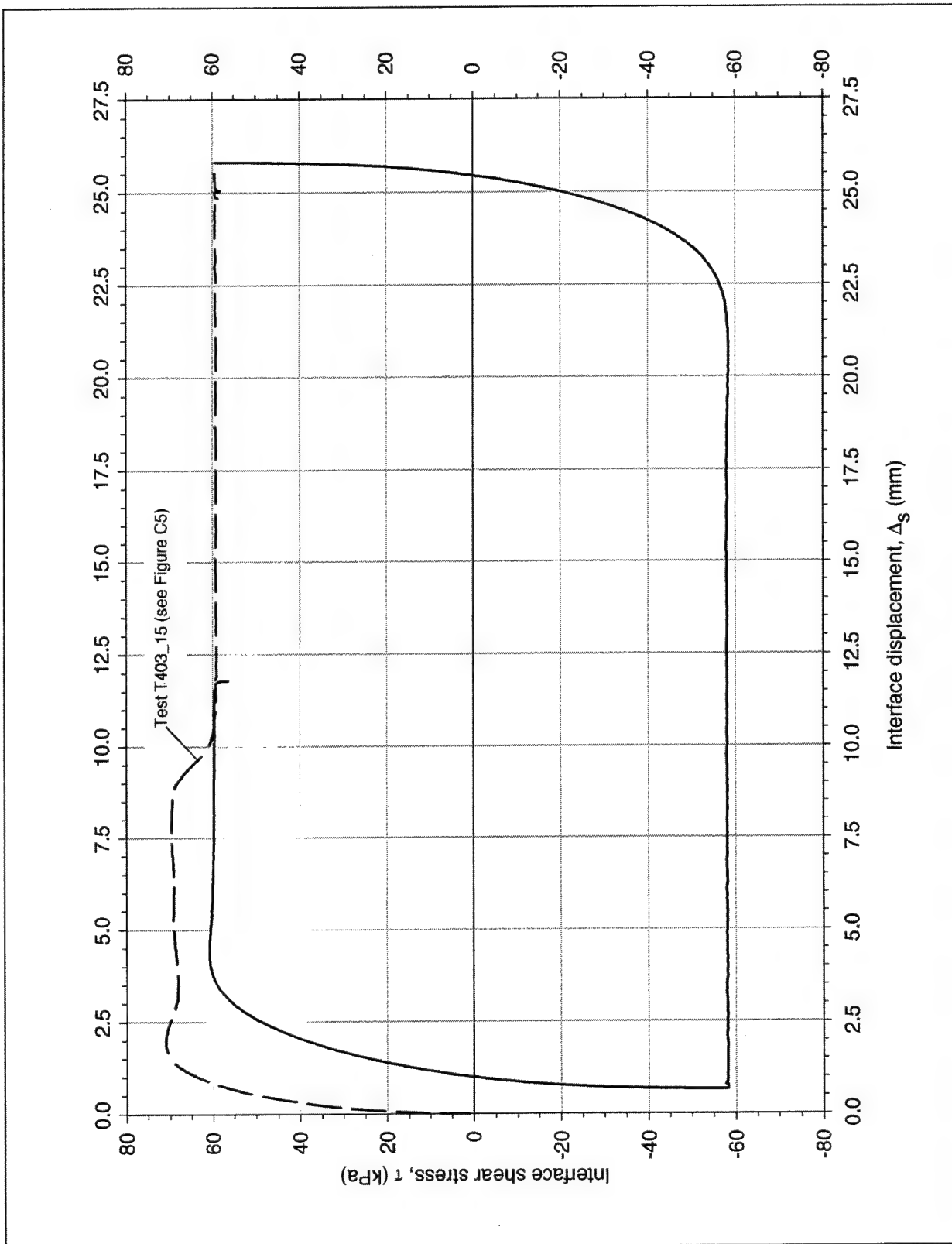
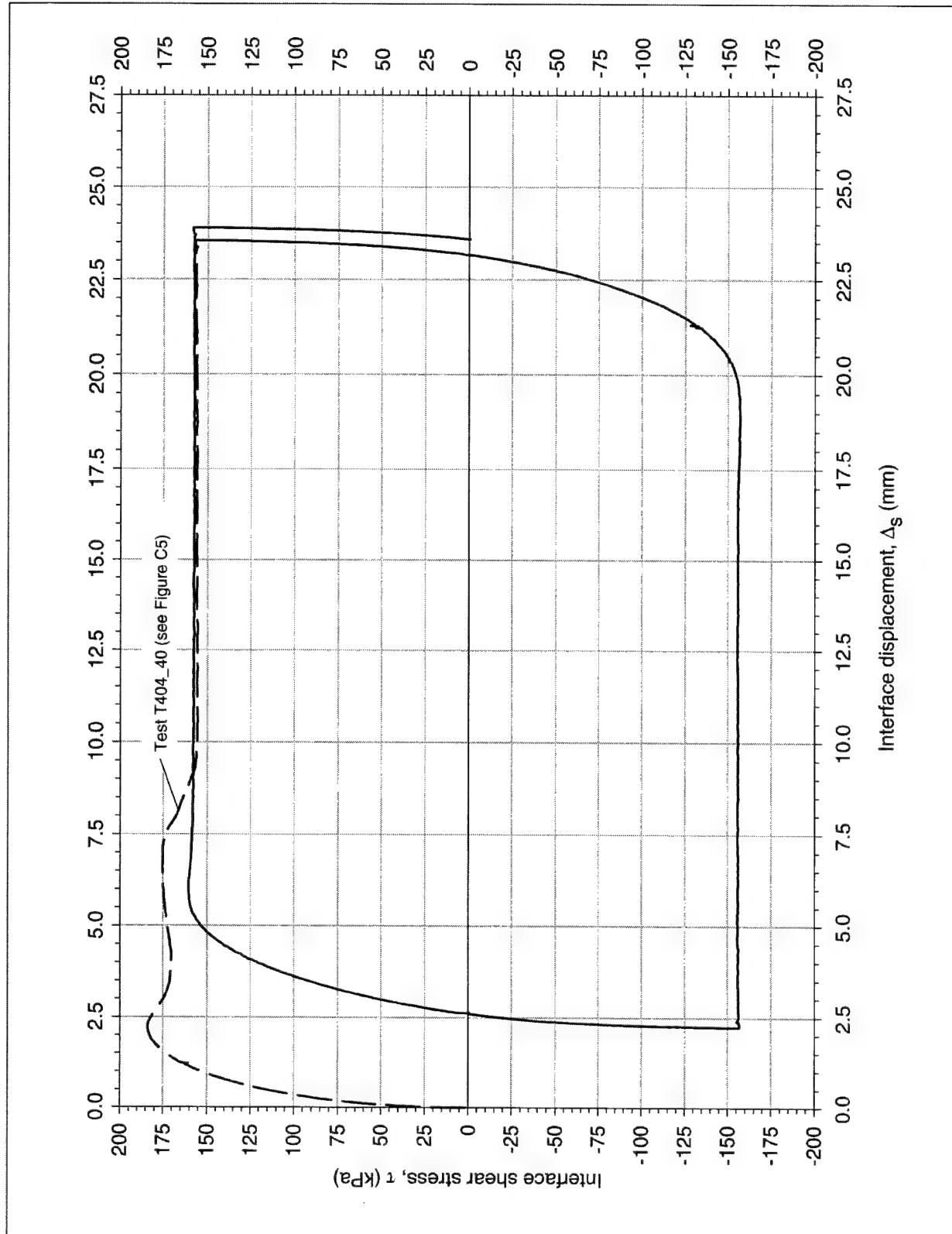
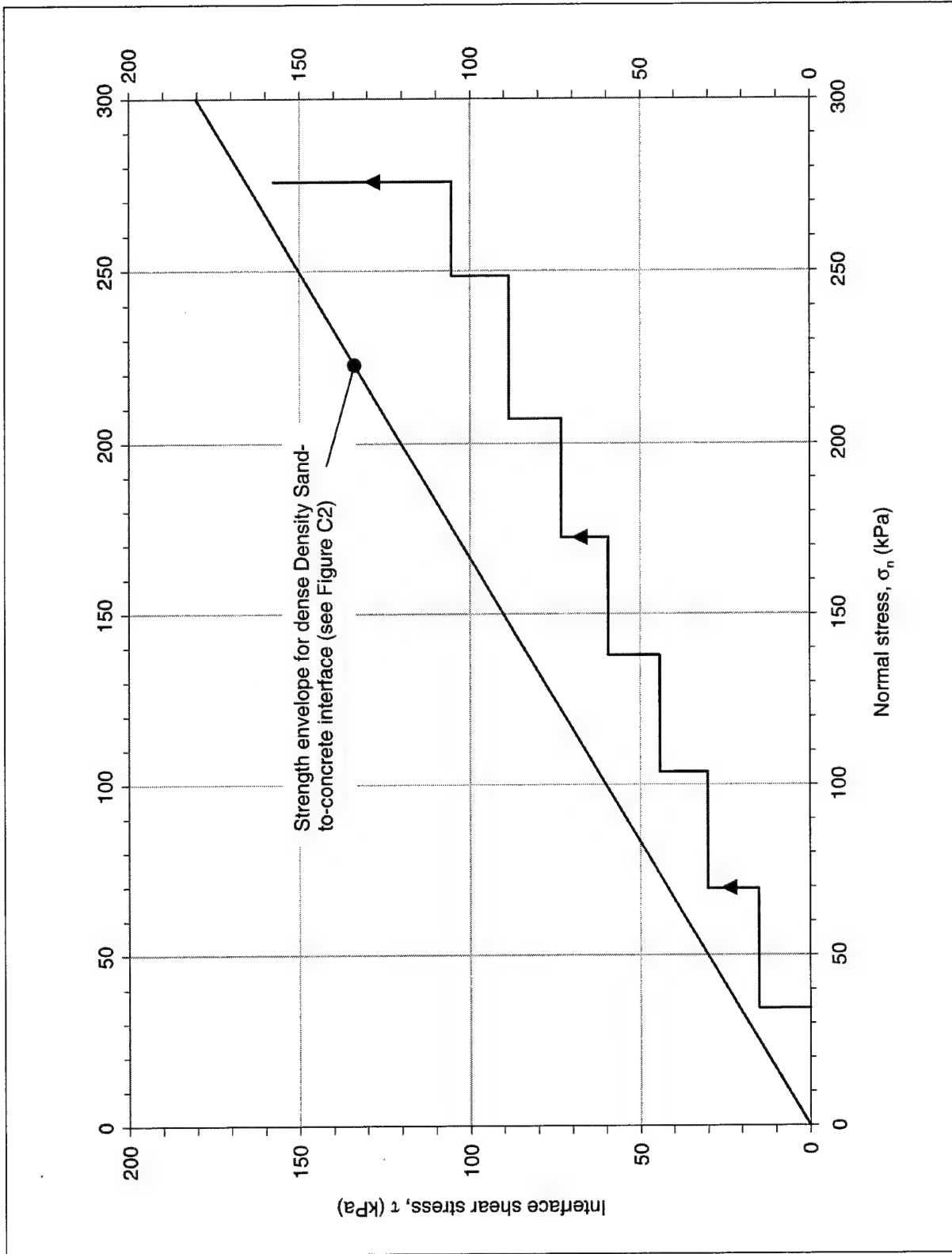
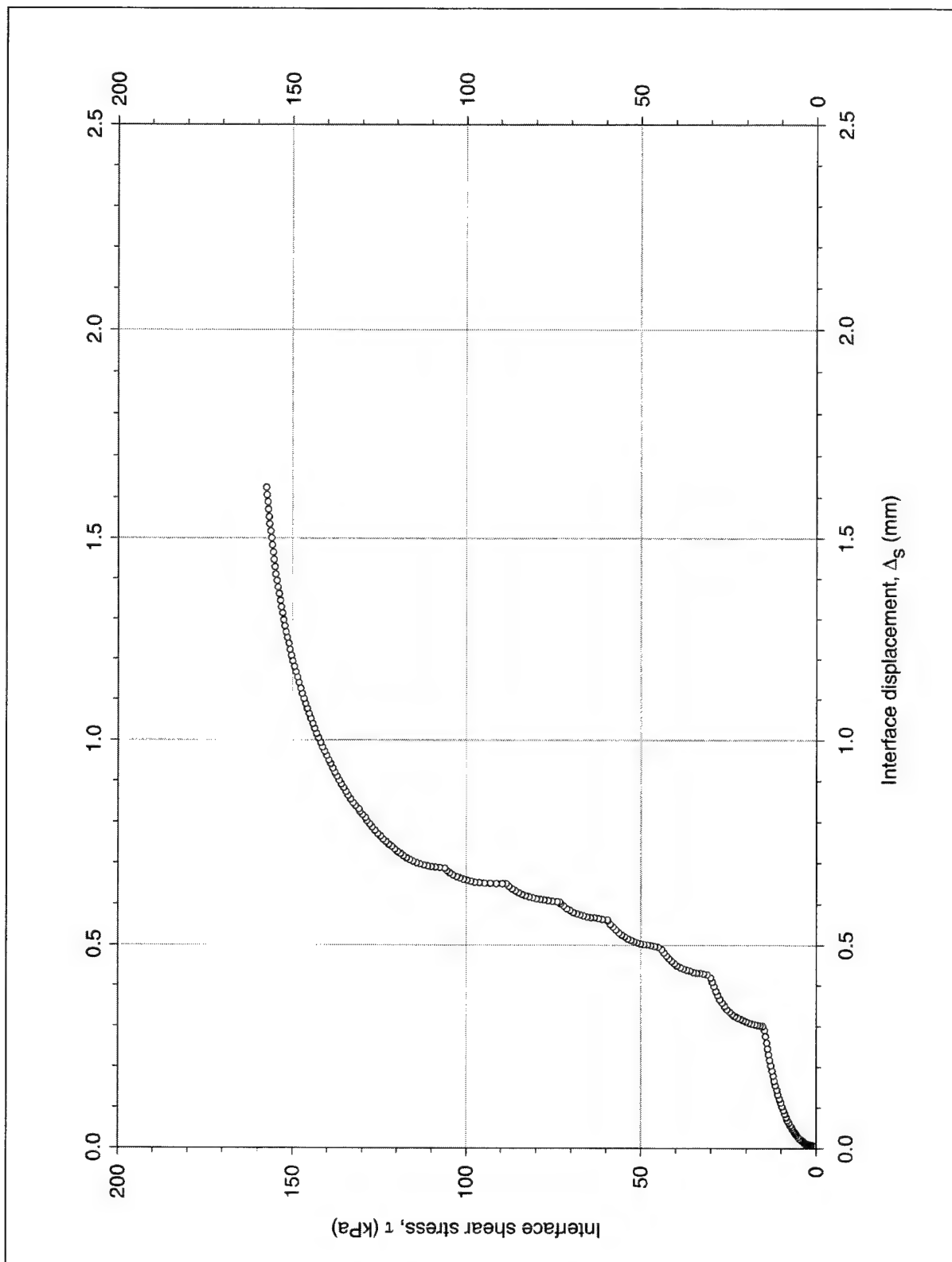


Figure C24. Cycle of shear reversals on dense-Light-Castle-sand-to-concrete interface, $\sigma_n = 104$ kPa, Specimen S403

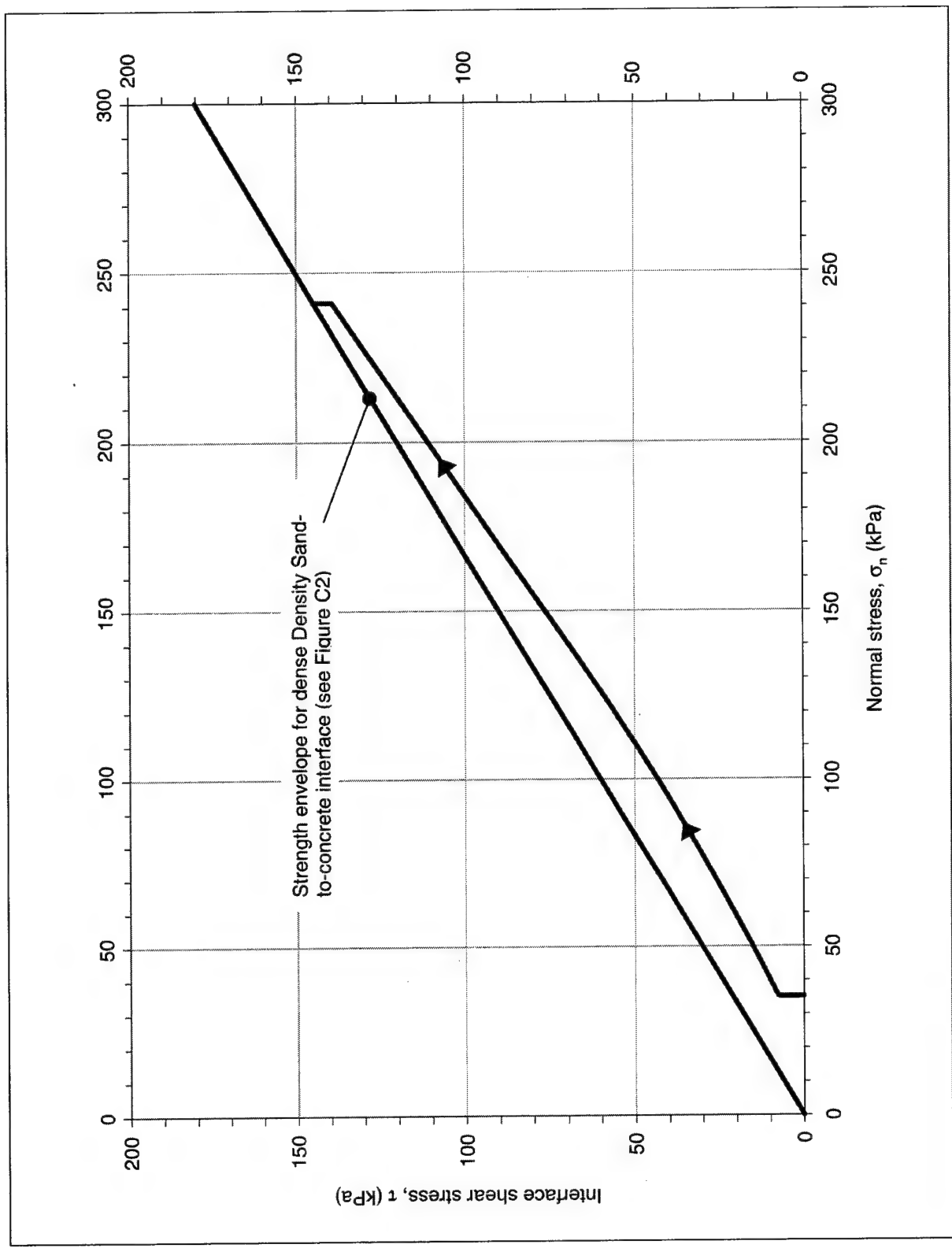




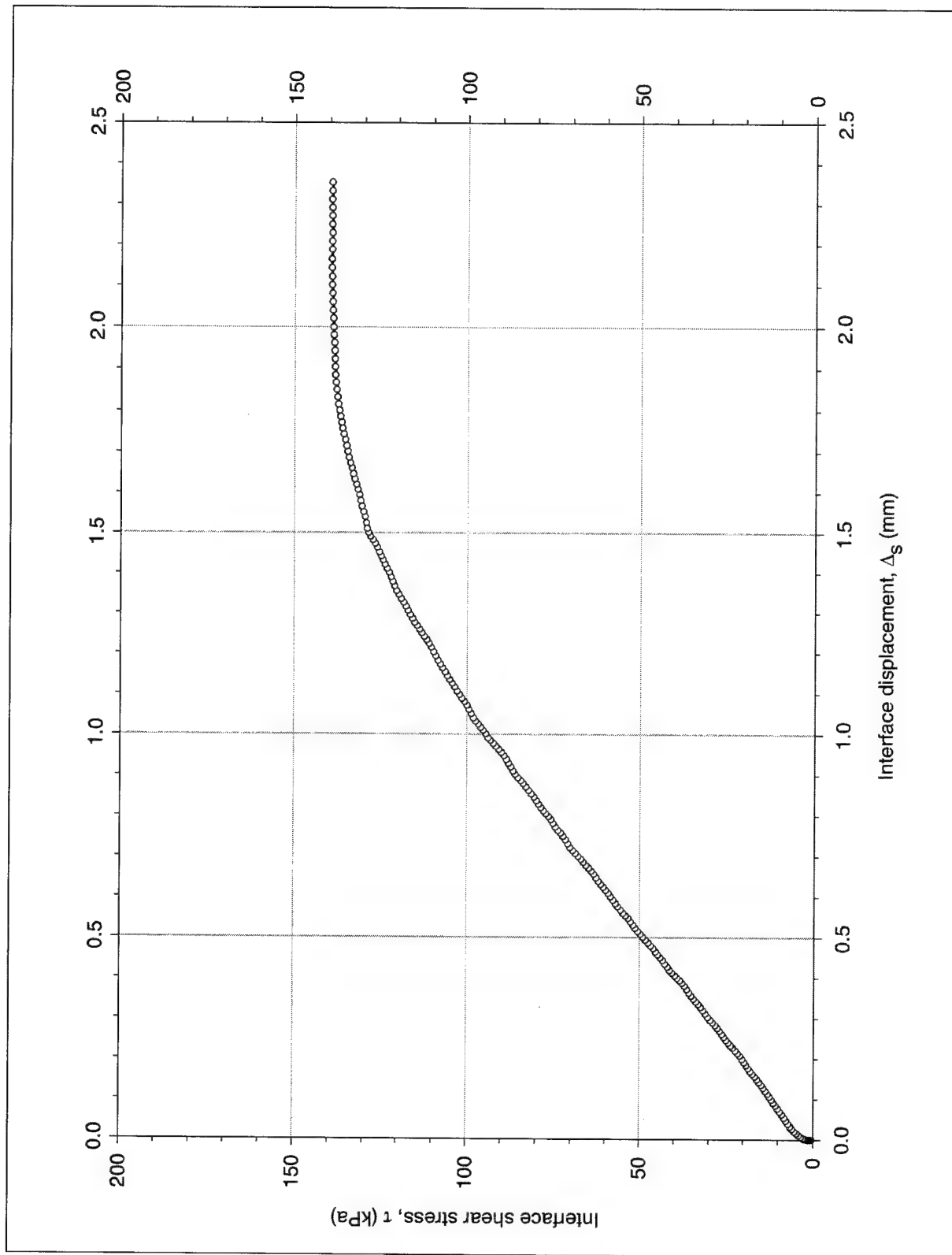
a. Stress path applied during test
Figure C26. Multidirectional stress path Test T204_5 on dense-Density-Sand-to-concrete interface (Continued)



b. Shear stress versus interface displacement data
Figure C26. (Concluded)

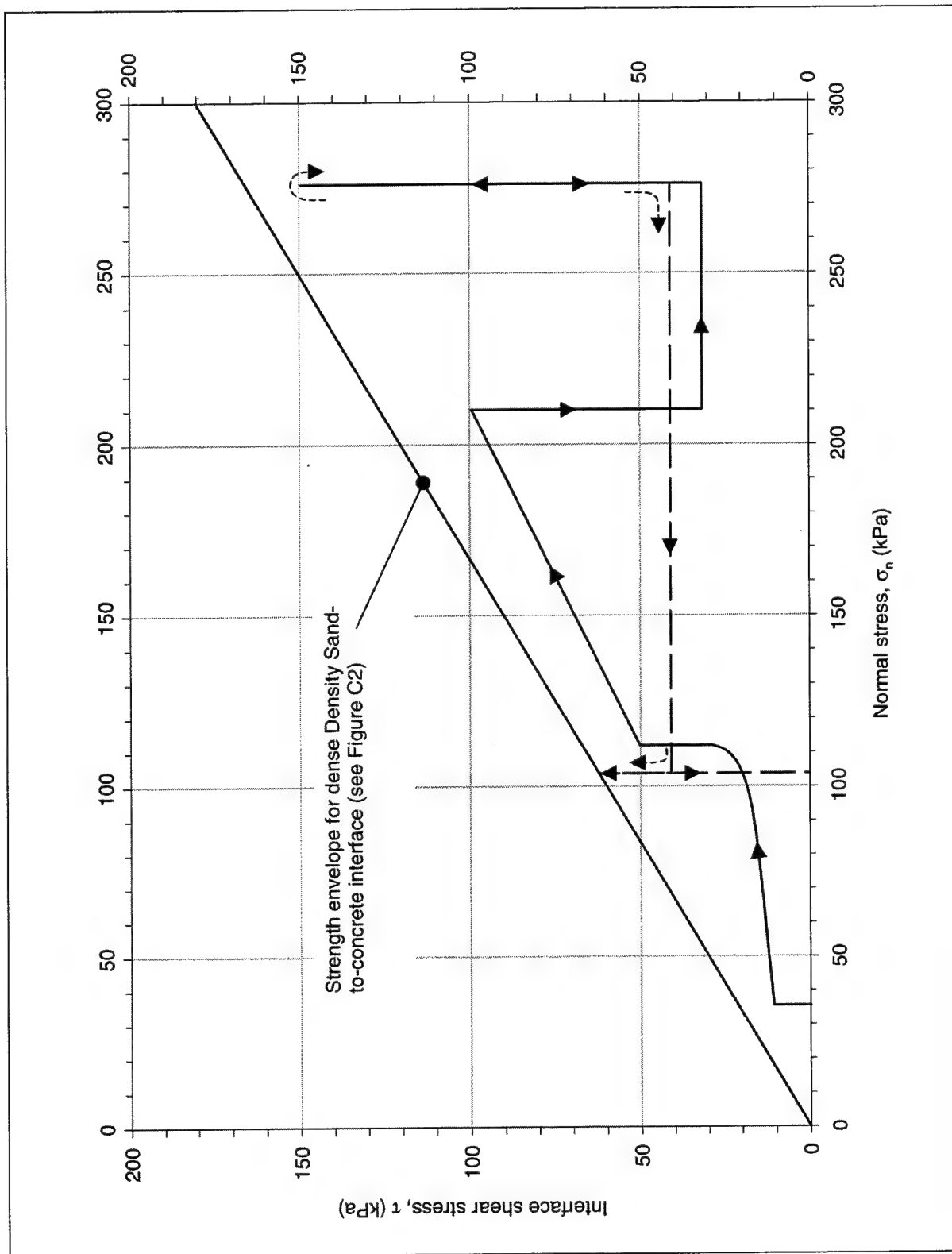


a. Stress path applied during test
Figure C27. Multidirectional stress path T205_5 on dense-Density-sand-to-concrete interface (Continued)

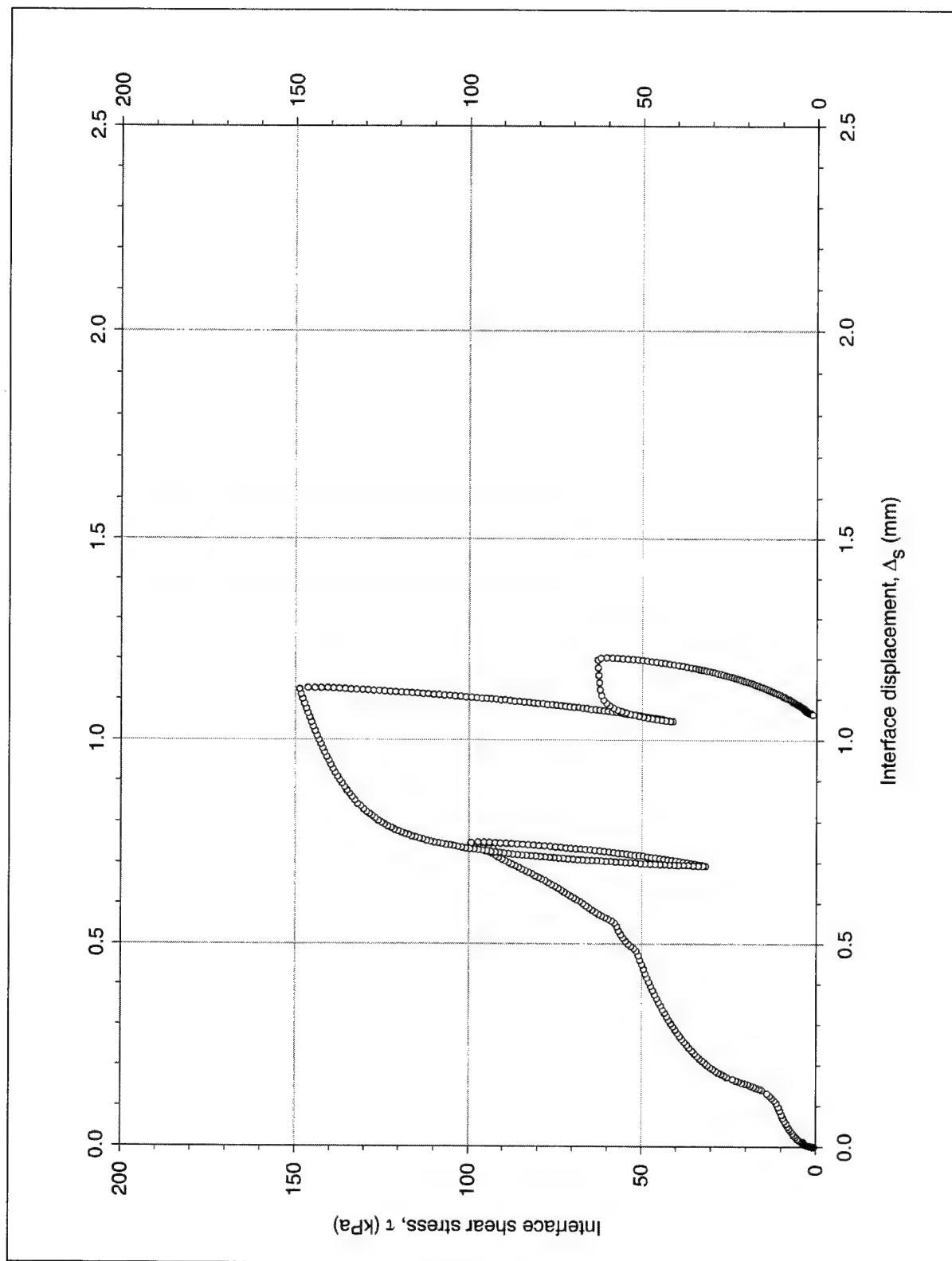


b. Shear stress versus interface displacement data

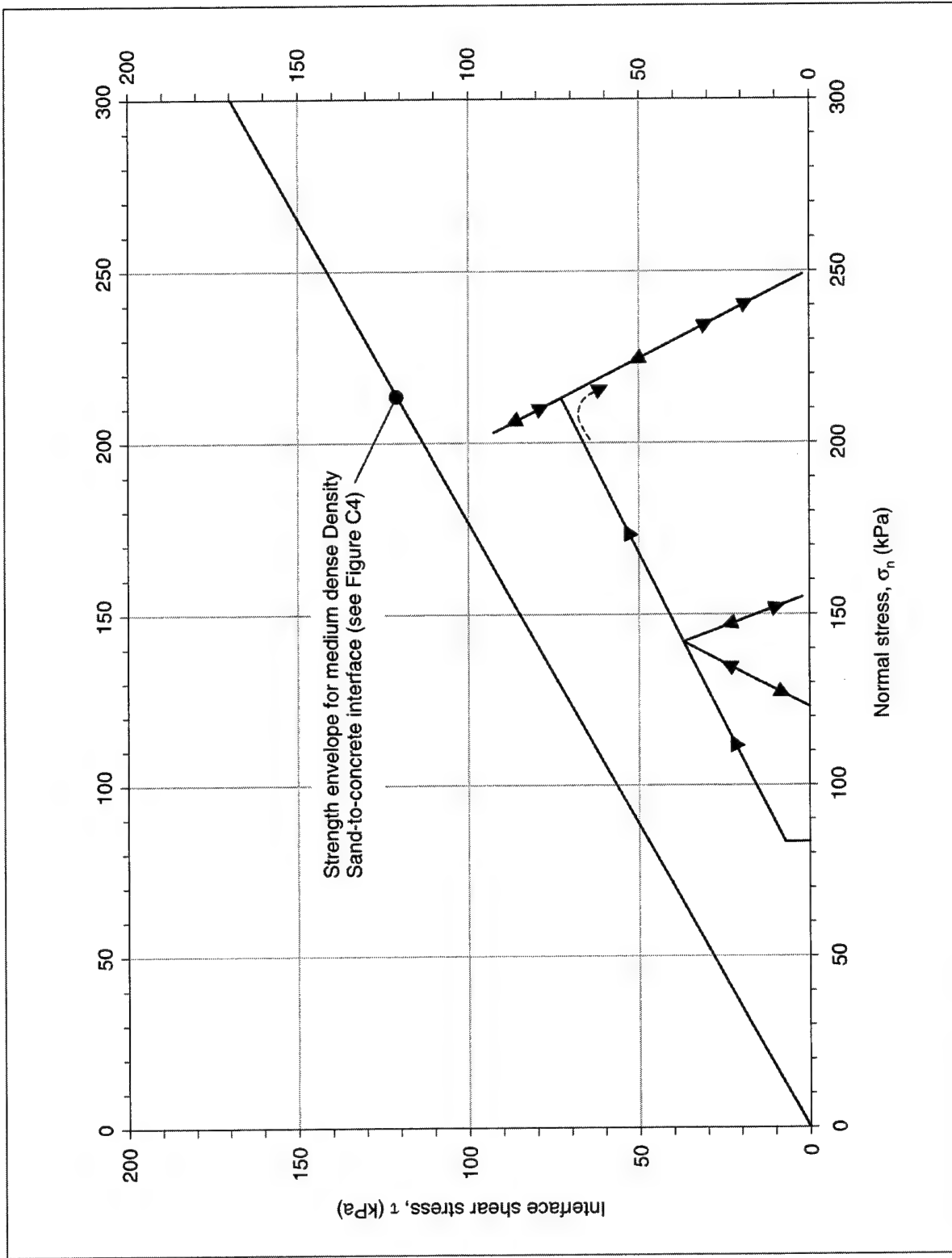
Figure C27. (Concluded)



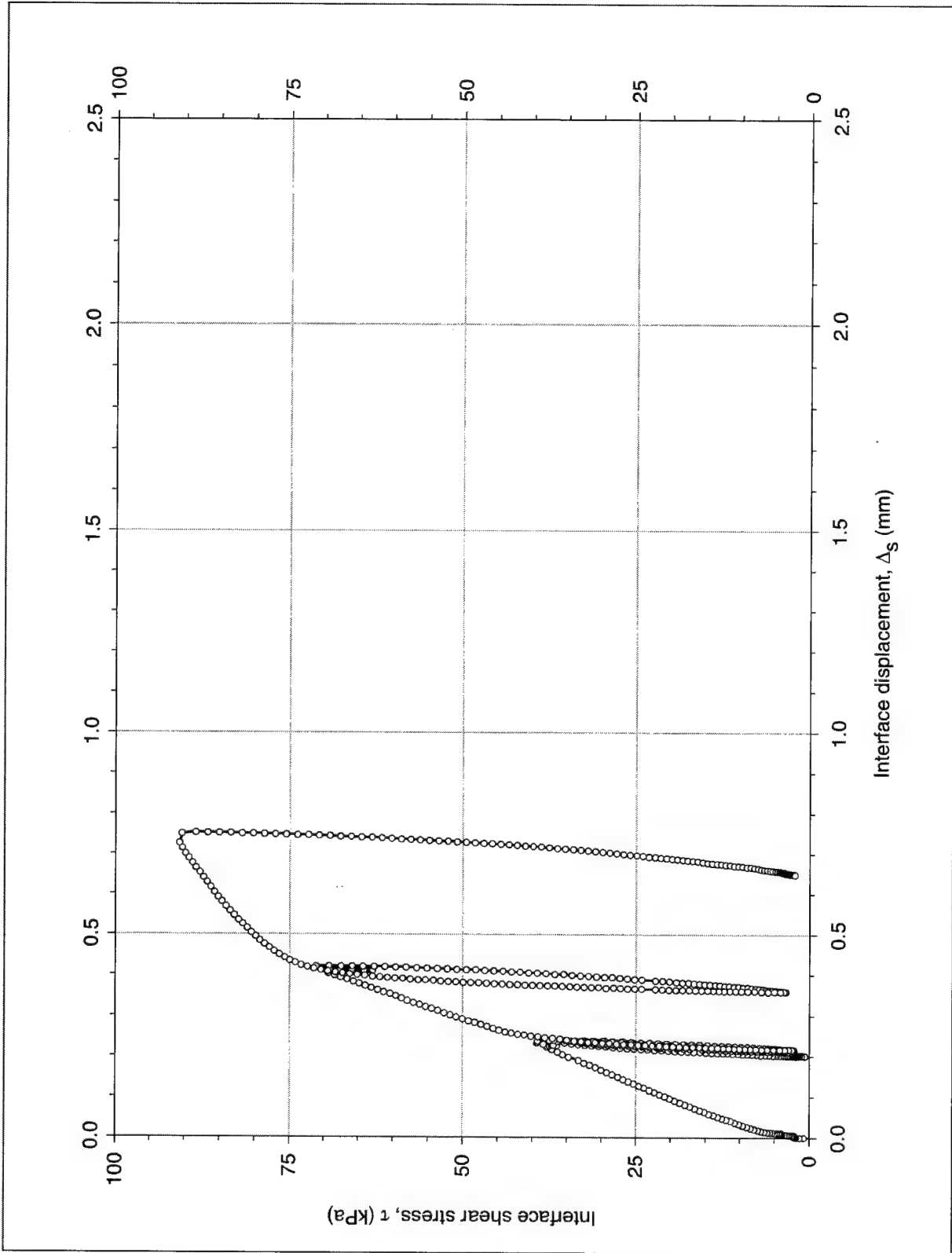
a. Stress path applied during test
Figure C28. Multidirectional stress path Test T206_5 on dense-Density sand-to-concrete interface (Continued)

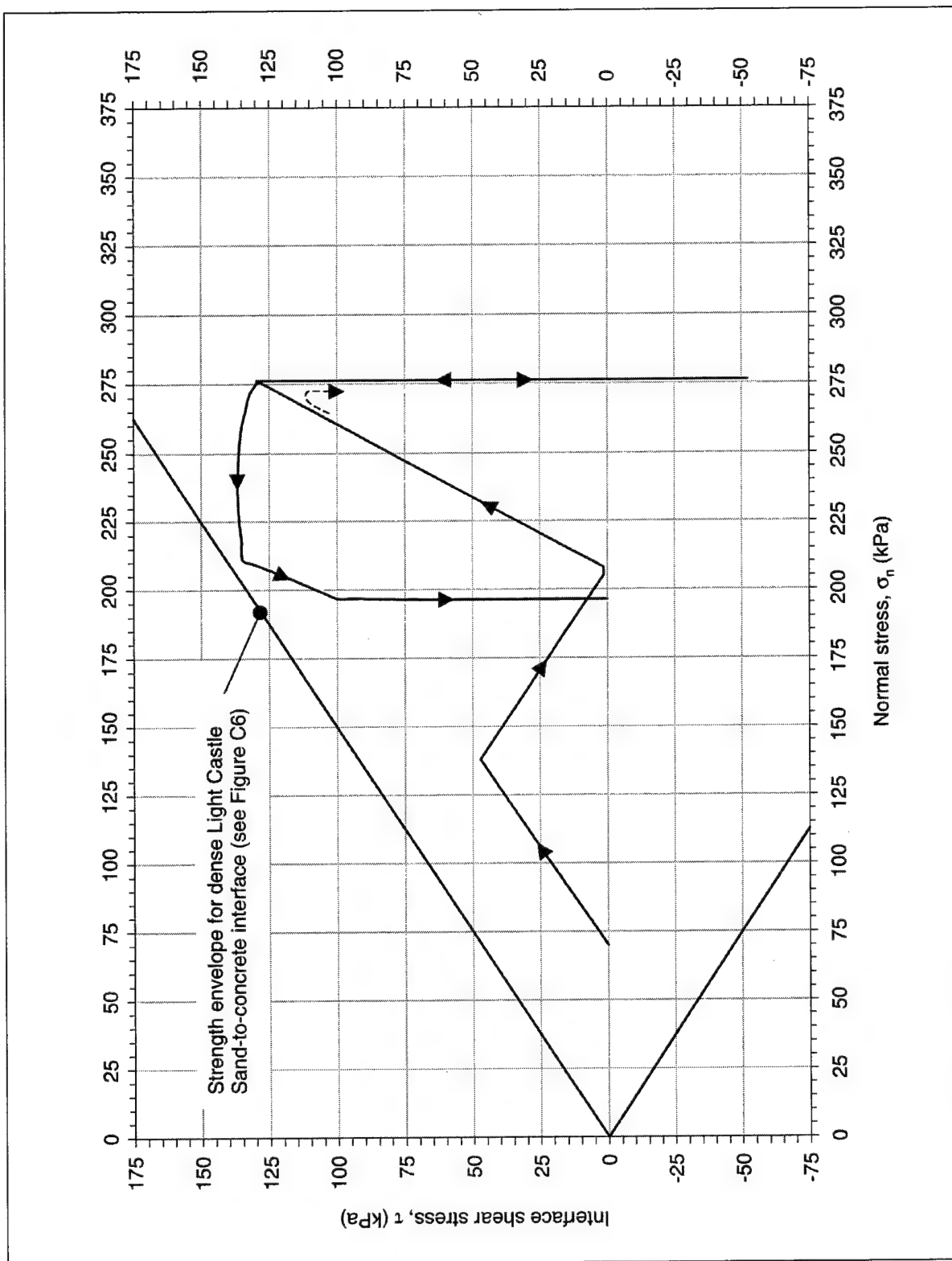


b. Shear stress versus interface displacement data
Figure C28. (Concluded)

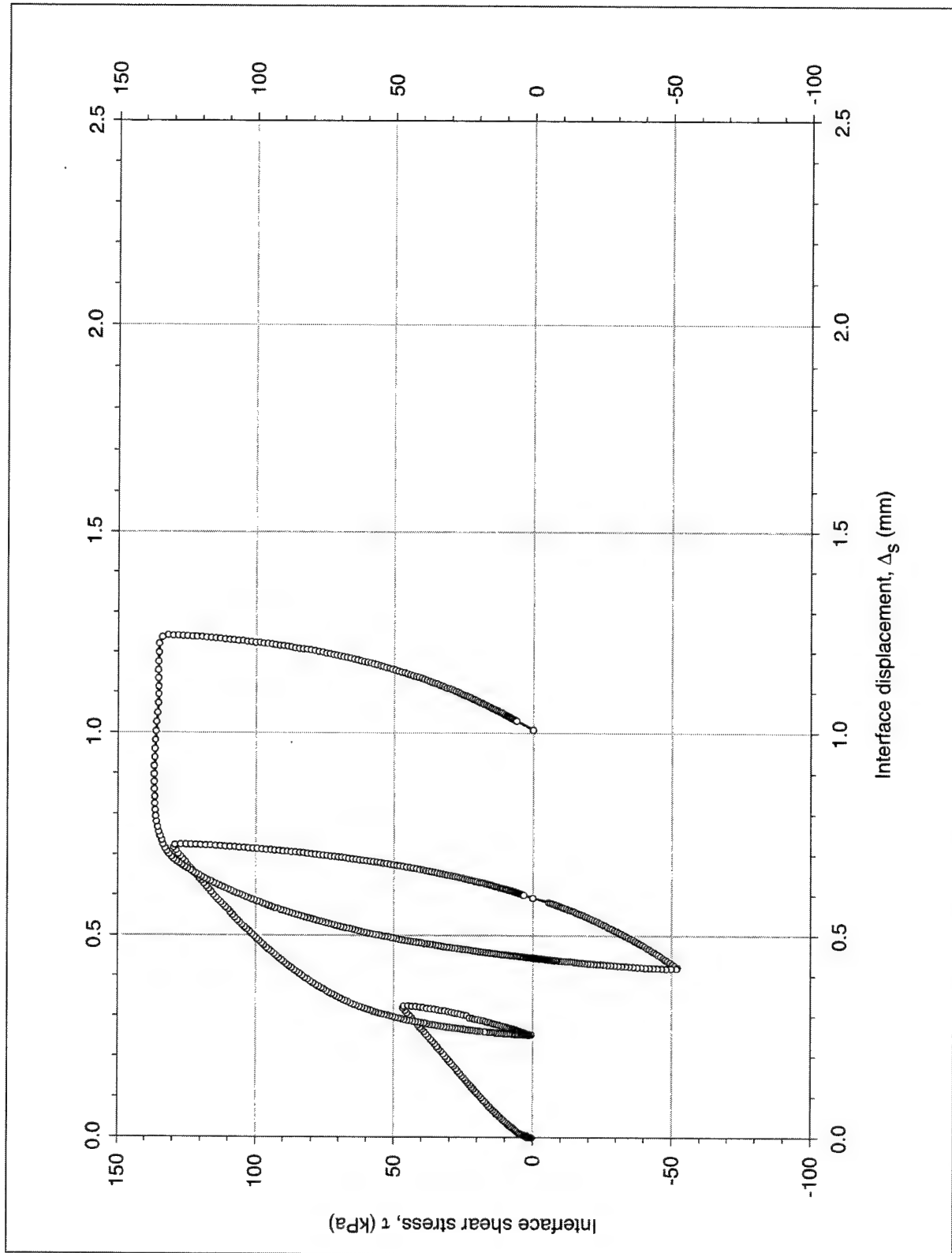


a. Stress path applied during test
Figure C29. Multidirectional stress path Test T305_10 on medium-dense-Density-sand-to-concrete interface (Continued)





a. Stress path applied during test
Figure C30. Multidirectional stress path Test T405_10 on dense-Light-Castle-sand-to-concrete interface (Continued)



b. Shear stress versus interface displacement data

Figure C30. (Concluded)

Appendix D

Determination of Interface Hyperbolic Parameter Values

This appendix describes the procedure developed by Clough and Duncan (1971)¹ for the determination of hyperbolic parameter values for interfaces. Hyperbolic parameter values of the interfaces between concrete and dense Density sand, medium-dense Density sand, and dense Light Castle sand are determined based on the results of the initial loading tests presented in Appendix C. Example calculations of hyperbolic parameter values for the interface between dense Light Castle sand and concrete are presented in the last section of this appendix.

D.1 Transformed Plots

The procedure for determination of hyperbolic parameters is illustrated using the data from initial loading tests on dense-Density-sand-against-concrete interface. The data from the initial loading tests, which is shown in Figure C1c of Appendix C, is represented in the transformed diagram of Figure D1 following the procedure described by Clough and Duncan (1971). In this transformed diagram, the value of interface displacement² Δ_s measured during the test is divided by the corresponding value of shear stress τ and plotted against the interface displacement. If the shear stress-displacement relationship measured during the triaxial test is hyperbolic, the transformed plot is a straight line. The intercept a of this straight line on the Δ_s/τ axis is the reciprocal of the initial shear stiffness K_{si} of the interface. The slope b of the line is the reciprocal of the asymptotic shear stress τ_{ult} .

The shear stress-displacement relationship of an interface usually differs from a hyperbola. Clough and Duncan (1971) indicated that the values of parameters a and b can be determined from a straight line passing through the points in the transformed plot that correspond to 70 and 95 percent of the interface shear strength. The transformed plot in Figure D1 shows the 70 and 95 percent strength

¹ References cited in this Appendix are included in the References at the end of the main text.

² For convenience, symbols are listed and defined in the Notation (Appendix F).

data points for each of the tests performed on the dense-Density-sand-against-concrete interface. Straight lines are drawn through each pair of these points.

It can be seen in Figure D1 that the lines drawn through the 70 and 95 percent data points match closely the transformed data sets. This type of comparison may be useful for avoiding errors in the determination of hyperbolic parameter values that can arise from inconsistencies in the data. Transformation of the entire set of test data is easily achieved in an electronic spreadsheet. The use of a spreadsheet also facilitates modification of the values of parameters a and b to obtain the best possible fit to the data.

D.2 Hyperbolic Parameter Values

D.2.1 Determination of K_i and n_j

The values of the parameters a and b determined from the transformed plots are presented in the table included in Figure D1. The values of initial interface shear stiffness and asymptotic shear stress are determined using the following equations:

$$K_{si} = \frac{I}{a} \quad (D1)$$

$$\tau_{ult} = \frac{I}{b} \quad (D2)$$

The values of K_{si} and τ_{ult} for each of the tests performed on the interface between dense Density Sand and concrete are presented in the table in Figure D1. It can be seen that the value of K_{si} increases with increasing normal stress σ_n . The following relationship is used to relate the value of initial interface stiffness to the magnitude of normal stress:

$$K_{si} = K_I \cdot \gamma_w \cdot \left(\frac{\sigma_n}{p_a} \right)^{n_j} \quad (D3)$$

where

K_I = stiffness number

γ_w = unit weight of water

p_a = atmospheric pressure

n_j = stiffness exponent

This relationship implies that there is a linear relationship between the logarithm of the initial interface shear stiffness and the logarithm of the normal stress. Figure D2 is a logarithmic diagram that shows the values of normalized initial stiffness K_{si}/γ_w represented against the values of normalized normal stress σ_n/p_a . A best-fit straight line is drawn through the data points. The value of the stiffness number K_I is equal to the value of normalized initial stiffness given by this best-fit line for a normal stress of 1 atm. The slope of the line is the stiffness exponent n_j .

D.2.2 Determination of R_{ff}

The table in Figure D1 shows the values of shear stress at failure τ_f , determined from the shear stress-displacement data from the tests, which are presented in Figure C1c of Appendix C. It can be seen in the table that the values of τ_{ult} are larger than the values τ_f in all the tests. The value of the failure ratio R_{ff} for each of the tests is determined from the following expression:

$$R_{ff} = \frac{\tau_f}{\tau_{ult}} \quad (D4)$$

The table contains the values of R_{ff} determined for each of the tests. For modeling, an average value of R_{ff} is determined from the test results as shown at the bottom of the table. According to Table 4-9 in Chapter 4 of this report, typical values of R_{ff} range between 0.4 and 0.95.

D.3 Comparison of Model to Test Data

Once the hyperbolic parameter values are determined, it is necessary to compare the model response to the test data. The shear stress-displacement response from the model is calculated using the following expression:

$$\tau = \frac{\Delta_s}{\frac{1}{K_I \cdot \gamma_w \cdot \left(\frac{\sigma_n}{p_a}\right)^{n_j}} + \frac{R_{ff} \cdot \Delta_s}{\sigma_n \cdot \tan \delta}} \quad (D5)$$

where δ is the interface friction angle. This expression is valid for frictional interfaces with zero adhesion intercept.

The shear stress-displacement response of the interface between dense Density sand and concrete was calculated using Equation D5 and the hyperbolic parameters determined following the procedure described previously. Figure D3 compares the test data and the calculated hyperbolic response. In the figure, the

shear stress-displacement hyperbola is interrupted at the value of shear stress at failure τ_f . A horizontal shear stress-displacement relationship, i.e., zero interface stiffness, is used to model the response of the soil after failure is attained.

An identical procedure was followed for the determination of the hyperbolic parameters of the interfaces between concrete and medium dense Density sand and dense Light Castle sand, as illustrated in Figures D4 through D9. It can be seen that the hyperbolic model provides an accurate approximation to the interface response measured during each of the tests.

Further adjustments of these parameter values may be required for the application of the extended hyperbolic model. These adjustments are fully described in Chapter 4 of this report.

D.4 Example Calculations of Hyperbolic Parameter Values

This section presents an example of the determination of hyperbolic parameter values. The data from the initial loading tests performed on the interface between dense Light Castle Sand and concrete are used for this example. The presentation of the example calculations is based on the procedure described by Duncan et al. (1980) for the determination of hyperbolic parameter values in soils.

The first step in the determination of hyperbolic parameter values is checking for inconsistencies in the data from the interface tests. Figure D10 shows the results of the tests performed on the dense-Light-Castle-sand-against-concrete interface. The data points shown in the figure are identical to those shown in Figures C5 and D9. Frequently, data from interface tests may present some inconsistencies that can be minimized by developing an assumed shear stress-displacement response. The response assumed for the determination of the hyperbolic parameters in this example is represented as a solid line in Figure D10. Because of the relatively large precision of displacement and shear stress measurements, few inconsistencies can be seen in the data and the assumed response is practically identical to the measured response.

The next step is the determination of the shear stress at failure τ_f for each normal stress. The values of τ_f can be determined from the shear stress-displacement plots of the tests. Column (2) in the table presented in Figure D11 contains the values of shear stress at failure determined from Figure D10. The values of shear stress corresponding to 70 and 95 percent of τ_f are calculated as shown in columns (3) and (6), respectively.

The values of interface displacement corresponding to 70 and 95 percent of the shear stress at failure are determined from the shear stress-displacement plots. Columns (4) and (7) in Figure D11 contain the displacement values determined as shown in Figure D10.

The values in columns (2), (3), (4), (6), and (7) are the basis for the determination of the values of initial interface stiffness K_{si} and failure ratio R_f . The sequence of calculations leading to the determination of the values of K_{si} and R_f is shown in Figure D11, and corresponds to the procedure presented in the previous sections.

It must be noted that in the method presented in Figure D11, the data are not plotted in transformed coordinates. Only the two data points corresponding to 70 and 95 percent of the shear strength are transformed as shown in columns (5) and (8). Although not strictly necessary, it is recommended always to plot the complete data set in transformed coordinates. The transformed plots are useful to check the data for inconsistencies and to verify the values of initial interface stiffness and failure ratio determined from the procedure presented in Figure D11. Transforming the data following the procedure described previously in this chapter can be accomplished easily with electronic spreadsheets.

The value of failure ratio R_f to be used for modeling is the average of the values determined in Figure D11. The values of K_f and n_f are determined by plotting the normalized values of initial interface stiffness against the normalized normal stress in logarithmic scale as shown in Figure D12.

It must be noted that none of the values presented in Figure D11 was determined graphically. They were obtained directly or by interpolation of data in an electronic spreadsheet. Although graphical determination of values of shear stress and displacement from a figure such as D10 may provide fewer significant decimal places than their numerical determination, the overall precision of the values of the hyperbolic parameters is similar using both procedures. The use of an electronic spreadsheet is recommended, not for increased precision, but for ease in the calculations and verification of the results.

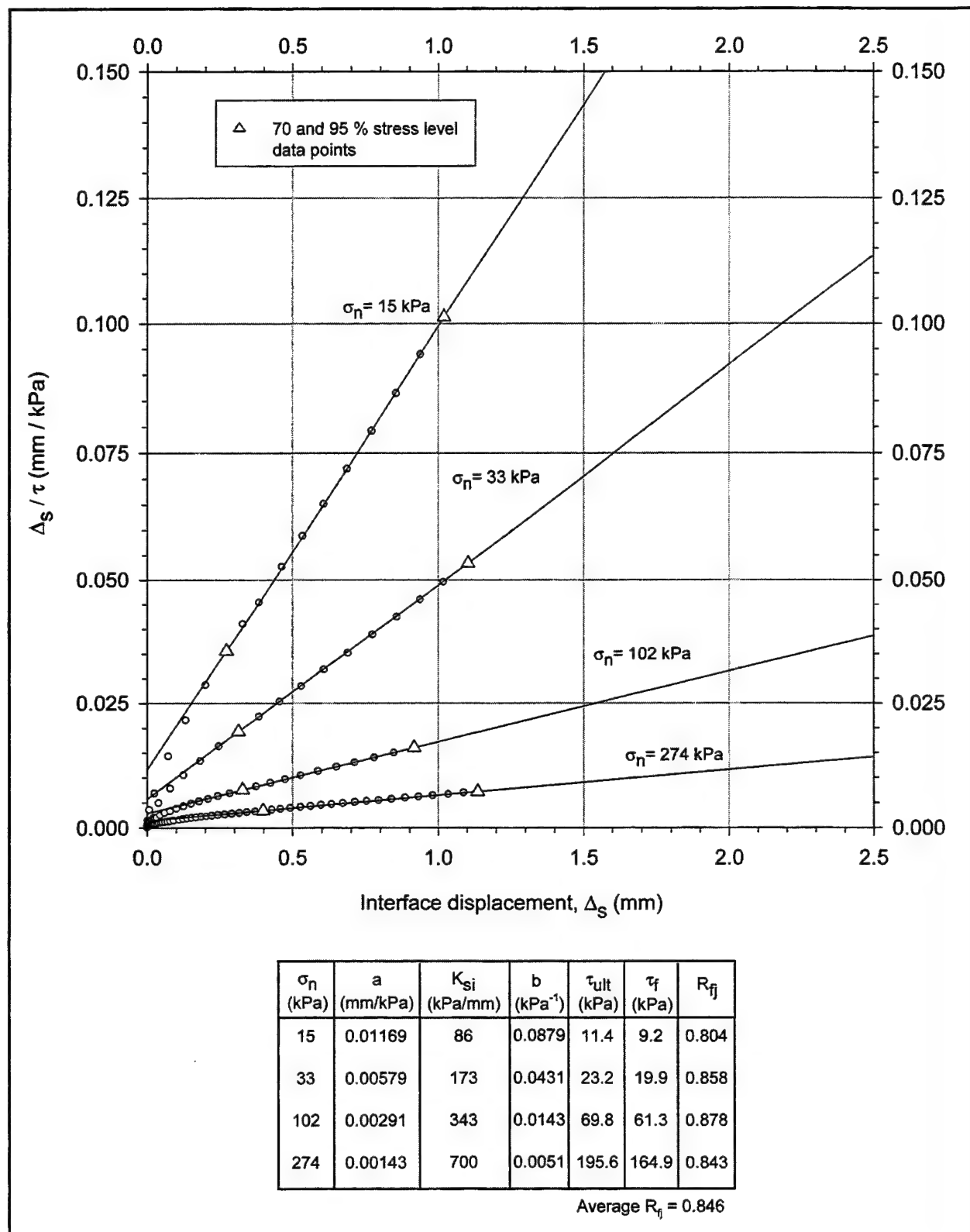


Figure D1. Transformed plots for initial loading tests on dense-Density-sand-to-concrete interface

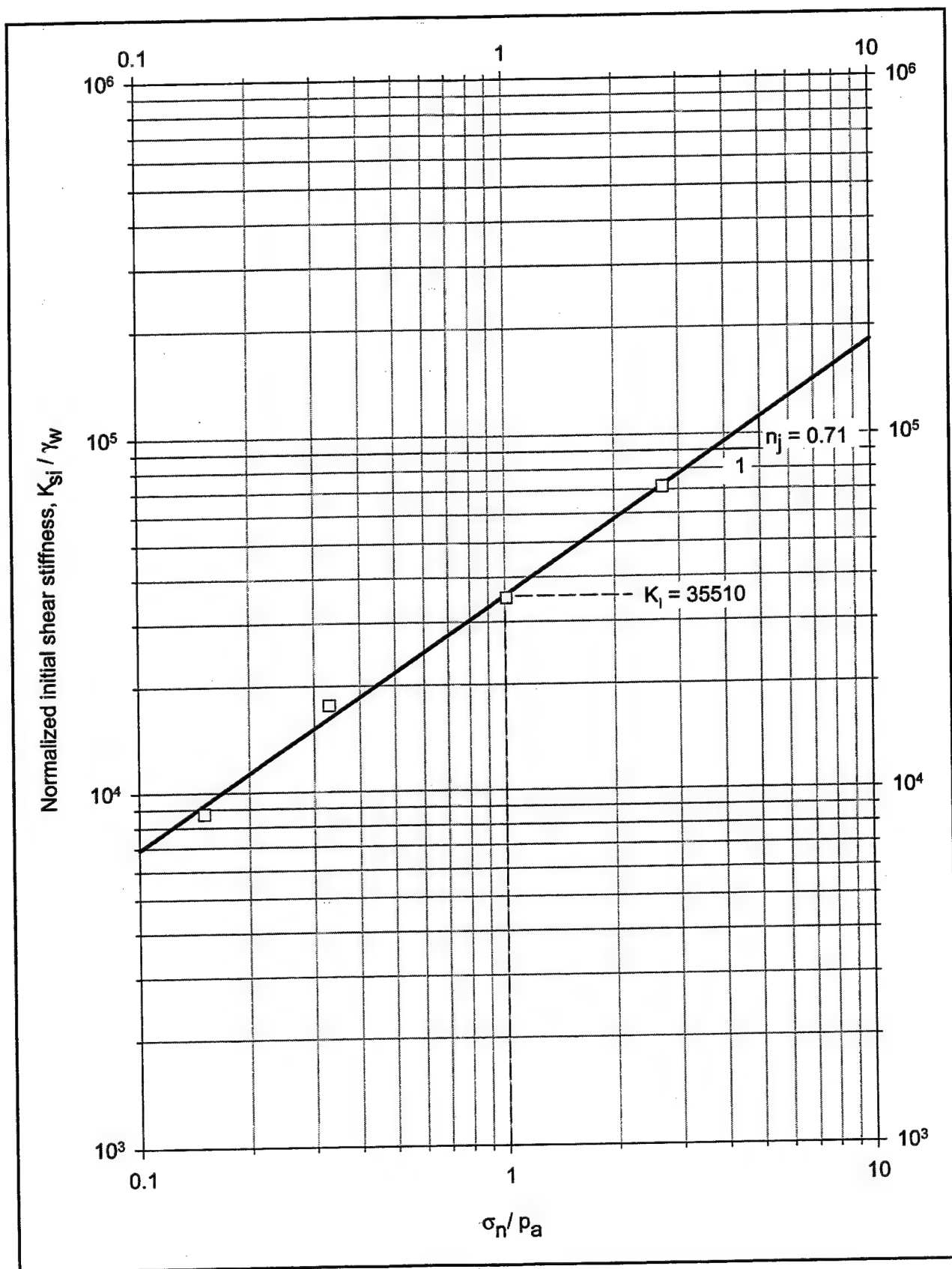


Figure D2. Determination of hyperbolic parameters K_i and n_j for dense-Density-sand-to-concrete interface

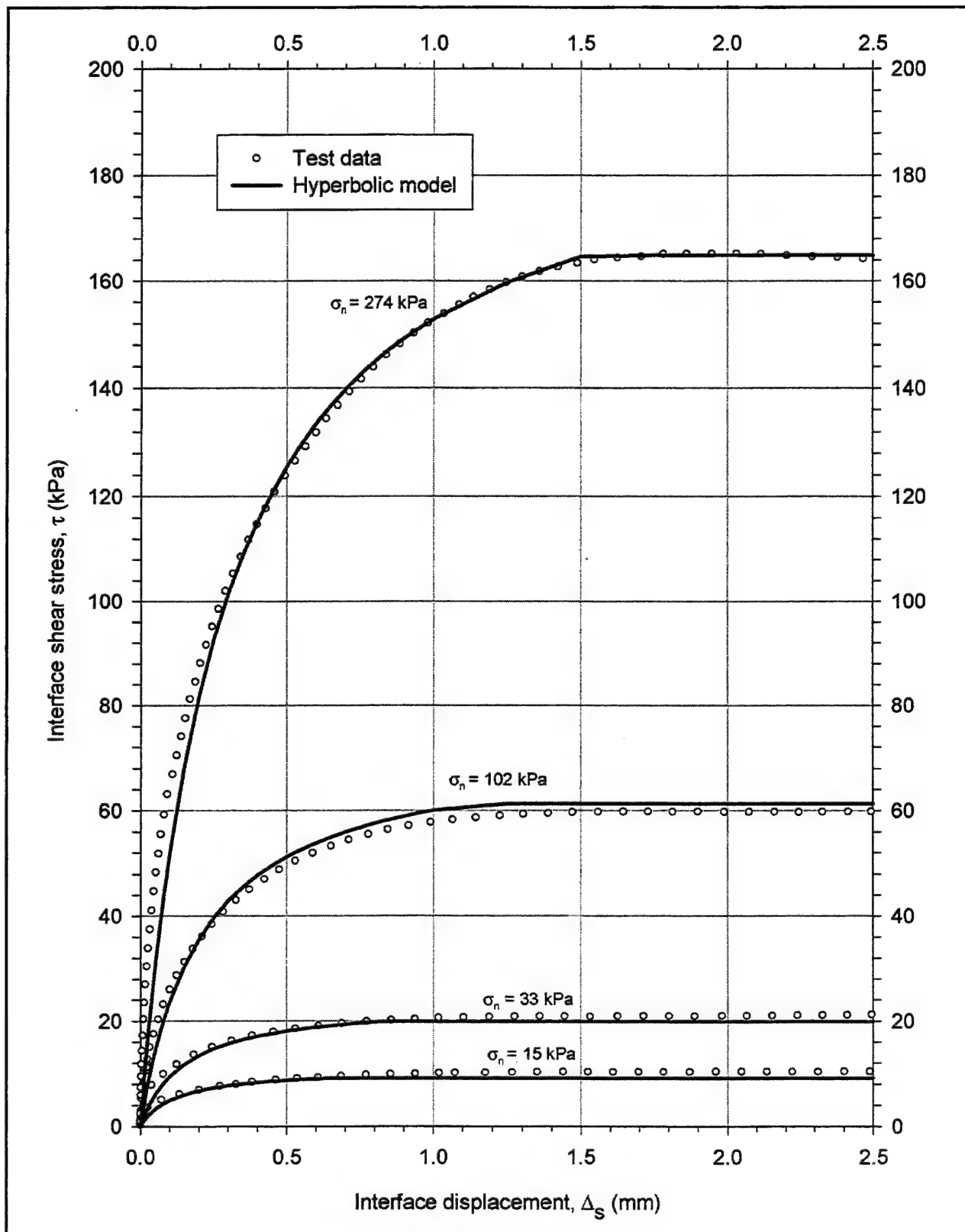


Figure D3. Comparison between the hyperbolic model and data from initial loading tests on dense-Density-sand-to-concrete interface

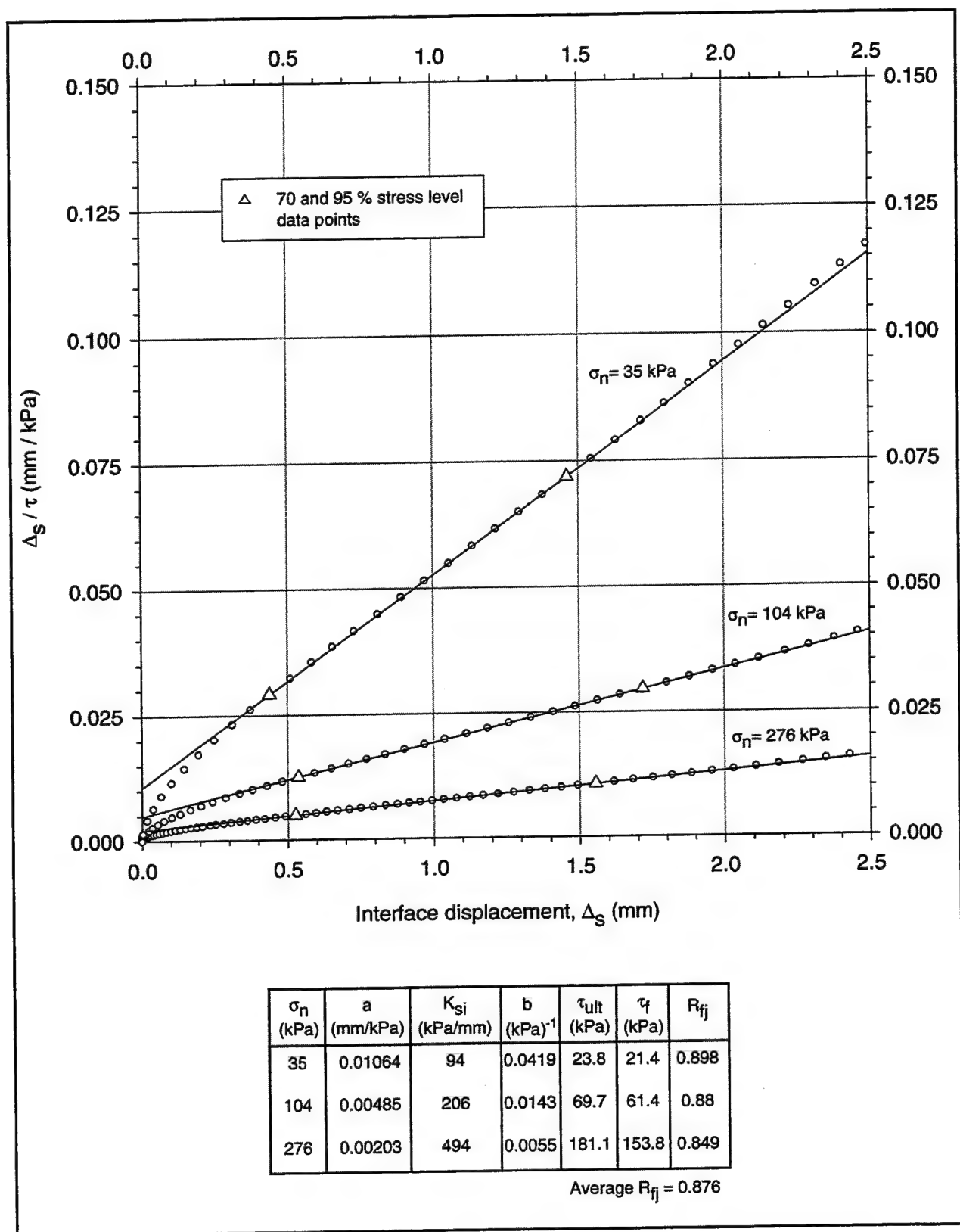


Figure D4. Transformed plots for initial loading tests on medium-dense-Density-sand-to-concrete interface

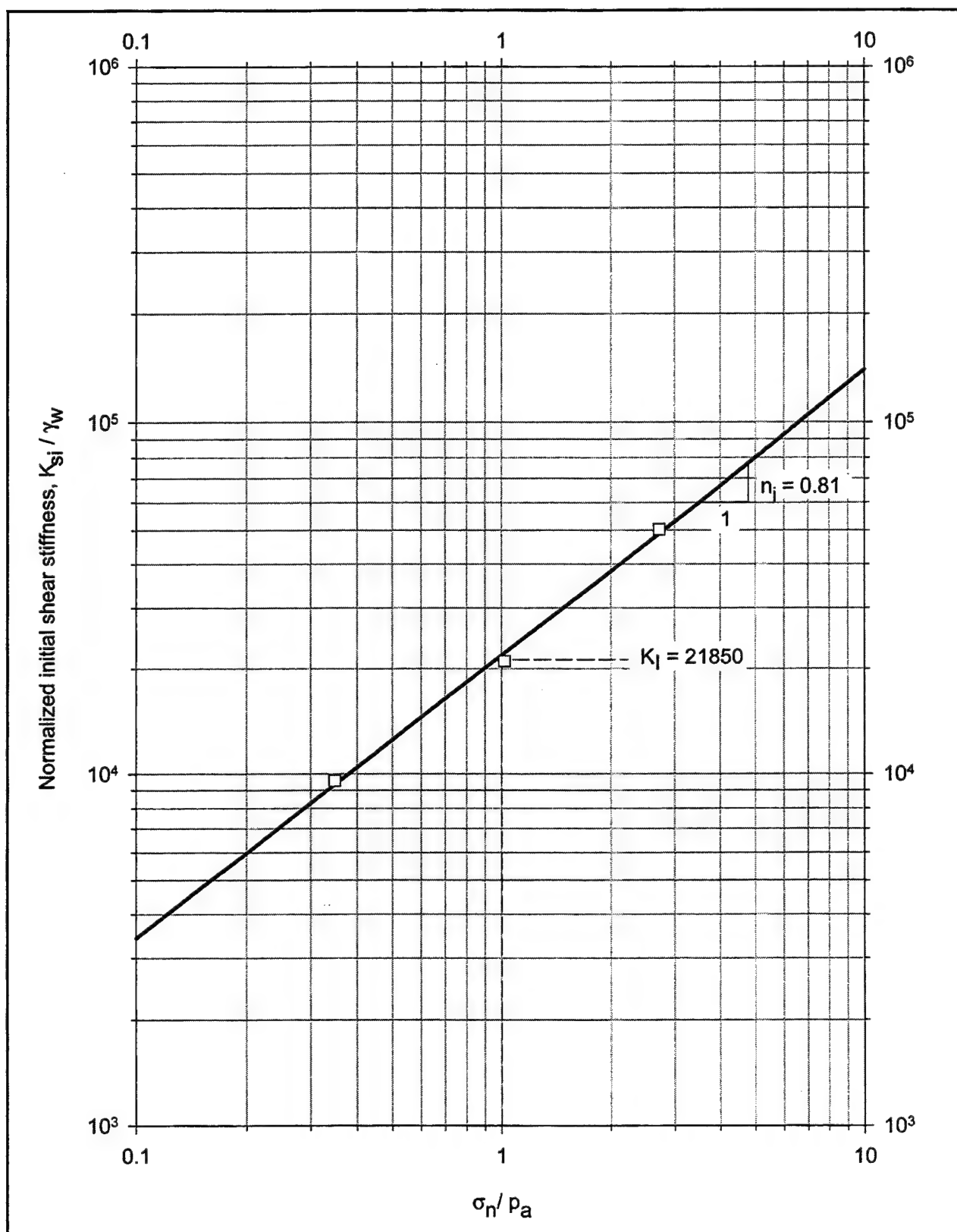


Figure D5. Determination of hyperbolic parameters K_I and n_i for medium-dense-Density-sand-to-concrete interface

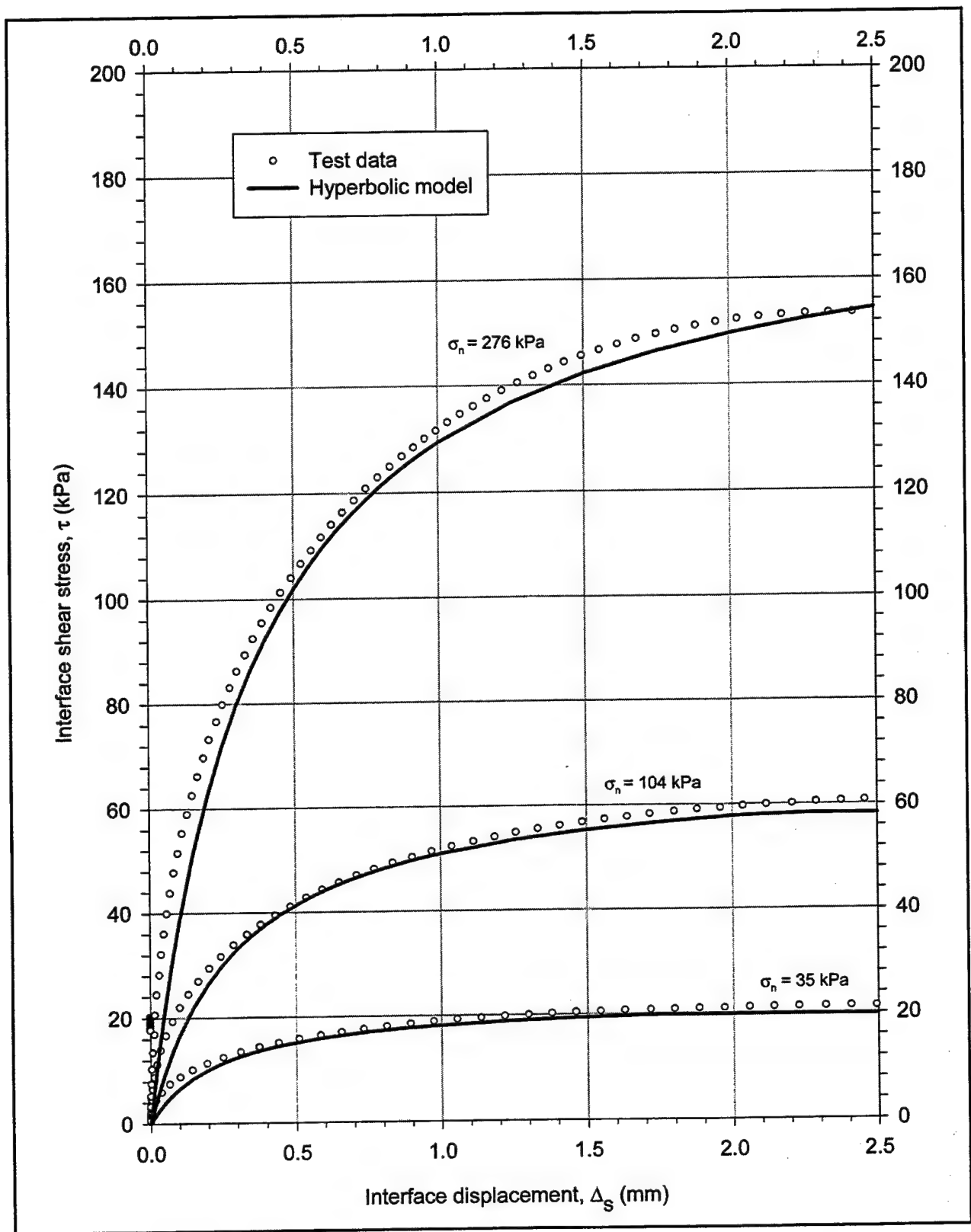


Figure D6. Comparison between the hyperbolic model and data from initial loading tests on medium-density sand-to-concrete interface

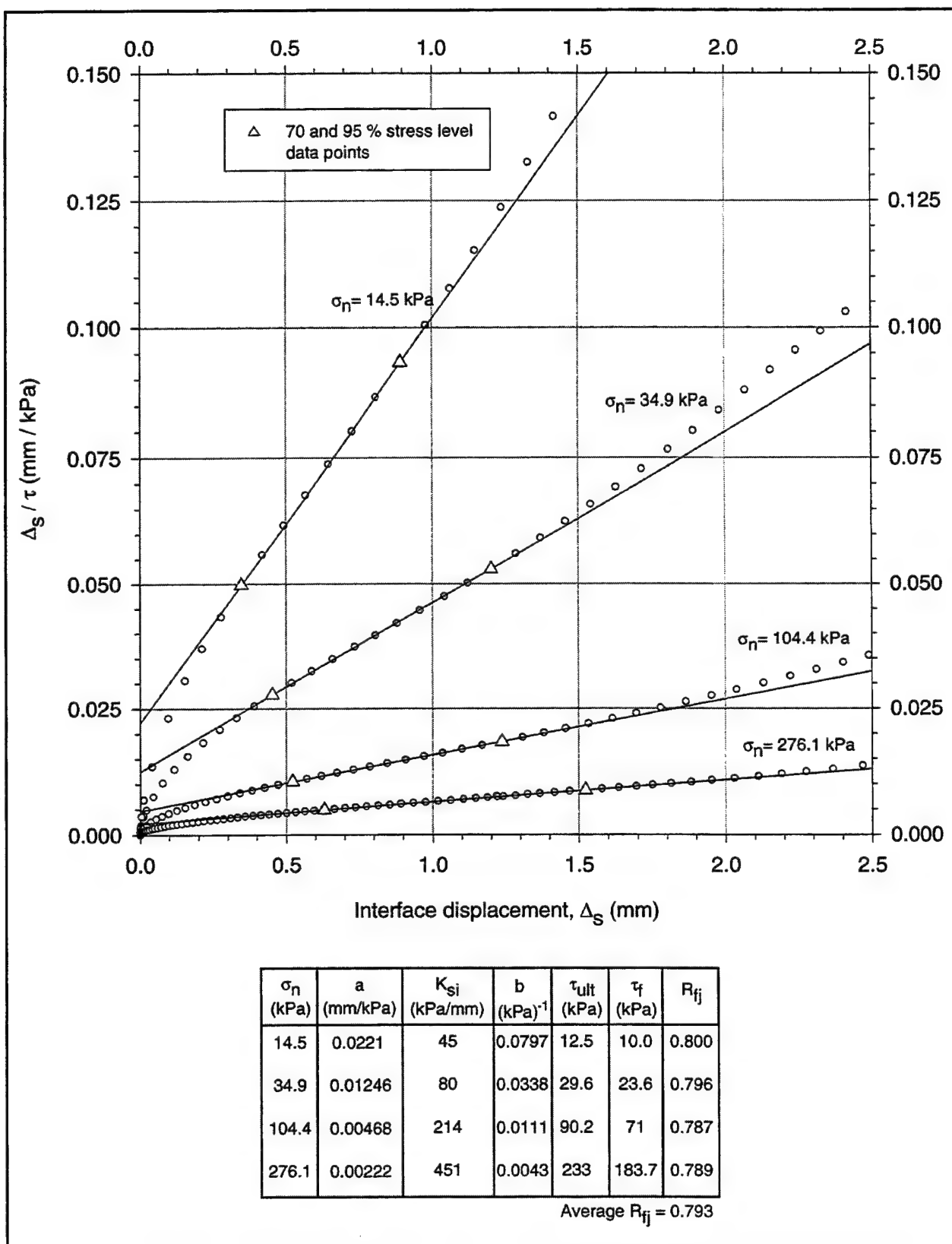


Figure D7. Transformed plots for initial loading tests on dense-Light-Castle-sand-to-concrete interface

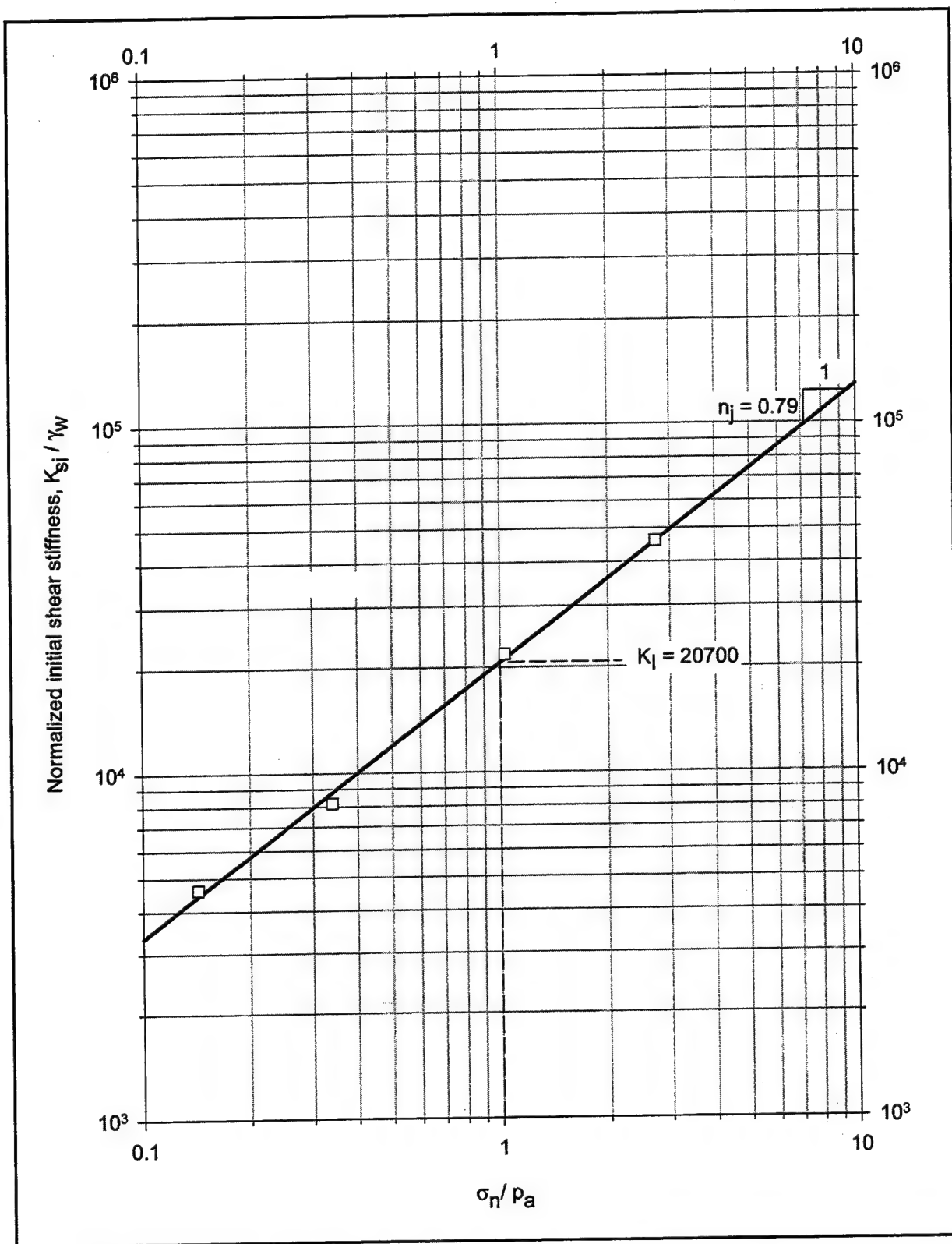


Figure D8. Determination of hyperbolic parameters K_I and n_j for dense-Light-Castle-sand-to-concrete interface

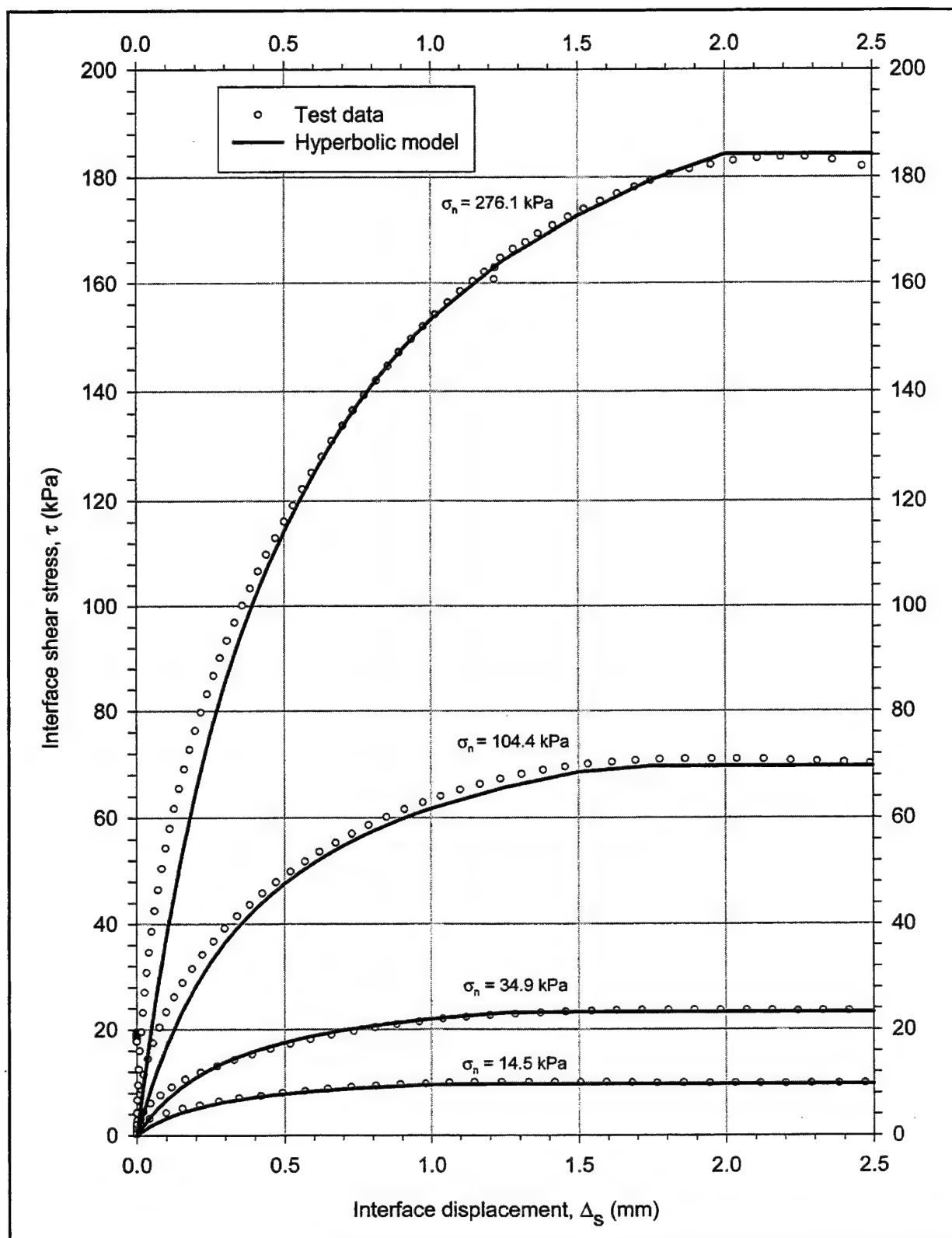


Figure D9. Comparison between the hyperbolic model and data from initial loading tests on dense-Light-Castle-sand-to-concrete interface

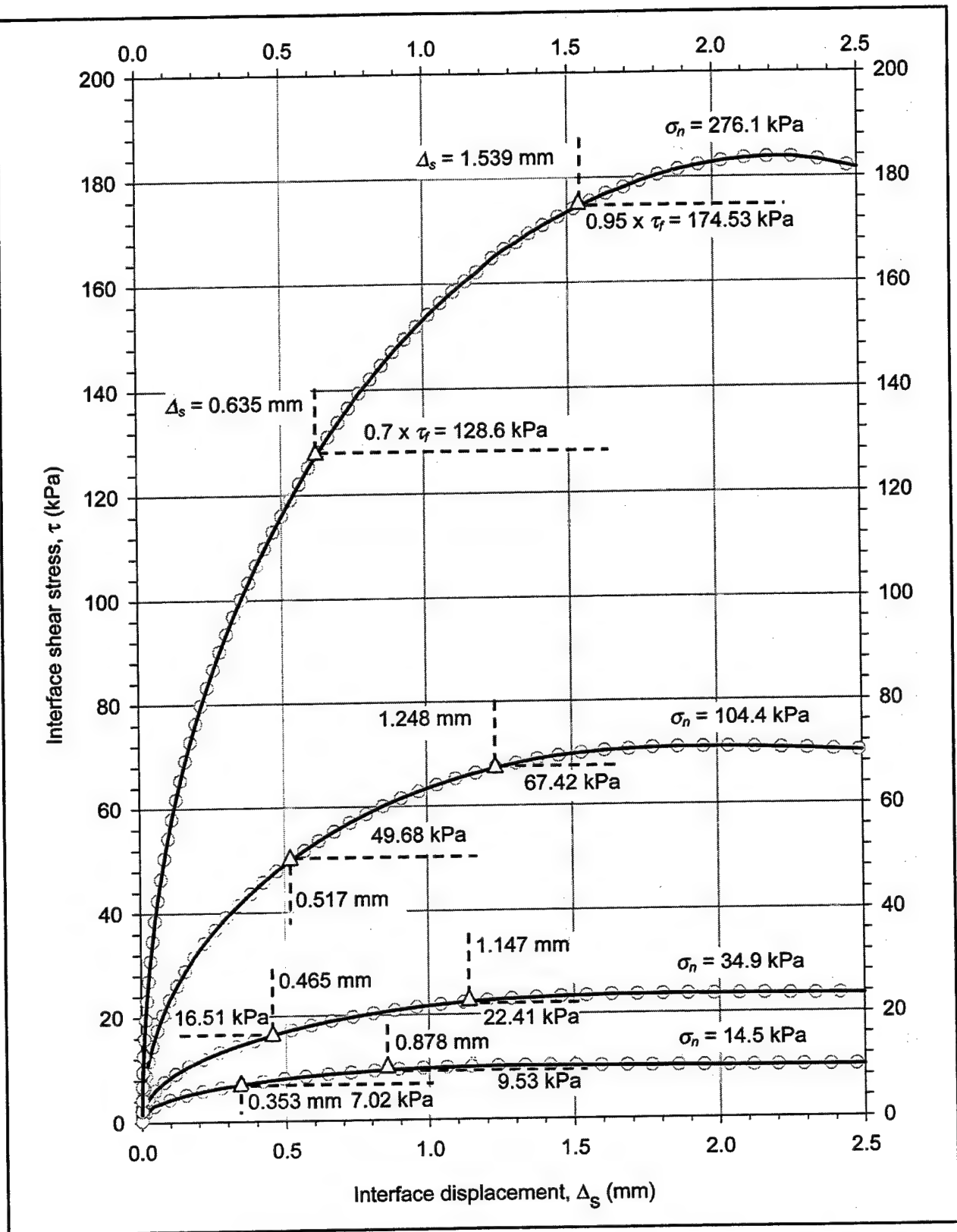


Figure D10. Example determination of interface displacements at 70 and 95 percent of strength. Data from interface tests on dense Light Castle sand

σ_n (kPa)	τ_f (kPa)	Data for Determination of Hyperbolic Parameters K_i and n_i					Determination of Normalized Initial Stiffness				
		70% Stress Level		95% Stress Level			$\frac{\sigma_n}{p_a}$	$\frac{1}{\tau_{ult}}$ (kPa) ⁻¹	R_{ff}	$\frac{K_{si}}{\gamma_w}$	
		τ (kPa)	Δ_s (mm)	$\frac{\Delta_s}{\tau}$ (mm kPa ⁻¹)	τ (kPa)	Δ_s (mm)					$\frac{\Delta_s}{\tau}$ (mm kPa ⁻¹)
(1)	(2)	(3)	(4)	(5)	(6)	(7)	(9)	(10)	(11)	(12)	
14.5	10.03	7.02	0.353	0.0503	9.53	0.878	0.143	0.0796	0.798	4595	
34.9	23.59	16.51	0.465	0.0282	22.41	1.147	0.345	0.0337	0.795	8138	
104.4	70.97	49.68	0.517	0.0104	67.42	1.248	1.031	0.0111	0.787	21924	
276.1	183.71	128.6	0.635	0.0049	174.53	1.539	2.726	0.0043	0.789	46895	

(1) Normal stress. Use effective normal stress, σ'_n , for effective stress analyses. Use total normal stress, σ_n , for total stress analyses

(2) Shear stress at failure. Determined from the shear stress-displacement plots of the data of each interface test.

(3) 70 percent of τ (4) Interface displacement corresponding to (3) determined as illustrated in Figure D10 (5) $\frac{\Delta_s}{\tau} = \frac{(4)}{(3)}$

(6) 95 percent of τ (7) Interface displacement corresponding to (6) determined as illustrated in Figure D10 (8) $\frac{\Delta_s}{\tau} = \frac{(7)}{(6)}$

(9) $\frac{\sigma_n}{p_a} = \frac{(1)}{101.3 \text{ kPa}}$ (10) $\frac{1}{\tau_{ult}} = \frac{(8) - (5)}{(7) - (4)}$ (11) $R_{ff} = (2) \cdot (10)$ (12) $\frac{K_{si}}{\gamma_w} = \frac{2 \cdot 1000 \frac{\text{mm}}{\text{m}}}{(5) + (8) - (10) \cdot [(4) + (7)]} \cdot \frac{1}{\gamma_w}$

Notes:

$$p_a = 101.3 \text{ kPa}$$

$$\gamma_w = 9.8 \text{ kN/m}^3$$

Figure D10 illustrates the procedure for the determination of the values of shear stress and interface displacement used for this example

See Chapter 2 and Appendix D for a complete explanation of the interface hyperbolic model and procedure for determination of hyperbolic parameter values

The data from the initial loading tests performed on dense-Light-Castle-sand-against-concrete interface were used for this example

Figure D11. Determination of the normalized values of K_{si} for each of the initial loading tests performed on the dense-Light-Castle-sand-to-concrete interface

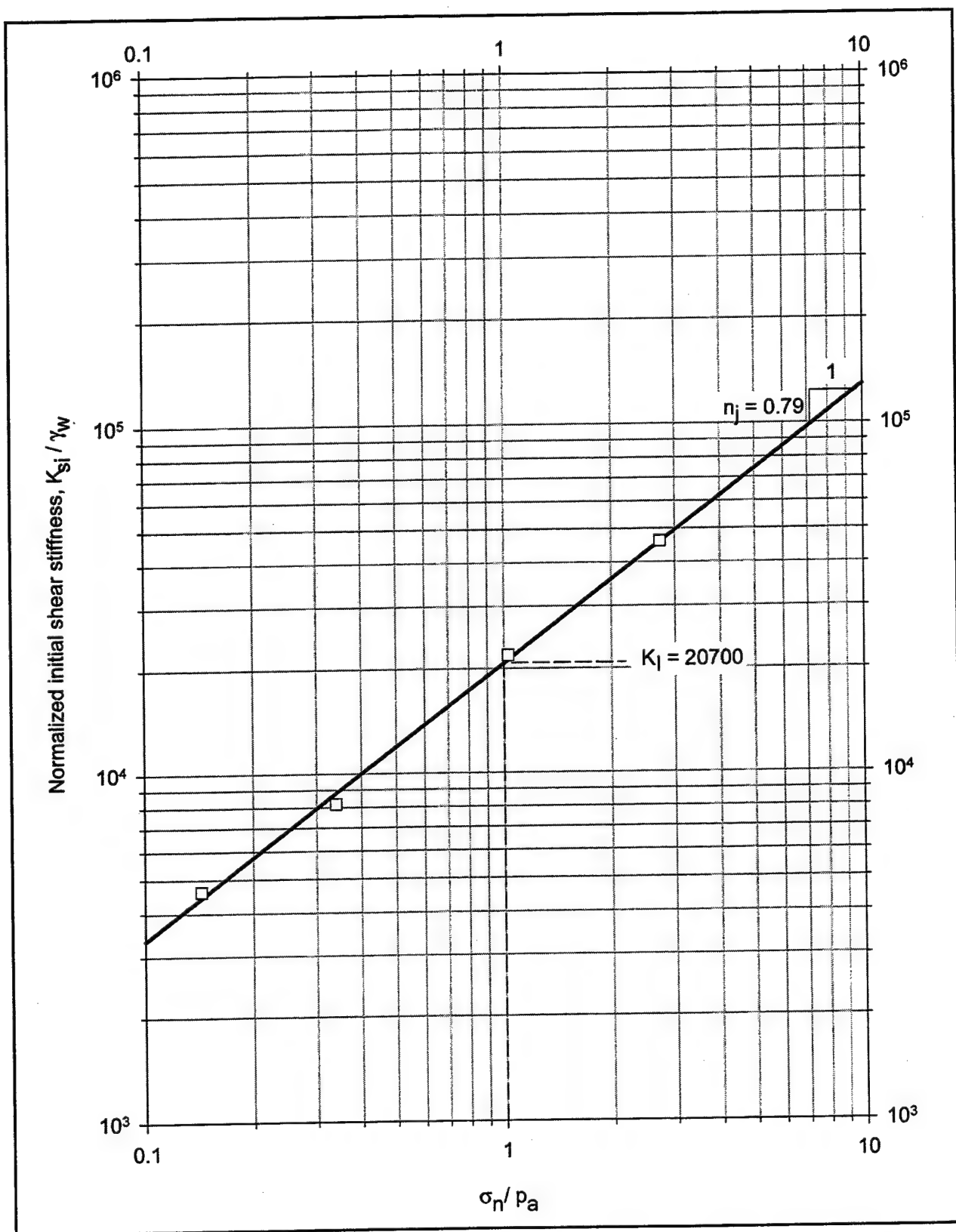


Figure D12. Determination of hyperbolic parameters K_i and η_j from the K_{si} / γ_w values determined in column (12) of Figure D11

Appendix E

Example Calculations of Interface Response in the Extended Hyperbolic Model

This appendix contains example calculations of interface stiffness using the extended hyperbolic model described in Chapter 4 of this report. The stress path applied during multidirectional stress path Test T405_10 was used as the basis for these examples.

Figure E1a shows the stress path applied during Test T405_10, performed on the interface between concrete and dense Light Castle sand. The interface response measured during the test is shown in Figure E1b for illustration. In this test, the interface was sheared following the sequence *A-B-C-D-E-D-F-G-H*. Table E1 contains information on some points along this stress path that is pertinent for the example calculations presented herein.

The parameter values for yield-inducing shear of the dense Light Castle sand against concrete interface were presented in Chapter 4, and they are reproduced in Table E2.

The parameter values for unloading-reloading are calculated according to the criteria presented in Chapter 4. The unload-reload stiffness number K_{urj} is calculated as follows:¹

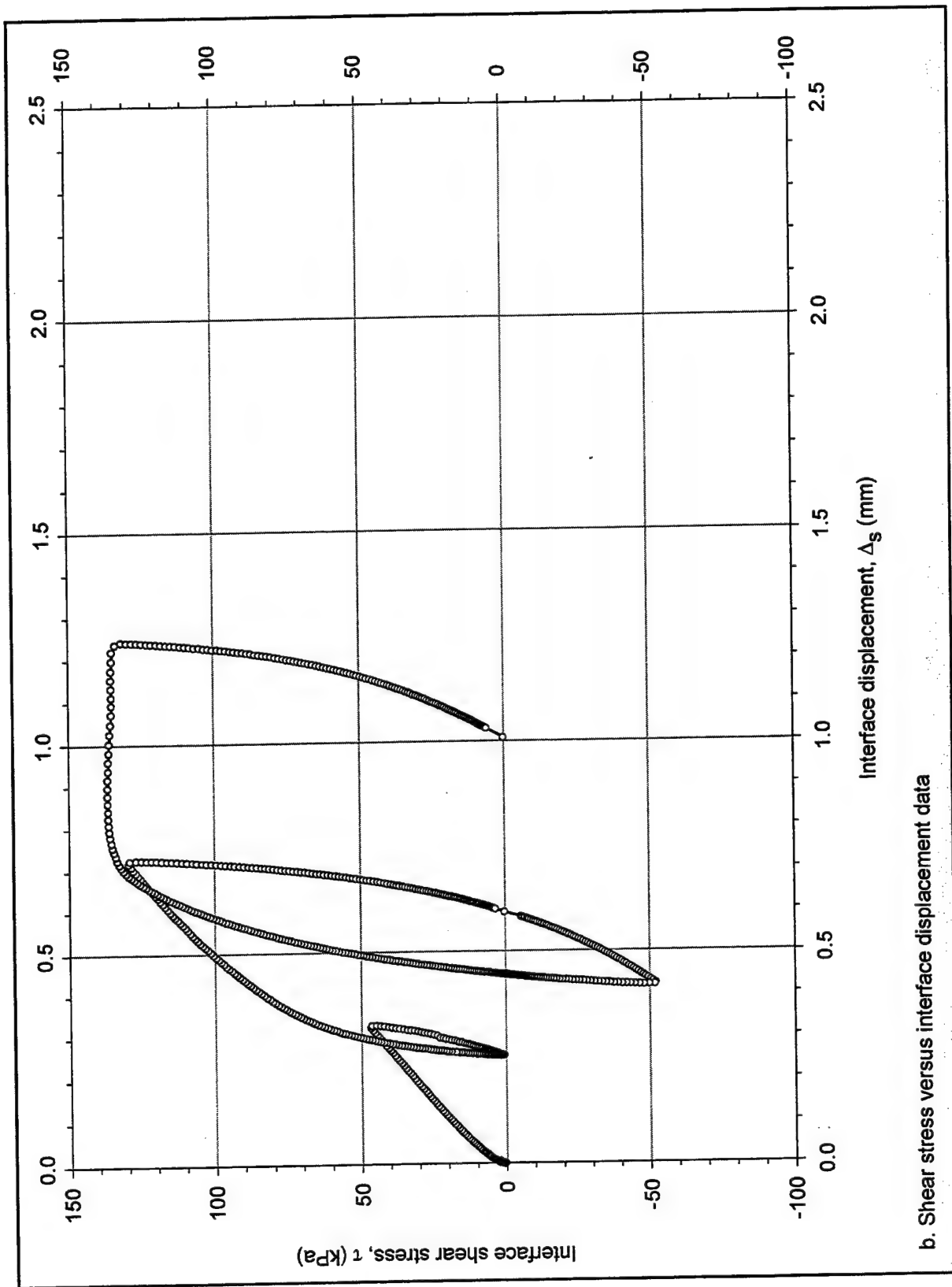
$$K_{urj} = C_k \cdot K_I \quad (4-37 \text{ bis})$$

where C_k is the interface stiffness ratio and K_I is the interface stiffness number for initial loading.

For Version I of the extended hyperbolic model, the following expression is used for the determination of the stiffness ratio C_k :

¹ For convenience, symbols used in this Appendix are listed and defined in the Notation (Appendix F).





b. Shear stress versus interface displacement data

Figure E1. (Concluded)

Table E1 Summary of State Parameters at Selected Points along Multi-Directional Stress Path T405_10									
Point	σ_n , kPa	τ , kPa	SL	Tan θ	Origin	Loading Type	SL+	SL-	q
A	70	0	0	1.43	-	Virgin shear	0	0	+1
1	105	25	0.36	1.43	-	Virgin shear	0.36	0	+1
B	137.5	47.5	0.52	-	-	Virgin shear	0.52	0	-
2	170	25	0.22	-1.48	B	Unloading	0.52	0	-1
C	207.5	0	0	-	B	Unloading	0.52	0	-
T	232.5	47.5	0.31	0.54	C	Reloading	0.52	0	+1
3	247.5	75	0.45	0.54	C	Transition loading	0.52	0	+1
Y1	255	89	0.52	0.54	-	Virgin shear	0.52	0	+1
D	277	130	0.70	-	-	Virgin shear	0.70	0	-
4	277	50	0.27	0	D	Unloading	0.70	0	-1
Y2	277	0	0	0	-	Virgin shear	0.70	0	-1
5	277	-25	-0.14	0	-	Virgin shear	0.70	-0.14	-1
E	277	-52.5	-0.28	0	-	Virgin shear	0.70	-0.28	-
Y2	277	0	0	0	E	Unloading-reloading	0.70	-0.28	+1
D	277	130	0.70	-	E	Reloading	0.70	-0.28	+1
6	253	137	0.81	-8.93	-	Virgin shear	0.81	-0.28	+1
Note: Definitions of parameters are presented in Chapter 4 and the Notation (Appendix F).									

Table E2 Summary of Hyperbolic Parameter Values for the Dense-Light-Castle-Sand-against-Concrete Interface	
Parameter	Value
K_I	20700
n_f	0.79
R_{ff}	0.79
δ	33.7°
Note: Parameters are defined in the Notation (Appendix F).	

$$C_k = 0.5 \cdot (1 + R_{ff})^2 \quad (\text{Table 4-11})$$

where R_{ff} is the failure ratio.

According to these equations, the value of K_{urj} for the dense-Light-Castle-sand-against-concrete interface is determined using the values of K_I and R_{ff} presented in Table E2, as follows:

$$C_k = 0.5 \cdot (1 + 0.79)^2 = 1.602$$

$$K_{urj} = 1.602 \cdot 20700 = 33160$$

This value of K_{urj} is used for modeling unloading-reloading of the interface in Version I of the model.

For Versions II and III, C_k is calculated as follows:

$$C_k = (1 + R_{ff})^2 \quad (\text{Table 4-11})$$

For the dense Light Castle sand against concrete interface, the following value of K_{urj} is obtained:

$$C_k = (1 + 0.79)^2 = 3.204$$

$$K_{urj} = 3.204 \cdot 20700 = 66320$$

The scaling factor α , which is used in Versions II and III of the model, is calculated according to the following expression:

$$\alpha = 1 + R_{ff} \quad (4-47 \text{ bis})$$

For the dense-Light-Castle-sand-against-concrete interface, the value of the scaling factor is determined as follows:

$$\alpha = 1 + 0.79 = 1.79$$

Table E3 summarizes the values of K_{urj} and α for the dense-Light-Castle-sand-against-concrete interface.

Table E3 Summary of Parameter Values for Unloading-Reloading of the Dense-Light-Castle-Sand-against-Concrete Interface		
Parameter	Value for Version I	Value for Versions II and III
K_{urj}	33160	66320
α	Not applicable	1.79

In each of the following sections, calculation of the interface stiffness for some points along the stress path is explained. Chapter 4 gives thorough explanations of the criteria and derivations of the equations used for these calculations.

E.1 Interface Stiffness at Point 1

The first step in the determination of the interface stiffness during shear is the determination of the type of loading applied. As explained in Chapter 4, the type of loading is defined by comparing the magnitude of the stress level acting on the interface to the positions of the yield surfaces $SL+$ and $SL-$. The stress level is calculated as follows:

$$SL = \frac{\tau}{\sigma_n \cdot \tan(\delta)} \quad (2-10 \text{ bis})$$

The value of the interface friction angle δ for the dense-Light-Castle-sand-against-concrete interface is given in Table E2. For point 1, the values of σ_n and τ given in Table E1 yield a stress level of 0.36. During shearing along *A-1-B*, the stress level increases continuously. Because the interface had not been sheared previously, the interface is subject to virgin shear. The formulation for interfaces at yield presented in Chapter 4 is then applicable. In this formulation, it is necessary to determine the inclination of the stress path $\tan(\theta)$, which is defined as:

$$\tan \theta = \frac{d\sigma_n}{d\tau^i} \quad (4-19 \text{ bis})$$

The inclination at point 1, which is determined graphically in Figure E1, is 1.43. It is also necessary to determine the direction of shearing. The shear direction parameter q is equal to +1 if the stress level increases during shear, and it is equal to -1 if the stress level decreases. For point 1, q takes on a value of +1.

The interface stiffness K'_{st} for yield-inducing shear is calculated from the following equations:

$$K'_{st} = K_{st} \cdot I \quad (4-17 \text{ bis})$$

$$I = \frac{1}{1 + SL \cdot [n_j(q \cdot R_{ff} \cdot SL - 1) - q \cdot R_{ff} \cdot SL] \tan \delta \tan \theta} \quad (4-21 \text{ bis})$$

$$K_{st} = K_I \cdot \gamma_w \cdot \left(\frac{\sigma_n}{P_a} \right)^{n_j} \cdot (1 - q \cdot R_{ff} \cdot SL)^2 \quad (4-22 \text{ bis})$$

where γ_w is the unit weight of water.

The values of the hyperbolic parameters K_I , n_j , and R_{ff} for the dense-Light-Castle-sand-against-concrete interface are given in Table E2. The value of K_{st} corresponds to the interface stiffness for a vertical stress path. For an inclined stress path, the interface stiffness is calculated by multiplying K_{st} by the correction factor I for stress path inclination. For point 1, the calculations are as follows:

$$K_{st} = 20700 \cdot 9.8 \frac{kN}{m^3} \cdot \left(\frac{105}{101.3} \right)^{0.79} \cdot (1 - (+1) \cdot 0.79 \cdot 0.36)^2 = 106867 \frac{kPa}{m}$$

$$I = \frac{1}{1 + 0.36 \cdot \{0.79 [(+I) \cdot 0.79 \cdot 0.36 - 1] - (+I) \cdot 0.79 \cdot 0.36\} \tan (33.7^\circ) \cdot 1.43}$$

$$K'_{st} = 106867 \frac{kPa}{m} \cdot 1.41 = 150886 \frac{kPa}{m}$$

E.2 Interface Stiffness at Point 2

The stress level at point 2, which is calculated as described previously, is 0.22. During the previous shearing history of the interface, a greater value of stress level was reached at point B. Consequently, point 2 is inside the unloading-reloading zone defined in Chapter 4. The interface stiffness for unloading-reloading can be calculated using one of the three versions of the model.

E.2.1 Version I

In Version I, the interface stiffness is determined according to the following equation:

$$K'_{st} = K_{wj} \cdot \gamma_w \cdot \left(\frac{\sigma_n}{P_a} \right)^{n_j} \quad (4-23 \text{ bis})$$

According to this expression, the interface response is assumed linear, normal stress-dependent, and independent of the inclination of the stress path. For point 2, the interface stiffness is calculated as follows:

$$K'_{st} = 33160 \cdot 9.8 \frac{kN}{m^3} \cdot \left(\frac{170}{101.3} \right)^{0.79} = 489174 \frac{kPa}{m}$$

E.2.2 Version II

In Version II, the interface response is assumed hyperbolic, normal stress dependent, and independent of the inclination of the stress path. The following equation is used for the determination of the interface stiffness:

$$K'_{st} = K_{wj} \cdot \gamma_w \cdot \left(\frac{\sigma_n}{P_a} \right)^{n_j} \cdot \left[1 - \frac{q}{\alpha} R_f \cdot (SL - SL_o) \right]^2 \quad (4-25 \text{ bis})$$

The values of the hyperbolic parameters K_{urj} , n_j , α , and R_f for the dense-Light-Castle-sand-against-concrete interface are presented in Tables E-2 and E-3. As defined in Chapter 4, the origin of unloading-reloading corresponds to the last point where the direction of shear was reversed. The stress level at the origin SL_o is calculated using the following equation:

$$SL_o = \frac{\tau_o}{\sigma_{no} \cdot \tan \delta} \quad (4-26 \text{ bis})$$

where τ_o and σ_{no} are, respectively, the shear stress and normal stress at the origin. For point 2, the origin is at point B, as indicated in Table E-1. The stress level at the origin corresponds to the stress level at point B, which is calculated as follows:

$$SL_o = \frac{47.5}{137.5 \cdot \tan(33.7^\circ)} = 0.52$$

The shear direction parameter q at point 2 is -1 because the stress level decreases continuously along segment B-C of the stress path. The interface stiffness K'_{st} at point 2 then becomes

$$\begin{aligned} K'_{st} &= 66320 \cdot 9.8 \frac{kN}{m^3} \cdot \left(\frac{170}{101.3} \right)^{0.79} \cdot \left[1 - \frac{(-1)}{1.79} 0.79 \cdot (0.22 - 0.52) \right]^2 \\ &= 736429 \frac{kPa}{m} \end{aligned}$$

E.2.3 Version III

In Version III, it is necessary to distinguish between unloading-reloading and transition loading. As indicated in Chapter 4, transition loading occurs if ($SL_- < SL < SL_+$) and ($\tau \leq \tau_-$ or $\tau \geq \tau_+$).

The transition surfaces τ_- and τ_+ are defined respectively as the minimum and maximum values of shear stress reached during interface shear. For point 2, the upper transition surface τ_+ is defined by the shear stress at point B. The lower transition surface τ_- is defined by the shear stress at point A. It can be seen that the value of shear stress at point 2 does not meet the criteria presented previously. Therefore, point 2 corresponds to unloading-reloading, and a formulation identical to that for Version II applies. In Version III, the interface stiffness at point 2 is then identical to that calculated previously using Version II:

$$K'_{st} = 66320 \cdot 9.8 \frac{kN}{m^3} \cdot \left(\frac{170}{101.3} \right)^{0.79} \cdot \left[1 - \frac{(-1)}{1.79} 0.79 \cdot (0.22 - 0.52) \right]^2$$

$$= 736429 \frac{kPa}{m}$$

E.3 Interface Stiffness at Point T

As indicated in Table E1, the stress level at point *T* is lower than the past maximum stress level *SL*+ reached during shear along *A-B-C-T*. Consequently, any of the three versions of the model for unloading-reloading can be used for the determination of the interface stiffness.

E.3.1 Version I

As indicated previously, the interface stiffness is determined according to the following equation:

$$K'_{st} = K_{urj} \cdot \gamma_w \cdot \left(\frac{\sigma_n}{p_a} \right)^{n_j} \quad (4-23 \text{ bis})$$

For point *T*, the interface stiffness is calculated as follows:

$$K'_{st} = 33160 \cdot 9.8 \frac{kN}{m^3} \cdot \left(\frac{232.5}{101.3} \right)^{0.79} = 626445 \frac{kPa}{m}$$

E.3.2 Version II

During shear along segment *C-D* of the stress path, the origin, or last point of change in shearing direction, is *C*. The value of the shear direction parameter *q* is +1 because the stress level increases during shear along *C-D*. As indicated previously, the interface stiffness is calculated using

$$K'_{st} = K_{urj} \cdot \gamma_w \cdot \left(\frac{\sigma_n}{p_a} \right)^{n_j} \cdot \left[1 - \frac{q}{\alpha} R_{ff} \cdot (SL - SL_o) \right]^2 \quad (4-25 \text{ bis})$$

The interface stiffness K'_{st} at point *T* then becomes

$$K'_{st} = 66320 \cdot 9.8 \frac{kN}{m^3} \cdot \left(\frac{232.5}{101.3} \right)^{0.79} \cdot \left[1 - \frac{(+1)}{1.79} 0.79 \cdot (0.31 - 0) \right]^2$$

$$= 933513 \frac{kPa}{m}$$

E.3.3 Version III

During shear along segment *C-D* of the stress path, the past maximum shear stress τ_+ , which is given by point *B*, is reached at point *T*. The past maximum stress level, SL_+ , determined by the stress level at point *B*, is reached at point *YI*. Consequently, all the points belonging to segment *T-YI* of the stress path are inside the transition region. In Version III, the normalized interface stiffness K_{sn} during transition loading is calculated using the following equation:

$$K_{sn} = K_{sn}^{ts} \cdot 10^{m(SL - SL^{ts})} \quad (4-27 \text{ bis})$$

where

K_{sn}^{ts} = transition stiffness number

m = stiffness degradation parameter

SL^{ts} = transition stress level

The transition stiffness number is the value of normalized interface stiffness at the point where the stress path crosses the transition surface, τ_+ or τ_- . For any point on segment *T-YI* of the stress path, K_{sn}^{ts} is the normalized stiffness at point *T*. Similarly, the transition stress level SL^{ts} is the stress level at the point where the stress path crosses the transition surface, τ_+ or τ_- . For any point on segment *T-YI* of the stress path, SL^{ts} is equal to the stress level at point *T*. It can be seen that by substituting these values of K_{sn}^{ts} and SL^{ts} in the equation, the following normalized interface stiffness is obtained for point *T*:

$$K_{sn} = K_{sn}^{ts}$$

The value of K_{sn}^{ts} depends on the previous shearing history of the interface. For the case under analysis, it may be assumed that point *T* corresponds to unloading-reloading (stress path *C-T*). The value of K_{sn}^{ts} can then be calculated using the values of the state variables of point *T* and the formulation for unloading-reloading.

A calculation of K'_{st} at point T , identical to that presented for Version II in the previous section, yields the following:

$$K'_{st} = 66320 \cdot 9.8 \frac{kN}{m^3} \cdot \left(\frac{232.5}{101.3} \right)^{0.79} \cdot \left[1 - \frac{(+1)}{1.79} \cdot 0.79 \cdot (0.31 - 0) \right]^2$$

$$= 933513 \frac{kPa}{m}$$

This is the value of interface stiffness at point T . It is also convenient to determine the value of normalized stiffness, K'_{sn} . The value of K'_{sn} is calculated from the following equation:

$$K'_{sn} = \frac{K'_{st}}{\gamma_w \cdot \left(\frac{\sigma_n}{p_a} \right)^{n_j}} = \frac{933513}{9.8 \cdot \left(\frac{232.5}{101.3} \right)^{0.79}} = 49414$$

This value will be used for the calculation of the interface stiffness at point 3.

E.4 Interface Stiffness at Point 3

As indicated in Table E1, the stress level at point 3 is lower than the past maximum stress level $SL+$ reached during shear along $A-B-C-3$. Consequently, any of the three versions of the model for unloading-reloading can be used for the determination of the interface stiffness.

E.4.1 Version I

For point 3, the interface stiffness is calculated as follows:

$$K'_{st} = 33160 \cdot 9.8 \frac{kN}{m^3} \cdot \left(\frac{247.5}{101.3} \right)^{0.79} = 658163 \frac{kPa}{m}$$

E.4.2 Version II

During shear along segment $C-D$ of the stress path, the origin, or last point of change in shearing direction, is C . The value of the shear direction parameter q is +1 because the stress level increases during shear along $C-D$. The interface stiffness K'_{st} at point 3 then becomes

$$\begin{aligned}
K'_{st} &= 66320 \cdot 9.8 \frac{kN}{m^3} \cdot \left(\frac{247.5}{101.3} \right)^{0.79} \cdot \left[1 - \frac{(+1)}{1.79} 0.79 \cdot (0.45 - 0) \right]^2 \\
&= 845393 \frac{kPa}{m}
\end{aligned}$$

E.4.3 Version III

As indicated previously, all the points located on segment $T-YI$ of the stress path correspond to transition loading. In Version III, the normalized interface stiffness K_{sn} during transition loading is calculated using the following equation:

$$K_{sn} = K_{sn}^{ts} \cdot 10^{m(SL - SL^{ts})} \quad (4-27 \text{ bis})$$

The transition stiffness number is the value of interface stiffness at the point where the stress path crosses the transition surface $\tau+$ or $\tau-$. For point 3, K_{sn}^{ts} is the normalized interface stiffness at point T , which was calculated in the previous section as:

$$K_{sn}^{ts} = K_{sn} \text{ at point } T = 49414$$

The transition stress level is the stress level of the point where the stress path crosses the transition surface $\tau+$ or $\tau-$. For point 3, SL^{ts} is the stress level at point T :

$$SL^{ts} = 0.31$$

The stiffness degradation parameter is calculated from the following equation:

$$m = \left(\frac{\log K_{sn}^{ts} - \log K_{sn}^{ys}}{SL^{ts} - SL^{ys}} \right) \quad (4-31 \text{ bis})$$

where

K_{sn}^{ys} = yield stiffness number

SL^{ys} = stress level for the current position of the yield surface

The yield stiffness number K_{sn}^{ys} is the value of normalized stiffness corresponding to the current position of the yield surface SL^{ys} . It is assumed that the inclination of the stress path does not influence the value of K_{sn}^{ys} ($I = 1$). The following expression is used to calculate the yield stiffness:

$$K_{sn}^{ys} = K_I \cdot (1 - q \cdot R_{ff} \cdot SL^{ys})^2 \quad (4-32 \text{ bis})$$

The current position of the yield surface SL^{ys} is defined mathematically as

$$SL^{ys} = SL + \text{for shear inside the transition zone of the first quadrant}$$

$$SL^{ys} = SL - \text{for shear inside the transition zone of the fourth quadrant}$$

Point 3 is located inside the first quadrant; therefore:

$$SL^{ys} = SL + = 0.52$$

During shear along segment C-D of the stress path, the stress level increases continuously. Therefore, the value of the shear direction parameter q is equal to +1. The yield stiffness number K_{sn}^{ys} can now be calculated:

$$K_{sn}^{ys} = 20700 \cdot (1 - (+1) \cdot 0.79 \cdot 0.52)^2 = 7186$$

The value of the stiffness degradation parameter m then becomes:

$$m = \left[\frac{\log(49414) - \log(7186)}{0.31 - 0.52} \right] = -3.987$$

Finally, the normalized stiffness at point 3 can be calculated:

$$K_{sn} = 49414 \cdot 10^{-3.987 \cdot (0.45 - 0.31)} = 13667$$

Once the normalized stiffness is calculated as described, the interface stiffness can be calculated using the following expression:

$$K'_{st} = K_{sn} \cdot \gamma_w \cdot \left(\frac{\sigma_n}{P_a} \right)^{n_j} \quad (4-28 \text{ bis})$$

For point 3, the following value of K'_{st} is obtained:

$$K'_{st} = 13667 \cdot 9.8 \frac{kN}{m^3} \cdot \left(\frac{247.5}{101.3} \right)^{0.79} = 271264 \frac{kPa}{m}$$

E.5 Interface Stiffness at Point 4

The stress level at point 4 is 0.27. During the previous shearing history of the interface, a greater value of stress level was reached at point *D*. Consequently, point 4 is inside the unloading-reloading zone, and the interface stiffness is calculated following identical procedures to those described for point 2.

E.5.1 Version I

For point 4, the interface stiffness is calculated as follows:

$$K'_{st} = 33160 \cdot 9.8 \frac{kN}{m^3} \cdot \left(\frac{277}{101.3} \right)^{0.79} = 719396 \frac{kPa}{m}$$

E.5.2 Version II

The origin of unloading-reloading for point 4 is point *D*. Therefore, the stress level at the origin SL_o is 0.7. The shear direction parameter q at point 4 is -1 because the stress level decreases continuously along segment *D-E* of the stress path. The interface stiffness K'_{st} at point 4 then becomes

$$\begin{aligned} K'_{st} &= 66320 \cdot 9.8 \frac{kN}{m^3} \cdot \left(\frac{277}{101.3} \right)^{0.79} \cdot \left[1 - \frac{(-1)}{1.79} 0.79 \cdot (0.27 - 0.70) \right]^2 \\ &= 944513 \frac{kPa}{m} \end{aligned}$$

E.5.3 Version III

Point 4 is not located within any of the transition regions. Therefore, the interface stiffness at point 4, according to Version III, is identical to that calculated previously using Version II:

$$K'_{st} = 66320 \cdot 9.8 \frac{kN}{m^3} \cdot \left(\frac{277}{101.3} \right)^{0.79} \cdot \left[1 - \frac{(-1)}{1.79} \cdot 0.79 \cdot (0.27 - 0.70) \right]^2$$

$$= 944513 \frac{kPa}{m}$$

E.6 Interface Stiffness at Point 5

Point 5 is located inside the fourth quadrant and has a stress level of -0.14. During shearing along *Y2-E*, the stress level decreases continuously. Because the interface had not been sheared previously into the fourth quadrant, the interface is subject to virgin shear, as indicated in Table E-1. The formulation for interfaces at yield presented in Chapter 4 is then applicable.

The inclination of the stress path at point 5 is zero, i.e., the stress path is vertical. The shear direction parameter q is equal to -1 because the stress level decreases continuously along *Y2-E*.

The interface stiffness at point 5 is calculated following an identical procedure as for point 1. The calculations are as follows:

$$K_{st} = 20700 \cdot 9.8 \frac{kN}{m^3} \cdot \left(\frac{277}{101.3} \right)^{0.79} \cdot [1 - (-1) \cdot 0.79 \cdot (-0.14)]^2 = 355237 \frac{kPa}{m}$$

$$I = \frac{1}{1 + (-0.14) \cdot \{0.79[(-1) \cdot 0.79 \cdot (-0.14) - 1] - (-1) \cdot 0.79 \cdot (-0.14)\} \tan(33.7^\circ) \cdot 0} = 1$$

$$K'_{st} = 355237 \frac{kPa}{m} \cdot 1 = 355237 \frac{kPa}{m}$$

It must be noted that after point *E* of the stress path is reached and the shear direction is reversed, subsequent shear along segment *E-D* induces unloading-reloading of the interface. Consequently, the interface stiffness at all points of this segment, including point 5, must be calculated using procedures identical to those described for points 2 and 4. If Versions II or III are used, the origin for unloading-reloading along *E-D* corresponds to point *E*.

E.7 Interface Stiffness at Point 6

Point 6 is located inside the first quadrant and has a stress level of 0.81. During shearing along *D-F*, the stress level increases continuously and the

interface undergoes yielding. The formulation for interfaces at yield presented in Chapter 4 is then applicable.

The inclination of the stress path at point 6 is -8.93 (decreasing normal stress and increasing shear stress). The shear direction parameter q is equal to +1.

The interface stiffness at point 6 is calculated following an identical procedure as for points 1 and 5. The calculations are as follows:

$$K_{st} = 20700 \cdot 9.8 \frac{kN}{m^3} \cdot \left(\frac{253}{101.3} \right)^{0.79} \cdot [1 - (+1) \cdot 0.79 \cdot 0.81]^2 = 54210 \frac{kPa}{m}$$

$$I = \frac{1}{1 + 0.81 \cdot \{0.79 [(+1) \cdot 0.79 \cdot 0.81 - 1] - (+1) \cdot 0.79 \cdot 0.81\} \tan(33.7^\circ) \cdot (-8.93)} = 0.183$$

$$K'_{st} = 54210 \frac{kPa}{m} \cdot 0.183 = 9920 \frac{kPa}{m}$$

It can be seen that the inclination of the stress path may have a substantial effect on the value of the interface stiffness, as evidenced by the low value of the correction factor I at point 6.

Appendix F

Notation

a	Reciprocal of the initial shear stiffness of the interface K_{si} under initial loading; reciprocal of the initial tangent modulus K_t of the soil
a_r	Reciprocal of the initial shear stiffness K_{sr} upon shear reversal
b	Reciprocal of the asymptotic shear stress τ_{ult} of the interface; reciprocal of the asymptotic deviator stress $(\sigma_1 - \sigma_3)$ of the soil
b_r	Reciprocal of the relative-asymptotic shear stress τ_{ur} upon shear reversal
B	Bulk modulus of the soil
c'	Cohesion intercept in terms of effective stresses
C_c	Coefficient of curvature
C_k	Correction factor for a rock-founded gravity retaining wall with an inclined backfill surface; interface stiffness ratio
C_N	Correction factor for the number of steps in the backside of a rock-founded gravity wall
C_u	Uniformity coefficient
C_{wt}	Correction factor for determination of the vertical shear force coefficient during submergence of the backfill
C_θ	Correction factor for inclination of the backside of a rock-founded gravity wall
$d\tau$	Infinitesimal shear stress increment along inclined stress path
D_r	Relative density

D_1	Thickness of the backfill above the hydrostatic water table
D_2	Thickness of the submerged backfill above the heel of the wall
D_{10}	Particle size diameter corresponding to 10 percent passing in the gradation curve
D_{30}	Particle size diameter corresponding to 30 percent passing in the gradation curve
D_{60}	Particle size diameter corresponding to 60 percent passing in the gradation curve
E_i	Initial tangent (or Young's) modulus
E_t	Tangent modulus of the soil
E_{ur}	Young's modulus for unloading-reloading
F'_h	Equal to F'_x
F_v	Vertical force or downdrag per unit length of wall
$F_{v,q}$	Vertical earth force due to a sloping backfill surface and/or an applied surcharge pressure
$F_{v,soil}$	Vertical earth force due to the self-weight of the backfill soil
F_w	Hydrostatic force on the wall
F_x	Total horizontal force
F'_x	Effective horizontal force per unit length of wall
G_s	Specific gravity
h	Height of the horizontal earth force above the base of the wall
H	Height measured along a vertical plane passing through the heel of the wall and extending through the backfill
H_b	Total backfill height as measured in Figure 2-5
i	Inclined stress path
I	Correction factor for the inclination of the stress path
k_n	Normal interface stiffness
k_s	Interface shear stiffness

K	Modulus number; stiffness number
$[K]$	Global stiffness matrix
K_b	Bulk modulus number
$K_f\text{-line}$	Line joining the failure points in the p' - q plane
K_h	Earth pressure coefficient for effective horizontal forces
K_i	Stiffness number for yield-inducing shear
K_I	Dimensionless interface stiffness number for initial loading
K_{Ir}	Dimensionless interface stiffness number for shear reversals
K_{Irl}	Dimensionless interface stiffness number for reloading
K_{Ist}	Dimensionless interface stiffness number for staged shear
K_{Iul}	Dimensionless interface stiffness number for unloading
K_n	Interface normal stiffness
K_o	At-rest pressure coefficient
K_{si}	Dimensionless interface initial shear stiffness of the interface
K_{sn}	Normalized stiffness of the matrix
K_{sn}^{ts}	Transition stiffness number
K_{sn}^{ys}	Yield stiffness number
K_{sno}	Normalized stiffness at zero stress level
K_{sr}	Initial shear stiffness for shear for initial loading of the interface reversals
K'_{ssec}	Secant interface stiffness
K_{st}	Interface tangent stiffness
K'_{st}	Tangent interface shear stiffness
K_{ur}	Unload-reload modulus number
K_{urj}	Interface stiffness number for unload-reload
K_v	Earth pressure coefficient for vertical forces

$K_{v,q}$	Vertical shear force coefficient for sloping backfill and surcharge
$K_{v,q,ref}$	Reference value of $K_{v,q}$ obtained for a value of $S = 0$
$K_{v,soil}$	Vertical shear force coefficient for self-weight of the backfill
$K_{v,soil,ref}$	Reference value of $K_{v,soil}$ obtained for an inclination of the back of the wall θ of 90 deg
m	Bulk modulus exponent
m_k	Stiffness degradation parameter
n	Dimensionless interface stiffness exponent for initial loading; modulus exponent
n_i	Dimensionless stiffness exponent
n_r	Dimensionless interface stiffness exponent for shear reversals
n_{rl}	Dimensionless interface stiffness exponent for reloading
n_{st}	Dimensionless interface stiffness exponent for staged shear
n_{ul}	Dimensionless interface stiffness exponent for unloading
N	Number of steps in the back of a stepped wall
p'	$(\sigma'_1 + \sigma'_3)/2$
p_a	Atmospheric pressure
q	$(\sigma_1 - \sigma_3)/2$
q	Shear direction parameter
q_s	Applied surcharge pressure
r	Subscript denoting shear reversal
R_f	Failure ratio for initial loading
R_{ff}	Failure ratio
R_{fr}	Failure ratio for shear reversals
R_{frl}	Failure ratio for reloading
R_{fst}	Failure ratio for staged shear
R_{ful}	Failure ratio for unloading

st	Subscript denoting staged shear of the interface
S	Horizontal distance from the vertical plane through the wall heel to the top of the backfill slope
SL	Stress level
SL_o	Stress level at the origin of unloading-reloading
SL_r	Relative stress level
SL_{ur}	Stress level at the unload or reload points
SL^{ts}	Transition stress level
SL^{ys}	Stress level for current position of yield surface
ur	Subscript denoting that a parameter has the same values for both unloading and reloading of the interface
α	Dimensionless scaling factor for unloading-reloading
α_{rl}	Dimensionless scaling factor for reloading
α_{ul}	Dimensionless scaling factor for unloading
β_{ub}, β_{rl}	Nondimensional coefficients for unloading and reloading, respectively
γ	Unit weight of the soil
γ_b	Buoyant unit weight of submerged backfill
$\gamma_{max}, \gamma_{min}$	Maximum and minimum density, respectively
γ_{moist}	Moist unit weight of the backfill above the water table
γ_{sat}	Saturated unit weight
γ_w	Unit weight of water
δ	Peak interface friction angle
δ_r	Residual interface friction angle
Δ_{actual}	Actual sliding displacement between soil particles and concrete
Δ_{dis}	Deformation of the sand mass due to distortion under applied shear stresses

Δ_{meas}	Displacement measured between the soil box and concrete specimen
Δ_n	Displacement normal to the interface
Δ_o	Interface displacement at the unload or reload point
$\Delta_{r,l}, \tau_{r,l}$	Coordinates in the shear stress-displacement plane at the shear reversal point <i>RI</i>
Δ_{rl}	Interface displacement at the reload point <i>RL</i>
Δ_s	Displacement along the interface; interface shear displacement
$\Delta_s^{i-1}, \Delta_s^i$	Consecutive interface displacement readings
Δ_{so}	Interface displacement at the origin of unloading or reloading
Δ_{sp}	Displacement to peak
Δ_{sr}	Displacement to residual
Δ_{ul}	Interface displacement at the unload point <i>UL</i>
Δ_v	Vertical displacement during interface testing
ΔP	Vector of nodal forces
Δu	Vector of unknown incremental displacements
$\Delta\gamma_{xy}$	Shear strain increment
$\Delta\epsilon_x, \Delta\epsilon_y$	Horizontal and vertical strain increments, respectively
$\Delta\sigma_n$	Normal stress increment
$\Delta\sigma_x, \Delta\sigma_y$	Horizontal and vertical stress increments, respectively
$\Delta\tau$	Shear stress increment
$\Delta\tau_{xy}$	Shear stress increment
$\Delta\tau^i$	Shear stress increment between points <i>P</i> and <i>Q</i>
$\Delta\tau^v, \Delta\tau^o$	Components of the shear stress increment in the orthogonal directions <i>v'</i> and <i>o'</i> , respectively
$\Delta\phi$	Reduction in the peak friction angle value for a tenfold increase in σ'_3

$\Delta\Delta_s$	Increment of interface displacement
ε	Axial strain
ε_v	Volumetric strain
θ	Angle between the stress path direction and τ -axis
ν	Vertical stress path; Poisson's ratio
ν_{nom}	Nominal Poisson's ratio
σ_h	Horizontal pressure
σ_n	Normal stress acting on the interface
σ_n^{ts}	Normal stress corresponding to point <i>TS</i>
σ_{no}	Normal stress at the origin
σ_v	Vertical stress
σ_v'	Effective vertical stress
σ_1	Major principal stress
σ_1'	Major principal effective stress
σ_3	Minor principal stress
σ_3'	Effective confining stress; minor effective principal stress
$(\sigma_1 - \sigma_3)$	Deviator stress
$(\sigma_1 - \sigma_3)_f$	Deviator stress at failure
$(\sigma_1 - \sigma_3)_{ult}$	Asymptotic strength in triaxial testing
τ	Interface shear stress
τ_f	Interface shear strength for initial loading
τ_{fr}	Interface relative shear strength for shear reversals
τ_o	Interface shear stress at the origin of unloading or reloading
τ_{rl}	Interface shear stress at the reload point <i>RL</i>
τ_{ur}	Relative-asymptotic interface shear stress for shear reversals

τ_{ul}	Interface shear stress at the unload point <i>UL</i>
τ_{ult}	Asymptotic interface shear stress value for initial loading
τ^i, τ^{i-1}	Consecutive shear stress readings
τ^s	Shear stress at point <i>TS</i>
ϕ	Secant friction angle
ϕ'	Internal friction angle of the soil
ϕ_{cv}	Friction angle at a strain of 15 percent
ϕ_o	Peak secant friction at a confining pressure of 101.4 kPa (1 atm)

WATERWAYS EXPERIMENT STATION REPORTS PUBLISHED UNDER THE COMPUTER-AIDED STRUCTURAL ENGINEERING (CASE) PROJECT

	Title	Date
Technical Report K-78-1	List of Computer Programs for Computer-Aided Structural Engineering	Feb 1978
Instruction Report O-79-2	User's Guide: Computer Program with Interactive Graphics for Analysis of Plane Frame Structures (CFRAME)	Mar 1979
Technical Report K-80-1	Survey of Bridge-Oriented Design Software	Jan 1980
Technical Report K-80-2	Evaluation of Computer Programs for the Design/Analysis of Highway and Railway Bridges	Jan 1980
Instruction Report K-80-1	User's Guide: Computer Program for Design/Review of Curvilinear Conduits/Culverts (CURCON)	Feb 1980
Instruction Report K-80-3	A Three-Dimensional Finite Element Data Edit Program	Mar 1980
Instruction Report K-80-4	A Three-Dimensional Stability Analysis/Design Program (3DSAD) Report 1: General Geometry Module Report 3: General Analysis Module (CGAM) Report 4: Special-Purpose Modules for Dams (CDAMS)	Jun 1980 Jun 1982 Aug 1983
Instruction Report K-80-6	Basic User's Guide: Computer Program for Design and Analysis of Inverted-T Retaining Walls and Floodwalls (TWDA)	Dec 1980
Instruction Report K-80-7	User's Reference Manual: Computer Program for Design and Analysis of Inverted-T Retaining Walls and Floodwalls (TWDA)	Dec 1980
Technical Report K-80-4	Documentation of Finite Element Analyses Report 1: Longview Outlet Works Conduit Report 2: Anchored Wall Monolith, Bay Springs Lock	Dec 1980 Dec 1980
Technical Report K-80-5	Basic Pile Group Behavior	Dec 1980
Instruction Report K-81-2	User's Guide: Computer Program for Design and Analysis of Sheet Pile Walls by Classical Methods (CSHTWAL) Report 1: Computational Processes Report 2: Interactive Graphics Options	Feb 1981 Mar 1981
Instruction Report K-81-3	Validation Report: Computer Program for Design and Analysis of Inverted-T Retaining Walls and Floodwalls (TWDA)	Feb 1981
Instruction Report K-81-4	User's Guide: Computer Program for Design and Analysis of Cast-in-Place Tunnel Linings (NEWTUN)	Mar 1981
Instruction Report K-81-6	User's Guide: Computer Program for Optimum Nonlinear Dynamic Design of Reinforced Concrete Slabs Under Blast Loading (CBARCS)	Mar 1981
Instruction Report K-81-7	User's Guide: Computer Program for Design or Investigation of Orthogonal Culverts (CORTCUL)	Mar 1981
Instruction Report K-81-9	User's Guide: Computer Program for Three-Dimensional Analysis of Building Systems (CTABS80)	Aug 1981
Technical Report K-81-2	Theoretical Basis for CTABS80: A Computer Program for Three-Dimensional Analysis of Building Systems	Sep 1981
Instruction Report K-82-6	User's Guide: Computer Program for Analysis of Beam-Column Structures with Nonlinear Supports (CBEAMC)	Jun 1982

(Continued)

WATERWAYS EXPERIMENT STATION REPORTS PUBLISHED UNDER THE COMPUTER-AIDED STRUCTURAL ENGINEERING (CASE) PROJECT

(Continued)

	Title	Date
Instruction Report K-82-7	User's Guide: Computer Program for Bearing Capacity Analysis of Shallow Foundations (CBEAR)	Jun 1982
Instruction Report K-83-1	User's Guide: Computer Program with Interactive Graphics for Analysis of Plane Frame Structures (CFRAME)	Jan 1983
Instruction Report K-83-2	User's Guide: Computer Program for Generation of Engineering Geometry (SKETCH)	Jun 1983
Instruction Report K-83-5	User's Guide: Computer Program to Calculate Shear, Moment, and Thrust (CSMT) from Stress Results of a Two-Dimensional Finite Element Analysis	Jul 1983
Technical Report K-83-1	Basic Pile Group Behavior	Sep 1983
Technical Report K-83-3	Reference Manual: Computer Graphics Program for Generation of Engineering Geometry (SKETCH)	Sep 1983
Technical Report K-83-4	Case Study of Six Major General-Purpose Finite Element Programs	Oct 1983
Instruction Report K-84-2	User's Guide: Computer Program for Optimum Dynamic Design of Nonlinear Metal Plates Under Blast Loading (CSDOOR)	Jan 1984
Instruction Report K-84-7	User's Guide: Computer Program for Determining Induced Stresses and Consolidation Settlements (CSETT)	Aug 1984
Instruction Report K-84-8	Seepage Analysis of Confined Flow Problems by the Method of Fragments (CFRAG)	Sep 1984
Instruction Report K-84-11	User's Guide for Computer Program CGFAG, Concrete General Flexure Analysis with Graphics	Sep 1984
Technical Report K-84-3	Computer-Aided Drafting and Design for Corps Structural Engineers	Oct 1984
Technical Report ATC-86-5	Decision Logic Table Formulation of ACI 318-77, Building Code Requirements for Reinforced Concrete for Automated Constraint Processing, Volumes I and II	Jun 1986
Technical Report ITL-87-2	A Case Committee Study of Finite Element Analysis of Concrete Flat Slabs	Jan 1987
Instruction Report ITL-87-1	User's Guide: Computer Program for Two-Dimensional Analysis of U-Frame Structures (CUFRAM)	Apr 1987
Instruction Report ITL-87-2	User's Guide: For Concrete Strength Investigation and Design (CASTR) in Accordance with ACI 318-83	May 1987
Technical Report ITL-87-6	Finite-Element Method Package for Solving Steady-State Seepage Problems	May 1987
Instruction Report ITL-87-3	User's Guide: A Three-Dimensional Stability Analysis/Design Program (3DSAD) Module	Jun 1987
	Report 1: Revision 1: General Geometry	Jun 1987
	Report 2: General Loads Module	Sep 1989
	Report 6: Free-Body Module	Sep 1989

(Continued)

WATERWAYS EXPERIMENT STATION REPORTS PUBLISHED UNDER THE COMPUTER-AIDED STRUCTURAL ENGINEERING (CASE) PROJECT

(Continued)

	Title	Date
Instruction Report ITL-87-4	User's Guide: 2-D Frame Analysis Link Program (LINK2D)	Jun 1987
Technical Report ITL-87-4	Finite Element Studies of a Horizontally Framed Miter Gate Report 1: Initial and Refined Finite Element Models (Phases A, B, and C), Volumes I and II Report 2: Simplified Frame Model (Phase D) Report 3: Alternate Configuration Miter Gate Finite Element Studies—Open Section Report 4: Alternate Configuration Miter Gate Finite Element Studies—Closed Sections Report 5: Alternate Configuration Miter Gate Finite Element Studies—Additional Closed Sections Report 6: Elastic Buckling of Girders in Horizontally Framed Miter Gates Report 7: Application and Summary	Aug 1987
Instruction Report GL-87-1	User's Guide: UTEXAS2 Slope-Stability Package; Volume I, User's Manual	Aug 1987
Instruction Report ITL-87-5	Sliding Stability of Concrete Structures (CSLIDE)	Oct 1987
Instruction Report ITL-87-6	Criteria Specifications for and Validation of a Computer Program for the Design or Investigation of Horizontally Framed Miter Gates (CMITER)	Dec 1987
Technical Report ITL-87-8	Procedure for Static Analysis of Gravity Dams Using the Finite Element Method – Phase 1a	Jan 1988
Instruction Report ITL-88-1	User's Guide: Computer Program for Analysis of Planar Grid Structures (CGRID)	Feb 1988
Technical Report ITL-88-1	Development of Design Formulas for Ribbed Mat Foundations on Expansive Soils	Apr 1988
Technical Report ITL-88-2	User's Guide: Pile Group Graphics Display (CPGG) Post-processor to CPGA Program	Apr 1988
Instruction Report ITL-88-2	User's Guide for Design and Investigation of Horizontally Framed Miter Gates (CMITER)	Jun 1988
Instruction Report ITL-88-4	User's Guide for Revised Computer Program to Calculate Shear, Moment, and Thrust (CSMT)	Sep 1988
Instruction Report GL-87-1	User's Guide: UTEXAS2 Slope-Stability Package; Volume II, Theory	Feb 1989
Technical Report ITL-89-3	User's Guide: Pile Group Analysis (CPGA) Computer Group	Jul 1989
Technical Report ITL-89-4	CBASIN—Structural Design of Saint Anthony Falls Stilling Basins According to Corps of Engineers Criteria for Hydraulic Structures; Computer Program X0098	Aug 1989

(Continued)

WATERWAYS EXPERIMENT STATION REPORTS **PUBLISHED UNDER THE COMPUTER-AIDED** **STRUCTURAL ENGINEERING (CASE) PROJECT**

(Continued)

	Title	Date
Technical Report ITL-89-5	CCHAN—Structural Design of Rectangular Channels According to Corps of Engineers Criteria for Hydraulic Structures; Computer Program X0097	Aug 1989
Technical Report ITL-89-6	The Response-Spectrum Dynamic Analysis of Gravity Dams Using the Finite Element Method; Phase II	Aug 1989
Contract Report ITL-89-1	State of the Art on Expert Systems Applications in Design, Construction, and Maintenance of Structures	Sep 1989
Instruction Report ITL-90-1	User's Guide: Computer Program for Design and Analysis of Sheet Pile Walls by Classical Methods (CWALSHT)	Feb 1990
Technical Report ITL-90-3	Investigation and Design of U-Frame Structures Using Program CUFRBC Volume A: Program Criteria and Documentation Volume B: User's Guide for Basins Volume C: User's Guide for Channels	May 1990
Instruction Report ITL-90-6	User's Guide: Computer Program for Two-Dimensional Analysis of U-Frame or W-Frame Structures (CWFRAM)	Sep 1990
Instruction Report ITL-90-2	User's Guide: Pile Group—Concrete Pile Analysis Program (CPGC) Preprocessor to CPGA Program	Jun 1990
Technical Report ITL-91-3	Application of Finite Element, Grid Generation, and Scientific Visualization Techniques to 2-D and 3-D Seepage and Groundwater Modeling	Sep 1990
Instruction Report ITL-91-1	User's Guide: Computer Program for Design and Analysis of Sheet-Pile Walls by Classical Methods (CWALSHT) Including Rowe's Moment Reduction	Oct 1991
Instruction Report ITL-87-2 (Revised)	User's Guide for Concrete Strength Investigation and Design (CASTR) in Accordance with ACI 318-89	Mar 1992
Technical Report ITL-92-2	Finite Element Modeling of Welded Thick Plates for Bonneville Navigation Lock	May 1992
Technical Report ITL-92-4	Introduction to the Computation of Response Spectrum for Earthquake Loading	Jun 1992
Instruction Report ITL-92-3	Concept Design Example, Computer-Aided Structural Modeling (CASM) Report 1: Scheme A Report 2: Scheme B Report 3: Scheme C	Jun 1992 Jun 1992 Jun 1992
Instruction Report ITL-92-4	User's Guide: Computer-Aided Structural Modeling (CASM) -Version 3.00	Apr 1992
Instruction Report ITL-92-5	Tutorial Guide: Computer-Aided Structural Modeling (CASM) -Version 3.00	Apr 1992

(Continued)

WATERWAYS EXPERIMENT STATION REPORTS PUBLISHED UNDER THE COMPUTER-AIDED STRUCTURAL ENGINEERING (CASE) PROJECT

(Continued)

	Title	Date
Contract Report ITL-92-1	Optimization of Steel Pile Foundations Using Optimality Criteria	Jun 1992
Technical Report ITL-92-7	Refined Stress Analysis of Melvin Price Locks and Dam	Sep 1992
Contract Report ITL-92-2	Knowledge-Based Expert System for Selection and Design of Retaining Structures	Sep 1992
Contract Report ITL-92-3	Evaluation of Thermal and Incremental Construction Effects for Monoliths AL-3 and AL-5 of the Melvin Price Locks and Dam	Sep 1992
Instruction Report GL-87-1	User's Guide: UTEXAS3 Slope-Stability Package; Volume IV, User's Manual	Nov 1992
Technical Report ITL-92-11	The Seismic Design of Waterfront Retaining Structures	Nov 1992
Technical Report ITL-92-12	Computer-Aided, Field-Verified Structural Evaluation	
	Report 1: Development of Computer Modeling Techniques for Miter Lock Gates	Nov 1992
	Report 2: Field Test and Analysis Correlation at John Hollis Bankhead Lock and Dam	Dec 1992
	Report 3: Field Test and Analysis Correlation of a Vertically Framed Miter Gate at Emsworth Lock and Dam	Dec 1993
Instruction Report GL-87-1	User's Guide: UTEXAS3 Slope-Stability Package; Volume III, Example Problems	Dec 1992
Technical Report ITL-93-1	Theoretical Manual for Analysis of Arch Dams	Jul 1993
Technical Report ITL-93-2	Steel Structures for Civil Works, General Considerations for Design and Rehabilitation	Aug 1993
Technical Report ITL-93-3	Soil-Structure Interaction Study of Red River Lock and Dam No. 1 Subjected to Sediment Loading	Sep 1993
Instruction Report ITL-93-3	User's Manual—ADAP, Graphics-Based Dam Analysis Program	Aug 1993
Instruction Report ITL-93-4	Load and Resistance Factor Design for Steel Miter Gates	Oct 1993
Technical Report ITL-94-2	User's Guide for the Incremental Construction, Soil-Structure Interaction Program SOILSTRUCT with Far-Field Boundary Elements	Mar 1994
Instruction Report ITL-94-1	Tutorial Guide: Computer-Aided Structural Modeling (CASM); Version 5.00	Apr 1994
Instruction Report ITL-94-2	User's Guide: Computer-Aided Structural Modeling (CASM); Version 5.00	Apr 1994
Technical Report ITL-94-4	Dynamics of Intake Towers and Other MDOF Structures Under Earthquake Loads: A Computer-Aided Approach	Jul 1994
Technical Report ITL-94-5	Procedure for Static Analysis of Gravity Dams Including Foundation Effects Using the Finite Element Method – Phase 1B	Jul 1994

(Continued)

WATERWAYS EXPERIMENT STATION REPORTS PUBLISHED UNDER THE COMPUTER-AIDED STRUCTURAL ENGINEERING (CASE) PROJECT

(Continued)

	Title	Date
Instruction Report ITL-94-5	User's Guide: Computer Program for Winkler Soil-Structure Interaction Analysis of Sheet-Pile Walls (CWALSSI)	Nov 1994
Instruction Report ITL-94-6	User's Guide: Computer Program for Analysis of Beam-Column Structures with Nonlinear Supports (CBEAMC)	Nov 1994
Instruction Report ITL-94-7	User's Guide to CTWALL – A Microcomputer Program for the Analysis of Retaining and Flood Walls	Dec 1994
Contract Report ITL-95-1	Comparison of Barge Impact Experimental and Finite Element Results for the Lower Miter Gate of Lock and Dam 26	Jun 1995
Technical Report ITL-95-5	Soil-Structure Interaction Parameters for Structured/Cemented Silts	Aug 1995
Instruction Report ITL-95-1	User's Guide: Computer Program for the Design and Investigation of Horizontally Framed Miter Gates Using the Load and Resistance Factor Criteria (CMITER-LRFD)	Aug 1995
Technical Report ITL-95-8	Constitutive Modeling of Concrete for Massive Concrete Structures, A Simplified Overview	Sep 1995
Instruction Report ITL-96-1	User's Guide: Computer Program for Two-Dimensional Dynamic Analysis of U-Frame or W-Frame Structures (CDWFRM)	Jun 1996
Instruction Report ITL-96-2	Computer-Aided Structural Modeling (CASM), Version 6.00 Report 1: Tutorial Guide Report 2: User's Guide Report 3: Scheme A Report 4: Scheme B Report 5: Scheme C	Jun 1996
Technical Report ITL-96-8	Hyperbolic Stress-Strain Parameters for Structured/Cemented Silts	Aug 1996
Instruction Report ITL-96-3	User's Guide: Computer Program for the Design and Investigation of Horizontally Framed Miter Gates Using the Load and Resistance Factor Criteria (CMITERW-LRFD) Windows Version	Sep 1996
Instruction Report ITL-97-1	User's Guide: Computer Aided Inspection Forms for Hydraulic Steel Structures (CAIF-HSS), Windows Version	Sep 1997
Instruction Report ITL-97-2	User's Guide: Arch Dam Stress Analysis System (ADSAS)	Aug 1997
Instruction Report ITL-98-1	User's Guide for the Three-Dimensional Stability Analysis/Design (3DSAD) Program	Sep 1998
Technical Report ITL-98-4	Investigation of At-Rest Soil Pressures due to Irregular Sloping Soil Surfaces and CSOILP User's Guide	Sep 1998
Technical Report ITL-98-5	The Shear Ring Method and the Program Ring Wall	Sep 1998
Technical Report ITL-98-6	Reliability and Stability Assessment of Concrete Gravity Structures (RCSLIDE): Theoretical Manual	Dec 1998

(Continued)

**WATERWAYS EXPERIMENT STATION REPORTS
PUBLISHED UNDER THE COMPUTER-AIDED
STRUCTURAL ENGINEERING (CASE) PROJECT**

(Concluded)

	Title	Date
Technical Report ITL-99-1	Development of an Improved Numerical Model for Concrete-to-Soil Interfaces in Soil-Structure Interaction Analyses	
	Report 1: Preliminary Study	Jan 1999
	Report 2: Final Study	Aug 2000
Technical Report ITL-99-5	River Replacement Analysis	Dec 1999
ERDC/ITL TR-00-1	Evaluation and Comparison of Stability Analysis and Uplift Criteria for Concrete Gravity Dams by Three Federal Agencies	Jan 2000
ERDC/ITL TR-00-2	Reliability and Stability Assessment of Concrete Gravity Structures (RCSLIDE): User's Guide	Jul 2000

REPORT DOCUMENTATION PAGEForm Approved
OMB No. 0704-0188

Public reporting burden for this collection of information is estimated to average 1 hour per response, including the time for reviewing instructions, searching existing data sources, gathering and maintaining the data needed, and completing and reviewing this collection of information. Send comments regarding this burden estimate or any other aspect of this collection of information, including suggestions for reducing this burden to Department of Defense, Washington Headquarters Services, Directorate for Information Operations and Reports (0704-0188), 1215 Jefferson Davis Highway, Suite 1204, Arlington, VA 22202-4302. Respondents should be aware that notwithstanding any other provision of law, no person shall be subject to any penalty for failing to comply with a collection of information if it does not display a currently valid OMB control number. **PLEASE DO NOT RETURN YOUR FORM TO THE ABOVE ADDRESS.**

1. REPORT DATE (DD-MM-YYYY) August 2000		2. REPORT TYPE Report 2 of a series		3. DATES COVERED (From - To)	
4. TITLE AND SUBTITLE Development of an Improved Numerical Model for Concrete-to-Soil Interfaces in Soil-Structure Interaction Analyses; Report 2, Final Study				5a. CONTRACT NUMBER	
				5b. GRANT NUMBER	
				5c. PROGRAM ELEMENT NUMBER	
6. AUTHOR(S) Jesús E. Gómez, George M. Filz, Robert M. Ebeling				5d. PROJECT NUMBER	
				5e. TASK NUMBER	
				5f. WORK UNIT NUMBER 31589	
7. PERFORMING ORGANIZATION NAME(S) AND ADDRESS(ES) Virginia Polytechnic Institute and State University Blacksburg, VA 24061-0105; U.S. Army Engineer Research and Development Center Information Technology Laboratory 3909 Halls Ferry Road Vicksburg, MS 39180-6199				8. PERFORMING ORGANIZATION REPORT NUMBER Technical Report ITL-99-1	
9. SPONSORING / MONITORING AGENCY NAME(S) AND ADDRESS(ES) U.S. Army Corps of Engineers Washington, DC 20314-1000				10. SPONSOR/MONITOR'S ACRONYM(S)	
				11. SPONSOR/MONITOR'S REPORT NUMBER(S)	
12. DISTRIBUTION / AVAILABILITY STATEMENT Approved for public release, distribution unlimited.					
13. SUPPLEMENTARY NOTES					
14. ABSTRACT Soil-Structure Interaction (SSI) analyses have proven to be powerful tools for use in analyzing, designing, and monitoring geotechnical structures. SSI analyses are particularly useful in problems of complex geometry and loading conditions such as lock walls. Several SSI analyses of Corps of Engineers lock walls have shown that the behavior of the soil-structure interface has a significant influence on the magnitudes of the loads acting against a lock wall. They have also illustrated that the pre- and post-construction field stress paths followed by interface elements often involve simultaneous changes in normal and shear stresses, as well as shear stress reversals. The hyperbolic formulation for interfaces, used commonly in SSI analyses, models interface behavior in the primary loading stage very closely. However, it has not been extended to accurately model simultaneous changes in shear and normal stresses or unloading-reloading of the interface. The purpose of this research was to develop an interface model capable of giving accurate predictions of the interface response under field loading conditions. In order to develop the necessary test data, the Large Displacement Shear Box (LDSB) at Virginia Polytechnic Institute and State University, Blacksburg, VA, was modified to permit soil-to-concrete interface testing. A concrete specimen for interface (Continued)					
15. SUBJECT TERMS Earth retaining structures, Interface constitutive model, Interface testing, Shear reversal, Staged shear, Unloading-reloading					
16. SECURITY CLASSIFICATION OF:			17. LIMITATION OF ABSTRACT	18. NUMBER OF PAGES 401	19a. NAME OF RESPONSIBLE PERSON
a. REPORT UNCLASSIFIED	b. ABSTRACT UNCLASSIFIED	c. THIS PAGE			19b. TELEPHONE NUMBER (include area code)

14. ABSTRACT

testing was prepared with a surface texture similar to that of concrete retaining walls in service. A number of tests were performed on interfaces formed by this concrete specimen and two different types of uniform sand compacted at varying densities: initial loading, staged shear, and unloading-reloading of the interface. The extended hyperbolic model was developed based on the results of these tests. Additional tests consisted of the application of multidirectional stress paths to the interface and served to verify the accuracy of the model formulation.

This research was conducted in two phases. Report 1, Preliminary Study, was completed, which included part of the interface testing results and a preliminary version of the extended hyperbolic model. This report contains the results of all the interface tests performed, including those reported in the Preliminary Study. It also contains the final version of the extended hyperbolic model for interfaces. This model is based on the hyperbolic formulation, which has been extended to model the interface response to a variety of stress paths. The model gives accurate approximations to the interface response to staged shear, unloading-reloading, and simultaneous changes in shear and normal stresses. The model was implemented in the finite element program SOILSTRUCT-ALPHA, used by the Corps of Engineers for analysis of lock walls.

A pilot-scale test was performed in the Instrumented Retaining Wall (IRW) at Virginia Tech that simulated construction and operation of a lock wall. After placement and compaction of the backfill, cycles of surcharge application and inundation of the backfill were applied. Measurements were made of the magnitudes of vertical and horizontal forces acting on the wall during the test. Finite element analyses of the IRW, performed using the updated version of SOILSTRUCT-ALPHA, revealed that the model provides accurate estimates of the vertical forces acting on the wall throughout the test.

It is anticipated that the use of the updated version of SOILSTRUCT-ALPHA, containing the extended hyperbolic model developed during this investigation, will introduce significant benefits for design or evaluation of lock walls and other U.S. Army Corps of Engineers structures.